Design and development of novel self-assembled luminescent lanthanide complexes in solution and in responsive soft materials

Samuel J. Bradberry, MChem

March 2017

Trinity College Dublin
The University of Dublin

Based on research carried out under the direction of
Prof. Thorfinnur Gunnlaugsson

A thesis submitted to the School of Chemistry,
Trinity College Dublin, The University of Dublin, for the degree of
Doctor of Philosophy

“I'm always learning something. Learning never ends.”

-Raymond Carver
1938-1988

Declaration

This thesis is submitted for the degree of Doctor of Philosophy to the University of Dublin, Trinity College and has not been submitted before for any degree or examination to this or any other university. Other than where acknowledged, all work described herein is original and carried out by the author alone. Permission is granted so that the Library may lend or copy this thesis upon request. This permission covers only single copies made for study purposes, subject to normal conditions of acknowledgment.

_____

Samuel J. Bradberry

Abstract

This thesis, entitled "Design and development of novel self-assembled luminescent lanthanide complexes in solution and in responsive soft materials" describes the design, synthesis and characterisation of naphthyl-dipicolylamide (naphthyl-**dpa)** ligands for sensitisation lanthanide (Ln^{III}) emission, particularly for Eu^{III}, in a range of solvent environments as well as soft materials.

Chapter 1 provides an introduction to the fundamental physical and chemical properties of Ln^{III} ions with particular focus on the photophysical properties. The characteristic spectral features of the emissive Ln^{III} ions will be reviewed, an overview given to the mechanisms available to access this *f*-metal-centred luminescence and the key design features for ligands highlighted. This is followed by a review of the available literature, describing recent advances in acyclic ligands for sensitising Ln^{III} emission in solution and the solid-state. The later sections will concentrate on the inclusion of emissive Ln^{III} complexes in soft matter, soft- and polymer-based materials. As a conclusion to the survey of research from the wider scientific community, the immediate prior art from the Gunnlaugsson laboratory will be highlighted.

Chapter 2 will describe the design and synthesis of naphthyl-**dpa** derivatives functionalised with sulfonate (SO_3^-) solubilising groups. A pair of enantiomeric ligands will be presented, the photophysical properties of these ligands and their complexes with Eu^{III} are probed in both aqueous and organic solutions, showing Φ_{tot} enhancements in the aqueous environment. The self-assembly behaviour of the ligands is investigated in H_2O through spectroscopic titrations using a range of techniques including UV-visible absorption, fluorescence and time-gated emission spectroscopy. Chiral spectroscopy (circularly polarised luminescence and circular dichroism) is exploited to analyse the photophysical properties and self-assembly in greater depth and global stability constants (β) determined by non-linear regression analysis, indicating $\log\beta_{\mathbf{ML_3}}$ *ca*. 18.5 – 20.0 for the saturated (**ML_3**) assemblies. This chapter concludes by discussing the self-assembly and aggregation behaviour of the ligands in solution and in the formation of gelled soft matter at higher concentration, using insights from dynamic light scattering (DLS), isothermal titration calorimetry (ITC) and scanning electron microscopy (SEM).

In Chapter 3, the extension of the naphthyl-**dpa** scaffold into responsive luminescent probes will be investigated. A family of chiral ligands is synthesised and their photophysical properties characterised as free ligands and as complexes with Eu^{III} in CH_3CN and CH_3OH

using UV-visible absorption, CD, fluorescence, time-gated luminescence and CPL spectroscopy. The influence of the ligand substitution pattern and peripheral covalent structure is probed, revealing 'spectral fingerprints' and responsive behaviours in ligand- and metal-centred emissions. A fine balance of electronic and structural features are highlighted and photoinduced electron transfer (PET) quenching effect indicated under various experimental conditions. Self-assembly processes are probed in CH_3CN and CH_3OH, showing similar processes between ligands ($\log\beta_{ML3}$ *ca.* 19.0). However, these differ significantly in their emission properties during self-assembly and this is discussed in the context of PET. The PET response is exploited in the development of acidity probes and one complex is calibrated in 5% CH_3OH:H_2O as a pH probe, showing a sensitive pH response in both ligand- and metal-centred emissions. This chapter concludes by describing the fabrication of a hydrogel-based pH sensor using Eu^{III}-centred luminescence, clear spectroscopic and visual responses are demonstrated to both solution and vapour stimuli.

Chapter 4 presents an extension to the responsive complexes described in Chapter 3 and focusses on the design of molecular logic gate mimics (MLGMs) in solution and polymer gels. This example represents one of the first soft materials-based MLGMs using Ln^{III} luminescence. Firstly, a brief introduction will present the fundamentals of logical analysis and the limited examples of exploiting Ln^{III} luminescence. A mixed Eu^{III}:Tb^{III} system combining both naphthyl-**dpa** and 2,6-bis(1,2,3-triazol-4-yl)pyridine (**btp**) ligands will be discussed showing luminescence responses to H^+ and F^-. These responses are characterised in CH_3OH and p(HEMA-*co*-EGMDA-*co*-MMA) organogels and parameterised as logic functions; both clear logical and visual outputs are demonstrated to unambiguously identify input states. This chapter concludes by highlighting the key limitations of this proof-of-concept and approaches to address these are set out.

Chapter 5 details the preliminary studies undertaken towards the covalent grafting of naphthyl-**dpa** binding sites to a bulk polymer chain and introduction of Eu^{III}-based supramolecular crosslinks. Two naphthyl-**dpa** ligands with pendent methacrylamide moieties, and their Eu^{III} complexes, are synthesised, in symmetrical and asymmetrical arrangements. The photophysical properties characterise by standard techniques of UV-visible absorption, fluorescence and time-gated emission. The self-assembly processes are characterised in CH_3CN, showing consistent behaviours to the respective ligand families, and particular attention is made to the luminescence lifetime distributions in a range of other solvents. Copolymers with p(HEMA-*co*-EGMDA) are synthesised and characterised thermally, showing inclusion of the novel monomers. Luminescent hydrogels are

demonstrated and the emission properties characterised to elucidate the nature of the crosslinking complexes, showing preference of **ML_3** and **ML_2** in the symmetrical and asymmetrical cases, respectively. The chapter concludes by presenting the preliminary mechanical analysis, showing inconclusive results, is described along with the limitations; approaches to address, extend and exploit these preliminary results are presented.

Finally, Chapter 6 outlines experimental, analytical and synthetic procedures used for the studies described throughout this thesis, as well as compound characterisation for the ligands and complexes discussed. This is followed by literature references and appendices containing relevant supplemental experimental data to that presented herein.

Acknowledgements

My first thanks must go to Prof. Thorfinnur Gunnlaugsson (Thorri) for many number of reasons from being a fantastic supervisor who has given me freedom, challenge, encouragement, opportunity, and guidance throughout the last four-and-a-bit years. Not only being an important teacher but also being a friend. Thank you for making me feel welcome and at home in the group, and in Ireland, from the very first time I visited. I will be forever grateful for the assistance and understanding offered to me when times were tough both in and out of the lab.

I am grateful for the opportunities to work with others and the warm reception by collaborators, to Prof. Amir Khan (TCD) and Prof. Colin McCoy (QUB) who have been a pleasure to work with, inspring in their individual weays and engaged even at the times when the collaborations were slow. I hope we can continue to work together in the future.

To Prof. A.P de Silva, many thanks for being welcoming to general discussion on my visit to Belfast and the hospitality shown to myself and Anna out of pure interest in science, friendship and concern for others.

Mr. Aramballi Jayant Savyasachi and Ms. Amy Lynes are thanked for their help with DSC and SEM, coming to help at the last minute and at the expense of their own time so many times. There are many people without whom this work could have been completed, who work behind the scenes: to Dr. Robert D. Peacock, for CPL measurements used throughout this thesis for the expedience of turnaround and advice. Drs. Gary Hessman and Martin Feeny for keeping the mass spec running vital to our work. To Dr Manuel Reuther for keeping the instrumentation from falling apart and technical assistance. Dr. John O'Brien, as always, must be singled out for the high-quality NMR, never-ending enthusiasm to help us solve our problems and coming to my rescue, particularly near the end! I thank, from the past, Prof. Phil Gale, Dr. Nathalie Busschaert and Dr. Kate Howell for preparing me for the opportunity to complete a PhD and making me the scientist I am today.

In the present every day, during this short time in Ireland, I have been fortunate to have befriended people from all over the world, of every background and of every personality. You have all taught me something and I am thankful for those opportunities. I have learned patience from the examples of Oxana and Sachi; the power and importance of curiosity from Joe; that I am not the 'best' at panicking from Helen and Fergus; Italian from Anna. From every person in the group past-and-present I can take away something new, thank you for that. To Jenn and Joe, I say thank you one-million times over for being there

to keep me thinking straight and to talk about crazy ideas whether in the same room or hundreds of miles apart.

I extend thanks to those in College who have come to my aid when in trouble, the health and counselling services, Dr. Lawless and Dr. Paris, who helped me out of some scary and difficult times; I had never expected to need to meet you both but I am better for having done so. I thank those who I have met that have made me a life away from the lab. To Hans for the friendship that helped me through the first years here and I hope will continue going forward. To Joao, Australian Sarah, American Sarah, James, Alex, Giangi and Gianna who welcomed me into their homes; to Viola, Fergus and Fergus' Mum for the friendship to help me when I was briefly homeless. I am thankful for, and to, those friends who have been supportive and inspiring in their own ways: Frs. Terence, John, Philip, Alan and the other Dominicans, Aileen, Maria, Pietro, Claudia, and Chiara.

I thank my family for the patience of a workaholic, never-in-contact son living abroad for four years. I thank Mum and Dad for having put up with this, and always being there to help when I was in trouble and needed help; knowing you have been there has been more help that you can imagine. To Rachel and Daniel for being the best sibling-hotels you could imagine, always available when I have been visiting the UK, and I hope you know we don't just come to you for the free bed…it's a bonus to getting to see everyone. I thank Ethan for letting me come play cars and electricity sets when times got tough. I am thankful to the new family which I have been lucky to inherit, to Attilio, Emanuela, Luca and Nonna, who have made me feel welcome in their home many, many times over the last three years; and have trusted me to look after their daughter and sister. Grazie mille!

Last, but by no means least, in fact the most, I thank the new family 'of my own', to Anna for being there for me always, with every stress, every up and every down. I cannot imagine where I would be, how I would be, what I would be, if I would even have finished, if I had not had your support in and out of the lab. Thank you for putting up with my journey while also on your own and I thank you for starting a journey of our own together into the future. I have learned a lot from you already, and I look forward to learning more from and with you as we go into our future!

Abbreviations

-*co*-	copolymer
@	non-covalently incorporated
1D	one dimensional
2D	two dimensional
3D	three dimensional
^{3}T	triplet excited state
Å	angstrom
acac	acetylacetonate
AIBN	azobissisobutyronitrile
AMP	adenosine monophosphate
app	apparent
ar	aromatic
atm.	atmosphere(s)
ATP	adenosine triphosphate
ATR	attenuated total reflection
bbpy	2,6-bis(benzimidazol-2-yl)pyridine
bipy	bipyridine
Boc_2O	di-*tert*-butyl dicarbonate
BODIPY	boron dipyrromethene
br s	broad singlet
btp	2,6-bis(1,2,3-triazol-4-yl)pyridine
BYzBP	bis-1,2,3-triazole-bipyridine
CB[n]	cucurbit[n]uril
CD	circular dichroism
CLSM	confocal laser scanning microscopy
COSY	correlation spectroscopy
CPL	circularly polarised luminescence
CP-NPs	coordination polymer nanoparticles
CuAAC	copper(I)-catalysed alkyne-azide 'click'
cyclen	1,4,5,10-tetraazacyclododecane
d	doublet
D-A	Diels-Alder

DEPT	distortionless enhancement by polarisation transfer
DLS	dynamic light scattering
DMF	*N,N*-dimethylformamide
DMSO	dimethylsulfoxide
DOPC	1,2-Dioleoyl-sn-glycero-3-phosphocholine
DOTA	1,4,5,10-tetraazacyclododecane
dpa	pyridine-2,6-dicarboxamide
DSC	dynamic scattering calorimetry
E	energy
ED	electric dipole
ED	electron donating
EDCI	1-ethyl-3-(3-dimethylaminopropyl)carbodiimide
EDTA	ethylenediamine tetra acetate
EGDMA	ethylene glycol dimethacrylate
equiv.	equivalent(s)
ES	excited state
ESI	electrospray ionisation
Et_2O	diethyl ether
EtOAc	ethyl acetate
EW	electron withdrawing
EWC	equilibrium water content (%)
FLIM	fluorescent lifetime microscopy
fluor	fluorescence
FT-IR	fourier-transform infrared spectroscopy
g_{lum}	luminescence dissymmetry factor
GMP	guanosine monophosphate
GS	ground state
gY	greeny yellow (CIE colour description)
HEMA	(2-hydroxylethyl)methacrylate
hfac	hexafluoroacetylacetone
HMBC	heteronuclear multiple-bond correlation spectrscopy
HOBt	1-hydroxybenzotriazole hydrate
HOMO	highest occupied molecular orbital

HOPO	1-hydroxypyridin-2-one
HPLC	high-performance liquid chromatography
HRMS	high resolution mass specrometry
HSQC	heteronuclear single quantum coherence spectroscopy
IAM	2-hydroxyisophthalamide
IED	"induced" electric dipole
ILCT	intra-ligand charge transfer
INH	INHIBIT
IR	infrared
ISC	inter-system crossing
ITC	isothermal titration calorimetry
J	NMR coupling constant
J	total angular momentum quantum number
K	formation equilibrium constant
K	kelvin
L	total orbital angular momentum quantum number
L	ligand
LA	lactic acid
LB	Langmuir-Blodgett
LbL	layer by layer
LCs	liquid crystals
LIS	lanthanide induced shifts
Ln	lanthanide
LOD	limit of detection
logP	octanol:water partition coefficient
LUMO	lowest unoccupied molecular orbital
M	molar ($mol.dm^{-3}$)
MD	magnetic dipole
MES	2-(*N*-morpholino)ethanesulfonic acid
m_l	orbital angular momentum quantum number
ML	complex with metal-to-ligand ratio of 1:1
ML_2	complex with metal-to-ligand ratio of 1:2
ML_3	complex with metal-to-ligand ratio of 1:3

MLCT	metal-to-ligand charge transfer
MLGM	molecular logic gate mimic
MMA	methyl methacrylate
MR	magnetic resonance
MRI	magnetic resonance imaging
m_s	spin angular momentum quantum number
NAND	inverse AND
NEt_3	triethylamine
NIPAM	*N*-isopropylacrylamide
NMR	nuclear magnetic resonance
NOR	NOT OR
NOTA	1,4,7-triazacyclononane-N,N',N''-triacetate
OLED	organic light emitting diodes
OPV	oligo(phenylenevinylene)
p-	para
p( )	poly( )
PAA	poly(acrylic acid)
PAAm	poly acrylamide
PAMPSA	poly(2-acrylamide-2-methyl propane sulfonic acid)
PDDA	poly(diallyldimethylammonium)
PDI	poly dispersion index
PE	polyethylene
PEG	polyethylene glycol
PET	photo-induced electron transfer
pH	$-\log_{10}[H^+]$
phen	1,10-phenanthroline
phosph	phosphorescence
PLIM	phosphorescent lifetime microscopy
PMT	photo-multiplier tube
pO_2	partial pressure of O_2
PS	polystyrene
PTFE	poly(tetrafluoroethene)
pybox	2,6-Bis[2-oxazolinyl]pyridine

q	number of bound water molecules (to a Ln^{III} on)
q_{Tb}, q_{Eu}	hydration state of Tb^{III}, hydration state of Eu^{III}
RGB	red-green-blue
RT	room temperature
S	total spin angular momentum quantum number
S_0	singlet ground state
S_1	singlet excited state
sal	salicylic acid
SDS	sodium dodecyl sulfate
SEM	scanning electron microscopy
SOMO	singularly occupied molecular orbital
T_1	triplet excited state
TBA	tetrabutyl ammonium
tBu	*tert*-butyl
TFA	trifluoroacetic acid
T_g	transition temperature
THF	tetrahydrofuran
TL	total luminescence
TRD	time resolved detection
TRIS	tris(hydroxymethyl)aminomethane
tta	2-thenoyltrifluoroacetone
UV	ultra-violet
UV-Vis	ultra-violet and visible
v/v	volume/volume
VA	vinyl acetate
VdW	van der waals
WOLED	white organic light emitting diodes
wt%	weight percent
XNOR	exclusive NOT OR
XOR	exclusive OR
y	yellow (CIE colour description)
YG	yellow green (CIE colour description)
α	proportional to

β	global stability constant
β-CD	beta cyclodextrin
δ	chemical shift (NMR)
ΔH	enthalpy
ΔS	change in entropy
ε	molar extinction coefficient
η_{sens}	efficiency of sensitisation of lanthanide luminescence
η_{sens}	sensitisation efficiency (%)
λ	wavelength
λ_{abs}	absorbance wavelength
λ_{em}	emission wavelength
λ_{exc}	excitation wavelength
λ_{max}	absorbance maxima wavelength
ν	frequency (cm^{-1})
τ	luminescence lifetime
τ_1	luminescence lifetime 1
τ_2	luminescence lifetime 2
τ_{em}	emission lifetime
τ_{obs}	observed luminescence lfetime
τ_{OD}	luminescence lifetime in D_2O
τ_{OH}	luminescence lifetime in H_2O
τ_R	radiative lifetime
ϕ	quantum yield (%)
ϕ_{tot}	total quantum yield

Note on publications

Sections of this work have been published in peer-reviewed journals prior to submission of the thesis.

From Chapter 1, Section 1.8, concerning the research of the Gunnlaugsson group, this has been partly described in a review article entitled "Development of responsive visibly and NIR luminescent and supramolecular coordination self-assemblies using lanthanide ion directed synthesis" co-authored with Aramballi Jayant Savyasachi, Miguel Martínez-Calvo and Prof. Thorfinnur Gunnlaugsson in *Coordination Chemistry Review* (*Coord. Chem. Rev* **2014**, 273, 226 – 241).

Chapter 2 was mostly described in the article "Quantifying the formation of chiral luminescent lanthanide assemblies in an aqueous medium through chiroptical spectroscopy and generation of luminescent hydrogels" co-authored with Aramballi Jayant Savyasachi, Dr. Robert. D. Peacock and Prof. Thorfinnur Guannlaugsson in *Faraday Discussions. (Faraday Discuss.* **2015**, 185, 413 – 431)- The same article was presented at the *Faraday Discussions* meeting on "Supramolecular Photochemistry" in Cambridge, UK (2015).

In Chapter 3, reference is made to a publication on pH sensing hydrogels published as the article "Luminescent lanthanide cyclen-based enzymatic assay capable of diagnosing the onset of catheter-associated urinary tract infections both in solution and within polymeric hydrogels" co-authored with Dr. Esther Surender, Dr. Sandra A. Bright, Prof. Colin P. McCoy, Prof. D. Clive Williams and Prof. Thorfinnur Gunnlaugsson in the *Journal of the American Chemical Society* (*J. Am. Chem. Soc*. **2017**, 139, 381 – 388)

Chapter 4 is based upon research published in the communication "Lanthanide luminescent logic gate mimics in soft matter: $[H^+]$ and $[F^-]$ dual-input device in a polymer gel with potential for selective component release" co-authored with Dr. Joseph Byrne, Prof. Colin P. McCoy and Prof. Thorfinnur Gunnlaugsson in *Chemical Communications* (*Chem. Comm.* **2015**, 51, 16565 – 16568).

Table of Contents

1. Introduction

1. Introduction

Photoactive, optical and photonic materials have been the subject of intense scientific interest since materials, both molecular and bulk, coloured or emissive and that respond to physical and chemical stimulus, have become embedded into daily life and fundamental to the modern world.

In recent times, developments in molecular photochemistry and photophysics have progressed from the study and application of discrete molecules and molecular materials to larger structures, and modular assemblies of interest to supramolecular chemistry.[1] For example, there has been increasing interest in the fundamental efficiency of the photosynthetic light harvesting systems, other natural supermolecules and the desire to mimic these principles in a controlled manner to build new optical chemical technologies.[2-5] Such interest has also grown extensively from coordination chemistry, along with the popularity of supramolecular chemistry, and supramolecular approaches are found addressing the behaviour of discrete complexes[6] and coordination polymers.[7-11]

Broadly, supramolecular chemistry involves the development of complex architectures through the directed- or templated-assembly of subcomponents through non-covalent interactions such as from ordered hydrogen bonding arrays,[12,13] electrostatic attraction,[14] various types of π-π interactions[15-17] and metal coordination.[18] An alternative approach is through the use of dynamic covalent bonding.[19] The first examples of supramolecular chemistry were shown by Lehn, Pederson Vögtle and Sauvage in the 1960s with the inception of crown ethers,[20] cryptands[21] and podands.[22] Of significant interest in recent supramolecular chemistry has been the assembly of extended frameworks,[13,23] interlocked,[24] and mechanically-active systems[25,26] as well as host receptors for small guest species (*e.g.* anions,[27] cations,[28,29] neutral organic molecules[30]) in pursuit of selective sensing molecules.

Modern supramolecular chemistry is now widely applied and the term 'supramolecular' has rightly become assimilated into all fields of science where dynamic intermolecular, or more generally inter-species and through-space, interactions are significantly involved.[14] This significance was first recognised in the award of the Nobel Prize in Chemistry in 1987. Since then, supramolecular photochemistry and supramolecular photophysics have contributed much towards modern photonic materials and optical technologies.[31] The complementary and interconnected disciplines of supramolecular photochemistry and photophysics were defined by Balzani[32] and Bassani[33] in 1987 and 2015

as "an appropriate assembly of suitable molecular components capable of performing light-induced functions" and "a field where interactions between light and matter are controlled by intermolecular forces", respectively. This brief encompasses both chemical and physical functions that may be static or dynamic in nature and supramolecular approaches have been taken up by researchers in photocatalysis,[34] energy conversion,[35] sensing and imaging,[36] and notably by 2016 Nobel Laureates Feringa, Sauvage and Stoddart within the "design and synthesis of molecular machines."[37,38] The approaches adopted have been vast and varied invoking traditional organic chromophores,[39] extended conjugates[40] and transition metal ions[6] to produce systems of various emissive and responsive character with equally various control and functionality.

Of the approaches in coordination chemistry those involving lanthanide complexes have converged neatly with supramolecular chemistry to provide a versatile platform for photophysically-rich materials, supermolecules and self-assembled architectures. This lanthanide supramolecular chemistry[41-44] and ligand engineering allows the intrinsically inactive lanthanide ions to be taken advantage of to great effect.[45-48]

The research described in this thesis is centred on the use of emissive lanthanide ions (particularly Eu^{III}) in discrete complexes as well as in supramolecularly-engineered materials. This introduction will first set out the principle which underlie the research, such as the physical properties of the Ln^{III} ions in addition to the mechanisms which allow access to their characteristic emissions. The later sections provide a survey of key and recent literature in the development of acyclic lanthanide-based complexes, supramolecular architectures and soft materials as well as specific attention to the contributions of the Gunnlaugsson Group.

1.1 Lanthanide Metal Cations

The lanthanoids, known alongside Sc and Y as 'rare earth elements', are a group of relatively abundant elements[49] in the first row of the *f*-block (Z = 57 - 71) which start popularly with lanthanum, includes the fourteen succeeding elements and ends with lutetium. As a result of decades of interest and development in coordination chemistry, the 'rare earth' elements find themselves fundamental to many technological fields for their optical and magnetic properties including in telecommunications as amplifier and waveguide materials,[31] pure colour emitters in OLED/WOLED devices,[50] organic complexes for cell imaging[51,52] and biosensing,[53] paramagnetic shift reagents for NMR spectroscopy and MR imaging,[54,55] as well as more niche fields as molecular magnets.[56-58]

1.2 Electronic Structure and Physical Properties of Ln ions

The preferred and most stable oxidation state has been found to be +3 and the entire series tend to exist as the tricationic (Ln^{III}) species. Over various years, the +2 (Ln^{II}) ions have been stabilised in organometallic complexes at low temperature and in Schlenk conditions by Evans and co-workers.[59,60] The lanthanides are a remarkable series in their broadly similar chemical properties showing little systematic diversity in oxidation state, coordination behaviour or reactivity.[45] These notable phenomena arise from the electronic structure of the Ln^{III} ions and presents electronic behaviour entirely different from that familiar from transition metal chemistry.[61]

1.2.1 Lanthanide *s, p, d* and *f* orbital configurations

The trivalent cations of the lanthanoid elements have a common electron configuration of $[Xe]4f^n$ where n = 0, 2 - 11 and, the case of Ce^{3+}, a $[Xe]5d^1$ configuration.[62] The 4*f* orbitals, shown in Figure 1.1a, represent seven possible 4*f* wavefunctions and therefore may accept 14 electrons with spin ± 1/2 and fill naturally following Hund's rule. Therefore, with the notable exceptions of La^{III} and Lu^{III}, which have empty and full 4*f* orbitals respectively, the Ln^{III} ions are characterised by partially filled *f*-orbitals and are paramagnetic.[63] This nature results in variable ground-state degeneracies and magnetic moments throughout the lanthanide series. The early ions (Ce – Eu) have small magnetic moments, while the later ions (Gd – Yb) have large overall moments.[64] Exploiting these properties, Gd^{III} has been employed extensively as MRI contrast agents because of the half-filled 4*f* orbitals giving a total of S = +7/2, a non-degenerate ground-state and strong magnetic moment.[65]

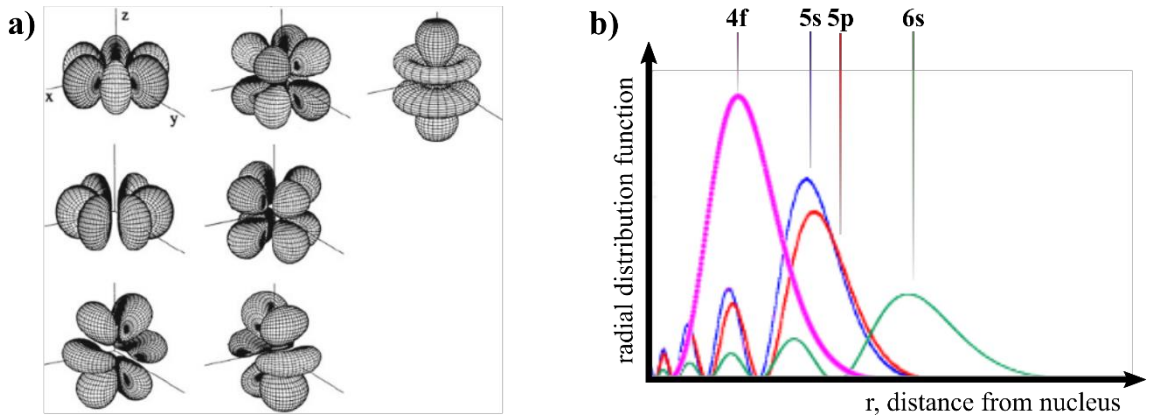

Figure 1.1 a) 3D representations of the shapes of 4*f* orbitals, showing the various lobes and high angular nodality of the orbital set, reproduced from Ref. 62; **b)** Schematic representation of the radial distribution functions for 4*f,* 5*s*, 5*p* and 6*s* orbitals showing the core nature of the 4*f* orbitals and external screening by 5*p*, 5*s*. In Ln^0 the 4*f* orbitals are also shielded from the external environment by *6s* electrons. Each schematic plot for the individual radial distribution functions were obtained from Orbitron™ ©2002 Mark Winter (University of Sheffield).

The 4*f* orbitals are in fact contracted, as shown by the schematic radial distribution function in Figure 1.1b, so that they are situated within the [Xe] core and are closer to the nucleus than the 5*s* and 5*p* orbitals. As a result, there is inefficient 'shielding' of electrons associated with the 4*f* orbitals against the increasing nuclear charge from La^{III} to Lu^{III} and substantial contraction (termed the 'lanthanide contraction') in the ionic radii is observed (from 103 – 86 ppm for La^{III} – Lu^{III}, respectively).[63] Therefore, due to the increasing charge density across the lanthanide series there is some variation in the inorganic chemistry and physical properties of the ions.

It is often noted that the coordination chemistry of the Ln^{III} ions is broadly invariant across the series, particularly in comparison to the diversity found across the transition metals[61] as the 4*f* electrons rarely participate in bonding. This phenomenon is also understood from the core nature of the Ln^{III} valence electrons. These electrons are not only held increasingly close to the nucleus but are also shielded from the external chemical environment by the electrons associated with 5*s* and 5*p* orbitals. As a result those phenomena associated with orbital overlap such as coordination and exchange interactions are weaker[64] compared to those with *d*-orbitals. Therefore, coordination interactions are mostly electrostatic in nature and the role of covalent interaction in first-sphere Ln^{III}-ligand interactions is small.[66] Despite this screening of 4*f* electrons from a ligand environment, it is a misconception that Ln^{III} are devoid of ligand field effects and, while indeed small, the effects of electrostatic ligand-field effects on Ln^{III} ions have been established.[62,64,67]

1.2.2 Electrostatic ligand-field effects and spectroscopic term symbols

As the theoretical free ion, Ln^{III} can be viewed as spherically symmetrical and the electronic structure is subsequently established as shown schematically in Figure 1.2a. Term symbols of LS (or Russell-Saunders) nomenclature are used regularly, and will appear throughout this thesis, to describe Ln^{III}-centred electron configurations.

The valence electronic configuration has been established as $4f^n$ and becomes split into ground- and excited-states by the inter-electron repulsion between those electrons situated within the seven available 4*f* orbitals. These seven 4*f* orbitals have orbital angular momentum quantum numbers (m_l) ± 0,1,2,3 and therefore combine to give the total orbital angular momentum (L). The distribution of spins (m_s, ± ½) within the degenerate orbitals sum to give the total spin quantum number (S) from which the base LS term is constructed in the form ^{2S+1}L. The ground-states of Eu^{III} and Tb^{III} are both ^7F (6 unpaired electrons).[63]

Spin-orbit coupling subsequently generates sub-levels to the ^{2S+1}L configuration. Spin-orbit coupling manifests as a result of the interaction between the magnetic moments

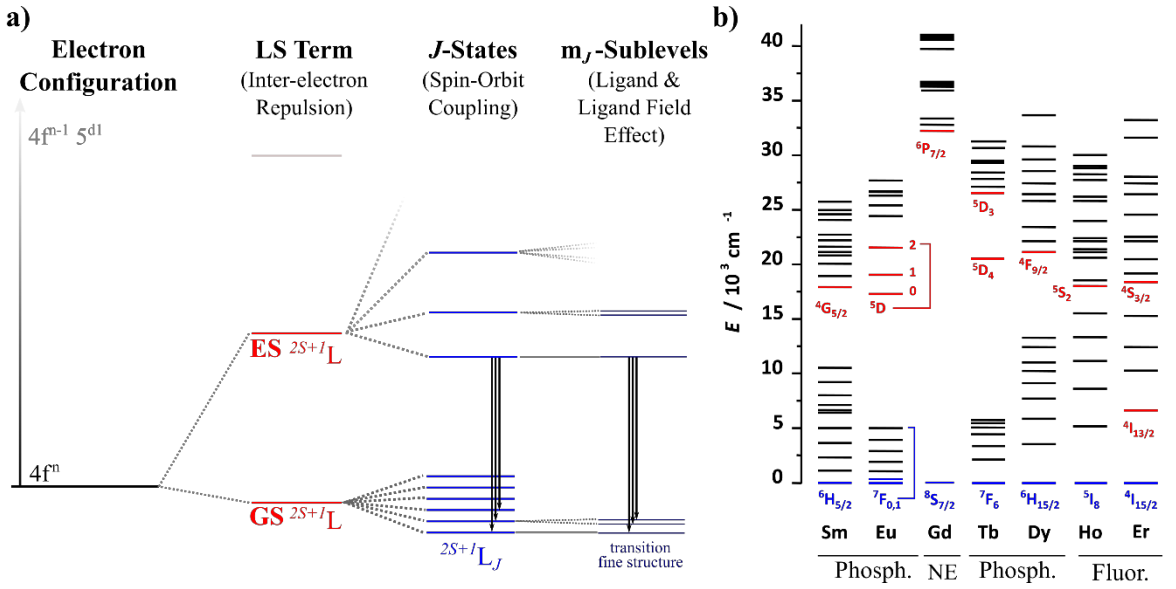

Figure 1.2 a) Schematic representation of the effects on the energy levels arising from $4f^n$ electron configurations by inter-electronic repulsion, spin-orbit coupling and electrostatic ligand-field effects along with the LS-type terms that correspond to each state. Potential emissive transitions are shown as arrows (black). Adapted from Ref. 64. **b)** Partial energy level diagram of $\mathbf{[Ln.(H_2O)_6]^{3+}}$ ions showing the term symbols for key excited (red) and ground (blue) states and the types of emission observed when sensitised by the "antenna effect". Phosphorescence ions ($\Delta S \neq 0$) are Sm^{III}, Eu^{III}, Tb^{III} and Dy^{III}, fluorescent ions ($\Delta S = 0$) are Ho^{III} and Er^{III} while Gd^{III} is not emissive (NE). Adapated from Ref 49.

(μ) associated with the spin and orbital angular momenta (m_s and m_l respectively) for each individual 4*f* electron. This coupling serves to lifts the degeneracy of 4*f* energy levels and each ^{2S+1}L level is split by quantum number *J* to give electron configurations of the form $^{2S+1}L_J$- The possible values for *J* are between L+S and |L-S| and for the ground state, *J* is given by L+S or |L-S| for ions with less than and over half-filled *f*-orbitals, respectively. The ground-state configurations of Eu^{III} and Tb^{III} are therefore given as $^7F_0$ and $^7F_6$, respectively. The determination of the ground-state terms for Ln^{III} are straightforward while the excited-states derivation is a more involved process, however these have been determined[68] extensively as can be seen from the examples shown in Figure 1.2b.[49]

Further sublevels (m_J) are induced by electrostatic ligand-field effects from coordinated organic ligands. The coupling interactions between electrons on ligands and the metal-centre result in small perturbations to the energy levels in $^{2S+1}L_J$ and further non-degeneracy arises. The extent of the splitting and non-degeneracies are also influenced by the symmetry of Ln^{III} ions and the ligand-field parameters vary with point group of the Ln^{III} site[69] and in magnetic fields, Zeeman splitting[64] may also contribute. The extent of microstates is large with $f^{6,8}$ and f^7 electron species providing 119 possible LS-type terms and over 3,000 microstates for each.[62] Overall, the *J* and m_J states are fundamental to the characteristic absorption and emission spectroscopies of the Ln^{III} series.

1.3. *f-f* electronic transitions in Ln^{III} ions

As a result of the energy separation of over 32,000 cm^{-1} between the [Xe]$4f^n$ and the [Xe]$4f^{n-1}5d^1$ electron configurations,[62] transitions from $f \rightarrow d$ occur only at high energy and are rarely observed.[70] Therefore, the main accessible electronic transitions are magnetic dipole (MD) and electric dipole (ED) *f-f* transitions. Unlike the potential $f \rightarrow d$ ED transitions which are u→g transitions and parity allowed, $f \rightarrow f$ ED transitions are u→u and conversely parity forbidden.[71] The *f-f* transitions therefore directly absorb very weakly and their absorption spectra are characterised by narrow bands with $\varepsilon < 4$ $M^{-1}cm^{-1}$.[72] This fundamental selection rule also underpins the emission spectroscopy of Ln^{III} ions and are considered advantageous for a number of applications across many disciplines, as highlighted above.

1.3.1 Magnetic and Induced Electric Dipole Transitions – Selection Rules

The electronic transitions of Ln^{III} ions are governed by certain selection rules for intra-configurational *f-f* transitions based upon the total quantum numbers described in the LS-type coupling scheme above, namely ΔS, ΔL and ΔJ.[45,62,67] Electron transitions fall within two categories: magnetic dipole (MD) and electric dipole (ED) transitions.

Those electronic transitions with MD character are associated with the magnetic component of electromagnetic radiation and, as such, are transitions of even parity and allowed; these transitions obey the selection rules of $\Delta S = 0$, $\Delta L = 0$ and $\Delta J = 0, \pm 1$ (except for $J \rightarrow J'$ being $0 \rightarrow 0$). The intermediate coupling scheme relaxes the selection rules of ΔS and ΔL and transitions of MD character are observed.[73] However, often these have intrinsically low intensity as a result of the nature of the magnetic dipole vector.[74]

ED transitions are forbidden since they are of odd parity and becomes allowed only due to the relaxed selection rules by mixing of other opposite parity states or vibronic coupling to other species. These transitions are much weaker than true ED transitions on account of the Laporte selection rule and therefore the term of "induced" electric dipole transitions is applied.[75] These "induced" ED transitions obey the selection rules of $|\Delta S| = 0$, $|\Delta L| = \leq 6$ and $|\Delta J| = \leq 6$ (or in the case of J or $J' = 0$, $|\Delta J| = 2, 4, 6$). Again, the intermediate coupling scheme relaxes the selection rules. The transition selection rules become relaxed further due to the phenomenon of *J*-mixing allowing both MD and "induced" ED transitions of various types to gain intensity and be observed in absorption and emission spectra.

1.3.2 Hypersensitive *f-f* transitions

Additional to classification of "induced" ED transition, electronic transitions which follow the ED mechanism and obey the selection rules $|\Delta J| \leq 2$, $\Delta L \leq 2$ and $\Delta S = 0$ are known to be "hypersensitive".[76,77] Unlike most "induced" ED transitions, which have intensities not

perturbed greatly by their coordination environment, hypersensitive transitions show intensities sensitive to the local environment of the Ln^{III} ion. Judd called these transitions "pseudo-quadrupole transitions" on account of their equivalent selection rules to pure quadrupole transitions.[78] However, the mechanism to hypersensitivity has yet to be explicitly established amongst various models.[67] Hypersensitive transitions have been observed experimentally in the absorption of Pr^{III}, $Nd^{III,}$ Sm^{III}, Gd^{III}, Dy^{III}, Ho^{III}, Er^{III} and Tm^{III}.[73] While in emission spectra hypersensitivity is observed in Eu^{III} and ligand-induced pseudo-hypersensitivity in Tb^{III} ions.[62] Beyond the physical curiosity, hypersensitivity has been employed to probe structural properties of complexes, site symmetries[69] and Ln^{III}–ligand bond strengths through resolved vibronic coupling to hypersensitive transitions.[79]

1.3.3 Selected spectral features of luminescent Ln^{III} ions

The unique electronic structure of the Ln^{III} ions gives rise to characteristic features to the luminescence spectra. The various energy gaps, Figure 1.2b, between excited- and ground-state configurations results in emission with UV emission for Gd^{III} ($^6P_{7/2} \rightarrow {}^8S_{7/2}$, ΔE = 32,200 cm-$^{1)}$ through visible emissions from Eu^{III} ($^5D_0 \rightarrow {}^7F_0$, ΔE = 12,300 cm^{-1}), Tb^{III} ($^5D_4 \rightarrow {}^7F_6$, ΔE = 14,800 cm^{-1}), Sm^{III} ($^4G_{5/2} \rightarrow {}^6F_{11/2}$, ΔE = 7,400 cm^{-1}) and Dy^{III} ($^4F_{9/2} \rightarrow {}^6F_{3/2}$, ΔE = 7,850 cm^{-1}) to near infrared (NIR) for Nd^{III} ($^4F_{3/2} \rightarrow {}^4I_{9/2}$), Yb^{III} ($^2F_{5/2} \rightarrow {}^3F_{7/2}$) and Er^{III} ($^2F_{5/2} \rightarrow {}^2F_{7/2}$).[45] These spectra are characterised by sharp line-like emission bands (with small linewidths), as a result of the forbidden nature of the transition and, therefore, colour purity is high. Some example spectra[80] of the visibly emissive lanthanides and solutions of emissive complexes[81] are shown in Figure 1.3a and Figure 1.3b, respectively.

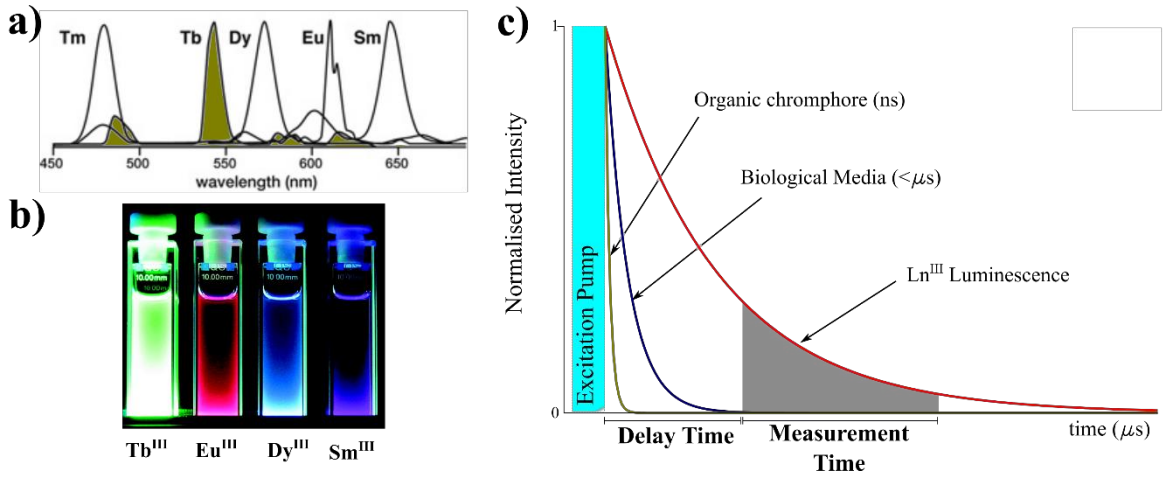

Figure 1.3 Luminescence features of selected emissive Ln^{III} ions; **a)** Luminescence spectra of UV and visible-emitting Ln^{III} ions, Tb^{III}-centred emission spectrum highlighted (green). Adapted from Ref. 80; **b)** Observed emission from Ln^{III}-IAM complexes under λ_{exc} = 365 nm by Raymond *et. al.* Reproduced from Ref. 81; **c)** Schematic representation of time-resolved detection (TRD), the delay time following excitation prior to measurement allows for Ln^{III}-emission detection free from ns and > µs fluorescence emissions.

Eu^{III} and Tb^{III} are the most commonly used ions and give pure red and green emissions, respectively. The line-like emission spectra give the Ln^{III} ions predictable and structured spectra which can reveal differences in solid and solution structure or behaviour from the splitting or relative intensities of the transitions.[67,69,73,82,83] This has been established in Judd-Ofelt theory[84,85] and is particularly well-developed in the case of Eu^{III} where the spectra can possess rich information due to both MD transitions ($^5D_0 \rightarrow {}^7F_{0,1}$) and true "induced" ED hypersensitivity ($^5D_0 \rightarrow {}^7F_2$).[67]

For the same physical reasons, Ln^{III} ions display much longer luminescence lifetimes compared to the nanosecond (ns) lifetimes of organic dyes and biological media. The lifetimes are found in the millisecond (ms) range for Eu^{III} and Tb^{III} and microsecond (μs) range for Sm^{III} and Dy^{III} ions. These long-lived excited-states enable the use of Ln^{III}-centred luminescence in time-resolved detection (TRD) in biological media, where Ln^{III}-emission can be distinguished from background auto-fluorescence by imposing a time-delay after the excitation pump before measurement, as shown schematically in Figure 1.3c. In TRD fluorescence emissions with ns and sub-microsecond lifetimes are able to decay prior to measurement and, therefore, the detected Ln^{III}-centred signal has an improved signal-to-noise ratio. Small complex probes that operate in this fashion have been established for various applications in biological media.[52,86,87]

1.4 Sensitised Ln^{III} Emission - The "Antenna Effect"

Despite the inefficiency of direct excitation of *f-f* electronic transitions, emission from Ln^{III}-centred excited states is observed as sensitised emission. Sensitised emissions are those which arise from radiative deactivation of metal-centred excited states which were initially populated indirectly by an energy transfer mechanism from a donor species rather than direct absorption by the metal centre.[88] This approach was first observed in 1942 by Weissman[89] and later became termed the "antenna effect".[90] Various aspects of this effect are described in the following sections. From various theories, this was refined into the readily accepted mechanism of Crosby and Whan invoking a ligand-centred triplet-excited-state energy transfer mechanism to populate the Ln^{III} excited state.[91] This has now been successively developed, extended and exploited for a range of novel Ln^{III}-based systems in recent years.[62]

1.4.1 Approaches to Antenna Sensitisation – ^3T, ILCT, MLCT

In brief, the general principles and component processes involved in indirect sensitisation, or the "antenna effect" are shown schematically in Figure 1.4a. An emissive Ln^{III} ion (such as Eu^{III}, Tb^{III} *etc.*) is coordinated by a ligand species that contains chromophores which absorb within the UV and visible regions and these ligand units are excited. The ligand-

centred excited states may deactivate *via* various possible processes that do not facilitate Ln^{III}-centred emissions including internal or external non-radiative processes (*e.g.* vibrational relaxation or vibronic coupling to solvent, respectively) or ligand-centred emissions. However, when the chromophores are held in proximity (*i.e.* first coordination sphere) to the Ln^{III} ion deactivation of the ligand-centred excited state can result in populating that of the coordinated ion. It is this energy transfer route which constitutes sensitisation. Antenna sensitisation is tuneable to different situations and the efficiency depends upon the competition of these radiative and non-radiative processes and therefore is influenced by the balance of various factors in ligand design, chromophore moieties, target lanthanide and conditions of use.[47]

Classically, energy transfer occurs from an organic triplet excited-state, this mechanism is elaborated in the Jablonski diagram shown in Figure 1.4b. The direct excitation of the chromophore moieties of the ligands gives an initial singlet excited state (S_1) which does not interact with the Ln^{III} centre. However, due to the heavy atom effect the intersystem crossing (ISC) of $S_1 \rightarrow T_1$ is promoted in most chromophores.[92,93] In brief, 'heavy atoms', such as those of the *f*-block, which hold higher nuclear charge (Z = 57 – 71 for La - Lu) possess proportionally larger nuclear magnetic field strength and consequently a larger spin-orbit coupling is observed. In turn, more substantial singlet-triplet mixing is achieved which produces excited states of mixed multiplicity, allowing a respective increase in the rate of forbidden processes such as ISC in the perturbed molecules. Moreover, in the case of all the Ln^{III} ions (excluding the diamagnetic ions La^{III} and Lu^{III}) their paramagnetic nature, and therefore increased overall angular momentum, may also contribute to the promotion of these effects.[94]

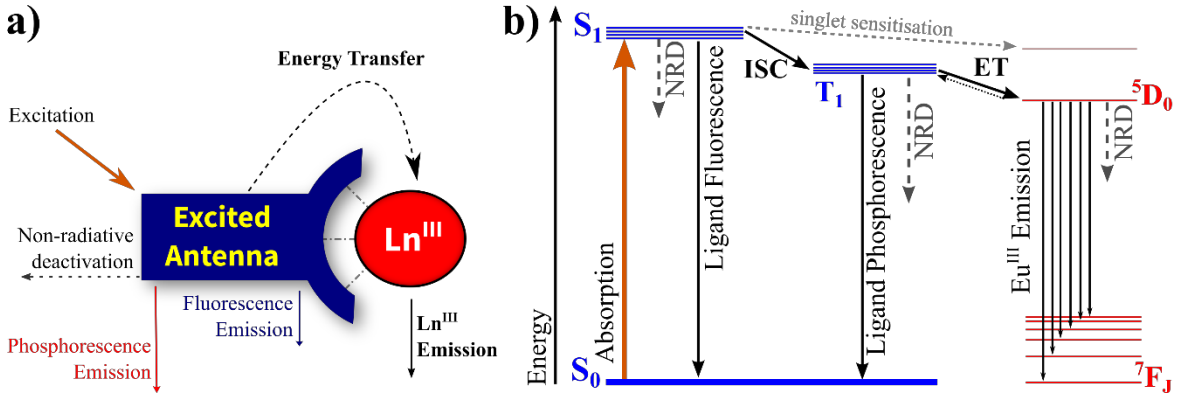

Figure 1.4 a) Schematic representation of the "antenna effect" showing various deactivation pathways of the antenna excited-state; **b)** Summary Jablonski energy level diagram demonstrating the sensitisation of $Eu(^5D_0)$ *via* excitation of the ligand from the ground-state (S_0) to the first excited-state (S_1) subsequent ligand-centred ISC to the triplet excited-state (T_1) and energy transfer (ET) to the lanthanide ion; shown also are the corresponding NRD pathways seen in panel a).

These longer-lived triplet excited-states can effectively relax to their ground-state through an energy transfer process leaving the metal-centre in an excited state (the Ln^{III} becomes excited indirectly). The excited-states of various Ln^{III} ions were presented in Figure 1.2b and, in most cases, upon sensitisation internal non-radiative relaxation will arrive at emissive excited-states (*i.e.* $^5D_{1,2}$ for Eu^{III}, $^5D_4$ for Tb^{III} or $^5I_4$ For Ho^{III}). As discussed above, in all cases, *f*-metal emissive transitions are parity forbidden and furthermore, in many of those cases, also spin-forbidden which results in a smaller overall rate constant. As a result of this, sensitised Ln^{III} emissions can be both intense and have long luminescence lifetimes. Simple and conjugated organic chromophores are often used for this mechanism.[95]

In a number of scenarios, the use of energy transfer from alternative donors such as triplet-based metal-to-ligand charge transfer (^{3}MLCT) excited-states have been utilised.[96,97] Hybrid and dyad complexes have been used which combine *d*- and *f*- block metals coordinated by chromophore-containing ligands.[98,99] Much like the classical triplet mechanism, a singlet excited-state (^{1}MLCT) is achieved by excitation of the MLCT band followed by ^{1}MLCT → ^{3}MLCT intersystem crossing that is achieved efficiently in second- and third-row transition metal complexes.[100] Energy transfer from the ^{3}MLCT then can occur in a similar manner as from a ligand-centred T_1 excited-state.[101,102] For example, amongst others, transition metal complexes of Cr^{III}, Co^{III} and Ru^{II}, **1**, have been used to sensitise the emission from Yb^{III} and Nd^{III} ions.[101,103,104] The ^{3}MLCT sensitisation mechanism, however, highlights the ever-present subtleties in ligand design for individual application and tends to be notably inefficient for the sensitisation of Eu^{III} and Tb^{III}-centred emissions.[105] In fact, even in *d-f* dyads of Cr^{III} paired with Yb^{III} or Nd^{III}, the MLCT was used as a mechanism to quench Eu^{III} luminescence *via* $Eu(^5D_0) \rightarrow Cr(^4A_2)$ energy transfer.[106]

Despite the accepted dismissal of Kleinerman's proposed $S_1 \rightarrow Ln^{III}$ energy transfer mechanism.[107] Importantly, sensitisation of Ln^{III} emission directly from singlet excited-states has recently been reported. However, these occur specifically *via* energy transfer from intra-ligand charge transfer (^{1}ILCT) singlet excited-states.[88] The extension of the classical

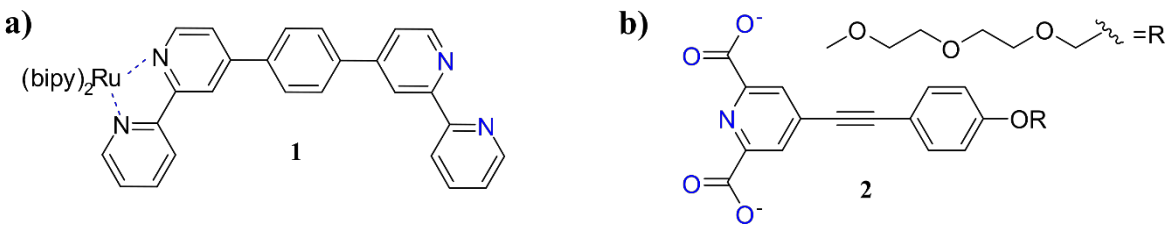

Figure 1.5 Example donor chromophore types suitable for sensitised Ln^{III}-centred emission *via*: **a)** ^{3}MLCT sensitisation. Compound **1** sensitises Yb^{III} and Nd^{III} emission from Ru^{II}-bipy ^{3}MLCT; and **b)** ILCT sensitisation. Compound **2** sensitises Eu^{III}, Yb^{III} and Nd^{III} emission.

use of simple small chromophores to the usage of larger conjugated units for example as CT-ready phenyl-ethynyl derivatives[108], **2**, as well as BODIPY-conjugates or pyridine-tetrathiofulvalene conjugates.[88]

Although ^{3}MLCT and ILCT sensitisation are fundamental to the future developments in luminescence Ln^{III} complexes and materials, the classical organic triplet (T_1) sensitisation remains the most popular approach taken by researchers for Eu^{III} and Tb^{III} emission.

1.4.2 Energy Transfer Mechanisms

The energy transfer from chromophore excited-state to the Ln^{III} ion generally will take place through the classical energy transfer mechanisms that are termed Förster or Dexter-type.[101,109] However, Horrocks[110] and Faulkner[111] have noted that in cases of Eu^{III} and Yb^{III}, a third redox-mediated mechanism is possible since readily accessible Ln^{II} oxidation states are available. The Förster- and Dexter-type mechanisms are quite different in nature and this should not be overlooked since optimisation of energy transfer efficiency often serves to dictate many aspects of antenna and ligand design.

The traditional schematics of these energy transfer mechanisms are perhaps confusing and ambiguous in the context of Ln^{III} sensitisation since the excited-states of the ligand and the Ln^{III} ion should be considered in different terms, as electron promotions within molecular orbitals and atomic orbital configurations, respectively. Therefore, in Figure 1.6, the Förster- and Dexter-type energy transfer mechanisms are represented in terms

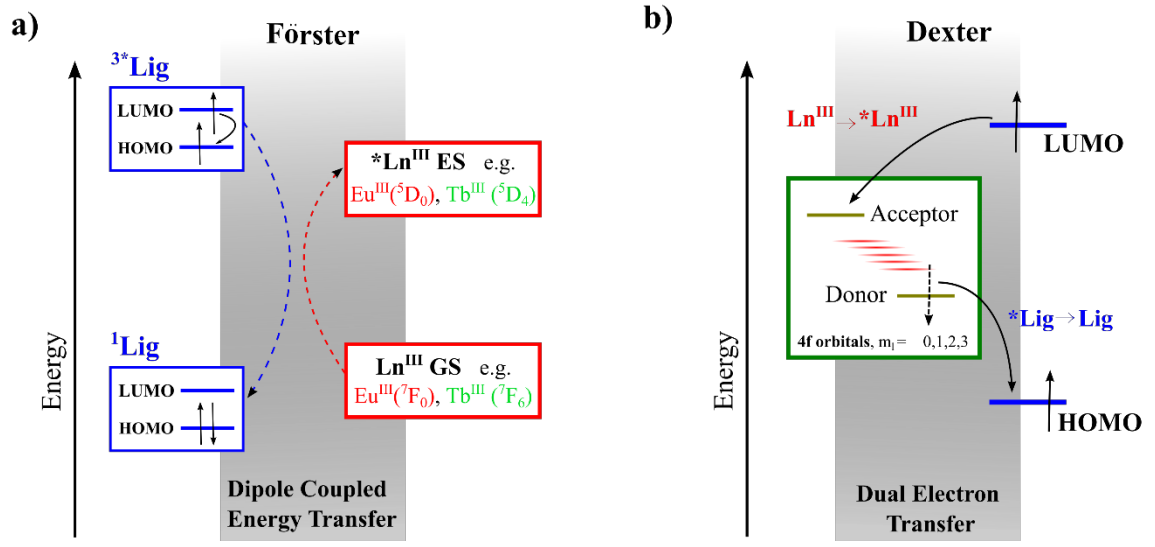

Figure 1.6 Schematic representations of Förster- and Dexter-type energy transfer in Ln^{III} complexes. **a)** Förster mechanism, the dipole-dipole coupled relaxation of ligand triplet excited-state to a singlet ground-state gives intra-configurational promotion of the Ln^{III} ground state (GS) to *Ln^{III} excited state (ES) Energy scale represents those of electronic configurations for Ligand (blue boxes) and Ln^{III} (red boxes); **b)** Dexter-type mechanism, simultaneous electron exchange of a 4f electron from Ln^{III} quenching ligand triplet excited state (blue) and an electron from the ligand to 4f orbital (green box) to generate a *Ln^{III} ES configuration; only electrons involved in the transfer are shown. Energy scale represents electron energy level.

of electron configurations which correlate more appropriately with the reality of Ln^{III} sensitisation.

The Förster mechanism of coulombic energy transfer, shown in Figure 1.6a, follows a dipole coupling mechanism where the donor transition dipole (ligand $T_1 \rightarrow S_0$ relaxation) is coupled with the acceptor transition dipole (the $*Ln^{III}$ ES ← Ln^{III} GS excitation) and allows population of the metal-centred excited-state indirectly. The rate of energy transfer (k_{ET}) can be described by Equation 1.1:

$$k_{ET} = k\frac{\kappa^2 k_D^o}{r_{DA}^6}J(\epsilon_A) \qquad \textbf{Equation 1.1}$$

Where k is a condition dependent constant, k_D^o describes the oscillator dipole strength while κ^2 reflects their respective orientation. The $J(\epsilon_A)$ term relates to the overlap integral of the donor chromophore emission and Ln^{III} absorption spectra. Appropriate spectral overlap is required for this mechanism of ET, with a larger overlap giving rise to a faster energy transfer rate. However, the narrow linewidth and low-extinction coefficients of *f-f* transitions are restrictive and highly efficient ET of sensitised emission can be challenging to achieve, even when overlap exists. The mixed multiplicity of the antenna excited-state, by the HA effect, can be understood to allow this formally forbidden relaxation ($\Delta S \neq 0$) to function efficiently for energy transfer through the dipole mechanism. The subsequently radiative relaxation of the $*Ln^{III}$ ES, assuming there is no reverse energy transfer (see Section 1.4.3), will take the form of Ln^{III}-centred luminescence. Furthermore, this mechanism is distance (r) dependent with the strength of the electric fields associated with both the donor and acceptor transition dipoles and falls off as r^{-6}. These restrictions can be addressed in ligand design.

The Dexter-type mechanism, shown in Figure 1.6b, involves a two-electron exchange. An electron is transferred from the highest energy SOMO in the ligand T_1 excited-state to an acceptor *f* sub-orbital of the Ln^{III} ion, while simultaneously another electron is transferred from a donor *f*- electron to the lower energy SOMO of the ligand. This results in quenching of the excited ligand ($T_1 \rightarrow S_0$) and change in the Ln^{III} $4f^n$ configuration ($*Ln^{III}$ ES ← Ln^{III} GS). As an electron transfer process, the distance-dependence of Dexter-type is more limiting and the efficiency decreases as e^{-2r} therefore requiring smaller chromophore-Ln^{III} (compared to Förster's mechanism) in order to be efficient. Förster's mechanism has been suggested to be more likely for Ln^{III} sensitisation,[45] while Faulkner and Ward have shown the occurrence of Dexter-type energy transfer at both short[112] and long[104] antenna-Ln^{III} distance, particularly so in ^{3}MLCT sensitisation of *d-f* dyads.[96,101] Irrespective of which mechanism operates,[81] the efficiency of sensitisation is proportional to antenna proximity.

1.4.3 Ligand design considerations – efficiency and quenching of luminescence

In the design of ligand structures for sensitisation a number of considerations are necessary. As established above, the proximity of the sensitising chromophores to the Ln^{III} centre is fundamental to the efficiency of the energy transfer process. Therefore, coordination sites have been developed to complement the hard Lewis acidity of the Ln^{III} ions. Hard Lewis bases such as carboxylates, amides and nitrogen-containing heterocycles are commonly used to maximise the Ln^{III}-ligand bond strength and shorten the Ln^{III}-ligand distance.[53]

For organic chromophores, in the T_1 excited-state mechanism consideration of the HOMO-LUMO gap is required. Despite the HA effect of the Ln^{III} resulting in easier $S_1 \rightarrow T_1$ intersystem crossing, in order to ensure efficient T_1 population, the HOMO-LUMO gap should ideally be ΔE = 5,000 cm^{-1}.[72] Furthermore, the relative energy of the ligand-centred T_1 and the Ln^{III} excited-state configuration will influence the efficiency of ligand-to-metal energy transfer. An energy gap which is too large (*i.e.* $E(T_1) \gg Ln^{III}$ ES) will likely result in ligand fluorescence and poor energy transfer efficiency. On the other hand, should the energy gap be too small (*i.e.* $E(T_1) \approx {}^*Ln^{III}$ ES) then thermal back-energy transfer results in desensitisation of the Ln^{III} centre *via* repopulation of the ligand-centred excited state and, again, poor energy transfer efficiency. In general terms, the $\Delta E(T_1 - Ln^{III}$ ES) should be between 2500 – 3500 cm^{-1} to balance these two effects.[72]

Similarly significant is the influence of post-sensitisation processes that act to quench the Ln^{III} excited-states through non-radiative pathways. Lanthanide luminescence quenching arises from vibronic coupling of high energy oscillating dipoles associated with N-H, O-H and C-H bonds. These oscillators may be located in solvent molecules (both coordinated and bulk) or in the ligand covalent structure itself as the effect occurs in both first- and second-coordination spheres of the Ln^{III} ions.[48] The effect arises from the fact that the third vibrational overtone of the O-H oscillator is close in energy to the excited-states of various Ln^{III} ions, particularly so for Eu($^5D_0$) and Tb($^5D_4$). The effect of N-H and C-H was expected due to the similarity in vibrational stretching frequencies of coordinated amide N-H ($\nu_{NH} \approx$ 3,300 cm^{-1}) and methylene C-H ($\nu_{CH} \approx$ 2,950 cm^{-1}) with that of O-H ($\nu_{OH} \approx$ 3,400 cm^{-1}).[113] These have been experimentally verified and the deactivating effect of N-H oscillators is significant.[48,114] Although the effect of C-H oscillators tends to be less, Wahsner showed substantial efficiency in Tm^{III} sensitisation from perdeuterated bis(**bipy)** complexes.[115] The exclusion of first-coordination sphere is central to limiting the O-H oscillator deactivation and this is usually approached through the use of polydentate, macrocyclic and pre-organised ligands that fully and efficiently occupy the coordination sphere with ligand donors.[53]

Furthermore, the influence of second-coordination sphere oscillators can be minimised through supramolecular approaches and hydrophobic exclusion of water molecules from the antenna and sensitisation process, for example through micellar structures.[116-118]

With these ideas in mind, researchers have designed and developed versatile Ln^{III}-containing systems. Recent developments in the design of luminescent Ln^{III} complexes formed from acyclic ligands are reviewed in the following section. In order to place the novel materials described later in this thesis into more specific context, the hierarchical self-assembly of small Ln^{III} complexes into solution-based and bulk soft matter will be introduced and is described in Section 1.6. The extension to the synthesis of composite, blended and doped luminescent organic polymers and polymer-gels containing emissive Ln^{III} complexes is of distinctive interest and will be reviewed separately in Section 1.7.

1.5 Discrete luminescent Ln^{III} complexes

The hard Lewis acid character of the Ln^{III} series has led to the use of the corresponding hard oxygen donors and heterocyclic nitrogen donors in a variety of different ligand classes.[47] The coordination of Ln^{III} tends to be demanding with high and variable coordination numbers needed. For example, Eu^{III} and Tb^{III} have coordination numbers of 9 – 10 and this requirement can range from 6 to 12 within the Ln^{III} series. This demanding coordination has often required polydentate macrocyclic or chelating ligands to saturate the ion with thermodynamic stability and kinetic inertness. The use of 1,4,5,10-tetraazacyclododecane (**3**, *cyclen*) and NOTA (**4,** 1,4,7-triazacyclononane-1,4,7-triacetic acid) as macrocyclic chelates for Ln^{III} ions with coordinating pendent arms for ion saturation and, where appropriate, sensitisation of the Ln^{III} excited states have been reported in a range of photophysical and magnetic applications.[119] Raymond and co-workers have extended ligand structures to open poly-dentate structures that bind with strong chelating and cooperative effects.[81] The motifs such as IAM, HOPO and ligands of the form of **5** have permitted the design of extremely luminescent and strongly coordinated complexes and probes.[120]

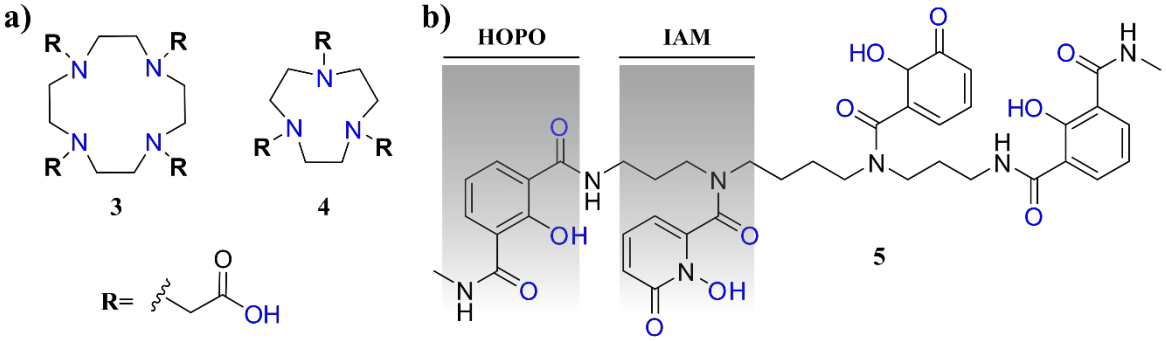

Figure 1.7 Structures of **a)** classical macrocyclic *cyclen* **3** and NOTA **4** ligands for Ln^{III} coordination; and **b)** structure of **5** a podand-like ligand for Ln^{III} containing the HOPO and IAM sub-units.

Similarly, Petoud and co-workers have contributed encapsulating oligomeric ligands (employing amino and carboxylate-based structures) and their emissive Ln^{III} complexes for in cellular applications for imaging.[121-123] These macrocyclic and chelating designs tend to provide complexes with high kinetic stability in solution accounting for their continued attention.

In the contrary approach, Bünzli, Piguet and Gunnlaugsson have pioneered the use of small acyclic ligands to promote Ln^{III}-directed self-assembly and supramolecular chemistry.[44,46,47,66,95] In recent years, it has been found that small bi- and tri-dentate structures can afford kinetically stable systems yet, unlike the corresponding macrocycles are dynamic, reversible and able to form with more varying stoichiometry.[124] These have been applied as probes and materials to great effect with recent developments which has led to a rapid progress in Ln^{III}-directed self-assembly; key and contemporary examples are discussed in the following section.

1.5.1 Acyclic ligands and their luminescent Ln^{III} complexes

For the formation of Ln^{III} complexes with acyclic ligands small molecules have been developed with appropriate donor moieties and of various denticities. Weismann[89] first described the antenna-sensitised emission of Ln^{III} ions from bidentate chromophore-containing β-diketonate ligands - a system which has been used extensively to date.[125]

Perhaps the most frequently used acyclic structures are terdentate ligands and therein the dipicolinate motif has been shown to be a versatile terdentate binding motif. The non-derivatised dipicolinic acid **6** forms various saturated complexes with emissive Ln^{III} ions (*i.e.* Eu^{III} and Tb^{III}) through a *O-N-O* binding site formed from the pyridine nitrogen and anionic carboxylate oxygen atoms. Werts showed the formation of complexes of various stoichiometry with Eu^{III}, demonstrating from the emission spectra the existence of **[Eu.(6)]**$^{+}$, **[Eu.(6)$_2$]**$^{-}$ and **[Eu.(6)$_3$]**$^{3-}$ in aqueous solutions.[126]

The saturated complexes of Cs_3[**Eu.(6)$_3$**] and Cs_3[**Tb.(6)$_3$**] were parameterised by Chauvin and Bünzli in TRIS-buffered solutions as a quantum yield standard for pyridine-based Eu^{III} and Tb^{III} complexes.[127] Recently, Chauvin and co-workers showed the parent M_3[**Ln.(6)$_3$**] complexes (M = Li^+, Na^+, K^+, Cs^+ or Rb^+, Ln = Eu, Tb) alongside the commercial luminescent cyan ink Firefly™ (Vermont PhotoInkjet, LLC) as a RGB inkjet ink for the preparation of anti-counterfeit documents. The water-based inkjet printing produced invisible images under ambient light and full-colour images visible only under irradiation with appropriate UV light.[128] The complexes of **6** have been shown to adopt D_3 symmetry and Λ and Δ configurations in racemic solution. Müller has demonstrated the use

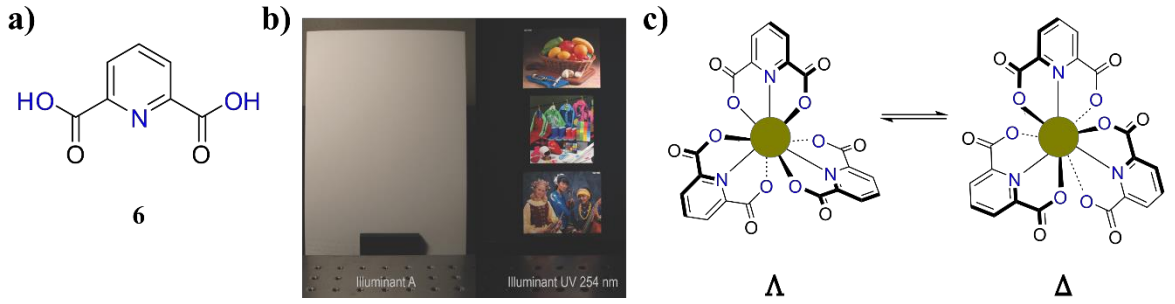

Figure 1.9 a) Structure of dipicolinic acid, **6**; **b)** inkjet printed images on A4 paper using **Cs_3[Eu.(6)$_3$], Cs_3[Tb.(6)$_3$]** and Firefliy™ inks under ambient (left) and UV (right) light. Reproduced from Ref. 128; and **c)** the Λ and Δ stereochemistry of Ln^{III} centres in tris-(dipolinate) complexes.

of simple **[Eu.(6)$_3$]$^{3-}$** for analytical purposes through Pfeiffer effect perturbation of the Λ ⇆ Δ equilibrium by amino acids and showed the determination of absolute configuration from polarised emission measurements.[129,130]

Discrete complexes have been reported using dipicolinic acid structures functionalised from the pyridine 4-position. Gassner, Bünzli and Grossel showed the 'remarkable' fine-tuning of photophysical properties of **ML_3** stoichiometry in tri(ethyleneglycol) substituted structures **7 - 13** with varying terminal functionalities.[131,132] The total quantum yield could be varied between *ca*. 13 and 30 % between the -OMe and -NH_2 terminated ligands, while the structure of the Eu^{III}-centred emission spectrum demonstrated that the coordination structure was unperturbed by the 4-position substituent.

Andres and Borbas showed chelidamic acid **7** as a readily functionalised platform in the screening of antenna chromophores for eventual use in NOTA-derived systems.[133] Ligand **14** was synthesised with appended visibly absorbing dyes and screened for the

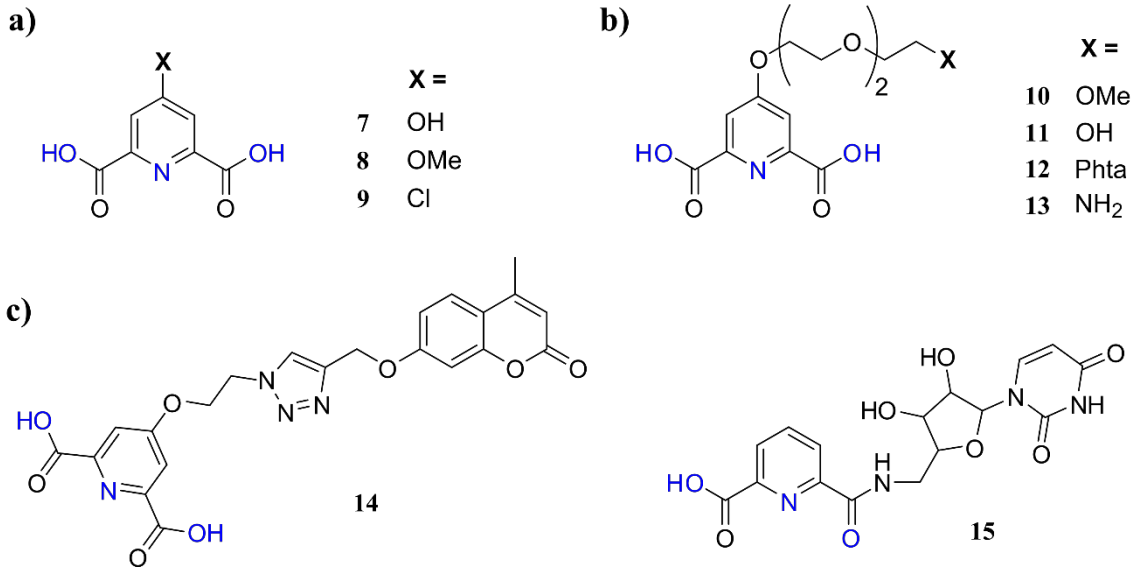

Figure 1.8 Structures of **a)** derivatised dipicolinic acids **7 - 9**; **b)** PEG-functionalised dipicolinic acids **10 - 13** with different terminal functionalities; and **c)** larger coumarin (**14**) and uridine (**15**) derivatives of dipicolinic acid.

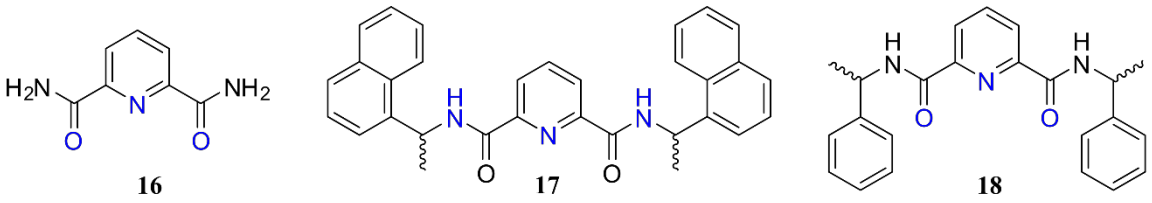

Figure 1.10 Structures of **dpa (16)** and simple chiral derivatives **(17** and **18)**.

efficiency of sensitised emission from Eu^{III}, Tb^{III}, Sm^{III} and Dy^{III} while triplet-state energies were determined from the respective Gd^{III} complexes. The results from the dipicolinate analogues were used to estimate the efficiency of sensitisation when linked to NOTA through a triazoyl linkage and 4-methyl-7-*O*-alkylcoumarin was demonstrated as a promising antenna which indeed translated to the *cyclen* platform. This approach has been further developed by the authors to realise the nucleotide-functionalised dipicolinate-based ligands. A uridine derivative **15** was synthesised and complexes of the form **[Eu.(15)$_3$]** gave exclusively Eu^{III}-centred emission with a total quantum yield of 3% without residual ligand fluorescence. The system was proposed as a precursor to oligonucleotide-attached Ln^{III} probes of interest to biochemical studies; however, example oligomers have yet to be demonstrated.[134]

Further derivatives have been reported from the basic dipicolinate scaffold to append chromophores with lower energy absorbance suitable for sensitisation. Piguet and Bünzli utilised *N,N,N',N'*-tetraethylpyridine-2,6-dicarboxamide, **16**, as a ternary ligand, rather than

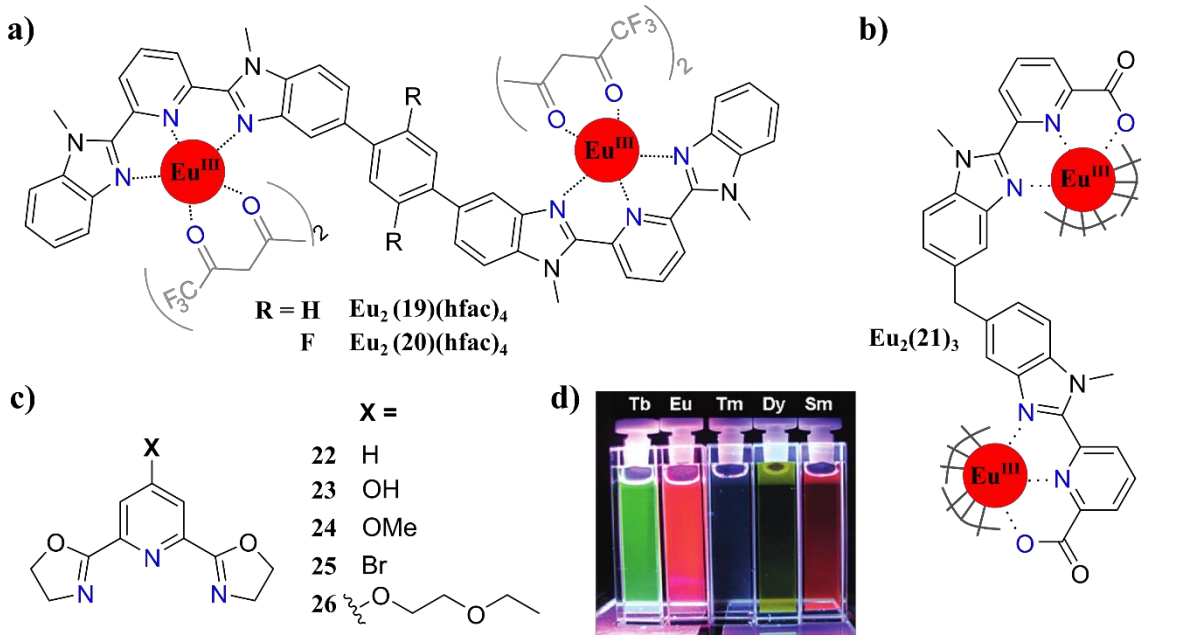

Figure 1.11 a) Structure of ditopic **bbpy** edifices **[Eu$_2$(19)](hfac)$_4$** and **[Eu$_2$(20)](hfac)$_4$**; **b) s**tructure single strand of a triple-stranded dimetallic helicate with Eu^{III} from three ligand **21; c)** structure of **Pybox** (**22**) and simple derivatives to tune photophysical performance (**23** - **26**); and **d)** photographs of visible emission from complexes of **22** with Tb^{III}, Eu^{III}, Tm^{III}, Dy^{III} and Sm^{III} ions. Reproduced from Ref. 148.

sensitising chromophore in order to optimise the geometry of triple-stranded helicates in organic solution.[135] Müller and co-workers, in parallel with Gunnlaugsson,[136] extended the use of dipicolylamide (**dpa**) derivatives and synthesised ligands **17** and **18** attaching chiral phenyl chromophores.[137,138] Efficient sensitisation of both visible and NIR emitting Ln^{III} ions was observed from these systems and circularly polarised luminescence was recorded from the complexes implying a Λ or Δ excess directed by enantiomer configuration. The **dpa** motif has been developed by Gunnlaugsson *et al.* in great depth and is specifically discussed in Section 1.7 below. Bünzli and Piguet introduced the terdentate 2,6-bis(benzimidazol-2-yl)pyridine (**bbpy**) ligand which was synthesised by heterocyclic condensation of benzimidazole from **dpa** precursors. Piguet used **bbpy** in bimetallic **Eu_2.(19)$(hfac)_4$** and **Eu_2.(20)$(hfac)_4$** to demonstrate the benefit of perfluorinated aromatics spacers for extending π-conjugation length of the chromophore units in the improvement of sensitisation efficiency of Eu^{III}-centred emission.[139] The balance of non-radiative deactivation was shown to optimise the efficiencies of ISC and in turn the intrinsic quantum yields of the Eu^{III} centre. This binding site has mostly been used in the formation of triple-stranded helicates,[140] such as those formed from ligand **21**, and thermodynamic properties of their formation studied in detail.[124] The cooperative stability, kinetic inertness and favourable millisecond lifetimes of Eu^{III}-containing methylene-**bbpy** triple-stranded helicates have been investigated for cellular staining.[82,141-144] The various options for functionalisation were highlighted for specific targeting and solubilisation for staining cellular cytoplasm, late endosomes or lysozomes, and therefore have been hypothesised for use in monitoring cellular processes using time-gated luminescence imaging.

Another direct **dpa** derivative binding site pyridine bis(oxazoline), or **Pybox**, **22** was reported by de Bettencourt-Dias[145] and showed that the ligand could be functionalised, **23 - 25**, to tune the sensitisation efficiencies in organic solvent[146,147] or, in the case of **26**, give large quantum yields in aqueous solution, Figure 1.11d.[148] There have been fewer reports of developments in **Pybox**-based ligands compared to **dpa** and **bbpy** over recent years. However, chiral absorption and emission from the corresponding Λ and Δ configurations have been shown by Yuasa and co-workers comparable to Muller's observations in dipicolinate Ln^{III} complexes.[149] Ligands containing nitrogen-rich heterocycles, such as triazoles and tetrazoles, have been of increasing interest to researchers and have generated tri- and higher-dentate scaffolds. These ligand types have been introduced as versatile alternatives to terpyridine (**tpy**). The **tpy** moiety has been used extensively for sensors of small molecules,[150] local polarity probes[151] and the generation of white-light-emitting

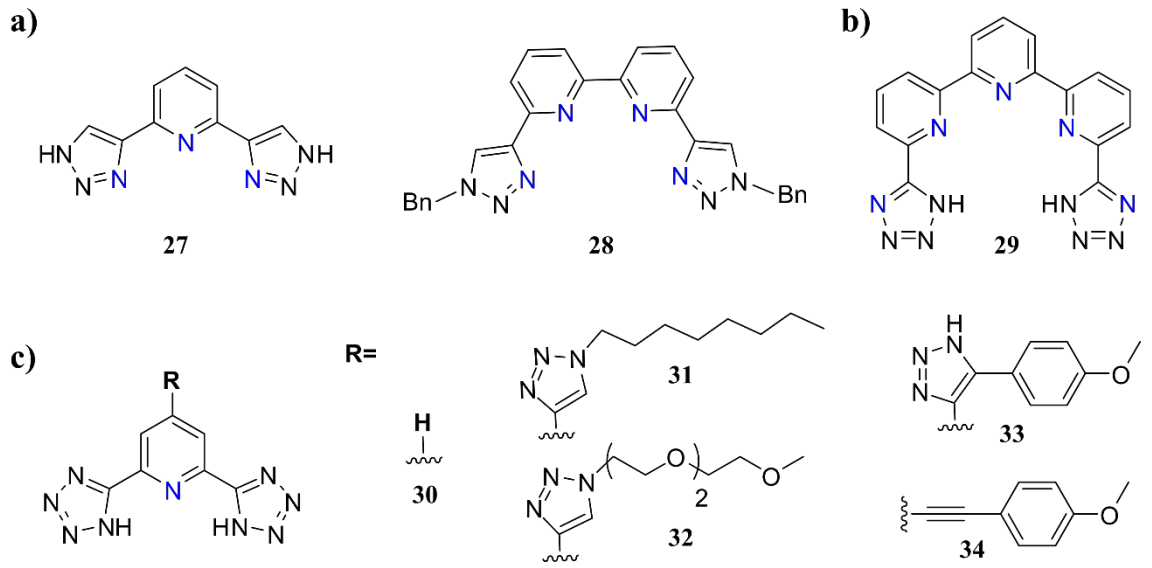

Figure 1.12 Structures of **a)** 1,2,3-triazoyl derivatives ligands from pyridine (**27)** and **bipy (28); b)** tetrazole-derived **tpy** (**29);** and **c)** 4-position functionalised ligands with various conjugated units (**30 - 34**)

fluids[152] since **tpy** sensitises Eu^{III} (red emitting), Tb^{III} (green emitting) and itself has a blue fluorescence.

Expanding upon the **tpy** moiety, Byrne and Gunnlaugsson introduced bis(1,2,3-triazolyl)pyridine (**btp, 27**) for Ln^{III} coordination, see Section 1.7, while Nash and co-workers used this triazole isomer in the synthesis of bis-1,2,3-triazole-bipyridine (**28**, BYzBP). Ligand **28** was synthesised containing triazole-attached phenyl substituents and were found to aid in the selective separation of lanthanide and actinide salts in the presence of suitably lipophilic anions.[153] However, despite being a chromophore-rich species, the sensitisation efficiency of these ligands for emissive Ln^{III} ions have not been explicitly explored. A similar approach was taken by Mazzanti *et al.* using tetrazoles and an extended **tpy** central core. Ligand **29** was reported as a poly-dentate scaffold which could assemble into complexes of various topologies and was shown to form highly luminescent double- and triple-helical complexes with various Ln^{III} ions (Ln = Eu, Tb or Nd).[154] The use of tetrazoles has been further developed by Mazzanti with the familiar pyridine ligand core.[155,156] The self-assembly of pyridine-2,6-bis-tetrazolates was demonstrated with various substitutions, **30** - **34**, with triazoles and other π-conjugated chromophores. The parent scaffold, **30**, was able to sensitise visible emission from Eu^{III} and Tb^{III} ions in water with quantum yields of 18% and 63%, respectively. Substitution of the pyridine 4-position with triazolyl units was not disruptive of self-assembly and photophysical properties and, in fact, demonstrated enhancement in the luminescence quantum yields to 43% and 98% for Eu^{III} and Tb^{III}, respectively.

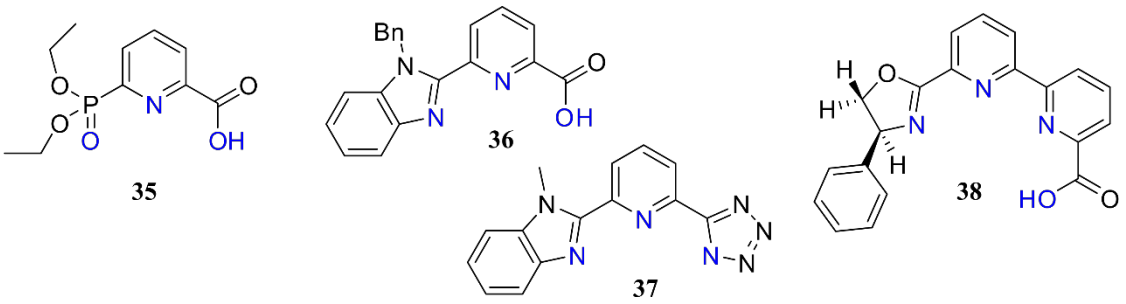

Figure 1.13 Structures of asymmetrical ligands **35 - 38** with central pyridine cores.

Most examples of Ln^{III} coordinating ligands have been symmetrical and have tended to form highly symmetrical complexes (*e.g.* D_3). However, enhancement of Ln^{III}-centred luminescence and the modulation of sensitive emission spectra have recently been achieved with asymmetrical units. Chauvin demonstrated that 6-phosphoryl picolinic acids with varying phosphorylester type could give rise to Eu^{III} and Tb^{III} complexes with greater stability, particularly with the ethyl ester **35**. However, for the majority of ligands lower luminescence quantum yields than the dipicolinic acid analogue were observed.[157] Bünzli and Eliseeva showed that asymmetrical benzimdazoyl-pyridinecarboxylic acids, **36**, complexed to Eu^{III} gave complex symmetry with varying symmetry (C_3 to C_1) and luminescence enhancements concomitant with lower symmetry - consistent with the nature of *f-f* transitions described in Section 1.3 above.[158,159]

The same authors synthesised the benzimidazole-pyridine-tetrazolate ligand, **37**, which interestingly showed better photophysical performance in CH_2Cl_2 solution than the solid materials, with quantum yields of 41% and 12%, respectively. This was accounted for by the formation of hydrated complexes exhibiting 3-3.5 waters of crystallisation in the solid state, strongly quenching emission which were dispersed from the coordination sphere in organic solution.[83] The asymmetrical tetradentate oxazoline-**bipy** derivative (**38**, **Phbipox**$^-$) reported by Mazzanti *et al.* underwent concentration-dependent diastereoselective self-assembly with Eu^{III} to give Δ- or Λ- **[Eu.(38)$_2$]**$^+$ (in ratio Λ/Δ ≈ 1.8) at low concentration and enantiopure ΔΔΔ triangular assembles at higher concentrations (these structures were assigned in both organic solution and the solid-state).[160]

The developments of emissive Ln^{III} complexes have led to the evolution of an extensive range of responsive probes and Ln^{III}-based sensors. A number of biomarker probes have been reported using acyclic ligands.[161-165]

Discrete emissive complexes have been used in the real-time sensing of enzyme activity, although most being macrocycle-based.[53,166-168] However, recently, Miller *et al.* used Eu^{III} and Tb^{III} complexes of the multi-dentate polyaminocarboxylate ligand **39**, with an

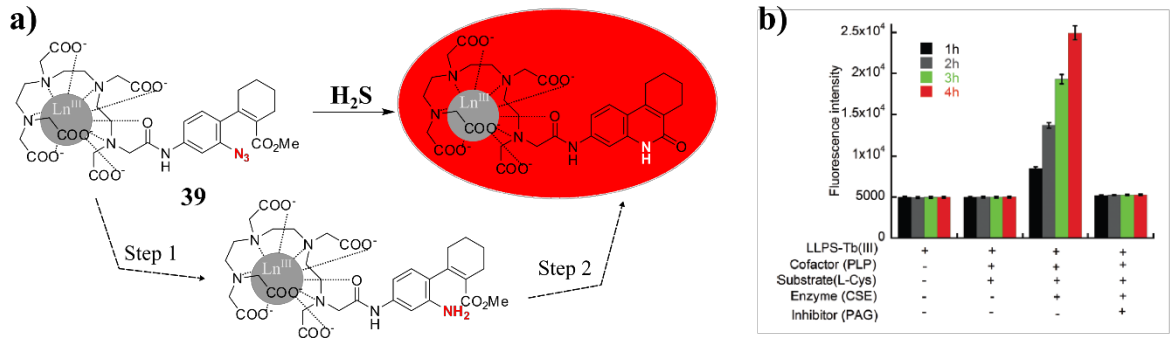

Figure 1.14 a) Mechanism of luminescence 'switch-on' response of **[Ln(39)]**$^-$ upon exposure to H_2S to generate an active antenna; and **b)** the fluorescence intensity responses upon exposure to lyase enzyme, substrate and inhibitor showing selective response to exposure to active enzyme. Reproduced from Ref. 169.

attached azido- and ester-functionalised quinolinone precursor, to monitor Cystathionine γ-Lyase activity using time-gated Ln^{III} emission.[169] The generation of H_2S by the enzymatic activity was found to convert the precursor chromophore (which was not suitable for Ln^{III} sensitisation) into the 7-amino-4-methyl quinolinone (which was a good sensitising antenna) and gave rise to the Eu^{III}- or Tb^{III}-centred emission. Luminescence enhancements of >25-fold were observed with low false-positive rates for the Eu^{III} complexes and an overall performance comparable to established commercially available alternatives.

Lu and Blight have independently reported Eu^{III}-based biomarker sensors for *B. anthracis* (popularly, anthrax) which is, in fact, dipicolinic acid (**6**). The approach of Lu *et. al* was to implement a "switch-on" sensor in which with EDTA-bound Eu^{III} complexes become emissive upon the coordination of trace dipicolinic acid. The probe was shown to be selective over related carboxylic acids with a limit of detection (LOD) of 0.2 nM and a response time of two minutes.[170]

On the other hand, Blight and co-workers used a "switch-off" approach with complex **40**, shown in Figure 1.15, in which the presence of dipicolinic acid was shown to compete with and displace the **phen** antenna reducing the sensitisation efficiency when irradiated at λ_{exc} = 340 nm. The operation of the probe was shown to be selective for dipicolinic acid in the presence of coordinating phosphates and H_2O while also maintaining sensitivity at

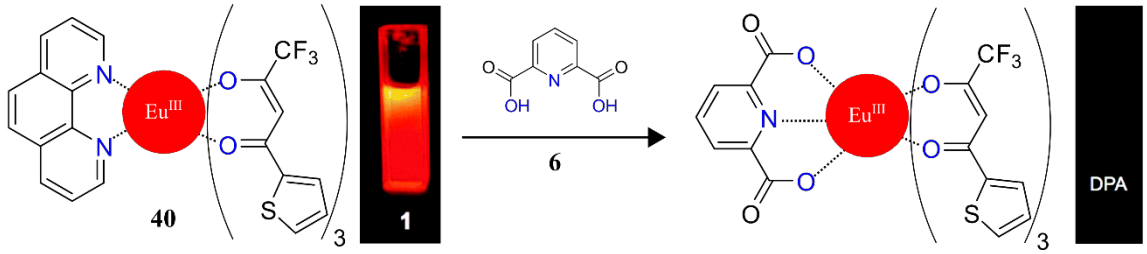

Figure 1.15 'Switch-off' sensor for *B. anthracis* biomarker dipicolinic acid, **6** showing **phen** sensitised emission in the resting state which becomes displaced upon exposure to **6**. The offset excitation wavelength between **phen** and **6** resulted in poorer sensitisation by 6 at λ_{exc} = 340 nm. Images reproduced from Ref. 171.

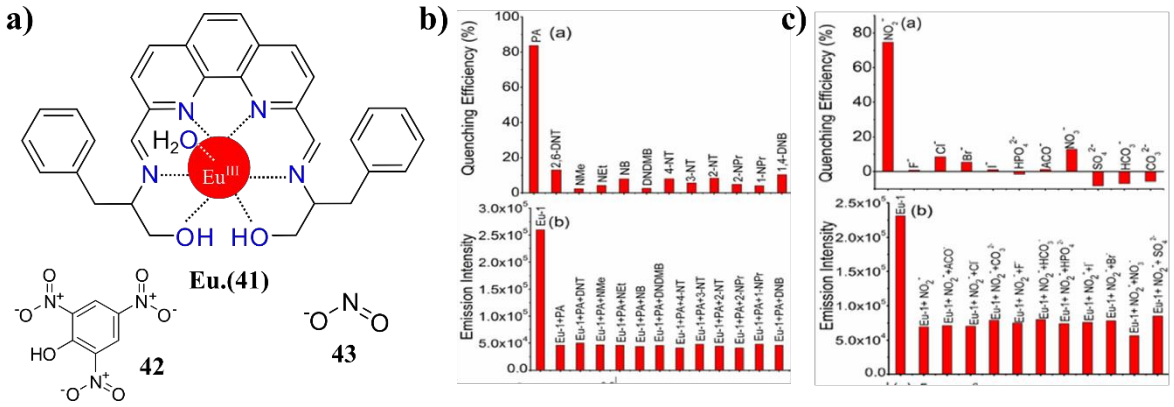

Figure 1.16 a) Structure of responsive probe **[Eu.(41)(H₂O)]**$^{3+}$ and selective analytes picric acid **42** and nitrite **43; b)** Selective response of **[Eu.(41)(H₂O)]**$^{3+}$ for 42 by quenching efficiency over other nitro-aromatic compounds; and **c)** selective response of **[Eu.(41)(H₂O)]**$^{3+}$ for **43** by quenching efficiency over other coordinating anions. Graphs reproduced from Ref. 172.

nanomolar concentrations of the biomarker.[171] Also, in order to address the consequences of warfare, Albrecht and co-workers have efficiently shown the Eu^{III}-based probe **[Eu.(41)(H₂O)]**$^{3+}$ to be selective for the explosive marker picric acid over other nitro-aromatic compounds. The **phen**-Schiff base ligand **41** sensitises Eu^{III} emission but in the presence of picric acid, **42**, is quenched with a selective efficiency of *ca*. 80%.[172] The same complexes operated as selective anion sensors for nitrite **43**; showing 8-fold selectivity over other anions as a result of discrimination in coordination abilities. Albrecht has also described related Schiff base systems to be responsive to other anions including adenosine triphosphate (ATP) both quantitatively[173,174] and as a cellular phospholipid stain.[175]

The recent trends of research in luminescent Ln^{III} complexes have been towards materials and spans between both hard and soft matter.[176] A number of immediately applicable materials have been achieved from fabrication of thin films using discrete complexes for OLED[177-179] and sensing applications.[180] However, the potential for emergent properties in supramolecular assembly and the corresponding materials, particularly polymeric and soft matter, has required more extensive research and will be reviewed in the following sections.

1.6 Luminescent Ln^{III}-containing assemblies and soft matter

The hierarchical self-assembly of smaller components *via* supramolecular interactions leads to a range of materials both hard (*e.g.* crystalline powders, polymers) and soft (*e.g.* amphiphilic assemblies, liquid crystals, gels). Those materials that are considered 'soft matter' are finding applications in bioengineering fields due to their mimicry of natural constructs and tissues where soft materials dominate[181] and coordination-based systems have received interested.[182] Hydrogels have received particular interest due to their increased

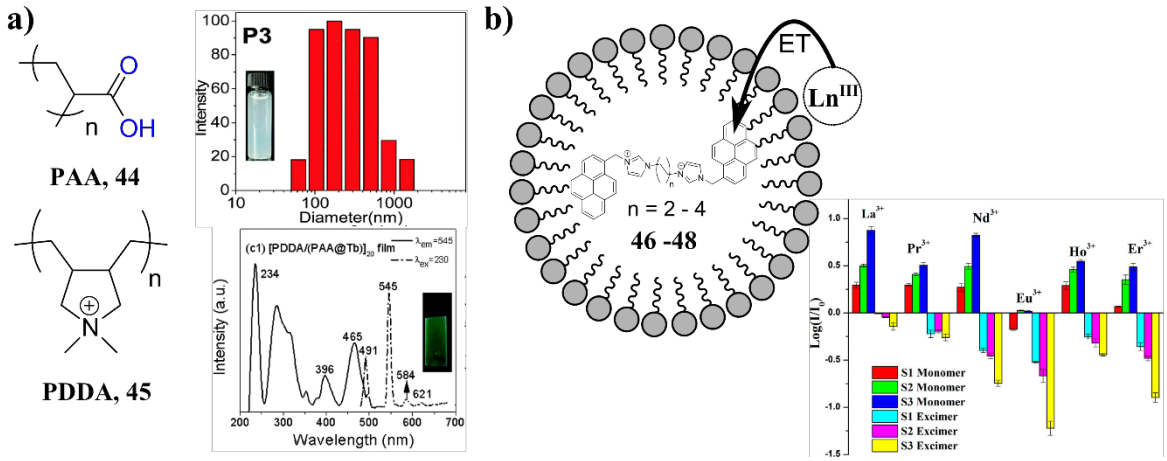

Figure 1.17 a) Structures of **44** and **45** which form LbL assembled films and colloidal particles doped with Tb^{III}. *Top right:* colloidal suspension of **44/45@Tb^{III}** and particle size distribution determined from DLS. *Bottom right:* Visible emission and corresponding spectrum from 20-layer LbL-assemblies of **45/44@Tb^{III}** on excitation at (λ_{exc} = 254 nm). Graphs reproduced from Ref. 186; **b)** Schematic representation of SDS micelle sensor array containing **46 - 48** and electrostatic association of Ln^{III} ions. *Bottom right*: cluster patterns of excimer emissions from **46 - 48** that unique identify the individual Ln^{III} ions. Graph reproduced from Ref. 187.

biocompatibility and bio-similar nature.[183] Over time there has been steady-development of luminescent soft assemblies in solution and soft bulk materials formed from acyclic and small-molecule Ln^{III} complexes.

1.6.1 Supramolecular assemblies and frameworks in solution and soft matter

Surfactants and amphiphiles naturally undergo self-assembly processes driven by hydrophobic, electrostatic and selective solvation interactions. These soft assemblies are concentration- and condition-dependent generating different morphologies including lamellar phases, micellar and bicellar systems or extended columnar structures.[184,185]

The use of amphiphilc assembly can allow layer-by-layer (LbL) assembly of thin films and colloidal soft matter. Indeed, the colloidal particles and LbL assemblies of poly(acrylic acid) (PAA) and poly(diallyldimethyl ammonium) (PDDA) were studied by Yang through lanthanide luminescence.[186] Mixed LbL-assembled films (20 layers) containing Ce^{III}, Eu^{III} and Tb^{III} were able to give blue, purple and green emissions, respectively. Burrows *et al*. also studied surfactant interactions with Ln^{III} and PAA.[187] In both these cases Ln^{III}-to-amphiphile interactions were promoted by carboxylate binding and relied on direct excitation of the Ln^{III}-centres.

Wang and co-workers reported the use of non-coordinating surfactant-assemblies as a microenvironment to encapsulate and solubilise hydrophobic sensitising chromophores in aqueous systems. A sensor array of three pyrene-based dyes, **46 - 48**, was developed using the anionic surfactant SDS that gave luminescence responses to various Ln^{III} ions and a multicomponent analysis allowed pattern-based identification of specific ions. The specific use of the surfactant self-assembly was justified in a clear correlation between the

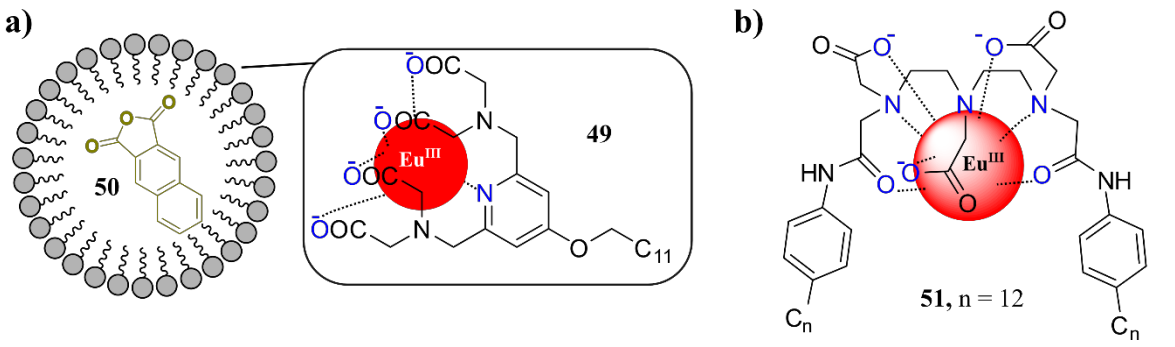

Figure 1.19 a) Structures of coordinating amphiphile **49** and sensitising chromophore **50** within a schematic representation of micelle formations of **[Eu.(49)]**$^-$ within encapsulated naphthalimide antenna; and **b)** structure of **[Eu.(51)]** with DTPA core and pendent phenyl antenna chromophores.

electrostatic interaction between anionic surfactant and cationic Ln^{III} in the modulation of the fluorescence responses.[188] Bonnet and Tóth extended the use of directly coordinating antennae in the development of Eu^{III} complexes of chelate **49** which contained C_{12} chains.[118] The complexes were shown to assemble into micellar structures, shown schematically in Figure 1.19, resulting in a hydrophobic core coated with net anionic Eu^{III} complexes. Emission was achieved by energy transfer from the excited states of the pyridine, however the hydrophobic core could be used as a 'cargo hold' for other hydrophobic antennae. The inclusion of 2,3-naphthylic anhyride (**50)** within the micellar solution resulted in *ca*. 400% enhancement in emission intensity. Total quantum yields of 0.14% were achieved, however the assemblies size and morphology were not determined.[118] Parac-Vogt and Eliseeva used a similar approach with ligand **51** and characterised the luminescent assemblies in greater detail demonstrating average assembly sizes of *ca*. 33 nm by light scattering experiments and found improved quantum yields *ca*. 1%.[189]

Maitra and co-workers have also reported emissive Eu^{III}-coated vesicles as a result of coordination of Eu^{III} by natural phospholipid DOPC, **52**, which contain hydrophobic

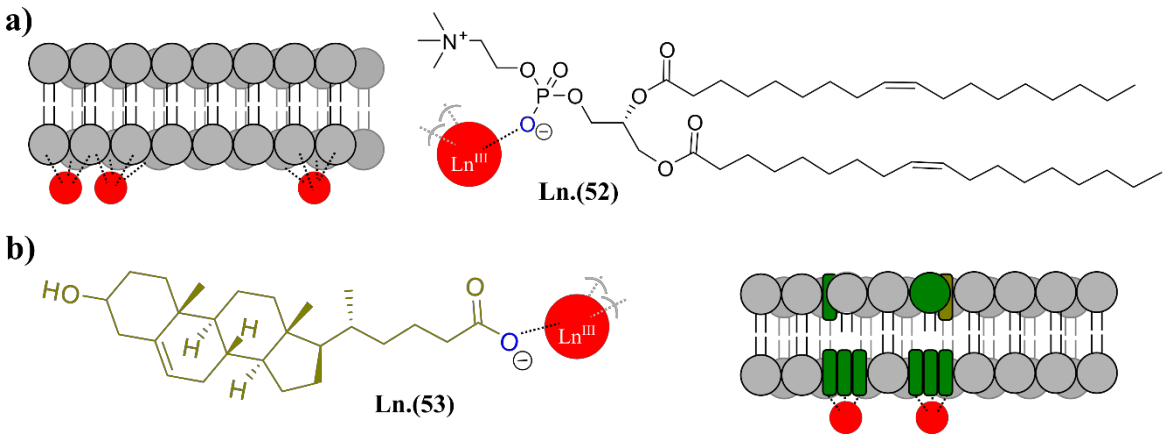

Figure 1.18 a) Schematic representation of the interaction of Ln^{III} ions with membrane phospholipid DOPC (**52**) within a bilayer soft assembly and the structure of the **52**; and **b)** structure of cholate derivative (**53)** and schematic representation of the interaction of Ln^{III} ions with the bilayer soft assemblies.

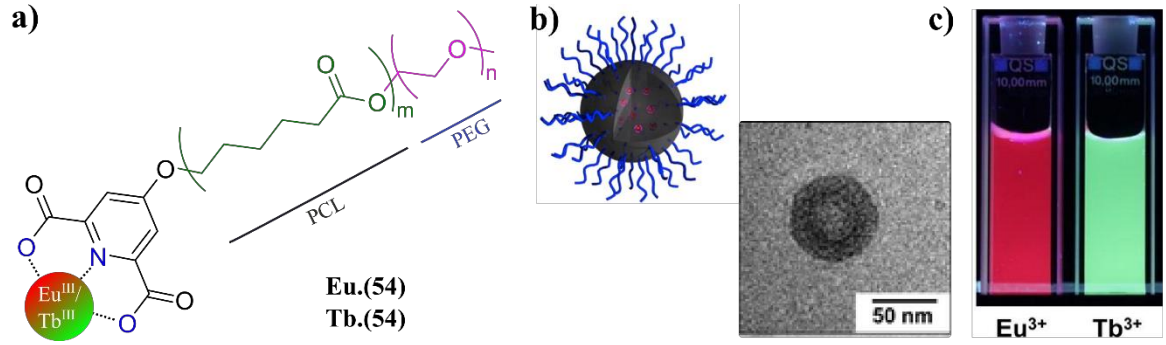

Figure 1.20 a) Structure of [**Eu.(54)**]$^+$ or [**Tb.(54)**]$^+$ complexes containing dipicolinate binding sites and poly(caprolactam) and PEG block copolymer functionalities to direct self-assembly; **b)** *top left:* schematic representation of the metal-centred micelles formed by [**Eu.(54)**]$^+$ or [**Tb.(54)**]$^+$ complexes in H_2O presenting a PEG-ylated surface. *Bottom right:* TEM image showing micelle self-assembly diameter *ca.* 50 nm; and **c)** emissive solutions of [**Eu.(54)**]$^+$ or [**Tb.(54)**]$^+$ micelles in H_2O following excitation at 254 nm. Images in **b)** and **c)** reproduced from Ref. 192.

antennae such as pyrene and naphthalene imbedded within the bilayer membrane.[190] Similarly, DOPC vesicles were decorated with Eu^{III} in a mixed-phase bilayer using embedded cholate units, **53**, and luminescence sensitised by various membrane-encapsulated chromophores. Others have shown that Ln^{III} decoration can also dictate the morphology of membranes formed.[191]

Fiore and co-workers showed the PEGylated dipicolinic acid conjugate, **54**, self-assembled into spherical nanoparticles and in the presence of Eu^{III} or Tb^{III} ions gave rise to strong luminescence.[192] Unlike the hydrophobic cores of the previous examples the Ln^{III} ions were embedded within the interior of the particle and the PEG chains forming the external coating, as shown in Figure 1.20b. The coordinating amphiphilic block copolymer formed both solid spherical particles (micelle-like) and vesicles with sizes variable between 20 – 66 nm. The micelles and vesicles were stable for multiple weeks and the driving force was suggested to be the amphiphilic interactions rather than the Ln^{III} coordination itself.

The inclusion of luminescent Ln^{III} complexes within soft matrices other that amphiphilic systems can result in soft assemblies and, eventually, soft materials. Ionic liquids have served as suitable alternative solvents often providing enhanced luminescence quantum yields.[193-198] Thermotropic liquid crystals (LCs) are unique soft matter phases closely related to amphiphilic assemblies and lyotropic phases[199] into which Ln^{III} complexes have also been successfully integrated.[195,200,201] The design of lanthanidomesogens[202] is a unique challenge given clashes arising between the relative bulk of the Ln^{III} coordination sphere with calamitic and discotic LC phases requiring rigid rod- and disc-like mesogens, respectively. However, substitution and grafting of Ln^{III} binding motifs with extended alkyl

chains (*e.g.* $C_{10} - C_{18}$) have been used to impose anisotropy and a large range of mesophases have been achieved including smectic,[203,204] columnar[205] and nematic phases.[206-208]

The dynamic assembly of Ln^{III}-based materials can rather be achieved through reversible and directed coordination of monomer ligands containing multiple binding sites. These extended and/or ordered structures form the class of materials characterised as supramolecular and coordination polymers.

1.6.2 Supramolecular coordination polymers

Metallo-supramolecular polymers are dynamic and reversible supramolecular polymers that form due to the coordination interactions of multidenate monomers.[209] The process of supramolecular polymerisation of ditopic ligands and Ln^{III} ions is shown schematically in Figure 1.21. The sequential coordination of the terminal binding sites results in a growth of a extended 'polymer' chain with each ditopic ligand acting as a monomer. Depending on the coordination requirement, or degree of saturation, of the metal sites independent 1D polymers or cross-linked chains may form, particularly in the case of tripodal monomers[209]. Rehahn described metal-containing polymers in three classes[210] dependent on the nature of the polymer chain and coordination sites. Supramolecular coordination polymers as described above are classed as Type II metallopolymers (which are equivalent to Wolf's Type-III classification[211,212]) while Rehahn Type I and Type II polymers are based upon classical organic polymers and discussed in Section 1.7 below.

A large number of coordination polymers or Ln^{III}-organic frameworks have been reported using small monomers in hard crystalline materials[213-221] or deposited thin films[222,223] for static emission or responsive applications. Stanley and Holliday have given a recent overview of progress in luminescent Ln^{III} supramolecular metallo-polymers and the field continues to develop rapidly in both hard and soft mateirals.[224-227]

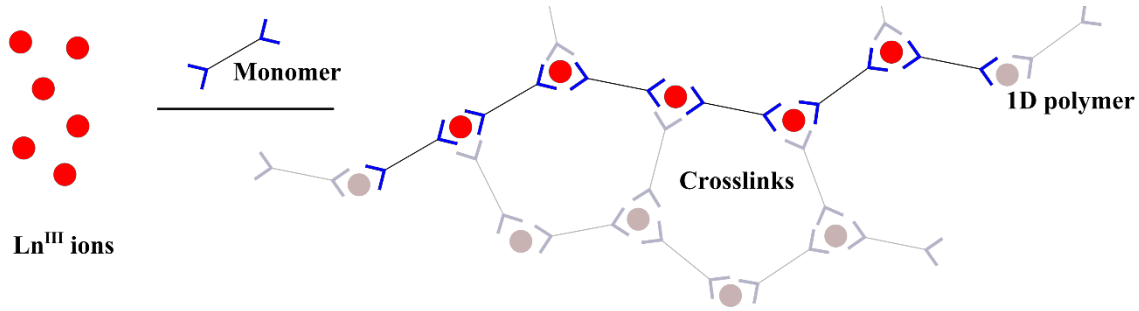

Figure 1.21 Schematic representation of metallo-supramolecular polymerisation of Rehahn II / Wolf III polymers from Ln^{III} ions (red dots), ditopic monomers (blue units) showing the formation of a bulk 1D polymer (bold chain) from 1D growth and potential crosslinks (faded chains) from tris-complexes formed due to the high coordination number of the Ln^{III} ions.

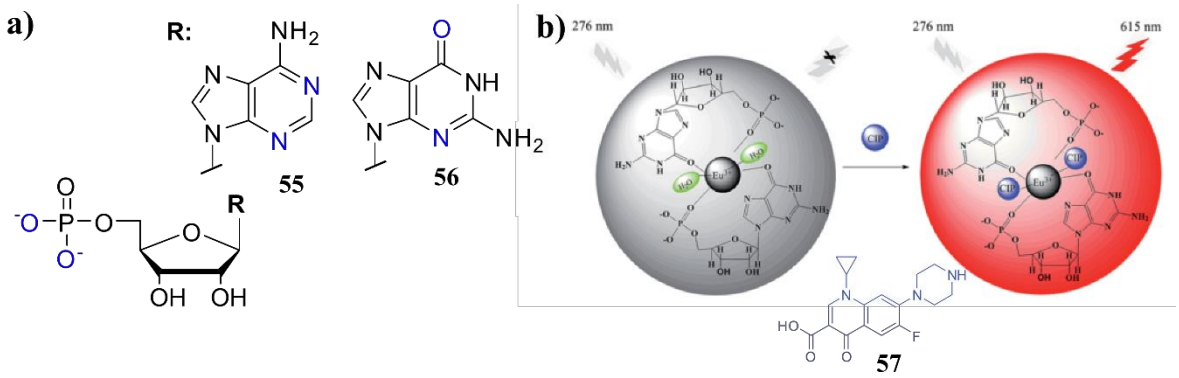

Figure 1.22 a) Structures of AMP (**55**) and GMP (**56**) used in the formation of CP-NPs; and **b)** schematic representation of GMP-based CP-NPs formed by Eu^{III} coordination. A 'switch-on' response to CIP (**57**) occurs due to displacement of H_2O, coordination of **57** and energy transfer to Eu^{III} when excited at λ_{exc} = 276 nm. Reproduced from Ref. 229.

The self-assembly of coordination polymer nanoparticles (CP-NPs) has been used in the generation of sensor arrays. An interesting array of natural ditopic monomers for self-assembled CP-NPs found in nucleotide phosphates such as ATP,[228] AMP **55**, and GMP **56**. Ln^{III} ions can coordinate with both the nucleobase and phosphate units of the monomer resulting in the formation of a coordination polymer formation. Xu and co-workers showed the ability of GMP-Eu^{III} CP-NPs to detect the presence of ciprofloxacin (**57**, CIP), an active medical ingredient of which excessive uptake can result in acute adverse physiological effects.[229] In a simple assay, Figure 1.22b, the self-assembled CP-NPs were initially non-emissive as the Eu^{III} was di-hydrated. Displacement of the coordinated H_2O molecules by **57** allowed CIP→Eu^{III} energy transfer and sensitised emission. As would be expected, the favourable performance of the CP-NPs was accounted for by strong coordination of **57** and a hydrophobic interior to the NP itself. Mao *et. al* used kinetically-assembled AMP-Tb^{III} CP-NPs to sense Cu^{II} ions from biological samples.[230] An antenna was encapsulated within the CP-NPs acting to sensitise the Tb^{III}-centred emission however this antenna was more strongly bound by Cu^{I}, deactivating the antenna sensitisation to give a "switch-off" response.

Independently Huang and Velders have reported the formation of Eu^{III}-driven coordination polymers of ditopic ligand **58**.[231,232] The self-assembly processes were monitored in aqueous solutions to elucidate the dynamic polymer structures formed at different proportions of **58**/Eu^{III} from between 1 and 3 equivalents. The lifetime measurements suggested four *in-situ* structures, Figure 1.23b, consistent with increasing degrees of saturation of the Eu^{III} centres by dipicolinate sites (replacing bound H_2O) extending the luminescence lifetimes. Both groups also showed the encapsulation of the coordination within cationic block copolymer micelles which resulted in quantum yield enhancement and further luminescence lifetime extension. This was not unexpected but

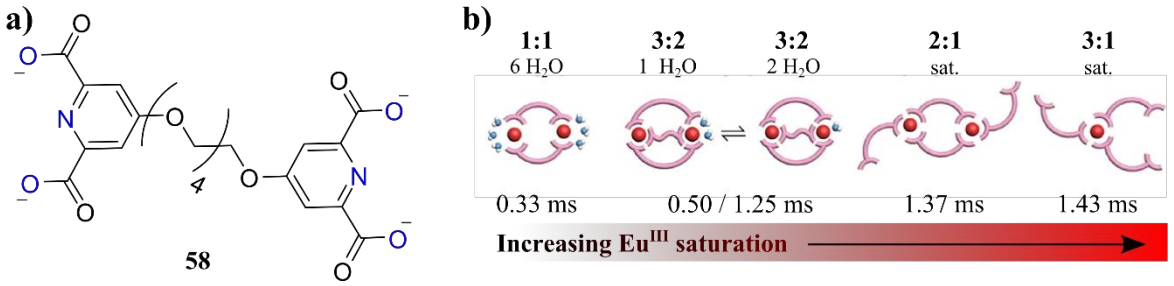

Figure 1.23 a) Structure of ditopic ligand **58;** and **b)** schematic representation of the suggested solution species dominant at various ratios of **58**-to-Eu^{III} and the corresponding luminescence lifetimes recorded. The increasing lifetime was consistent with increasing Eu^{III} saturation by non-water coordinating sites. Reproduced from Ref. 231.

showed consistent behaviour to the micellar systems described in Section 1.6.1 above, and the micelle structures assisted in the exclusion of bound H_2O from the Eu^{III} centres.[233]

Similar ditopic ligands **59**-**60** have been shown by Weder and co-workers beyond solution-based soft assemblies in the formation of solid-state malleable and flexible metallopolymers. Earlier examples employed the poly(*p*-xylylene), **59**, linearly polymerised through Zn^{II}, Fe^{II} or La^{III} coordination (**ML_2** stoichiometry) and crosslinked by La^{III} complexes (**ML_3** stoichiometry).[234,235] However, lanthanide luminescence was not exploited with examples limited to non-emissive La^{III} ions and the material colour was dictated by the *d*-metal complexes, as shown in Figure 1.24b. The thermal stability of the resulting material was shown to depend on the counter anions with triflate or bis(triflimide) offering greater stability than the perchlorate salts.[234]

Rowan and Balkenende the use of Eu^{III} and Fe^{II} coordination for polymerisation of **60** was shown.[236] Similar solid materials to the poly(*p*-xylylenes) could be formed with the telechelic poly(ethylene-*co*-butylene) linked monomer **60**, Figure 1.25a. Again, the Fe^{II} complexes acted to direct linear growth of the metallopolymer chains while Eu^{III} acted as a crosslinking agent forming **ML_3** complexes. In this case, the material was luminescent, Figure 1.24d, and characteristic Eu^{III}-centred luminescence was used as an optical probe for crosslink dissociation under mechanical stress, showing quenching upon exposure to ultrasonic pulses (and thus dissociation of the coordinating antennae from the Eu^{III} ions). The recovery and self-healing was also observed in the luminescence intensity of Eu^{III} emission at 615 nm, Figure 1.24c. This ultrasound- and thermally- initiated dissociation and the self-healing effects allowed for discrete polymer films to be welded together, Figure 1.24e, with the welds showing reasonable robustness to strain. The solid polymers were swellable in CH_3CN solutions with the polymerisation complexes remaining stable in the presence of other metal ions (*i.e.* Fe^{II}) and may be considered therefore to be 'gel-like' in nature, although the authors did not assess this directly.

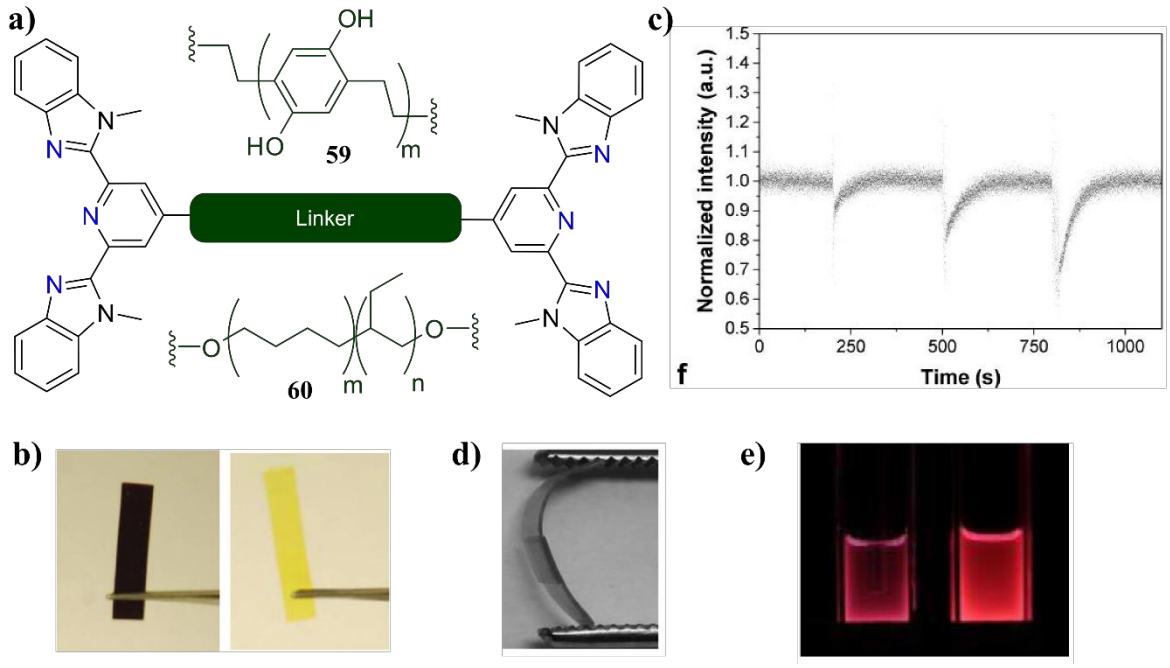

Figure 1.24 a) Structures of ditopic **bbpy** ligands **59** and **60** with different polymeric spaces; **b)** supramolecular polymers of **59** with Fe^{II}/Ln^{III} (left) and Zn^{II}/Ln^{III} (right) showing different optical properties dominated by the transition metal, Ref. 234; **c)** Eu^{III} luminescence quenching and recovery of supramolecular polymers of **59** with Zn^{II} and Ln^{III} upon treatment with ultrasound for increasing periods; **d)** welding strength of supramolecular polymers of **60** with Zn^{II}/Ln^{III}; and **e)** characteristic Eu^{III}-centred emission from supramolecular polymers of **60** with Zn^{II}/Eu^{III}. Reproduced from Ref. 236.

1.6.3 Self-assembled soft gel materials

Gels form sets of soft matter that are characterised by intertwined and, mostly, fibrous networks of molecules that form a bulk material while encapsulating a solvent environment. The structures of gelators may be classed as *organo*- or *hydro*-gelators depending on whether they gel organic or aqueous solutions. There has been much interest in designing low-molecular-weight gelators that act at very low concentration, are robust and biocompatible, and that are functional or responsive.[237] Ln^{III} luminescence has found some utility within this field to provide optical response.

The ditopic ligand **61** (comparable to **59** and **60**, above) was reported by Rowan and co-workers to act as a small molecule organogelator for CH_3CN.[238] Gels were generated from CH_3CN at *ca*. 11 wt% incorporating transition metal and Ln^{III} ions at 95% and 5%, respectively. Robust gels were formed, Figure 1.25b, with yield stresses of *ca.* 160 Pa. The materials were 'self-healing' and recovery speed varied with solvent content while more dilute gels recovered slower. Various other features included thermo-response (*i.e.* the gel was reverted to solution upon heating) and chemo-response (*i.e.* the gel structure was destroyed by the addition of formic acid or TBA perchlorate). The luminescence properties corresponded with the gel formation, where **61**:Zn/La showed blue ligand fluorescence and strong Eu^{III}-centred emission was observed in the static gel of **61**:Zn/Eu. The chemo- or

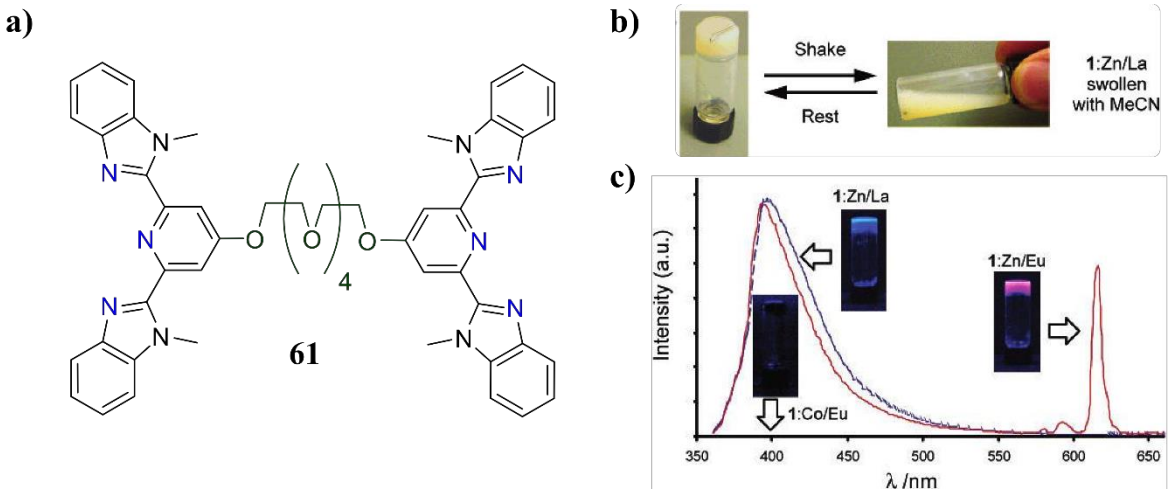

Figure 1.25 a) Structure of a ditopic **bbpy** organogelator, **61**; **b)** organogels formed from **61** at 11 wt% in CH_3CN showing resistance to flow in inversion testing and thixotropic behaviour on agitation by shaking; **c)** emission spectra and 'naked-eye' emission of various co-metallic CH_3CN gels of **61** showing Eu^{III} emission quenching in Co^{II}/Eu^{III}, blue ligand fluorescence for Zn^{II}/La^{III} and characteristic red emission in Zn^{II}/Eu^{III}. Reproduced from Ref. 238.

thermo- stimulated systems showed quenched Eu^{III}-centred emission due to larger chromophore-Eu^{III} distances consistent with fewer coordination polymer crosslinks being present. Interestingly, the **61**:Zn/Eu and **61**:Zn/La gels were found to be thixotropic- upon shaking the material was not completely reverted to sol but was able to flow and then reform on resting. This behaviour was accounted for by the gel network being constructed as a secondary structure from CP-NPs or flocs at lower shear stress (low shear velocity or static conditions) which then break down into smaller aggregates under higher shear stress allowing continuous deformation or flow.[239]

Maitra *et.* al. described a range of cholate hydrogels showing Eu^{III} or Tb^{III}-centred luminescence. The cholate derivative **53** was previously demonstrated in vesicle formation, Figure 1.18b above. Hydrogel matrices were formed from **53**.$\mathbf{Eu^{III}}$ and **53**.$\mathbf{Tb^{III}}$ giving an intertwined fibrous network and was characterised by TEM and SEM, Figure 1.26a. Encapsulated within the fibres were non-coordinating antenna such as pyrene[240] or 2,3-dihydroxynaphthalene[241] **62**, and despite not being covalently bound to the Eu^{III} or Tb^{III} ions these chromophores acted as antennae to sensitise weak red and strong green metal-centred luminescence, respectively. Indeed, varied molar ratios of Eu^{III} and Tb^{III} in mixed gels allowed mixing of RGB colours to achieve blue, green, yellow or purple emissions, as shown in Figure 1.26b. The 100% Eu^{III} gel gave weak metal-centred emission and the overall colour dominated by blue antenna fluorescence while the Eu^{III}-centred emission was in fact stronger in mixed gels of Tb^{III} and Eu^{III}. Therefore, the mixed gels gave rise to yellow and red luminescence from the gels at Tb^{III}:Eu^{III} ratios of 49:1 and 4:1, respectively, due to internal $Tb^{III} \rightarrow Eu^{III}$ energy transfer sensitising the red emission.

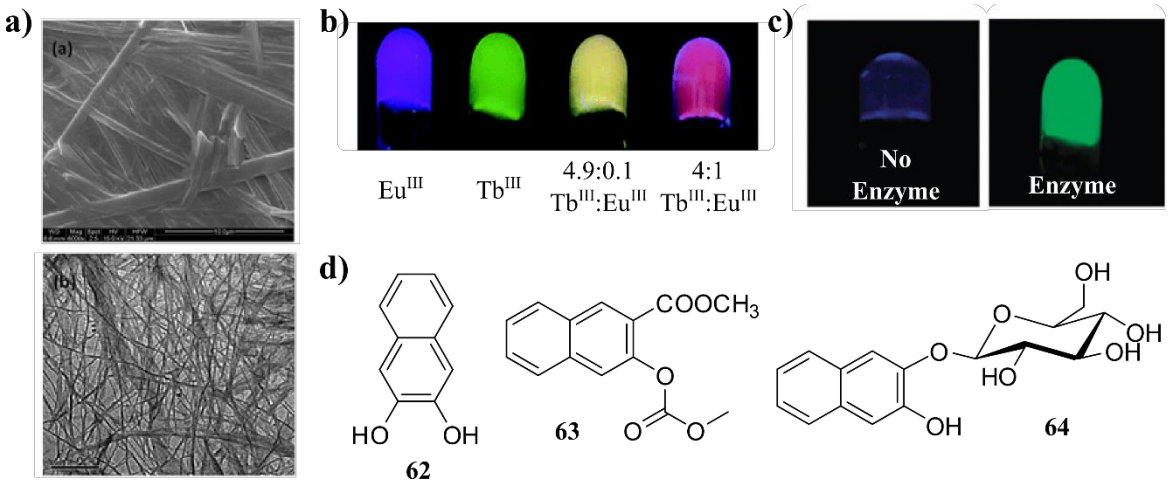

Figure 1.26 a) SEM (top) and TEM (bottom) images of cholate gels formed from **53** and doped with Eu^{III} or Tb^{III} and **62** showing a fibrous network, Ref. 240; **b)** colour of gels to the 'naked eye' in **[Eu.(53)]**$^{2+}$, **[Tb.(53)]**$^{2+}$ and mixed gels showing efficient Eu^{III} sensitisation due to Tb→Eu energy transfer, Ref. 241; **c)** 'switch on' response of **[Tb.(53)]**$^{2+}$ hydrogels doped with pro-sensitiser **63** in the presence of lipase, Ref. 244; and **d)** structures of chromophore **62** and pro-sensitisers for enzyme assays of lipase (**63**) and β-glucosidase (**64**).

Tb^{III}-cholate gels have been diversely applied.[242,243] For example, soft materials responsive to enzyme activity were developed in which novel 'pro-sensitisers' were designed for enzymatic transformation and subsequent activation of the antenna chromophores. Maitra also designed 'pro-sensitiser' **63** for β-lipase as it was initially found to be unsuitable to sensitise Tb^{III}-centred emission. However, upon cleavage of the esters to generate **62** the chromophore became active and Tb^{III}-centred emission could be switched on.[244] This simple assay was also developed for β-glycosidase in which **64** was synthesised as a 'pro-sensitiser'.[245]

Similarly, other small molecules have been shown to be appropriate for luminescent Ln^{III}-containing hydrogels. Liu and co-workers generated the hybrid supramolecular hydrogel from bolaamphiphile **65** and isophthalic acid **66** doped with Eu^{III} ions.[246] Transparent, colourless gels were achieved that were mechanically responsive with

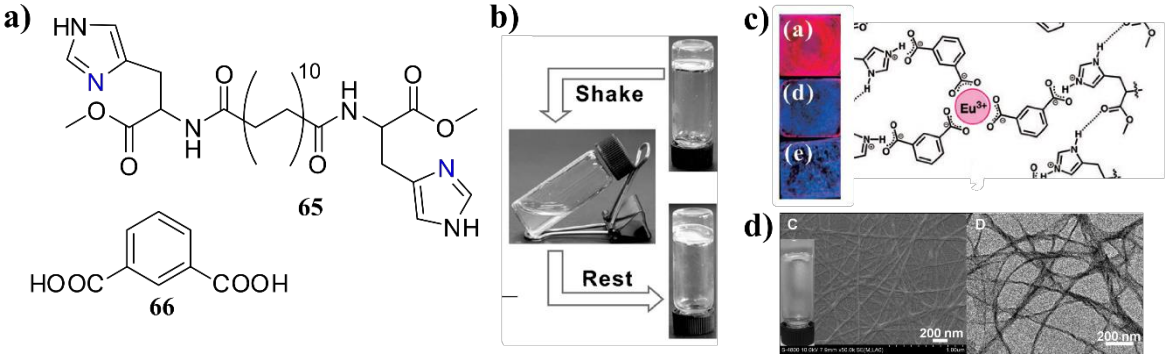

Figure 1.27 a) Structures of bolaamphiphile **65** and **66**; **b)** photographs of physical hydrogels of **65** and **66** doped with Eu^{III} ions showing gelation resistant to inversion and mechanical reversibility; **c)** red emission visible to the eye from deposited gels and schematic representation of proposed gelation mechanism from **[Eu.(66)$_3$]** crosslinks; and **d)** SEM (left) and TEM (right) images of the fibrous gel network formed. Images reproduced from Ref. 246.

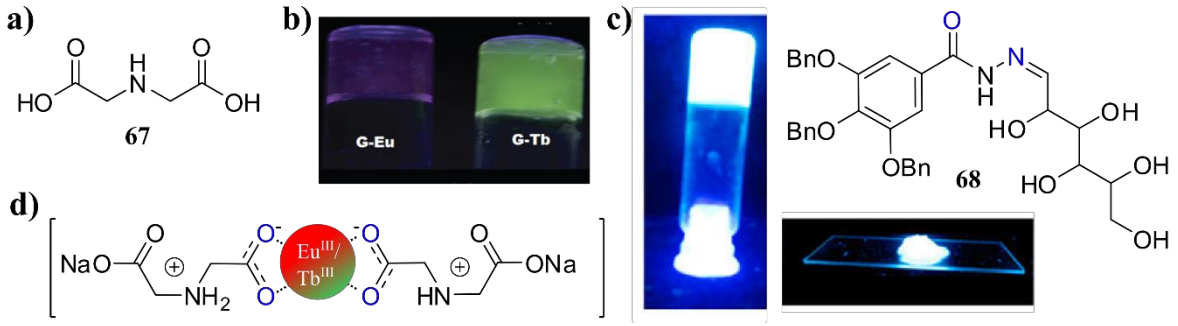

Figure 1.28 a) Structure of iminodiacetic acid, **67**; **b)** Eu^{III} and Tb^{III} hydrogels of **67** showing weak Eu^{III} emission and strong Tb^{III} emission on direct excitation, reproduced from Ref. 247; **c)** proposed gelating dimer responsible for hydrogels of **67**; and **c)** structure of dendron ligand **68** and Eu:Tb mixed hydrogels resulting in white-light emission from Eu^{III}/Tb^{III} emissions and blue antenna fluorescence. Reproduced from Ref. 248.

thixotropic nature, Figure 1.27b, however the Eu^{III} doping resulted in characteristic red emission when irradiated with UV-light (λ_{exc} = 254 nm), Figure 1.27c. The gels were shown by SEM and TEM to consist of interconnected molecular fibres as expected of classical molecular gels, Figure 1.27c, formed by the supramolecular polymerisation of **65** through the bridging of amphiphilic assemblies with $\mathbf{(66)_2}$ carboxylate dimers. However, it was suggested that a number of these $\mathbf{(66)_2}$ bridges are formed as **66**-Eu-**66**, shown schematically in Figure 1.27c, with **66** also acting as an appropriate sensitising antenna for Eu^{III}-centred emission accounting for the luminescence properties.

Da Silva *et. al* also used carboxylates to form the first LMW hydrogels containing Eu^{III} and Tb^{III} from the simple iminodiacetic acid **67**. In this case it was also suggested that carboxylate-Ln^{III} dimers corresponded to the monomer gelator.[247] The pure Eu^{III} and Tb^{III} hydrogels, shown in Figure 1.28b, were formed with characteristic luminescence following direct excitation of the Ln^{III} ions rather than incorporating a sensitising antenna, and mixed $\mathbf{(67)_2.Eu^{III}_{0.5}Tb^{III}_{0.5}}$ gels showed excitation-wavelength-dependent emission colours; the system was highlighted as a potential precursor for a full colour system.

Prasad and co-workers in fact showed a full colour system from the dendron **68**-based hybrid hydrogels.[248] A single hydrogel containing both Eu^{III} and Tb^{III} ions which was doped with three sensitising chromophores (pyrene, **phen** and napththalene) gave white-light, as shown in Figure 1.28c; blue emission was due to antenna-centred fluorescence and incomplete energy transfer.

Additionally, hybrid or blended gels including hydro-[249] and organo-gels,[250] liquid-crystalline physical gels[251,252] or ionogels[201,253] have been reported directly doped with luminescent lanthanide complexes which take advantage of distinct properties of discrete materials. Among the Ln^{III} luminescent LMW organogels reported,[152,254,255] Kim and Chang generated white-light emitting organogels of *n*-decane using ligand **69**.[256] Organogelating

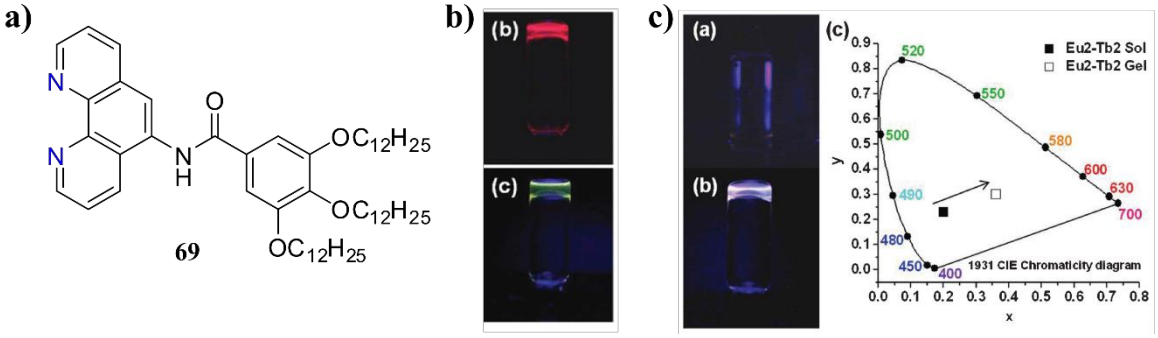

Figure 1.29 a) Structure of super-organogelator **69**; **b)** Eu^{III} (top) and Tb^{III} (bottom) based gels formed in *n*-decane at <1 wt% **69** showing robustness to inversion; and **c)** mixed Eu^{III}:Tb^{III} gels of **69** in *n*-decane showing white-light emission; and **d)** CIE colour diagram showing absolute colour shift between the mixed Eu^{III}:Tb^{III} with **69** in solution and gel showing red to white shift. Images reproduced from Ref. 256.

complexes of **Ln.(69)$_2$** were formed with β-diketonate auxiliary ligands (Ln = Eu^{III}, Tb^{III}) and stable gels synthesised at super-gelator concentrations 0.4 – 1 wt% in *n*-decane. The pure Eu^{III} and Tb^{III} gels were strongly emissive with characteristic red and green luminescence, respectively, as shown in Figure 1.29b, while mixed **Eu.(69)$_2$:Tb.(69)$_2$** gels gave white-light emission, Figure 1.29c. Interestingly, the equivalent solutions were not strongly emissive while the corresponding gels showed strong metal-centred luminescence-demonstrating the sensitivity of the photophysical properties to the local environment, Figure 1.29c. In fact, variation in sensitisation efficiency was observed in different organic solvents (*i.e.* toluene, chloroform, *n*-decane).

The enhancement of luminescent properties and the generation of composite or blended materials has been noted in small-molecule self-assembly but also to similar success in organic polymer-derived matrices and form a distinctive collection of materials.

1.7 Organic polymer-based luminescent Ln^{III}-containing materials

Luminescent Ln^{III}-containing materials based on organic polymer chains fall into two classes of metal-containing polymers as defined by Rehahn[210] – Type I and Type III, Figure 1.30a and Figure 1.30b, respectively, while Type II are the supramolecular metallo-polymers

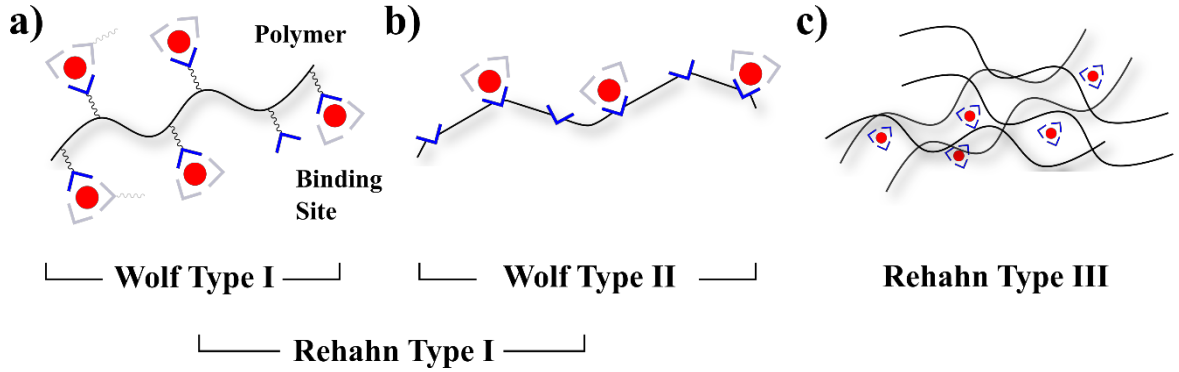

Figure 1.30 Schematic representations of metallo-supramolecular polymers formed from classical organic polymers: **a)** Rehahn Type I / Wolf Type I with grafted binding sites; **b)** Rehahn Type I/ Wolf Type II with binding sites intrinsic to the polymer backbone; and **c)** Rehahn Type III with doped Ln^{III} complexes included within the polymers non-covalently.

discussed in Section 1.6.2 above. Type I polymers are those in which an organic polymer chain has been covalently-functionalised with binding sites suitable for metal binding and allow immobilisation of complexes on the polymer, or indeed act as a crosslink between polymer chains. On the other hand, Type III polymers are those in which the inclusion of the metal complexes is purely physical and the interactions between polymer chains non-covalent and non-coordinative in their nature.

1.7.1 Hard Ln^{III}-doped polymer films and assemblies

Type III metallo-polymer materials with homogenously distributed, non-covalently included (doped) luminescent Ln^{III} complexes have been reported widely in the last two decades.[257] The motivation behind these approaches has been the early and persistent observations of photophysical optimisation and luminescence enhancement in Ln^{III} complexes embedded within polymer matrices.[258] Moreover, the use of blended materials and doped polymers has tended to offer improved mechanical and thermal properties with respect to flexibility, ability to be processed and often thermal stability, while retaining photoactivity.[259] In fact, a great deal of attention has been placed on poly(methyl methacrylate) (p(MMA), **70**) as the dopant matrix. This interest can be assigned to various factors including a low cost, high optical transparency, facile preparation as well as other optical properties. p(MMA) has been shown to be resistant to high energy excitation and has a tuneable refractive index dependent on molecular weight.[260]

Numerous ligand types and structural variations have been included in p(MMA) films. Classical β-diketonate ligands, for example, were used as early dopants with quantum yield enhancements of up to 150% reported.[261-265] Zhang and co-workers have shown the emission enhancement of Eu^{III} complexes doped (5 wt%) with dibenznoylmethide **71** and **phen** in p(MMA) and also demonstrated the co-doping with other Ln^{III} (Ln = La, Gd, Dy,

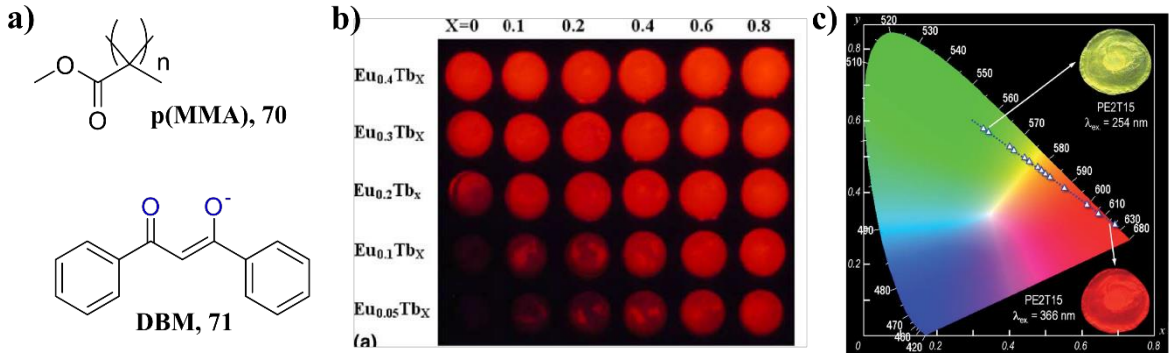

Figure 1.31 a) Structures of p(MMA) (**70**) and antenna DBM (71); **b)** emission visible to eye from p(MMA) doped with **71** and Eu^{III} and Tb^{III} in various ratios showing poor sensitisation of Eu^{III} by **71** but enhanced emission from Tb→Eu energy transfer with increasing Tb^{III} content; **c**) CIE colour diagram showing variable colour output (green to yellow to red) from the p(MMA) films dependent on excitation wavelength (λ_{exc} = 254 – 366 nm). Reproduced from Ref. 262.

Y, Ce, Tb) ions to further enhance Eu^{III}-centred emission by resonance energy transfer.[261,266] The co-dopant complexes of Tb^{III} were shown to enhance luminescence intensity by >20-fold in both cases, Figure 1.31b, and was accounted for by the well-established $Tb^{III} \rightarrow Eu^{III}$ energy transfer process.

Malta and co-workers characterised a similar system and doped p(MMA) with simple β-diketonate complexes of Eu^{III} and Tb^{III}, **[Eu.(tta)$_3$.(H$_2$O)$_2$]** and **[Tb.(acac)$_3$.(H$_2$O)$_2$]**, respectively.[262] The polymer matrix was responsible for an emission enhancement which is most realistically explained by exclusion of the bound H_2O molecules from the coordination sphere by p(MMA) carbonyls. Again, $Tb^{III} \rightarrow Eu^{III}$ energy transfer *via* the **tta**-centered T_1 excited was observed. Moreover, the emission colour was tuneable across yellow, green and red areas of CIE colour space, Figure 1.31c. A key advantage of the p(MMA) films was shown in improved photo-stablity under extended irradiation with UVA (λ_{em} = 254 nm) and UVC (λ_{em} = 330 nm), after prolonged exposure showed recovery of Eu^{III} emission; this was assigned to photo-initiated surface modification of the matrix.

Bünzli and Biju also showed the Eu^{III} complexes of the tetrapodal β-diketonate **72** within p(MMA) employing similar doping (4 wt%) and demonstrated substantial total quantum yields of 67 – 69%.[267] A dimeric, dinuclear stoichiometry was predicted within the matrix and accounted for some of the largest total quantum yields reported. In addition to the generation of bulk films, the doped p(MMA) was electrospun into uniform fibres suitable for further device fabrication and which, importantly, retained the same luminescence properties. Moreover, both the bulk doped p(MMA) films and spun fibres were emissive under ambient sunlight and Eu^{III}-centred luminescence observed without the need for intense

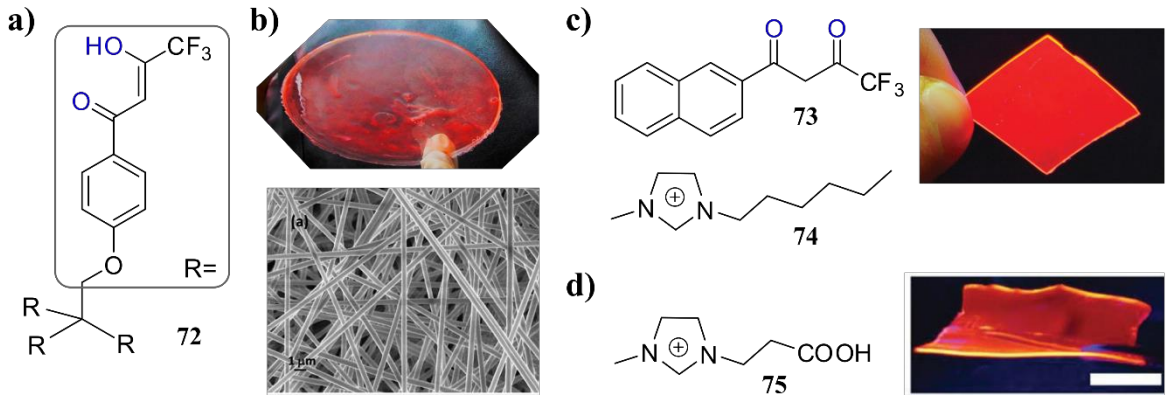

Figure 1.32 a) Structure of tetrapodal β-diketonate **72**; **b)** *top:* monolithic p(MMA) fabricated with **[Eu.(72)$_4$]**$^-$ as dopant showing characteristic red Eu^{III}-centred emission sensitised under ambient light, *bottom:* SEM image of the fibrous network of polymer chains, Ref. 264; **c**) structures of **nta** (**73**) and ionic liquid plasticiser **74** (left) for p(MMA) and the visible Eu^{III} emission from the resulting flexible film under λ_{exc} = 360 nm, reproduced from Ref. 263; and **d**) structure of IL carb-mim (**75**) and visible Eu^{III} emission from the resulting flexible film under λ_{exc} = 360 nm, reproduced from Ref. 277.

UV irradiation, Figure 1.32b. Indeed, the use of p(MMA) has also been demonstrated to enhance NIR emissive ions readily susceptible to quenching.[268] Bünzli, Jones and Wang have reported independently the utility of p(MMA) to enhance NIR-centred emissions readily susceptible to solvent quenching.[269-276]

While being easily fabricated into films and fibres suitable for optical devices, p(MMA) remains intrinsically brittle, Binnemans *et. al* addressed this for Eu^{III}-doped luminescent materials using the complex **[Eu.(73)$_4$]$^-$** as the p(MMA) dopant but also an ionic liquid plasticiser, **74**.[264] The dry films were synthesised from evaporation of solutions containing **74**-[**Eu.(73)$_4$**] and the plasticiser achieved flexible luminescent films, as shown in Figure 1.32c, that displayed enhancement in Eu^{III}-centred luminescence to the same extent as observed in brittle p(MMA). Li and co-workers also blended ionic liquids and p(MMA) to generate ionogels using **75** containing **[Eu.(tta)$_3$]** and **[Eu.(sal)$_3$]** to achieve similar results, Figure 1.32d.[277]

Others have sought polymer matrices based upon different polymer backbones rather than IL blended materials that mimic the optical properties of p(MMA) while exhibiting unique structural and mechanical properties. Mazzanti and co-workers doped the Eu^{III} complexes of **76** with **tta** ancillary ligands into poly(vinyl acetate) (p(VA), **77**) and found equivalent photophysical enhancement to those in p(MMA) films with total quantum yield showing a 3-fold enhancement compared to solid samples, Figure 1.33a.[278] Again, this phenomenon was rationalised in p(VA) due to displacement of the two H_2O molecules coordinated to Eu^{III} by polymer carbonyl groups; in p(VA) this interaction can be expected

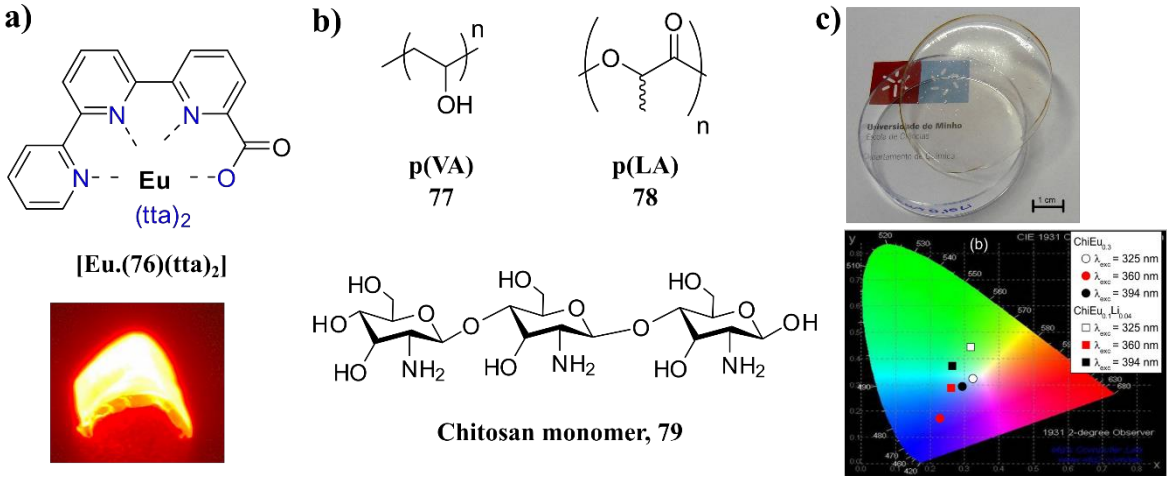

Figure 1.33 a) Structure of **[Eu.(76)(tta)$_2$]** and photograph of the strong Eu^{III}-centred emission visible to eye upon UV irradiation of a flexible p(VA) doped film, reproduced from Ref. 278; **b)** Structures of various polymers **77-79** reported as doping matrices for luminescent Ln^{III} complexes; and **c)** transparent chitosan **79** polymer doped with Eu^{III} complex **40** at 30 mol% (top) and the CIE colour of the emission showing excitation wavelength dependent emission across the spectrum of blue to green; white-light was emitted at λ_{exc} = 325 nm. Images reproduced from Ref. 291.

to be strong from acetate carbonyls compared to ester. It was also interesting to note that the ternary [**76.(tta)$_2$**] complexes were not dissociated under the influence of the polymer matrix. Unlike the p(MMA) films, however, the doped p(VA) were flexible under varied concentrations of dopant (1 mM to 5 mM) and in films prepared from THF solutions at 5% and 10% w/w. The flexibility of the films highlights them as being more appropriate for large-area optoelectronics.[279]

Over time there have been gradual progression in the selection of polymer matrices motivated by application and processability which showed enhancements compared to the equivalent p(MMA) and complex co-polymers.[280,281] Garcia-Torres and co-workers explored systematically the influence of different acryl, vinyl, styrene and urethane polymer matrices on the photophysical performance of Eu^{III} complexes elucidating a complex balance of factors such as rigidity to the behaviour.[282-284] Conjugated polymer matrices of various types that may participate in the Ln^{III} sensitisation process have been employed for Eu^{III}-based photo-[285] and electro- luminescence[286-288].

The drive for tissue engineering polymer materials has led to the exploration of biodegradable as well as 'eco-friendly' and natural polymers.[289] Indeed, luminescent Eu^{III}-containing materials of this type have been shown in the generation of biodegradable fibres of p(LA), **78**, doped with the classical Eu^{III} emitter **40**.[290] The use of chitosan (**79**) has been reported as a biodegradable polymer host for Eu^{III}-centred emission to give flexible transparent films with tuneable emission dependent on dopant and excitation wavelength. However, quantum yields were severely limited (*ca*. 2%) compared to p(MMA) and related synthetic polymers due to the quenching by –OH oscillators within the matrix.[291]

While the development of these polymer films has mostly been driven for light emitting, particularly white light,[292] and solar concentration applications[46] there have also been efforts towards their use as probes and sensors. Doped p(MMA) films have been suggested as biocompatible temperature dependent probes, for example the Eu^{III} complex **40** was used as a dopant in p(MMA) and the Eu^{III}-centred emission calibrated against temperature.[293] A mostly linear response with temperature across the broad range of 50 to 320K was observed which operated with sensitivities at 1% and 1.75% below and above 298K, respectively, Figure 1.34a.

Thick films of p(MMA) doped with Eu^{III} complexes of **80** were used by Zheng and co-workers to generate anion responsive materials. The complexes and materials were strongly luminescent and underwent large colour changes when exposed to F^- dosages in DMSO solution varying between red, purple and green emission, as shown for DMSO

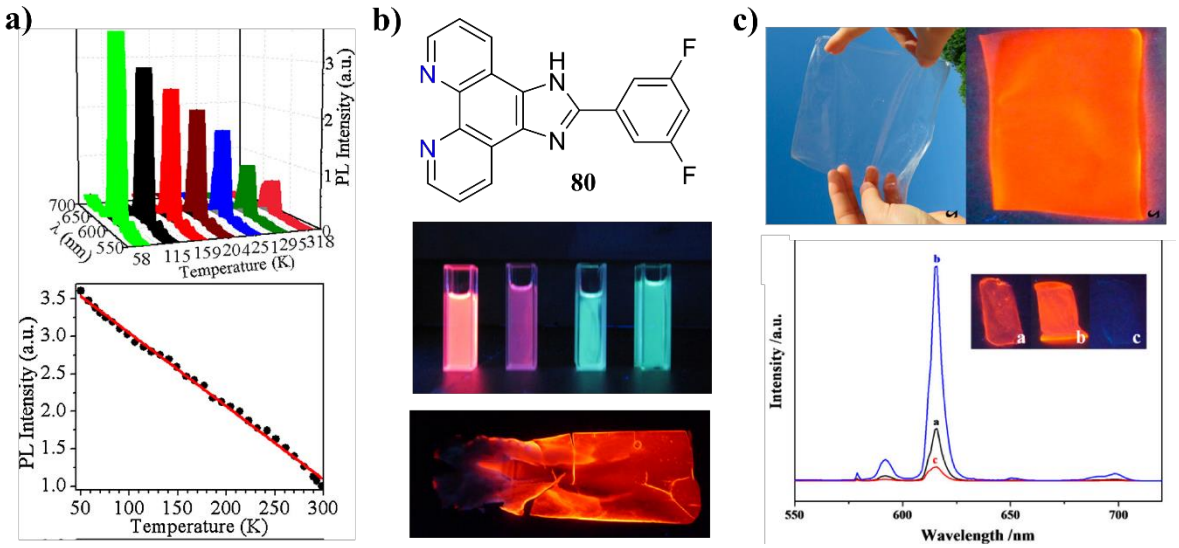

Figure 1.34 a) Luminescence response of p(MMA) doped with Eu^{III} complex **40** (*top*: full spectrum, *bottom*: intensity at λ_{em} = 615 nm, showing linear response between 50 and 300 K, Ref. 293; **b)** *top:* Structure of imidazole-**phen** ligand **80**, *middle:* luminescence response of **[Eu(80)(tta)$_2$]$^+$** in solution upon exposure to TBAF showing clear colour changes (λ_{exc} = 360 nm) with increasing equivalents, *bottom:* p(MMA) film doped with **[Eu(80)(tta)$_2$]$^+$** following immersion in DMSO showing structural damage to the film by solvent, Ref. 295; and **c)** *top*: Chitosan films doped with **[Eu(tta)$_3$]** under ambient (left) and UV (right, λ_{exc} = 360 nm) light showing transparent and emissive properties, respectively, *bottom:* emission spectra and 'naked eye' colour of doped films exposed to Et_3N vapour (b) and HCl vapour (c) showing 'switch on' and 'switch off' responses, respectively. Images reproduced from Ref. 296.

solutions in Figure 1.34b. However, the materials were mechanically unstable upon exposure to DMSO, as clearly seen in Figure 1.34b (bottom panel), and were critically damaged by the solvent exposure.[294,295]

Responsive thin films were more effectively generated from an ionic liquid-blended chitosan polymer by Yang *et. al* where Eu^{III}-centred luminescent responses to HCl/Et_3N vapours were achieved.[296] Simple **[Eu.(tta)$_3$]** complexes were doped within the chitosan films providing strong Eu^{III}-centred emission under basic conditions, as shown in Figure 1.34c. The exposure of the films to HCl vapours resulted in the 'switch-off' of Eu^{III}-centred luminescence through a dissociative mechanism in which the strong H^+ activity results in destabilisation of the complexes. Furthermore, the films were physically robust, optically transparent and flexible while the chemical response reversible and robust to repetitive cycling between Et_3N and HCl vapours.

Non-covalent interactions between the polymer matrix and the Ln^{III} complexes are responsible for the many photophysical enhancements in Type III metallopolymer materials however issues of homogeneity and concentration quenching can arise.[297] To address these problems a number of developments have involved the direct covalent attachment of the ligands and complexes to the polymer.

1.7.2 Polymers containing covalently-attached coordinating sites

Those polymers of Rehahn Type I, Figure 1.30a above, are further subdivided into polymers with metal binding sites tethered to the polymer backbone (Wolf Type I) and those where the coordination site is intrinsic to the polymer chain (Wolf Type II). Piguet modelled the cooperative effects in Wolf Type II systems with polymeric ligands.[298,299] O'Reilly and co-workers used controlled polymerisation to construct MMA, butyl styrene and styrene polymers of the **btp** binding motif, **81 - 83**, as shown in Figure 1.35a. The complexation of the resulting polymer ligands with Eu^{III} ions gave 'metallostar' structures with a bright yellow emission which generated colloidal spherical particles *ca*. 240 nm in diameter.[300]

Akcelrud and co-workers synthesised the **tpy** containing conjugated poly(fluorene) polymer **84** and used it to complex Eu^{III} ions with **71** ancillary ligands at *ca*. 37% metal loading.[301] The close spatial proximity of conjugated polymer backbone and Ln^{III} complexes opens the opportunity for electronically coupling and sensitisation energy transfer. Indeed, strong blue poly(fluorene) fluorescence was observed in the neat polymer yet only strong red luminescence observed when coordinated to **[Eu.(71)$_3$]** as a result of polymer-to-Eu^{III} energy transfer. Furthermore, Ln^{III} containing conjugated polymers of this type, and similar, also have interest for electroluminescence.[302,303] Hecht and Weng have also both reported polymers of Rehahn Type I / Wolf Type II using **btp** coordination sites in the generation of Ln^{III} containing soft matter, see Section 1.7.3 below.

The tethering, or *grafting*, of binding sites in Rehahn Type I / Wolf Type I polymer materials has been exploited extensively. Post-synthetic modification approaches were employed by Rocha *et al.* to functionalise genetically encoded elastin-like polymers.[304] The bulk polymers were expressed by genetically modified *E. coli* followed by post-polymerisation attachment of **tpy** coordinating units through standard peptide coupling protocols. The bulk elastin-like polymers **85** were fluorescent under irradiation with UV-light (λ_{em} = 300 -350 nm). However, treatment of the polymers with Eu^{III}, Tb^{III} or Dy^{III} ions

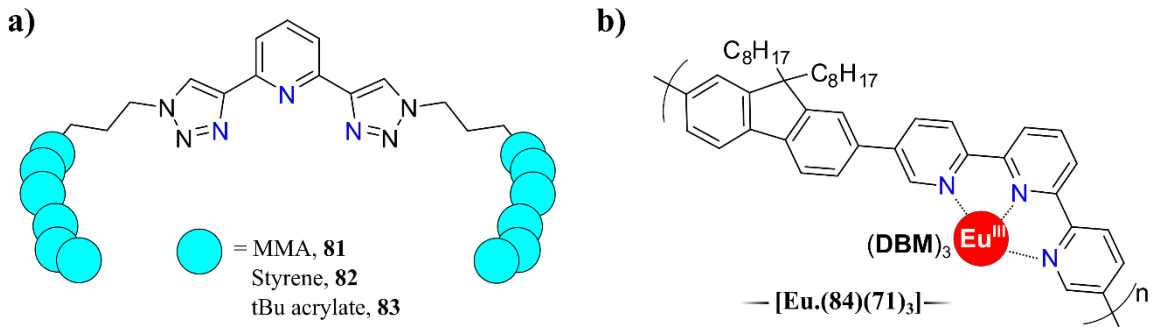

Figure 1.35 Rehahn Type I / Wolf Type II polymers used for Ln^{III}-supramolecular polymers, structures of: **a) 81 - 83**; and **b)** poly(fluorene) polymer **84**.

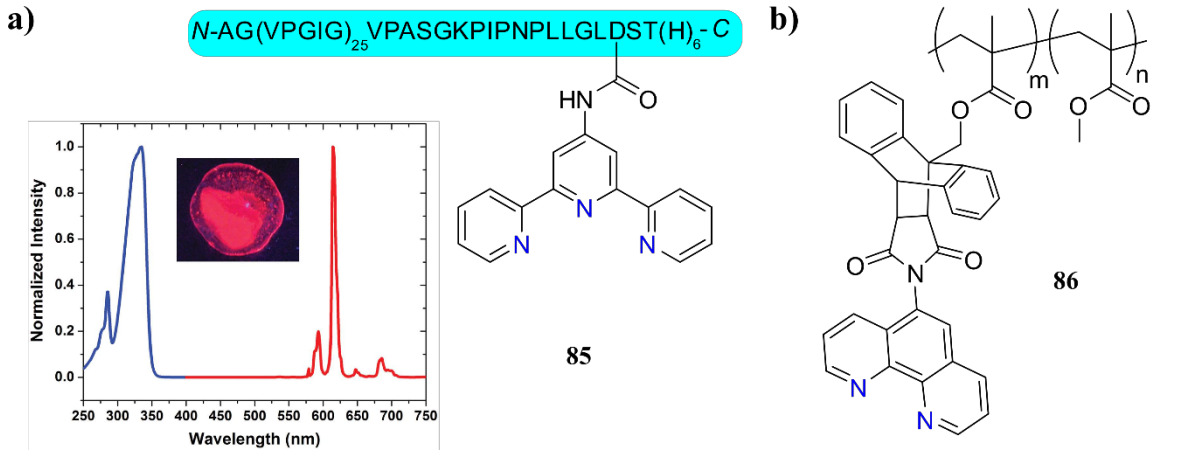

Figure 1.37 a) Schematic structure of **85**, a **tpy**-functionalised elastin-like polymer and the emission spectrum recorded from the resulting Eu^{III} doped polymers, *inset:* inhomogeneity in the distribution of **tpy** sites and corresponding Eu^{III} complexes clearly seen to the 'naked eye', Ref. 304; **b)** Structure of **phen**-derived poly-acrylate polymer formed by post-polymerisation Diels-Alder condensation.

gave rise to dominant Ln^{III}-centred emission (the emission from Eu^{III} was visible, shown in Figure 1.37a). Thin films were generated from spin-coating and drop-casting methods, however the inhomogeneity of these films was clearly evident from the naked-eye emission.

Feng and co-workers also used post-synthetic modification and synthesised p(**86**-*co*-MMA) possessing pendent anthracene units which were subsequently coupled to **phen** derivatives through Diels-Alder (D-A) condensation reactions.[305] Strongly emissive materials were produced upon complexation with Eu^{III} ions and the quantum yields up to 14% were recorded. The authors suggest the D-A post-synthetic modification as a route to optimised in-polymer quantum yields, however it is perhaps more realistic to expect case-by-case absolute changes.

Alternatively, direct co-polymerisation of coordinating ligands carrying pendent polymerisable groups has been used in the synthesis of grafted metallopolymers.[306-310] Binnemans *et al*. took the commercially available PS-based Merrifield Resin and grafted **phen** binding sites to the surface of the polymer beads through facile chemistry from the 5-amino **phen**-derivative to generate decorated beads, **87**. Ln^{III} complexes were formed from

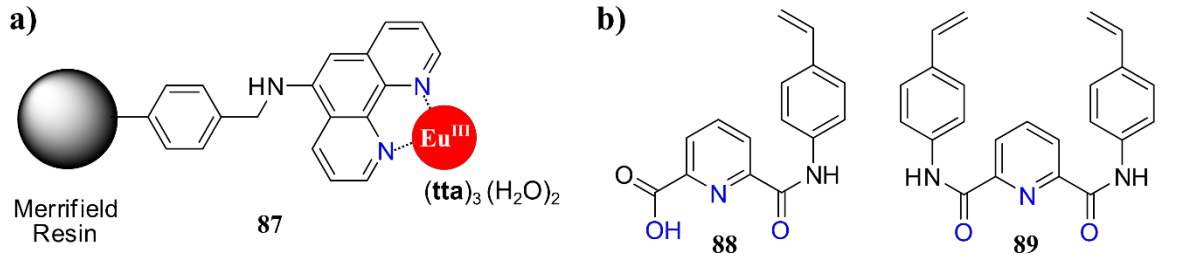

Figure 1.36 a) Schematic structure of Merrifield Resin **87** decorated with amino-**phen** complexes of Eu^{III} with **tta** that give rise to emissive polystyrene beads upon excitation of the **phen** chromophore; **b)** Structures of styrene monomers **88** and **89**, derived from dipicolinic acid copolymerised into polystyrene materials for Ln^{III} extraction.

various ions (Ln = Nd, Sm, Eu, Gd, Tb, Er, Yb) with **tta** ancillary ligands and gave excellent emissive materials in both visible and NIR regions dependent on the selected Ln^{III} ion.[297] Similarly, Chauvin and Bünzli also functionalised PS-based resins by copolymerising dipicolinic acid-based monomers **88** and **89** within bulk PS for the extraction of ^{90}Y and heavy Ln^{III} cations; Eu^{III} luminescence was employed as a spectroscopic probe to characterise the coordination environment within the imprinted polymer.[311] The splitting of $^5D_0 \rightarrow {}^7F_{1,2,4}$ transitions were used to identify D_2 and D_3 symmetry for the model complexes **[Eu.(88)$_3$]** and **[Eu.(89)$_3$]$^{3+}$** respectively. In the case of **88**, lack of broadening on polymerisation and similar spectral structure demonstrated retention of suitable coordination within the PS-material. This was not the case for symmetrical **89** where major distortion of the coordination site was suggested and poor Ln^{III} cation retention observed corresponding with weak Eu^{III}-centred emission intensity.

Jayakannan and co-workers generated an elegant Eu^{III}-based probe for temperature sensing from copolymers of the form of **90** containing oligo(phenylenevinylene) (OPV) and PEG chains.[312] The OPV units acted as sensitising chromophores for Ln^{III} emission while the blended PEG units improved the solubility and ability to process the materials. The polymers **90** in the absence of Eu^{III} were stable, displaying blue emission (characteristic of the OPV chromophore) while in the presence of Eu^{III} the temperature dependent metal-centred emission was observed. The system functioned in both solution (solvents such as chlorobenzene, THF, *p*-xylene) and as deposited films, as shown in Figure 1.38a. In both cases, the red Eu^{III} luminescence was observed at low temperature while upon heating decreased in intensity and a complete 'switch off' effect was observed at ≈ 100 °C; the emission was fully recovered upon cooling. The mechanism of action was determined to be the thermal dissociation of the **[Eu.(90)$_2$]$^+$** complexes and subsequent restriction of **90**→Eu^{III} energy transfer resulting in quenching of sensitised emission. However, the cooperativity of

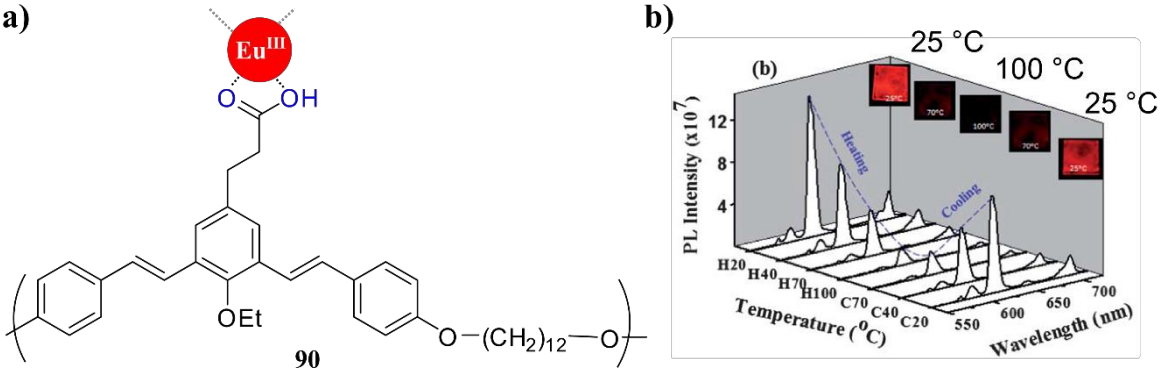

Figure 1.38 a) Structure of temperature sensitive Eu^{III}-appended polymer **90**; and **b)** the temperature responses of deposited films of **[Eu.(90)$_2$]$^+$** between 25 °C and 100 °C showing decreasing intensity with increasing temperature, complete 'switch off' at 100°C and reversible behaviour, graph reproduced from Ref. 312.

the polymer system allowed efficient reversal of the system; indeed, this improved upon problems of low robustness and reversibility in a small molecule system operating on dissociative mechanisms.

The Rehahn Type I, II and III approaches to solution and film metallo-polymers has also been exploited to generate soft matter of various descriptions including polymeric liquid crystals from polymer-based lanthanidomesogens[313-317] and hybrid ionogels.[318] It should be noted that in the examples above homogeneity of the Ln^{III} distribution within the polymer matrices was varied and inconsistent. The distribution was not actively investigated by the authors but this was clear from qualitative inspection of visible emission (*e.g.* **71**, **72**, **85**, **90**). The most homogenous films were observed for the more flexible matrices (*e.g.* chitosan, IL-modified p(MMA) and p(VA)), consistent with the increased solid-state mobility of the polymer chains. Increased homogeneity has also been observed in luminescent Ln^{III}-containing bulk soft gel materials and these are reviewed in the following section.

1.7.3 Polymer-based soft gel materials

Soft matter gels, despite being physically weaker, often provide improved responsive behaviour compared to their solid thin film analogues and demonstrate quicker analyte equilibration times and the corresponding faster response rates.[237,319] Specifically, polymer-based hydrogels and organogels that exhibit Ln^{III} luminescence have been achieved through a number of approaches and offer a range of properties combining unique luminescence and mechanical features.

Alginate, **91**, a polymer of glucuronic acids, has emerged as a candidate for Ln^{III} luminescence hydrogels as a result of their natural gelling ability with cations and abundant pendent $–COO^-$ and –OH groups available for coordination interactions.[320,321] Chen and co-workers used Eu^{III}-carboxylate and Tb^{III}-carboxylate interactions with alginate/polyacrylamide to improve the mechanical performance of the hydrogel materials while also imparting photoluminescent properties to the gels.[322] The alginate/polyacrylate underwent thermo-reversible gelation only in the presence of $EuCl_3$ or $TbCl_3$, as shown in Figure 1.39b, and produced gels that were robust and mouldable. The pure Eu^{III}- and Tb^{III}-containing materials were luminescent following direct-excitation of the metal ions. There were no antenna chromophores present in the polymer chains or doped within the matrix however, the emission from direct-excitation was visible to eye and the colour was tuneable between red, green and yellow dependant on the Eu:Tb ratio selected in mixed systems. Furthermore, the mechanical properties of the Ln^{III}-alginate/polyacrylamide gels were remarkable with extensive tensile and compressive strength (≈ 1 and 3.4 MPa tensile and

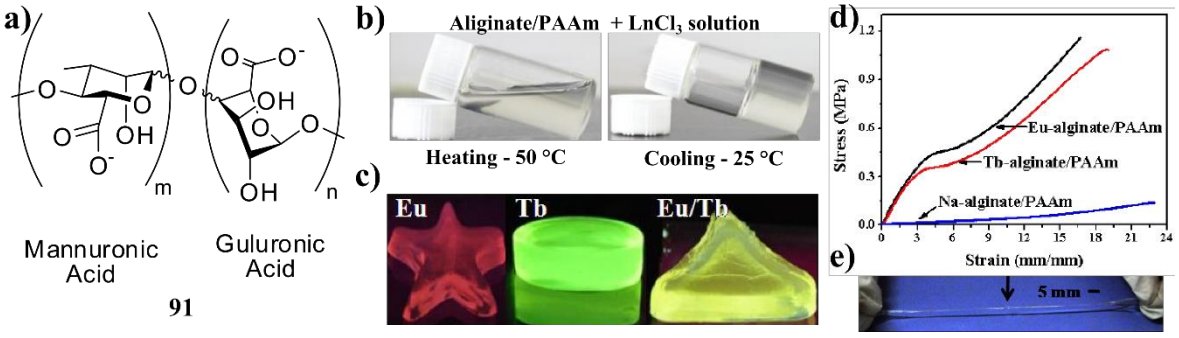

Figure 1.39 a) Structure of alginate, **91**, co-polymer; **b)** thermo-responsive and reversible formation of transparent **91**/polyacrylamide hydrogels from $EuCl_3$ and $TbCl_3$ solutions when cooling from 50 °C to 25 °C; **c)** Eu^{III}, Tb^{III} and mixed Eu^{III}:Tb^{III} doped alginate/polyacrylamide hydrogels under direct excitation conditions showing red, green and yellow emissions, respectively; **d)** Stress/Strain curve for the Eu^{III}, Tb^{III} and un-doped hydrogels showing the mechanical enhancement of Ln^{III} coordination; **e)** tensile extension of a 15 mm sample knotted in the centre of Eu^{III}-alginate/polyacrylamide showing significant robustness. Images from Ref. 322.

compressive moduli, respectively) allowing approximately 20-fold extension prior to yielding. In fact, the materials could be strained extensively even under additional lateral stresses such as knotting as shown in Figure 1.39c.

The 'antenna effect' was employed by Wang and Ma to produce responsive Eu^{III} and Tb^{III} luminescent alginate gels suitable for the detection of the bacterial biomarker dipicolinic acid, **6**.[323] In the same fashion as above, the gels were generated from aqueous solutions of sodium alginate (5% w/v) by the addition of $EuCl_3$ and $TbCl_3$, respectively, at a dopant level of *ca*. 1.5 wt%. Upon exposure of these gels to dipicolinates the Ln^{III}-centred emissions were enhanced with high sensitivity and the emission intensities were doubled following exposure to 10 μM sodium dipicolinate. In fact, LODs were determined *ca.* 80 - 90 nM in the Ln^{III} gels. The mechanism of action was clearly related to the coordination of the dipicolinate to the Ln^{III} centres resulting in both the removal of bound H_2O molecules while simultaneously acting as a sensitising antenna.

Polymer hydrogels have been used by a number of researchers to generate tunable[324] and responsive[325-327] hydrogels exhibiting Ln^{III}-centred luminescence. Hao co-polymerised the vinyl derivatives of dipicolinic acid with p(NIPAM) to generate transparent hydrogels.[328] However, more relevantly Lu[325] and Wang[326] have independently used p(NIPAM) hydrogels as chemosensors for $H_2PO_4^-$ and HSO_4^-, respectively; the probes **92** and **94** are shown in Figure 1.41a and Figure 1.41c, respectively. Both system operated *via* a dissociative mechanism of polymer-bound and doped Eu^{III} or Tb^{III} complexes, respectively, following competitive binding of the analyte anions that resulted in 'switch off' effects in the Ln^{III}-centred luminescence.

Also developing responsive polymer hydrogels, Li *et al*. described a responsive system of poly(2-acrylamido-2-methyl-1-propanesulfonic acid) (PAMPSA, **95**) as the host

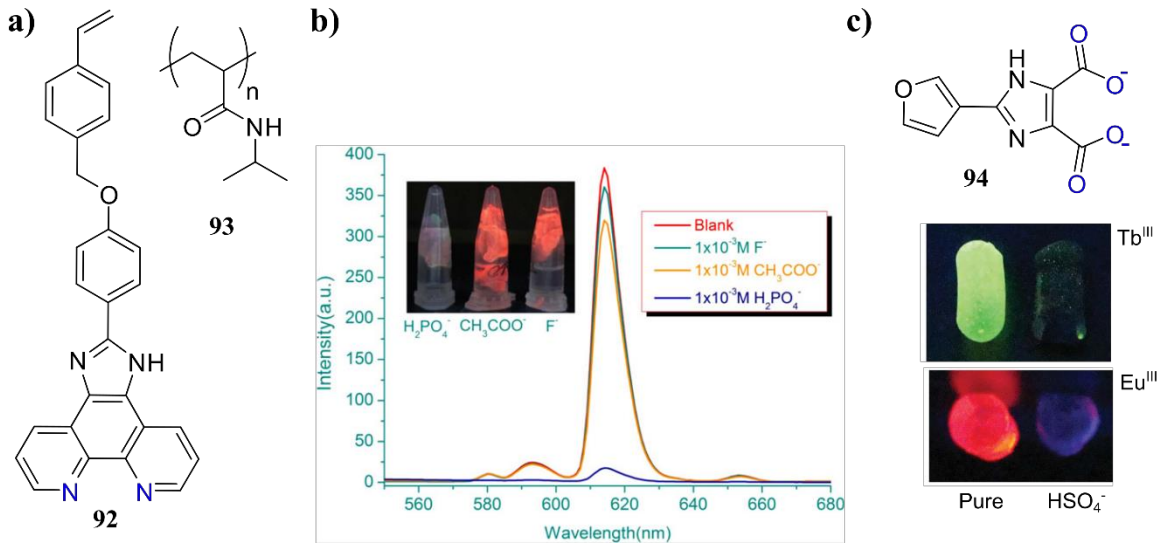

Figure 1.41 a) *left:* Structure of imidazole-**phen** derived styrene monomer (**92**) and p(NIPAM) (**93**) to yield hydrogels; ; **b)** the emission spectra and 'naked eye' appearance of the selective responsive of the hydrogels to $H_2PO_4^-$ over other competitive anions such as CH_3COO^- and F^-, Ref. 324; and **c)** structure of **94** (top) and p(NIPAM) hydrogels doped with **[Tb.(94)$_2$]$^{3+}$** and **[Eu.(94)$_2$]$^-$** (bottom) showing 'switch off' responses with HSO_4^- anions. Reproduced from Ref. 327.

hydrogel doped with simple **[Eu.(tta)$_3$(H$_2$O)$_2$]** or **[Tb.(sal)$_3$.(H$_2$O)$_2$]** to generate hydrogels sensitive to HCl and NH_3 vapours. Both Eu^{III} and Tb^{III} hydrogels were strongly luminescent and showed similar responses, as shown in Figure 1.40b. Again, following dissociative mechanisms of the emissive complexes within the host matrix, rapid 'switch on' and 'switch off' luminescence responses for basic and acidic vapours were observed, respectively.[329] Interestingly, the hydrogen-bonding of the sulfonic acids in **95** also gave these hydrogels self-healing and adhesive properties, Figure 1.40c, which allowed the formation of mixed Eu^{III} and Tb^{III} gels in a modular fashion *via* macroscale assembly.

The use of Ln^{III} ions to directly crosslink and entangle polymer fibres (through coordination interactions) and induce gelation has extended to synthetic systems and have contributed to self-healing metallo-supramolecular materials.[330] Key advances have

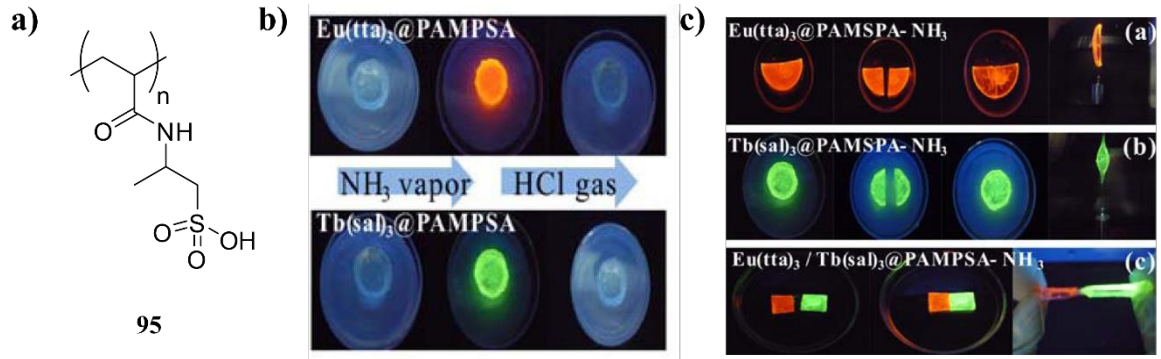

Figure 1.40 a) Structure of PAMPSA polymer **95**; **b)** PAMPSA hydrogels doped with **[Eu.(tta)$_3$]** or **[Tb.(sal)$_3$]** under UV irradiation (λ_{em} = 254 nm) showing 'switch on' responses with NH_3 vapour and 'switch off' responses with HCl vapour; and **c)** self-healing of emissive PAMPSA hydrogel doped with **[Eu.(tta)$_3$]** (top), **[Tb.(sal)$_3$]** (middle) and adhesion of separate Eu^{III} and Tb^{III} gels (bottom). Reproduced from Ref. 329.

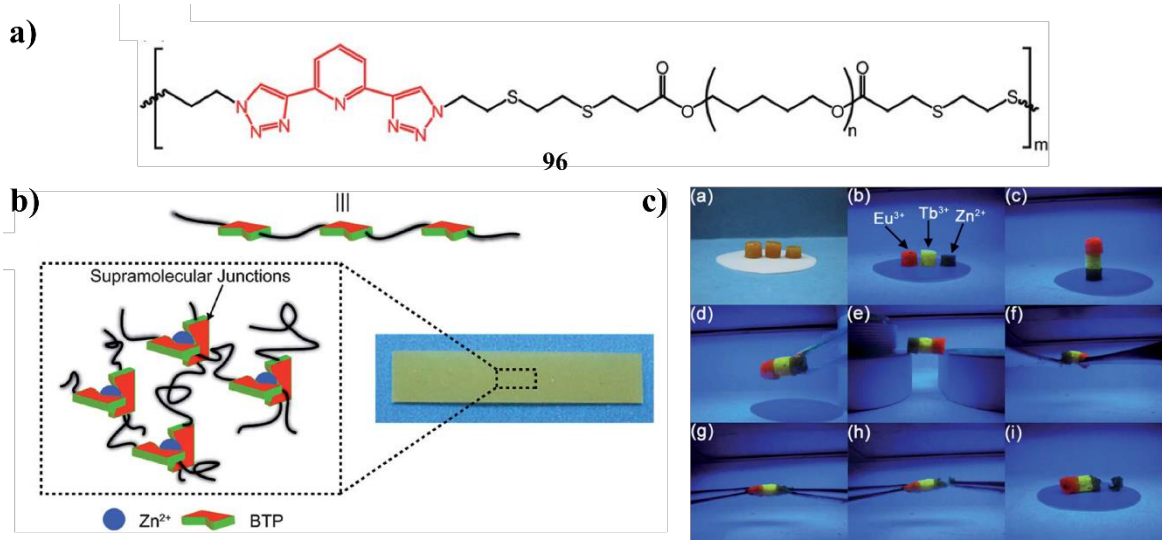

Figure 1.42 a) Structure of **btp** containing poly(urethane) **96**, an organogelator for toluene; **b)** Schematic representation of the cross-linking mechanism of supramolecular junctions due to coordination interactions; and **c)** self-healing of the organogels formed from **96** using Eu^{III}, Tb^{III} and Zn^{II} showing their welding and resistance to strain. Reproduced from Ref. 333.

focussed on the **btp** motif and Hecht first showed the polymerisation of these units into poly(**btp**-*alt*-(1,2,3-triazol-4-yl-1,3-pheylene)) type polymers that in the presence of metal ions including Eu^{III} caused the gelation of CH_3CN solutions.[331] This has since been developed more extensively by Weng and co-workers who synthesised Rehahn Type I / Wolf Type II polymer **96** containing **btp** sites copolymerised with functionalised poly(urethane) backbone polymers, Figure 1.42 below.[332-334] The resulting macromolecular ligand was soluble in organic solvents, as expected by its hydrophobicity, and **96** formed organogels in toluene. Those gels which were formed in the presence of Eu^{III} or Tb^{III} showed red and green metal-centred emission, respectively, upon irradiation with UV light due to sensitisation by the **btp** chromophores. In mixed systems with Zn^{II} additional blue emission could be achieved and the colour tuned by varying the molar ratio of the metal ions. In addition to showing photoluminescence the gels were mechanically interesting showing thermo-reversibility and self-healing properties. The self-healing behaviour was characterised through the rheology of the materials. The storage/loss moduli were restored to their original magnitudes within 30 minutes healing time although the recovery varied with the ratios of Ln^{III} to Zn^{III} ions. The subtle and varied mechanical enhancements with Ln^{III} and Zn^{II} can be rationalised by the higher coordination number but weaker bond strength of Ln^{III} ions compared to *d*-metals and therefore the absolute nature of each crosslink can vary widely.

The drive for luminescent materials that can be easily processed remains current with the desire for printable, smart materials and the motivation for soft LMW and polymer materials remaining at the forefront of these efforts. Indeed, much focus rests with transition

metal ions,[330] however the privileged properties of Ln^{III} luminescence remain fundamental to soft electronic and biomedical materials.[276] Within the field of Ln^{III} luminescent materials, Gunnlaugsson and co-workers have contributed various advances which are reviewed in the following section as direct precedence to the research described in this Thesis.

1.8 Recent advances from Gunnlaugsson and co-workers

In recent research efforts Gunnlaugsson and co-workers have focussed attention away from macrocyclic Ln^{III} coordination chemistry[335] towards purely acyclic systems to understand their self-assembly processes,[95] potential antennae[336,337] and responsive nature.[338,339]

Amongst the antenna systems developed the naphthyl **dpa** scaffold, **17**, was introduced for the self-assembly of luminescent coordination bundles.[136] These bundles were formed from enantiopure acyclic ligands **17** with *S,S* and *R,R* configurations at the chiral centre of the naphthyl ethylamine and self-assembled with Ln^{III} ions (Ln = Eu, Tb, Sm, Nd or Yb) into their corresponding saturated enantiopure $\mathbf{ML_3}$ complexes with Δ and Λ metal stereochemistry, respectively. In the case of the Eu^{III} complexes, the naphthyl groups were shown to be acceptable antennae for ligand-to-ion energy transfer and therefore strong sensitised emission was observed (both spectroscopically and to the naked-eye) showing extended millisecond lifetime (τ = 1.66 ms) and total quantum yields *ca*. 6-8%. Moreover, the Eu^{III}-centred emission was circularly polarised as a result of the enantiopure stereochemistry at the Eu^{III} centre induced by the chiral ligands; as expected the Δ and Λ enantiomers gave equal but opposite CPL signals. As observed in the crystal structure, Figure 1.43a, the assembly of the chiral bundles was characterised by π-π interactions with each ligand pyridine intercalating naphthyl groups from the two remaining ligands, thus wrapping the Ln^{III} ion within a helical ligand environment.

Indeed, this π-π stacking motif was found to be common to a number of derivatives that possessed pendent chains substituted at the 4-position of the pyridine core.[340] Ligands **97** – **100** were synthesised with various functionalities from small PEG, ethoxy, propargyl

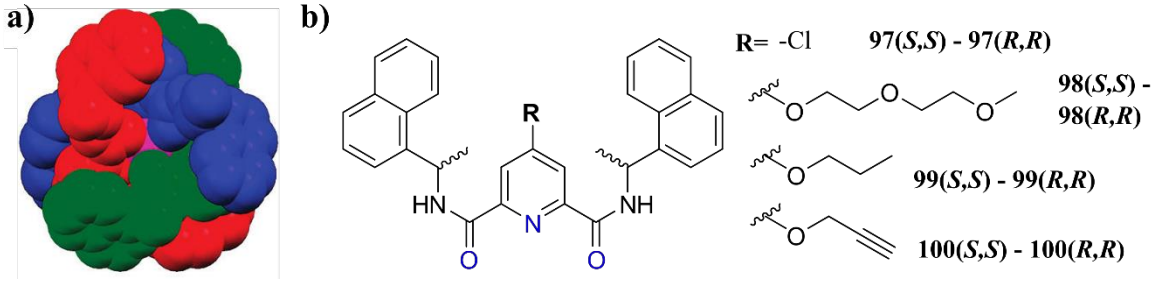

Figure 1.43 a) Crystal structure of **[Eu.(17)$_3$]** showing tight helical bundle formed from self-assembly of **17** with $Eu(CF_3SO_3)_3$, reproduced from Ref. 336; and **b)** structures of selected naphthyl-**dpa** derivatives **97-100** with 4-pyridyl ether substituents.

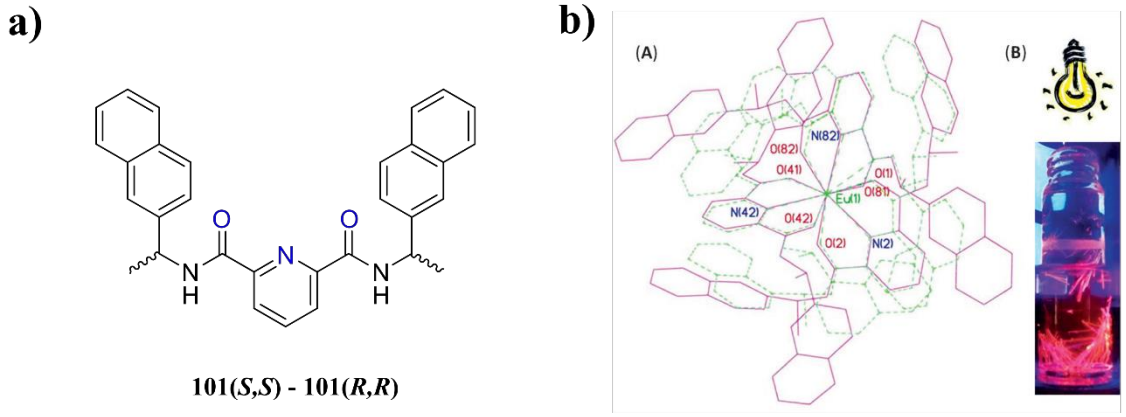

Figure 1.45 a) Structure of ligand **101**, a 2-naphthyl isomer of naphthyl-**dpa 17**; and **b)** overlaid crystal structures of **[Eu.(17)$_3$]**$^{3+}$ (dashed) and [**Eu.(101)**$_3$]$^{3+}$ (solid) showing a more open packing arrangement in the case of **101** compared to the complex of **17** and more exposure of the central Eu^{III} ion, also shown is the crystals under λ_{exc} = 254 nm showing red Eu^{III} emission to the 'naked eye'. Figures reproduced from Ref. 341.

units and, in fact, larger motifs such as crown ethers and carbohydrates were also formed and studied.[340] In every case, the **ML$_3$** species could be assembled in organic solvents and the size of the pendent functionality was found to be of limited importance in the formation of the self-assembly beyond effecting solubility. This accessible versatility arose from the 4-position of the pyridine extruding directly away from the cavity formed from the π-π stacking between adjacent ligands and, therefore, with appropriate spacers the pendent chain did not disrupt π-π interactions or prevent the self-assembly processes.

More significant perturbation of the self-assembly ability of naphthyl **dpa** ligands was found in the isomers of the naphthyl ethylamine antenna. Ligand **101** was reported, possessing the 2-naphthyl antenna instead to the 1-naphthyl isomer of **17**, and was shown to have weaker photophysical performance.[341] In single crystals of the Eu^{III} complexes of **101**, the central ion was more exposed to the external environment because of less ideal inter-ligand π-π interactions, as shown in Figure 1.45b. This was reflected in the photophysical performance in organic solutions and the total quantum yield was 4-fold reduced from 4%

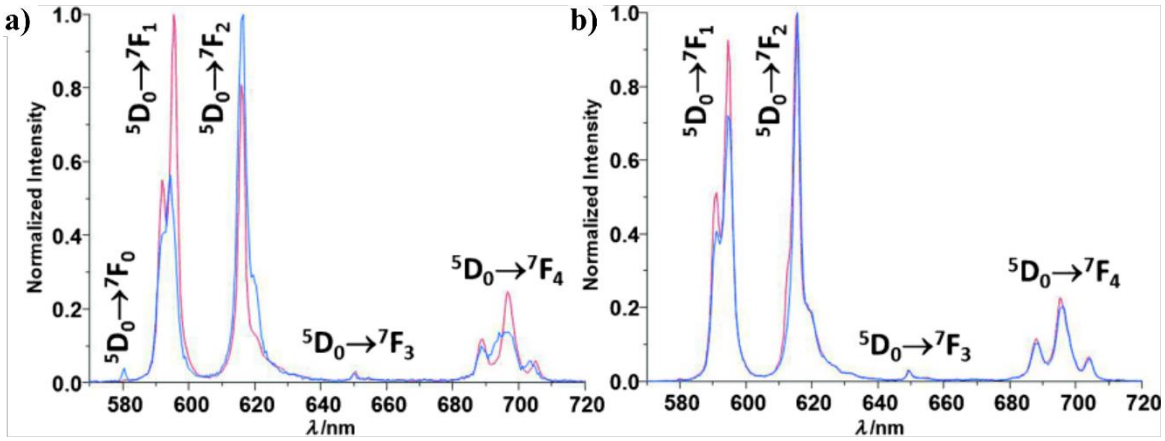

Figure 1.44 Indicative emission spectra for **[Eu.(17)$_3$]**$^{3+}$ (red) and [**Eu.(101)**$_3$]$^{3+}$ (blue) in: **a)** CH_3OH and **b)** CH_3CN, showing small changes in the transition intensities but equivalent line structure. Reproduced from Ref 341.

to 1% between **17** and **101**, respectively. The structure of the Eu^{III} emission spectra, Figure 1.44, were similar for **97-101** and can be considered characteristic for the scaffold. A concomitant reduction in the sensitisation efficiency was observed reducing by 5-fold between **17** and **101** which reflected the slightly increased naphthyl-to-Eu^{III} distance and increased exposure of the Eu^{III} centre to solvent deactivation.

Elaborate symmetrical supramolecular assemblies have been developed from these small mono-nuclear complexes, including the first examples of true Ln^{III}-templated [2]- and [3]-catenanes.[342] Building directly upon the naphthyl-**dpa** bundles a family of dimetallic, triple-stranded helicates, **102-104**, have been developed in which two naphthyl **dpa** units are linked by xylene spacers of varying substitution pattern.[343-345] In every case, triple-stranded helicates of stoichiometry $\mathbf{M_2L_3}$ (**M** = Eu^{III}, Tb^{III}, **L** = **102-104**) were formed by self-assembly in high yield (*ca.* 90% solution distribution) with visibly emissive Ln^{III} ions (Ln = Eu, Tb, Sm) in organic solution (CH_3OH or $CH_3CN/CHCl_3$). The ditopic ligands which were again enantiopure in their configurations gave complexes that were naturally strongly emissive and gave rise to Ln^{III}-centred CPL upon excitation of the naphthalene antennae.

The asymmetrical building block **105** of helicates **102-104** was shown to be itself a versatile scaffold for luminescent Ln^{III} complexes and Ln^{III} soft matter. The self-assembly of the Eu^{III} complexes of **105** was shown to be comparable to the symmetrical naphthyl **dpa** systems, **17**, forming saturated **ML** and $\mathbf{ML_3}$ species in organic solution with similar global stability constants, as estimated by spectroscopic titrations, with $\log\beta_{ML} \approx 7$ and $\log\beta_{ML3} \approx 20$.[346] As may be expected, the coordination geometries match closely those observed in the triple-stranded helicates above and absolute metal stereochemistry was determined as being

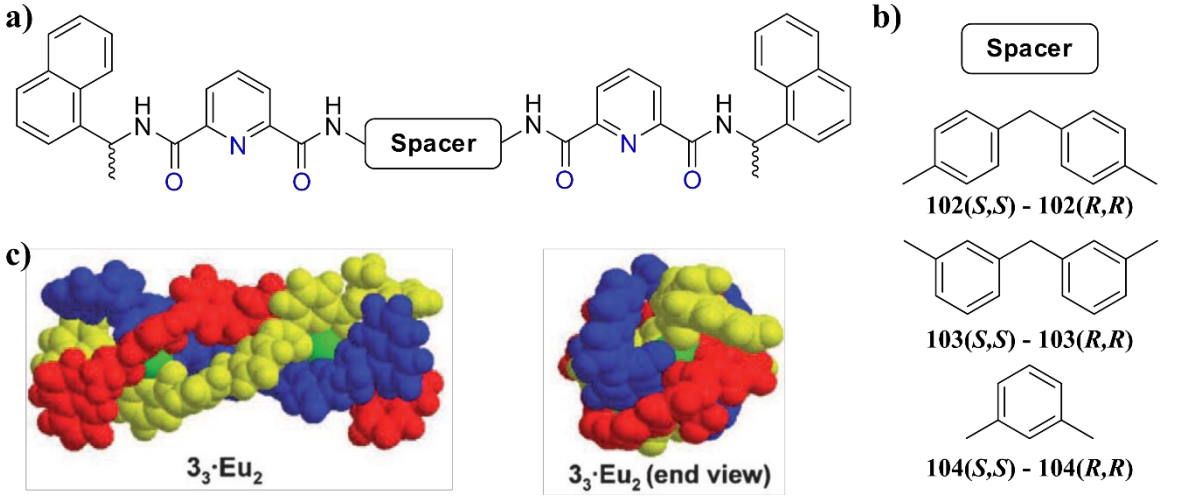

Figure 1.46 a) Schematic representation of ditopic ligand strands for the formation of dimetallic triple stranded helicates; **b)** the representative spacers for helicate strands **102-104** capped by naphthyl-**dpa** units are shown in a); and **c)** space-filling models estimated by MM2 calculations showing the packing of the three-strands and overall helical nature of the $L_2.Eu_2$ assemblies (L = **102-104**). Models reproduced from Fig. 345.

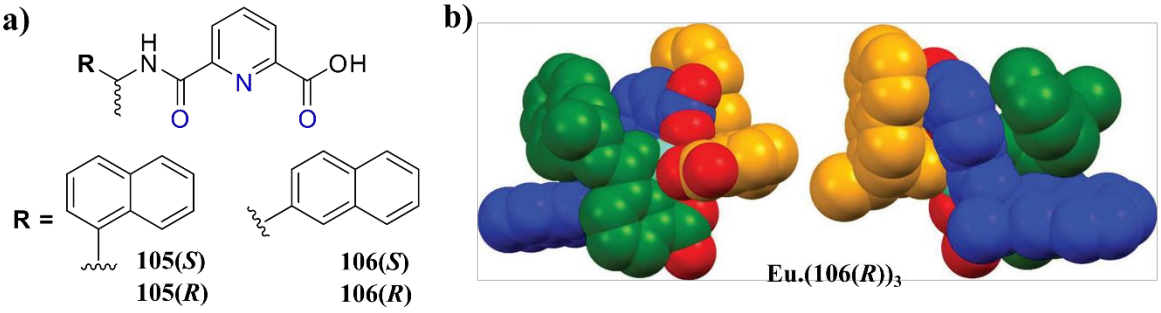

Figure 1.47 a) Structures of **105** and **106**, naphthyl-**dpa** half-helicates; and **b)** crystal structures of the Eu^{III} complexes formed from the 2-naphthyl isomer **106** showing the helical nature of the self-assembled bundles. Reproduced from Ref. 347.

Λ and Δ for the *R* and *S* enantiomers, respectively. This was established by combining X-ray crystal data from the solid state with the structure of CPL spectra from the solution state and comparing to similar systems.

Moreover, the self-assembly of Eu^{III} with **105** and **106** represented, for the first time, the use of CD spectroscopy to both monitor and estimate stability constants for solution species. Again, the naphthyl isomer was found to be significant in the self-assembly with photophysical performance being lower in the 2-naphthyl system **106** compared to **105** while total quantum yields were again 4-fold reduced (8% vs. 2% in CH_3CN and 2% vs. 0.5% in CH_3OH). Furthermore, for **105** and **106**, the exposure of the central core to solvent was found to affect solution stability and while 100% formation of $\mathbf{[Eu.(105)_3]^{3+}}$ was observed in solution, only 80% was found for the corresponding $\mathbf{[Eu.(106)_3]^{3+}}$ complex.[347] However, both ligands **105** and **106** were suitable precursors for the generation of soft monolayers and deposited Langmuir-Blodgett (LB) films.[348-350] Ligands **107** and **108** were derived from **105** and **106**, respectively, by coupling of the carboxylate with *N*-hexadecylamine to introduce a hydrophobic C_{16} chain to one side of the *O-N-O* binding site of **dpa** and subsequently gave amphiphilic character to the ligands. Complexes with Eu^{III} and Nd^{III} were formed with the 1-naphthyl isomer **107** and the $Ln(CF_3SO_3)_3.6H_2O$ salts under microwave irradiation.

The complexes of **107** showed photophysical properties comparable to the parent half-helicates **105** and demonstrated that the introduction of the C_{16} chain did not significantly perturb the coordination environment. LB monolayers were subsequently formed on the air-water interface and assembled with the Ln^{III}-**dpa** complex at the water surface and C_{16} chain projected to the air, shown schematically in Figure 1.48a below. Equivalent behaviours were observed for the *SSS* and *RRR* enantiomers and films were stable until collapse at *ca*. 30 mN m^{-1} and corresponding to areas of 75 $Å^2$ - consistent with the expected size of $\mathbf{ML_3}$ complexes. The films were transferred to quartz slides with high

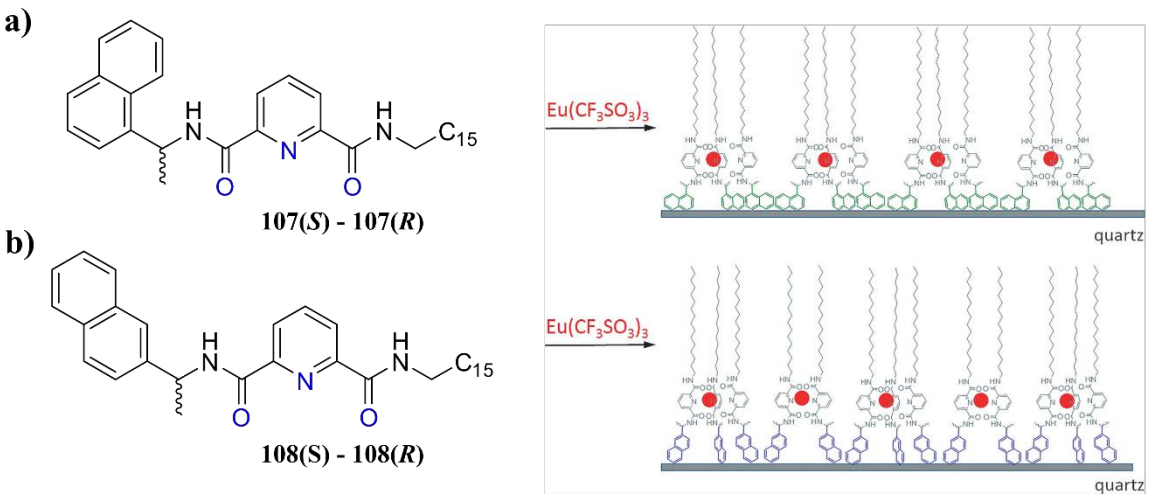

Figure 1.48 Structures of Langmuir-Blodgett monolayer forming naphthyl-**dpa** half-helicate ligands alongside the schematic representation of the LB films formed from their Eu^{III} complexes. **a)** ligand **107** with 1-naphthyl antenna formed uniform films of $[\mathbf{Eu.(107)_3}]^{3+}$; and **b)** ligand **108** with 2-naphthyl antenna formed mixed films of $[\mathbf{Eu.(108)_3}]^{3+}$ and $[\mathbf{Eu.(108)_2}]^{3+}$. Reproduced from Ref. 349.

transfer ratios from monolayer to LB film. In the case of Eu^{III}, the slides gave rise to characteristic emissive transitions of $^5D_4 \rightarrow {}^7F_J$ for Eu^{III} and, as for the individual complexes in solution, showed CPL emission.[348] Similarly, the Nd^{III}-centred complexes gave LB films on quartz slides that showed characteristic emission; however, CPL was not recorded for these NIR emitting samples as a result of the limitations of current spectrometers.[350] Again, corresponding to the self-assembly behaviour of the parent half-helicates, in the case of **108**, the monolayers and LB films formed from Eu^{III} were found to be of mixed stoichiometry.[349] Similarly, the photophysical performance of the 2-naphthyl isomers was weaker than that of the 1-naphthyl, mirroring the parent compounds once again. The speciation of complexes in the LB films was estimated by the fitting of luminescence lifetime data as 85% $\mathbf{ML_3}$ and 15% $\mathbf{ML_2}$ stoichiometry complexes resulting in different amphiphile packing and larger surface area of the monolayer, as illustrated in Figure 1.48b.

Further approaches to the formation of soft matter by Gunnlaugsson have included the use of micellar domains in the optimisation of photophysical properties for photolabelling[351] and *in vivo* imaging[55] as solution assemblies. However, most significantly, bulk soft gels have been developed from novel Ln^{III} binding motifs. Byrne and Gunnlaugsson introduced **btp** more broadly for Ln^{III} coordination and described a range of derivatives with amino acids and chiral chromophores that were formed in facile, one-pot CuAAC "click" syntheses.[352,353]

Ligands based upon **btp** were found to be a particularly efficient sensitising antenna for Tb^{III}-centred emission with total quantum yields *ca*. 70% (while being less effective for sensitising Eu^{III} giving total quantum yields *ca*. 3%). A tri-carboxylic acid derivative of **btp**,

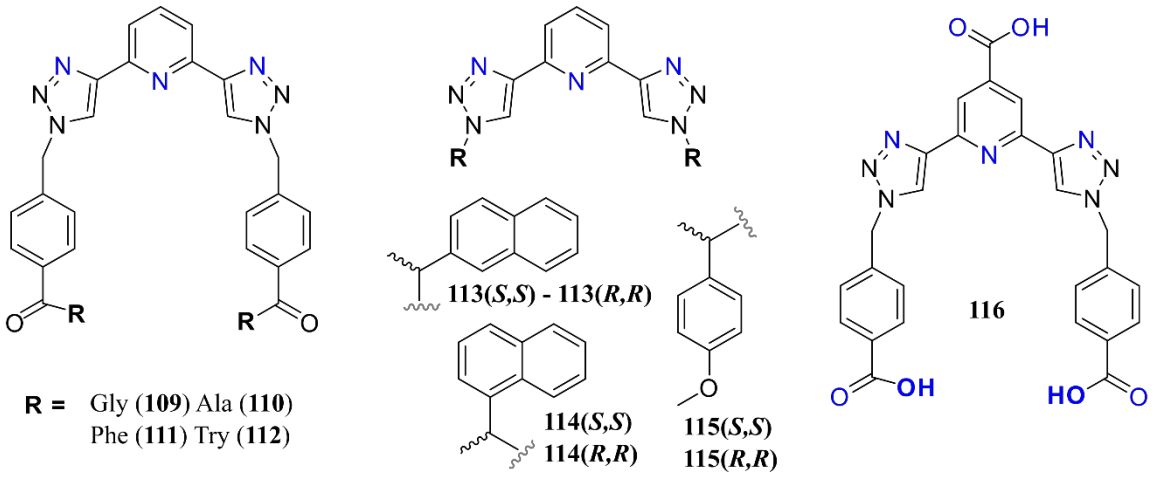

Figure 1.49 Structures of ligands **109 – 116** based upon the **btp** central motif and used in the binding of Eu^{III} and Tb^{III} ions.

116, was found to form hydrogels, and, in the presence of Eu^{III} ions, gave materials that were strongly red emissive, as shown in Figure 1.51a above.[354] Representative spectra for the sensitised emission from Eu^{III} and Tb^{III} from **btp**-based ligands are shown in Figure 1.49; these, like the naphthyl-**dpa** systems, have the same line structure of the emission spectra but vary amongst the derivatives in the relative intensities of the *f-f* transitions.

Interestingly, the Eu^{III}-doped hydrogels were more robust than the corresponding ligand gels and self-healing. Ln^{III}-induced rapid self-healing was found and the recovery of the storage moduli of the metallogels was upon straining to their yield points observed within 250s, but not the ligand gels. SEM revealed a fibrous gel network while luminescence lifetimes implied two Eu^{III} centres within the gel, corresponding to $\mathbf{ML_3}$ complexes and Eu^{III} crosslinking the complexes contributing to the gelation behaviour.

Martínez-Calvo and Kotova generated metallogels (in CH_3OH) from **117**, a phenyl **dpa** derivative.[355] The alcogels were formed in the presence of both Eu^{III} and Tb^{III} ions, with the bridging of ligands through coordination of the terminal carboxylates by Ln^{III} resulting

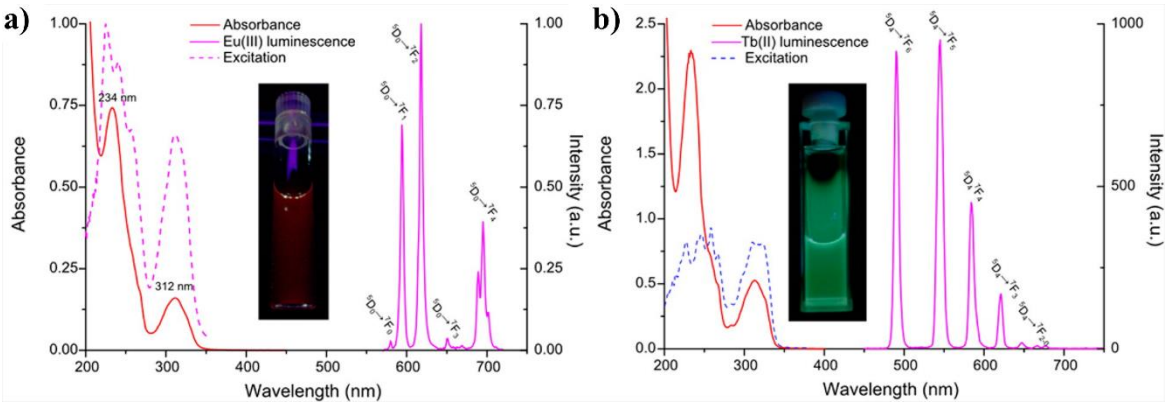

Figure 1.50 Representative absorbance (red), emission (pink) and excitation (dashed pink) spectra for **btp**-based complexes showing: **a)** Eu^{III} **btp** derivative and **b)** $[\mathbf{Tb.111}]^{3+}$ in CH_3CN showing the characteristic f-f transitions. Reproduced from Ref. 353.

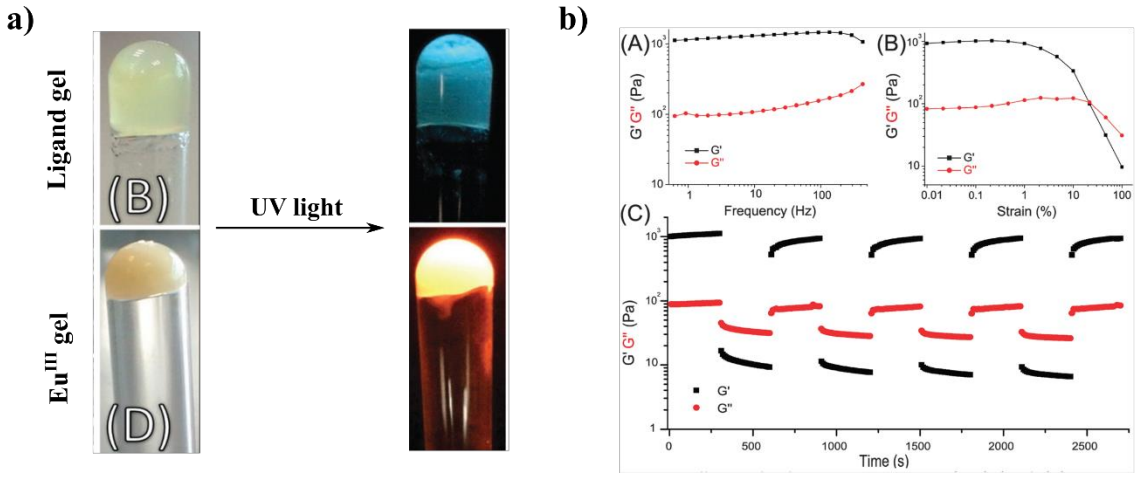

Figure 1.51 a) Photographs of the ligand gel of **116** (top) and **[Eu.(116)$_3$]$^{3+}$** (bottom) under ambient (left) and UV light (right, λ_{exc} = 365 nm) showing strong red Eu^{III}-centred emission in the metallogel and ligand fluorescence from the ligand gel; and **b)** 4 Oscillatory rheology measurements of **[Eu.(116)$_3$]$^{3+}$**gel. *(A)* Frequency sweeps at 0.1% strain amplitude of the storage modulus G' (black) and loss modulus G'' (red). *(B)* The corresponding strain dependence at at = 1 Hz showing yield strain at ≈ 20%. *(C)* Recovery test for **[Eu.(116)$_3$]$^{3+}$** gel showing self –healing properties. Reproduced from Ref. 354.

in an extended network. Both Eu^{III} and Tb^{III} gels were strongly emissive with the respective metal-centred emission with minimal contribution from ligand fluorescence. Indeed, the colour could be mixed by varying the molar ratio of Eu^{III}:Tb^{III}, allowing the generation of orange luminescent gels with no Tb→Eu energy transfer being observed. However, due to the lack of ligand fluorescence white-light was not achieved. Interestingly, the hydrogels of Eu^{III} and Tb^{III} with **117** were physically different and the gel network was much denser with Tb^{III} compared to Eu^{III}, clearly visible in the swelling sizes and morphology observed by SEM, as shown in Figure 1.52b. All the gels were self-healing with quick recovery times of

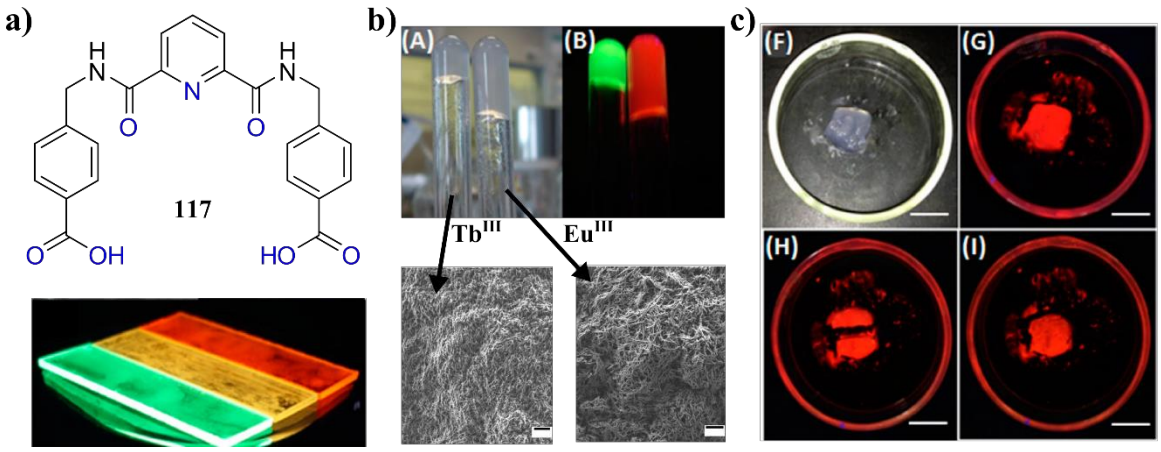

Figure 1.52 a) Structure of **117**, an organogelator in the presence of Ln^{III} ions, *bottom:* deposited films of Tb^{III}, Tb^{III}:Eu^{III} and Eu^{III} containing gels showing green, orange and red emission, respectively; **b)** photographs of Tb^{III} and Eu^{III} doped CH_3OH gels of **117** (top) under ambient (left) and UV light (right, λ_{exc} = 365 nm), also shown are the corresponding SEM images for the Eu^{III} and Tb^{III} gels with a more dense fibrous network observed in the case of Tb^{III}-based gels; and **c**) photographs of the self-healing of an Eu^{III}-based gel of **117** *(F)* gel under ambient light, *(G)* gel under UV-light, *(H)* gel separated by cutting, (*I*) welding of the cut gel. Reproduced from Ref. 355.

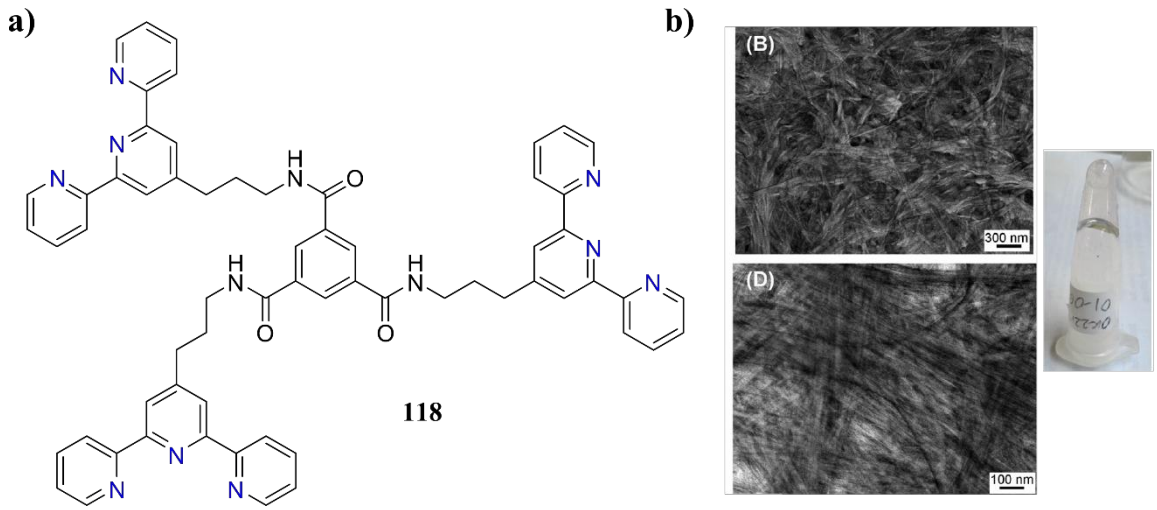

Figure 1.53 a) Structure of **118**, a tripodal **tpy** functionalised **bta** ligand; **b)** *left:* SEM images of the fibrous gel network of ligand gels of **118** (top) and metallogels of **[Eu$_3$.(118)]$^{9+}$** (bottom) showing an increased density in the metallogel consistent with Eu^{III}-based crosslinking of the fibres, *right:* photograph of the **[Eu$_3$.(118)]$^{9+}$** metallogel showing resistance to flow upon inversion. Figures reproduced from Ref. 357.

ca. 100 seconds. The Eu^{III} and Tb^{III} gels were also found to adhere, Figure 1.52c, and 'heal' together. However, their interfacial interaction was clearly different, as evidenced by morphology, demonstrating the subtleties that exist in the behaviours of the Ln^{III} ions.

The generation of luminescent Eu^{III}-based metallogels were achieved by Kotova and Daly using tripodal ligand **118** inspired by the **bta** supramolecular polymers of Meijer and Feringa.[356,357] A well-established helical supramolecular polymer can be formed in solution by the hydrogen bonding interactions of the **bta** core, resulting in unidirectional growth, while the addition of **tpy** units in **118** allowed cross-linking of the supramolecular polymers. Indeed, the addition of Eu^{III} ions (as Cl^-, $CF_3SO_3^-$ or NO_3^- salts) to **118** in H_2O:CH_3OH solution resulted in the formation of metallogels that exhibited Eu^{III}-centred emission. The gels formed from a combination of **bta** hydrogen-bonding, additional π-π interactions of the **tpy** units and supramolecular crosslinking by Eu^{III} at a critical concentration of 9 wt%. The **118** gel and Eu^{III}-containing metallogel formed from dense fibrous networks, a denser networks was found in the metallogel the consistent with the 'supramolecular glue' Eu^{III} crosslinks, as seen in Figure 1.53b.

Finally, luminescent lanthanide polymer hydrogels of Rehahn Type III have been developed. The pH responsive *cyclen* complex **119** was doped non-covalently within a matrix of poly(MMA-*co*-HEMA-*co*-EGDMA) *via* direct encapsulation during polymerisation.[358] The resulting polymer materials swelled as polymer hydrogels with equilibrium water content being *ca*. 40% at a 1:3 of MMA:HEMA and was found to be adequate for efficient equilibration (90 minute response time) with the bulk supernatant solution. Representing a versatile manufacturing method to produce *in situ* probes that are

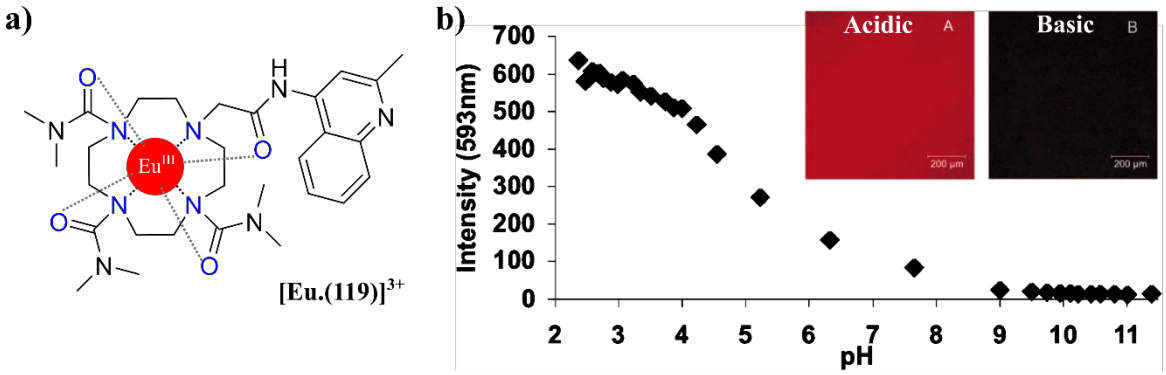

Figure 1.54 a) Structure of *cyclen* complex **[Eu.(119)]**$^{3+}$; and **b)** pH calibration of **[Eu.(119)]**$^{3+}$ in aqueous solution showing decreasing intensity (λ_{em} = 593 nm) with increasing pH, *inset*: CLSM images of p(HEMA-*co*-MMA-*co*-EGDMA) doped with **[Eu.(119)]**$^{3+}$ in acidic and basic conditions showing strong Eu^{III}-centred emission and no emission, respectively. Reproduced from Ref. 358.

easily fabricated and processed, the hydrogels were strongly emissive despite doping levels of only 0.05 wt% and retained the pH dependence of **[Eu.119]**$^{3+}$ with a "switch-off" response upon submersion in basic media, Figure 1.54. Although, leeching of the water-soluble probe **[Eu.119]**$^{3+}$ from the hydrogel into the bulk was observed as a limitation to be addressed and implied that the size exclusion of the internal porous structure was insufficient to retain the active compound.[359]

These examples from Gunnlaugsson over the past decade have led to the directed interests in optimising and exploring the scope of naphthyl **dpa**-based luminescent Ln^{III} complexes. The central aims of this current research, and the specific drive of the work to be discussed in this Thesis, has been to develop these systems further both in solution but also in assembled or polymeric materials. A range of novel developments will be described in the following chapters.

1.9 Works described in this thesis

The research presented in the following chapters will address a range of advances in the use of naphthyl-**dpa** ligands of the basic scaffold represented by **17** and **97** - **100** discussed above. The potential application of Ln^{III}, and particularly Eu^{III}, emission was discussed above; the systems studied herein are of interest since they give rise to strong Eu^{III} emission from a scaffold which is both chiral and readily derivatised. These properties allow for the introduction of responsive or functional units that report in the luminescence output or provide access to material forms more appropriate for exploring application in luminescent materials technology. The chiral nature of the ligands opens a new avenue to study their behaviour using chiral spectroscopies, allowing analysis of their absorbance and emission of (circularly) polarised light to gain further insight into their behaviour. Throughout the work is underlined by the aims: to optimise naphthyl-dpa Ln^{III} complexes (*e.g.* in their

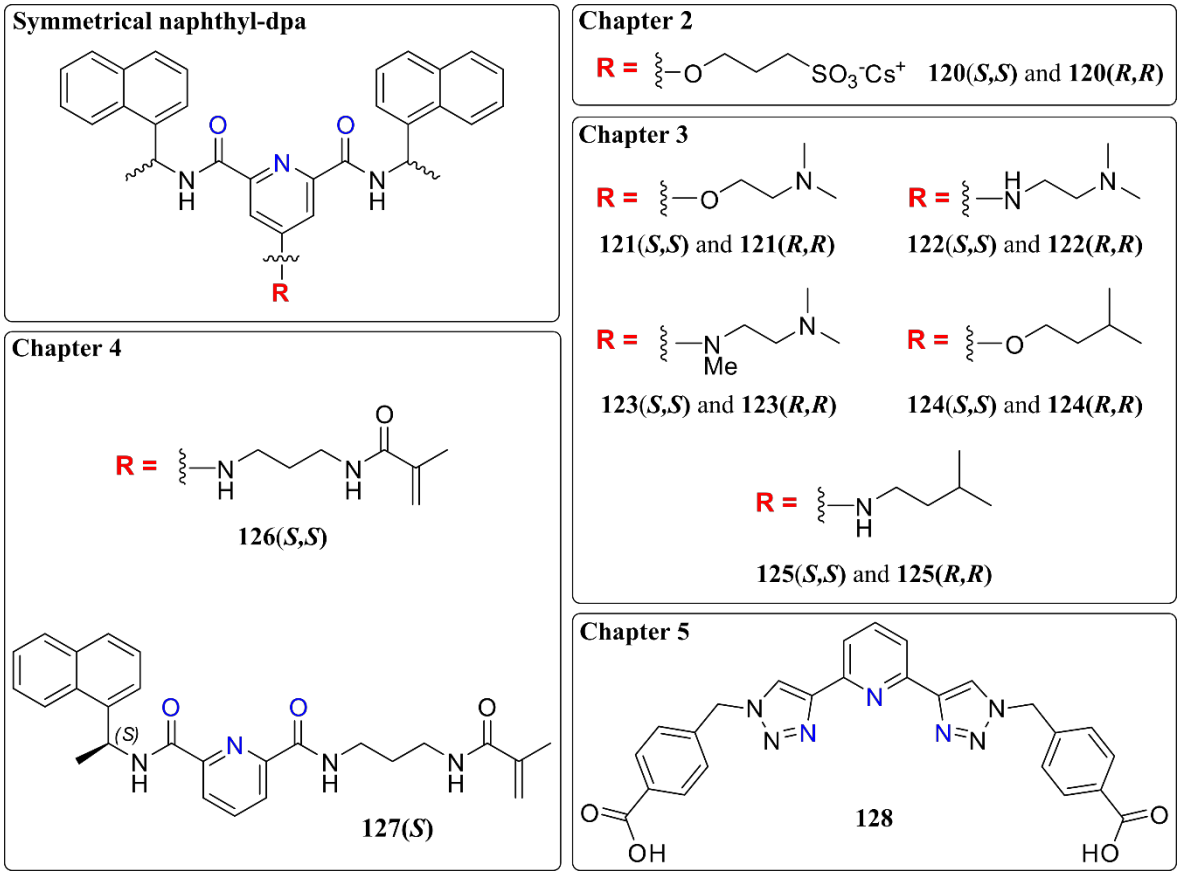

Figure 1.55 Summarised structures of key structures to be discussed in this Thesis.

photophysical properties and accessible solubility); expand these systems from being static luminescent Ln^{III} complexes into responsive probes; and, at each stage, evaluate their mode of application in materials designed to be more versatile and robust compared to solution. The key structures to be discussed are presented in Figure 1.55.

Chapter 2 will address the solubility of naphthyl-**dpa** systems through the development of an enantiomeric pair of derivatives, **120(*S,S*)** and **120(*R,R*)**, grafted with the powerful sulfonate ($R\text{-}SO_3^-$) solubilising group. The photophysical performance will be evaluated using classical spectroscopic techniques (UV-visible absorption and luminescence spectroscopy) as well as chiral analogues (CD and CPL) and important enhancements discussed. Similar methods will be used to probe the self-assembly processes in H_2O and the application of CD titrations developed further. The formation of a soft solution assemblies and a self-assembled 'gel-like' material will also be presented.

Chapter 3 will report the full photophysical characterisation of a larger family of naphthyl-**dpa** derivatives, (**121(*S,S*)** - **125(*S,S*)** and **121(*R,R*)** - **125(*R,R*)**, in order to systematically explore the effects of structural diversity of pyridyl substitution and solvent environments on the luminescent properties of the resulting complexes. A set of amine-containing ligands and their corresponding Eu^{III} complexes will be explored for their

interesting acid sensitivity and the unique spectroscopic features of their self-assembly (compared to **17**). With these responsive complexes, the formation of Eu^{III}-based pH probes and polymer hydrogels with luminescent response to pH will be presented as a readily manufactured chemical device.

Chapter 4 will subsequently introduce the field of molecular logic gate mimics (MLGMs) and describe the development of Ln^{III} luminescent MLGMs in solution and polymer gels. Responsive Eu^{III} complex **122(*S,S*)** developed in Chapter 3 will be combined with responsive Tb^{III} complexes formed from **btp** ligand **126** and probed for their responsive behaviours to H^+ and F^- stimuli simultaneously. The systems in solution and soft materials will be combined to generate a parallel circuit of dual input MLGMs through logical binary analysis of the luminescent behaviour characterised.

Finally, Chapter 5 will present methacrylate derivatives of naphthyl-**dpa** and the preliminary studies of their inclusion within polymer hydrogels based upon methyl methacrylate (MMA) and 2-hydroxyethyl methyl methacrylate (HEMA). Ligands **127(*S,S*)** and **128(*S*)** will be discussed which represent symmetrical and asymmetrical naphthyl-**dpa** derivatives, respectively. Photophysical characterisation of the ligands, their Eu^{III} complexes and resulting co-polymer gels will be described in addition to initial mechanical measurements of compressive and tensile moduli.

Chapter 6 will describe detailed experimental procedures including synthesis, analysis techniques and spectroscopic methods for all the research described herein. The combined references are listed in Chapter 7 while supplemental materials for each chapter (*i.e.* graphs, tables, spectra and photographs) are included in chapter specific appendices.

2. Sulfonate-grafted naphthyl dpa ligands and their complexes with Eu^{III} in polar and aqueous media

2.1 Introduction

The chemistry and physics of biology is naturally dominated by aqueous systems and, therefore, presents a fundamental environment for synthetic and supramolecular chemistry aimed at application (*e.g.* biosensors, imaging agents, theranostics).[360] In fully synthetic systems, water has been highlighted as a versatile 'green' solvent.[361-363] Water itself, in fact, can present "unique" qualities[364,365] and influence properties diverse in reactivity[366,367], physical behaviour and solution-based processes[368,369] in a variety of contexts can lead to unique and emergent properties.[360,370,371] The photophysical properties and self-assembly of pyridine di-amide ligands in their interactions with Ln^{III} cations were reviewed in Chapter 1, and the examples discussed were shown to be sensitive to the nature of the peripheral organic structure as well as the external environment. The naphthyl **dpa** ligand family has also been shown to be versatile by means of various scaffold modifications.[340] A number of derivatives have shown excellent solubility in both polar (CH_3CN and CH_3OH) and non-polar (CH_2Cl_2 and $CHCl_3$) organic solvents allowing the photophysical properties of the ligands to be probed in solution. However, attempts to monitor and analyse the *in-situ f*-metal-directed formation in more competitive media, such as water or buffered aqueous solution has not been achieved to date due to unsuitable solubility. In fact, to progress this class of ligand and complex for application, appropriate solubility and stability in desired operating conditions is of importance; for biological application, this requires access to the aqueous environment.

This chapter discusses the design of ligand derivatives **120(*S,S*)** and **120(*R,R*)** following an approach to aqueous solubility through *grafting* appropriate solubilising moieties. The resulting ligands and complexes were studied for unique behaviour as aqueous systems in comparison to the parent generation and sibling ligands, previously developed by Gunnlaugsson and co-workers, in organic media.

2.1.1 Design rationale and solubilisation strategies

Ligands in the naphthyl-**dpa** family have strongly lipophilic character (calculated $logP^{372}$ = 5.0 - 5.6 for structures such as **6**, **133** and **98**) and, therefore, have lower solubility in polar media. Compared to dipicolinate **6**, which is readily soluble in basic aqueous solution, the solubility is lowered by the substitution of the polar and anionic carboxylates by hydrophobic naphthyl amides. There are numerous potential approaches to solubilise lipophilic molecules in aqueous environments. Solubility can be achieved through addition of polar moieties, hydrogen bond donors and acceptors within the structure; approaches that are commonly

employed in medicinal chemistry.[373-376] Furthermore, g*rafting* can introduce moieties to the periphery of the organic scaffolds without being disruptive to other key functionalities.

Previous studies with the pyridine diamides have considered the 4-position of the pyridine in naphthyl **dpa**, and helicate molecules[377] related to **104**, by using this site to graft potential solubilising groups. The limited scope of the prior studies only explored the use of diethylene glycol units. The grafted ethylene glycol moiety introduced polarity and provided additional hydrogen bonding ability to the lipophilic scaffold. Mixed solvent solubility in modest ratios of H_2O:CH_3OH could be obtained in this way for symmetrical '*Trinity Sliotar*' ligands such as **98**, asymmetrical half-helicate derivatives and di-topic helicate-forming ligands.[340,377] This was effective for both types of system allowing the passage from neat methanolic solutions to mixed solvents of H_2O:CH_3OH and arriving at stable 50:50 mixtures that showed adequate photophysical performance; neat, or buffered, aqueous studies could not be achieved.

Wider research has demonstrated that the use of poly(PEG) chains (*e.g.* PEG-400, PEG-800, PEG-5000) is more effective in solvating hydrophobic moieties than short oligomers as co-solvent[378,379] and covalent adducts,[380-382] however, with increasing chain length comes an increased potential for additional, interfering or competing interactions. In the design of ligands **120(*S,S*) and 120(*R,R*)**, the strategy of grafting was extended to a non-PEG_n moiety to overcome the drawbacks of solubility.

Alkyl sulfonates, for example those shown in Figure 2.1, have received attention for solubilisation[383] and the group is extremely effective in the controlling solubility in aqueous and polar media. O'Shea *et al.* demonstrated the covalent grafting of propylsulfonate moieties in the design of fluorescent BODIPY dyes, **129**, for cellular imaging.[384] The organic-soluble dyes were efficiently brought into aqueous media through the grafting of propylsulfonate to a phenol arm producing the anionic species as salts with K^+ and Cs^+ counter-ions, both of which were soluble in aqueous and cellular environments.

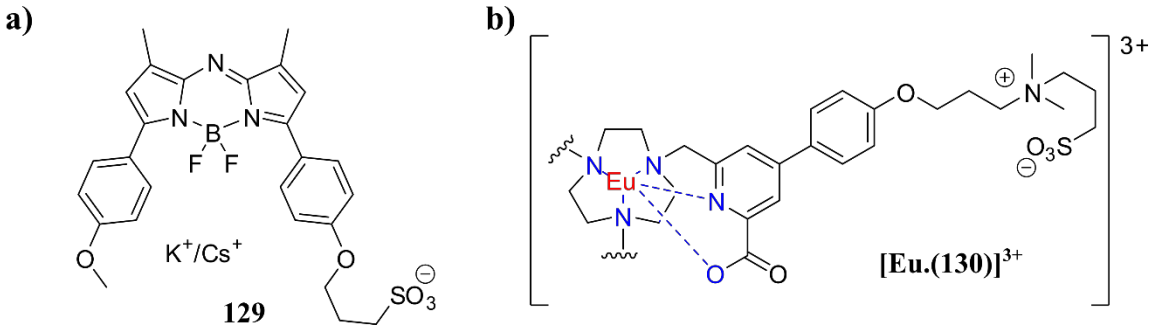

Figure 2.1 Structures of sulfonate-containing structures for solubility in aqueous media: **a)** anionic BODIPY dye **129**; and **b)** complex **[Eu.(130)]$^{3+}$** formed from neutral sulfobetaine-containing NOTA ligand **130**.

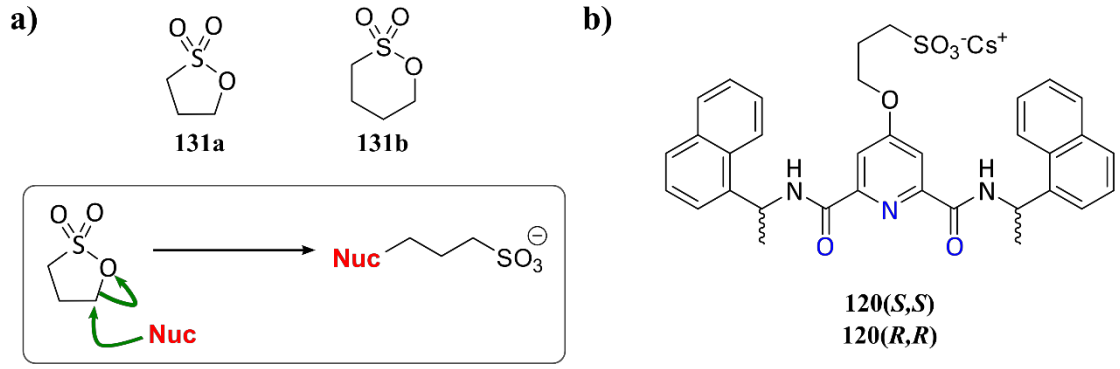

Figure 2.2 a) Structures of sultones **131a** and **131b**, along with the schematic reaction mechanism for their sulfonation action; and **b)** structures of proposed naphthyl **dpa** derivatives **120(*S,S*)** and **120(*R,R*)**.

Likewise, applied to cellular imaging, Maury and co-workers developed the NOTA-based Eu^{III} complex **130** with pendent picolinate antennae.[87] The antenna moieties were further substituted with sulfonate-betaine groups which corresponded to a charge-neutral sulfonate graft. This gave aqueous solubility to the relatively hydrophobic core-structure and efficient localisation within cells.

The sulfonate moiety (SO_3^-) is soft and polarisable so is able to provide beneficial interactions with the bulk solvent accounting for the solubility and can be readily introduced from sultone reagents such as 1,3-propanesultone **131a** or 1,4-butanesultone **131b** in rapid nucleophilic substitution reactions.[385] The proposed ligands, **120(*S,S*)** and **120(*R,R*)**, were synthesised introducing the propane sulfonate moiety to the naphthyl **dpa** scaffold providing enantiopure ligands with increased water solubility; their synthesis and water solubility properties are described in the following sections. The later sections of this chapter concentrate on the studies of coordination, solution self-assembly and photophysical properties of **120(*S,S*)** and **120(*R,R*)** in fully aqueous media.

2.2 Synthesis and structural characterisation of 120(S,S) and 120(R,R)

The synthesis of ligands **120(*S,S*)** and **120(*R,R*)** is shown in Scheme 2.1. The commercially-available chelidamic acid was first coupled with optically-resolved (ee > 98%) *R*- or *S*- 1-(1-naphthyl)ethylamine in anhydrous THF. The di-acid was activated at low temperature with EDCI with HOBt in the presence of 2 equivalents of Et_3N, followed by the addition of the appropriate amine drop-wise at 0 °C and stirred at RT to obtain the hydroxyl intermediates **133(*S,S*)** and **133(*R,R*)** as off-white solids in good yields (71% and 70%, respectively) after elution on silica (RediSep® 12g, 0 → 5% CH_3OH : CH_2Cl_2).

The amide coupling and successful inclusion of the naphthyl moieties were confirmed by HRMS and in ^1H NMR with the appearance of naphthyl CH resonances between 7 – 9 ppm which were characteristic of the 1-naphthyl isomer. The formation of the

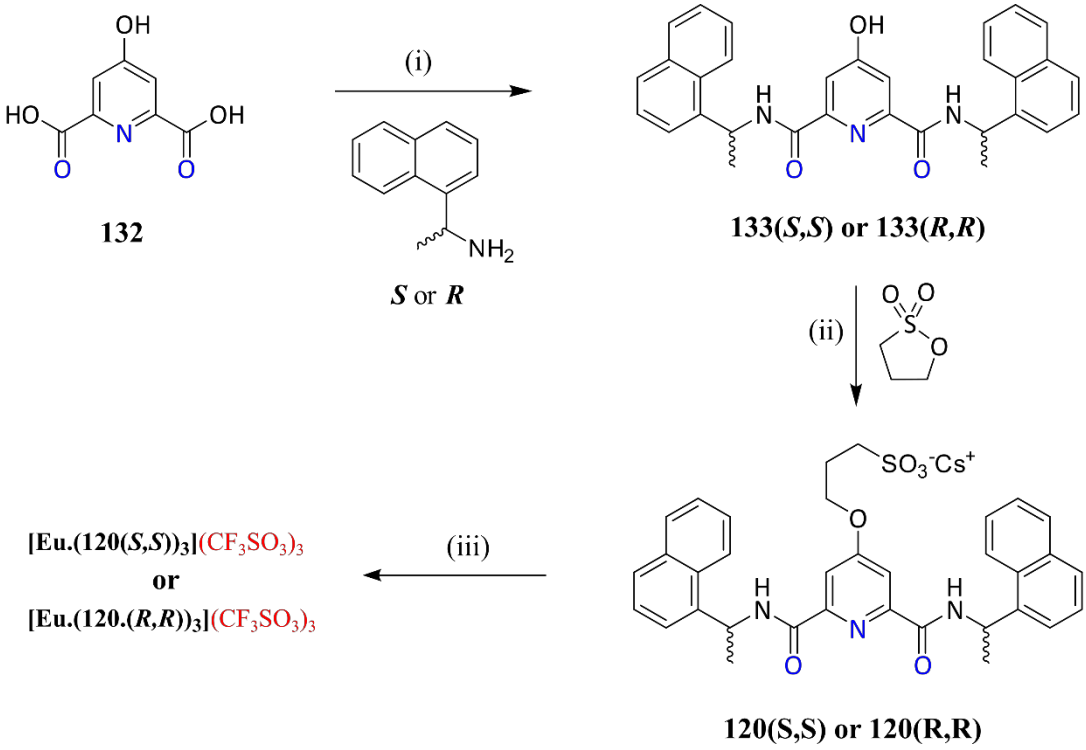

Scheme 2.1 Synthesis of **120(*S,S*)** and **120(*R,R*)**. (i) EDCI (2 eq.), HOBt (4 eq.), Et_3N (2 eq.), 0 °C → RT, THF (dry); (ii) Cs_2CO_3, THF (dry), Δ reflux, 2h; (iii) $Eu(CF_3SO_3)_3$ (0.33 eq.), CH_3OH.

amide was also evidenced by the resonance at 6.1 ppm which corresponded to the aliphatic CH of the chiral carbon (H_i) which becomes deshielded by ≈ 1 ppm upon amide formation compared to the starting 1-(1-naphthyl)ethylamine. Moreoever, the ^{13}C NMR showed that the chemical shift of the carbonyl carbon which was consistent with the amide formation. The NMR characterisation in all cases showed a single set of resonances which demonstrated a C_2 symmetry in the molecule which was consistent with enantiopure configurations *S,S* and *R,R* for **133** and no evidence of the *S,R* diastereoisomer was observed. This was also supported by paramagnetic shift NMR upon formation of Eu^{III} complexes with **133**. The IR spectra of **133(*S,S*)** and **133(*R,R*)** showed the exchange of the carboxylic acid of chelidamic acid with an amide showing a reduction in C=O stretching frequency from 1720 cm^{-1} to 1652 cm^{-1} and also supported this structural assignment; furthermore, this characterisation was consistent with previous reports.[386]

The synthesis of **120(*S,S*)** and **120(*R,R*)** was subsequently achieved from an adapted literature procedure of O'Shea *et al.*[384] The intermediates **133(*S,S*)** and **133(*R,R*)** were heated to reflux with 1,3-propanesultone and Cs_2CO_3 in anhydrous THF for two hours. The reaction mixture was concentrated under reduced pressure and afforded an oil which then precipitated as a white solid with sonication in acetone. The filtration of the resulting solids and washing with acetone and diethyl ether gave crude products which were purified from

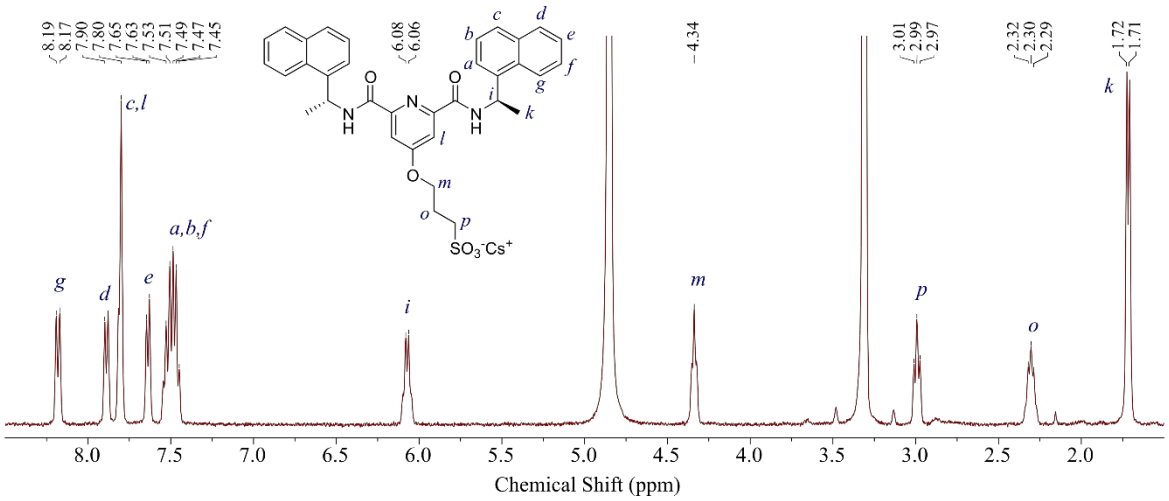

Figure 2.3 ^{1}H NMR spectrum of **120(*S,S*)** (CD_3OD, 400 MHz) showing a single set of signals and C_2 symmetry.

excess 1,3-propanesultone by reversed-phase flash chromatography (C_{18}-functionalised silica, 0 → 100% CH_3CN in H_2O). After elution, the ligands were recovered pure as their caesium salts in 51% and 71% yields, respectively, which corresponded to an overall yield *ca.* 50%.

Again, the ^{1}H NMR spectra were simplified and well resolved. The spectrum for **120(*S,S*)** is shown in Figure 2.3, showing a single set of resonances which corresponded to *S,S* and *R,R* configurations being retained in **120(*S,S*)** and **120(*R,R*)**, respectively. Similarly, the substitution was shown not to restrict conformational freedom within the structure and no rotational isomerism was observed. The same key resonances that confirmed the base scaffolds **133(*S,S*)** and **133(*R,R*)** were observed - seven protons $H_{a\text{-}g}$, which correspond to the naphthalene protons, and H_l, arising from the pyridine core. The chemical shift and integration of pyridyl proton was equivalent to **133** and demonstrated the same 4-position oxygen substituent. The chiral proton, H*i*, appeared as a single resonance at the same shift of 6.1 ppm indicating again the retention of configuration at the chiral carbons in the basic conditions of the sulfonate substitution. A single substitution in the molecule with the propylsulfonate moiety was confirmed by the appearance of three new resonances at 2.3, 3.0 and 4.3 ppm corresponding to the methylene protons of the propyl chain and integrated in a ratio of 1:1 with the pyridine scaffold. The ligand mass was confirmed by HRMS while the IR spectra showed new stretching frequencies at 1360 cm^{-1} and 1180 cm^{-1} which were assigned to the sulfonate S=O asymmetric and symmetric stretching modes, respectively.[387]

Ligands **120(*S,S*)** and **120(*R,R*)** were readily soluble in both CH_3OH and H_2O, while **133** and PEG-ylated **98** showed flocculation of the solid material. The UV-visible absorption

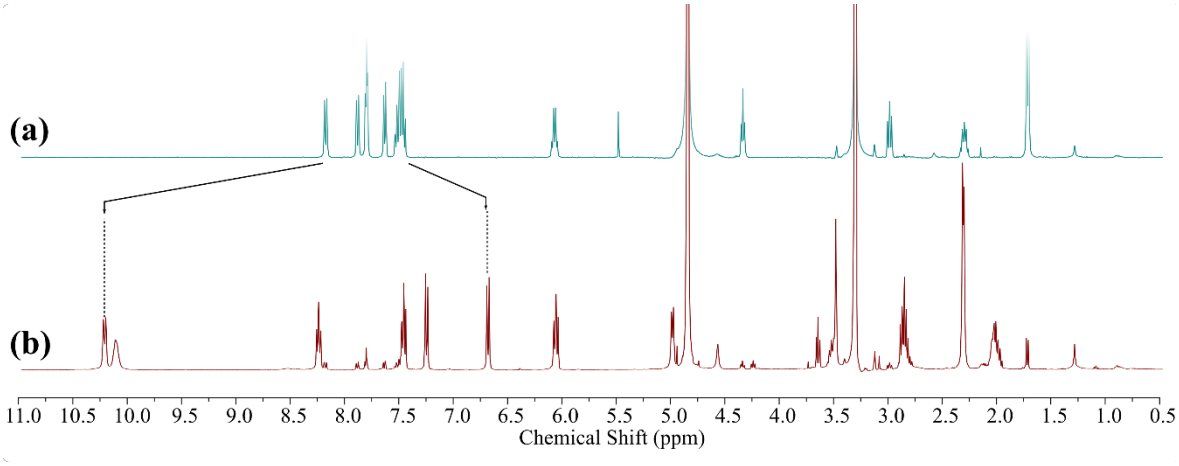

Figure 2.4 ^{1}H NMR spectra (CD_3OD, 400 MHz) showing: **a)** free ligand **120(*S,S*)**; **b) [Eu.(120(*S,S*))$_3$]** showing paramagnetic chemical shift and also uncoordinated **120(*S,S*)** clearly distinguishable from Eu^{III} containing species.

spectra recorded of filtered CH_3OH and H_2O solutions after sonication showed that only in the case of **120(*S,S*)** and **120(*R,R*)** was appreciable dissolution observed.

The complexes of **120(*S,S*)** or **120(*R,R*)** with Eu^{III} were prepared thermodynamically by reacting the respective ligands with 0.33 equivalents of $Eu(CF_3SO_3)_3$ in CH_3OH. The complexes were synthesised by heating the mixtures under microwave irradiation at 70 °C for 20 minutes in a sealed vial and then isolated by precipitation by slow injection of the cooled reaction mixtures into excess diethyl ether. After stirring at RT for 30 minutes, the suspended precipitate was removed by centrifuge and dried under high vacuum. Initial visual observation indicated successful complex formation with both the CH_3OH solution and isolated solids being red emissive when irradiated with UV light (λ_{em} = 254 nm).

^{1}H NMR spectra of the complexes were recorded in CD_3OD which demonstrated the coordination of **120(*S,S*)** and **120(*R,R*)** to Eu^{III}, as shown in Figure 2.4. The relatively small net magnetic moment for Eu^{III} resulted in a small shift range between 10.5 and 0.5 ppm from LIS paramagnetic effects. The efficient binding of **120(*S,S*)** and **120(*R,R*)** at NMR concentrations gave well resolved signals that clearly demonstrated a single complex stoichiometry in solution, Figure 2.4c. Those circumstances in which dissociation, or incomplete coordination, occurred were clearly identified from the ^{1}H NMR spectra, Figure 2.4b, with ligand not bound to Eu^{III} being clearly distinguishable.

The IR spectra were recorded of the solid complexes and, similarly to **133** and **[Eu.(133)$_3$]$^{3+}$**, a decrease in the stretching frequency of the amide carbonyl was observed from 1651 cm^{-1} to 1619 cm^{-1}. Furthermore, a concomitant increase in the amide N-H bend from 1521 cm^{-1} to 1557 cm^{-1} consistent with a coordination interaction was also observed. In complexes **[Eu.(120(*S,S*))$_3$]** and **[Eu.(120(*R,R*))$_3$]**, the propyl sulfonate SO_2 asymmetric

and symmetric stretches were overlapped with SO_2 and C-F stretches of the $CF_3SO_3^-$ counter-ions. However, there was evidence that no reduction in the frequencies in the IR stretches of the propylsulfonate occurred and, therefore, indicated that the pendant chain was not coordinated to a Eu^{III} ion, see Appendix A2. HRMS only showed the mass expected for **ML_2**. This has been observed previously in naphthyl-**dpa** derivatives and is not unexpected given the harsh conditions in MALDI mass spectrometry and the potential for dissociation; the stoichiometry was suggested to be **ML_3** photophysical measurements of luminescence lifetimes (*vide infra)*. Both the ligands and their complexes were then characterised for their fundamental photophysical properties.

2.3 Photophysical characterisation of ligands 120(*S,S*) and 120(*R,R*)

The photophysical properties of ligands **120(*S,S*)** and **120(*R,R*)** were initially studied in deionised water for both UV-visible absorption and emission characteristics; in addition, the effect of the structural chirality was observed through CD absorption spectroscopy.

The absorption spectra from aqueous solutions of ligands **120(*S,S*)** and **120(*R,R*)** were identical and are shown in Figure 2.5 at $c = 1 \times 10^{-5}$ M. Electronic transitions characteristic to the pyridine $n \rightarrow \pi^*$ and $\pi \rightarrow \pi^*$ transitions as well as the naphthyl $\pi \rightarrow \pi^*$ transitions were observed. A strongly absorbing feature was found at $\lambda_{max} = 224$ nm ($\epsilon \approx 120 \times 10^3$ $dm^3.mol^{-1}.cm^{-1}$) and a weaker band at 270 – 290 nm ($\epsilon_{281} \approx 15 \times 10^3$ $dm^3.mol^{-1}.cm^{-1}$) which possessed a fine structure consisting of bands at 275, 281 and 290 nm. The fine structured absorbance band was mostly naphthyl-centred and the overall profiles were consistent in the aqueous solution to related naphthyl-**dpa** ligands, such as **133**. Compared to organic solution, the molar extinction at $\lambda_{abs} = 224$ nm was slightly reduced in aqueous solution and was likely a result of solvent-screening of chromophore coupling.

Ligands **120(*S,S*)** and **120(*R,R*)** were studied for their chiroptical properties; the results were consistent in each case with the presence of single chiral stereoisomers in solution. The CD spectra of the ligands **120(*S,S*)** and **120(*R,R*)** are presented in Figure 2.5b. As expected the isomers gave mirror-image spectra, with transitions of equal magnitude but of opposite signs.

Moreover, these CD spectra showed strong Cotton effects, which could be characterised by Davydov splitting of 6 and 5 nm, respectively.[388-390] Intense bisignate CD Cotton effects were observed in both enantiomers and could indicate a coupling between the naphthyl antennae. The intensity and wavelength of chiral absorption maxima associated with exciton coupling mechanisms often show temperature dependence,[391] therefore, the CD spectra of **120(*S,S*)** and **120(*R,R*)** was recorded also as a function of temperature.

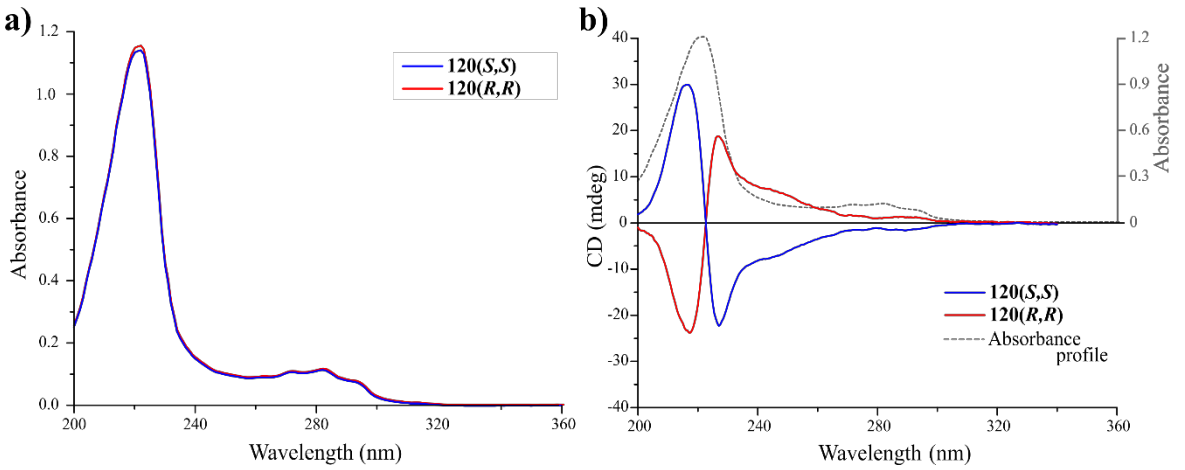

Figure 2.5 a) UV-visible absorption spectra of **120(*S,S*)** (blue) and **120(*R,R*)** (red), showing equivalent absorption profiles for the two enantiomers; **b)** CD spectra recorded for **120(*S,S*)** (blue) and **120(*R,R*)** (red), showing equal but opposite ellipticity for the two enantiomers; overlaid absorbance profile of **120** (dashed) shows key features with chiral absorption reflect regions of the absorption. All spectra were recorded in H_2O at $c = 1 \times 10^{-5}$ M at 24 °C.

The CD spectra from aqueous solutions of **120(*S,S*)** and **120(*R,R*)**, at a constant concentration ($c = 1 \times 10^{-5}$ M), were recorded at various temperatures between -6 °C and +55 °C and are shown in Figure 2.6a for **120(*S,S*)**. Small changes in one component of the Cotton effect absorbance between λ_{abs} = 200 – 230 nm were observed, shown enlarged in Figure 2.6b. While being small in magnitude, as the temperature increased a red-shift (*ca.* 3 nm) of the chiral absorption maxima occurred; this resulted in a minor hypochromism in absorbance from the maximum at -6 °C by approximately 10% upon heating to +55 °C.

The naphthyl π → π* transitions, inset Figure 2.6a, showed no established changes since chiral absorption was low in this region and could not be distinguished from experimental noise. These variable temperature experiments showed a minimal, but

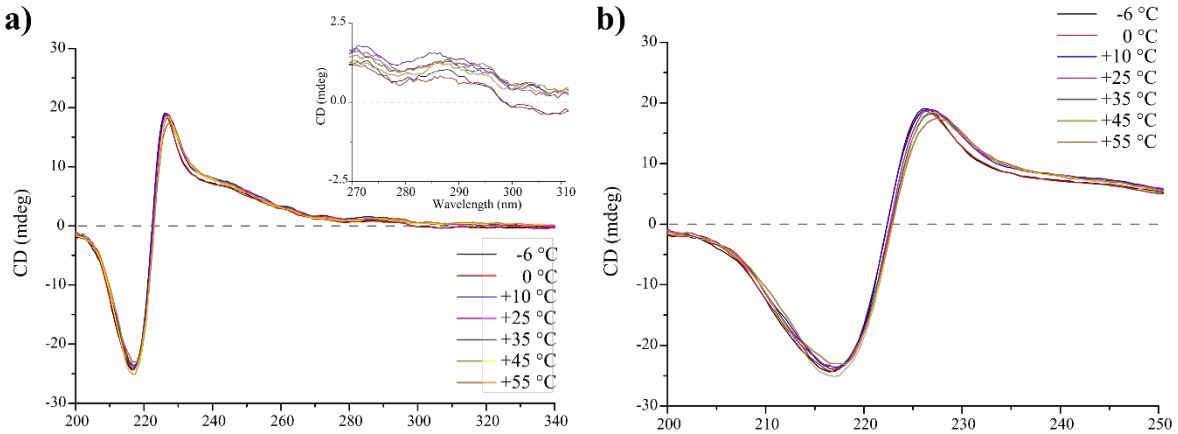

Figure 2.6 Variable temperature CD spectra of **120(*S,S*)** recorded between -6 °C and +55 °C showing: **a)** full absorption profile and small red shift in λ_{abs} = 228 nm, *inset*: zoomed region of naphthyl absorbance showing no systematic trend; **b)** zoomed region (200 -250 nm) clarifying the red shift and hypochromism of λ_{abs} = 228 nm with increasing temperature.

measureable, temperature dependence in the ligands and further supported some extent of exciton coupling (in addition to the observed Cotton effect).

To determine the emission properties intrinsic to ligand **120(*S,S*)** and **120(*R,R*)** in aqueous media, **120** was irradiated into the λ_{max} = 281 nm $\pi \rightarrow \pi^*$ transitions and the concomitant fluorescence spectrum measured. This did not result in measurable ligand fluorescence, which was consistent with efficient non-radiative deactivation of *O*-linked naphthyl **dpa** ligands in H_2O. Similarly, behaviour was observed upon excitation directly of the pyridyl core in the band at λ_{max} = 224 nm. Following the characterisation of the photophysics of **120(*S,S*)** and **120(*R,R*)**, showing the expected enantiomeric relationship, the respective complexes with Ln^{III} cations were studied.

2.4 Photophysical parameterisation of Eu^{III} complexes of 120(*S,S*) and 120(*R,R*)

It was expected that sensitised emission would be obtained from complexes of **120(*S,S*)** and **120(*R,R*)** based on emissive Ln^{III} ions. However, from the luminescent ions, measurable emission was only obtained from Eu^{III} while the other complexes gave no appreciable emission even in degassed solution. Full parameterisation was pursued only for complexes **[Eu.(120(*S,S*))$_3$]** and **[Eu.(120(*R,R*))$_3$]**. The lifetimes of Ln^{III} emissions are commonly extended to the millisecond timescale, therefore, luminescence studies were carried out on two time-scales to measure both ligand fluorescence and metal-centred luminescence.

2.4.1 UV-visible absorption, fluorescence and phosphorescence emission

In a similar manner to the ligands, both the absorption and the emission spectra of the Eu^{III} complexes of **120(*S,S*)** and **120(*R,R*)** were recorded in water, these are shown in Figure 2.7 and Figure 2.8 for **[Eu.(120(*S,S*))$_3$]** and **[Eu.(120(*R,R*))$_3$]**, respectively. The absorption spectra of complexes **[Eu.(120(*S,S*))$_3$]** and **[Eu.(120(*R,R*))$_3$]** showed hypochromic shifts at λ_{abs} = 220 and 281 nm with de-convolution of the high energy band into two features, shifted by 5 nm; one band was red-shifted (λ_{max} = 225 nm) and the other band blue-shifted (λ_{max} = 215 nm). These shifts may be accounted for by changes in the chromophore coupling[392,393] arising from the direct-assembly and concomitant interactions of adjacent ligands. A simultaneous hyperchromic shift of the region of 300 - 310 nm was observed and corresponded to conformational changes and the associated coordination to the Eu^{III} ion.

The 'fine structure' of the naphthyl $\pi \rightarrow \pi^*$ bands at λ_{max} = 281 nm was less resolved in the spectra of the complexes (as has been observed in other naphthyl **dpa** systems[340,341]) and would correspond to reduced rotational freedom of the ligands in the directed-assembly.

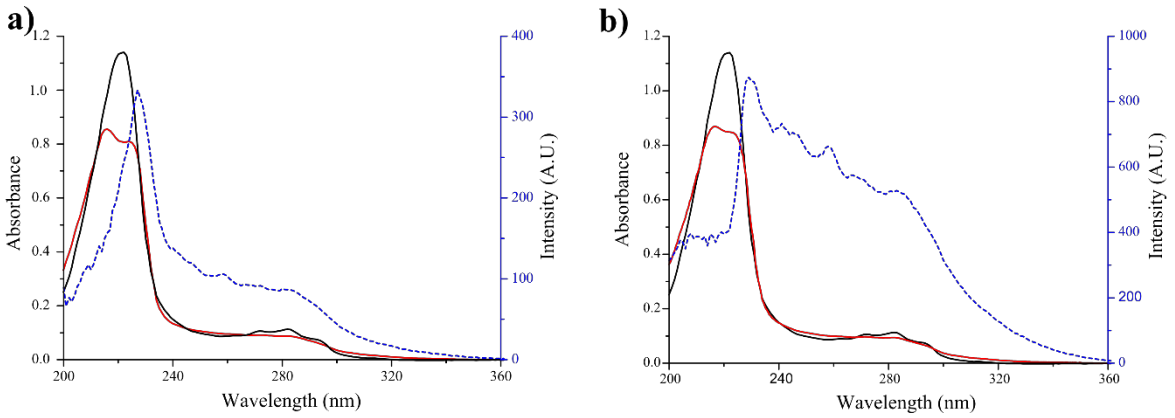

Figure 2.7 Overlaid UV-visible absorption spectra of ligands (black, $c = 1 \times 10^{-5}$ M), Eu^{III} complexes (red, $c = 3.3 \times 10^{-6}$ M) and the excitation spectrum (blue dashed) of Eu^{III}-centred fluorescence ($\lambda_{em} = 615$ nm), showing sensitisation arising from ligand-centred energy transfer, for: **a) 120(*S,S*)** and **[Eu.(120(*S,S*))$_3$]**; **b) 120(*R,R*)**, **[Eu.(120(*R,R*))$_3$]**.

Complexes **[Eu.(120(*S,S*))$_3$]** and **[Eu.(120(*R,R*))$_3$]** were excited *via* electronic absorption of the naphthyl chromophores of the ligands ($\lambda_{exc} = 281$ nm) and pseudo-Stokes shifted[75] luminescence was observed. The sensitisation of Eu^{III}-centred luminescence from the ligand-centred excited-states was confirmed through the excitation spectra recorded for the Eu^{III}-centred luminescence ($\lambda_{em} = 615$ nm). The excitation spectra for characteristic Eu^{III} emission are also shown in Figure 2.7a and Figure 2.7b and had structures which agreed with the features of the absorbance spectra of **120(*S,S*)** and **120(*R,R*)**, respectively.

A characteristic structure in the emissive *f-f* transitions was evident and the emerging line-like emission at long wavelengths was assigned to the $^5D_0 \rightarrow {}^7F_J$ transitions of Eu^{III}, where $J = 1 - 4$, shown in Figure 2.8. This emission was clear in the fluorescence emission spectra, as shown in Figure 2.8a (inset), and suggested a fast and efficient overall sensitization process from the ligand excited-states to the $^5D_0$ excited-state of Eu^{III}. Furthermore, the red Eu^{III}-centred emission was also clearly visible to the naked eye when both the solid complexes and their aqueous solutions were irradiated under UV-light (λ_{exc} = 254 nm) as demonstrated in Figure 2.8b (inset). The extended (millisecond) lifetime emission, however, was confirmed by observing the Eu^{III}-centred emission in time-resolved spectroscopy (in phosphorescence mode). The luminescence spectra recorded after a delay of 0.1 ms are shown in Figure 2.8a and Figure 2.8b for **[Eu.(120(*S,S*))$_3$]** and **[Eu.(120(*R,R*))$_3$]**, respectively. No strong evidence of the $^5D_0 \rightarrow {}^7F_0$ transition of Eu^{III} was observed in these emission spectra. Since the relaxation of the selection rules by *J*-mixing is often insufficient to give appreciable intensity to the transition and observances are restricted to C_n, C_1 and C_s type symmetries.[69] It was suggested that **[Eu.(120(*S,S*))$_3$]** and

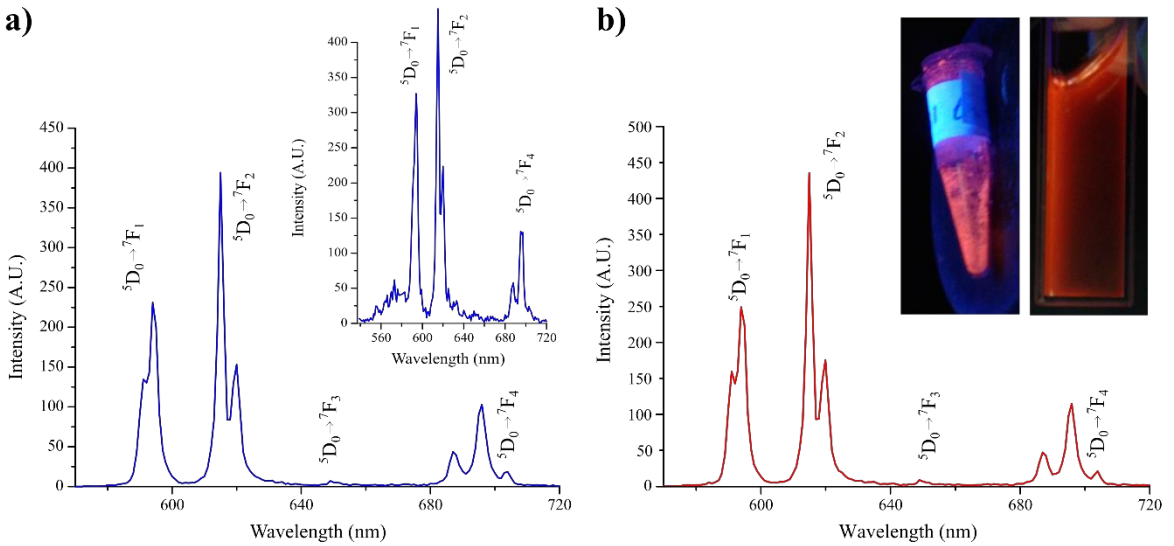

Figure 2.8 Luminescence solution spectra of Eu^{III}-centred emissive transitions showing $^5D_0 \rightarrow {}^7F_{1,2,3,4}$ characteristic transitions in both enantiomers. **a) [Eu.(120(*S,S*))$_3$]**, *inset*: fluorescence-timescale emission; **b) [Eu.(120(*R,R*))$_3$]** phosphorescence emission, *inset*: photographs of **[Eu.(120(*R,R*))$_3$]** solid (left) and aqueous solution (right). All spectra were recorded at $c = 1 \times 10^{-5}$ M in H_2O at 24 °C.

[Eu.(120(*R,R*))$_3$] adopted more D_3-like geometry in solution (rather than C_3) and, indeed, this was consistent with previous observations.[67,130,135,137,341,354,394]

The $^5D_0 \rightarrow {}^7F_1$ and $^5D_0 \rightarrow {}^7F_2$ transitions were both strongly observed in a ratio of 1:1.3, respectively, which was consistent with emission spectra for **[Eu.(133)$_3$]$^{3+}$** and related naphthyl-**dpa** derivatives *O*-substituted at the pyridyl 4-position.[340,386] Additionally, these strongest transitions were split to show m_J states by the ligand environment surrounding the Eu^{III} centre. The $^5D_0 \rightarrow {}^7F_1$ transition was resolved into two sub-components at λ_{em} = 589 and 592 nm, while $^5D_0 \rightarrow {}^7F_2$ also showed two resolved peaks at λ_{em} = 613 and 621 nm. The ratio between the integrated (and arbitrary) intensities of the subcomponents was consistent between **[Eu.(120(*S,S*))$_3$]** and **[Eu.(120(*R,R*))$_3$]** in aqueous solution and **[Eu.(133(*S,S*))$_3$]$^{3+}$** and **[Eu.(133(*R,R*))$_3$]$^{3+}$** in organic solutions. This indicated that there was minimal direct perturbation of the coordination environment of the Eu^{III} centre by pendent carbon chain or solvent environment. The $^5D_0 \rightarrow {}^7F_3$ transition was of (very) weak intensity which was consistent with the theoretical selection rules for "induced"-electric-dipole transitions from $J = 0$ excited states configurations ($\Delta J = 2, 4, 6$ for emissive transitions) in Ln^{III} complexes.[67] As was expected, the $^5D_0 \rightarrow {}^7F_4$ transition was also weaker than $^5D_0 \rightarrow {}^7F_{1,2}$ transitions and showed a splitting pattern that was resolved into three sub-components in a ratio of *ca.* 3:5:1 in integrated (and arbitrary) intensity. Overall, the Eu^{III}-centred emission spectra strongly suggested that the fundamental core structural geometry in **[Eu.(120(*S,S*))$_3$]** and **[Eu.(120(*R,R*))$_3$]** was closely correlated to those of the Eu^{III} complexes of **97** - **100** (*O*-

substituted naphthyl **dpa** systems). Therefore, it was suggested that observed photophysical perturbations were not likely a result of distortions in first coordination sphere geometry.

2.4.2 Luminescence emission lifetimes and Eu^{III} hydration states

Luminescence life-time (τ_{obs}) measurements for the Eu^{III}-centred emission were recorded from aqueous solutions of **[Eu.(120(*S,S*))$_3$]** and **[Eu.(120(*R,R*))$_3$]** in H_2O and D_2O, Figure 2.9a. The decay of luminescence at λ_{em} = 615 nm was measured at various gate times to allow calculation of the average radiative lifetime of the phosphorescence emission. The lifetimes of the $^5D_0$ excited-state of Eu^{III} were best fitted as a mono-exponential decay, shown in Figure 2.9b for **[Eu.(120(*R,R*))$_3$]**. This indicated that there was a single emissive species in solution. This species was assigned by the complimentary spectroscopy to be the **ML$_3$** complexes and confirmed the complex structures as having stoichiometry consistent with **[Eu.(120(*S,S*))$_3$]** and **[Eu.(120(*R,R*))$_3$]**.

From the fitted decay curves, the excited-state lifetimes were determined as 1.61 ± 0.01 ms in H_2O and 3.9 ± 0.1 ms in D_2O; the lifetime values calculated for **[Eu.(120(*S,S*))$_3$]$^{3+}$** and **[Eu.(120(*R,R*))$_3$]$^{3+}$** were equivalent and demonstrated the expected corresponding behaviour between enantiomers. No substantial perturbation in the emission lifetime was observed with introduction of the sulfonate moiety and they were similar to those found for Eu^{III} complexes of ligands such as **133(*S,S*)** and **133(*R,R*)** when recorded as suspensions in H_2O and D_2O.[395] The luminescence lifetime values stated in Table 2.1 were eventually

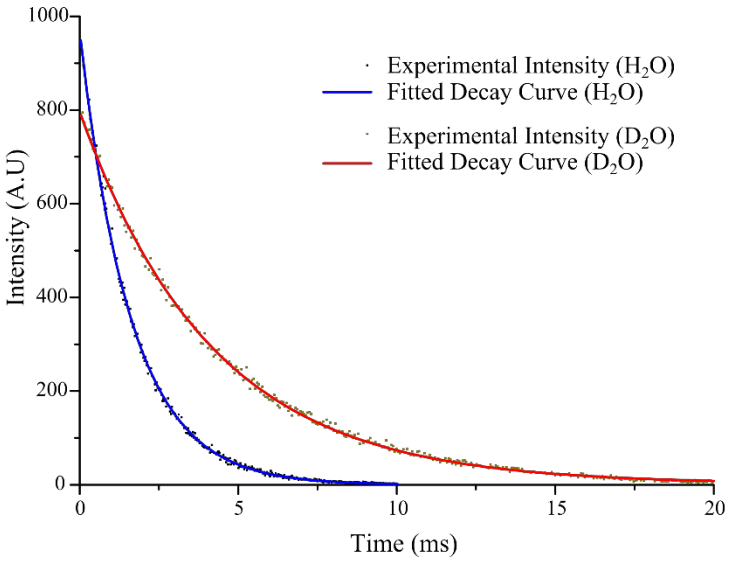

Model Fitted: $I = A_1 \times e^{\frac{-t}{\tau}} + y_0$

H_2O		
	Result	**S.E.**
τ	1.61016	0.00521
A_1	969.74238	1.66757
y_0	-0.17344	0.53216
Adj. R^2	0.99	

D_2O		
	Result	**S.E.**
τ	4.15961	0.01875
A_1	794.95463	1.62554
y_0	1.80035	0.74594
Adj. R^2	0.99	

Figure 2.9 a) Representative Eu^{III}-centred luminescence (λ_{em} = 615 nm, λ_{exc} = 281 nm) decay curves (points) and mono-exponential fit (line) for **[Eu.(120(*R,R*))$_3$]** recorded from solutions in H_2O (blue) and D_2O (red); **b)** Mono-exponential decay models results for single species in solution and giving luminescence lifetime values. Reported τ values in Table 2.1 are averages of 5 fitted decay models with varying gate times (shown gate time = 0.025 ms).

derived from the average lifetimes determined by five independent measurements, with different gate times between 0.015 – 0.035 ms, from the solutions or suspensions.

From these data, the hydration state, *q*, was also determined, using Horrocks' equation[396] for bound water molecules to Eu^{III}, with Parker's modification[114] for N-H oscillators:

$$q^{Eu^{III}} = A\left[\left(\frac{1}{\tau_{OH}} - \frac{1}{\tau_{OD}}\right) - 0.25 - 0.075x\right] \qquad \textbf{Equation 2.1}$$

The proportionality constant (*A*) specific to Eu^{III} in aqueous systems was determined as 0.525 ms per O-H oscillator and, therefore, 1.2 ms for each bound H_2O molecule (increased to 2.1 ms in methanolic solution). The correction factor of −0.25 ms^{-1} accounted for the quenching effects of second-sphere water molecule.[397] Parker's modification, the term $-0.075x$ ms^{-1}, corresponded to a correction for the effect of N-H oscillators in the coordinated amide moieties, where *x* was equal to the number of N-H oscillators. Table 2.1 also summarises the *q* values determined *via* Horrocks' and Parker's modified equations. The values were determined to be zero for all complexes and indicated that the complexes had no aqua ligands coordinated to Eu^{III} and was fully saturated by coordinating ligands.[136]

Table 2.1 Luminescence lifetimes (τ) recorded from aqueous solution (**[Eu.(120(*S,S*))$_3$]** and **[Eu.(120(*R,R*))$_3$]**) and suspensions (**[Eu.(133(*S,S*))$_3$]** and **[Eu.(133(*R,R*))$_3$]**) with *q*-value (hydration states) as determined by Horrocks' and Parker's equation(s) (Equation 2.1). Lifetimes were determined as averages of five independent measurements.

Complex	τ (H_2O), ms	τ (D_2O), ms	Horrocks *q* (± 0.5)	Parker *q* (± 0.5)
[Eu.(**120(*S,S*)**)$_3$]	1.60 ± 0.01	3.9 ± 0.1	0.14	~ 0
[Eu.(**120(*R,R*)**)$_3$]	1.61 ± 0.01	4.0 ± 0.1	0.14	~ 0
[Eu.(**133(*S,S*)**)$_3$]$^{3+}$	1.53 ± 0.08	2.3 ± 0.3	-0.03	~ 0
[Eu.(**133(*R,R*)**)$_3$]$^{3+}$	1.4 ± 0.1	2.9 ± 0.3	0.11	~ 0

The *q*-values determined by Parker's equation (following correction for the six N-H oscillators present in the complex) returned negative values. This was likely due to the complexes being in suspension and, therefore, the empirical corrections (determined in solution) deviated from Parkers's proposed models.[398] The lifetimes and *q*-values of zero were, however, consistent with the **ML$_3$**, the complex of stoichiometry with one Eu^{III} to three ligands existing uniquely in solution; the **ML$_3$** stoichiometry fulfilled the coordination

requirements of Eu^{III} which is 9 - 10.[63] The general consistency with the parent ligands indicated that the pendent sulfonate moiety was removed from the immediate photophysical processes and did not influence the stoichiometry of the thermodynamically-formed complexes as both **[Eu.(133)$_3$]$^{3+}$** and **[Eu.(120)$_3$]** gave hydration states of zero. The complexes for **[Eu.(120(*S,S*))$_3$]** and **[Eu.(120(*R,R*))$_3$]** were found to be stable in water and in buffered aqueous solution over the period of several months and these lifetimes and hydration states were reproducible.

2.4.3 Photophysical parameters, quantum yields and sensitisation efficiencies

The ligands **120(*S,S*)** and **120(*R,R*)**, along with their Eu^{III} complexes, were studied in neat aqueous solutions due to the solubility provided by the sulfonate moiety. However, to compare their behaviours more fully, parameterisation of Eu^{III}-centred emission was made in three systems: i) CH_3OH (as a competitive organic medium); ii) neat H_2O; and iii) HEPES-buffered aqueous solution (to evaluate ionic aqueous media for stabilisation or quenching effects). The key photophysical parameters are summarised in Table 2.2 for **[Eu.(120(*S,S*))$_3$]** and **[Eu.(120(*R,R*))$_3$]**.

The photoluminescence quantum yields (Φ_{tot}, %) were determined in CH_3OH, H_2O, 0.1M HEPES buffer using a relative method against the **Cs$_3$[Eu.(6)$_3$]·9H$_2$O** standard established by Bünzli and co-workers.[127,399] The relative method for quantum yield determination is described in Equation 2.2:

$$\Phi_{REL}^{Eu,L} = \frac{\Phi_S}{\Phi_R} = \frac{E_S}{E_R} \times \frac{A_R(\lambda_R)}{A_S(\lambda_S)} \times \frac{I_R(\lambda_R)}{I_S(\lambda_S)} \times \frac{n_S^2}{n_R^2} \qquad \textbf{Equation 2.2}$$

In Equation 2.2, Φ_{REL} represented a ratio of the total quantum yield of the sample (Φ_S) and the known absolute quantum yield of a reference standard (Φ_R). This quantum yield is denoted as $\Phi_{REL}^{Eu,L}$ and should be distinguished from Φ_{Ln}^{Ln}, the intrinsic quantum yield of Ln^{III}-centred emission. The ratio of quantum yields is determined from the relative relationships of integrated luminescence intensity (E_S and E_R, for sample and reference, respectively), the absorbance at the relevant excitation wavelength (A_S and A_R), the intensities of the source of excitation (I_S and I_R), and the refractive indices of solution (n_S and n_R).

Three additional parameters were determined. Firstly the τ_R (k_R^{-1}), the radiative lifetime of Eu^{III}, describing both non-radiative and radiative deactivation processes, was calculated by Equation 2.3:

$$\frac{1}{\tau_R} = A_{MD,0} \cdot n^3 \cdot \left(\frac{I_{tot}}{I_{MD}}\right) \qquad \textbf{Equation 2.3}$$

where $A_{MD,0}$ corresponded to the Einstein coefficient for the spontaneous emission probability of the magnetic-dipole-allowed $^5D_0 \rightarrow {}^7F_1$ emissive transition of Eu^{III}, determined as 14.65 s^{-1} for this transition;[126] n was the refractive index of the solvent; and, I_{tot}/I_{MD} the ratio of total integrated emission spectrum to the integrated emission of the $^5D_0 \rightarrow {}^7F_1$ transition of Eu^{III}.

The intrinsic quantum yield of the Eu^{III} emission, Φ_{Eu}^{Eu}, was determined. This parameter compared the observed luminescence of sensitised emission to the theoretical lifetime. Therefore the intrinsic quantum yield described the maximum emission quantum yield from Eu^{III} assuming 100% sensitisation efficiency and was calculated by Equation 2.4:

$$\Phi_{Ln}^{Ln} = \frac{\tau_{obs}}{\tau_R} \qquad \textbf{Equation 2.4}$$

where τ_{obs} was the measured luminescence lifetime and τ_R the calculated theoretical lifetime, Equation 2.3. Furthermore, the antenna-to-ion energy transfer efficiency, η_{sens}, was also calculated and compared Φ_{Eu}^{Eu} to Φ_{Ln}^{Ln}, as shown in Equation 2.5:

$$\eta_{sens} = \frac{\Phi_{tot}}{\Phi_{Ln}^{Ln}} \qquad \textbf{Equation 2.5}$$

where Φ_{tot} was the experimental relative quantum yield and Φ_{Ln}^{Ln} was the calculated instrinsic quantum yield.

Table 2.2 Photophysical parameters in H_2O, 0.1M HEPES and CH_3OH at 25 °C: lifetime values (τ, τ_R), total and intrinsic quantum yield percentages (Φ_{tot}, Φ_{Eu}), and antenna-to-Eu^{III} sensitisation efficiencies (η_{sens}) for Eu^{III} complexes of **120(*S,S*)** and **120(*R,R*)**. Calculations made using Equations 2.1 – 2.5, excitation at λ_{exc} = 279 nm.[127] Estimated error associated with quantum yields (Φ_{tot}) is ±10%.[137] Uncertainties were determined through averaging independent measurements and represent standard deviations from the mean value.

Complex	Solvent	τ_{obs}, ms	Φ_{tot}, %	τ_R, ms	Φ_{Eu}^{Eu}, %	η_{sens}, %
[Eu.(120(*S,S*))$_3$]	H_2O	1.59(2)	11.4(3)	11.0(2)	14.5(3)	78.5(4)
	$HEPES_{(aq)}$	1.58(1)	10.9(5)	11.4(1)	13.9(3)	78.0(4)
	CH_3OH	1.62(1)	4.5(3)	12.7(4)	12.8(3)	35.0(2)
[Eu.(120(*R,R*))$_3$]	H_2O	1.60(1)	11.8(3)	9.5(3)	16.9(4)	69.6(4)
	$HEPES_{(aq)}$	1.58(2)	11.6(4)	10.4(3)	15.2(4)	76.6(3)
	CH_3OH	1.68(2)	3.4(2)	12.9(2)	13.0(2)	26.4(2)

The total quantum yields (Φ_{tot}) of **[Eu.(120(*S,S*))$_3$]** and **[Eu.(120(*R,R*))$_3$]** in aqueous solution were determined as *ca.* 12% in water as well as in buffered solution. These values were significantly higher than **[Eu.(133)$_3$]$^{3+}$** and **[Eu.(6)$_3$]$^{3+}$** in organic solution which showed Φ_{tot} *ca.* 4% and 7.5%, respectively.[340,341] The photophysical parameters determined

in CH_3OH were in agreement with the Eu^{III} complexes of **133** and clearly demonstrated the changes to be solvent-specific dependent. Since the O-H oscillator is a prevalent first and second sphere quencher, it could be expected that luminescence be more extensively quenched in aqueous environments. However, the **[Eu.(120(*S,S*))$_3$]** and **[Eu.(120(*R,R*))$_3$]** gave more intense luminescence n the aqueous environment despite the increased quenching ability of the aqueous solvent. The observed enhancement in quantum yield could not be accounted for by the electronic effect of solvent polarity alone, with equivalent ground-state features and behaviour in both H_2O and CH_3OH observed.

For all previous naphthyl **dpa** complexes, it has been observed that the quantum yields in CH_3CN are higher than in CH_3OH because of the quenching ability of the O-H bonds. However, it is interesting to note that enhancement was seen in **[Eu.(98)$_3$]$^{3+}$** when studied in 1:1 ratios of CH_3OH:H_2O co-solvent.[340] The enhancement of emission in CH_3OH:H_2O co-solvent can only indicate that selective solvation and hydrophobic effects influence the excited-state photophysical properties. The enhancements in Φ_{tot} seen for **[Eu.(120(*S,S*))$_3$]** and **[Eu.(120(*R,R*))$_3$]** could be accounted for through hydrophobic self-assembly of the complexes which may result in improved exclusion of second-coordination sphere H_2O quenchers and decrease chromophore-Eu^{III} distances.

The luminescence lifetimes (τ_{obs}), that were previously recorded in D_2O and H_2O, were also measured in 0.1M HEPES and CH_3OH. The values of τ_{obs} were not substantially affected by the solvent environment. This suggested that the naphthyl groups provided some protection of the Eu^{III} centre from interaction with the external solvent environment and the influence of second-sphere O-H quenchers was limited.

Small changes to the Eu^{III} environment were suggested by the theoretical radiative lifetimes (τ_R) and intrinsic quantum yield (Φ_{Eu}^{Eu}); the values are shown in Table 2.2. The τ_R is influenced by the ion surrounding and refractive index of the system, and therefore so is Φ_{Eu}^{Eu} (Equation 2.4).[126,400,401] The τ_R values were extended *ca.* 1-2 ms extended in CH_3OH and almost equivalent in H_2O and 0.1M HEPES. The determined values were not substantially different and would represent only very small intrinsic changes to the complexes. This would be consistent with small perturbations induced in the hydrophobically-driven conformation of the ligands around the metal centre or perturbation of the electrostatic ligand field by the bulk solvent.

The key parameter for the photophysical performance of **[Eu.(120(*S,S*))$_3$]** and **[Eu.(120(*R,R*))$_3$]** was the sensitisation efficiency (η_{sens}); values are shown in Table 2.2. In

CH_3OH, the sensitisation efficiency, η_{sens}, were determined as *ca.* 30 – 35 % and were in agreement with Eu^{III} complexes of **97 - 100** with *O*-substituted pyridines in CH_3OH, although corresponded to a less efficient sensitisation process than the underivatised napthyl **dpa, 17**, under the same conditions. Upon moving to aqueous media from CH_3OH, substantial enhancement in the efficiency of sensitisation was observed. In 100% H_2O and 0.1 M HEPES the efficiency was doubled compared to CH_3OH and increased by *ca.* 75 - 80%. This indicated that Φ_{tot} was approaching the intrinsic value of Φ_{Eu}^{Eu} and represented the highest magnitude observed to-date for this scaffold. The increase in η_{sens} was accounted for by hydrophobic effects upon complex assembly with the lipophilic cores of the ligands interacting closer together in the **ML_3** complexes. As a result, if ligands became more tightly packed around the Eu^{III} centre it would be expected that chromophore-to-Eu^{III} distances be slightly reduced. Furthermore, hydrophobic exclusion of quenching H_2O solvent from around the chromophores and Eu^{III} centre can be expected to be enhanced in the aqueous environment because of this highly lipophilic character. In this scaffold, while structural modification of the pyridine was able to provide solubility in H_2O, the overall limitations to Eu^{III} emission arise from the symmetry of the complexes formed.

The photophysical parameters also revealed the limited effect of ionic strength on the system. The absorbance and emission features were also recorded in buffered (0.1 M HEPES) solution and were found to be consistent with neat water. Emission lifetimes in buffered H_2O and the quantum yields agreed between neat and buffered H_2O systems. The ionic strength was, therefore, not substantially impacting the luminescence or self-assembly and suggested that the emissive complexes could be taken into more complex media in the future without immediately unfavourable effects.

2.4.4 Circular dichroism and circularly polarised luminescence of [Eu.(120(*S,S*))$_3$] and [Eu.(120(*R,R*))$_3$]

Complimentary to the chiral studies of the ligands, the chirality of the Eu^{III} complexes was confirmed by using CD and CPL spectroscopy. CD and CPL spectra were recorded in 100% H_2O by Dr. Robert D. Peacock at the University of Glasgow and are shown in Figure 2.10. The results were consistent with the presence of single enantiomer in solution and showed consistencies between the complexes and their respective ligands.

The CD spectra of **[Eu.(120(*S,S*))$_3$]** and **[Eu.(120(*R,R*))$_3$]** were of equal shape and magnitude but of opposite sign and as expected for the enantiomeric pair. The strong Cotton effect, positive in the case of **[Eu.(120(*S,S*))$_3$]** and negative for **[Eu.(120(*R,R*))$_3$]**, was again observed indicating a possible coupling between naphthyl and pyridyl chromophores in the

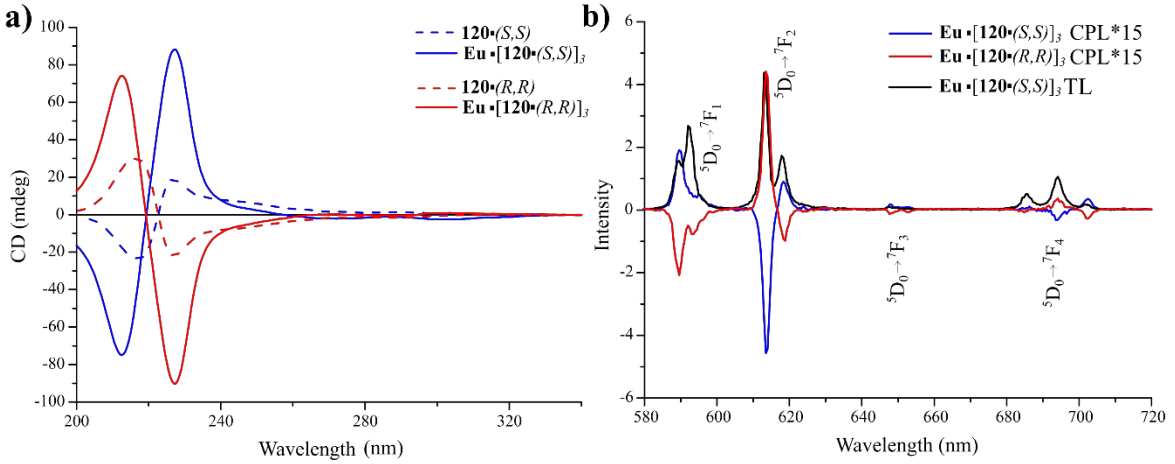

Figure 2.10 Chiroptical spectra of ligands **120(*S,S*)** (blue dashed), **120(*R,R*)** (red dashed) and their complexes **[Eu.(120(*S,S*))$_3$]** (blue solid), **[Eu.(120(*R,R*))$_3$]** (red solid): **a)** CD absorption spectra showing enhancement and maxima wavelength shifts between ligands (dashed, $c = 1 \times 10^{-5}$ M) and complexes (solid, $c = 3.3 \times 10^{-6}$ M); and **b)** CPL emission spectra including total luminescence of **[Eu.(120(*S,S*))$_3$]** (black solid).

complexes as well as the free ligand. At the same effective ligand concentrations, the CD signals were of the same sign but enhanced significantly (*ca*. 300%) compared to the respective ligands, as can be seen in Figure 2.10a. While maintaining the same bulk profile as their respective ligands, **[Eu.(120(*S,S*))$_3$]** and **[Eu.(120(*R,R*))$_3$]** possessed small structural differences to spectra with measurable increases in the Davydov splitting to 6 and 7 nm along with the enhancements in the signal intensity. This corresponded to the assembly of the complexes which directed the relative conformations of the chromophores while placing naphthyl and pyridyl chromophores of adjacent ligands into close proximity.

In order to probe the potential exciton coupling in the complexes, in the same manner as for the ligands above, the CD spectra of both Eu^{III} complexes were measured as a function of temperature. CD spectra were recorded varying the temperature from –10 to +40 °C; the

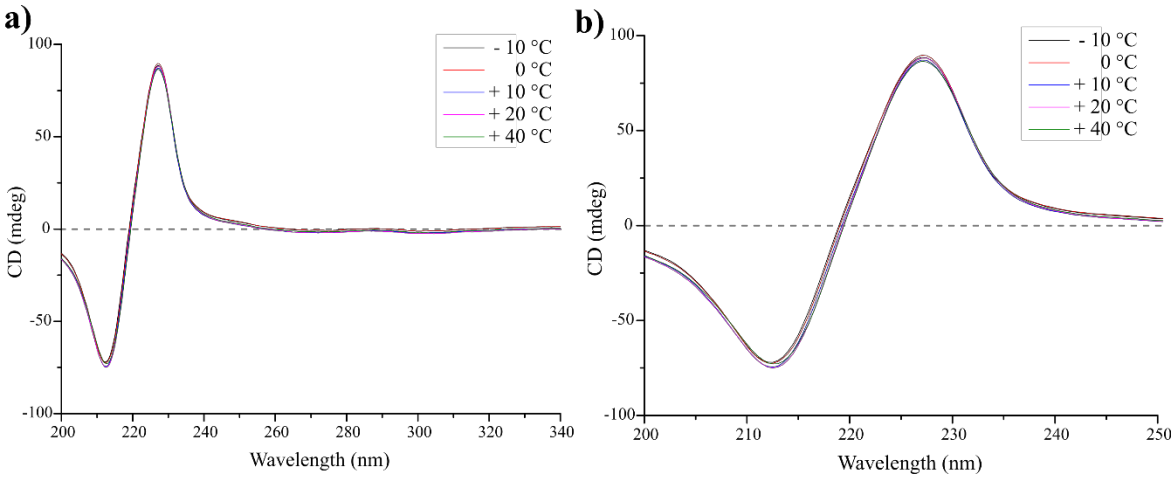

Figure 2.11 Variable temperature CD spectra of **[Eu.(120(*S,S*))$_3$]** recorded between -10 °C and +40 °C showing small intensity and minor wavelength shifts in the 213 nm negative CD band; **a)** full spectrum (200 – 340 nm); and **b)** zoomed region (200 – 250 nm) of higher energy absorption showing only minimal changes.

spectra are shown in Figure 2.11 for **[Eu.(120(*S,S*))$_3$]**. However, unlike the ligands insignificant changes were observed with temperature. While there was a lack of changes in the CD with temperature, it has been noted that couplets with strong Cotton effect have been shown to imply this exciton mechanism. [402-404] Indeed, the minimal temperature dependence was likely due to the restriction of freedom in the ligand conformation and corresponding chromophore orientations on forming the complexes.

As the complex bundles showed strong chiral nature through their CD, the specific chiral environment of the Eu^{III} ion was probed by CPL spectroscopy following excitation of the ligand naphthyl-centred absorption bands. The chiral nature of coordinating ligands and assemblies may be transferred to the Eu^{III}-centred emission in the formation of enantiopure bundles should the metal ion be placed in a suitably chiral environment.[130,136,405]

The CPL spectra of **[Eu.(120(*S,S*))$_3$]** and **[Eu.(120(*R,R*))$_3$]** were recorded by Dr. Robert D. Peacock and are shown in Figure 2.10b. The Eu^{III} emission gave rise to mirror-image CPL spectra showing the appearance of $^5D_0 \rightarrow {}^7F_J$ (J = 1–4) transition bands. The total luminescence spectra displayed the same splitting and ratiometry while and the CPL measurements showed a characteristic structure for both **[Eu.(120(*S,S*))$_3$]** and **[Eu.(120(*R,R*))$_3$]** complexes. The $^5D_0 \rightarrow {}^7F_1$ transition was split into two emission maxima at λ_{em} = 589 and 592 nm, and the $^5D_0 \rightarrow {}^7F_2$ transition was split into the components 615 nm and 621 nm. The structure in the dissymmetry magnitude and signs of these two transitions differed whle the two enantiomers gave equal but opposite spectra. The complex **[Eu.(120(*S,S*))$_3$]** showed positive CPL signals for the $^5D_0 \rightarrow {}^7F_1$ and $^5D_0 \rightarrow {}^7F_3$ transitions while the $^5D_0 \rightarrow {}^7F_2$ and $^5D_0 \rightarrow {}^7F_4$ transitions were both split to give bisignate CPL signals containing positive and negative components.

Luminescence dissymmetry factors g_{lum}, were determined in order to quantify the chiral character of each Eu^{III}-centred emissive transitions. The values of g_{lum} were calculated for each transition as a ratio of the CPL magnitude to total luminescence (TL) intensity through the relationship shown in Equation 2.6 and Equation 2.7:

$$g_{lum} = \frac{2 \times CPL}{TL} \qquad \textbf{Equation 2.6}$$

$$g_{lum} = 4 \frac{|\mu_{i,j}| . |m_{j,i}| . \cos\theta_{\mu,m}}{|\mu_{i,j}|^2 + |m_{j,i}|^2} \qquad \textbf{Equation 2.7}$$

The CPL signals were well resolved and of reasonable intensity which allowed dissymmetry factors (g_{lum}) to be determined for the different $^5D_0 \rightarrow {}^7F_J$ transitions calculated. Selected g_{lum} values are presented in Table 2.1.

Table 2.1 Summary of dissymmetry factors (g_{lum}) calculated from CPL measurements of **[Eu.(120(*S,S*))$_3$]** and **[Eu.(120(*R,R*))$_3$]** emissive transitions in H_2O. g_{lum} values were in agreement when calculated from both arbitrary and integrated intensities. *weak transition in TL and CPL.

λ_{em}	[Eu.(120(*S,S*))$_3$] g_{lum}	[Eu.(120(*R,R*))$_3$] g_{lum}	Transition	Nature
589	0.16	-0.18	$^5D_0 \rightarrow {}^7F_1$	MD
592	0.03	-0.03		
614	-0.14	0.13	$^5D_0 \rightarrow {}^7F_2$	IED
618	0.07	-0.08		
652	0.24	-0.24	$^5D_0 \rightarrow {}^7F_3$	IED*
685	0.03	-0.02	$^5D_0 \rightarrow {}^7F_4$	IED
694	-0.04	0.05		
702	0.31	-0.22		

The ratios in CPL dissymmetry differed from intensity ratios from classical emission spectra, notably for $^5D_0 \rightarrow {}^7F_1$ and $^5D_0 \rightarrow {}^7F_2$. The $^5D_0 \rightarrow {}^7F_{0,1}$ transitions in Eu^{III} are considered the most appropriate for CPL analysis since they give the strongest intensities and dissymmetry because of their MD-allowed nature.[406] The value of g_{lum} is given by the coupling of magnetic and electric dipole components of the transition (see Equation 2.7 above) and the magnitude depending on whether the transition is ED or MD allowed/forbidden. The larger g_{lum} values, therefore, come from MD allowed and ED forbidden transitions.[405]

In fact, the largest g_{lum} value was seen for the $^5D_0 \rightarrow {}^7F_1$ transition at 589 nm which is the only MD-allowed $^5D_0 \rightarrow {}^7F_J$ transition in Eu^{III} ions. The values of g_{lum} for $^5D_0 \rightarrow {}^7F_2$ are indeed slightly smaller than for $^5D_0 \rightarrow {}^7F_1$, however, remain appreciable despite being an ED-allowed/MD-forbidden *f-f* transition. This is likely due to the hypersensitivity associated with this ED-transition under many ligand fields and favourable $\theta_{m,\mu}$ term.[407] In the case of the $^5D_0 \rightarrow {}^7F_1$ transition, the 589 nm component showed a g_{lum} value of 0.16 while the second component showed negligible chiral emission. Similarly for the two components of the $^5D_0 \rightarrow {}^7F_2$ transition, the second component (λ_{em} = 618 nm) gave half the chiral emission of the first component (λ_{em} = 614 nm).

The dissymmetry factors for $^5D_0 \rightarrow {}^7F_3$ and $^5D_0 \rightarrow {}^7F_4$, which were both observed in TL and CPL measurement, were calculated but treated with caution. The intrinsically lower

TL intensity of $^5D_0 \rightarrow {}^7F_J$ transitions where $\Delta J \geq 2$, on account of *J*-mixing, reduced the confidence in which these g_{lum} values could be determined. The intensity of the $^5D_0 \rightarrow {}^7F_3$ emission was very low, and should be treated with greater experimental uncertainty. However, the magnitude of all these g_{lum} values were similar to those that have been observed for the naphthyl-**dpa** scaffold.[95] In addition, the dissymmetry factors for all transitions (including $^5D_0 \rightarrow {}^7F_{3,4}$) were also comparable to those seen in phenyl-**dpa** analogues.[138] The order of magnitudes of g_{lum} were of the same order typically seen for emissive enantiopure Eu^{III} and Tb^{III} complexes where g_{lum} is observed between 0.1 and 0.5 (the upper limit being considered "*extraordinarily*" large).[408,409] For the $^5D_0 \rightarrow {}^7F_1$ transition (λ_{em} = 589 nm) g_{lum} values were calculated to be +0.16 and –0.15, while for $^5D_0 \rightarrow {}^7F_2$ (λ_{em} = 615 nm) to be +0.13 and -0.14. These were relatively large within the naphthyl-**dpa** scaffold demonstrating efficient de-symmetrisation of the 'spherical' Eu^{III} emitter.

The chiral environment dissymmetry factors (g_{lum}) are sensitive to the magnetic and electric transition dipole moments and the angle through which they are coupled.[410] Therefore, the magnitude, sign and distribution can be considered to reflect the absolute geometry around the central ion.[137] In fact, for the Eu^{III} complexes symmetrical naphthyl **dpa** the sign of the CPL intensity and g_{lum} values have aided in analysis of geometry in solution, due to the *J* levels of ^7F_J being split in a consistent manner by the immediate environment.[341] This CPL structure has been used to act as a structural signature for the absolute complex stereochemistry as Λ or Δ isomers, in solution. [136,341]

The CPL spectra of both **[Eu.(120(*S,S*))$_3$]** and **[Eu.(120(*R,R*))$_3$]**, were identical in their main transition structures, and sign distribution of g_{lum}, to that observed for the previously studied naphthyl **dpa** complexes. Therefore, it was assigned that **[Eu.(120(*R,R*))$_3$]** gave the **Λ** complex and **[Eu.(120(*S,S*))$_3$]** gave the **Δ** complex in solution. The consistency in overall CPL (in agreement with total emission spectra) indicated that in aqueous environments the complex coordination geometry was not affected significantly by the competitive environment. The subtle differences within the magnitudes of g_{lum} from **[Eu·(120(*S,S*))$_3$]** and **[Eu·(120(*R,R*))$_3$]** and related complexes[340,341] were likely due to vicinal perturbation effects[411] of the true conformation of **120(*S,S*)** or **120(*R,R*)** as a result of the pendent chain and corresponding solvent interactions.[410]

Following this characterisation of the **[Eu.(120(*S,S*))$_3$]** and **[Eu.(120(*R,R*))$_3$]** from thermodynamic synthesis, the kinetically-controlled self-assembly processes of ligand **120(*S,S*)** and **120(*R,R*)** in aqueous systems, and the resulting complexes, were studied.

2.5 Solution self-assembly studies of 120(*S,S*) and 120(*R,R*) with Eu^{III} in H_2O

The formation and characterisation of **[Eu.(120(*S,S*))$_3$]** and **[Eu.(120(*R,R*))$_3$]** described in the previous section concerned the thermodynamic products of high-temperature synthesis. Self-assembly in ambient conditions represents the kinetically favourable assemblies and complexes that tend to be more dynamic, fluxional and of varied stoichiometry. These processes were studied for **120(*S,S*)** and **120(*R,R*)** with $Eu(CF_3SO_3)_3$ in H_2O

Consequently, the spectroscopic titrations were carried out at ligand concentrations of 1×10^{-5} M. At this concentration the lanthanide-directed self-assembly was also observed to be fast and no substantial equilibration period was needed at each equivalence. The ligand solutions were titrated by sequential additions of aqueous $Eu(CF_3SO_3)_3$ and the relevant spectra recorded immediately after each addition. The trends discussed in the following sections represent behaviours that were reproducible from at least three independent experiments; stability constants could therefore be determined as averages. For clarity only the self-assembly of **120(*S,S*)** with Eu^{III} will be discussed; **120(*R,R*)** behaved equivalent and the corresponding data and spectra can be found in Appendix A2.

2.5.1 UV-visible absorption and luminescence titrations

The speciation of the lanthanide-directed assembly was monitored by multiple spectroscopic methods in parallel. Spectroscopic changes in the ground-state were monitored using UV-visible absorbance spectroscopy while the solution emission was recorded with both fluorescence and time-gated luminescence (phosphorescence mode) spectroscopies.

The absorption spectra recorded during a titration of **120(*S,S*)** are shown in Figure 2.12a, and the overall binding isotherms for absorbance at key wavelengths are shown in Figure 2.12b. Significant and large changes were observed in the higher energy $n \rightarrow \pi^*$ transitions at 220 nm while substantial changes of smaller magnitude were seen in the naphthyl $\pi \rightarrow \pi^*$ transitions at 270 - 300 nm. There was an average hypochromic shift of the absorbance band at 220 nm with concomitant deconvolution of the absorbance into two separate maxima that were shifted from each other by 10 nm (λ_{max} = 214 nm and 224 nm). Hypochromism was also observed for the naphthyl $\pi \rightarrow \pi^*$ absorbance between λ_{abs} = 260 – 290 nm with the fine structure of the maxima being lost to a broad and unresolved absorbance at 0.33 equivalents of Eu^{III} being added.

An enhancement of the absorbance at longer wavelength (λ_{abs} > 290 nm) was observed, with a clear isosbestic point appearing at λ_{abs} = 291 nm as shown in Figure 2.12a (inset). A second isosobestic point could be seen at λ_{abs} = 255 nm accompanying hyperchromism of the region of λ_{abs} = 235 – 255 nm. These points indicated that there was

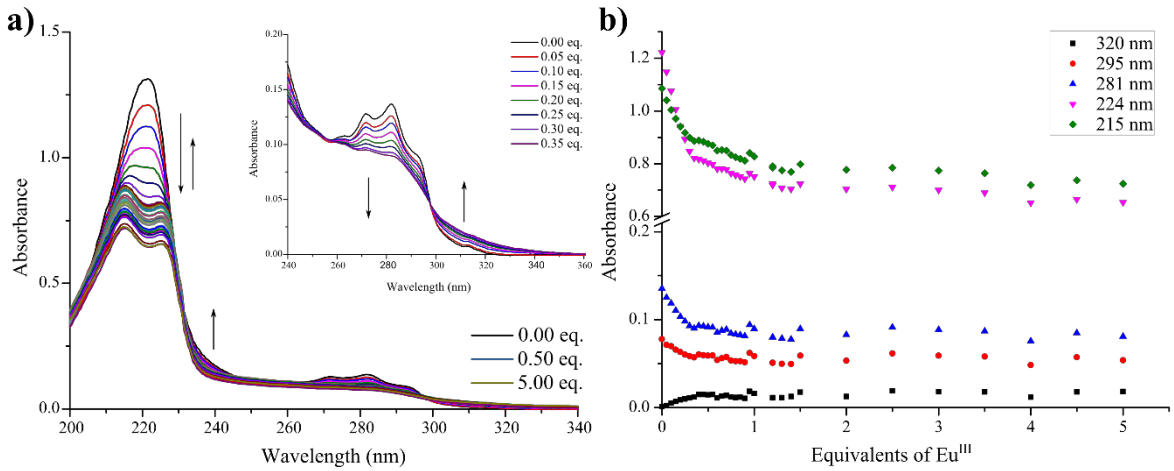

Figure 2.12 Overall changes for UV-visible absorption spectra upon titration of **120(*S,S*)** with $Eu(CF_3SO_3)_3$; **a)** overlaid UV-visible absorption spectra from 0.00 → 5.00 equivalents of Eu^{III}, ***inset***: zoomed region of naphthyl π → π* electron transitions, clearly showing two isosbestic points; **b)** corresponding binding isotherms from titration a) for key absorption maxima (λ_{abs} = 320, 295, 281, 224, 215 nm) showing changes with increasing Eu^{III} concentration. Spectra were recorded in CH_3CN at 24 °C with initial [**120(*S,S*)**] = 1 × 10-5 M. This titration is representative of triply reproduced trends.

at least two correlated species in solution, one being ligand **120(*S,S*)** and was consistent with complex formation. The speciation was elucidated further by fitting of the titration data using non-linear regression analysis and is discussed in the Section 2.5.4. As can be seen in Figure 2.12b, the main changes in the absorption spectra occurred within the addition of 0.3 equivalents of Eu^{III}, with rapid hyper- or hypo-chromism seen across the spectrum. At higher equivalents of Eu^{III} (0.3 → 4.00 equivalents) only relatively minor changes occurred with a minor hypochromism seen in the two bands centred at λ_{abs} = 214 and 224 nm, before both reaching an effective plateau in absorbance at > 1.00 equivalents of Eu^{III}. After the addition of 0.33 equivalents of Eu^{III}, the changes were relatively small and did not provide much useful insight into the speciation in solution. However, the changes in the region 0 → 0.33 equivalents of Eu^{III} were dominantly due to the formation of the desired **ML_3** complexes and after reaching 1.00 equivalent of Eu^{III} the plateau attributed to **ML** complexes uniquely in solution.

It was notable that the splitting for the band centred at λ_{abs} = 220 nm into two separate features was considerably more resolved in the aqueous studies of **120(*S,S*)** and **120(*R,R*)** compared to related naphthyl **dpa** ligands in organic solutions, indicating a stronger chromophore coupling. However, in comparison, despite still being resolved in the hyperfine structure the changes in naphthyl π → π* absorption were much smaller in magnitude and the feature found to be less sensitive in H_2O than in CH_3CN or CH_3OH solutions. In general, this impacted the quality in modelling the titration data, and the ability to distinguish the types of complex existing in solution such as **ML_3**, **ML_2** and **ML** (or higher order

stoichiometries). To address this further the changes in the luminescence and the CD spectra during the step-wise assembly process were probed.

2.5.2 Eu^{III}-centred luminescence titrations (emission and time-gated emission)

As discussed earlier, ligand **120(*S,S*)** gave rise to weak intrinsic fluorescence and changes in the ligand-centred emission could not be monitored accurately. However, upon addition of Eu^{III} to **120(*S,S*)**, evolution of the Eu^{III}-centred emission was observed as a result of the sensitisation by the coordinating ligands. The Eu^{III} luminescence was monitored as time-gated emission and the appearance and intensity enhancement of the characteristic Eu^{III}-centred $^5D_0 \rightarrow {}^7F_{1,2,3,4}$ transitions occurring at λ_{em} = 585, 615, 621 and 700 nm, respectively, were clearly observed. The spectra and corresponding single wavelength isotherms are shown in Figure 2.13a and Figure 2.13b, respectively.

The emission showed enhancement from 0 → ≈ 0.35 equivalents of Eu^{III} before reaching a maximum and subsequent quenching by approximately 10% in the phosphorescence measurements with further additions of Eu^{III}. The most emissive state in solution was seen between 0.3 – 0.35 equivalents of Eu^{III}, which is consistent with previous experiments, and was likely due to the existence of higher stoichiometry species in solution such as **ML_3** and **ML_2**. Nevertheless, upon further additions of Eu^{III} (up to 5 equivalents) there was a gradual quenching in the sensitised Eu^{III} emission as expected from the increasing formation of **ML** complexes that are susceptible to solvent quenching.

The intensities of the $^5D_0 \rightarrow {}^7F_J$ transitions changed at the same rate with the relative ratios between and splitting in $^5D_0 \rightarrow {}^7F_1$ and $\rightarrow {}^7F_2$ remaining constant. This suggested that

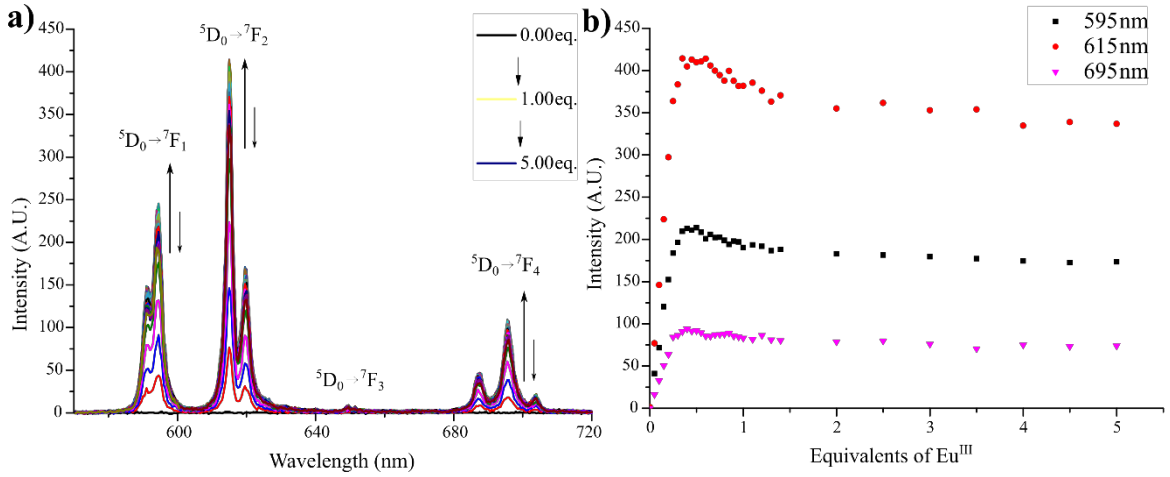

Figure 2.13 Overall changes for Eu^{III}-centred luminescence spectra upon titration of **120(*S,S*)** with $Eu(CF_3SO_3)_3$ in H_2O; **a)** overlaid luminescence spectra showing $^5D_0 \rightarrow {}^7F_{1,2,3,4}$ emissive transitions from Eu^{III} for 0.00 → 5.00 equivalents of Eu^{III}; and **b)** binding isotherms for the phosphorescence intensity of $^5D_0 \rightarrow {}^7F_{1,2,4}$ transitions at λ_{em} = 595, 615, 695 nm, respectively, with increasing Eu^{III} concentration. Spectra were recorded at 24 °C with initial [**120(*S,S*)**] = 1 × 10^{-5} M. This titration is representative of triply reproduced trends.

throughout the titration, the coordination sphere in both saturated and unsaturated Eu^{III} complexes shared many characteristics. The $^5D_0 \rightarrow {}^7F_0$ transition (which while being usually very weak[397] due to the strictly forbidden nature can arise at 580 nm in certain C_n geometries[69] and vary with solvent)[412] was not observed. In previous studies of naphthyl **dpa** ligands the appearance of this transition was in fact observed in CH_3OH but not CH_3CN, and assigned to the formation of both **ML₂** and **ML** stoichiometries in polar solvents.[341] The lack of the emergence of this transition in the case of **120(*S,S*)** with Eu^{III} could be attributed to the dynamic hydrophobic associations of **ML₂** and **ML** complexes in solution generating different chemical environments to those expected from discrete naphthyl-**dpa** complexes.

2.5.3 Chiroptical titrations using CD spectroscopy

It was established that with the coordination of **120(*S,S*)** and **120(*R,R*)** to Eu^{III} there were significant changes in their respective CD properties, as shown in Section 2.4.4. These changes were monitored in real time for the progressive behaviour in the CD bands upon the *in-situ* formation of $\mathbf{ML_n}$ species. These titrations were completed in 100% H_2O to minimise noise in the important features of chiral absorbance between λ_{abs} = 200 – 220 nm. The use of ionic strength and buffering has been exploited to stabilise the intermediate species and aid in the determination of binding constants, however, wavelengths close to 200 nm are disrupted by scattering in buffered systems.[347]

The titrations were carried out in an identical manner to those described above using ligand concentrations of 1×10^{-5} M and sequential additions of aqueous Eu^{III} as $Eu(CF_3SO_3)_3$. Ligands **120(*S,S*)** and **120(*R,R*)** showed opposite CD features with large

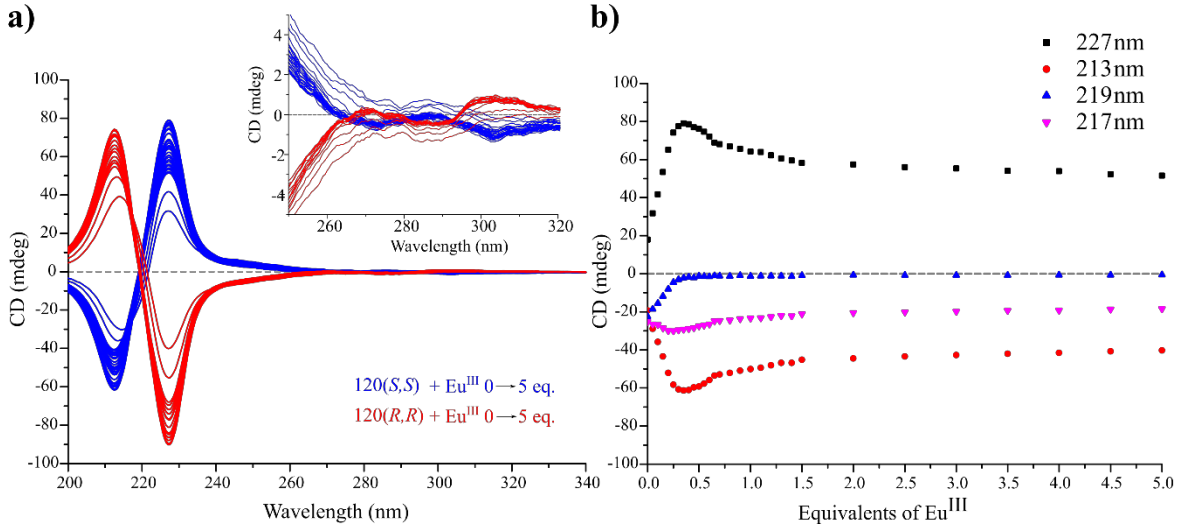

Figure 2.14 a) Overlaid CD titrations of **120(*S,S*)** (blue) and **120(*R,R*)** (red) between 0.00 → 5.00 equivalents of Eu^{III} showing hyperchromism in the main CD features and minor wavelength shifts in the ligand λ_{abs} = 217 nm band, ***inset*:** zoomed region of 250 – 320 nm showing small CD intensity changes in the naphthyl $\pi \rightarrow \pi^*$ features; **b)** binding isotherms of key CD absorbance features λ_{abs} = 213, 217, 219, 227 nm from the high energy Cotton effect bands with increasing Eu^{III} concentration. Spectra were recorded in H_2O at 24 °C from an initial ligand concentration *(c)* = 1×10^{-5} M. This titration is representative of triply reproduced trends.

ellipticity of the absorbance band centred at 224 nm and minor signal for the naphthyl $\pi \rightarrow \pi^*$ transitions at λ_{abs} = 275 nm; the progressive changes were clearly observed in the higher energy absorbance (λ_{abs} = 200 - 260 nm). The overall titrations for both **120(*S,S*)** and **120(*R,R*)** are shown in Figure 2.14a, the structure of the naphthyl $\pi \rightarrow \pi^*$ region are shown as inset. There was an instantaneous enhancement in both Cotton effect bands in the bisignate feature between λ_{abs} = 210 - 230 nm observed upon addition of Eu^{III}. These Cotton effect bands corresponded to the absorbance maxima observed in **[Eu.(120(*S,S*))$_3$]** and **[Eu.(120(*R,R*))$_3$]** formed under thermodynamic control. A bathochromic shift in the first Cotton band was observed while the second component only showed increased intensity but not shift in the absorbance maxima. The shift in the Cotton band started immediately upon the first addition of Eu^{III} (0.05 equivalents) and was complete after 0.3 equivalents of Eu^{III}; for further additions of Eu^{III} only intensity changes occurred. The naphthyl $\pi \rightarrow \pi^*$ CD bands (which absorbed much more weakly) decreased in magnitude upon the first additions of Eu^{III} until 0.30 equivalents (which was consistent with the formation of complexes) and then showed no appreciable changes during the course of titration. Binding isotherms for the titration of **120(*S,S*)** with Eu^{III} are plotted in Figure 2.14b, and indicated three regions of changes and multiple equilibria throughout the titration.

Following the initial enhancements in CD signal and the maxima of ellipticity at 0.35 equivalents of Eu^{III}, the CD intensity was decreased in two distinct regions; the first between $0.35 \rightarrow 0.60$ equivalents of Eu^{III} and the second from $0.60 \rightarrow 1.50$ equivalents of Eu^{III}. These modes were consistent with the formation of **ML$_2$** and **ML** species after dominant formation of **ML$_3$** complexes. The weaker CD signals were in agreement with the reducing stoichiometry and the associated reduction in ligand chromophore interactions.

Concomitantly, the emergence of isoeliptic points was observed at various points of the titration, for example at λ_{abs} = 217, 219 and 240 nm as highlighted in Figure 2.15a and Figure 2.15b. These isoeliptic points were observed sequentially and indicated multiple solution equilibria. Between $0 \rightarrow 0.60$ equivalents of Eu^{III} two isoeliptic points were observed at λ_{abs} = 217 and 240 nm. Upon further additions of Eu^{III} an additional isoeliptic point was observed at λ_{abs} = 219 nm for both ligands. These suggested that at least three, and potentially four, correlated species were formed in solution. This was consistent with the formation of **ML$_3$** complexes from **L** (**120(*S,S*)**) followed by a shift in the equilibrium processes towards the dissociation of **ML$_3$** into **ML$_2$** and eventually the formation of **ML** species. These observations in CD spectroscopy supported the changes described in classical absorption and the luminescence experiments and were considered suitable for determining

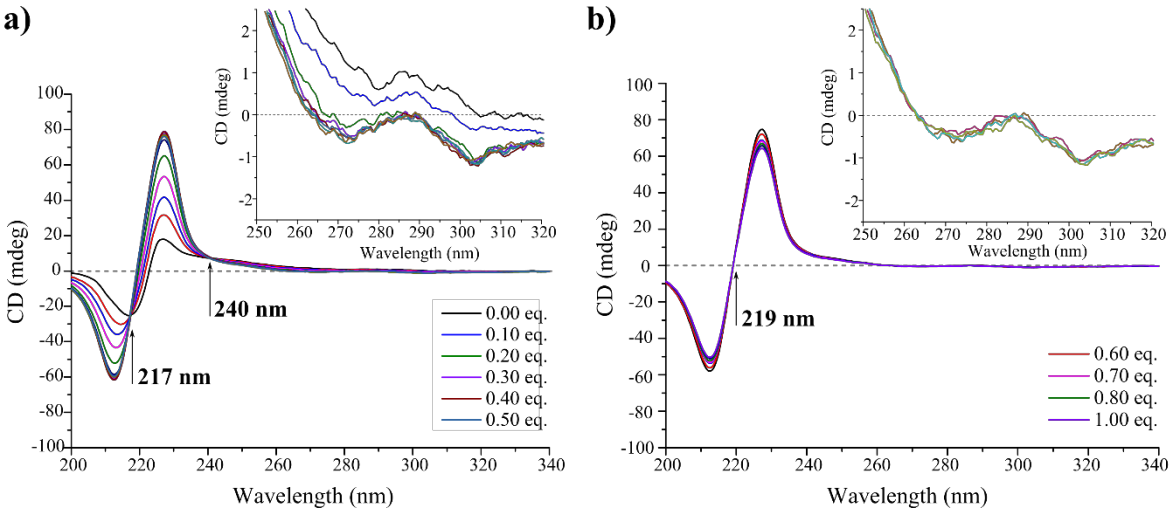

Figure 2.15 Partial overlaid CD titration of **120(*S,S*)** with $Eu(CF_3SO_3)_3$ in H_2O; **a)** overlaid CD spectra from 0.00 → 0.50 equivalents of Eu^{III} showing two isosbestic points at λ_{abs} = 217 and 240 nm, ***inset*:** zoomed region of naphthyl π → π* absorbance showing initial changes only from 0.00 → 0.30 equivalents of Eu^{III}; **b)** overlaid CD spectra from 0.60 → 1.00 equivalents of Eu^{III} showing an isosbestic point at λ_{abs} = 219 nm, ***inset*:** zoomed region of naphthyl π → π* absorbance showing no general trend. Spectra were recorded in H_2O at 24 °C from an initial ligand concentration *(c)* = 1×10^{-5} M. This titration is representative of triply reproduced trends.

the binding modes and speciation. The measurements from all the spectroscopic techniques were analysed by non-regression analysis to estimate the binding model and stability constants.

2.5.4 Estimation of stability constants by data fitting to theoretical models

The changes observed in both the absorption and the emission spectra were analysed with respect to established binding models. The following solution equilibria were considered valid based upon the facts that the coordination number of Eu^{III} is most commonly nine and the *O-N-O* binding motif of **120(*S,S*)** and **120(*R,R*)** was terdentate and converging, so each ligand would likely account for three coordination bonds.

$$Eu^{III} + (\mathbf{120}) \leftrightarrows [\mathbf{Eu(120)}]^{2+} \qquad \beta_{ML}$$

$$Eu^{III} + 2(\mathbf{120}) \leftrightarrows [\mathbf{Eu(120)_2}]^{+} \qquad \beta_{ML2}$$

$$Eu^{III} + 3(\mathbf{120}) \leftrightarrows [\mathbf{Eu(120)_3}] \qquad \beta_{ML3}$$

These global stability constants, β, represent the product of the step-wise formation constants, K, of the equilibria expressed as:

$$Eu^{III} + (\mathbf{120}) \leftrightarrows [\mathbf{Eu(120)}]^{2+} \qquad K_{ML}$$

$$[Eu(\mathbf{120})]^{2+} + (\mathbf{120}) \leftrightarrows [\mathbf{Eu(120)_2}]^{+} \qquad K_{ML2}$$

$$[Eu(\mathbf{120})_2]^{+} + (\mathbf{120}) \leftrightarrows [\mathbf{Eu(120)_3}] \qquad K_{ML3}$$

So that:

$$\beta_{\mathbf{ML}} = K_{\mathbf{ML}},$$

$$\beta_{\mathbf{ML2}} = K_{\mathbf{ML}} \times K_{\mathbf{ML2}} \quad \text{and}$$

$$\beta_{\mathbf{ML3}} = K_{\mathbf{ML}} \times K_{\mathbf{ML2}} \times K_{\mathbf{ML3}}$$

K and β are a simple expression of the relative concentrations and are obtained, for monometallic complexes by:

$$\beta_{ML_n} = \frac{[ML_n]}{[M][L]^n} \qquad \text{therefore, for } \mathbf{ML}: \qquad \beta_{ML} = \frac{[ML]}{[M][L]} = K_{ML}$$

Therefore, from estimated values of $\beta_{\mathbf{ML_n}}$ the concentration of each particular $\mathbf{ML_n}$ species can be calculated; the simultaneous regression of these concentration profiles and the recalculated spectra for each species against the experimental data forms the basis of non-linear regression of spectral data and $\beta_{\mathbf{ML_n}}$ can be refined.[413]

The proposed binding models considered the direct formation of complex species and, therefore, $\beta_{\mathbf{ML_n}}$ parameters were estimated. To provide robust constant estimation a global analysis method was used that regressed the entire spectra together, simultaneously fitting every wavelength to arrive at the estimated values for the stability constants. This allowed the determination of the equilibrium processes in solution elucidating the $\mathbf{ML_n}$ stoichiometry species present and their respective stability constants, expressed as $\log\beta_{\mathbf{ML_n}}$.

In the refinement of $\log\beta_{\mathbf{ML_n}}$ by non-linear regression, concentration profiles were predicted for each equilibrium species describing the speciation distribution of each species at each addition of Eu^{III} from initial estimates. This analysis was made using the commercial software ReactLab EQUILBRIA® for coherent replicate titrations and the estimated values determined as averages.[413] The parameters estimated from the UV-visible and CD absorption spectra, as well as luminescence measurements, are summarised in Table 2.2.

The UV-visible absorption titration spectra were analysed and the experimental fits to the spectra are shown in Figure 2.16a. However, the modelling of the data was found to be ambiguous. Two different binding models could be fitted acceptably to the data, one consisting of three species (**L**, **ML** and $\mathbf{ML_3}$) and the other with four components (**L**, **ML**, $\mathbf{ML_2}$ and $\mathbf{ML_3}$). This ambiguity was accounted for most likely due to lower sensitivity of the naphthyl $\pi \rightarrow \pi^*$ transitions and relatively small overall changes seen in the naphthalene

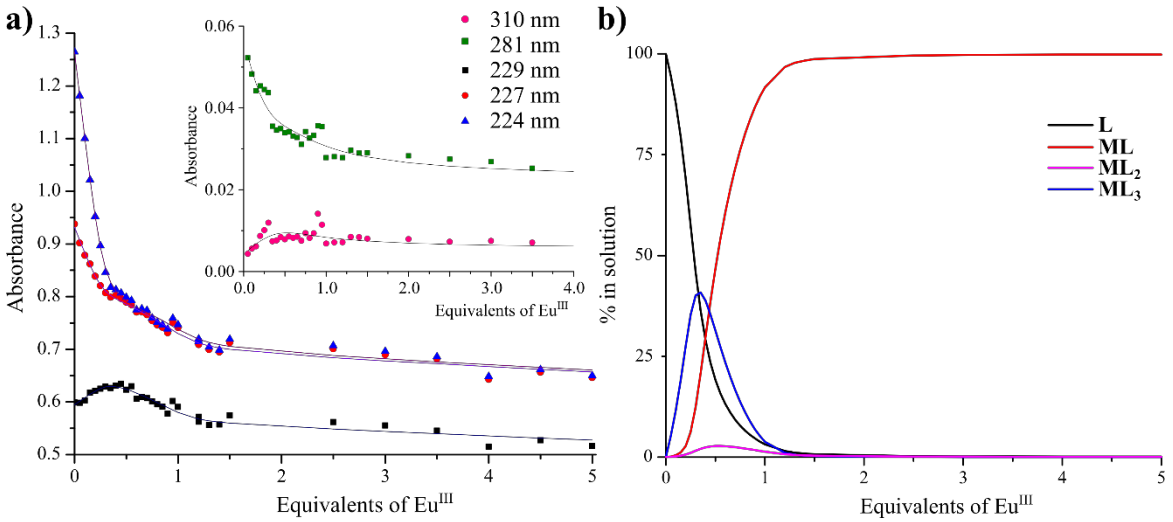

Figure 2.16 a) The fitted model (line) calculated by ReactLab EQUILBRIA® from UV-visible absorption titration data of **120(*S,S*)** showing the experimental binding isotherms (points) for λ_{abs} = 224, 227 and 229 nm considering a four-component binding model and, ***inset***: for λ_{abs} = 281 and 310 nm corresponding to naphthyl $\pi \rightarrow \pi^*$ transitions; and **b)** The speciation diagram (expressed as mol % formation) obtained from the non-linear regression. Data was fitted to individual titrations that were coherent upon repetition in triplicate.

absorption, with the main changes in the absorption spectra occurring at the higher energy pyridyl transition.

While a model with fewer free parameters can be considered preferable statistically, the UV-visible absorption data was fitted to the four component based upon the observations in the parallel spectroscopic techniques (*vide infra*). The fitting of the concentration profiles and recalculated spectra determined both log$\beta_{\mathbf{ML}}$ and log$\beta_{\mathbf{ML_3}}$ to be major species with their binding constants calculated as 7.4±0.1 and 19±0.1, respectively. The **ML$_2$** species was identified as a smaller component with an intermediate stability constant of logβ_{ML2} = 12.2±0.1. The increases between each logβ values were of equivalent magnitude for each species indicating that the $K_{\mathbf{ML_n}}$ for each ligand association was similar and that there was not substantial intrinsic or cooperative stabilisation in the higher order complexes (*i.e.* **ML$_3$** over the **ML$_2$** and **ML** species).

The speciation distribution for the self-assembly of **120(*S,S*)** (and **120(*R,R*)**) with Eu^{III} was derived, and is shown in Figure 2.16b (Appendix A2). It was seen that the **ML$_3$** stoichiometry was primarily formed at the beginning of the titration, but to a lesser extent, (*ca.* 45%) than seen for similar systems in organic solvents such as CH_3CN (which can normally give rise to formation of *ca.* 70-90%).[341] In fact, the **ML** stoichiometry was predicted to be present in solution ≈ 0.3 equivalent of Eu^{III} at approximately 25%, alongside the still dominant **ML$_3$**, while the remaining speciation was accounted for by free ligand **L** and only a small amount of the 1:2 complex **ML$_2$**. The lower percentage formation of **ML$_3$** in these studies would perhaps be accounted for by the more competitive aqueous solvent

(which may coordinate to the Eu^{III} centre) while also increasing the rate and degree of Eu^{III} hydration and, therefore, complex dissociation. At higher Eu^{III} concentrations, the **ML** complex is the main species in solution with **ML_2** being present but never becoming a dominant stoichiometry. The hydrophobic effects associated with amphiphilic ligands appeared to improve the luminescence properties of the **ML_3** species when in H_2O systems but were not responsible for driving their formation.

The absorption data was ambiguous during modelling and, therefore, the other techniques were necessary to support conclusions about the behaviour of **120(*S,S*)** and **120(*R,R*)**. Therefore, analysis of the Eu^{III}-centred emission was desirable, particularly with respect to analysis of the **ML_2** complexes, due to the significantly larger changes observed during the titrations. The binding isotherms for the $^5D_0 \rightarrow {}^7F_J$ ($J = 1, 2, 4$) transitions, the fits obtained from the non-linear regression analysis of the time-gated emission spectra and the corresponding speciation distribution diagrams are shown in Figure 2.17a and Figure 2.17b, respectively.

Fits were obtained for these transitions (in both fluorescence and phosphorescence modes) that agreed closely with the data when fit using the four component **L**, **ML**, **ML_2** and **ML_3** model. The data fitting using the fluorescence timescale Eu^{III} emission was in agreement to the phosphorescence, however, were subject to more experimental error and uncertainty because of the intrinsically weaker emission measurements. In fact, neither of the luminescence modes could be fitted satisfactorily to the data without the inclusion of the **ML_2** complex equilibrium species.

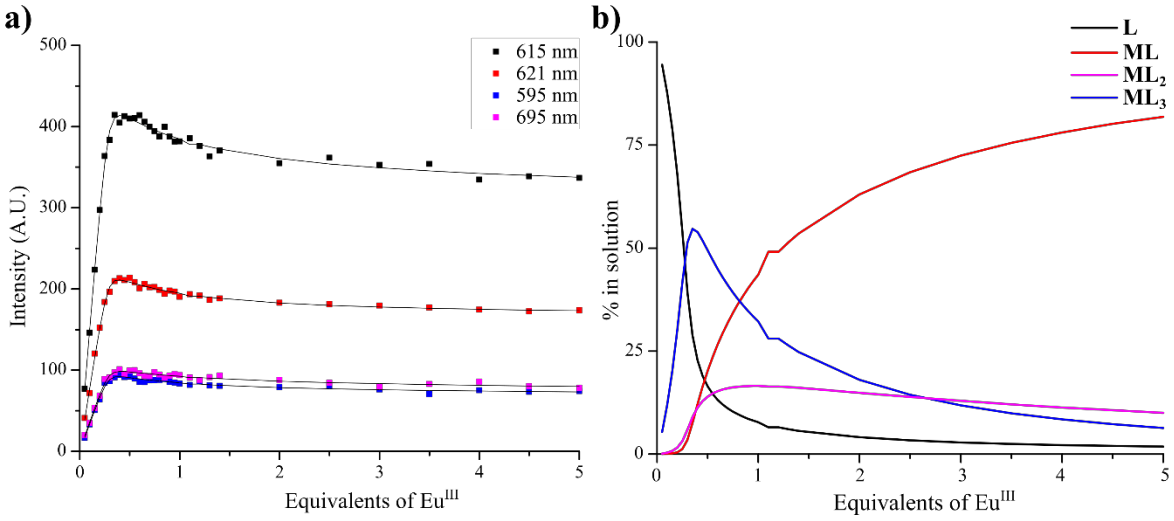

Figure 2.17 a) The fitted model (line) calculated by ReactLab EQUILBRIA® from time-gated emission titration data of **120(*S,S*)** with Eu^{III} showing the experimental binding isotherms (points) for $^5D_0 \rightarrow {}^7F_{1,2,4}$ at 595, 615/621 and 695 nm; **b)** The speciation diagram (expressed as mol % formation). Data was fitted to individual titrations that were coherent upon repetition at least in triplicate.

From these data, the binding constants of 6.1±0.1, 12.1±0.1 and 18.7±0.1 were determined for logβ_{ML}, logβ_{ML2} and logβ_{ML3}, respectively; these matching well with that observed previously for similar systems. As was determined for the changes in the absorption spectra, the **ML$_3$** stoichiometry was suggested to be formed initially, but unlike that seen from UV-visible absorption, the **ML$_2$** stoichiometry was also prominent even at the early stages of the titration. The overall percentage formation of the **ML$_3$** alone was in agreement to the models of absorption at approximately 50%. The formation of **ML$_2$** and **ML** was suggested to begin at approximately the same equivalents of Eu^{III} with the **ML** species dominating over **ML$_2$**, but both persisting into excess additions of Eu^{III}.

The outcomes of UV-visible absorption and luminescence analysis gave consistent results. However, the speciation distributions were notably different, particularly with respect to **ML$_2$** in the models. This was addressed later through changes observed in the CD spectra which were also analysed using non-linear regression.

While using chiroptical changes to investigate the binding interactions of biomolecules with drug candidates, such as DNA and Ru(II) polypyridyl complexes,[36] is well documented, very few reports have to-date focused on studying the other supramolecular processes. Only recently has it been shown, by Kotova and Gunnlaugsson, as effective in the analysis of self-assembly between chiral organic ligands and lanthanide ions in solution.[347] When appropriate, the use of CD is highly attractive for gaining insight into equilibrium processes because potentially changes can be significantly larger than those seen in conventional UV-visible absorption spectroscopy, resolve further certain absorption

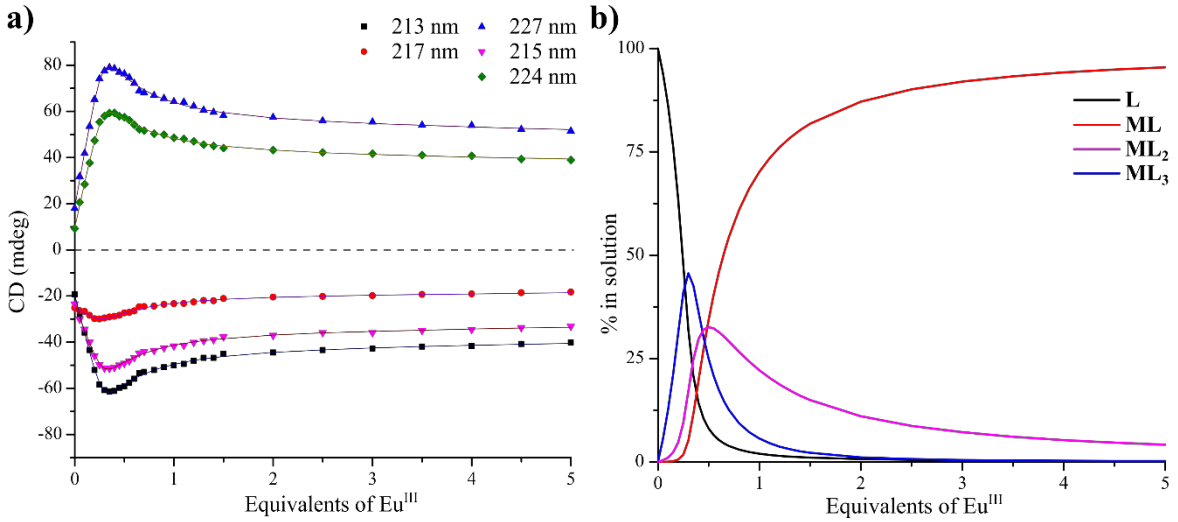

Figure 2.18 a) The fitted model (line) calculated by ReactLab EQUILBRIA® from CD titration data of **120(*S,S*)** showing the experimental binding isotherms (points) for λ_{abs} = 213, 215, 217, 224, and 227 nm considering a four-component binding model and, **b)** the speciation diagram (expressed as mol % formation) obtained from the non-linear regression. Data was fitted to individual titrations that were coherent upon repetition at least in triplicate.

features should their ellipticity be inverse, and can provide further 'spectral fingerprints' representing each stoichiometry uniquely in solution.

The changes in the CD spectra of both **120(*S,S*)** and **120(*R,R*)** were quite significant upon coordinating to Eu^{III}, Figure 2.10a and Figure 2.18a. As above, the data was fitted to binding models consisting of **L**, **ML**, **ML$_2$** and **ML$_3$**; all of which gave excellent fit as shown in Figure 2.18. This analysis gave greater confidence to the conclusions of the existence of four total species in solution, including the presence of **ML$_2$** stoichiometry. In fact, only supporting the model where the **ML$_2$** species was included. The speciation distribution was calculated using the chiral absorbance data, Figure 2.18b, and agreed with the luminescence measurements. The formation of a more substantial percentage (*ca.* 40%) of **ML$_2$** species in solution. Again, **ML$_3$** was shown to be the dominant assembly following the initial additions of Eu^{III} forming to 45% while **ML$_2$** and **ML** were suggested to form significantly around 0.30 → 0.50 equivalents of Eu^{III}, with almost equal distribution around 0.50 equivalents. The **ML$_3$** complex was suggested to be persistent into excess Eu^{III} which was consistent with other symmetrical naphthyl **dpa** ligands. Eventually **ML** was the dominant species in solution. The model estimated the binding constants $\log\beta_{\mathbf{ML}}$, $\log\beta_{\mathbf{ML_2}}$ and $\log\beta_{\mathbf{ML_3}}$, as 7.0±0.1, 13.4±0.1 and 19.7± ± 0.1, respectively, for **120(*S,S*)** with similar results being seen for **120(*R,R*)**. These values also compared well with those seen above from the more 'classical' approach of fitting the changes in the absorption and emission spectra. Moreover, the magnitude of $\log\beta$ compared to similar **dpa** systems of Bunzli, Piguet and Muller.[135,137,138,394]

Table 2.2 Summarised global stability constants ($\log\beta_{MLn}$) estimated and refined by ReactLab EQUILIBRA® global analysis for **120(*S,S*)** and **120(*R,R*)** with $Eu(CF_3SO_3)_3$ in H_2O. [Ligand]: $c = 1 \times 10^{-5}$ M. Values and associated errors (standard deviations) were determined as the average of three independent titrations. [a]Value fixed manually.

		$\log\beta_{ML}$	$\log\beta_{ML2}$	$\log\beta_{ML3}$
120(*S,S*)	UV-Vis	7.4 ± 0.1	12.2 ± 0.1	19.1 ± 0.1
	Phosph.	6.1 ± 0.1	12.1 ± 0.1	18.7 ± 0.1
	CD	7.0 ± 0.1	13.4 ± 0.1	19.7 ± 0.1
120(*R,R*)	UV-Vis	7.4[a]	14.0 ± 0.3	19.7 ± 0.2
	Phosph.	6.7 ± 0.1	12.6 ± 0.2	18.7 ± 0.2
	CD	6.9 ± 0.1	13.6 ± 0.1	19.8 ± 0.1

The recalculated CD spectra were extracted from the data fitting for each of the complex species; the spectra are shown in Figure 2.19a. These clearly showed that each of the **ML**,

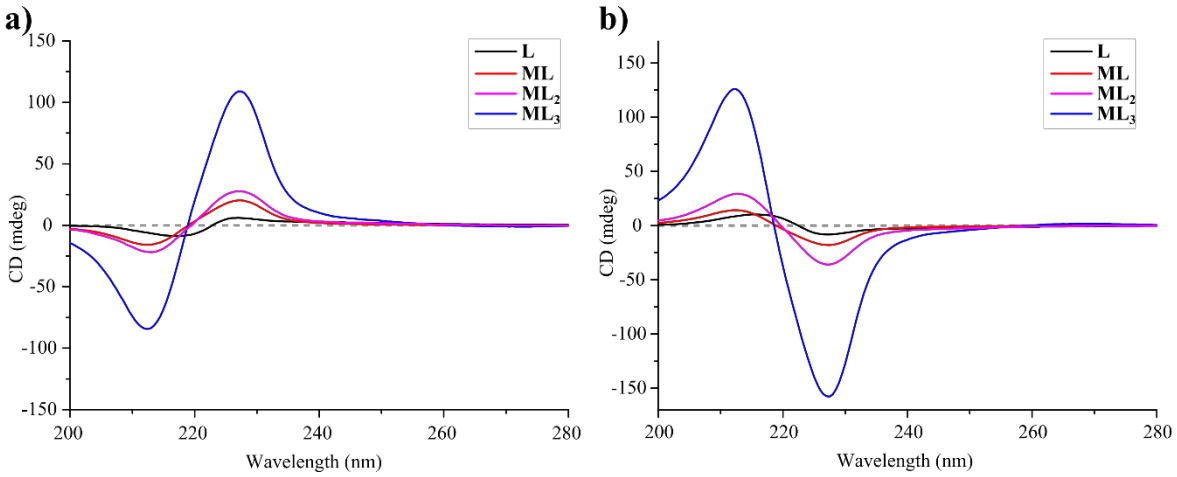

Figure 2.19 Recalculated spectra of **L**, **ML**, **ML$_2$** and **ML$_3$** stoichiometry complexes obtained from non-regression analysis of CD titration data with Eu(CF_3SO_3) of **a) 120(*S,S*)**; **b) 120(*R,R*)**.

ML$_2$ and **ML$_3$** have characteristic spectra that can be treated as 'fingerprint' descriptions for each species in solution.[347] As described above, these reflected the appropriate negative and positive Cotton effects for *S,S* and *R,R* isomers, respectively, as well as the wavelength shift and splitting of each species in the higher energy absorbance band as well as the lower energy naphthyl-centred feature. The isoeliptic points that were observed during the titration were evidenced in the overlaid recalculated spectra with the profiles of key correlated complexes coinciding at the wavelengths at which isoelipticity was observed during titrations, for example at λ_{abs} = 217 and 219 nm. Additionally, the spectra also clearly indicated the largest enhancement occurring for the highly bundled **ML$_3$** species compared to both **ML$_2$** and **ML** which agreed with the expected additional helical character of the closely π-π stacked arrangement of naphthyl **dpa** ligands in the higher stoichiometry complex.[136,414] Concluding the studies of **120** and Eu^{III} at lower concentration, it was demonstrated that changes in the CD spectra can be treated quantitatively to monitor binding and can became significant when classical absorption changes are ambiguous.

The amphiphilic nature of **120(*S,S*)** and **120(*R,R*)** resulted in changes in physical behaviour including solution self-assemblies and aggregated soft materials at higher concentrations which were characterised by various techniques.

2.5.5 Towards thermodynamic characterisation of the self-assembly between 120 and Eu^{III}

The quantitative assessment of Ln^{III} binding and resulting complex stability has been explored extensively through spectroscopic measurements in this, and previous work. For the chromophore-rich and chiral naphthyl **dpa** scaffold this has provided suitably diverse information, however other techniques are available to provide additional insight and confirmation. For example, Piguet and co-workers have regularly studied thermodynamic

properties of Ln^{III}-containing supramolecular assemblies through the use of NMR techniques. In the wider fields of supramolecular[415] and coordination chemistries[416-421] direct calorimetry has been employed to study associative interactions using isothermal titration calorimetry (ITC) protocols. Few examples have been reported, however, of the direct Ln^{III}-ligand ITC measurements and most employ the Ln^{III}-perchlorate salts.[422-428]

With this in mind, the feasibility of direct calorimetry in the measurement of naphthyl **dpa** complexes with $EuCl_3$ was explored. The preliminary viability studies of direct calorimetric measurement of the association of naphthyl **dpa** with $EuCl_3$ were investigated using ITC measurements in collaboration with Prof. Amir Khan (School of Biochemistry and Immunology, Trinity College Dublin).

Ligands **120(*S,S*)** and **120(*R,R*)** were prepared in buffered-solutions (10 mM, pH 7.4) that were filtered and dialysed against a bulk buffer to remove suspended particle and equilibrate ionic strength. Initial screening of non-coordinating buffers[429] (HEPES, MES and TRIS) suggested that HEPES was the most appropriate buffer and showed the minimal background heat associated with injection, ionisation and buffer dilution. Solutions of $EuCl_3$ were prepared from the dialysed buffer to $c = 5 \times 10^{-6}$ M and were used as the receiving solution of the titration to favour **L** → **ML** formation with the initial injections (to allow characterisation of **ML** formation and potential cooperativity in subsequent **ML** → **ML₂** formation). To the Eu^{III} solutions (held at 25°C), ligands **120(*S,S*)** or **120(*R,R*)** were injected in aliquots ≈ 0.1 equivalents and the differential heat was measured. Additionally, various control titrations were completed for the injections of: i) blank HEPES into blank HEPES; ii) blank HEPES into $LnCl_3$; and iii) ligand **120(*S,S*)** or **120(*R,R*)** into blank HEPES. In the cases of i) and ii), minimal heat above that of the noise was observed and indicated that neither buffer nor $LnCl_3$ dilution gave a substantial calorimetric change.

The ITC data from the titration of ligand **120(*S,S*)** with $EuCl_3$ and the direct dilution of **120(*S,S*)** into blank HEPES shown in Figure 2.20a and Figure 2.20b, respectively. Overall the results from the ITC were inconclusive. The difference ITC data obtained by treating the ligand dilution titration as a background was not of a suitable quality to be fitted.[430] As can be seen from the titrations of **120(*S,S*)** with Eu^{III} and dilution with HEPES while overall endothermic heat for the initial injections of the **120(*S,S*)** solution were observed these were suggested to be mostly due to the dilution of **120(*S,S*)**. The magnitude of any binding processes could not be extracted and, as of yet, appropriate unambiguous data has not been achieved. Indeed, in the case of some interactions the heats of coordination are not always

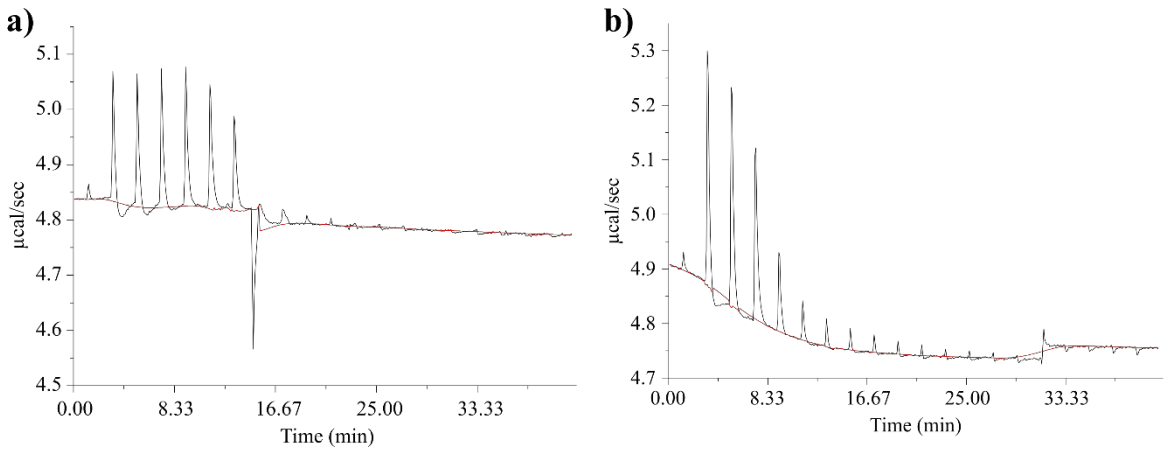

Figure 2.20 Raw ITC data for: **a)** Titration of **120(*S,S*)** into $EuCl_3$ (200 µL) showing initial large endothermic heats. Each injection corresponds to 2 µL, first injection 0.2 µL.; and **b)** dilution of **120(*R,R*)** into HEPES (200 µL) showing initial large endothermic heats and small systematic drift of the baseline (red spline). Each injection corresponds to 2 µL, first injection 0.2 µL. ***inset*:** calculated molar heats (KCal/mole) on each injection. Cell held at 25 °C.

measurable, particularly in water,[431] In our studies, the reverse titration of **L → ML$_3$ → ML$_2$** was also unable to provide measurable heats for the complex formations.

Nevertheless, the ITC experiments did reflect some of the solution behaviour of **120(*S,S*)** and **120(*R,R*)** described above and was consistent with hydrophobic effects of the ligands. It was suggested previously that photophysical enhancements observed in H_2O were the result of hydrophobic effects in the directed Eu^{III}-assemblies. The endothermic heat pulses would be consistent with dissociation or reorganisation of amphiphilic and hydrophobic ligand assemblies upon dilution and coordination (these processes are often endothermic and entropy-driven).[432] Furthermore, in a number of titrations a small baseline drift was observed which has also been associated with slow equilibration by aggregation phenonema[430,433,434] and low critical concentrations for interaction were implied by the decreasing dilution heats. Although inconclusive at this time, the full thermodynamic and kinetic characterisation remains of interest for this and other scaffolds and these studies should be completed the future in other solvents, such as CH_3OH or CH_3CN. However, these opportunities have yet to arise.

To further support the suggested assemblies of ligand and **ML$_n$** species additional preliminary investigations were made using light scattering techniques that would respond to larger assemblies and are discussed in the following section.

2.5.6 Dynamic light scattering and SEM assessment of solution soft-assemblies

A number of the behaviours observed for ligands **120(*S,S*)** and **120(*R,R*)** and their complexes have been suggested to correspond to hydrophobic effects and assemblies forming in

solution as a result of the amphiphilic character of the ligands. Solution assemblies of various types often will result in the scattering of light[435] and therefore, in order to provide further evidence, DLS measurements were taken from solutions of **120(*S,S*)** and **120(*R,R*)**. Samples were prepared as solutions in H_2O that was filtered at least 6 times to remove dust particles and the backscattered light at 25 °C measured.

Initially, solutions were prepared of **120(*S,S*)** and **120(*R,R*)** in H_2O at $c = 1 \times 10^{-5}$ M and 1×10^{-3} M in order to replicate the conditions of the titrations as well as higher concentrations where aggregation could be more obviously promoted. The solutions at $c = 1 \times 10^{-5}$ M were also prepared with 0.33 equivalents of $Eu(CF_3SO_3)_3$. The DLS results (size distributions) for **120(*S,S*)** at 1×10^{-5} M and with 0.33 equivalents of Eu^{III} added are shown in Figure 2.21and Figure 2.21b, respectively.

Scattered light was detected which suggested that self-assembly was occurring and would be consistent with the implications from the ITC measurements. The samples were not mono-disperse with polydispersity index (PDI) values *ca*. 0.6. This was not unexpected due to the dynamic and varied nature of possible self-assembly interaction that could occur.

Upon the addition of 0.33 equivalents of Eu^{III} to the ligand solutions there was a change in the distribution of solution assemblies, as shown by the change in distribution seen in Figure 2.21b. The PDI (*ca.* 0.4) was reduced and the range of assembly sizes was suggested to be narrower. This can be expected to arise from the effect of reduced ligand freedom following coordination in the directed-assembly. However, while these data demonstrated scattering effects, they were treated as indicative and mostly qualitative due to the absorbing and fluorescent nature of **120** and **[Eu.(120)$_3$]** potentially introducing artefacts to the measurements.[436,437] At higher equivalents of Eu^{III}, although scattering was still

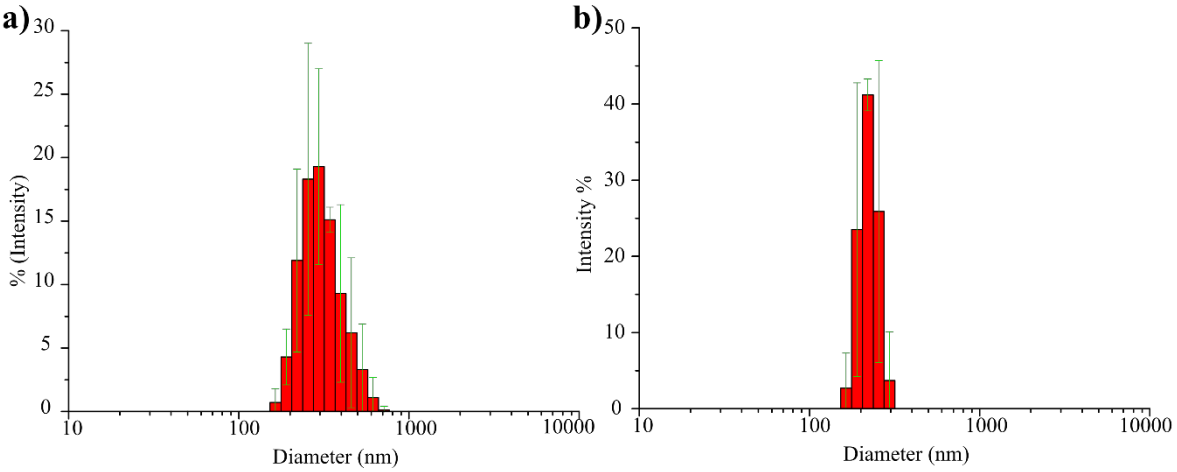

Figure 2.21 Particle size distrbution profiles (by intensity) determined by DLS backscatter measurements in aqueous solution for: **a) 120(*S,S*)** at $c = 1 \times 10^{-5}$ M; and **b) 120(*S,S*)** at $c = 1 \times 10^{-5}$ M in the presence of 3.3×10^{-6} M $Eu(CF_3SO_3)_3$. Error bars are standard deviations determined from 3 repeats measurements.

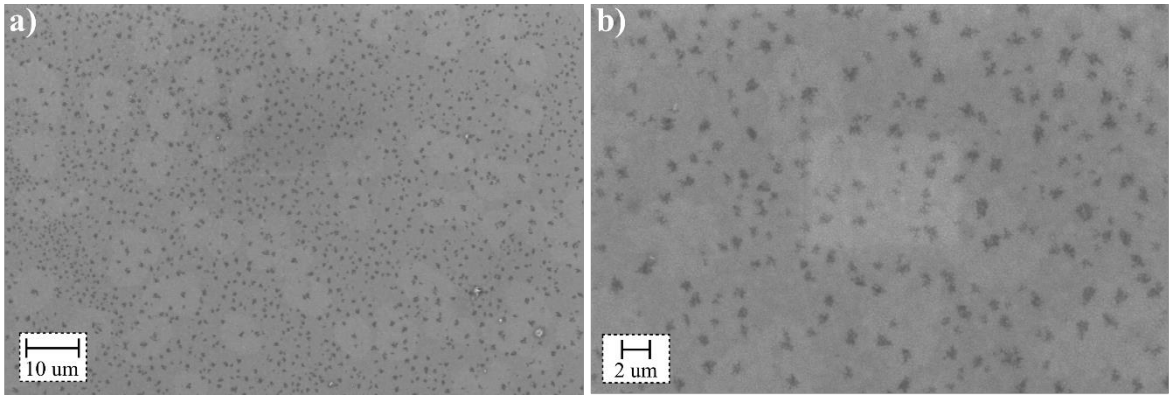

Figure 2.22 SEM images recorded of **120(*S,S*)** drop-cast from aqueous solution at $c = 1 \times 10^{-5}$ M at two different magnifications in **a)** and **b)**. Images taken in collaboration with Ms. Amy Lynes (TCD).

observed the quality of the DLS data was poor and no meaningful analysis could be made. Similarly, at higher concentration (see Appendix A2) there was evidence of multiple scattering, which while indicating that solution assemblies were present, was inappropriate for additional analysis.

Self-assembled materials can be probed for their morphology by various microscopy techniques such as scanning electron, transition electron and He-ion microscopies. The solution from DLS analysis were drop-cast onto silica substrates and imaged using SEM in collaboration with Ms. Amy Lynes (School of Chemistry, Trinity College Dublin) at the Advanced Microscopy Laboratory. The SEM images for solutions at 10^{-5} and 10^{-3} M are shown in Figure 2.22 and Figure 2.23, respectively. At 1×10^{-5} M, the dried samples showed the formation of aggregates with an average diameter of 0.4 μm which was consistent with the DLS measurements. Upon treatment with Eu^{III} the SEM images showed precipitation that was likely $Eu(CF_3SO_3)_3$ salts and the organic materials were not clearly observed. The samples at 1×10^{-3} M showed the formation of uniform aggregates with a larger diameter of *ca*. 20 μm and suggested that the higher concentration leads to increased bulk aggregation.

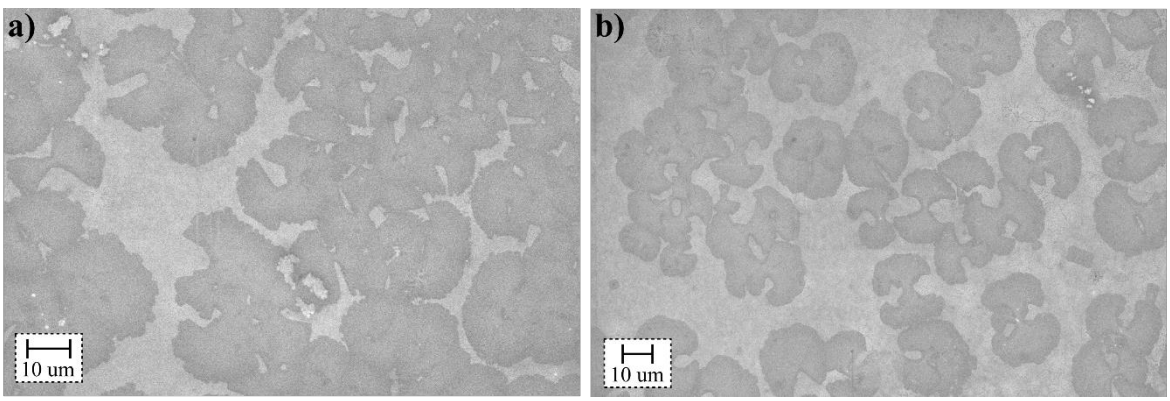

Figure 2.23 SEM images recorded of **120(*S,S*)** drop-cast from aqueous solution at $c = 1 \times 10^{-3}$ M at two different magnifications in **a)** and **b)**. Images taken in collaboration with Ms. Amy Lynes (TCD)

The differences between the aggregates seen in SEM at both these concentrations corresponds with the dissociation heats found in the ITC measurements.

In fact, as the concentration was increased further the aggregation was seen beyond solution soft-assemblies and the formation of gel-like bulk materials was observed.

2.6 Formation and characterisation of hydrogels of 120(*S,S*) and Eu^{III}

At spectroscopic concentrations ligands **120(*S,S*)** and **120(*R,R*)**, and their saturated complexes, existed as discrete molecules and molecular assemblies. However, at concentrations higher than 1×10^{-5} M, both enantiomers rapidly began to form viscous solutions and under certain conditions 'gel-like' materials (aggregated materials that encapsulated their solvent environment). Sulfonated materials,[438,439] including naphthyl-containing derivatives,[440] have been shown to act as hydrogelators and sulfonated Pt^{II} complexes to undergo self-assembly in aqueous media.[441] The 'gel-like' materials formed from **120(*S,S*)** were characterised by spectroscopic and SEM methods; the optical properties of the hydrogel aggregates are qualitatively shown in Figure 2.24. To generate the materials, ligand **120(*S,S*)** was dissolved in H_2O at various wt% ratios and with increasing concentration there was increased the viscosity of the solutions. However, no immediate 'gelation' was observed. To achieve the formation of gels for **120(*S,S*)**, the solutions were heated to fully dissolve in H_2O and give a viscous solution, a subsequent addition of Cs_2CO_3 resulted in gelation of the solution; dissolution directly into solutions of Cs_2CO_3 also gave the gel materials.

The critical "gelation", or aggregation, concentration was determined as 5 wt%, in the presence of Cs_2CO_3, and produced gels that resisted the "inversion test" as shown in Figure 2.24a. This method produced ligand gels of varying transparency dependent on the weight percentage of **120(*S,S*)** and the Cs_2CO_3 salt content; for example, the resulting

Figure 2.24 Optical images of **a)** ligand hydrogels formed from **120(*S,S*)** at 6 wt% (left) and 10 wt% (right) showing transparent and opaque materials, respectively; **b)** ligand hydrogels of **120(*S,S*)** at 6 wt% (left), 10 wt% (middle) and 5 wt% Eu^{III}-doped (right) under ambient light and; **c)** the same hydrogels in b) under UV light (λ_{exc} = 254 nm).

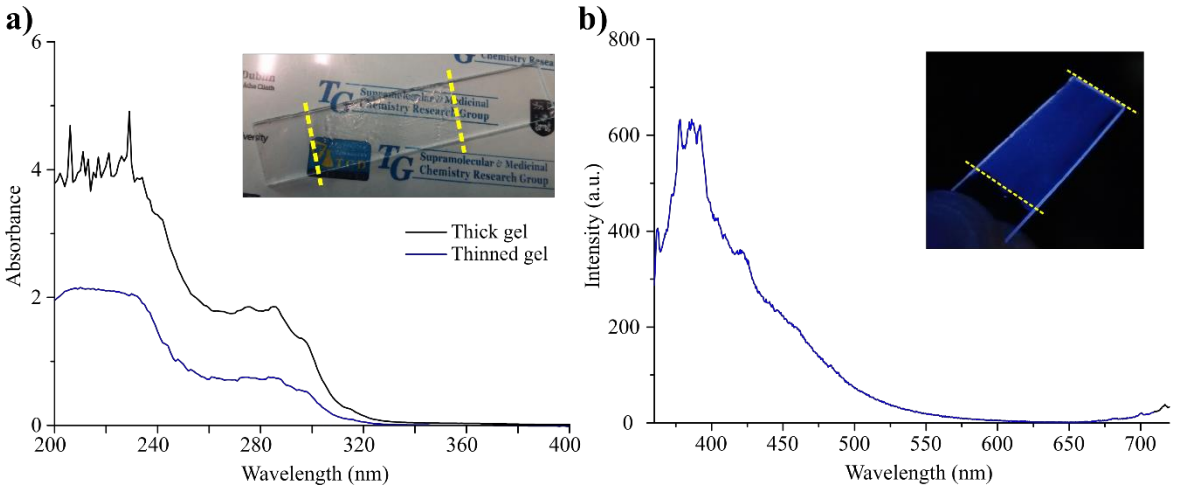

Figure 2.25 a) Absorbance spectra recorded from gelled **120(*S,S*)** coated onto a quartz slide (inset) as thick (black) and thinned (blue) films; and **b)** fluorescence emisson spectrum (λ_{exc} = 281 nm) of thick film of gelled **120(*S,S*)**, *inset*: photograph of gel-coated slide under UV-light (λ_{exc} = 254 nm) showing purple emission.

materials were shown to be clear and opaque at 6 and 10 wt%, respectively. Gels of both enantiomers could be formed reproducibly at these weight percentages, although compared to most LMWGs these represented very high concentrations.[237] As expected, under UV light (λ_{em} =254 nm) both gels gave a blue fluorescence emission, Figure 2.24c and Figure 2.25b.

The UV-visible absorption spectrum of the transparent ligand gels were recorded, Figure 2.25a, and contained the same features as the free ligand with small red-shifts (*ca*. 2 – 5 nm) in the naphthyl absorbance maxima to 275, 284 and 296 nm with broadening of the λ_{abs} = 200 – 240 nm region consistent with aggregation behaviour. Fluorescence spectra of the strong ligand-centred emission observed under UV irradiation was characteristic of naphthyl-**dpa** systems (without aggregation-induced shifts) showing an emission maximum 280 nm and broad tail to that emission band until 600 nm, as shown in Figure 2.25b.

Although the initial observation of the gelation was made from samples that were not purified from Cs_2CO_3 and it was found that gelation occurred in the presence of other metal

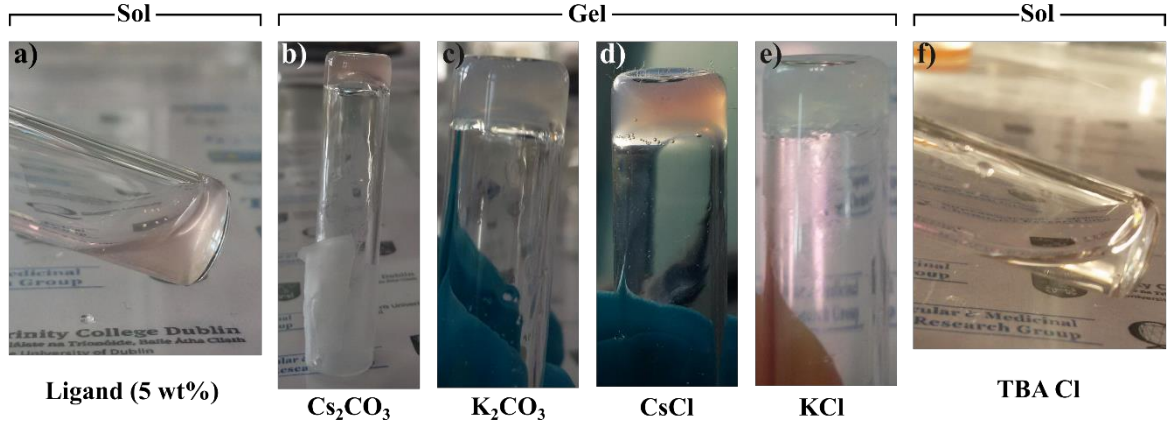

Figure 2.26 Photographs of gelating solutions showing the effect of metal cations: **a)** viscous solution of 120(*S,S*) at 5 wt%; **b)** inverted gel formed by addditon of Cs_2CO_3; **c)** inverted gel formed by addition of K_2CO_3; **d)** inverted gel formed by the addition of CsCl; **e**) inverted gel formed by the addition of KCl; and **e)** sol remaining after treatment with TBACl for which no gelation occurred.

cations, as shown in Figure 2.26. Viscous solutions of **120(*S,S*)** were prepared at 5 wt% concentration and treated with <0.1 wt% Cs_2CO_3, K_2CO_3, CsCl and KCl and gelation assessed through the standard inversion test. The solutions were found to gel when treated with all the Cs^+ and K^+ salts which indicated that the behaviour was cation-induced (and anion-independent) but not a specific caesium interaction. Moreover, when treated with TBACl the viscosity of the solutions was unaffected, as shown in Figure 2.26f, and no gelation occurred which suggested further the role of the spherical cation in the assembly processes. These interactions and conditions for the formation were consistent with reports of frameworks and assemblies in the solid-state of sulfonated materials bridged by alkali metal cations (which showed the most favourable interactions with the SO_3^- moiety).[442,443]

Eu^{III} was introduced to the gels by layering a solution of the Eu^{III} salt on top of the pre-formed gel material as well as by direct-gelation of Eu^{III}-containing electrolyte solutions. Initially, the luminescence of the materials changed and showed characteristic red luminescent, as demonstrated in Figure 2.24c for **[Eu.(120(*S,S*))$_3$]**. However, as can also be seen in Figure 2.24c, these Eu^{III} metallogels were unstable and aged rapidly and, over the period of only a few hours, the precipitation of the Eu^{III} complexes within the gel network occurred. The precipitation resulted in a collapse of the gel network and, in fact, was instantaneous in the direct gelation experiments (representative gels and precipitates are shown in Figure 2.27a). The corresponding spectra of the recovered precipitate suspended in H_2O, Figure 2.27b, showed ligand fluorescence equivalent to that seen from the ligand gels and the Eu^{III}-centred emission. Luminescence lifetimes of the precipitated complexes were best-fitted to bi-exponential decay which gave τ_{obs} of 1.52 and 0.42 ms consistent with

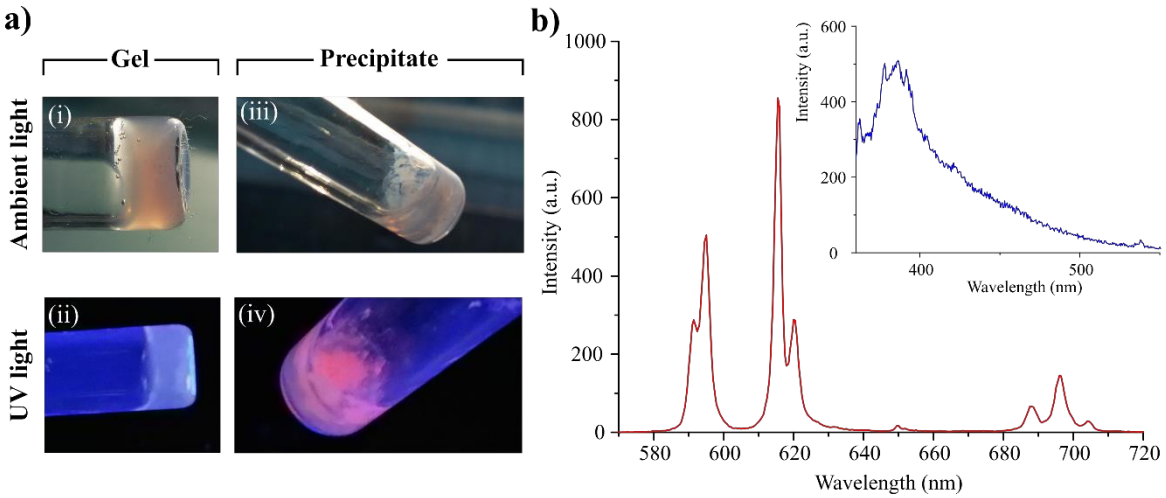

Figure 2.27 a) Photographs of: **i)** ligand gel of **120(*S,S*)** at 5 wt% under ambient light and **ii)** under UV light (λ_{exc} = 254 nm), **iii)** precipitate formed after treatment of ligand gel of **120(*S,S*)** with 0.33 equivalents $EuCl_3$ under ambient light and **iv)** under UV light (λ_{exc} = 254 nm); and **b)** luminescence spectra recorded of the precipitate from the collapsed as time-gated Eu^{III} emission, ***inset***: ligand fluorescence. (λ_{exc} = 281 nm)

the precipitation of charge neutral **ML_3** species as well as the presence of unsaturated species (**ML** and **ML_2)** with shorter-lived emission (as a result of increased solvent quenching).

Once formed within the gel, the **[Eu.(120(*S,S*))$_3$]** and **[Eu.(120(*R,R*))$_3$]** complexes were charge neutral, which resulted in less stabilisation in both aqueous solution and hydrogel phases, and rapidly precipitated as the solid complexes. In the cases of the other Eu^{III} salts, such as chloride and acetate, the same result was observed; the layering of salt solution initiated the phase transition and collapse of the material. No weight percentage could be determined at which the Eu^{III}-based materials were formed and remained stable.

SEM studies were carried out on the ligand hydrogels probe the morphology of the materials. However, the metallo-gels were unstable and meaningful analysis was not possible. SEM was performed in collaboration with Mr. Savyasachi A Jayanth of the Gunnlaugsson Group in Trinity College, Dublin.

SEM micrographs of the ligand gels are shown in Figure 2.28 – Figure 2.30 for samples prepared at 5 wt%, the critical concentration for ligand gelation. Samples were prepared by drop-casting the ligand hydrogels onto silica wafers then dried *in vacuo* prior to imaging. The SEM imaging did not suggest **120(*S,S*)** formed a traditional fibrous gel network and the gel material was shown to arise from an ordered aggregated state. Various areas of the bulk surface, Figure 2.28a, were of a smooth morphology with a featureless surface texture, much like that of a compacted solid. However, there were also areas which showed a more complex morphology, represented in Figure 2.28b, and the surface appeared 'wrinkled' through the dense packing of thick fibril-like extended assemblies; these features were seen throughout the materials.

Magnification of the 'wrinkled' surface showed that the thick fibre-like features had additional order. In places where the smooth surface and bulk material was broken, through

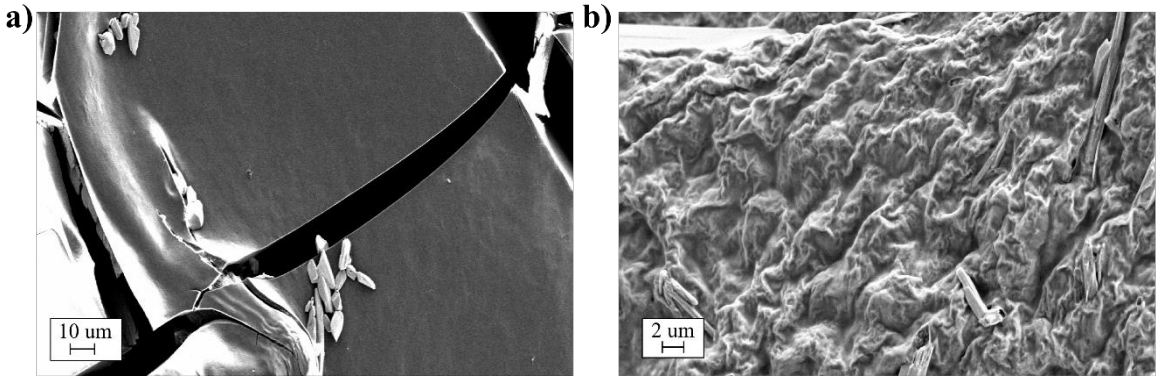

Figure 2.28 SEM micrographs of ligand hydrogels of **120(*S,S*)** drop-cast onto silica wafers and dried *in vacuo* prior to imaging. **a)** bulk material showing a smooth surface morphology appearing "compacted-solid-like" and showing Cs_2CO_3 salt on the surface, bar represents 10 μm; **b)** wrinkled surface morphology observed at various points of the gel, bar represents 2 μm.

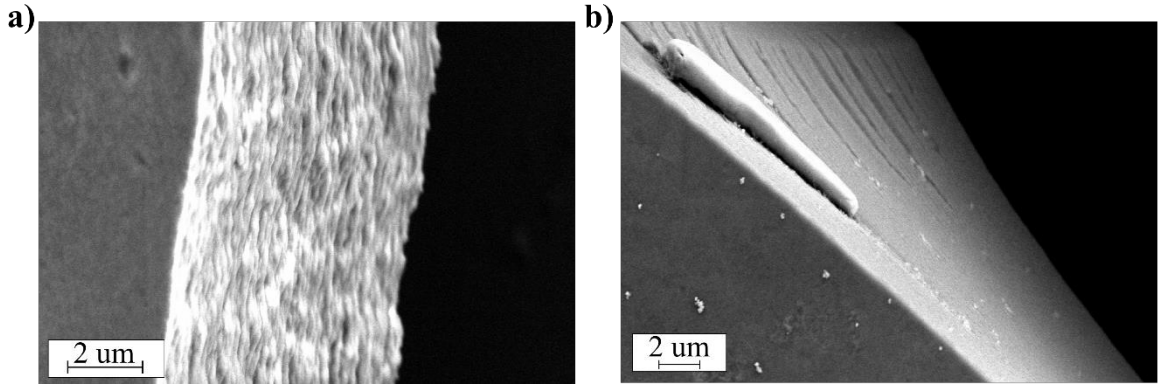

Figure 2.29 SEM micrographs of ligand hydrogels of **120(*S,S*)** drop-cast onto silica wafers and dried *in vacuo* prior to imaging. **a)** edge region of the gel aggregate showing layered morphology with directional order, bar represents 2 μm; **b)** edge region of the gel aggregate showing parallel splitting of the bulk material into layers, bar represents 2 μm.

cratering or cracking, edges were generated that revealed a more complex morphology. It appeared that layers were forming, as shown in Figure 2.29a, and that these layers were stacked to form bulk lamellar materials. In fact, where the material was compacted evidence of the layer could be seen in the splitting of the surface, as shown in Figure 2.29b.

Further to the above, a variation in morphology was observed for the interior of the material where the structure beneath the surface was exposed at the base of surface craters, as shown in Figure 2.30a and Figure 2.30b. Beneath the smooth surface, there were thick fibrous structures visible that were extended and intertwined. The form of these fibrous assemblies was consistent with the morphology of the materials seen at the exposed edges in Figure 2.29a and indicated that the bulk aggregate/gel material could be constructed from layered networks of these thick fibres. At 10 wt%, the gels of **120(*S,S*)**, as described, were fully opaque and this was reflected in the morphology. The materials again showed a smooth collapsed surface across large areas of the sample and the morphology was substantially more compacted across the entire material. The smooth surface could be accounted for by

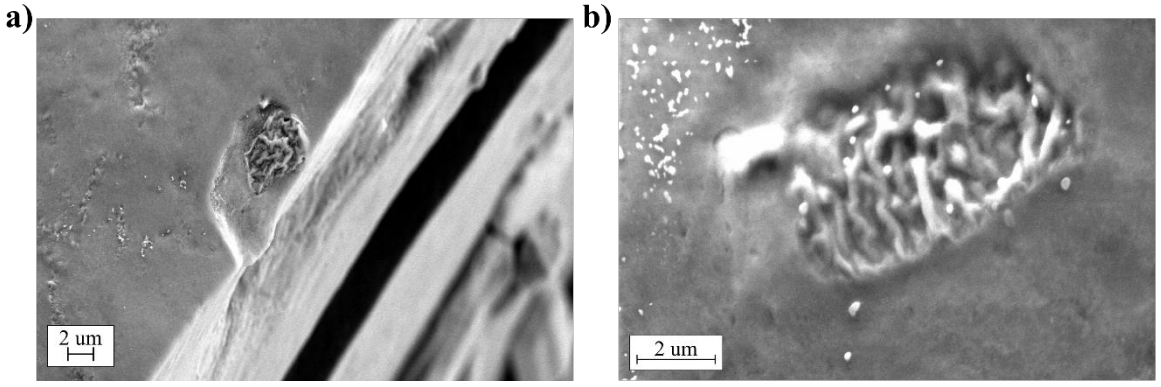

Figure 2.30 SEM micrographs of ligand hydrogels of **120(*S,S*)** drop-cast onto silica wafers and dried *in vacuo* prior to imaging. **a)** Bulk material showing damaged surface revealing a wrinkled, fibril-like internal morphology underneath the surface; bar represents 2 μm; **b)** additional 'cratering' of the gel surface revealing a thick, fibril-like morphology under the smooth compacted surface morphology, bar represents 2 μm.

the material compacting due to the collapse of weak gel at the surface when solvent evaporation and concentration occurred in sample preparation as the morphology changed notably beneath the surface.

The nature and definition of soft materials varies between simple single component gels to complex systems.[444,445] The thick entangled, fibre-like features that were observed within these material could be consistent with those available from "surfactant-gel" materials.[446] In the theory of traditional gel formation, fibres grow from the assembly of single molecules in a unidimensional fashion which subsequently entangle and form the gel network. "Surfactant gels", on the other hand, arise from the growth of extended amphiphilic structures and these non-conventional 'fibres' interact to form aggregated materials that are gel-like. This is shown schematically with the context of ligand **120** in Figure 2.31. As previously stated, ligands **120(*S,S*)** and **120(*R,R*)** have an amphiphilic nature and were expected to behave accordingly, parallel behaviour to surfactant molecules was therefore not unrealistic.

At low concentration, the ligands behave mostly as individual molecules and the sol state is dynamic and stable. With increasing concentration, however, it can be expected that the hydrophobic effects can drive self-assemblies that minimise the exposure of the naphthyl groups of the naphthyl **dpa** scaffold to the aqueous solvent. This potential behaviour was consistent with the solution studies and photophysical effects previously described. It is therefore proposed that, at much higher concentrations than the spectroscopic studies, hydrophobically-driven assembly grows thick fibre-like structures and gives rise to the extended network with "spaghetti-like" morphology as seen in the SEM images. The

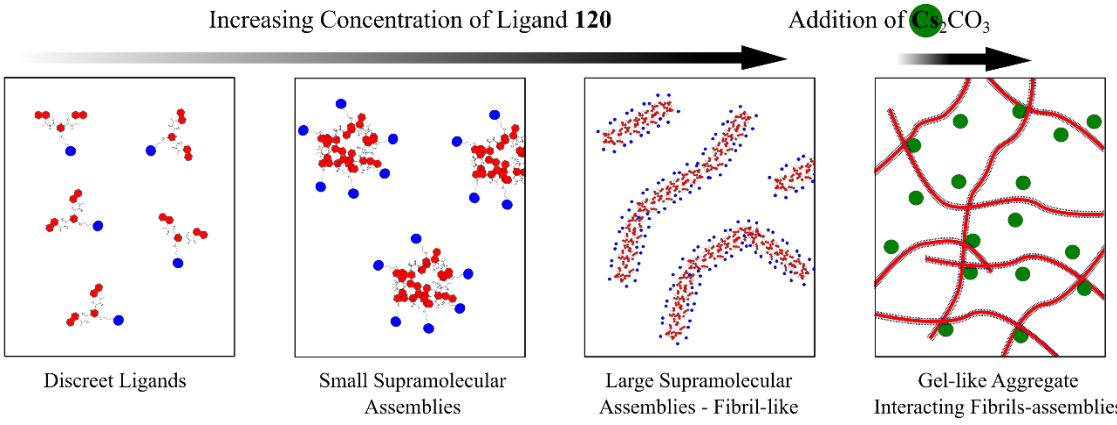

Figure 2.31 Schematic representation for a potential growth mechanism of ligand gels of **120(*S,S*)** and **120(*R,R*)** as 'surfactant gel'-like materials. **Panel 1** (left): discrete molecules which behave independently; **Panel 2**: increasing concentration 'micelle-like' self-assembly; **Panel 3**: further increasing concentration leading to fibril growth from the 'micelle-like' structures; **Panel 4** (right): addition of Cs_2CO_3 leads to partial electrostatic 'crosslinking' of fibril-like supramolecular assemblies and gel-like aggregates. Schematic adapted from Ref 446.

entanglement, partial cross-linking and subsequent layering of these structures (likely through sulfonate-cation bridging interactions) would be suggested to result in the formation of a gelating network.

Ligands **120(*S,S*)** and **120(*R,R*)** demonstrated limited utility compared to the majority of LMWGs since unstable gels were formed at relatively large weight percentages of gelator molecule and conversion to the metallogel was unsuccessful. While representing a proof of concept for naphthyl **dpa** systems in neat aqueous media as well as naphthyl **dpa**-based soft materials, there is no future application available to ligands **120(*S,S*)** and **120(*R,R*)**, but the approaches discussed in this work should form the basis of further research.

2.7 Conclusions and future work

In this chapter, two novel enantiomeric ligands based on the naphthyl **dpa** scaffold were designed, synthesised and characterised. Their abilities for use in formation of lanthanide-directed synthesis of supramolecular structures and materials was explored from their photophysical behaviours with the use of chiroptical spectroscopy for monitoring solution assembly highlighted in particular.

Ligands **120(*S,S*)** and **120(*R,R*)** were modified at the 4-position of the pyridyl unit to allow for the incorporation of a water-solubilising sulfonate (SO_3^-) moiety and represented the first examples of chiral **dpa** structures that could be studied in neat H_2O from the Gunnlaugsson laboratory. The ligands formed enantiopure complexes with Eu^{III} in a 1:3 ratio (metal-to-ligand) under microwave irradiation and gave **[Eu.(120(*S,S*))$_3$]** and **[Eu.(120(*R,R*))$_3$]** as confirmed by lifetime measurements in H_2O and D_2O solutions. The photophysical analysis of these complexes in H_2O and 0.1 M HEPES solutions showed strong sensitised Eu^{III}-centred with only minor ligand fluorescence emission. In fact, complexes **[Eu.(120(*S,S*))$_3$]** and **[Eu.(120(*R,R*))$_3$]** were highly luminescent with total quantum yields in H_2O *ca*. 14% for the Eu^{III}-centred emission. This was significantly higher than that seen previously for such systems in organic solution *ca*. 4%.[341] Moreover, in the highly competitive media, the antenna-to-ion energy transfer efficiency was also greatly improved; being *ca*. 80%, almost three-fold increased from CH_3OH and CH_3CN solutions. It was proposed that this enhancement was due to the amphiphilic nature of the ligands and the associated hydrophobic effects; this clearly demonstrated the important role that can be played by the pendent functionality of the pyridyl unit on the photophysical properties of the resulting systems.

The complexes were also analysed using chiroptical spectroscopy with the use of both CD and CPL measurements. Both these techniques confirmed that **[Eu.(120(*S,S*))$_3$]** and **[Eu.(120(*R,R*))$_3$]** were chiral and formed as pairs of enantiomers. In CD and CPL, the complexes gave rise to equal but opposite dichroism and polarised luminescence bands, respectively, with the CPL demonstrating the 'transfer' of chirality to the Eu^{III}-centred emission by generating a strongly chiral environment.

The directed-assembly between **120(*S,S*)** and **120(*R,R*)** with Eu^{III} *in-situ* was also investigated using changes in the absorption of the ligands as well as Eu^{III}-centred emission. The changes observed were used to probe the stoichiometry of the complexes formed, their concentration distributions and to estimate corresponding stability constants (logβ) through global non-linear regression analysis. Due to the relatively small changes in the absorption spectra, the changes in the CD spectra were also monitored and used to quantify the binding stoichiometry. The results from the CD measurements were in agreement with other methods and served as a more reliable absorption method to quantify the complex formation. Modelling of the spectroscopic data suggested that a four-component binding model was most appropriate to describe the solution equilibria and gave stability constants (logβ) of *ca.* 7, 13 and 19 for the **ML**, **ML$_2$** and **ML$_3$** species, respectively. The binding constants agreed closely between spectroscopic techniques.

Attempts were made to study the self-assembly of Eu^{III} complex through direct calorimetry using ITC and it was suggested that the coordination heats were not measurable. While the presence of amphiphilic assemblies of ligands **120(*S,S*)** and **120(*R,R*)**, as well as **[Eu.(120(*S,S*))$_3$]** and **[Eu.(120(*R,R*))$_3$]** were indicated by endothermic heats that were suggested to be associated with dissociation and disaggregation processes. Further evidence of solution assemblies, or aggregates, at spectroscopic concentrations was found in DLS measurements with scattering from ligand solutions both with and without Eu^{III} observed.

The formation of 'hydrogels' from electrolyte solutions by **120(*S,S*)** and **120(*R,R*)** was demonstrated in the cooling of hot solutions with both opaque and transparent gels being generated. A critical gelation point of 5 wt% was determined and soft materials were formed between 5 to 10 wt% of varying transparency. Morphological analysis of the ligand gels using SEM showed that the ligands formed layered materials consisting of more complex fibrous networks of thick assemblies that were intertwined underneath the smooth surface of the gel. The addition of Eu^{III} to the gels initially gave red luminescent metallogels, however the resulting Eu^{III} complexes were not stable within the gel matrix and resulted in precipitation of emissive solid materials with luminescence lifetimes consistent with the

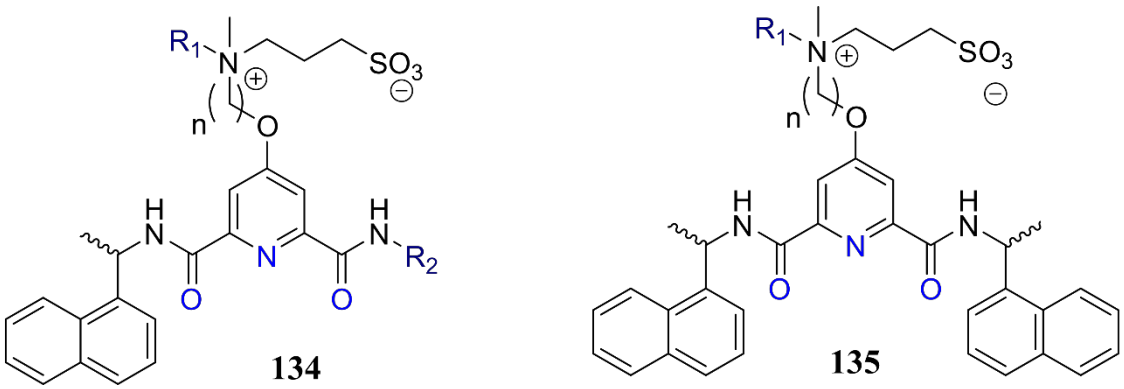

Figure 2.32 Structures of proposed derivatives of asymmetrical, **134**, and symmetrical, **135**, naphthyl **dpa** ligands possessing sulfonate moieties as charge-neutral zwitterionic sulfo-betaine groups

formation of neutral **[Eu.(120(*S,S*))$_3$]** or **[Eu.(120(*R,R*))$_3$]** complexes. The metallogel materials were unstable and unable to be studied individually.

There are a number of future prospects in the broader use of the sulfonate grafting to potentially improve both solubility and photophysical properties. The strategy of sulfonation to solubilise other naphthyl **dpa** derivatives, such as triple-stranded helicates[377], or indeed other hydrophobic ligands with limited solubility such as **btp**, is promising (on the condition of working at low concentration. Moreover, the efficiency of the approach could perhaps be improved through derivatives which will *not* be charge neutral upon formation of the **ML$_3$** stoichiometry complexes. To allow both sulfonation and maintaining the overall charge on the Ln^{III} complexes formed structures, like those shown schematically in Figure 2.32, could be considered for the naphthyl **dpa** scaffold; **134** and **135** represent the asymmetrical and symmetrical naphthyl **dpa** scaffolds, derived from previous[377] and current work in the Gunnlaugsson group, respectively. Grafting the sulfonate moiety by the quaternisation of a tertiary amine would produce betaine derivatives[87] and a sulfonated charge-neutral ligand; coordination to a Ln^{III} ion would therefore still give cationic complexes and have improved solution stability compared to a charge-neutral complex. These structures would be expected to retain the water solubility afforded by the sulfonate group and photophysical enhancements arising from the naphthyl-flanked coordination site. Furthermore, in the case of asymmetrical and sulfobetaine systems functionalisation sites remain available (R_1 and R_2 in Figure 2.32) for the introduction of other interacting or responsive groups. A range of simple responsive groups for naphthl-**dpa** complexes are under investigation within our group and one example is discussed in Chapter 3 of this thesis.

3. Photophysical behaviours of responsive naphthyl-dpa derivatives and their complexes with Eu^{III} in solution and soft materials

3.1 Introduction

The behaviour of naphthyl-**dpa** ligands in aqueous media was discussed in Chapter 1 as well as having been demonstrated through the design of ligand **120** (in the previous chapter). The use of the **dpa** ligands has much broader potential in organic systems as has been described in previous work by Gunnlaugsson,[335] Bünzli[135,394] and Muller.[137,138] As highlighted in Section 1.8, both the symmetrical and asymmetrical ligand scaffolds have been shown to produce discrete complexes,[341,346] helicates[344,346] and bundles[136] that are aesthetically beautiful in their helicity, solid-state geometry and symmetry.[43] Thus far, these superstructures have shown stable and uniform emissions yet have not yet been developed with responsive properties. Furthermore, the factors which influence their emission properties as well as their structural and coordination properties have not been studied systematically in any great detail. The demand for responsive materials is clear, particularly for analytical problems in environmental, biomedical and clinical contexts (for which lanthanide luminescence has long been considered a viable approach with various scaffolds).[31,44,45,53,62,151] However, the naphthyl-**dpa** scaffold has only been studied fully with non-functional pendent moieties (*i.e.* propyloxy-, propagyloxy-, diethyeleneglycol-) with minor, yet inconclusive, evidence of luminescence responsive behaviour in complexes of **136** upon host-guest interactions with the pendant crown[8] macrocycle.[340] The optical properties of the naphthyl-**dpa** scaffold have been demonstrated to be sensitive to isomeric variations, with respect to the antenna moiety,[341] and it has also been shown that modifications at the 4-position substitution of the pyridine core can be made without substantially changing the assembly behaviour or Ln^{III}-centred emission.[340]

Initially, in formation of this work, the feasibility of amide substitution was considered with simple alkylations of the secondary amides of **17** and **126**, resulting in derivatives such as **137** – **139**, Figure 3.1, foreseeing potential photophysical gains. However, it was found that even simple methylation resulted in prohibitive rotational restriction of the amide moieties and resulted in ineffective self-assembly of the rotamers. The poor self-assembly can be accounted for by the coordination interaction being

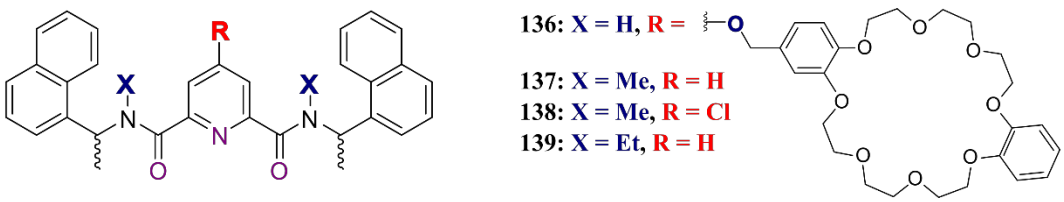

Figure 3.1 Structures of compounds **136**, a naphthyl-**dpa** showing partial responsive behaviour, and **137-138**, tertiary amide derivatives of **17** and **126**.

insufficient to overcome the conformational reorganisational energy barrier. In fact, attempts to coordinate Eu^{III} with **137 - 139** under thermodynamic conditions were also unsuccessful and in general the observed photophysical performance was overall decreased. This approach was therefore abandoned and will not be discussed in detail.

Prior work from the Gunnlaugsson laboratory demonstrated that in the solid-state, the 4-position of the pyridine extrudes from the cavity such that, regardless of identity, the substituent is unlikely to sterically hinder the π-π stacking interactions. This structural feature has been considered suitable for diverse functionalisation and to give broadly isostructural systems. Therefore, it was expected that higher function could be achieved by developing this handle further; indeed, this was highlighted in Chapter 2 through ligand **120** and the [**Eu.(120)$_3$**] complexes with respect to solubility. As a result of these positive developments, the sensitivity of the photophysical properties to variation at the 4-position of the naphthyl-**dpa** derivatives was probed with the aim of identifying perturbation in binding and photophysical character. Specifically, the influence of heteroatom substitutions at the pyridine 4-position and the introduction of responsive luminescence was of interest. Therefore, a series of five isosteric ligands was designed, shown in Figure 3.2, which varied the 4-position substitution with *O*-linked or *N*-linked pendant chains and an investigation into these phenomena was undertaken. In the cases of **121** - **123** these pendant chains possessed a bis-methylated amine. The isosteres **124** and **125** were studied to distinguish the influences of the *N* or *O* linking atom from those of the pendant chains which were found to participate in various interactions (*vide infra*). This chapter describes the structure-property relationships observed in the naphthyl-**dpa** scaffold and probes the photophysical data to characterise their solution behaviour more fully than previously studied. To facilitate these studies, attention was focussed to the complexes of **121** - **125** with Eu^{III},[67] these complexes were studied in enantiopure configurations.

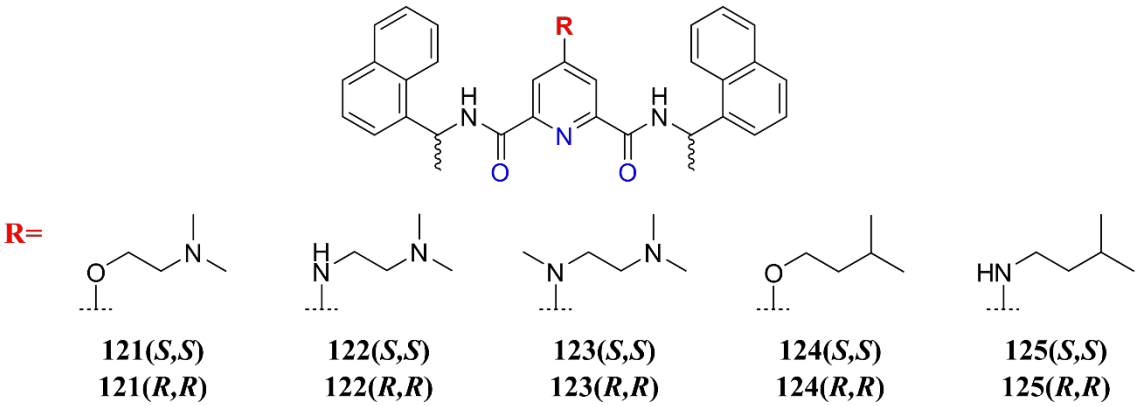

121(*S*,*S*) **122(*S*,*S*)** **123(*S*,*S*)** **124(*S*,*S*)** **125(*S*,*S*)**
121(*R*,*R*) **122(*R*,*R*)** **123(*R*,*R*)** **124(*R*,*R*)** **125(*R*,*R*)**

Figure 3.2 Summary of the structures of ligand series **121(*S*,*S*)** - **125(*S*,*S*)** and **121(*R*,*R*)** - **125(*R*,*R*)** which represent five short-chain naphthyl-**dpa** derivatives as *S,S* and *R,R* absolute configurations, respectively.

3.2 Design, synthesis and structural characterisation of ligands 121 - 125

A family of isosteric ligands **121 - 123**, were designed and synthesised, varying the linker to the naphthyl-**dpa** scaffold as ether (**121** and **124**) or as secondary (**122**, **125**) and tertiary (**123**) amines. The synthetic route, shown in Scheme 3.1, afforded the target structures from the common derivative **126** that was readily accessed from commercially available starting materials in a two-step synthesis.

Chelidamic acid **132** was suspended in thionyl chloride and heated with catalytic DMF at 51 °C under argon for 18 hours to afford the di-acyl chloride intermediate **132a** (simultaneously to the acid chloride formation the substitution of the pyridine 4-hydroxyl group as a chloro-substituent was achieved). Excess thionyl chloride was distilled from the mixture under reduced pressure to afford **132a** in quantitative yield as a white solid. Intermediate **132a** was dried under high vacuum for 2 hours prior to being dissolved in anhydrous CH_2Cl_2 and cooled to 0 °C. At low temperature, freshly distilled Et_3N was added to the reaction mixture followed by the slow addition of enantiopure *R*- or *S*- 1-(1-naphthyl)ethylamine. After 30 minutes, the reaction was warmed to ambient temperature

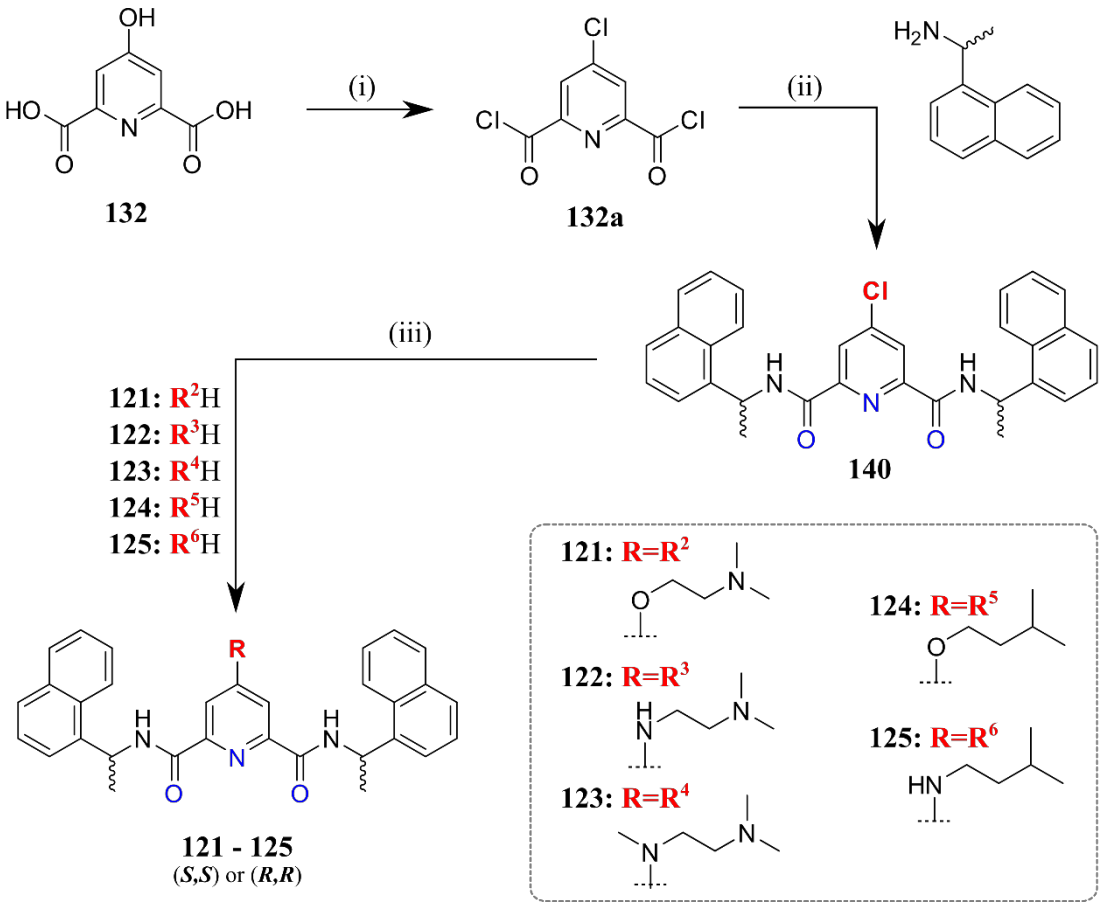

Scheme 3.1 Synthesis of intermediate **126** and ligands **121 - 125**: (i) $SOCl_2$, DMF (cat.), 51 °C; (ii) EDCI (2 eq.), HOBt (4 eq.), Et_3N (2 eq.), CH_2Cl_2, 0 °C → RT; (iii) Δ reflux.

and stirred under inert atmosphere for 48 hours. The resulting organic mixture was extracted with aq. 1M HCl, sat. aq. $NaHCO_3$ and sat. aq. NaCl. Following solvent evaporation from the dried (over $MgSO_4$) organic phase, the solid residues were triturated under ice-cooled CH_3OH and **126** was recovered in good yields (≈ 60%). The structures of **126** were confirmed by NMR and IR spectroscopy in addition to HRMS. In the IR spectra of **126** there was a shift in the carbonyl stretching frequency compared to **132** indicating the successful formation of the amide moiety showing $\nu_{C=O}$ at 1652 cm^{-1}.

In the ^{1}H and ^{13}C NMR spectra, a single set of sharp and well-resolved resonances were observed which corresponded the structure (shown in Appendix A3) which indicated that both symmetrical and enantiomerically pure forms (rather than diastereomers) were achieved. The chemical shift of the chiral ethylamine proton (H_*) at ≈ 6 ppm and the appearance of naphthyl aromatic signals supported the amide formation. A symmetrical structure was demonstrated by a singlet resonance for the pyridine protons, and the change in the chemical shifts of pyridine protons (H_ω) corresponded to the successful substitution of the hydroxyl for a chloro- group at the 4-position of the pyridine. Subsequently, ligands **121** - **125** were obtained by aromatic substitution of the 4-chloro substituent with relevant nucleophiles as primary alcohols (**121** and **124**) or amines (**122**, **123** and **125**).

Intermediate **126** was heated to reflux in neat *N,N*-dimethylethanolamine, *N,N*-dimethylethylenediamine*, N,N,N'*-trimethylethylenediamine to afford the pendent amine derivatives **121**, **122** and **123**, respectively. Ligands **124** and **125** were achieved by heating **126** at reflux in neat isopentanol and isopentylamine, respectively. After 18 hours, in each case, all the solids materials were dissolved and gave clear solutions from which crude ligands were precipitate from the rapid addition of the reaction mixture to iced-water. The resulting precipitates were isolated through filtration and excess alcohol or amine reagents removed by washing with distilled water, followed by purification of the desired products by column chromatography on silica (0 → 10 % CH_3OH in CH_2Cl_2). The pure products were isolated in good yields (50 – 60%). Ligands **121 - 123** were recovered as a mixture of neutral and protonated forms. Analysis of the respective derivatives confirmed these to be a single species by ^{1}H NMR with NaOD and DCl additives converging to a single set of resonances consistent with the expected structure. These resonances tended to be broader and less resolved in $CDCl_3$ and ^{1}H NMR spectra recorded in CD_3CN resolved better the vicinal coupling of the pendent chain, see Appendix A3.

The ^{1}H NMR spectra of **121** - **125** are shown in Figure 3.3. A single set of well resolved signals was observed in the ^{1}H NMR spectra of all the ligands, which confirmed the expected C_2 symmetry in the ligands structures, this corresponded to absolute configuration of *S,S* or *R,R* at the two chiral centres in the antennae and there was no evidence of *S,R*-configuration diastereoisomers. The aromatic region showed a set of multiplets which were in agreement between each ligand structure corresponding the naphthyl antennae (H_a to H_g). The small variations in chemical shifts of the naphthyl groups were consistent within the two groups of ligands which were *O*-linked (**121** and **124**) or *N*-linked (**122**, **123** and **125**) and supported the proposed substitution patterns. The deshielding of one naphthyl proton was observed of the *O*-linked ligands compared to the *N*-linked

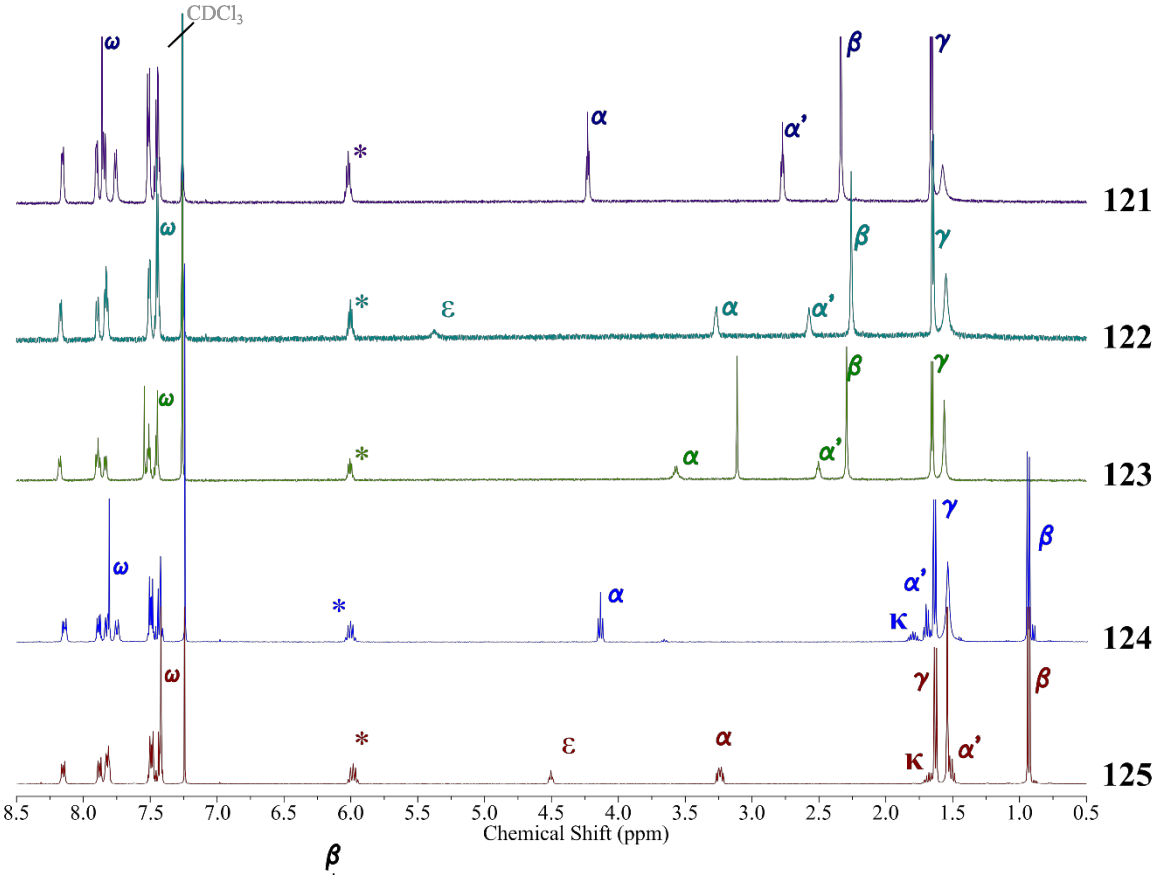

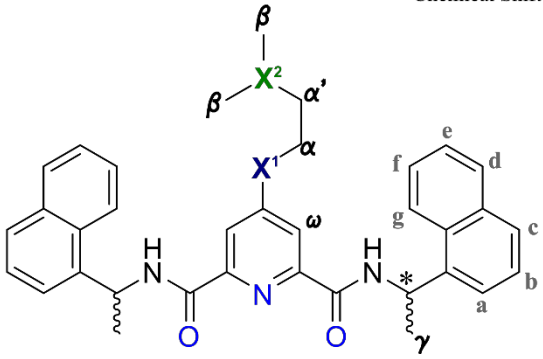

121: X^1 = O X^2 = N

122: X^1 = NH_ε X^2 = N

123: X^1 = $N(CH_3)$ X^2 = N

124: X^1 = O X^2 = CH_κ

125: X^1 = NH_ε X^2 = CH_κ

Figure 3.3 ^{1}H NMR spectra of **121(*S,S*)** - **125(*S,S*)** ($CDCl_3$, 600 MHz) with assigned key resonances based upon 2D NMR correlation experiments (Appendix A3).

substitution and was consistent with changes in EW/ED character influence on the magnetic anisotropy of the pyridine core. Furthermore, in the aromatic region, the resonance corresponding to the aryl protons of the pyridine core (H_ω) was indicative of the individual structures and was directly influenced by the 4-position substitution; with the pyridine core proton becoming more shielded upon substitution of the 4-position chlorine substituent with –OR or –NR moieties (producing a unique shift to each structure). The stereogenic centre (H_*) was reproduced as a single resonance with resolved coupling pattern and confirmed the symmetry of *S,S* and *R,R* configurations. The pendent chains were confirmed by the introduction of aliphatic resonances corresponding to methylene (H_α and $H_{\alpha'}$) and methyl (H_β) groups of the *N,N*-dimethyl ethylamine moieties. The relative deshielding of H_α reflected the electronegativity of the *O*- and *N*- linker atoms. In the cases of **124** and **125**, an additional resonance was observed for H_κ with a chemical shift of 1.75 ppm while the terminal CH_3 resonances were substantially shielded consistent with the purely hydrocarbon pendent chain. Key structural features were also confirmed by IR spectroscopy. In each case, the carbonyl stretch was unperturbed from the precursor compound which demonstrated no change in the amide moieties. Furthermore, in the case of **122** and **125** (both of which contained secondary anilines) an additional stretch was observed with $\nu_{N\text{-}H}$ at 3406 cm^{-1}, consistent with the aniline N-H stretch.

The fully characterised ligands were complexed to Ln^{III} salts (Ln = Eu, La, Lu) through the established microwave-assisted methodology, Scheme 3.2, that was used in Chapter 2. Ligands **121(*S,S*)** - **125(*S,S*)** (or **121(*R,R*)** - **125(*R,R*)**) were treated with 0.33 equivalents of the appropriate $Ln(CF_3SO_3)_3$ salt (Ln = Eu, La, Lu) in CH_3OH and heated at 70 °C in a sealed vial *via* microwave-assisted heating for 20 minutes. In each case, clear solutions were obtained that were emissive under UV light (λ_{exc} = 254 or 365 nm) and the complexes were precipitated by slow addition of excess diethyl ether to the CH_3OH

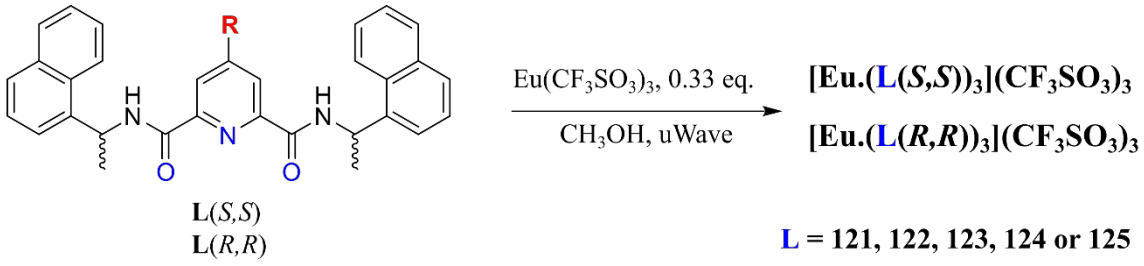

Scheme 3.2 Synthesis of Eu^{III}-centred complexes of **121** - **125** under thermodynamic control *via* microwave-assisted heating.

solutions. The complexes were recovered after centrifugation from the diethyl ether supernatant solutions and dried under high vacuum prior to further analysis.

The complexes were initially characterised by ^{1}H NMR and IR spectroscopy. The ^{1}H NMR spectrum, shown for **121(*S,S*)** in CD_3OD as a representative example in Figure 3.4. It was suggested in this case a single stoichiometry in solution and the single set of resonances consistent with **ML$_3$** having formed. The ligand resonances were broadened slightly and shifted modestly due to paramagnetic contact and pseudo-contact shifting (lanthanide induced shifts, LIS). This demonstrated the successful coordination of the ligands to the Eu^{III} ion. The magnitude of these LIS, while smaller than those observed in *cyclen* complexes,[447] were consistent with other systems of similar geometry[340,341,353] and corresponded with a small B_0^2 crystal field parameter.[448,449] Both the *S,S* and *R,R* complexes of **122** - **125** with $Eu(CF_3SO_3)_3$ showed LIS of similar magnitude which was in agreement with similar complexes geometry in each complexes of the ligand family (see Appendix A3). Similarly, in the IR spectra clear evidence of the coordination of Eu^{III} within the *O-N-O* binding site was observed. A reduction in the stretching frequency of the amide carbonyls from 1663 cm^{-1} to 1620 cm^{-1} consistent with bond lengthening with the coordination bond formation. The coordination of Eu^{III}, and the formation of these complexes with $(CF_3SO_3)^-$ counter-ions was also confirmed by HRMS. However, the stoichiometry could not be determined as a result of partial dissociation of the complexes under the experimental conditions. The

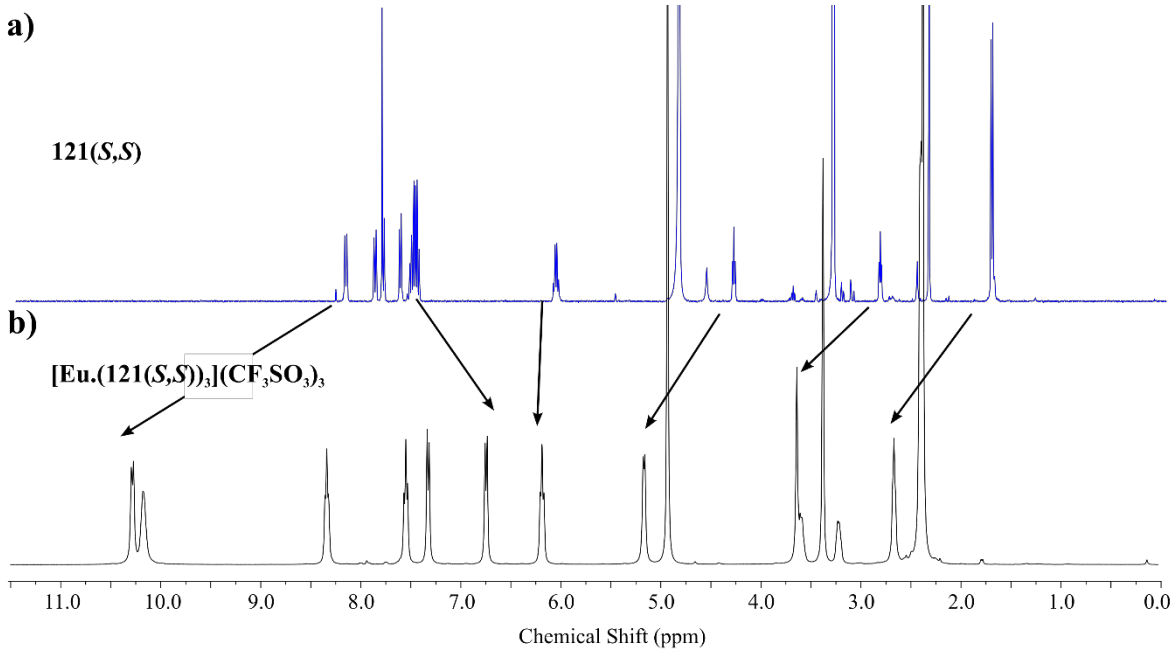

Figure 3.4 ^{1}H NMR spectra (400 MHz, CD_3OD) recorded for: **a)** ligand **121**; and **b)** complex $[Eu.(\mathbf{121})_3](CF_3SO_3)_3$ showing lanthanide induced shifting (LIS) of key resonances as a result of paramagentic proximity shifting effects. A single set of peaks demonstrated a single species in solution, confirmed to be **ML$_3$** by photophysical measurements.

stoichiometry of the complexes in the solid and solution states was later supported to be **ML_3** from photophysical measurements (*vide infra)*; however, first the photophysical properties of the free organic ligands were characterised in detail.

3.3 Photophysical characterisation of ligands 121 - 125

Spectroscopic characterisation of **121 - 125** was made using UV-visible absorption spectroscopy and fluorescence and time-gated emission spectroscopy. In a similar manner to that described in Chapter 2, the chiral absorbance properties were also probed. Similarly to the previously studied **dpa**-based scaffolds from the group[340,377] behaviour in increasingly competitive solvents was studied and **121 - 125** were characterised in both CH_3CN and CH_3OH. While the hydrocarbon isosteres **124** and **125** were less soluble in both CH_3CN and CH_3OH compared to the amine-appended structures; stable solutions could be achieved for all the ligands at $c = 1 \times 10^{-3}$ M (requiring sonication of **124** and **125**). Small differences emerged between the two sets of ligands dependent on whether the pendant chain was *O*-linked or *N*-linked and divided ligands **121** and **124** from ligands **122**, **123** and **125**, respectively. Solvent-dependency of various photophysical behaviours was also observed. The free-ligands were first characterised and in each case, the properties were in agreement between the *S,S* and *R,R* of the ligands (as expected for enantiomers), and hence, only the *S,S* configurations will be discussed in the following sections. The corresponding spectra from **121(*R,R*) - 125(*R,R*)** may be found in Appendix A3.

3.3.1 UV-visible absorption, CD and fluorescence characteristics of ligands 121 - 125

The structure of the UV-visible absorption features were broadly similar across the ligand series showing two main bands at λ_{abs} = 221 nm and 270 – 300 nm, corresponding to pyridine n→π* and high energy π → π* electronic transitions of the naphthalene and pyridyl moieties.

The lower energy feature showed a fine structure with maxima at 278, 281 and 290 nm and was consistent with naphthyl π→π* transitions from the antenna; a weakly absorbing tail to this naphthyl absorbance feature was observed in the region λ_{abs} = 300 – 350 nm. The basic features of the UV-vis absorption spectra of the ligands were similar when recorded in CH_3CN and CH_3OH. Molar extinction coefficients (ϵ, $cm^{-1}M^{-1}$) were determined for each ligand from the measurement of independent solutions at varying concentrations between 1 and 100 μm, and linear Beer-Lambert relationships were observed within this concentration range. The absorption characteristics (expressed as ϵ) for ligands **121(*S,S*) - 125(*S,S*)** in CH_3CN and CH_3OH, are shown in Figure 3.5a and Figure 3.5b, respectively.

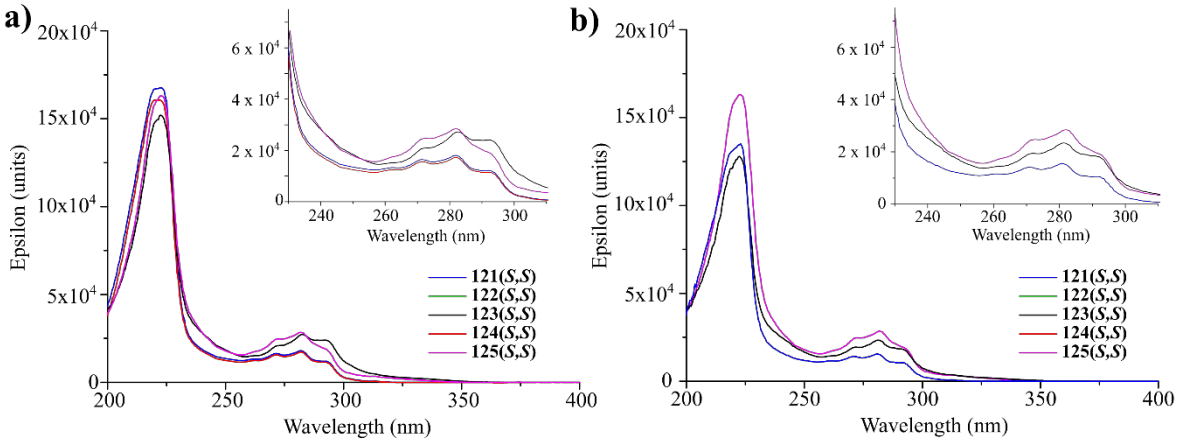

Figure 3.5 Overlaid UV-visible absorpton spectra comparing the molar excition coefficients (ϵ) of ligands **121** - **125** in: **a)** CH_3CN; and **b)** CH_3OH, showing common features and variation in ϵ with changes in *O*- or *N*-susbsitution of the 4-postion of the pyridine. Spectra recorded at 24 °C and ϵ determined as the average of measurements from at least 5 different solutions.

In CH_3CN, similar molar extinction coefficients were recorded for the absorbance band at λ_{abs} = 224 nm for all the ligands (*ca*. 15 - 16 × 10^4 $M^{-1}cm^{-1}$). However, the naphthyl π→π* feature at lower energy (270 – 300 nm and the tail in the region 300-350 nm) was more strongly absorbing in the *N*-linked ligands (**122**, **123** and **125**) compared to the analogous *O*-linked ligands. Solvent dependence was observed most significantly in the extinction coefficient for the λ_{abs} ≈ 224 nm feature, and only very small shifts in the absorbance maxima (*ca*. 1 - 2 nm) were seen. This was also reflected in CH_3OH where the *N*-linked ligands also showed stronger absorbance features at longer wavelengths.

The CD spectra of **121** - **125** were also recorded in CH_3CN and CH_3OH solutions; and those for **121(*S,S*)**, **121(*R,R*)**, **123(*S,S*)** and **123(*R,R*)** are summarised in Figure 3.6. The two enantiomers were expected to behave similarly and show strong, structurally similar dissymmetry in their chiroptical spectra. Indeed, the ligands showed strong Cotton effects, negative and positive in the case of *S,S* and *R,R* enantiomers, respectively, for the short wavelength absorption at λ_{max} = 224 nm in the UV-visible absorption spectra. The CD spectra showed this feature as two separate transitions to give a bisignate CD signal with one positive and one negative component. The region of absorbance between 230 – 260 nm gave positive CD for *S,S* and an equivalent negative signal for *R,R*. The finely structured pyridyl n → π* and naphthyl π → π* absorbance also showed a small Cotton effect which was positive and negative in the cases of *S,S* and *R,R*, respectively. The distributions of the ellipticity implied that the structures and conformations were also consistent to related ligands, such as **120(*S,S*)** and **120(*R,R*)**. The maxima of the Cotton effect were characterised by a Davydov splitting of 12 nm and 8 nm for the O-*linked* ligands (**121** and **124**) in CH_3CN

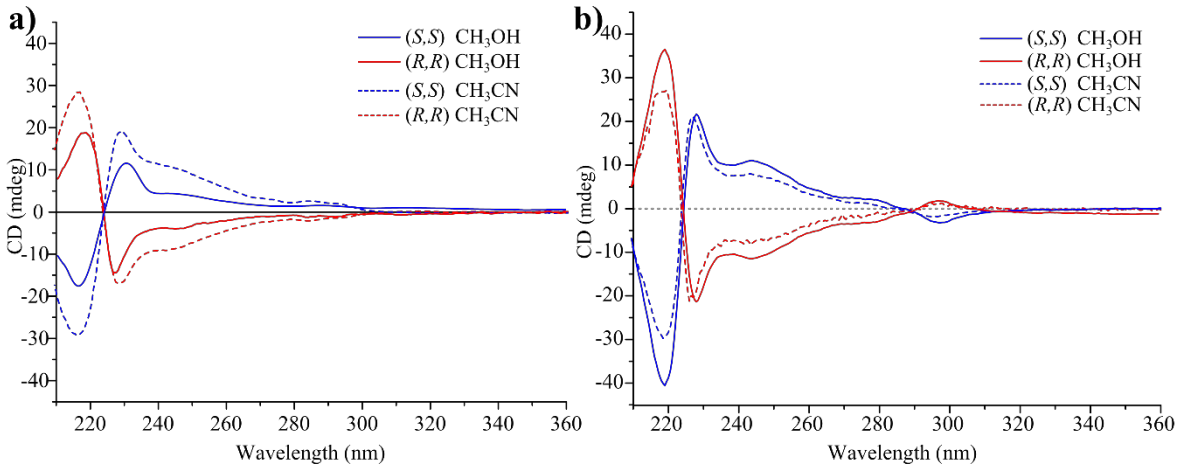

Figure 3.6 CD spectra recorded for: **a)** *O*-linked ligand **121** in CH_3CN (dashed) and CH_3OH (solid) for both *S,S* (blue) and *R,R* (red) enantiomers showing differences in elipticity with solvent; and **b)** *N*-linked ligand **123** in CH_3CN (dashed) and CH_3OH (solid) for both *S,S* (blue) and *R,R* (red) enantiomers showing similar shifts and enhancements in CD signals in CH_3CN. All spectra recorded at 24 °C with $c = 1 \times 10^{-5}$ M.

and CH_3OH, respectively. However, smaller splitting of *ca.* 7 nm and 9 nm in CH_3CN and CH_3OH, respectively, were observed for *N*-linked ligands (**122**, **123** and **125**).

Interestingly for **123(*S,S*)**, in contrast to **121(*S,S*)**, the magnitude of the negative Cotton effect bands (λ_{abs} = 219 nm) were enhanced by *ca.* 150% in CH_3OH compared to CH_3CN, while the positive band was red-shifted *ca.* 1 nm which resulted in the different splitting (the complementary changes were observed for the *R,R* configurations of **121** - **125**). This enhancement in CD signal did not correspond with the expected changes of solvent screening effects between CH_3CN and CH_3OH (the magnitudes being proportional to the square of the respective refractive indices of the solvent).[450] Therefore, the change was likely the result of a solvent-directed conformational change as a result of the polarity[451,452] and respective solvation (the amplitudes of Cotton effects, as dipole-coupled mechanisms, have distance[453,454] and extinction coefficient dependence[455]).

Excitation of the ligands, into both the pyridyl and naphthyl motifs (at λ_{exc} = 224 nm and 281 nm, respectively) gave rise to broad solvent-dependent fluorescence emission. The fluorescence spectra recorded for **121(*S,S*)** - **125(*R,R*)** in CH_3CN and CH_3OH are shown in Figure 3.7a and Figure 3.7b, respectively. A significant sensitivity to environment was observed. In CH_3CN, **121** and **124** gave fluorescence with λ_{max} = 410 nm while the *N*-linked ligands (**122**, **123** and **125**) gave emission with λ_{max} = 385 nm, while a red-shift *ca.* 15 nm was observed between CH_3CN and CH_3OH. Furthermore, both the intensities and absolute emission maxima varied greatly (between each ligand and solvent); however, these were reproducible in their λ_{max} values from independent batches of each ligand. In CH_3OH, the fluorescence maxima were not consistent between the ligands and was likely the result of

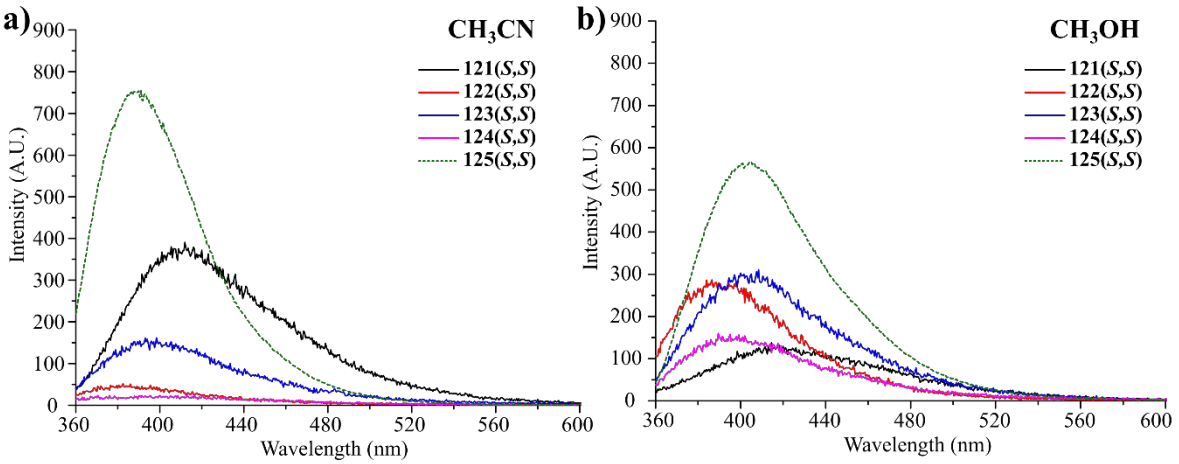

Figure 3.7 Fluorescence emission spectra recorded from ligands **121** - **125** in: **a)** CH_3CN; and **b)** CH_3OH, showing varying intensity and emission maxima in each ligand. Ligand **125** (green, dashed) was substantially more emissive and was recorded at a lower PMT voltage to demonstrate the maxima however intensity is not comparable to the other spectra. All spectra recorded at $c = 1 \times 10^{-5}$ M at 24 °C. $\lambda_{exc} = 281$ nm.

differences in the conformation (and therefore chromophore coupling) arising from variance in the solvent interactions of each ligand.

The fluorescence emissions of **121** - **123** were found to be acid-sensitive upon treatment with TFA and HCl in both CH_3CN and CH_3OH, respectively. The fluorescence emission spectra from **121(*S*,*S*)** and **123(*S*,*S*)** in neutral and acidic CH_3OH are shown in Figure 3.8a and Figure 3.8b, respectively. The two ligands showed opposite behaviours. Upon protonation of **121(*S*,*S*)** the fluorescence emission was quenched by *ca*. 90% while **123(*S*,*S*)** conversely showed a five-fold enhancement. In fact, equivalent behaviour to **123(*S*,*S*)** was observed for **122(*S*,*S*)** (both *N*-linked ligands with pendent amines) while **124(*S*,*S*)** and **125(*S*,*S*)** showed the same quenching as **121(*S*,*S*)**. The quenching behaviours are summarised in **Figure 3.9**a and two distinct groups were apparent. The quantitative

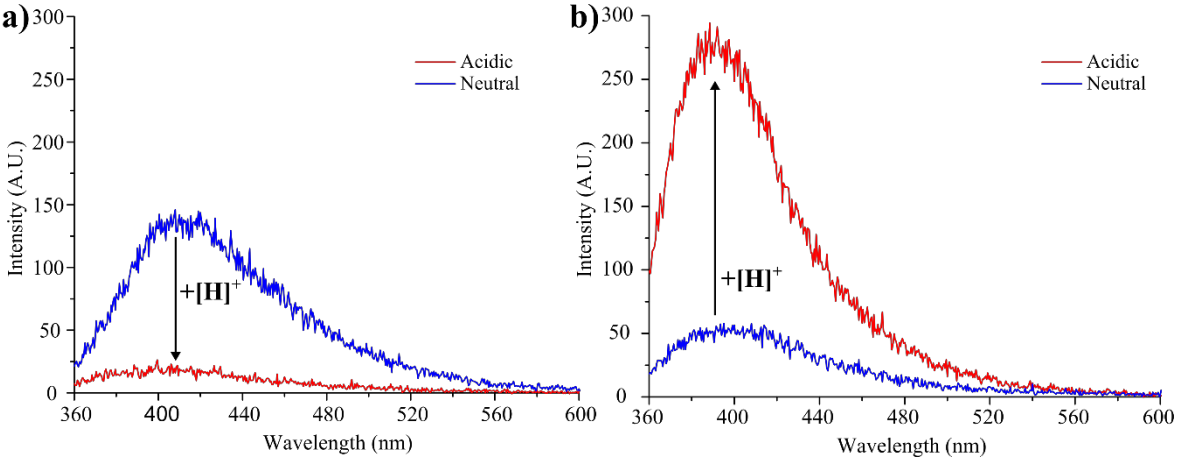

Figure 3.8 Fluorescence emission spectra in neutral (blue) and acidic (red) conditions in CH_3OH for: **a)** ligand **121** showing emission quenching upon protonation; and **b)** ligand **123**, showing emission enhancement upon protonation. All spectra recorded at $c = 1 \times 10^{-5}$ M at 24 °C. $\lambda_{exc} = 281$ nm. $[H^+]$ added as 0.5 HCl in CH_3OH. Spectra represent consistent trends from repeated measurements.

quenching in **124** and **125** was likely due to protonation of the pyridine core with concomitant deactivation of radiative pathways. The unique behaviour of **122** and **123**, however, suggested interaction of the amine lone pair with ligand-centred excited states. It was proposed that there was participation of photoinduced electron transfer (PET); this process is highlighted schematically in the frontier orbital diagram in Figure 3.9b.

The ligand-centred excited-states can deactivate *via* radiative (fluorescence, k_{fl}) or non-radiative (internal conversion or energy transfer, k_{IC} or k_{EnT}) pathways. In the case that a suitable electron donor is present ($HOMO_{amine}$), the excited-state can be quenched through a non-radiative pathway involving an electron transfer (k_{ET}). The suitability of a donor and efficiency of PET is strongly influenced by two factors: i) the distance between donor and acceptor frontier orbital and ii) the energy gap between the lone pair HOMO and acceptor SOMO.[456] This second factor is consistent with the diverse behaviour seen for the *O*- and *N*-linked ligands since molecular orbital distributions are intrinsically different (in both neutral and protonated forms) and, therefore, vary in PET quenching efficiency. The protonation of the pendent amine substantially increases its oxidation potential[457] and, therefore, in the *N*-linked ligands (where efficient PET was proposed) restricts the PET process and the associated quenching and therefore fluorescence intensity would be enhanced. The ligands alone demonstrated interesting and subtle photophysical properties. It was expected that the

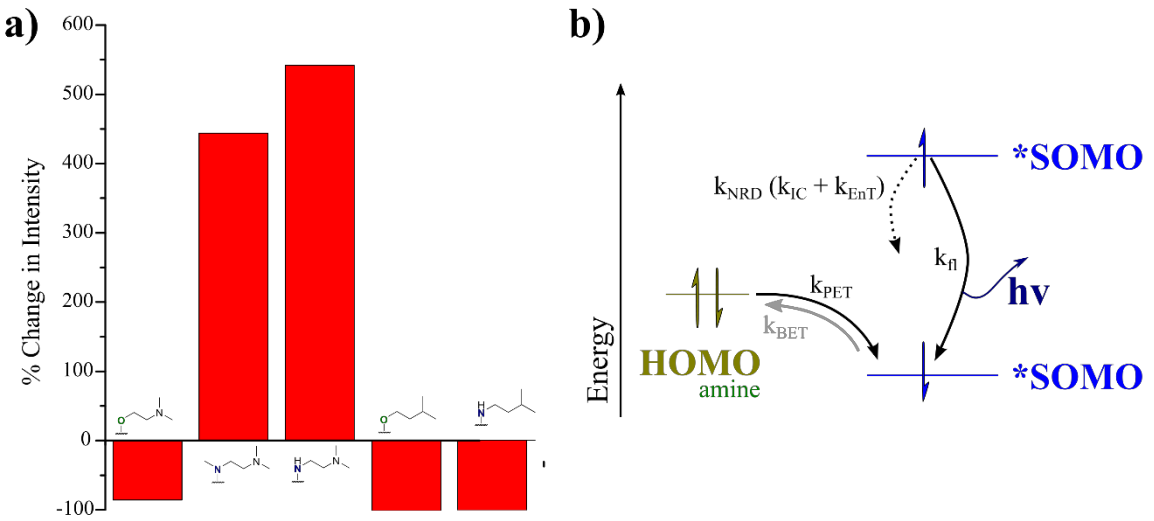

Figure 3.9 a) Summary of the percentage changes in fluorescence emission from ligands **121** - **125** upon protonation showing emission quenching from all ligands species except *N*-linked ligands possessing pendent amines (**122** and **123**) which gave enhanced emission; **b)** Schematic representation of S_1 excited-state SOMO (blue orbitals) processes associated with free ligands appended with ligands **122** ad **123**, showing additional excited-state processes due to the amine lone pair (green orbital). Excited state rate constants are shown for fluorescence emission (k_{fl}, solid arrow), non-radiative decay (k_{NRD}, dashed arrow) as a linear combination of internal conversion (k_{IC}) and solvent energy transfer (k_{EnT}) as well as possible photo-induced electron transfer (k_{PET}) and corresponding back electron transfer (k_{BET})

PET, and the general solvent effects, could influence the behaviour of the corresponding Eu^{III} complexes in a similarly rich and diverse manner. The Eu^{III} complexes formed under microwave irradiation were therefore fully characterised and are discussed in the following section.

3.3.2 UV-visible absorption, CD, fluorescence and Eu^{III}-centred emission from thermodynamic complexes of Eu^{III} with 121(*S,S*) - 125(*S,S*)

Coordination with Eu^{III} gave complexes which were shown to be of the stoichiometry **ML_3** by various spectroscopic techniques (*vide infra*) and resulted in clear changes in both absorbance and luminescence properties. Hypochromism of the λ_{max} = 221 nm absorbance was observed along with a minor broadening of the absorbance band. In the case of the *O*-linked ligands, this band was split into two separate maxima red- and blue-shifted by *ca.* 4 nm; this was consistent with the coordination of **120** described in Chapter 2. The absorption spectra of the *N*-linked ligands showed a lower degree of broadening and did not give rise to specifically resolved maxima. This dependence of the band splitting on the electronic character of the pyridine ring could be consistent with chromophore coupling upon direct-assembly of the ligand chromophores into close proximity.[392,393] This splitting, and the extent of hypochromism, was also found to be solvent dependent in the complexes (likely due to solvent screening effects on chromophore coupling) as seen from the spectra recorded in CH_3CN and CH_3OH (Appendix A3).

Additionally, upon the formation of the complexes hyperchromic shifts in the region of 300 – 310 nm were observed and were consistent with π-π interactions that would arise from the close proximities achieved by directed-assembly of the ligands around the Eu^{III}

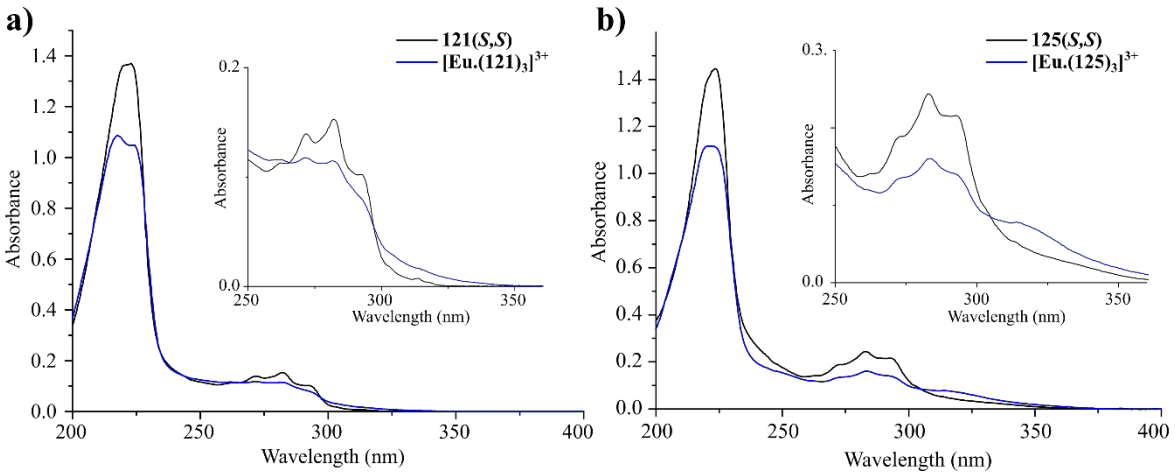

Figure 3.10 Overlaid UV-visible absorption spectra in CH_3CN for: **a)** *O*-ligand **121** and **[Eu.(121)$_3$]**$(CF_3SO_3)_3$; and **b)** *N*-ligand **123** and **[Eu.(123)$_3$]**$(CF_3SO_3)_3$; showing hypo- and hyper-chromic shifts at key wavelengths which varied with *O*- and *N*-linked ligands species. All spectra recorded at ligand $c = 1 \times 10^{-5}$ M at 24 °C and represent consistent observations from repeated measurements.

centre. In the case of *N*-linked ligands, shown for **123(*S,S*)** in Figure 3.10b, the enhancement in absorption was seen to a greater extent and extended to longer wavelengths than the corresponding *O*-linked ligand **121(*S,S*)** (Figure 3.10a). This hyperchromism was expected to arise from electronic coupling of the pyridine and naphthalene chromophores.[458] Furthermore, in various regions of the their spectra, the ligands and respective Eu^{III} complexes coincided and were consistent with isosbestic points seen in titrations (*vide infra*), as can be seen in Figure 3.10a and Figure 3.10b for **121(*S,S*)** and **123(*S,S*)**, respectively. The position of the isosbestic points corresponded to the electronic nature of the pyridine and were common for the *O*- and *N*-substituted ligands, respectively.

The use of chiroptical spectroscopy to aid understanding chiral systems, where classical methods have lower sensitivity, was demonstrated during Chapter 2 for the self-assembly of **120** with Eu^{III} ions. Similarly, the complexes of **121** - **125** were studied in solution using CD spectroscopy. A large change in the spectra was observed in CH_3CN while those in CH_3OH were much smaller in magnitude. The representative spectra for both enantiomers of **[Eu.(123)$_3$]$^{3+}$** and **[Eu.(121)$_3$]$^{3+}$** are shown in Figure 3.11 and Figure 3.12 with their respective ligand spectra in: a) CH_3CN; and b) CH_3OH.

The overall structure of the CD spectra were similar between each **ML$_3$** complex and the respective ligands. In each case, the *S,S* and *R,R* enantiomers behaved equivalently and differences in the absorbance at 270 – 320 nm arose between *O*- and *N*-linked systems. The spectra of the complexes consisted of the strong bisignate Cotton effect band between 220 – 230 nm and weaker CD of the naphthyl fine structure across 270 – 320 nm. Most notably changes in the magnitude of the CD bands occurred. In CH_3CN, the Cotton effect bands were enhanced by *ca*. 100% in both components while in CH_3OH, only the second

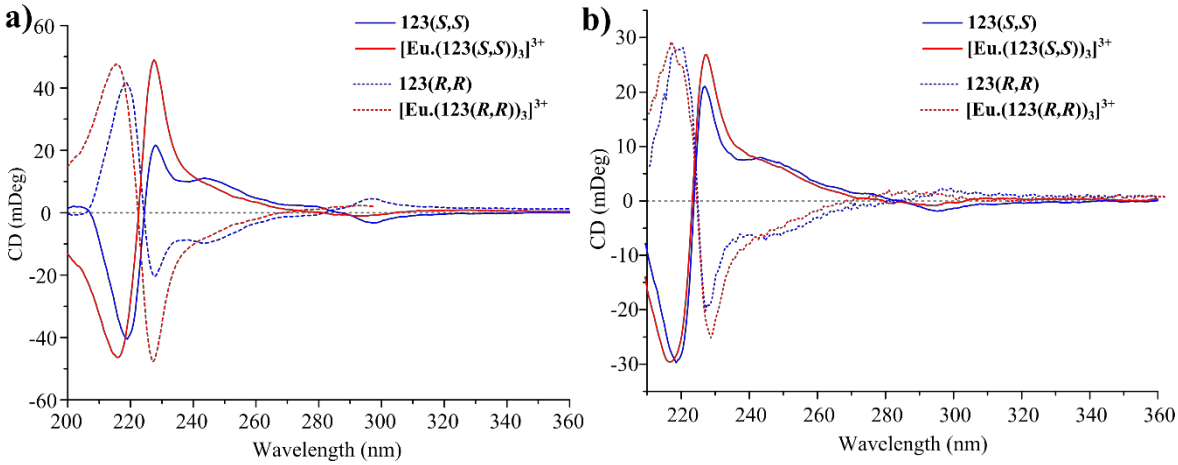

Figure 3.11 Overlaid CD spectra for ligands **123(*S,S*)** (blue solid) and **123(*R,R*)** (blue dashed) with their respective complexes **[Eu.(123(*S,S*))$_3$]$^{3+}$** (red solid) and **[Eu.(123(*R,R*))$_3$]$^{3+}$** (red dashed) in: **a)** CH_3CN and **b)** CH_3OH. Spectra were recorded at 25°C with ligand concentration $c = 1 \times 10^{-5}$ M.

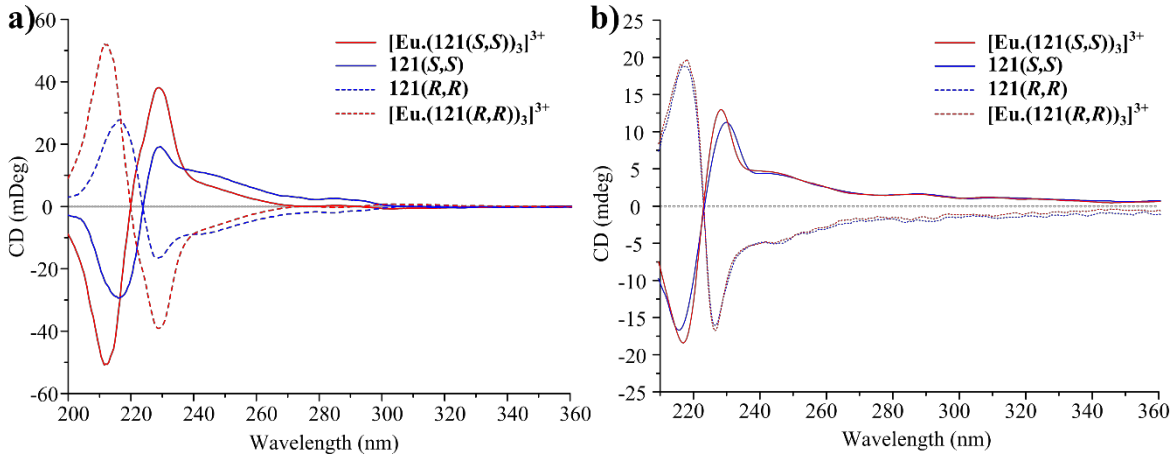

Figure 3.12 Overlaid CD spectra for ligands **121(*S,S*)** (blue solid) and **121(*R,R*)** (blue dashed) with their respective complexes **[Eu.(121(*S,S*))$_3$]$^{3+}$** (red solid) and **[Eu.(121(*R,R*))$_3$]$^{3+}$** (red dashed) in: **a)** CH_3CN and **b)** CH_3OH. Spectra were recorded at 25°C with ligand concentration $c = 1 \times 10^{-5}$ M.

component was enhanced, and to a smaller extent than above (*ca*. 15%). Simultaneously, the CD signal of the band between 270 – 300 nm was supressed from the *O*-linked ligands with the formation of the **ML$_3$** complexes. However, for *N*-linked derivatives, the ellipticity was redistributed around an isoeliptic point at 281 nm in the complexes, reflecting the different coupling with the pyridyl core. Additionally, the complexes showed increased Davydov splitting (as a result of shift in the bands of the Cotton effect) compared to the respective ligands. In CH_3CN, the first component of the Cotton effect was blue-shifted by *ca*. 3 and 4 nm for *O*- and *N*-linked derivatives, respectively (as shown for **123** and **121** in Figure 3.11 and Figure 3.12) while the second component remained unchanged. However, in CH_3OH both components underwent small shifts, blue- and red- shifts were observed in the first (*ca*. 3 nm) and second components (*ca*. 2 nm), respectively. These varied changes between the ligands and complexes demonstrated isoeliptic points at 218, 241 and 291 nm. The smaller magnitude of the complex CD signals in CH_3OH compared to CH_3CN was consistent with the increased solvent screening effect, while the less substantial enhancement suggested that CH_3OH directed conformation of the free-ligands that were more similar to that adopted in the directed assembly. In **121(*S,S*)** and **121(*R,R*)** only negligible changes were seen, with enhancement and shifts of the order of 2 mdeg and 2 nm, respectively. This highlighted the significance of the initial conformational conditions in the use of CD analysis of binding and the need to critically distinguish changes in CD arising from conformational change with those from stoichiometry changes. This is a fundamental consideration in the scope of CD as a tool to monitor self-assembly processes (*vide infra*).

The complexes formed with Eu^{III} under thermodynamic control were luminescent and gave characteristic emission spectra showing the $^5D_0 \rightarrow {}^7F_{1,2,3,4}$ transitions of Eu^{III} within

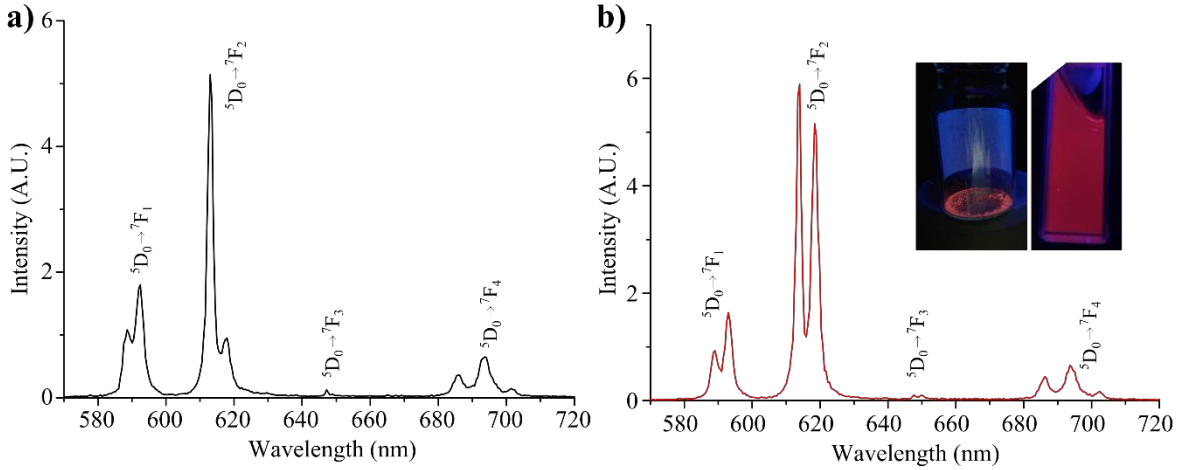

Figure 3.13 Representative Eu^{III} luminescence spectra from: **a)** complex **[Eu.(121(*S,S*)$_3$)]**$(CF_3SO_3)_3$ showing characteristic $^5D_0 \rightarrow {}^7F_{1,2,3,4}$ transitions; and **b)** complex **[Eu.(123(*S,S*)$_3$)]**$(CF_3SO_3)_3$ showing the same transitions but displaying a different ratiometry in the spectral structure, *inset*: photographs of complex **[Eu.(123(*S,S*)$_3$)]**$(CF_3SO_3)_3$ as solid and solution in CH_3CN under UV-light (λ_{exc} = 254 nm) showing visible red Eu^{III} emission. All spectra recorded in CH_3CN at c = 3.3 × 10^{-6} M at 24 °C. Spectral structures were reproducible between independent measurements on different instruments.

the region of 580 – 720 nm. The representative time-gated spectra from **[Eu.(121(*S,S*))$_3$]**$(CF_3SO_3)_3$ and **[Eu.(123(*S,S*))$_3$]**$(CF_3SO_3)_3$ in CH_3CN are shown in Figure 3.13a and Figure 3.13b, respectively. The same structure was maintained in both CH_3OH and the corresponding spectra can be found in Appendix A3. The most intense transitions was $^5D_0 \rightarrow {}^7F_2$ in each case, consistent with the selection rules for "induced"-ED transitions and the hypersensitivity of this transition. Similarly, the $^5D_0 \rightarrow {}^7F_{3,4}$ transitions were weaker with the $^5D_0 \rightarrow {}^7F_3$ being of negligible intensity from all the complexes. The lack of $^5D_0 \rightarrow {}^7F_0$ in the spectra of these complexes suggested the formation of saturated complexes of stoichiometry **ML$_3$** consistent with previous observations of the naphthyl-**dpa** scaffold.[341] The emission observed in CH_3OH was less intense compared to that in CH_3CN as was expected due to the more competitive quenching nature of CH_3OH (arising from the OH oscillator, see Appendix A3). More significantly differences were observed in the emission intensity dependent on the *O*-linked and *N*-linked species. In general, the overall intensity of the Eu^{III}-centred emission was lower in complexes of *O*-linked ligands *vs*. the *N*-linked analogues. Interestingly, the ratio between various features of the Eu^{III} spectra was found to act as a 'fingerprint' for the 4-position substituent atom; selected ratios are listed in Table 3.1, but for the present discussion the $^5D_0 \rightarrow {}^7F_{1,2}$ transitions were considered appropriate for analysis. The $^5D_0 \rightarrow {}^7F_1$ band was split into two components at 590 and 595 nm in a ratio of 1:2, respectively. This degree of splitting of this transition was consistent with the LIS observed in ^{1}H NMR spectra above (Section 3.2), a small B_0^2 crystal field parameter for the

systems[448,449] and the trigonal symmetry class expected for D_3 (or C_3) systems.[67] This transition remained independent of the 4-position linker type. The classical ratios between the integrated emission intensities of the two transitions (I_{J1} and I_{J2}, respectively) were determined for each complex and showed structure specific-trends.[459,460]

Table 3.1 Summary of ratiometry between the integrated intensities of emissive Eu^{III} transitions determined from emission spectra of **[Eu.(126(*S*,*S*))$_3$]$^{3+}$** and - **[Eu.(121(*S*,*S*))$_3$]$^{3+}$** - **[Eu.(125(*S*,*S*))$_3$]$^{3+}$** in CH_3CN.

Complex	Linker	I_{615}/I_{621}	I_{J2}/I_{J1}	I_{tot}/I_{J2}
[Eu.(17)$_3$]$^{3+}$	H	7.1	0.9	2.5
[Eu.(133)$_3$]$^{3+}$	O	3.7	1.0	3.4
[Eu.(126)$_3$]$^{3+}$	Cl	5.7	1.1	2.8
[Eu.(121(*S*,*S*))$_3$]$^{3+}$	O	3.7	1.6	3.5
[Eu.(122(*S*,*S*))$_3$]$^{3+}$	N	0.9	3.7	5.8
[Eu.(123(*S*,*S*))$_3$]$^{3+}$	N	1.1	3.3	5.5
[Eu.(124(*S*,*S*))$_3$]$^{3+}$	O	2.5	1.6	3.4
[Eu.(125(*S*,*S*))$_3$]$^{3+}$	N	0.9	3.1	5.3

Complex [**Eu.(126)$_3$]$^{3+}$** was considered as the reference compound and the integrated intensity of the $^5D_0 \rightarrow {}^7F_{1,2}$ transitions were found to be approximately equal giving $I_{J2}/I_{J1} \approx 1$. In the case of *O*-linked complexes the I_{J2} transition gained intensity and the ratio increased giving $I_{J2}/I_{J1} \approx 1.5$. In contrast, in the case of *N*-linked complexes, the I_{J2} transition gained intensity more significantly (*ca.* three-fold) giving $I_{J2}/I_{J1} \approx 3.5$. Similarly, the integrated intensity of the $^5D_0 \rightarrow {}^7F_1$ transition was compared to that of the total integrated emission intensity (I_{tot}) and consistent behaviour was observed with the complexes of *O*-linked, sharing a I_{tot}/I_{J1} ratio *ca*. 3.5, while this ratio for the complexes of *N*-linked ligands was increased to *ca*. 5.5.

The $^5D_0 \rightarrow {}^7F_2$ transition revealed interesting ratiometry, and this transition was also parameterised as a diagnostic 'fingerprint' to the substitution type. Unlike the original naphthyl-**dpa** ligand **17** which resolved a single component $^5D_0 \rightarrow {}^7F_2$ transition ($\lambda_{em} \approx 616$ nm), the hetero-substitution of the 4-position of the pyridine resolved a second m*J* component. The ratio between the two sub-components of the transition consistently correlated with the linker atom; these transitions are shown normalised in Figure 3.14b. In the case of the parent complex **[Eu.(126)$_3$]$^{3+}$** a small shoulder was resolved, however, upon *O*-substitution, the second component (at 621 nm) gained in intensity and increased further with *N*-substitution. The ratios of integrated intensity of the two components are also listed in Table 3.1 and showed a ratio between emission at 615 nm and 621 nm of 3:1 for *O*-linked

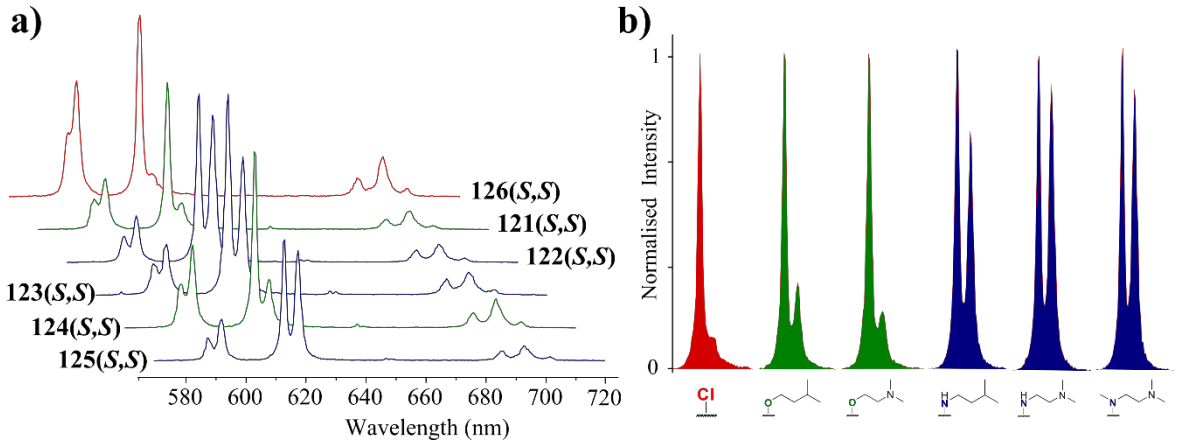

Figure 3.14 a) Stacked emission spectra recorded from the Eu^{III} complexes of **126(*S,S*)** and **121(*S,S*)** - **125(*S,S*)** demonstraing shared spectral features recorded at $c = 1 \times 10^{-5}$ M; and **b)** normalised spectra for the $^5D_0 \rightarrow {}^7F_2$ transition of Eu^{III} showing common intensity ratios in the transition components depending on the linker atom at the pyridine 4-position acting as a spectral 'fingerprint'. All spectra recorded at $c = 1 \times 10^{-5}$ M at 24 °C.

complexes and 1:1 for *N*-linked complexes. As an observational tool, it should be noted that the ratios between integrated and arbitrary intensities were in close agreement (Appendix A3). Again, these ratios were consistent within the *O*- and *N*-linked families and within the enantiomeric pairs. Indeed, the observed ratiometry was only significantly dependent on the 4-position linker atom and behaved independently of the periphery of the pendent chain. This was in agreement with the first coordination sphere of complexes formed from naphthyl-**dpa** based ligands being dictated uniquely by the pyridyl amides and naphthyl groups, both structurally as well as electronically. In fact, these 'fingerprints' for the linker atom can be observed retrospectively through the naphthyl-**dpa** bundles of **120** (discussed in Chapter 2) and **98** - **100** previously developed in the Gunnlaugsson group. The spectral 'fingerprint' was reproducible in from different batches of each complex and between different spectrophotometers (see Section 3.3.3). As a result of the structural similarity in the coordination sphere of both symmetrical and asymmetrical naphthyl-**dpa** systems, the same 'fingerprint' can be identified for *O*-substituted dimetallic triple-stranded helicates.[377] Changes in the ratiometry of emission Eu^{III} transitions are often assigned to changes in coordination sphere or coordination geometry.[67] However, the ratiometric behaviour here in most realistically accounted for by uniquely electronic effects. Therefore, the overall phosphorescence intensity enhancement and the ratiometry here was assigned to small changes in the HOMO-LUMO gaps of the different ligands and, predominantly, to the polarisability of central chromophore, which is larger in the more electron-rich *N*-substituted pyridines. A more polarisable ligand field can be expected to contribute to relaxation of

selection rules allowing certain transitions to gain intensity without substantial changes to geometry.[67]

3.3.3 Circularly Polarised Luminescence measurements of Eu^{III} complexes with ligands 121 - 125

The chiral environment generated around the central Eu^{III} ions in each **ML_3** complex was again transferred to the emission from the Eu^{III} ion, as shown by CPL measurements of the complexes in CH_3CN. CPL spectra were recorded by Dr. Robert D. Peacock at the University of Glasgow. The spectra from **121** and **123** in CH_3CN are shown in Figure 3.15. In the total luminescence spectra, the band ratios in the $^5D_0 \rightarrow {}^7F_{1,2}$ transitions were consistent with those observed previously and were an independent verification of the 'fingerprint' for the 4-position substitution. The enantiopure ligands were expected to give enantiopure Λ and Δ metal stereochemistry for *R,R* and *S,S* ligands, respectively, and gave therefore opposite CPL spectra.

The structure of the CPL spectra were familiar to the naphthyl-**dpa** scaffold and demonstrated a common structure to the family of complexes. Large CPL signals were only observed in the cases of the MD-allowed and hypersensitive $^5D_0 \rightarrow {}^7F_{1,2}$ transitions as expected by the selection rules and dipole transition vectors.[461] The $^5D_0 \rightarrow {}^7F_{1,3}$ transitions showed positive CPL for both resolved m*j* subcomponents while the $^5D_0 \rightarrow {}^7F_{2,4}$ transitions gave different ellipticity in their constituent m*j* subcomponents. While no crystals were forthcoming for ligands **121 - 125** nor their Eu^{III} complexes to support the assignment of stereochemistry, the structure of CPL spectra has increasing viability to elucidate metal stereochemistry by comparison to reference standards in structurally related systems.[138] The

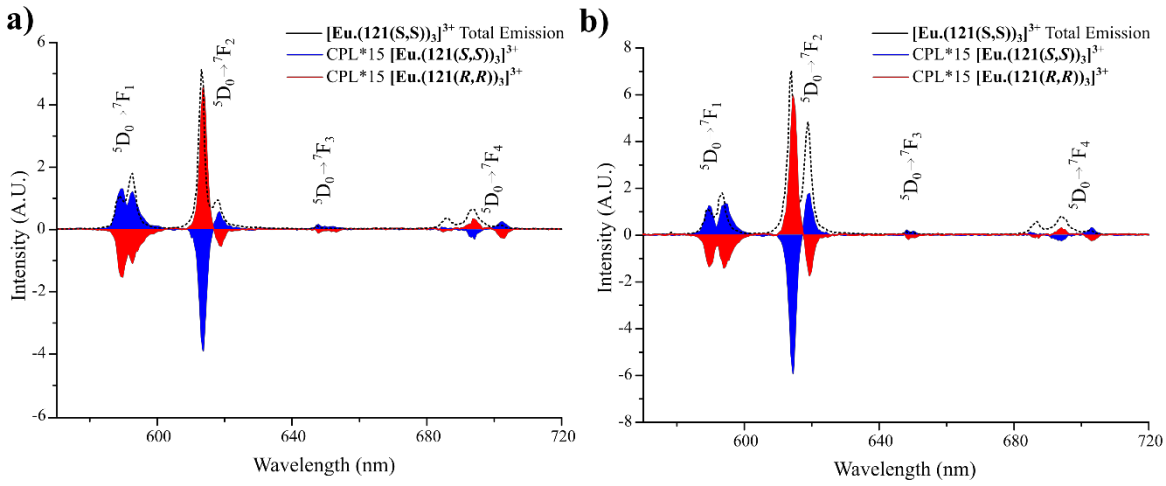

Figure 3.15 CPL spectra recorded in CH_3CN for *R,R* (red) and *S,S* (blue) isomers of: **a) $[Eu.(121)_3]^{3+}$**; and **b) $[Eu.(123)_3]^{3+}$** showing equal and opposite CPL emissions for each enantiomeric pair as well as similar intensities of dissymmetry. Total luminescence spectra are shown (black, dashed) demonstrating the Eu^{III} 'spectral fingerprint' of the *O*- and *N*- linked species in **a)** and **b)**, respectively.

Eu^{III} complexes of **121** - **125** clearly behaving similarly to each other but this was also in agreement to the wider ligand family and gave the corresponding CPL 'fingerprints'. Therefore, in each case, considering dipicolinate, **dpa** and other naphthyl-**dpa** systems as reference the assignment of Λ and Δ for the Eu^{III} stereochemistry was tentatively made for the complexes of *R,R* and *S,S* ligands, respectively.

Luminescence dissymmetry factors (g_{lum}) were calculated from the CPL and total luminescence spectra, using Equation 2.6, for the $^5D_0 \rightarrow {}^7F_{1,2,4}$ transitions which were strong enough for analysis. The CPL of chiral organic chromophores tends to be very small and difficult to measure,[462] while the CPL of metal complexes, particularly Ln^{III}-centred emission,[405] have tended to give stronger signals.[463] The values for g_{lum} for Eu^{III} and Tb^{III} complexes have been reported to vary between very weak (0.01) to strong (0.5).[405] and therefore the g_{lum} values calculated for the complexes of **121** - **125** are of significant magnitude for the $^5D_0 \rightarrow {}^7F_{1,2}$ transitions. The calculated values are summarised in Table 3.2 and were found to be consistent for ligands **121** - **125** and no dependence on the pendent chains was observed, which was not unexpected due to their isostructural connectivity.

Table 3.2 Summary of the dissymetry factors (g_{lum}) calculated for **[Eu.(126(*S,S*))$_3$]$^{3+}$** - **[Eu.(125(*S,S*))$_3$]$^{3+}$** from CPL measurements in CH_3CN.

	$^5D_0 \rightarrow {}^7F_1$				$^5D_0 \rightarrow {}^7F_2$			
	589 nm		**595 nm**		**614 nm**		**619 nm**	
Complex	***S,S***	***R,R***	***S,S***	***R,R***	***S,S***	***S,S***	***S,S***	***R,R***
[Eu.(126)$_3$]$^{3+}$	0.16	-0.16	0.02	-0.02	0.21	0.21	0.07	-0.04
[Eu.(121)$_3$]$^{3+}$	0.16	-0.17	0.09	-0.07	0.22	0.22	0.09	-0.07
[Eu.(122)$_3$]$^{3+}$	0.15	-0.15	0.09	-0.08	0.20	0.20	0.05	-0.05
[Eu.(123)$_3$]$^{3+}$	0.15	-0.15	0.10	-0.10	0.20	0.20	0.05	-0.05
[Eu.(124)$_3$]$^{3+}$	0.16	-0.17	0.09	-0.08	0.21	0.21	0.09	-0.08
[Eu.(125)$_3$]$^{3+}$	0.15	-0.13	0.08	-0.07	0.20	0.20	0.06	-0.05

In comparison to related complexes the g_{lum} values were smaller than those found for the un-substituted ligand **17**. However, they were in agreement with the magnitude to those recorded for the bulkier glycosylated naphthyl-**dpa** systems[340], triple-stranded helicates[345] and the half-helicates.[377] It was implied the smaller g_{lum} was a result of vicinal perturbation effects of the pendent chain that influence the conformations of the complexes.[411] For the reference complex **[Eu.(126)$_3$]$^{3+}$**, this was likely due to the larger radius of chlorine compared to hydrogen and oxygen. Previous studies which produced larger g_{lum} values have

been on un-substituted ligand and those functionalised with straight-chain moieties or longer linkers.[340] Therefore, it is likely that proximal steric effects, such as larger linker atoms and connectivity (*e.g.* early branching), contribute most strongly to this effect.

Further to this rich structural variation in the emission spectra the luminescence lifetimes of the complexes were probed in order to understand the quenching processes and stoichiometry of the complexes.

3.3.4 Luminescence lifetimes and Eu^{III} hydration states in Eu^{III} complexes of ligands 121 - 125

The lifetime of Eu^{III}-centred luminescence for each Eu^{III} complex with ligands **121 - 125** were determined in H_2O and D_2O and formalised by Horrocks and Parker to describe the number of Ln^{III}-bound solvent molecules (*q-value*) as was stated in Equation 2.1.

The emission lifetimes were measured for the Eu^{III} complexes **121 - 125** suspended[395] in H_2O and D_2O from monitoring the decay in intensity at 615 nm which corresponded to the most intense Eu^{III}-centred transition ($^5D_0 \rightarrow {}^7F_2$). Average luminescence lifetimes were determined from the fitting of at least five independent measurements of the decay profile acquired at different experimental gating time. The calculated lifetimes are summarised in Table 3.3 for **$[Eu.(121(S,S))_3]^{3+}$ - $[Eu.(125(S,S))_3]^{3+}$** while the values for **$[Eu.(121(R,R))_3]^{3+}$ - $[Eu.(125(R,R))_3]^{3+}$** were equivalent within experimental error and can be found in Appendix A3. From these lifetimes *q*-values were determined; each case suggesting that there were zero water molecules directly bound to the Eu^{III} ion. This corresponded with full saturation which would be achieved only in the **ML_3** stoichiometry, and demonstrated that the complexes were still susceptible to –OH oscillator quenching exclusively the result of second coordination sphere coupling interactions. Again, the Parker-modified equation corrected for the six amide –NH oscillators, which resulted in negative *q*-values (this still gave *q*-values of 0±0.5, consistent with the saturated stoichiometry). As described in Chapter 2, the existence of negative *q*-values has been reported previously and was suggested by Muller to be the result of sensitivity to scaffold N-H and C-H oscillators (distance and hydrogen-bonding affect quenching rates and deviates from the model corrections).[398] The empirical corrections, and full validity of the necessary assumptions, of the *q*-value method are challenged when conditions deviate from the conditions of the original model. This can be expected to be significant when dealing with suspensions and aggregating or self-assembling molecules. Therefore, **$[Eu.(121)_3]^{3+}$ - $[Eu.(125)_3]^{3+}$** highlight the use of *q*-values as just one method to support a physically rationale ligand arrangement since we must consider an increased the intrinsic error.

Table 3.3 Summary of Eu^{III} luminescence emission lifetimes (τ, ms) recorded from complexes in H_2O and D_2O and the number of bound water molecules (*q*-value) determined from Horrocks' and Parker's equations. Average lifetimes were determined from five independent measurements.

Complex	τ_{H_2O} (ms)	τ_{D_2O} (ms)	*q*-value (Horrocks)	*q*-value (Parker)
[Eu.(121(*S*,*S*))$_3$]$^{3+}$	1.54 ± 0.01	2.79 ± 0.02	0.05	~0 (-0.40)
[Eu.(122(*S*,*S*))$_3$]$^{3+}$	1.33 ± 0.01	2.44 ± 0.01	0.11	~0 (-0.34)
[Eu.(123(*S*,*S*))$_3$]$^{3+}$	1.26 ± 0.01	2.77 ± 0.02	0.22	~0 (-0.23)
[Eu.(124(*S*,*S*))$_3$]$^{3+}$	1.46 ± 0.01	2.17 ± 0.01	-0.05	~0 (-0.20)
[Eu.(125(*S*,*S*))$_3$]$^{3+}$	1.38 ± 0.02	2.54 ± 0.02	0.09	~0 (-0.35)

The extended luminescence lifetimes were consistent with that previously seen for **ML$_3$** complexes of naphthyl-**dpa** derived systems (with the **ML** or **ML$_2$** stoichiometry demonstrating substantially shorter lifetimes).[340,341] The complexes of *O*-linked ligands (**[Eu.(121(*S*,*S*))$_3$]$^{3+}$** and **[Eu.(124(*S*,*S*))$_3$]$^{3+}$**) exhibited slightly longer luminescence lifetimes than those seen for the equivalent *N*-linked complexes (despite giving less intense emission spectra). However, in all cases, the Eu^{III}-centred luminescence lifetimes were best-fitted to a mono-exponential decay which suggested the complexes were formed exclusively as the **ML$_3$** stoichiometry.

The balance of the metal-centred photophysical properties and influence of the peripheral ligand structure of these **ML$_3$** complexes was probed further and the emission parameterised in CH_3CN and CH_3OH solutions.

3.3.5 Quantum yields, sensitisation efficiency and photophysical parameterisation of Eu^{III} complexes of ligands 121 - 125

In order to complete the comparison of the Eu^{III} complexes of **121 - 125**, a broad parameterisation of the Eu^{III}-centered luminescence was undertaken and a number of parameters were calculated. The calculations of total luminescence quantum yield (Φ_{tot}), intrinsic quantum yield (Φ_{Ln}^{Ln}), radiative lifetime (τ_r) and sensitisation efficiency (η_{sens}) were previously described in Equation 2.2 to Equation 2.5. A summary of these parameters for **[Eu.(121)$_3$]$^{3+}$** - **[Eu.(125)$_3$]$^{3+}$** is given in Table 3.4 below. Luminescence quantum yields were determined from the relative method of Bünzli using Cs_3**[Eu.(6)$_3$]** acting as the standard (Φ = 24 ± 0.2 %)[127] and the remaining parameters calculated from the integrated luminescence spectra and corresponding lifetime measurements.

As a result of the acid sensitivity observed in the amine-appended ligands **121 - 123**, the transfer of the acid sensitivity to the Eu^{III}-centred luminescence in the **[Eu.(122)$_3$]$^{3+}$** and

[Eu.(123)$_3$]$^{3+}$ complexes was investigated. It was proposed that an approach for the development of Eu^{III} luminescent probes for acidity could be found through this modulation of the emission intensity. Therefore, the Eu^{III}-centred emission was parameterised in both 'neutral' conditions and in the presence of [H$^+$]. The emission was recorded in CH_3CN and CH_3OH with [H$^+$] added as trifluoroacetic acid (TFA) and HCl in CH_3OH, respectively; spectra in 'neutral' and 'acidic' conditions are presented in Figure 3.16a and overall changes summarised in Figure 3.16b.

Table 3.4 Photophysical parameters in neutral and acidic CH_3CN and CH_3OH at 24 °C: lifetime values (τ_{obs}, τ_R), total and *intrinsic* quantum yield percentages (Φ_{tot}, Φ_{Eu}), and antenna-to-Eu^{III} sensitisation efficiencies (η_{sens}) for Eu^{III} complexes of **121** - **125**. Calculations made using Equations 2.1 – 2.5, excitation at λ_{exc} = 279 nm.[127] Estimated error assosciated with quantum yields (Φ_{tot}) and the photophysical paramters is ±10%.[137] Uncertainties were determined through averaging independent measurements and are approximately ± 10%.

Complex	Solvent	τ_{obs}, ms	Φ_{tot}, %	τ_R, ms	Φ_{Ln}^{Ln}, %	η_{sens}, %
[Eu.(121)$_3$]$^{3+}$	CH_3OH	1.61	3.35	10.1	16.1	21.0
	CH_3OH (acid)	1.62	5.95	10.0	15.9	37.4
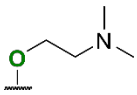	CH_3CN	1.58	5.60	8.82	17.9	31.3
	CH_3CN (acid)	1.56	5.82	8.48	18.4	31.7
[Eu.(122)$_3$]$^{3+}$	CH_3OH	1.41	3.65	6.75	20.9	17.5
	CH_3OH (acid)	1.43	5.59	7.50	19.0	29.4
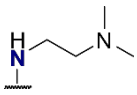	CH_3CN	1.50	2.71	6.72	25.3	10.7
	CH_3CN (acid)	1.51	5.94	6.82	21.5	26.8
[Eu.(123)$_3$]$^{3+}$	CH_3OH	1.35	2.21	6.89	19.6	11.3
	CH_3OH (acid)	1.36	6.08	6.86	19.0	32.1
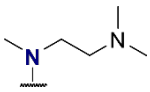	CH_3CN	1.50	2.31	6.69	22.4	10.3
	CH_3CN (acid)	1.52	4.95	6.34	23.9	20.7
[Eu.(124)$_3$]$^{3+}$	CH_3OH	1.54	4.65	10.3	16.0	29.0
	CH_3OH (acid)	1.54	4.56	10.2	15.2	30.2
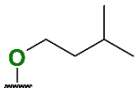	CH_3CN	1.78	5.67	9.81	18.2	31.24
	CH_3CN (acid)	1.76	5.85	9.91	17.7	32.9
[Eu.(125)$_3$]$^{3+}$	CH_3OH	1.42	6.60	6.95	20.4	34.0
	CH_3OH (acid)	1.43	6.57	7.19	19.9	33.1
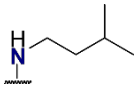	CH_3CN	1.53	11.1	6.63	23.1	48.2
	CH_3CN (acid)	1.51	11.0	6.46	23.4	47.0

The hydrocarbon isosteres **[Eu.(124)$_3$]$^{3+}$** and **[Eu.(125)$_3$]$^{3+}$** demonstrated the least number of competing effects and represented behaviour that was in agreement with other simple naphthyl-**dpa** systems reported previously.[341] The *O*-linked complex **[Eu.(124)$_3$]$^{3+}$** gave similar η_{sens} values to those determined for **[Eu.(120)$_3$]$^{3+}$** (*ca.* 30%, see Chapter 2), while

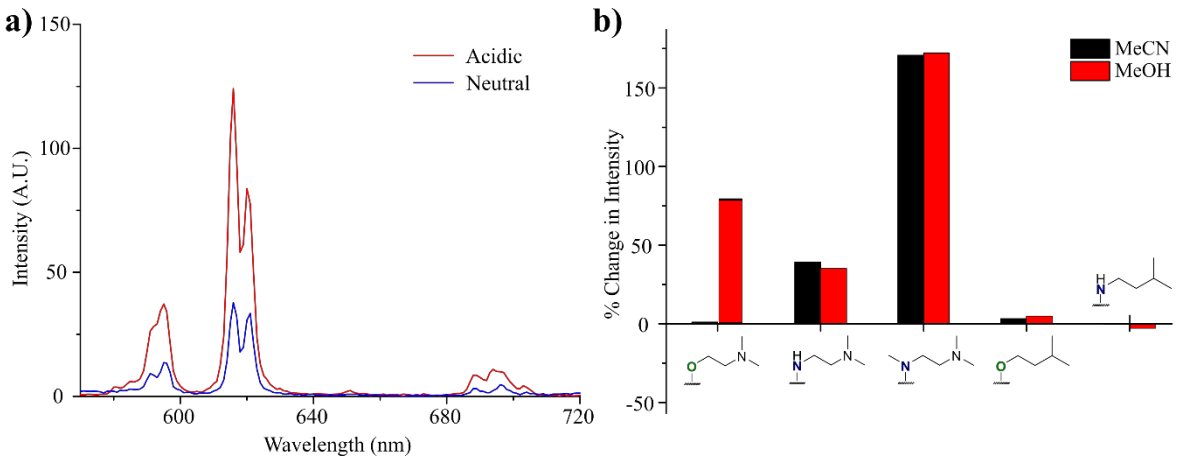

Figure 3.16 a) Representative Eu^{III} emission spectra from **[Eu.(123)$_3$]$^{3+}$** under neutral and acidic conditions in CH_3OH recorded during quantum yield determination, showing significant intensity enhancement in acidic conditons; and **b)** summary of the % change in Eu^{III} emission intensity (integrated total emission) in acidic conditions in CH_3CN/TFA (black) and CH_3OH/HCl (red), showing significant enhancements only in the case of **[Eu.(123)$_3$]$^{3+}$** and **[Eu.(122)$_3$]$^{3+}$** with the other complexes remaining mostly stable. All measurements made at 24 °C, at equivalent absorbance at λ_{abs} = 279 nm.

order of magnitude for both **[Eu.(124)$_3$]$^{3+}$** and **[Eu.(125)$_3$]$^{3+}$** was in agreement with **[Eu.(17)$_3$]$^{3+}$**.[341] Moreover, **[Eu.(124)$_3$]$^{3+}$** gave a lower Φ_{tot} than the *N*-linked analogue **[Eu.(125)$_3$]$^{3+}$**, which were both reduced in CH_3OH compared to CH_3CN, consistent with increased solvent quenching.

The spectra also revealed common features (within each solvent system) in the Φ_{Ln}^{Ln} values for groups of the ligands (summarised in Table 3.4). The Φ_{Ln}^{Ln} values were found to be common between **[Eu.(121)$_3$]$^{3+}$** and **[Eu.(124)$_3$]$^{3+}$** (16-17% and 18% in CH_3OH and CH_3CN, respectively) and, similarly, **[Eu.(122)$_3$]$^{3+}$** and **[Eu.(123)$_3$]$^{3+}$** showed equivalent Φ_{Ln}^{Ln} values to **[Eu.(125)$_3$]$^{3+}$** (20% and 25% in CH_3OH and CH_3CN, respectively). The τ_r values were also consistent within the same sets of ligands and therefore demonstrated that both the Φ_{Ln}^{Ln} and radiative lifetime τ_r were dictated by the substitution pattern at the 4-position of the pyridine. This implied the fundamental coordination was not disrupted with the changes in ligand structure but arose from electronic variations in the ligands. As a result, the changes in η_{sens} observed was suggested to be a specific effect of the pendent amine moiety.

Contrary to the hydrocarbon isosteres **[Eu.(124)$_3$]$^{3+}$** and **[Eu.(125)$_3$]$^{3+}$**, in neutral conditions of both CH_3OH and CH_3CN the complexes **[Eu.(121)$_3$]$^{3+}$** (an *O*-linked ligand derivatives) showed a larger quantum yields of Eu^{III} emission compared to the *N*-linked analogues of **[Eu.(122)$_3$]$^{3+}$** and **[Eu.(123)$_3$]$^{3+}$**. However, in fact, the less emissive species were suggested to have a larger intrinsic quantum yield of lanthanide luminescence which was likely due to the difference in polarisability of the surrounding electrostatic ligand field.

Therefore, the difference in the emission was a result of lower sensitisation efficiencies in **[Eu.(122)$_3$]$^{3+}$** and **[Eu.(123)$_3$]$^{3+}$** compared to that seen for **[Eu.(121)$_3$]$^{3+}$**.

The complex with strongest photophysical performance was **[Eu.(125)$_3$]$^{3+}$** (quantum yield of *ca*. 11% in all conditions as a result of significantly enhanced energy transfer efficiency). Indeed, as the Φ_{Ln}^{Ln} of the *N*-linked ligands were universally higher, the overall photophysical parameterisation strongly suggested a substantial participation of the pendent amine in control of metal-centred emission properties. These observations were consistent with different extents of competition from PET with the sensitisation process for the *O*- and *N*-linked ligands. Moreover, this was also suggested by the changes in the emission in CH_3CN compared to CH_3CN and measuring the luminescence properties in neutral and acidic conditions. Complexes **[Eu.(121)$_3$]$^{3+}$** and **[Eu.(124)$_3$]$^{3+}$** showed reduced quantum yields in CH_3OH compared to CH_3CN, this being consistent with the quenching effect of the –OH oscillators. Interestingly, **[Eu.(121)$_3$]$^{3+}$** showed a two-fold increase in quantum yield upon treatment with acid only in the case of CH_3OH. In contrast, no change seen in CH_3CN. In CH_3OH, the photophysical performance improved to match that of the **[Eu.(124)$_3$]$^{3+}$** (which did not possess a terminal amine) and indicated that the pendent amine was responsible for perturbation in the metal-centred photophysical performance. Different behaviour was seen for complexes **[Eu.(122)$_3$]$^{3+}$** and **[Eu.(123)$_3$]$^{3+}$** which were formed with *N*-linked ligands that possessed a terminal amine. An enhancement in the quantum yield for **[Eu.(122)$_3$]$^{3+}$** and **[Eu.(123)$_3$]$^{3+}$** in CH_3OH compared to CH_3CN was seen. This was proposed to be due to the hydrogen bonding of solvent to the PET donor which restricted the PET efficiency and concomitantly increased the ligand→Eu^{III} energy transfer efficiency. This was in agreement with the ligand fluorescence measurements discussed above. The complexes that did not possess pendent amines, **[Eu.(124)$_3$]$^{3+}$** and **[Eu.(125)$_3$]$^{3+}$**, did not show significant acid sensitivity and their quantum yields were equivalent (within experimental error) under both solvent conditions demonstrating the correlation of pendent amine and the influence of acid. The lack of acid response in **[Eu.(125)$_3$]$^{3+}$** demonstrated that the aniline –NH was not involved in perturbing the photophysical behaviours and that it was specific to the pendent amine moieties. This excluded the direct $Eu^{III} \rightarrow Eu^{II}$ reduction[464] as a route to quenching the Eu^{III}-centred luminescence.

Enhancement in photophysical performance was also observed for **[Eu.(121)$_3$]$^{3+}$**, **[Eu.(122)$_3$]$^{3+}$** and **[Eu.(123)$_3$]$^{3+}$** and upon acidification (an immediate enhancement in the Eu^{III}-centred emission was observed). In acidic conditions, these complexes showed *ca*. three-fold enhancement in quantum yield as a result of improved sensitisation efficiency. In

agreement with the expected behaviour, the Φ_{Ln}^{Ln} of Eu^{III} were unaffected by the acidity (not suggestive of substantial ligand field changes) and the improved sensitisation efficiency was, therefore, likely the result of reduced PET efficiency upon protonation of the donor amines. The UV-visible absorption spectra of all the complexes suggested that the complexes maintained their structure and stoichiometry.

A classical PET process was observed in ligands **122** and **123** above, which quenched the fluorescence emission (represented in the Jablonski diagrams in Figure 3.9b). However, in complexes **[Eu.(122)$_3$]$^{3+}$** and **[Eu.(123)$_3$]$^{3+}$** non-classical PET processes were suggested which resulted in the quenching of Eu^{III}-centred emission. A number of potential PET pathways may arise in the **ML$_3$** complexes, as shown in Figure 3.17a. As demonstrated for the free ligands an intramolecular quenching can occur (PET_{intra}) by electron transfer from a nitrogen lone pair donor to the pyridine acceptor of the same ligand molecule. Furthermore, the directed-assembly of the ligands in **ML$_3$** complexes around Eu^{III} brings three ligands together and may allow inter-ligand electron transfer (PET_{inter}) to the molecular orbitals of adjacent ligands in the same complex. The fate of these quenched excited-states may be: a) deactivation through internal conversion; or b) subsequent electron transfer to adjacent ligands or the Eu^{III} ions reducing it to Eu^{II}.[66,464,465] In each case the result could contribute to an overall quenching of Eu^{III}-centred emission by perturbing the classical sensitisation process. Most likely ligand-centred exited-states are quenched by PET_{inter} and PET_{intra} processes and deactivated rapidly by internal conversion, which competes with the energy transfer to Eu^{III}.[466,467] The protonation of the pendent amines would restrict the PET

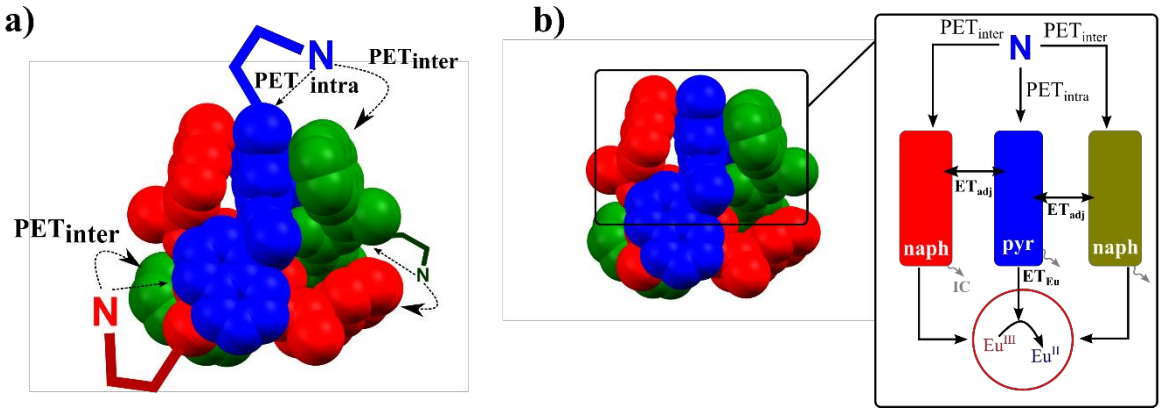

Figure 3.17 Schematic representation of PET pathways and emission characteristics in **[Eu.(L)$_3$]$^{3+}$** complexes where **L** = **122** or **123** (possessing *N*-linked pendent amines): **a)** cartoon representation showing expected proxmity of chromophores to the pendent chains potentially allowing both intraligand (PETintra) and interligand (PET_{inter}) PET processes; **b)** schematic representation of stacked chromophores from three adjcaent ligands indicating PETintra and PETintra processes, in additon to other fates of the quenched excited-state involving additional electron transfers to reduced Eu^{III} to Eu^{II} (ET_{Eu}), transfer to adjcaent ligands (ET_{adj}) and deactivaton by internal conversion (IC).

quenching of the excited-states allowing efficient ISC, ligand→Eu^{III} energy transfer and sensitised Eu^{III}-centred emission. The protonation was also demonstrated by the reversible nature of the effect with the addition of TBAOH to the solutions (see Appendix A3). It was suggested that the effect was weaker in **[Eu.(121)$_3$]$^{3+}$** likely due to the specific energy levels arising from the mixing of MOs in the directed-assembly and with the solvent environment. The UV-visible absorption spectra of the complexes showed significant changes in the ground-states in the complexes compared to the free ligands, which may also be reflected in the excited-states and the resulting acceptor ability. The true excited-state processes and fate of those quenched excited-states have not yet been fully understood, requiring study of the transient and ultrafast spectroscopy. However, since the behaviours were robust and reproducible, the calibration of the emission response was undertaken in order to exploit the system towards application as a pH probe within an aqueous medium.

3.3.6 pH Calibration of [Eu.(122)$_3$]$^{3+}$ in 5% CH_3OH in H_2O

The organic media in which naphthyl-**dpa** systems are most soluble, including **122** and **123**, presented a limitation to the calibration of the luminescence response as a continuous relationship with [H^+]. Therefore, since pH is an aqueous phenomenon, the solubility of **122**, **123**, **[Eu.(122)$_3$]$^{3+}$** and **[Eu.(123)$_3$]$^{3+}$** in aqueous media was investigated; neither the ligands nor the complexes were soluble in neat H_2O. The solubility in mixed solvent systems of CH_3OH and H_2O was investigated in order to find the maximum water content that allowed the formation of a stable solution. Initial attempts with **123** in CH_3OH:H_2O did not produce stable solutions > 50:50 while **122** could be stabilised in mixture of CH_3OH:H_2O (5:95). This was likely due to the increased number of hydrogen bonding interactions available to

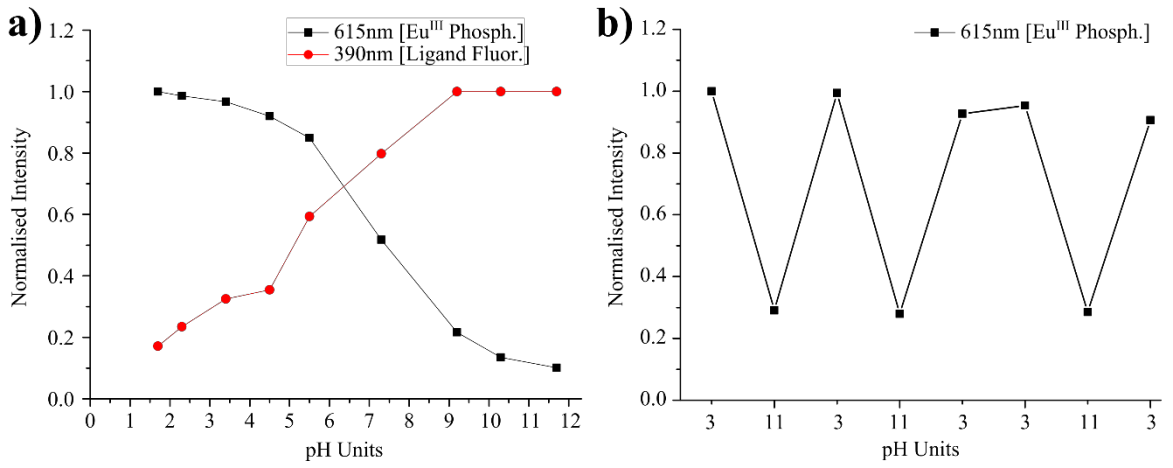

Figure 3.18 a) Normalised pH calibration of the emission intensity of the $^5D_0 \rightarrow {}^7F_2$ at 615 nm and ligand-centred fluorescence at 390 nm from **[Eu.(122)$_3$]**$(CF_3SO_3)_3$ in 5% CH_3OH:H_2O (100 mM NaCl) determined by titration with HCl(aq) and NaOH(aq); and **b)** normalised intensity when switching between pH 3 and pH 11, each sequential measurement was recorded after 10 minutes equilibration

stabilise the complexes in solution. Therefore complex **[Eu.(122)$_3$]$^{3+}$** was selected for investigation as a pH probe in aqueous media.

Complex **[Eu.(122)$_3$]**$(CF_3SO_3)_3$ was prepared at 1×10^{-5} M in 5% CH_3OH in 0.1M aqueous NaCl (to control ionic strength variation). This aqueous media allowed the measurement of pH using an AgCl electrode. The solution was subsequently titrated with $HCl_{(aq)}$ and $NaOH_{(aq)}$ at 24 °C recording the absorbance and luminescence spectra, in addition to luminescence lifetime measurements, at various pH values (between 1 and 12).

In 'neutral' conditions (pH 6-7) both ligand-centred and Eu^{III}-centred luminescence was recorded and pH dependence was observed in the Ln^{III}-centred emission. As the pH was decreased the ligand-centred luminescence was quenched by >80% while the Eu^{III}-centred emission was enhanced by 150%. Conversely, with increasing pH, the Eu^{III}-centred luminescence was 90% quenched while the ligand-centred emission was enhanced. These two continuous relationships are shown in Figure 3.18a. The corresponding fluorescence behaviour (contrary to that expect from classical PET quenching) was likely due to the combined effects of participation of the 4-position –NH. This moiety could potentially interact with the pendent amine through hydrogen bonding interactions under both acidic and basic conditions, contributing to electronic subtleties.[468] Nonetheless, ligand→Eu^{III} energy transfer efficiency increased in acidic media with the emissions being fully switchable and the intensity could be repeatedly switched "on" and "off" between pH 3 and 11, respectively, as shown in Figure 3.18b. Small decreases in the "on" state at pH 3 were observed on repeated switching. However, these tended to recover over time and suggested an equilibrium state was reached rapidly in each case. Complex **[Eu.(122)$_3$]$^{3+}$** was suggested

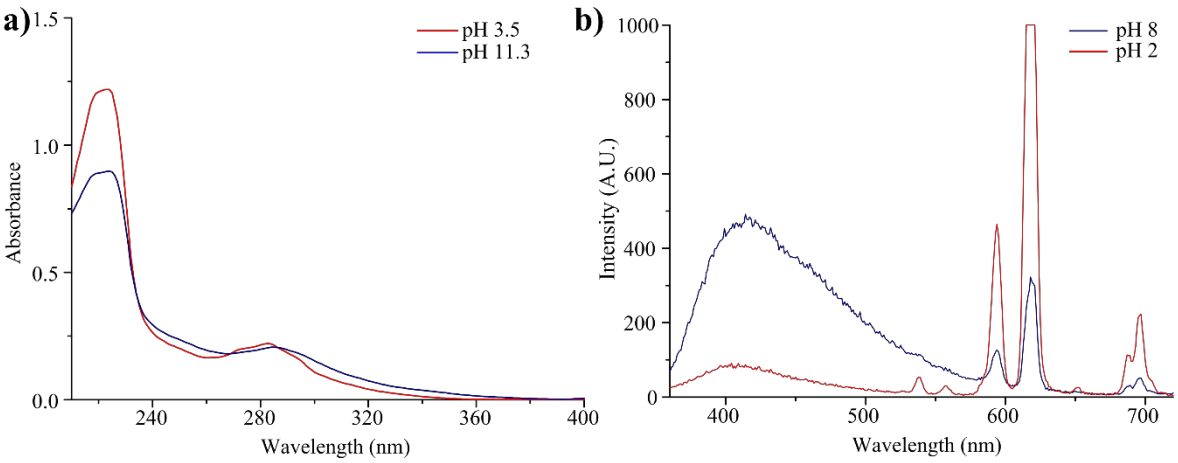

Figure 3.19 a) UV-visible absorbance spectra of **[Eu.(122)$_3$]**$(CF_3SO_3)_3$ 5% CH_3OH in H_2O under acidic (red, pH 3.5) and basic (blue, pH 11) conditions; **b) E**mission spectra of [Eu.(**122**)$_3$]$(CF_3SO_3)_3$ 5% CH_3OH in H_2O in acidic (red, pH 2) and basic (blue, pH 8) conditions. All spectra recorded with c = 1 × 10^{-5} M at 24 °C with 100 mM KCl ionic strength. pH was adjusted using conc. $HCl_{(aq)}$. λ_{exc} = 281 nm.

to remain intact in **ML3** stoichiometry at both extremes of pH. In acidic conditions, the strong Eu^{III}-centred emission indicated the pyridine nitrogen was not protonated and cause dissociation. Furthermore, luminescence lifetime measurements of the Eu^{III}-centred emission were mono-exponential and did not show reduced values (which suggested that **ML3** stoichiometry was maintained despite the strong potential positive charge on the protonated complexes). The UV-visible absorption spectra showed two "states" in acidic and basic conditions, respectively, although the behaviour was not consistent with dissociation processes, Figure 3.19a. Furthermore, the switchable nature of the emission, Figure 3.18b and Figure 3.19b, suggested that in strongly basic conditions there was no dissociation, or formation of $Eu(OH)_3$. These luminescence changes were visible to the 'naked-eye' at concentrations of 1×10^{-5} M suggesting that the probe could be used as a 'litmus-like' probe as well as a calibrated pH sensor. The acid-response of $\mathbf{[Eu.(122)_3]^{3+}}$ is discussed further in Section 3.7.3 below, however the influence of the solvent and PET effects on the ligands and complexes during the Eu^{III}-directed self-assembly was also studied and are discussed in the following sections for CH_3CN and CH_3OH.

3.4 Solution self-assembly studies of 121 – 125 in CH_3CN

The ligand family and respective **ML3** complexes showed interesting sensitivity to the covalent scaffold as well as their environments and a number of these effects were reflected in the study of kinetically-controlled assembly of Eu^{III} complexes. The self-assembly processes were probed through titrations of the ligands with Eu^{III}. These solutions studies (at initial ligand concentrations of $c = 1 \times 10^{-5}$ M= by UV-visible absorption, CD, NMR and emission spectroscopies in both CH_3CN and CH_3OH, are discussed in the following sections. For clarity only the *S,S* enantiomers will be discussed for non-chiroptical techniques; relevant results for the *R,R* ligands are presented in Appendix A3.

3.4.1 UV-visible absorption titrations of the self-assembly of Eu^{III} with ligands 121 - 125 in CH_3CN

The UV-visible absorption spectra, along with the changes observed during the titrations of **124** and **125** with $Eu(CF_3SO_3)_3$ in CH_3CN are shown in Figure 3.20a and Figure 3.20b, respectively. The differences in the structural and intensity of **124** and **125** and their Eu^{III} complexes were described in Section 3.3.5, however similar behaviours in the Eu^{III}-directed self-assembly was observed. At lower wavelengths, the strong absorbance band (λ_{max} = 221 – 224 nm) underwent a hypochromic shift with the first additions of Eu^{III} and the absorbance decreased between 0 → 0.40 equivalents of $Eu(CF_3SO_3)_3$ being added. This was consistent between both ligand types; however, in the case of **123** the overall percentage decrease in

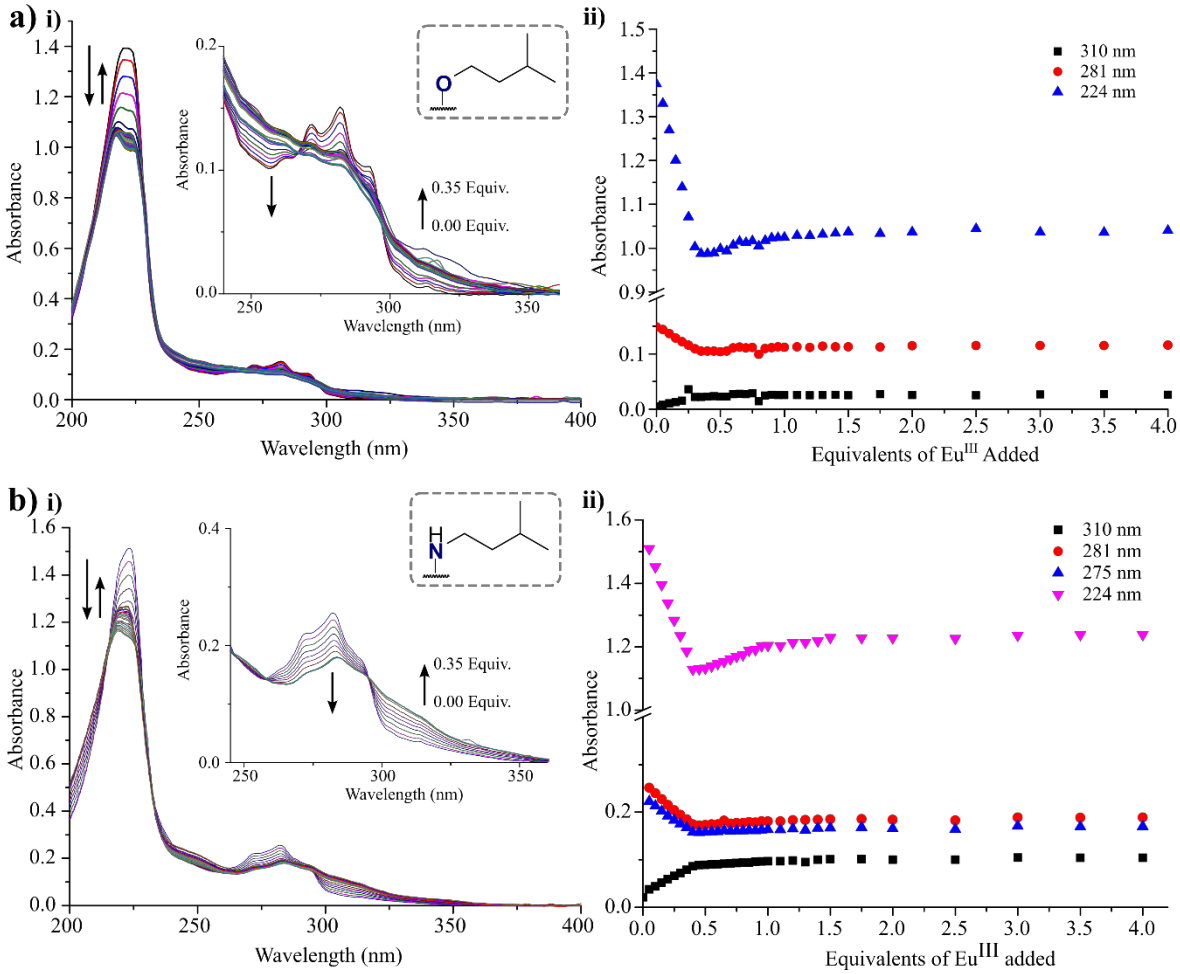

Figure 3.20 UV-visible absorption titrations in CH_3CN of: **a)** ligand **124** with $Eu(CF_3SO_3)_3$, **i)** overlaid spectra between 0.00 → 4.00 equivalents Eu^{III}, ***inset:*** zoomed region on naphthyl π→π* fine structure, **ii)** binding isotherms of key absorbance features λ_{abs} = 310, 281,, 224 nm; and **b)** ligand **125** with $Eu(CF_3SO_3)_3$, **i)** overlaid spectra between 0.00 → 4.00 equivalents Eu^{III}, ***inset:*** zoomed region on naphthyl π→π* fine structure, **ii)** binding isotherms of key absorbance features λ_{abs} = 310, 281, 275, 224 nm. Spectra were recorded at 24 °C from an initial ligand concentration of $c = 1 \times 10^{-5}$ M. This titration is representative of triply reproduced trends.

absorbance was greater. In the case of **121**, the splitting of the single absorbance maxima (λ_{max} = 222 nm) into two bands, centred at 217 and 224 nm was observed, and was in agreement to that previously observed in the thermodynamically synthesised complexes. Similarly, the subtle differences in the electronic nature of the pyridines from *O*- to *N*-linked system were again reflected and for **123** the maxima broadened but the two distinct maxima were not resolved. Simultaneously, hyperchromism was observed between 240 – 260 and 290 – 330 nm while the naphthyl fine structure also showed a hypochromic shift and the absorbance decreased, along with a loss of resolution in the fine structure. Additionally, a number of isosbestic points appeared between the addition of 0.00 → 0.40 equivalents of Eu^{III}, observed at λ_{abs} = 297, 267 and 241 nm for **124** and for **125** at λ_{abs} = 294, 257 and 246 nm. This correlated with the expected π-π stacking of naphthyl and pyridyl aromatic systems,

reduced freedom of the ligand moieties and their potential concomitant coupling interactions (which, as described above, had significant effect on the photophysical properties of the system).

With further additions of Eu^{III} (0.40 → 1.00 equivalents) the changes at λ_{abs} = 224 and 281 nm were reversed. The absorbance at λ_{abs} = 224 nm was recovered (by *ca*. 80%) while the absorbance at wavelengths longer than 300 nm, in each case, had reached a plateau and remained constant. Additional isosbestic points were observed at 231 and 214 nm, along with general hyperchromism at longer wavelengths, indicative of multiple species in solution. These changes would be consistent with the initial formation of a larger stoichiometry assembly (*i.e.* **ML$_3$**) and the changes associated with coordination and π-π

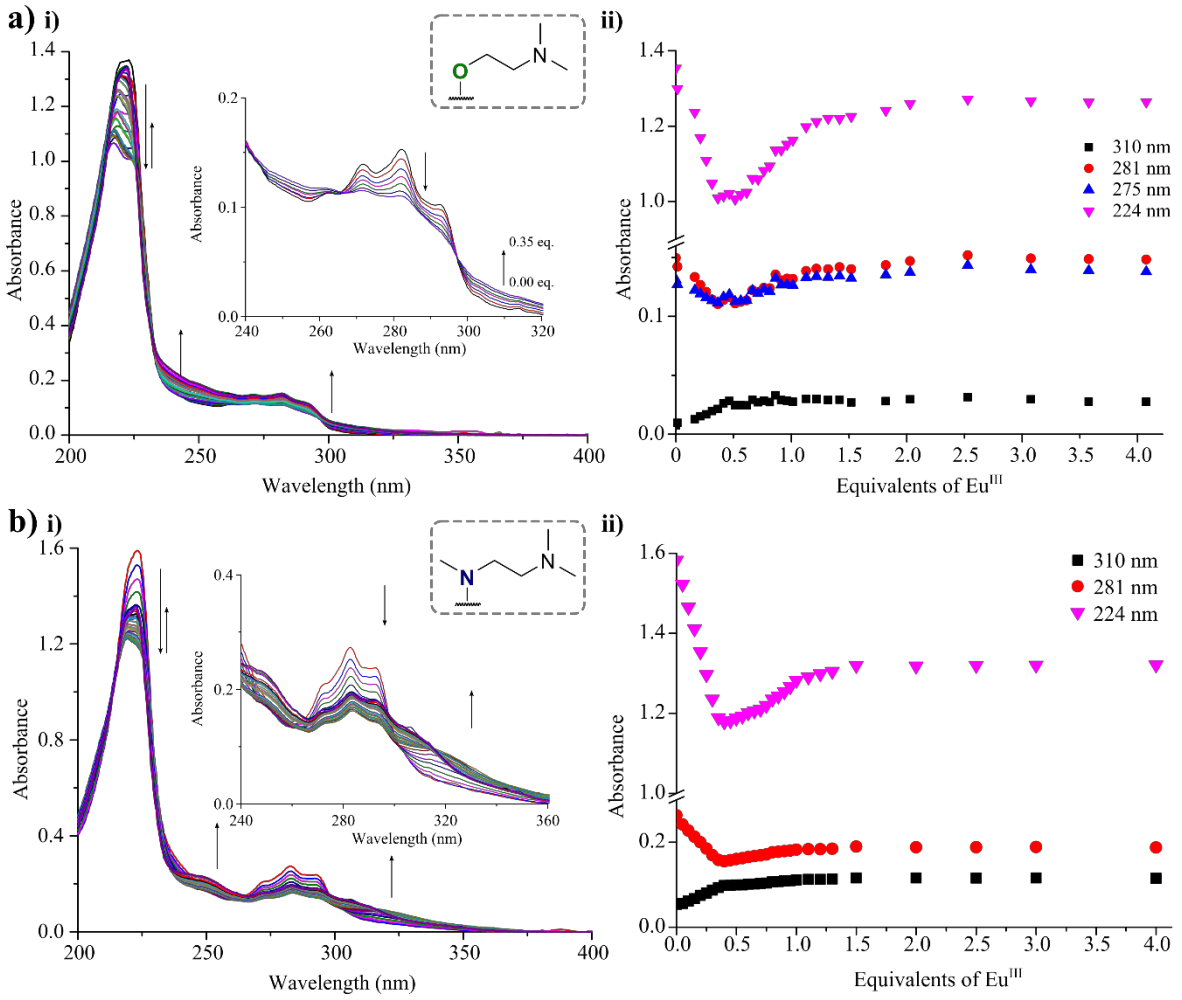

Figure 3.21 UV-visible absorption titrations in CH_3CN of: **a)** ligand **121** with $Eu(CF_3SO_3)_3$, **i)** overlaid spectra between 0.00 → 4.00 equivalents Eu^{III}, ***inset:*** zoomed region on naphthyl π→π* fine structure between 0.00 → 0.35 equivalents Eu^{III}, **ii)** binding isotherms of key absorbance features λ_{abs} = 310, 281, 275, 224 nm; and **b)** ligand **123** with $Eu(CF_3SO_3)_3$, **i)** overlaid spectra between 0.00 → 4.00 equivalents Eu^{III}, ***inset:*** zoomed region on naphthyl π→π* fine structure, **ii)** binding isotherms of key absorbance features λ_{abs} = 310, 281, 224 nm. Spectra were recorded at 24 °C from an initial ligand concentration of $c = 1 \times 10^{-5}$ M. This titration is representative of triply reproduced trends.

stacking. After the addition of 0.40 equivalents of Eu^{III} began to undergo dissociation into **ML$_2$** and **ML** species with fewer π-π interactions. The timeframe of the specific changes throughout the titrations suggested that the lower energy transitions (270 – 310 nm) may mostly reflect the conformational changes while the higher energy transitions (200 – 230 nm) represent more of the changes in complex speciation and inter-ligand chromophore coupling.[458] This behaviour in the absorption properties was familiar from previously reported naphthyl-**dpa** ligand self-assembly.[340,341]

The analogous absorbance spectra and spectral changes from the titrations of **121** (*O*-linked) and **123** (*N*-linked) are shown in Figure 3.21a and Figure 3.21b. The changes on coordination of Eu^{III} were equivalent to those seen with **124** and **125** implying an equivalent self-assembly behaviour and no significant participation of the pendent amine with the spatial assembly of the resulting complexes. However, upon observing both the ligand-fluorescence and Eu^{III}-centred emission during titrations of **121** - **123** differentiation arose between these behaviours and those seen for **124**, **125** as well previously reported naphthyl-**dpa** structures. Metal-centred luminescence was monitored as time-gated emission (rather than on the fluorescence time-scale) and ligand fluorescence was probed where measurable.

3.4.2 Luminescence titrations of the self-assembly of Eu^{III} with ligands 121 - 125 in CH_3CN

The *O*-linked ligand **124** did not show measurable ligand-centred fluorescence under the experimental conditions. However, the Eu^{III}-centred $^5D_0 \rightarrow {}^7F_{1,2,4}$ transitions could be observed weakly at this timescale (see Appendix A3). On the other hand, ligand **125** showed strong ligand-centred emission at λ_{em} = 390 nm, in addition to the metal-centred luminescence. The fluorescence titration of **125** with $Eu(CF_3SO_3)_3$ in CH_3CN is shown in Figure 3.22b.

Upon addition of Eu^{III}, immediate evolution of the Eu^{III}-centred emissions was observed. For **125**, a quenching of ligand-fluorescence also occurred. These changes continued linearly until the addition of 0.35 equivalents of Eu^{III} at which point the fluorescence from **125** was fully quenched and the Eu^{III}-centred emissions reached maximum intensity. The maximum Eu^{III}-centred luminescence at 0.35 equivalents was once again in agreement with formation of **ML$_3$** as the major species, as has been described by previous studies.[340] Subsequently, from 0.35 → 4.00 equivalents of Eu^{III}, the metal-centred luminescence was progressively quenched by *ca.* 25% and 45% for **124** and **125**, respectively; this corresponding to the formation of **ML$_2$** and **ML** (this, however, was better observed in the time-gated emission measurements, Section 3.4.3 below). Overall, these

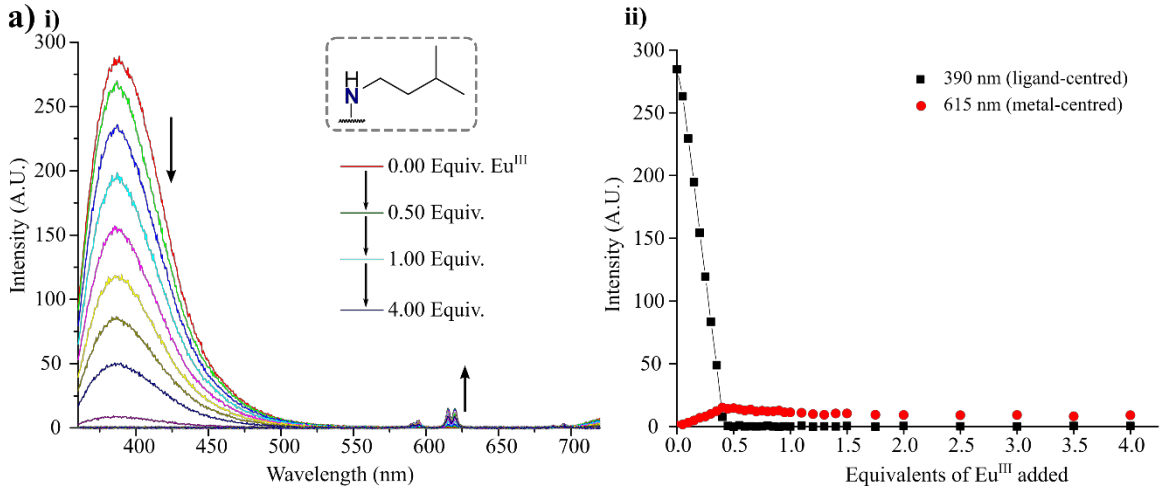

Figure 3.22 Luminescence titrations in CH_3CN of: **a)** ligand **125** with $Eu(CF_3SO_3)_3$, i) overlaid spectra between 0.00 → 4.00 equivalents Eu^{III}, showing ligand and Eu^{III}-centred emissions, ii) binding isotherms of fluorescence intensity of fluorescence at λ_{em} = 390 nm and the Eu^{III}-centred $^5D_0 \rightarrow {}^7F_2$ transition at λ_{em} = 615 nm. Spectra were recorded at 24 °C from initial ligand concentration of $c = 1 \times 10^{-5}$ M. This titration is representative of triply reproduced trends.

changes on Eu^{III}-directed self-assembly were characteristic of the basic scaffold and non-functional derivatives.

In contrast to the above, **121** and **123** showed more complicated behaviour; the fluorescence timescale luminescence spectra for which are shown in Figure 3.23a and Figure 3.23b for **121** and **123**, respectively. Again, the *O*-linked ligand **121** showed no measurable ligand-centred fluorescence and remained non-emissive throughout the titration (although upon sequential additions did give rise to the sensitised Eu^{III}-centred emission). The fluorescence timescale emission was weak and noisy; therefore, this was probed using only the time-gated emission. On the other hand, **123** was fluorescent in CH_3CN solution; however, an uncharacteristic behaviour to that previously seen was observed during the self-assembly process. The overlaid spectra and spectral changes for the self-assembly of **123** with Eu^{III} are shown in Figure 3.23b). Upon the first additions of Eu^{III}, the ligand fluorescence was enhanced, while only a negligible metal-centred emission was observed. An increase in the ligand fluorescence continued to reach a maximum (a two-fold increase) up on the addition of 0.35 equivalents of Eu^{III}. This was followed by a rapid quenching in the fluorescence (fully quenched by 0.40 equivalents and remained quenched for the remainder of the titration), while sensitised Eu^{III} emission rapidly evolved between 0.35 → 1.00 equivalents of Eu^{III}. The maxima for the $^5D_0 \rightarrow {}^7F_J$ transitions was reached at 1.00 equivalents followed by a partial quenching, *ca.* 20%, of the emission upon the addition of excess (1.00 → 4.00 equivalents) Eu^{III}. From these results, it was indicated that there was participation of the pendent amine throughout the titration, influencing the emission

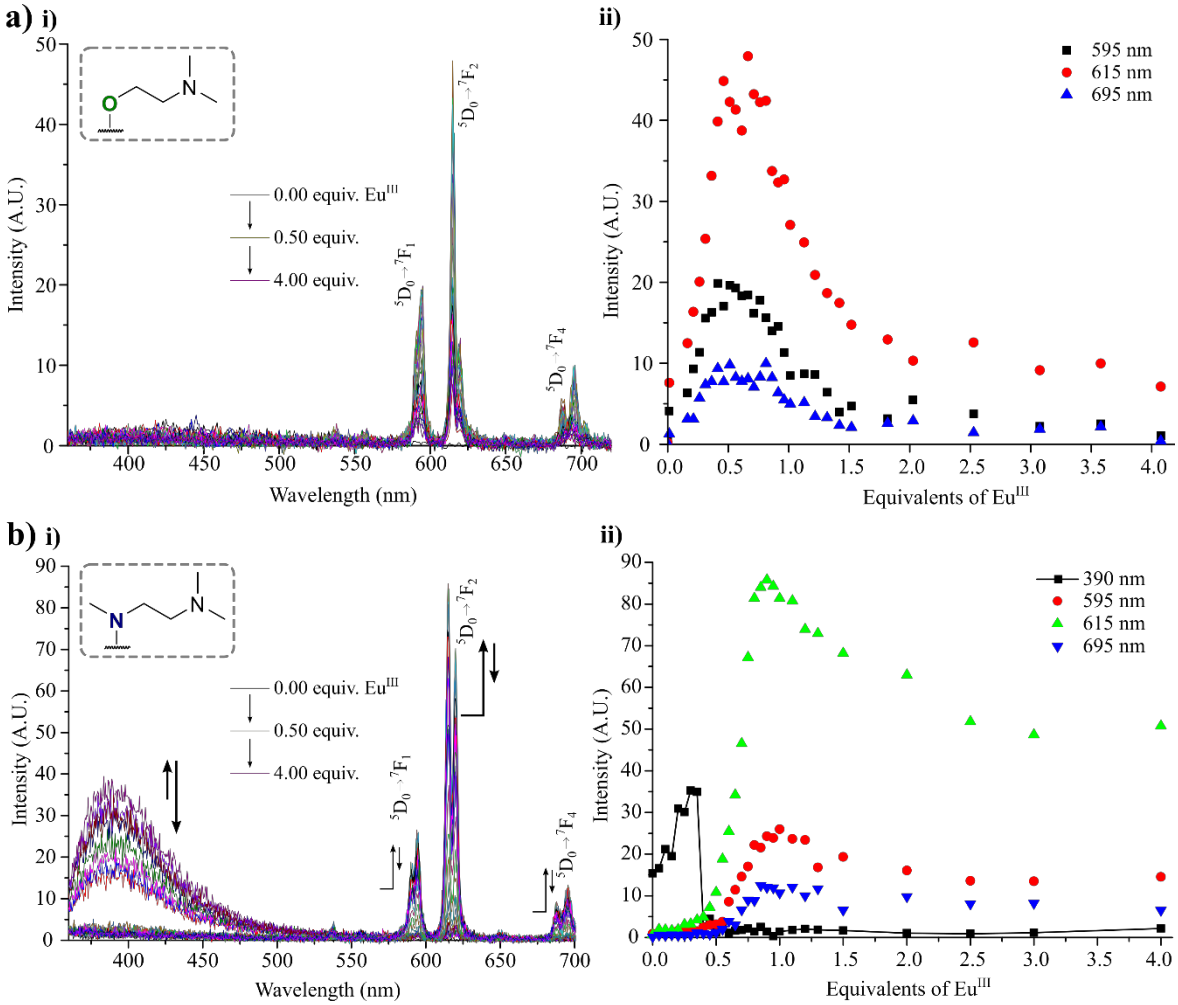

Figure 3.23 Luminescence titrations in CH_3CN of: **a)** ligand **121** with $Eu(CF_3SO_3)_3$, **i)** overlaid spectra between 0.00 → 4.00 equivalents Eu^{III}, showing no ligand and Eu^{III}-centred emissions, **ii)** binding isotherms of fluorescence intensity of Eu^{III} centred emissive transitions at 595, 615 and 695 nm; **b)** ligand **124** with $Eu(CF_3SO_3)_3$, **i)** overlaid spectra between 0.00 → 4.00 equivalents Eu^{III}, showing ligand and Eu^{III}-centred emissions, **ii)** binding isotherms of fluorescence intensity of ligand-cented fluorescence at λ_{em} = 390 nm and the Eu^{III}-centred $^5D_0 \rightarrow {}^7F_{1,2,4}$ transitions at λ_{em} = 595, 615 and 695 nm showing delay Eu^{III} emission onset complimentary to ligand fluorescence. Spectra were recorded at 24 °C from an initial ligand concentration of $c = 1 \times 10^{-5}$ M. This titration is representative of reproduced trends.

properties in both systems. This effect was most significantly in the *N*-linked systems, in agreement with the observed PET activity in the **ML₃** complexes (*c.f.* Section 3.3.5).

To explore this effect further the Eu^{III}-centred emission was measured as time-gated emission, providing improved data quality, and allowing greater analysis of the emission changes throughout the titration.

3.4.3 Time-gated luminescence titration of the self-assembly of Eu^{III} with ligands 121 - 125 in CH_3CN

As expected, no discrepancy was observed between the changes in Eu^{III}-centred emission in fluorescence or time-gated modes. In the case of both **124** and **125**, the metal-centred emission was immediately evolved and reached a maximum Eu^{III} at 0.35 – 0.40 equivalents of Eu^{III} as shown in Figure 3.24a and Figure 3.24b, respectively. This was again in agreement with the formation a major ML_3 species at *ca*. 0.33 equivalents of Eu^{III}. The maximum was followed by steady quenching of the emission with the addition of excess Eu^{III}.

As eluded to in the fluorescence spectra above, **121** and **123** showed modified behaviours. The overlaid spectra for the titrations are shown in Figure 3.25a and Figure 3.25b, respectively. The changes in the Eu^{III} emission spectra recorded for **121** were in

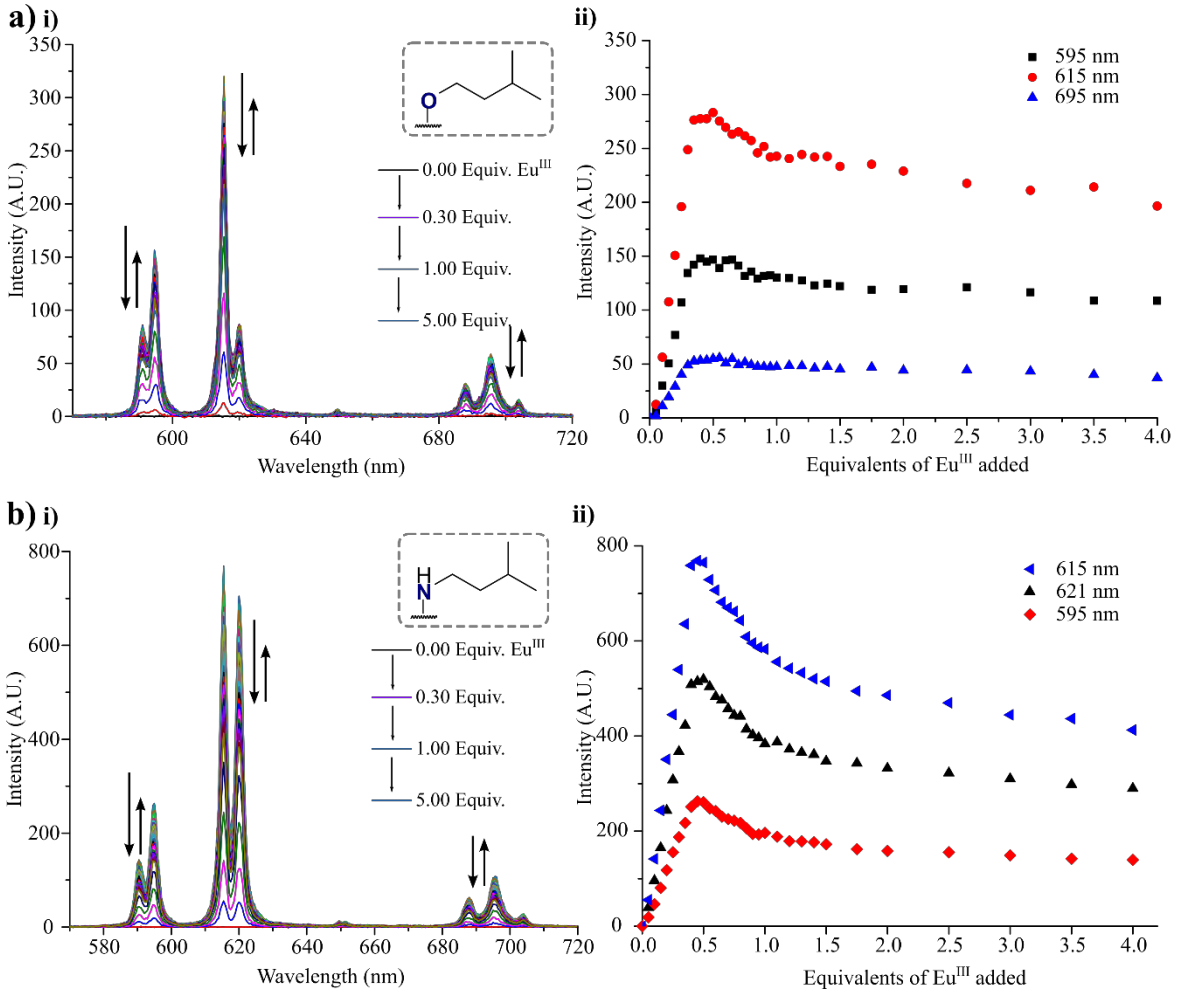

Figure 3.24 Time-gated emission titrations in CH_3CN of: **a)** ligand **124** with $Eu(CF_3SO_3)_3$, **i)** overlaid spectra between 0.00 → 4.00 equivalents Eu^{III}, showing $^5D_0 \rightarrow {}^7F_{1,2,3,4}$ transitions, **ii)** binding isotherms for phosphoresence intensity of $^5D_0 \rightarrow {}^7F_{1,2,4}$ transitions at λ_{em} = 595, 615 and 695 nm showing maximum emission *ca* 0.35 equivalents of Eu^{III}; and **b)** ligand **125** with $Eu(CF_3SO_3)_3$, **i)** overlaid spectra between 0.00 → 4.00 equivalents Eu^{III}, showing Eu^{III}-centred $^5D_0 \rightarrow {}^7F_{1,2,3,4}$ transitions, **ii)** binding isotherms for time-gated emission intensity of $^5D_0 \rightarrow {}^7F_{1,2,4}$ transitions at λ_{em} = 595, 615 and 695 nm. Spectra were recorded at 24 °C from an initial ligand concentration of $c = 1 \times 10^{-5}$ M. This titration is represenrtative of triply reproduced trends.

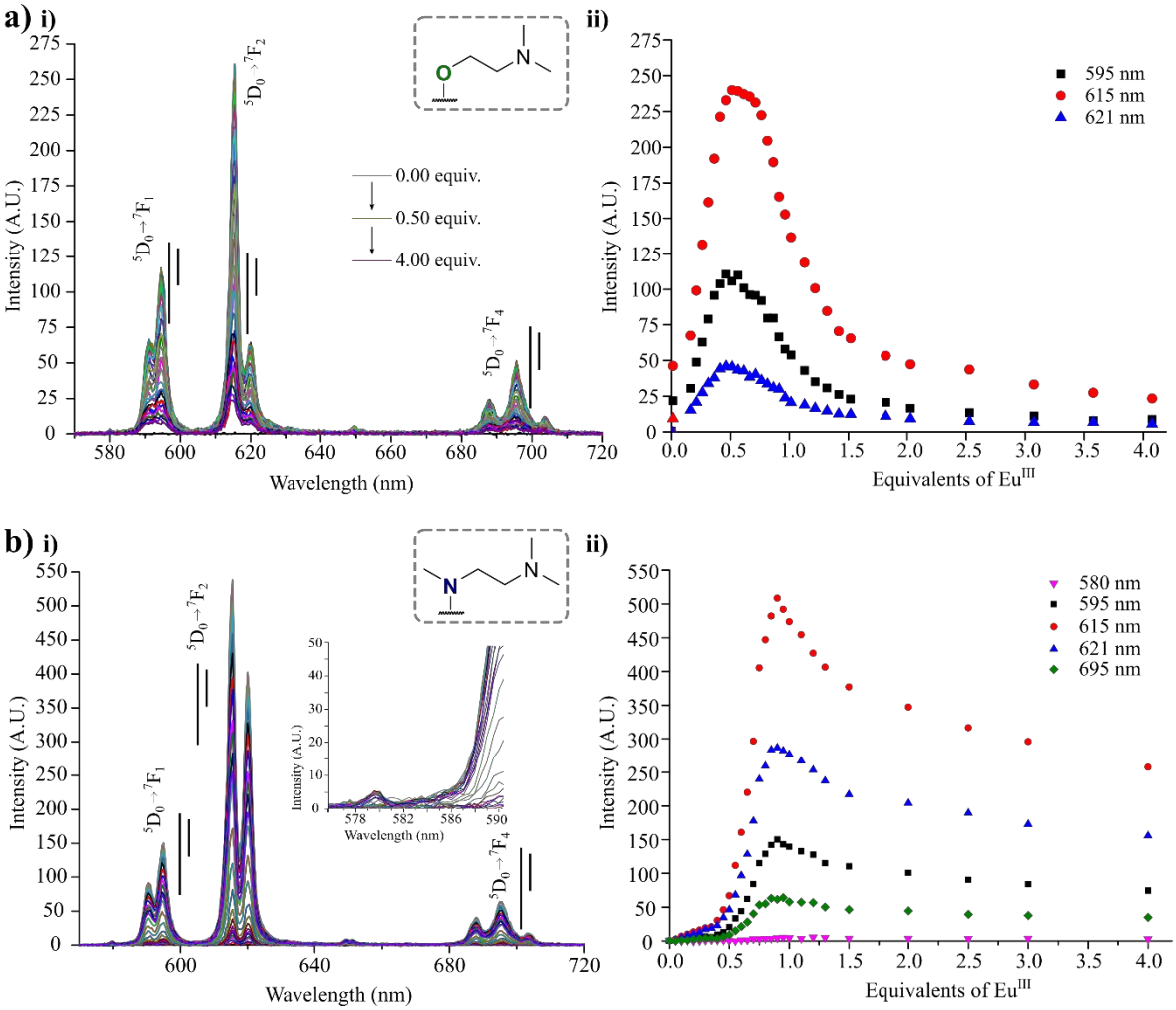

Figure 3.25 Phosphorescence titrations in CH_3CN of: **a)** ligand **121** with $Eu(CF_3SO_3)_3$, **i)** overlaid spectra between 0.00 → 4.00 equivalents Eu^{III}, showing Eu^{III}-centred $^5D_0 \rightarrow {}^7F_{1,2,3,4}$ transitions, **ii)** binding isotherms for phosphoresence intensity of $^5D_0 \rightarrow {}^7F_{1,2,4}$ transitions at λ_{em} = 595, 615 and 695 nm, showing maximum emission *ca* 0.5 equivalents of Eu^{III}; and **b)** ligand **125** with $Eu(CF_3SO_3)_3$, **i)** overlaid spectra between 0.00 → 4.00 equivalents Eu^{III}, showing Eu^{III}-centred $^5D_0 \rightarrow {}^7F_{1,2,3,4}$ transitions, *inset*: zoomed region showing the apperance of $^5D_0 \rightarrow {}^7F_1$ (λ_{em} =580 nm) at 0.50 → 1.00 equivalents of Eu^{III} **ii)** binding isotherms for time-gated emission intensity of $^5D_0 \rightarrow {}^7F_{0,1,2,4}$ transitions at λ_{em} = 580, 595, 615 and 695 nm showing delayed onset of Eu^{III} emission. Spectra were recorded at 24 °C from an initial ligand concentration of $c = 1 \times 10^{-5}$ M. This titration is representative of triply reproduced trends.

agreement to that observed in the fluorescence titration. The Eu^{III}-centred emission immediately evolved over the addition of 0.00 → 0.50 equivalents of Eu^{III} (maximum enhancement) followed by quenching of *ca*. 90% from the addition of 0.50 → 4.00 equivalents of Eu^{III}. This quenching was divided into two different steps. Firstly, immediately after reaching the maximum emission, minor decreases in the emission intensities were observed between 0.50 → 0.80 equivalents of Eu^{III}, Figure 3.25a. This was followed by rapid quenching at up to the addition 0.80 equivalents of Eu^{III}, continuing upon further additions. These regimens corresponded to the evolution of **ML₂** and **ML** species in solution. In the case of **123**, an overall different behaviour was observed. The initial additions

of Eu^{III} (0.00 → 0.35 equivalents) did not give rise to significant evolution of sensitised emission. Upon the addition of *ca*. 0.35 equivalents of Eu^{III}, the metal-centred emission began to enhance, resulting in maximum emission at *ca.* 1.00 equivalents of Eu^{III}. The more intense transitions (and better signal-to-noise resolution of weak signals) seen for **123** provided additional spectral information compared to **121** and the $^5D_0 \rightarrow {}^7F_0$ transition was weakly observed after 0.5 equivalents, Figure 3.25b. These observations were consistent with the UV-visible absorption changes and, despite the emission quenching, supported the formation of $\mathbf{ML_2}$ and **ML** species in solution.

This Eu^{III}-centred emission behaviour was rationalised through the same acid sensitivity and PET mechanisms discussed for the $\mathbf{ML_3}$ complexes (*c.f.* Section 3.3.5). In the saturated $\mathbf{ML_3}$ stoichiometry, the ligands were directed into their closest arrangement and the most significant quenching by PET_{inter} and PET_{intra} processes could be expected. At the initial stages of the titrations, $\mathbf{ML_3}$ is likely to form as the major species, with greatly quenched Eu^{III}-centred emission, with increasing additions of Eu^{III} dissociation into the $\mathbf{ML_2}$ and **ML** complexes occurs with a reduced the number of possible PET pathways (*i.e.* each ligand has one fewer neighbouring donor) and the PET quenching being less effective. Furthermore, a change in π-π stacking was indicated by the changes in UV-visible absorption upon titrations for complexes of ligand **121** - **125**, and it may be expected that the PET acceptor ability of the chromophores was also perturbed.

As a distance-dependent process (with $k_{ET} \alpha r^{-6}$) changes in the speciation and their coordination geometry may also contribute to reduced PET in $\mathbf{ML_2}$ and **ML** species. In unsaturated complexes, greater inter-ligand distances can indeed be expected, Piguet and co-workers have described the metal configurations of related phenyl-**dpa** systems in solution.[394] The solution state structures of the **dpa**-based $\mathbf{ML_2}$ species was shown to be fluxional in the coordination geometry and overall symmetry. An inter-conversion was suggested between D_3 and C_{2h} symmetry for the solution species. The C_{2h} arrangement would place the ligands such that the **dpa** *O-N-O* binding sites are 180° from each other (with solvent or water molecules interacting in about a meridional plane). Consequently, the dissociation equilibria would greatly increase the average PET donor-acceptor distance for PET_{inter} and reduce the overall efficiency of this quenching pathway. Therefore, in the titrations the maximum would not necessarily be observed when $\mathbf{ML_3}$ were formed as the major species in solution but rather at the equilibrium position where Eu^{III} emission was least quenched (*i.e.* a balance between PET and solvent quenching processes). As a result, the maximum emission was not expected to arise at any key ligand:Eu^{III} ratio.

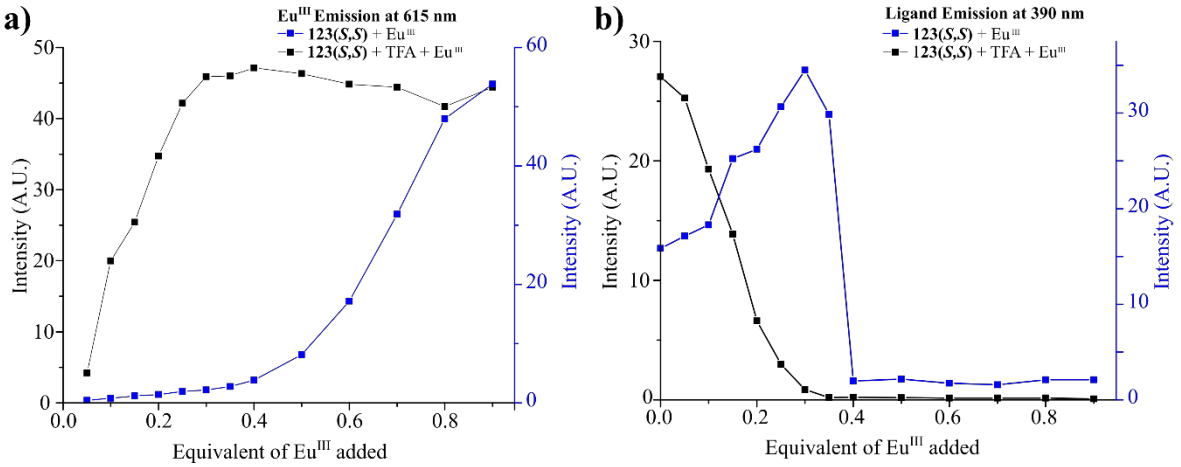

Figure 3.26 a) Emission intensities for Eu^{III}-centred $^5D_0 \rightarrow {}^7F_2$ transition (λ_{em} = 615 nm) during titration of **123** with Eu^{III} in CH_3CN in 'neutral' (blue) and acidic (black) conditions; and **b)** emission intensities for **123**-centred fluorescence (λ_{em} = 390 nm) during the titration of **123** with Eu^{III} in CH_3CN in 'neutral' (blue) and 'acidic' (black) conditions. All spectra were recorded in CH_3CN at 24 °C.

The above was demonstrated further by titration of acidified solutions of **123** (**123-H$^+$**) with $Eu(CF_3SO_3)$ in CH_3CN. The single wavelength isotherms for Eu^{III}-centred emission at 615 nm and ligand fluorescence at 390 nm are shown in Figure 3.26a and Figure 3.26b, respectively. When the ligand was acidified (no active PET) the changes observed were in agreement with those seen for **124** and **125**. The Eu^{III}-centred luminescence reached a maximum at *ca.* 0.35 equivalents of Eu^{III} and the ligand fluorescence was fully quenched also at this point, as can be seen in Figure 3.26; this behaviour was the inverse of that observed under neutral conditions (where PET is active). A consequence of the evident interference of excited-state quenching processes the luminescence titration data was not appropriate for data fitting and analysis of solution speciation or stability constants using the standard methodologies.[413] Therefore, to provide a secondary technique to model the solution behaviour of **121** - **123**, further studies using ground-state absorption spectroscopy were carried out. Both the ligand and **ML$_3$** complex CD spectra were discussed in Sections 3.3.1 and 3.3.2, respectively, and showed large chiral absorption changes between ligand and complex. Taking advantage of these changes, CD titrations were carried out to monitor the coordination process.

3.4.4 Chiroptical titrations of the self-assembly of Eu^{III} with ligands 121 - 125 in CH_3CN using CD spectroscopy

As described in Section 3.3.3, the naphthyl-**dpa** ligands **121** - **125** gave strong CD profiles and those of their respective Eu^{III} complexes were significantly different. As a result, the changes in the CD spectra could be used as an additional technique to assess the self-assembly processes in those cases where the luminescence measurements could not be used

accurately (*i.e.* for **121** - **123**). The CD titrations in CH_3CN for **121(*S*,*S*)** and **123(*S*,*S*)** and their corresponding single wavelength isotherms are shown in Figure 3.27a and in Figure 3.27b, respectively. In fact, ligands **121** - **125** all showed the same behaviour in their CD changes, as was seen previously in the UV-visible absorbance titrations. This again indicating that the pendent amine moieties did not participate in the fundamental assembly formation and did not promote a significant conformational change compared to **124(*S*,*S*)** and **125(*S*,*S*)**.

The changes were monitored across the whole absorbance spectrum and considered both the strong Cotton effect band at λ_{abs} = 224 nm as well as the weaker changes in the

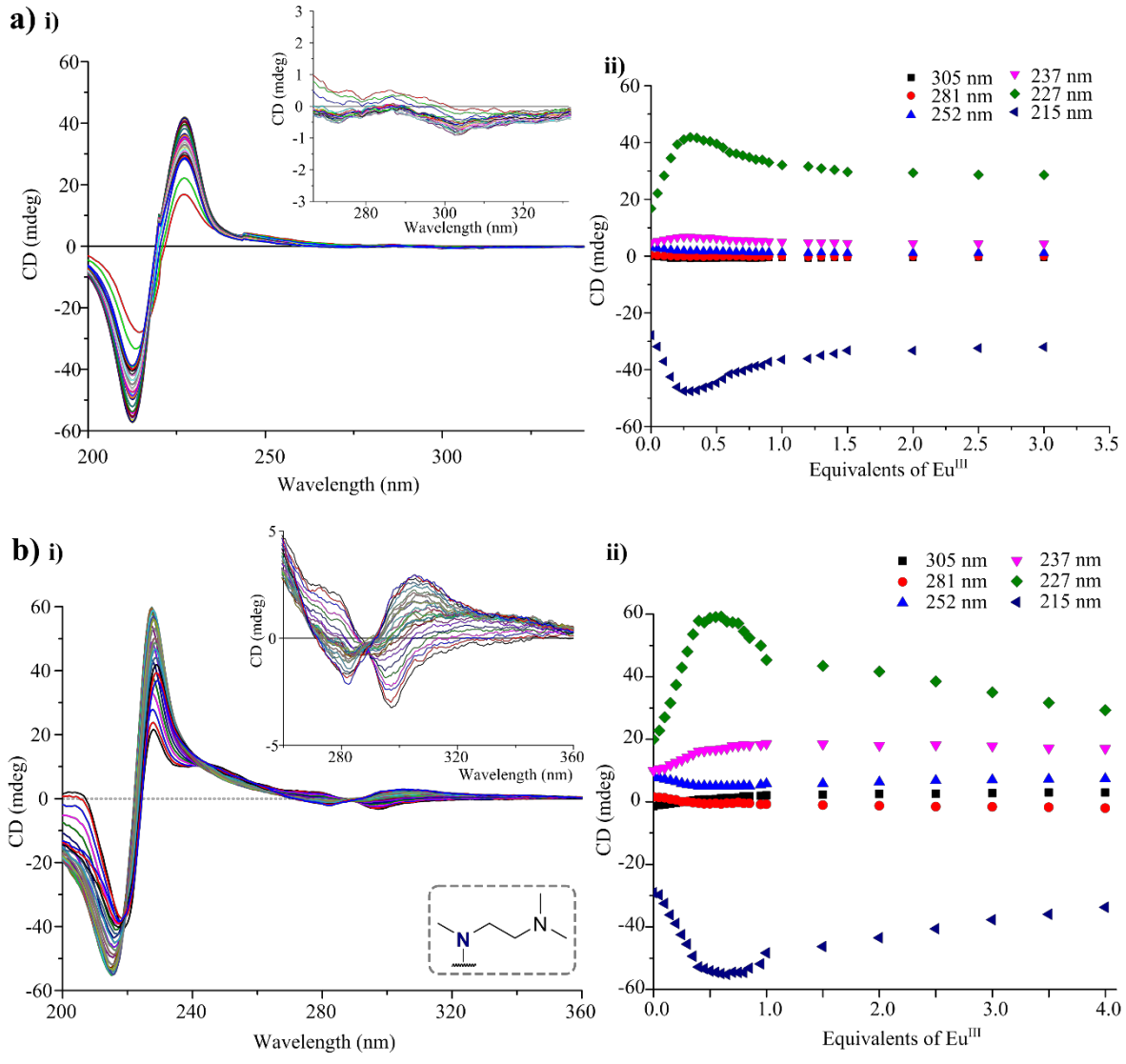

Figure 3.27 CD titrations in CH_3CN of: **a)** ligand **121** with $Eu(CF_3SO_3)_3$, i) overlaid spectra between 0.00 → 4.00 equivalents Eu^{III}, ***inset:*** zoomed region on naphthyl π→π* fine structure, **ii)** binding isotherms of key absorbance features λ_{abs} = 310, 281, 275, 224 nm; and **b)** ligand **123** with $Eu(CF_3SO_3)_3$, i) overlaid spectra between 0.00 → 4.00 equivalents Eu^{III}, ***inset:*** zoomed region on naphthyl π→π* fine structure, ii) binding isotherms of key absorbance features λ_{abs} = 310, 281, 224 nm. Spectra were recorded at 24 °C from an initial ligand concentration of $c = 1 \times 10^{-5}$ M. This titration is representative of triply reproduced trends.

naphthyl π→π* transitions at 270 – 360 nm. Upon addition of Eu^{III}, immediate changes were observed in both absorbance features with greater a sensitivity than the corresponding UV-visible absorption spectra. The two components of the Cotton effect band were enhanced between 0.00 → 0.35 equivalents, with the maxima λ_{abs} = 223 nm blue-shifted by *ca*. 2 nm and consequently increased the Davydov splitting to a total of 9 nm. This was consistent with the formation of **ML3** stoichiometry complexes as characterised from the thermodynamically-synthesised complexes in Section 3.3.2. Concomitantly, there was the reduction in the magnitude of the CD signals at 281 and 297 nm which gave 0 mdeg upon the addition of 0.35 equivalents of Eu^{III}. At the addition of *ca* 0.35 equivalents of Eu^{III} the magnitudes of the signals in the Cotton effect band (223 and 227 nm) reached a plateau, while steady changes continued in the naphthyl π→π* absorbance at longer wavelengths until the addition of 0.80 equivalents Eu^{III}. At this point, the changes ceased while the Cotton effect bands began to change once again, now showing a rapid reduction in absorbance until the addition of 1.00 equivalents of Eu^{III}. This was subsequently followed by steady decreases upon the addition of excess Eu^{III}; a plateau was observed in the longer wavelength absorbance throughout these additions.

Isoelipticity was noted in the comparison of the ligands and their respective **ML3** complexes and these points were observed again during the titrations. Isoeliptic points were observed sequentially throughout the titration between the key stoichiometric equivalences (*i.e.* 0.00 → 0.35 → 0.50 → 1.00 equivalents). The initial large enhancements were in agreement with the formation of **ML3** stoichiometry complexes, and the later changes with the formation of **ML2** and **ML** species in solution following dissociation of **ML3** complexes.

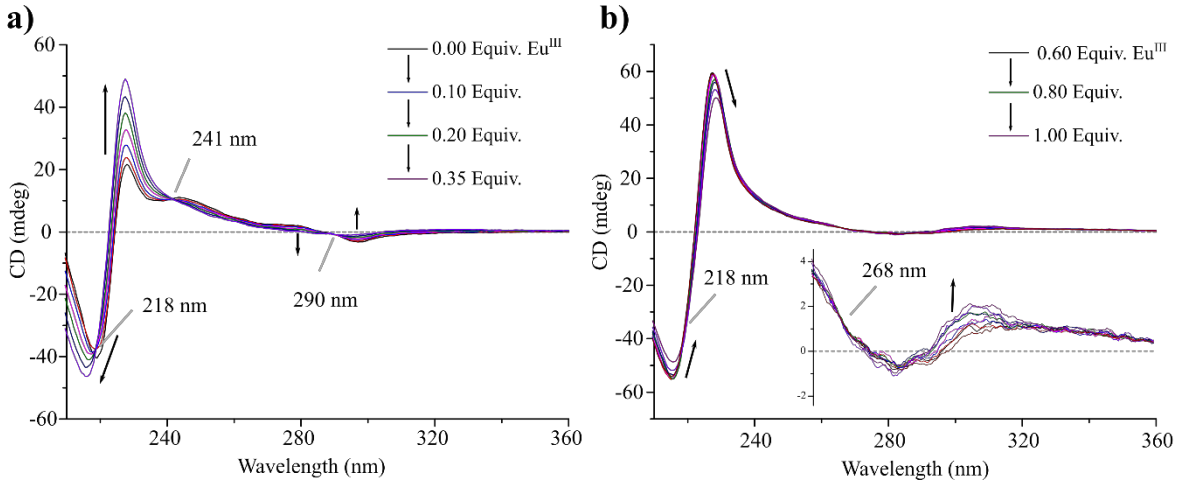

Figure 3.28 Representative plots of the CD titration of **123(*S,S*)** with $Eu(CF_3SO_3)_3$ in CH_3CN, showing isoeliptic points between: **a)** 0.00 → 0.35 equivalents of Eu^{III} at λ_{abs} = 218, 241 and 290 nm; **b)** 0.60 → 1.00 equivalents of Eu^{III} at λ_{abs} = 218 and 267 nm. Spectra were recorded at 24 °C with initial ligand concentration of $c \approx 1 \times 10^{-5}$ M.

In the final stages of the titration, similar isoeliptic points were observed and likely corresponded to the associated disassembly processes resulting in similar correlated species in solution (Appendix A3). The changes in the CD were suitable for modelling and, in fact, the richer spectral information (*e.g.* Davydov splitting, isoeliptic points and general intensity changes) can be particularly useful in elucidating the contribution of the **ML_2** species to the solution equilibrium *vs*. that seen in the luminescence and weak UV-visible absorbance measurements.

The luminescence behaviour was already highlighted as solvent-dependent during photophysical studies of the saturated **ML_3** complexes and the binding efficiency of many systems is often reduced in solvents which compete with the binding site (*e.g.* through hydrogen bonding). Therefore, to determine further the behaviour of naphthyl-**dpa** in CH_3OH compared to CH_3CN, the self-assembly processes were also studied in CH_3OH.

3.5 Solution self-assembly studies of 121 – 125 in CH_3OH

In a similar manner to that described above, self-assembly studies were undertaken in CH_3OH to compare the influence of the more polar solvent on the binding process at the **dpa** site. Different luminescence behaviours were expected as a result of the PET process and the potential influence of hydrogen-bonding solvent interactions with the PET donors. The self-assembly behaviour of **124** could not be reliably reproduced as a result of poorer solubility in CH_3OH and is, thus, not reported. The behaviour of **125** was largely equivalent in both solvents, except for the overall emission intensity (which was quenched appreciably) and, therefore, is not discussed in this section (the corresponding titrations can be found in Appendix A3). Again, the *S,S* configurations of **121** - **123** are discussed below while the results from the *R,R* enantiomers were in agreement and where relevant are presented in Appendix A3.

3.5.1 Absorption titrations (UV-visible and CD) of the self-assembly of Eu^{III} with ligands 121 - 125 in CH_3OH

The overall UV-visible absorption spectra and changes observed for the ligands **121** and **123** with additions of Eu^{III} are shown in Figure 3.29a and Figure 3.29b, respectively. Changes similar to those seen in CH_3CN were observed upon addition of Eu^{III} although in both cases the spectral changes were of much smaller magnitude. The changes were particularly small for the self-assembly of **121**, which had intrinsically lower molar absorption in the region 270 – 320 nm compared to the *N*-linked ligands (Figure 3.5 and Appendix A3).

A similar effect was observed for **120** in H_2O (Chapter 2) with the small spectral changes and, again, likely an effect of the solvent polarity. However, the changes that could

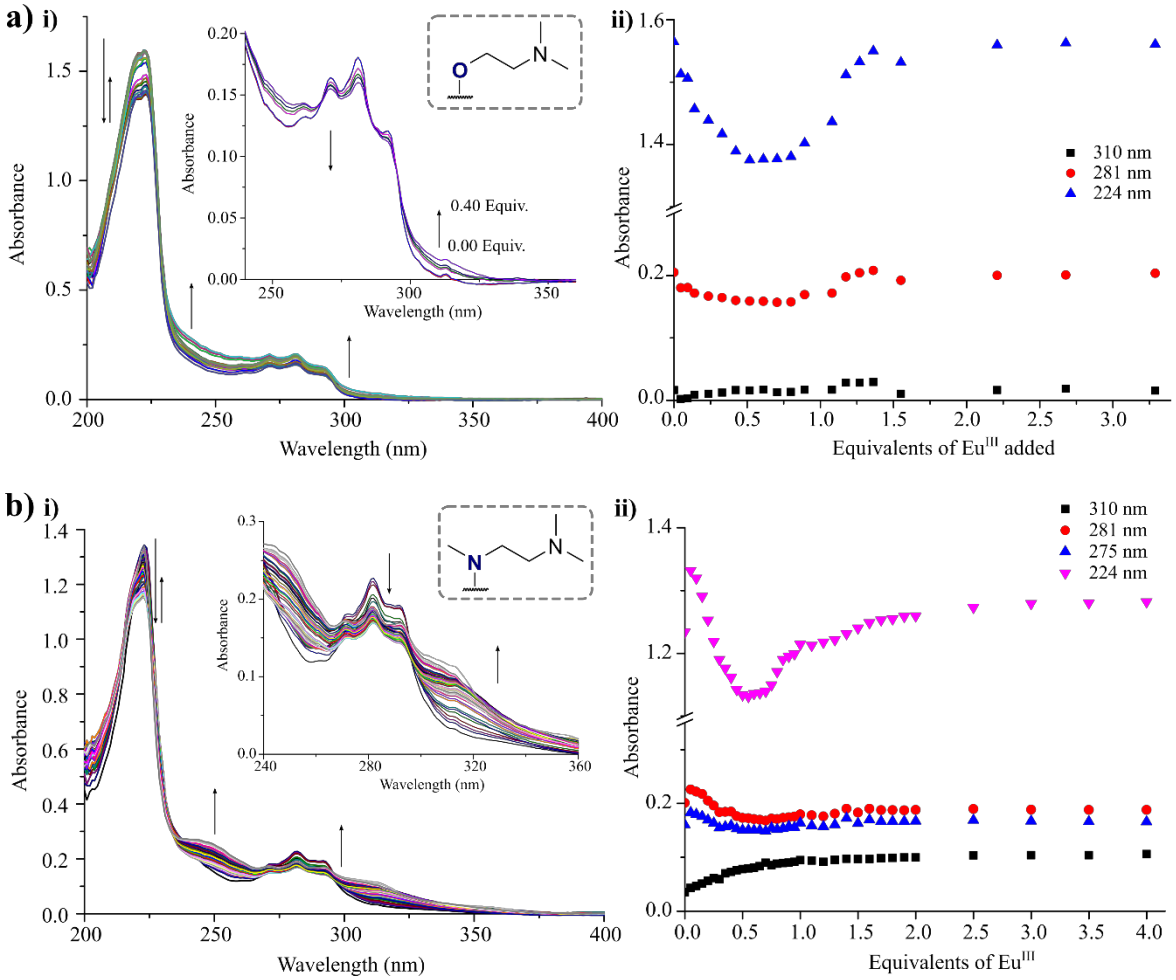

Figure 3.29 UV-visible absorption titrations in CH_3OH of: **a)** ligand **121** with $Eu(CF_3SO_3)_3$, i) overlaid spectra between 0.00 → 3.50 equivalents Eu^{III}, ***inset:*** zoomed region on naphthyl π→π* fine structure, ii) binding isotherms of key absorbance features λ_{abs} = 310, 281 and 224 nm; and **b)** ligand **123** with $Eu(CF_3SO_3)_3$, i) overlaid spectra between 0.00 → 4.00 equivalents Eu^{III}, ***inset:*** zoomed region on naphthyl π→π* fine structure, ii) binding isotherms of key absorbance features λ_{abs} = 310, 281, 275, 224 nm. Spectra were recorded at 24 °C from an initial ligand concentration of $c \approx 1 \times 10^{-5}$ M. This titration is representative of reproduced trends.

be observed were consistent between the *O*- and *N*-linked ligands, showing the changes that usually correspond with the **ML₃ → ML₂ → ML** binding model. Hypochromic shifts of the absorbance feature at λ_{abs} = 224 nm were observed, between 0.00 → 0.50 equivalents, along with hyperchromism at λ_{abs} = 250 and 310 nm. This hyperchromism continued until the addition of 1.00 equivalents of Eu^{III} while the feature at λ_{abs} = 224 nm regained absorption intensity to *ca*. 80% the initial value. In agreement with the changes observed in CH_3CN, a number of isosbestic points occurred during the titrations indicating a various correlated species occurring at different stages throughout the titrations. While the absorbance changes were smaller in CH_3OH compared to CH_3CN, the profile of absorbance maxima remained similar and the isosbestic points were in agreement with those in CH_3CN suggesting similar speciation changes. Isosbestic points were seen at at λ_{abs} = 297, 267 and 241 nm for **121** and

for **123** at λ_{abs} = 294, 257 and 246 nm between 0.00 → 0.40 equivalents of Eu^{III} then at λ_{abs} = 231 and 214 nm along with general hyperchromism between 0.40 → 2.00 equivalents of Eu^{III}.

It has been well established herein that the UV-visible absorption reflected the same binding modes in each case and was in agreement to the previously reported systems. On the other hand, the excited-state processes varied greatly and continued to show unique behaviour both in the fluorescence and time-gated emission properties, which were solvent dependent. Therefore, to support the elucidation of binding models the CD spectra were also probed during titrations **121** - **123** with Eu^{III} in CH_3OH and the representative titrations for

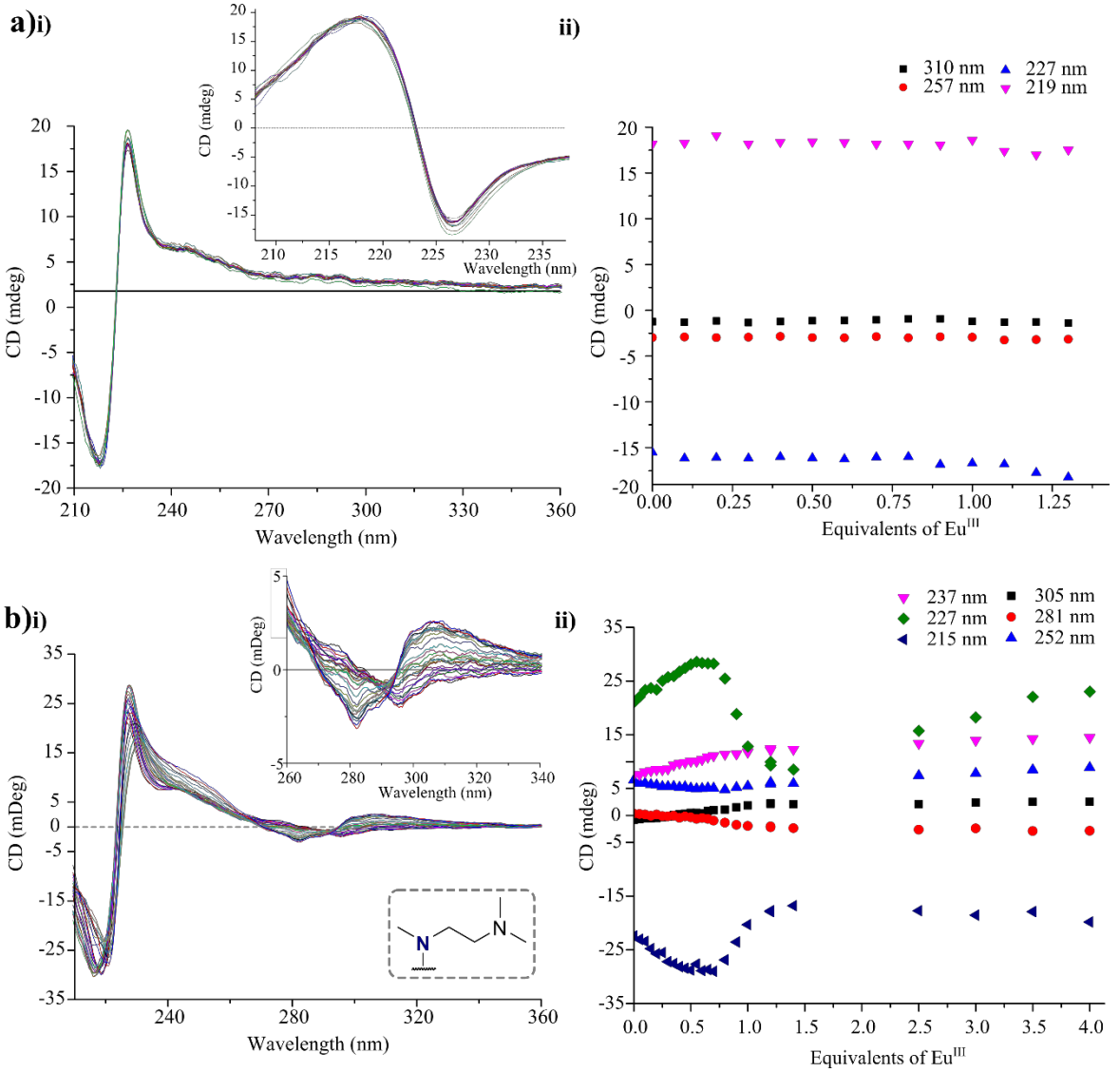

Figure 3.30 CD titrations in CH_3OH of: **a)** ligand **121** with $Eu(CF_3SO_3)_3$, i) overlaid spectra between 0.00 → 4.00 equivalents Eu^{III}, ***inset:*** zoomed region on naphthyl π→π* fine structure, ii) binding isotherms of key absorbance features λ_{abs} = 310, 281, 275, 224, 215 nm; and **b)** ligand **123** with $Eu(CF_3SO_3)_3$, i) overlaid spectra between 0.00 → 4.00 equivalents Eu^{III}, ***inset:*** zoomed region on naphthyl π→π* fine structure, ii) binding isotherms of key absorbance features λ_{abs} = 310, 281, 224, 215 nm. Spectra were recorded at 24 °C from an initial ligand concentration of $c = 1 \times 10^{-5}$ M. This titration is representative of triply reproduced trends.

121(*S,S*) and **123(*S,S*)** are shown in Figure 3.30a and Figure 3.30b, respectively. The behaviour for **123(*S,S*)** was similar to that seen in CH_3CN. However, as was found in the UV-visible absorption, the CD technique was also less sensitive in CH_3OH compared to CH_3CN, and the changes measured for these systems were less substantial in CH_3OH. The self-assembly process could not be measured in the CD changes of **121(*S,S*)** (or **121(*R,R*)**), consistent with the smaller enhancement noted between ligand complex profiles noted above. Nonetheless, the key points of the titrations were in agreement with the classical UV-visible absorption spectra. As can be seen from the single wavelength isotherm plots from UV-visible absorption and CD spectroscopy in Figure 3.29 and Figure 3.30, respectively. These changes varied around and between key points corresponding to the stoichiometries of **ML$_3$**, **ML$_2$** and **ML** at 0.35, 0.50 and 1.00 equivalents, respectively. It was expected that the same assembly processes were occurring in CH_3OH as had been noted in CH_3CN.

3.5.2 Fluorescence titrations of the self-assembly of Eu^{III} with ligands 121 - 125 in CH_3OH

The fluorescence was also monitored during the titration of **121** and **123** with Eu^{III} in CH_3OH and the spectral changes are shown in Figure 3.31a and Figure 3.31b, respectively. Significant differences were seen between **121** and **123,** as well as with their respective behaviours in CH_3CN. For **121**, a weak ligand fluorescence was observed. However, upon addition of Eu^{III} no changes in the intensity were observed, despite the evolution of Eu^{III}-centred emission. The Eu^{III}-centred emission had a delayed onset, similar to that seen for **123** in CH_3CN, at *ca*. 0.5 equivalents of Eu^{III}, metal-centred emission was evolved and enhanced to reach a maximum intensity after the addition of over 1.00 equivalents of Eu^{III}. The behaviour was consistent with the noted increase in PET quenching efficiency of **[Eu.(121)$_3$]$^{3+}$** in CH_3OH (see Section 3.3.5).

A delayed onset and progressive enhancement of Eu^{III}-centred emission during dissociation was likely for the same reasons as presented previously in Section 3.4.3. In the case of **123**, the converse changes in the ligand fluorescence and the Eu^{III}-centred emission to those observed in CH_3CN were observed. Upon addition of Eu^{III}, there was immediate onset of Eu^{III}-centred emission which increased constantly and reached a maximum emission at *ca*. 0.50 equivalents of Eu^{III}. Also, unlike in CH_3CN while the Eu^{III}-centred emission was evolved the ligand fluorescence remained constant. However, at 0.50 equivalents (when Eu^{III}-centred emission started to be quenched) the ligand fluorescence was enhanced. This continued until reaching a maximum emission at *ca*. 1.00 equivalents of Eu^{III} and subsequently quenched again upon the addition of excess Eu^{III}.

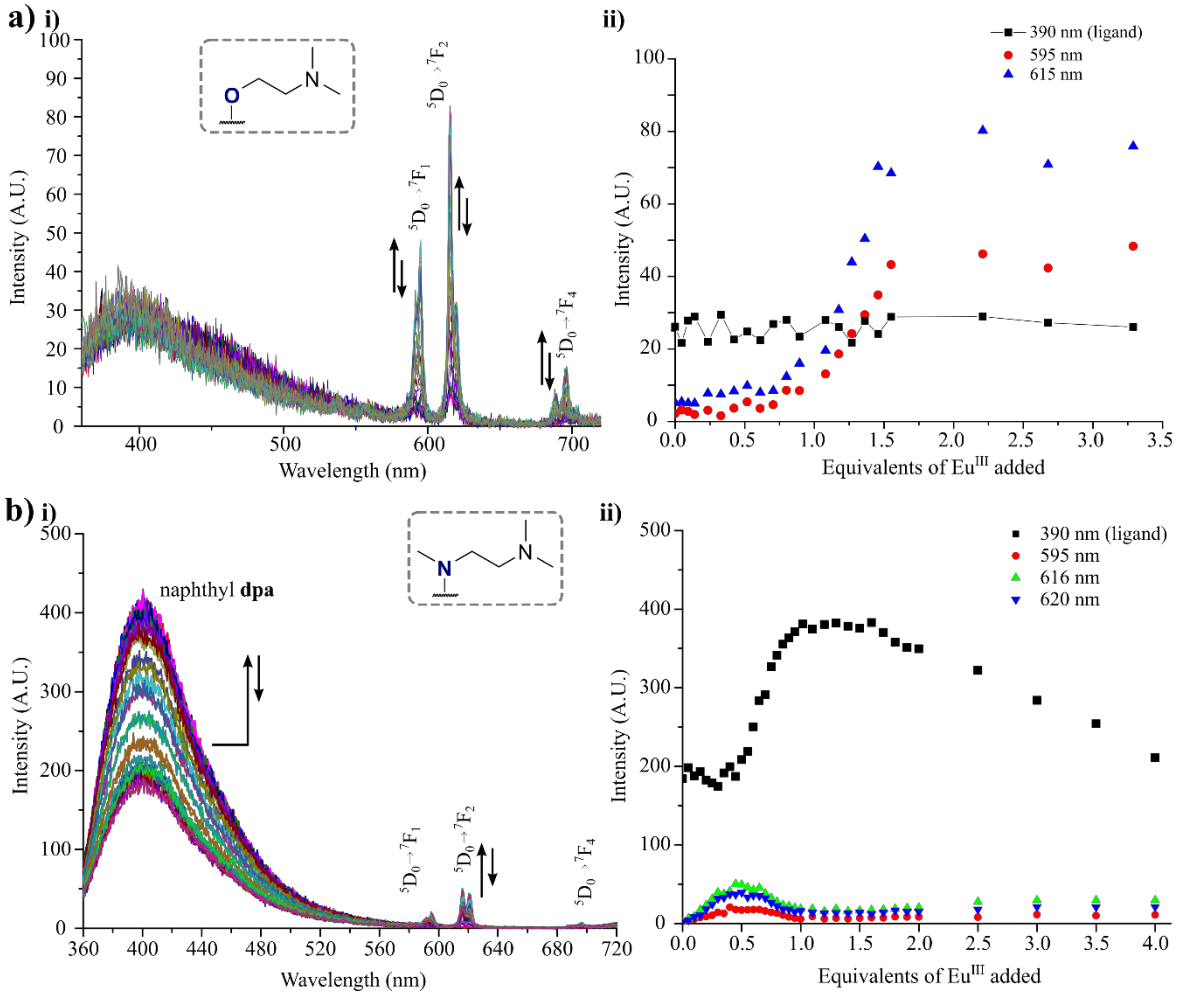

Figure 3.31 Luminescence titrations in CH_3OH of: **a)** ligand **121** with $Eu(CF_3SO_3)_3$, **i)** overlaid spectra between 0.00 → 3.50 equivalents Eu^{III}, **ii)** binding isotherms of fluorescence intensity of ligand- and Eu^{III} -centred emissive transitions at λ_{em} = 390 nm and 595, 615 nm, respectively; **b)** ligand **123** with $Eu(CF_3SO_3)_3$, **i)** overlaid spectra between 0.00 → 4.00 equivalents Eu^{III}, **ii)** binding isotherms of fluorescence intensity of ligand-centred fluorescence at λ_{em} = 390 nm and the Eu^{III}-centred at λ_{em} = 595, 615 and 695 nm. Spectra were recorded at 24 °C from an initial ligand concentration of $c \approx 1 \times 10^{-5}$ M. This titration is representative of reproduced trends.

This suggested that the **ML_2** stoichiometry was less efficiently sensitised in CH_3OH compared to CH_3CN, resulting in the ligand fluorescence becoming favourable deactivation pathway of the ligand-centred excited states.

3.5.3 Time-gated luminescence titration of the self-assembly of Eu^{III} with ligands 121 - 125 in CH_3OH

The changes in Eu^{III}-centred emission showed complementary trends for ligands **121** and **123**, being opposite to those previously described for CH_3CN (Section 3.4.3). Upon addition of Eu^{III} to a solution of **121**, no metal-centred emission was observed between 0.00 → 0.30 equivalents, while a rapid enhancement in the Eu^{III}-centred emission was seen between 0.35 → 1.00 equivalents. This was followed by steady quenching of the emission with the additions of excess Eu^{III} (till 4.00 equivalents). This behaviour was comparable to that observed for **123** with Eu^{III} in CH_3CN. This change in CH_3OH was in agreement that shown

in Section 3.3.5 as **[Eu.(121)$_3$]$^{3+}$** was found to be susceptible to PET in CH_3OH but not in CH_3CN.

The maximum Eu^{III}-centred emission was reached at *ca*. 1.00 equivalents (similar to that seen for **123** in CH_3CN). At excess Eu^{III}, the emission was quenched *ca*. 80%; this indicating the susceptibility of **ML** and **ML$_2$** to solvent quenching.

The titration of **123** with Eu^{III} in CH_3OH was comparable to that of **121** with Eu^{III} in CH_3CN. There was immediate onset of the Eu^{III}-centred emission which reached maximum emission after the addition of *ca*. 0.50 equivalents of Eu^{III}, followed by rapid quenching between 0.50 → 1.00 equivalents. The difference in behaviour suggested reduced PET efficiency in CH_3OH which resulted enhanced emission intensities from the **ML$_3$** and **ML$_2$**

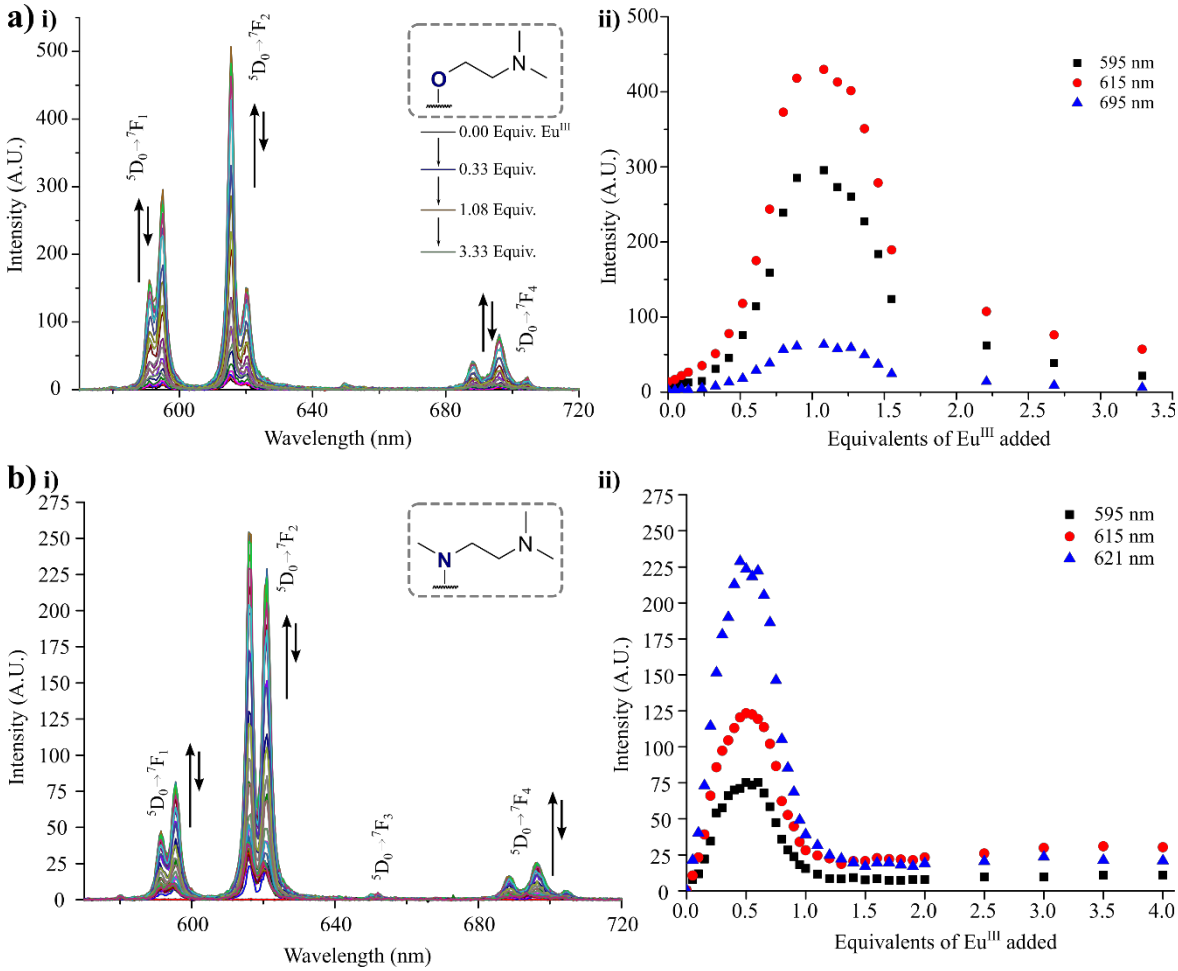

Figure 3.32 Time-gated emission titrations in CH_3OH of: **a)** ligand **121** with $Eu(CF_3SO_3)_3$, i) overlaid spectra between 0.00 → 3.50 equivalents Eu^{III}, showing Eu^{III}-centred $^5D_0 \rightarrow {}^7F_{1,2,3,4}$ transitions, ii) binding isotherms for phosphoresence intensity of $^5D_0 \rightarrow {}^7F_{1,2,4}$ transitions at λ_{em} = 595, 615 and 695 nm showing maximum emission *ca* 0.5 equivalents of Eu^{III}; and **b)** ligand **125** with $Eu(CF_3SO_3)_3$, i) overlaid spectra between 0.00 → 4.00 equivalents Eu^{III}, showing Eu^{III}-centred $^5D_0 \rightarrow {}^7F_{1,2,3,4}$ transitions, ii) binding isotherms for time-gated emission intensity of $^5D_0 \rightarrow {}^7F_{0,1,2,4}$ transitions at λ_{em} = 595, 615 and 695 nm showing delayed onset of Eu^{III} emission. Spectra were recorded at 24 °C from an initial ligand concentration of $c \approx 1 \times 10^{-5}$ M. This titration is representative of reproduced trends.

complexes. As was indicated for **121** with Eu^{III} in CH_3CN, the balance of partial PET and solvent quenching resulted in an arbitrary point of maximum emission due to multiple species in solution. The enhanced quenching upon addition of excess Eu^{III} in the titrations of **123** was consistent with established stronger solvent coupling with CH_3OH. Once again, the changes in the time-gated emission were not suitable for assessing the binding model through standard fitting methods. Therefore, the species in solution and their respectively stabilities were estimated from absorbance data only for ligands **121** - **123** and luminescence considered only for ligands **124** and **125**. The titrations were subsequently analysed by non-linear regression global analysis.

3.6 Fitting self-assembly titration data to determine stability constants for the Eu^{III} complexes of ligands 121 - 125

For ligands **121** - **123**, the various internal quenching processes observed for different stoichiometries did not allow for luminescence data to be modelled. However, the absorption data from both the UV-visible and the CD spectroscopy measurements were analysed using non-linear regression analysis in the same manner as described in Section 2.5. In the cases of **124** and **125** (which did not display the same quenching processes), the Eu^{III}-centred luminescence was used to analyse the solution behaviour using the same models. The same fundamental binding equilibria (as described in Section 2.5.4) were considered as discussed previously and the calculated stability constants are summarised in Table 3.5 below.

The data from the UV-visible absorption and CD titrations were fitted for all the ligands **121** - **125**, while the luminescence was only analysed in the case of **124** and **125**. A representative fit for **123** with Eu^{III} from the absorbance data is shown in Figure 3.33a and the corresponding speciation distribution profile for the **ML**, $\mathbf{ML_2}$ and $\mathbf{ML_3}$ complexes are shown in Figure 3.33b; the speciation diagrams were fundamentally equivalent for the other ligands. The model calculated values closely matching the experimental data across the entire spectrum and particularly for key spectral changes at 224, 281 and 310 nm. The data could only be reliably fitted with the binding model that included complexes of **ML**, $\mathbf{ML_2}$ and $\mathbf{ML_3}$ stoichiometry.

The exclusion of $\mathbf{ML_2}$ species resulted in similar estimated stability constant. However, the isotherm fits poorly described key spectral changes and, in the case of **124** and **125**, the estimated logβ values drifted on iterative fitting introducing larger uncertainties. The speciation diagram indicated that $\mathbf{ML_3}$ were species formed predominantly between 0.00 → 0.35 equivalents (in agreement to the previously reported naphthyl-**dpa** self-assembly.[340,341]) however, only being formed in *ca*. 50 – 60 % yield (compared to 80% in

simpler naphthyl-**dpa** derivatives). This was consistent to the solution behaviour suggested for the SO_3^--derived naphthyl-**dpa 120** described in Chapter 2. After ≈ 0.30 equivalents the proportion of **ML₃** rapidly decreased with the growth of **ML₂** and **ML** species simultaneously with the absorption data suggesting a smaller contribution of **ML₂** compared to **ML** throughout the course of the titrations. Stability constants (logβ) were extracted from the data fitted to these concentration profiles for each of these species giving $\log\beta_{MLn}$ = 7.1±0.1, 13.4±0.1 and 19.5±0.2 for the **[Eu.(123)]$^{3+}$**, **[Eu.(123)$_2$]$^{3+}$** and **[Eu.(123)$_3$]$^{3+}$**, respectively.

These binding constants were equivalent for the entire family of ligands, as can see in Table 3.5, and to those seen for the previous systems (despite the variation in speciation distribution) indicating that substitution of the pyridine 4-position did not improve stability in the *N*-linked ligands, as had been expected. This suggested that the carbonyl units of the *O*-*N*-*O* binding site were most significant in determining the strength of the coordinative interactions and, therefore, electron density at the pyridyl nitrogen could vary without substantial changes in stability. The lower formation of **ML₃** species in the early stages of the titrations was consistent within the ligand family and was suggested to be the result of steric influences of the pendent chains in the kinetically-controlled system. This was in agreement with vicinal perturbation effects suggested from CPL measurements in the **ML₃** complexes (Section 3.3.3). Indeed, the speciation distribution predictions from the absorbance measurements indicated the lesser quenched **ML₂** and **ML** species evolving simultaneously from ≈ 0.40 equivalents of Eu^{III} and **ML** becoming dominant after *ca*. 0.8 →

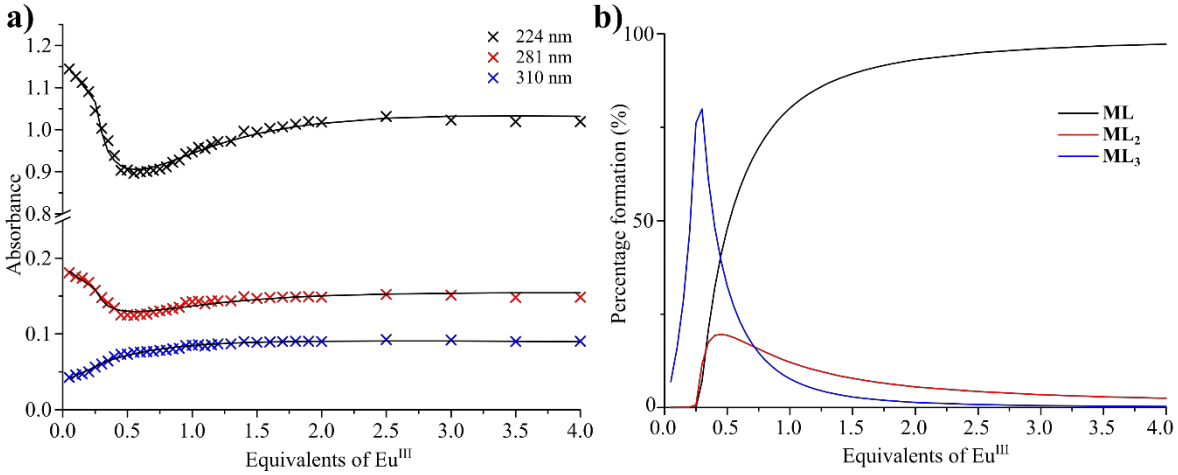

Figure 3.33 Representative fitting outputs from UV-visible absorption titration of **123 (L)** with Eu^{III} in CH_3CN. **a)** Experimental data (points) for various wavelengths and calculated fitting curves (lines); and **b)** calculated speciation distribution diagram showing the formation of **ML₃**, **ML₂** and **ML** species as a function of equivalents of Eu^{III}. This represents one fitted data set from ReactLab EQUILIBRIA®, three coinciding titrations to determine stability constants.

1.00 equivalents, which correlated well with those seen in titrations of the PET active complexes.

Table 3.5 Summarised global stability constant ($\log\beta_{MLn}$) estimated and refined by ReactLab EQUILIBRIA® non-linear global analysis for **121(*S,S*) - 125(*S,S*)** with $Eu(CF_3SO_3)_3$ in CH_3CN and CH_3OH. [Ligand]: $c = 1 \times 10^{-5}$ M. Values and assosicated errors (standard devitations) were determined as the average from independent titratons. [a]changes too small to fit; [b]stable solutions could not be obtained; [c]value fixed.

		$\log\beta_{ML}$		$\log\beta_{ML2}$		$\log\beta_{ML3}$	
		CH_3CN	**CH_3OH**	**CH_3CN**	**CH_3OH**	**CH_3CN**	**CH_3OH**
121	UV	7.1±0.1	-[a]	12.9±0.1	-[a]	19.9±0.1	-[a]
	CD	7.3±0.1	-[a]	13.1±0.1	-[a]	19.5±0.2	-[a]
122	UV	7.2±0.1	7.4±0.1	13.4±0.1	12.6±0.1	19.8±0.2	18.9±0.2
	CD	7.0±0.1	7.6±0.2	14.1±0.1	12.6[c]	19.5±0.1	19.5±0.2
123	UV	7.1±0.1	7.8±0.2	13.4±0.1	12.8±0.1	19.5±0.1	18.9±0.2
	CD	7.1±0.2	8.0±0.1	13.8±0.1	12.8[c]	19.7±0.2	19.5±0.2
124	UV	7.4±0.1	-[b]	14.7±0.1	-[b]	21.0±0.1	-[b]
	Lum.	7.4±0.1	-[b]	14.7±0.1	-[b]	20.4±0.1	-[b]
125	UV	7.3±0.1	7.4±0.1	14.6±0.1	13.4±0.1	20.5±0.1	20.0±0.2
	Lum.	7.1±0.1	7.5±0.1	14.4±0.2	13.4[c]	20.0±0.2	20.3±0.2

The significance of **ML_2** in solution carries most uncertainty as a result of the less clear absorbance changes in the region of 240 – 270 nm and a second technique to support the conclusion was desired. Therefore, the CD titrations were fitted in the same manner which yielded equivalent results, as shown in Figure 3.35. The results supported the formation of **ML_3** complexes dominantly between the additions of 0.00 → 0.35 equivalents of Eu^{III}, after which, the simultaneous formation of **ML_2** and **ML** occurred. Importantly, in the case of the CD titrations, the convergence of the models with experimental data was only achieved in the binding model considering the **ML_2** species. The global stability constants from CD were determined as $\log\beta_{MLn}$= 7.1±0.1, 13.8±0.2 and 19.7±0.2 for the **$[Eu.(123)]^{3+}$**, **$[Eu.(123)_2]^{3+}$** and **$[Eu.(123)_3]^{3+}$**, respectively. This was in agreement with the results from the UV-visible absorption fits. Moreover, the binding constants from CD titrations were also equivalent for ligands **121 - 125** independent of the substitution at the pyridyl 4-position as *O*- or *N*-linked chains. In CH_3OH, the smaller changes in the CD did not significantly improve the ability to assess the solution species quantitative and highlights the limitation to the scope of applying CD measurements.

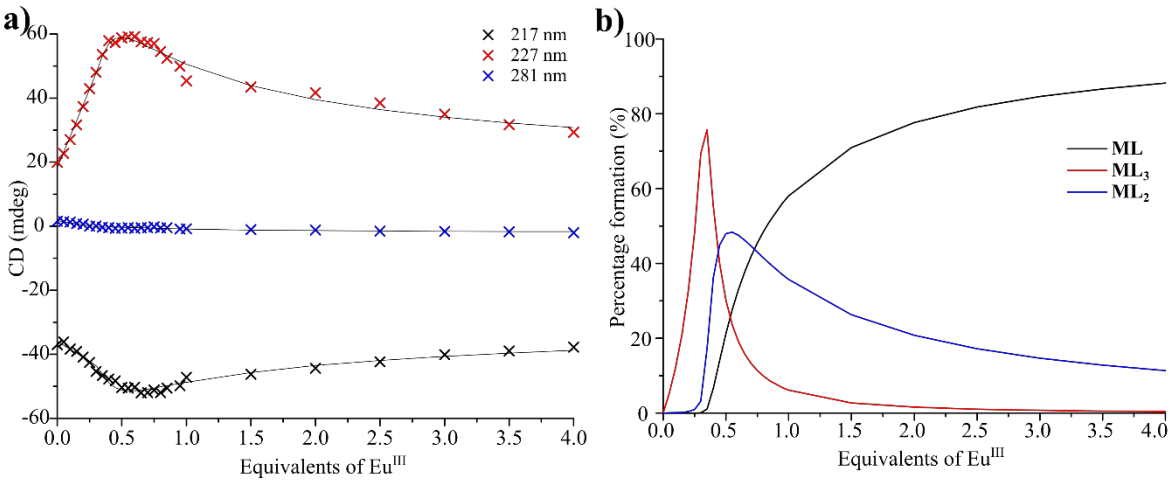

Figure 3.35 Representative fitting outputs from CD titration of **123 (L)** with Eu^{III} in CH_3CN. **a)** Experimental data (points) for various wavelengths and calculated fitting curves (lines); and **b)** calculated speciation distribution diagram showing the formation of $\mathbf{ML_3}$, $\mathbf{ML_2}$ and **ML** species as a function of equivalents of Eu^{III}. Fits were calculated using ReactLab EQUILIBRIA® for global spectral analysis.

The results demonstrated that the $\mathbf{ML_2}$ species formed as an important component to the solution (*i.e.* they did not dissociate instantaneously into the **ML** complexes) during the self-assembly of all the ligands. Additional support for this was available from luminescence titrations of **124** and **125,** since the Eu^{III}-centred emission from these species was not affected by PET quenching. A representative fit for the self-assembly formation of **124** with Eu^{III} is shown in Figure 3.34. As was seen in the analysis of the CD titrations, the luminescence changes could only be modelled considering solution equilibria that consisted of the presence of **ML**, $\mathbf{ML_2}$ and $\mathbf{ML_3}$ complexes which supported the assignment of $\mathbf{ML_2}$. Additionally, the same speciation distributions were determined and similar binding

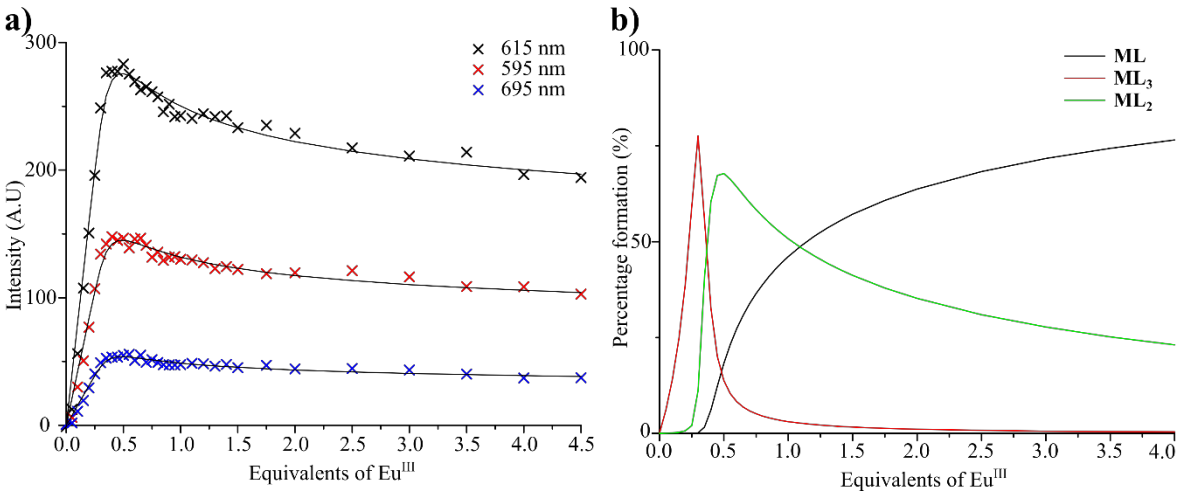

Figure 3.34 Representative fitting outputs from luminescence titrations of **124 (L)** with Eu^{III} in CH_3CN. **a)** Experimental data (points) for various wavelengths and calculated fitting curves (lines); and **b)** calculated speciation distribution diagram showing the formation of $\mathbf{ML_3}$, $\mathbf{ML_2}$ and **ML** species as a function of equivalents of Eu^{III}. Fits were calculated using ReactLab EQUILIBRIA® for global spectral analysis.

constants calculated from the model as $\log\beta_{MLn}$ = 7.1±0.1, 14.4±0.2 and 20.0±0.2 for the **[Eu.(123)]$^{3+}$**, **[Eu.(123)$_2$]$^{3+}$** and **[Eu.(123)$_3$]$^{3+}$**, respectively.

From these results, it can be deduced that the influence of *O*- or *N*-linker was not significant, and the only participation of the pendent moieties was in the possible stabilisation of **ML$_2$** species of Eu^{III} with **124** and **125**. While there were clear solvent effects on excited-state, and consequently the luminescence properties, the effect of solvent on the equilibrium and the estimated stability constants was not substantial with similar constants being determined for each ligand in both CH_3CN and CH_3OH solutions. Having studied the self-assembly behaviour using a series of spectroscopic techniques, the focus was returned to the development of the pH responsive complexes **[Eu.(123)$_3$]$^{3+}$** and **[Eu.(122)$_3$]$^{3+}$** with the aim of incorporating this functionality into soft materials, such as hydrogels.

3.7 Emissive Eu^{III}-luminescent poly(HEMA) hydrogels and responsive pH probes

The acid responsive complex **[Eu.(123)$_3$]$^{3+}$** and pH-calibrated complex **[Eu.(122)$_3$]$^{3+}$** could be effectively used as solution-based probes in organic solution and, indeed, could be considered as a potential route for the development of new, TRD acidity monitors in organic media. However, these probes were directly limited in their application in the common aqueous environment due to their inadequate solubility. In order to address this limitation a soft materials approach was considered to bring a Eu^{III}-luminescent response to pH into fully aqueous media.

As briefly discussed in Chapter 1, poly(HEMA) matrices swell in H_2O as a hydrogel and shows large internal water volumes (*ca*. 80%) on equilibration with an external aqueous environment.[469] If co-polymerised with ethyleneglycol dimethacrylate (EGDMA) the resulting polymer gel materials are covalently cross-linked and further endowed with an internal porous structure. These Rehahn-type III polymer gels (Section 1.7) allow for the non-covalent encapsulation of materials within a bulk polymer material that behave as though in solution and interact with their environment within the pores. This porosity also allows for potential size exclusion, encapsulation or selective equilibration of the interior and exterior environments of the bulk polymer hydrogel material.[470] In poly(HEMA-*co*-EGDMA) materials, species with molecular weights larger than 700 g mol^{-1} are often excluded from diffusion and isolated within the materials, while smaller molecules and solvent may equilibrate.[471,472]

During preparation of this thesis, it was shown in collaboration with Dr. Esther Surender (School of Chemistry, Trinity College Dublin), that a water-soluble *cyclen*

complex could be non-covalently incorporated into a poly(HEMA) hydrogel matrix for the detection of urease activity in the onset of bacterial infection in urinary catheters (see Appendix A6 - Publications).[473] This example utilised a methodology reported by McCoy and Gunnlaugsson[358] and which is developed more extensively herein.

The inclusion of water-soluble materials was established previously. However, it was proposed that the internal microenvironment of the polymer hydrogel could facilitate the solubilisation of compounds and complexes of partial aqueous solubility (or, indeed, water insoluble materials) inside the matrix. Therefore, materials were prepared from HEMA and EGDMA containing **[Eu.(122)$_3$]**$(CF_3SO_3)_3$ and **[Eu.(123)$_3$]**$(CF_3SO_3)_3$ as a responsive probe and unresponsive complex with partial to no solubility in aqueous media, respectively.

3.7.1 Synthesis and characterisation of [Eu.(122)$_3$]$^{3+}$@p(HEMA-*co*-EGDMA)

The polymer materials were doped with **[Eu.(122)$_3$]**$(CF_3SO_3)_3$ directly during the polymerisation process as described in Scheme 3.3. Complex **[Eu.(122)$_3$]**$(CF_3SO_3)_3$ and AIBN were dissolved into HEMA, containing 1 wt% ethylene glycol dimethacrylate (EGDMA) as cross-linker and stirred until the complexes had fully dissolved. After complete dissolution, the homogenous solutions were then transferred to glass moulds (see Appendix A3) that were lined with a non-stick PE-based coating (Siliconised PE, Lintec Graphic Films) and heated to 90 °C and cured for 6 hours in an oven. The solutions solidified to give hard, p(HEMA) monoliths which were allowed to cool substantially below the glass transition temperature (T_g, *ca.* 85 – 90 °C for p(HEMA) homo-polymers)[474,475] before removing the cast monoliths from the mould. The monoliths were hard, brittle and transparent, as shown in Figure 3.36. The monoliths were soaked in deionised water and swelled as expected to afford soft, flexible polymer gels, as shown in Figure 3.36a)ii). The hydrogels were conditioned further by soaking in H_2O to remove unreacted monomers and residual inhibitor from the interior.

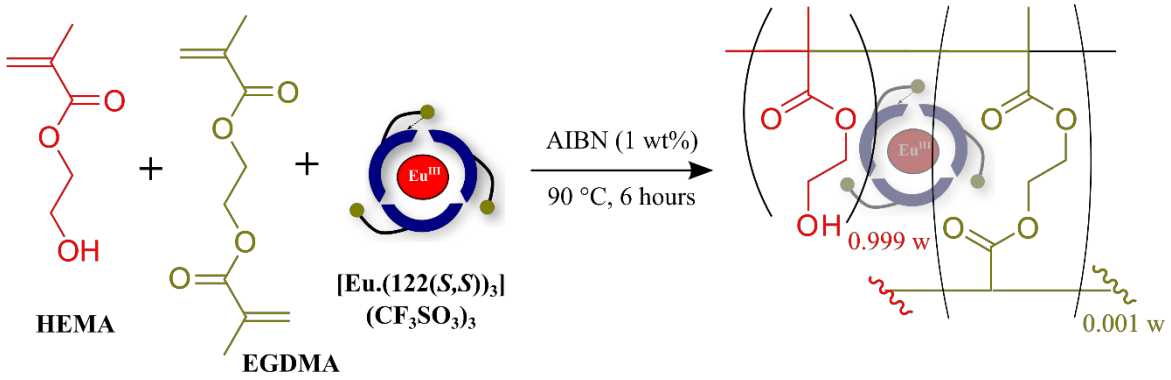

Scheme 3.3 Schematic representation of the synthesis of **[Eu.(122)$_3$]$^{3+}$@p(HEMA-*co*-EGDMA)** with the complex being non-covalently (@) incorportated in the random copolymer.

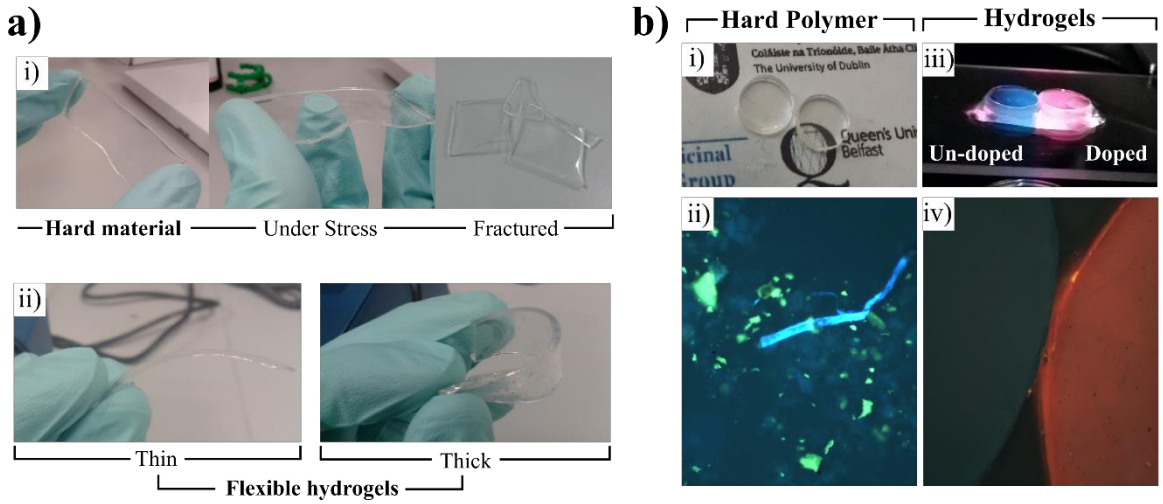

Figure 3.36 a) i) Photographs of *top:* hard brittle monoliths of **[Eu.(122)3]$^{3+}$@p(HEMA-*co*-EGDMA)** polymers shattering under stress, ii) swelled poylmer gels after 200 minutes equilibration in deionised H_2O showing flexible films derived from both thin and thick monoliths; and **b)** optical and fluorescence microscope images showing: **i)** die-cut hard polymer samples under amibent conditions, ii) filtered fluoresecence micrograph of doped p(HEMA-*co*-EGDMA) showing encapsulated solid clusters, iii) undoped and doped p(HEMA-*co*-EGDMA) swelled in H_2O under λ_{exc} = 254 nm, showing red emission to the 'naked eye' from the doped sample, and iv) fluorescence micrograph of p(HEMA-*co*-EGDMA) and**[Eu.(122)3]$^{3+}$@p(HEMA-*co*-EGDMA)** showing uniform red Eu^{III}-centred emisson from the internal solution of the doped polymer gel.

The inclusion of the complexes within the materials was confirmed by optical and fluorescence microscopy. Inspection of the materials under magnification showed the solid material embedded within the hard polymers, Figure 3.36b)ii), as small clusters of white solid which upon irradiation with UV light (λ_{exc} = 254 nm) was red emissive as expected from the Eu^{III} complexes. A relatively homogenous distribution of the embedded complexes in combination with the optical properties of the p(HEMA) resulted in uniform emission to the eye across the materials, as shown in Figure 3.36b. After swelling of the hydrogels the fluorescence microscopy showed the diffusion of the solid clusters to be a uniform encapsulated solution within the polymer matrix, Figure 3.36b; further quantitative photophysical analysis is discussed in Section 3.7.2 below.

A general mechanical analysis was made of the hard polymers and polymer hydrogels to determine whether the doping of the p(HEMA) with **[Eu.(122)$_3$]$^{3+}$** resulted in physical changes to the bulk material. The dry polymer was studied through dynamic scanning calorimetry (DSC) to determine the T_g and any phase-change behaviour of the doped polymers. The material was heated in cycles from -25 to 150 °C and, as shown in Figure 3.37a, the DSC demonstrated a single gel transition which was stable on cycling. For the doped p(HEMA) a T_g was determined at 87.5 ± 0.3 °C which was in agreement with neat 1% EGDMA cross-linked p(HEMA)[475] and, in general, the behaviour of the materials were equivalent to the neat materials. Similarly, the compressive modulus of the swelled hydrogel

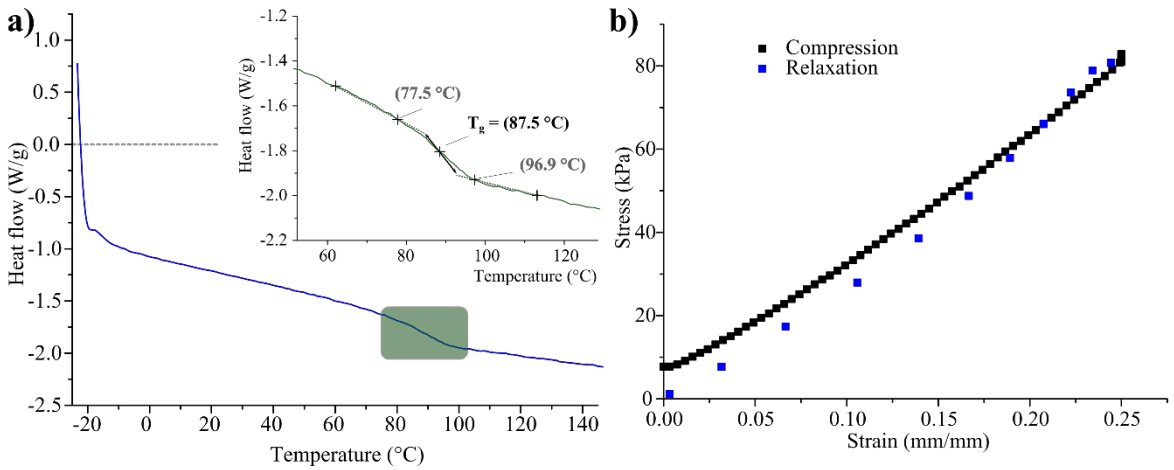

Figure 3.37 a) DSC heating cycle between -25 and +150 °C for **[Eu.(122)3]$^{3+}$@p(HEMA-*co*-EGDMA)** showing a single phase transition *ca*. 80 – 100 °C, ***inset:*** zoom region of glass transition and derivation of the T_g at 87.5 ± 0.3 °C. Tg was calculated by fitting the data using TA Universal Analysis®; and **b)** representative stress/strain plot for **[Eu.(122)3]$^{3+}$@p(HEMA-*co*-EGDMA)** under compressive strain (black) and relaxation (blue), the linear region between 0.05 mm/mm and 0.20 mm/mm was fitted to determine the modulus.

was measured, the data for which is shown in Figure 3.37b. Samples were die-cut as cylindrical (Ø = 5 mm, height = 1.2 mm) or cuboidal (10 mm x 10 mm x 1.2 mm) from swelled polymer gels (so that force was applied from a constant area in each measurement) and the samples were compressed by 25 % and the stress response force measured.

The modulus corresponded to the gradient of the linear region of the experimental stress/strain curve for the compression test. The average modulus was then calculated as the average of twelve replicate experiments and determined to be 309 ± 2 kPa which was again in close agreement to the un-doped materials.[475] As expected, the dopant complexes did not interact with the polymer matrix substantially to influence the physical behaviour of the polymer and the mechanical features of the doped p(HEMA) was predictable from the model materials. The fluorescence microscopy clearly showed the luminescence characteristics of the polymers and polymer-gels formed, therefore, spectroscopic characterisation of these photophysical properties was undertaken.

3.7.2 Photophysical characterisation of [Eu.(122)$_3$]$^{3+}$@p(HEMA-*co*-EGDMA) as hard polymers and soft polymer gels

The p(HEMA) matrix was absorbing at wavelengths shorter than 250 nm and therefore UV-visible absorbance measurements did not provide strong characterisation. However, the fine structural features of the naphthyl π→π* transitions were visible, as shown in Figure 3.38a. The ligand- and Eu^{III}-centred luminescence was recorded from the hard polymers, as shown in Figure 3.38b. These showed strong luminescence of substantially larger intensity than observed for the complexes in solution. Simultaneous ligand and Eu^{III}-centred luminescence was observed in agreement with the solution studies and both emissions contributed to the

colour perceived to the eye. This was consistent with the observations of others for intensity and quantum yield enhancements within polymer matrices (see Section 1.7.1). The ligand-fluorescence maximum was in agreement with that observed in CH_3OH (λ_{em} = 390 nm) and suggested that the encapsulation resulted in an environment of similar polarity allowing for responses similar to those observed in CH_3OH from fully aqueous solutions.

The structure of, and ratios between, the Eu^{III}-centred transitions in the emission spectra agreed with that observed in the solution-state. While the ratio between $^5D_0 \rightarrow {}^7F_1$ and $^5D_0 \rightarrow {}^7F_2$ were equivalent throughout the swelling process, the band shape of $^5D_0 \rightarrow {}^7F_2$ was, in fact, informative of the environmental change. The ratio of intensity in the sub-components in this band was consistent throughout with the fingerprint of *N*-substitution of the pyridine core discussed in Section 3.3.2 above. The luminescence lifetimes of Eu^{III}-centred emission were fitted to a mono-exponential decay and determined as τ_{em} = 1.38 ms and 1.45 ms in the hard and soft materials, respectively. This lifetime was constant when measured across the material which indicated a homogenous distribution of a single, strongly luminescent species within the gel. However, as shown in Figure 3.39b, the emission intensity at 617 nm decreased as the polymer gels hydrated (improving resolution of the two m*j* maxima) and that at 621 nm was enhanced.

After complete swelling (after 150 minutes) the spectral structure had stabilised. The changes in the structure of the $^5D_0 \rightarrow {}^7F_2$ transition throughout the swelling was accounted for due to the hypersensitivity to environment associated with the transition and expected variation in polymer interactions and solvent effects until equilibrium swelling was reached.

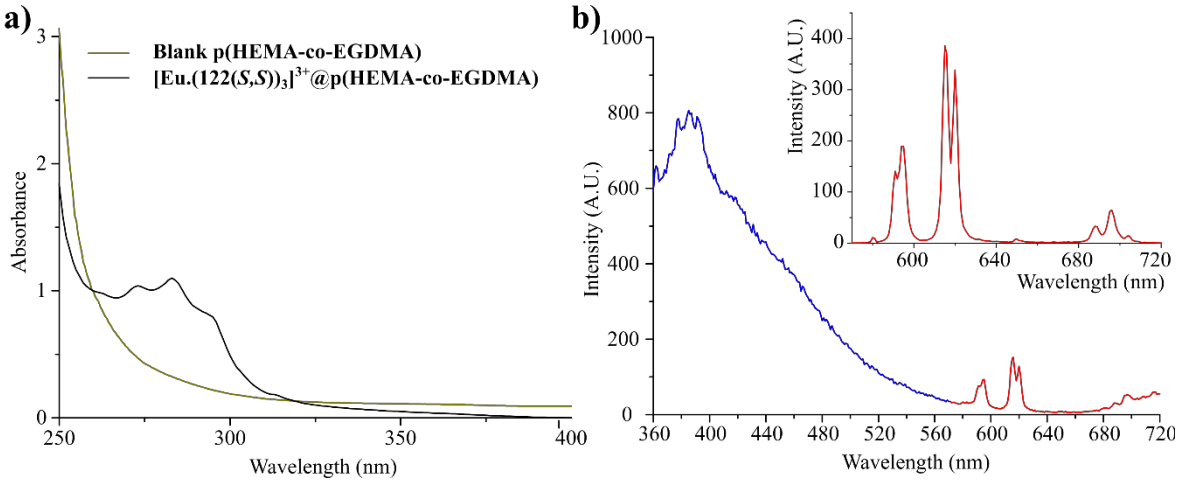

Figure 3.38 a) UV-visible absorption spectra of 1.2 mm dry films of p(HEMA-*co*-EGDMA) and **$[Eu.(122)_3]^{3+}$@p(HEMA-*co*-EGDMA)** showing the UV cutoff of the material and absorbance associated with **$[Eu.(122)_3]^{3+}$** at λ_{abs} = 279 – 320 nm; and **b)** fluorecence emission spectrum from dry **$[Eu.(122)_3]^{3+}$@p(HEMA-*co*-EGDMA)** showing ligand and Eu^{III}-centred emissions, ***inset**:* phosphorescence emission spectrum from dry **$[Eu.(122)_3]^{3+}$@p(HEMA-*co*-EGDMA)** showing Eu^{III}-centred $^5D_0 \rightarrow {}^7F_{0,1,2,3,4}$ transitions.

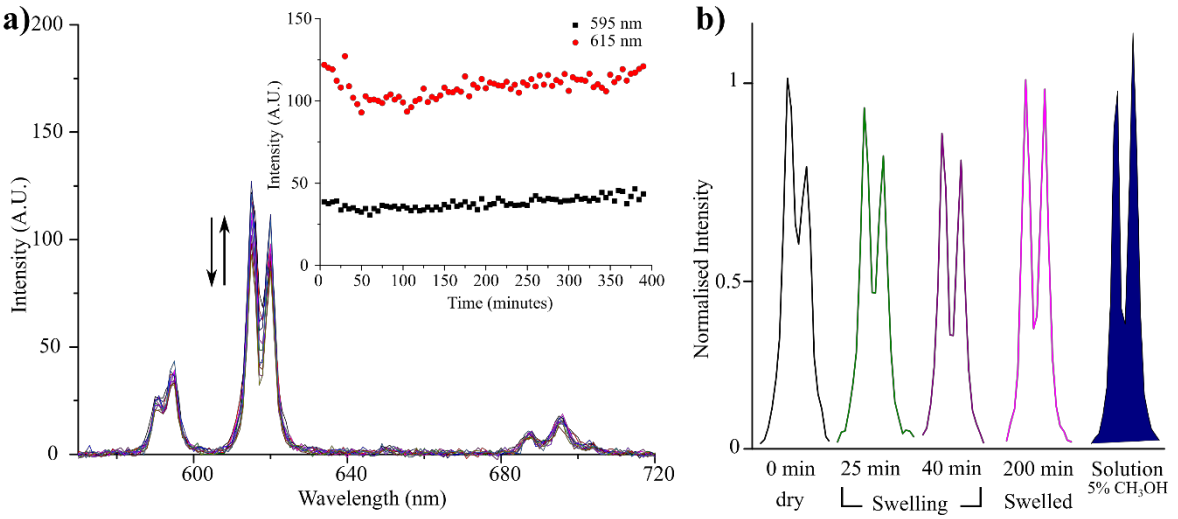

Figure 3.39 a) Overlaid Eu^{III}-centred emission spectra recorded during the swelling of hard polymer monolith as soft polymer gels in H_2O showing intensity and structural changes to the spectrum, ***inset***: emission intensity at λ_{em} = 595 and 615 nm during swelling, showing initial quenching and eventual recovery of Eu^{III} emission intensity; and **b)** Normalised $^5D_0 \rightarrow {}^7F_2$ transition at various stages of swelling, showing the changes in intensity and also in the ratio between the $^5D_0 \rightarrow {}^7F_2$ subcomponents in hard and soft materials. A comparison of spectra of the equilbrated internal complex to that of free solution (blue filled) implied structural similarity.

Strong and stable luminescence could therefore be achieved from **[Eu.(122)$_3$]$^{3+}$** in a fully aqueous system. The spectra in the equilibrated polymer was more closely in agreement to the free solution complex compared to the dry polymer and indicated the similarity between encapsulated and free solution. This suggested that no significant changes in the structure of the complexes had occurred within the swelled soft material.

The strong spectra and visible colours of the polymer gels was encouraging for the development of a gel-based visual probe for pH and, therefore, the materials were calibrated as a function of pH value.

3.7.3 pH calibration of [Eu.(122)$_3$]$^{3+}$@p(HEMA-*co*-EGDMA) polymer gels in aqueous media

The gel probes were calibrated for changes in their spectra, as for the solution complexes, through pH titration. However, additionally, the 'naked-eye' colours were qualitatively assessed within key pH ranges. The polymer gels were suspended in a supernatant solution of aqueous 0.1M NaCl, the pH adjusted through additions of $HCl_{(aq)}$ and $NaOH_{(aq)}$ within the pH range of 2 – 11 and the corresponding luminescence spectra at each pH value recorded. The pH calibration of Eu^{III}- and ligand-centred luminescence, shown in Figure 3.40a, matched with that of the complexes in solution. In basic conditions, the Eu^{III}-centred luminescence was almost completely quenched (*ca.* 90%) while strong **122**-centred fluorescence was observed. As the pH was reduced, a gradual quenching of the ligand fluorescence signal occurred with concomitant enhancement in the intensity of the

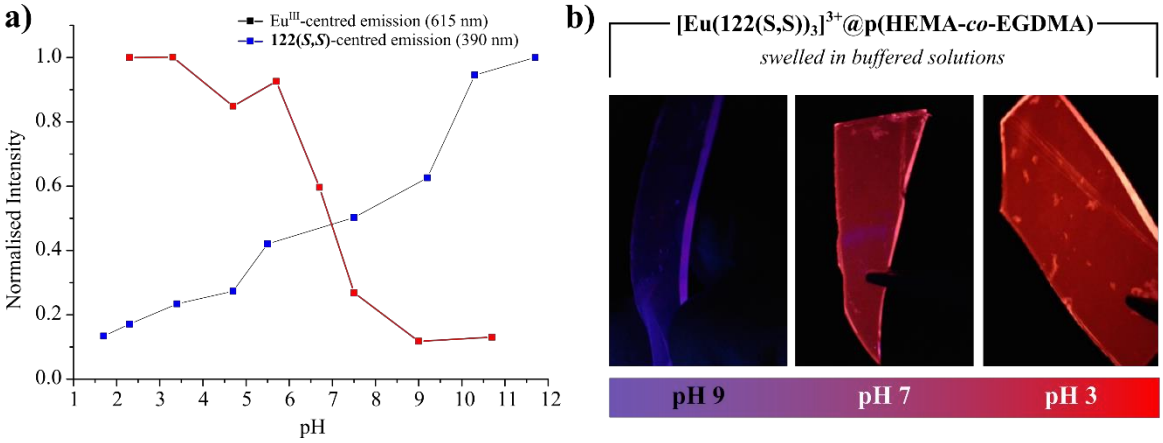

Figure 3.40 a) Calibration of pH with Eu^{III} emission intensity (λ_{em} = 615 nm) and ligand-centred emission (λ_{em} = 390 nm) recorded from **[Eu.(122)$_3$]$^{3+}$@p(HEMA-*co*-EGDMA)** after 20 minutes equilibration time, showing equivalent behaviour to the free solution; and **b)** photographs of visible colour-to-eye after exposure of **[Eu.(122)3]$^{3+}$@p(HEMA-*co*-EGDMA)** to pH buffered aqueous solutions at pH 9, pH 7.4 and pH 3, showing clear colour changes from blue-purple (pH 9), pink (pH 7.4) and red (pH 3).

Eu^{III}-centred emission. This behaviour was in agreement with the solution studies (Section 3.3.6 above) and the greatest sensitivity in Eu^{III} emission was observed between pH 5 - 9.

The sensitivity of the ligand fluorescence was shifted towards more basic conditions and was accounted for by the polarity changes in the hydrogel microenvironment. Overall quality of the calibration of the two emissions from **[Eu.(122)$_3$]$^{3+}$** was reduced when encapsulated within the hydrogel and this greater experimental variation was likely a result of the added diffusion processes. Nonetheless, both emissions were in the visible spectrum (λ_{em} = 390, 595, 615 and 695 nm) and consequently the gels were strongly coloured, as shown in Figure 3.40b. In basic conditions, the ligand fluorescence became dominant over the quenched Eu^{III} emission and the resulting gels were blue-purple in colour. Upon

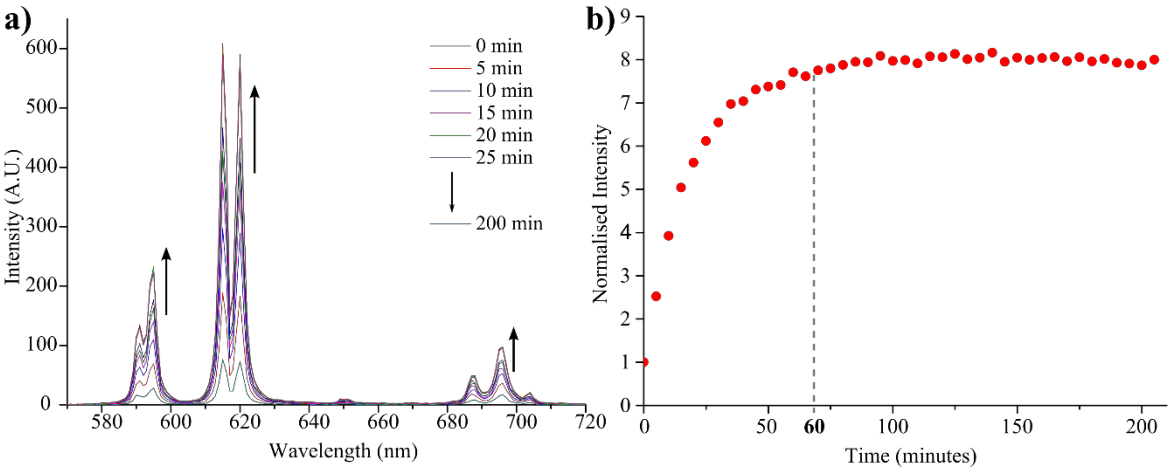

Figure 3.42 Kinetic study of **[Eu.(122)$_3$]$^{3+}$@p(HEMA-*co*-EGDMA)** switching from pH 7 to pH 3. **a)** Overlaid Eu^{III}-centred emission spectra showing significant enhancement over time. Intensity changes were observed but no ratiometric or structural changes occured; and **b)** kinetic isotherm (λ_{em} = 615 nm), showing equilibration of the external and internal solutions after *ca*. 60 minutes. Measurements made in gently stirred aqueous solution at 24 °C. The pH was adjusted to pH 3 with $HCl_{(aq)}$.

acidification, Eu^{III} began to enhance the mixing of purple and red emission affording gels that were pink, as perceived by the eye. Finally, in strongly acidic conditions the gels were intensely red to the naked-eye, consistent with an efficient energy transfer process to Eu^{III} from the ligand excited-states. The gels could be cycled and showed no leeching of **$[Eu.(122)_3]^{3+}$** over extended periods of time (Appendix A3).

A reusable gel probe based upon the luminescence of lanthanide complexes that was 'litmus-like' in response was developed. However, since the swelled polymer gels had a diffusion control on the equilibration of internal and external environments a longer time for the full response was required. The spectroscopic response of the gel switching from neutral (pH 7) to acidic (pH 3) conditions as a function of time is shown in Figure 3.42. An average response time for the encapsulated probes was determined in gels with thickness *ca*. 1.2 mm ('thick gels') of approximately 60 minutes after which equilibration time was mostly complete. The equilibration time to reach maximum emission was consistent and reproducible within ± 5 minutes, in independent measurements at constant temperature, consistent with the diffusion control. Furthermore, in thinner gels or films the response time could be reduced to 20 minutes, due to the shorter diffusion distance.

Furthermore, the **$[Eu.(122)_3]^{3+}$@p(HEMA-*co*-EGDMA)** materials were able to soften in vapours of H_2O and respond as thin films to acidic and basic vapours yielding the same colour response. Thin films of the polymers (*ca.* 0.5 mm) were exposed to HCl and NH_3 vapours in sealed vials containing HCl (aq. conc.) and NH_3 (40% in H_2O); physical and visual changes are shown in Figure 3.41. The films slowly became flexible (as a result of partial wetting) and luminescence responses were observed. A colour change occured that was visible to the 'naked-eye; the films changed from the original pink colour to strong red

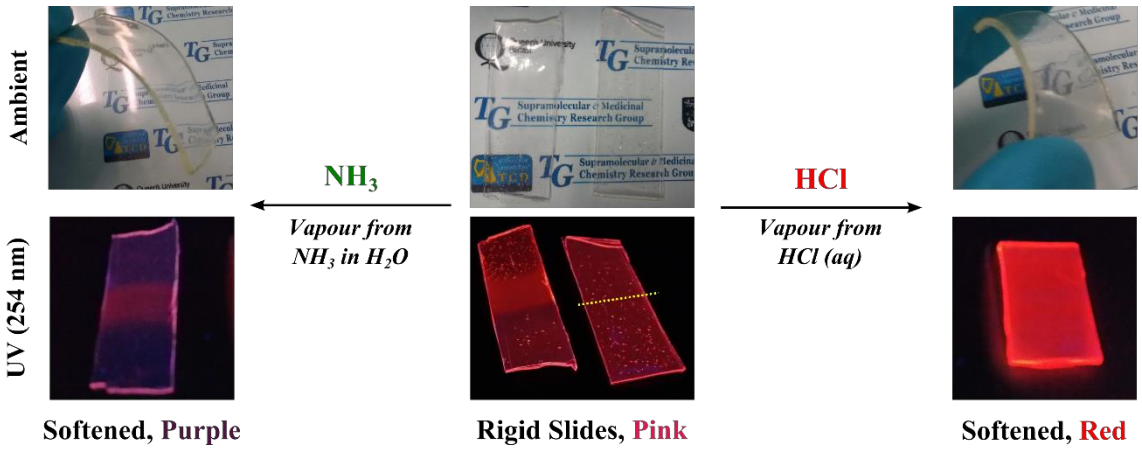

Figure 3.41 Photographs of colour changes as seen to the naked eye of **$[Eu.(122)3]^{3+}$@p(HEMA-*co*-EGDMA)** rigid thin films (*ca*. 0.5 mm) after 48 hours: **a)** exposure to NH_3 vapours; **b)** in neutral condtions as fabricated; **c)** exposure to HCl vapours. Top images: ambient light, bottom images: UV-light, λ_{em} = 254 nm.

and blue-purple when exposed to HCl or NH_3, respectively. This corresponded with the same luminescence responses seen in solution as a result of PET competiton of the red Eu^{III}-centred emission in basic conditions. Once again, the response time was slow (while flexibiltiy was observed after 5 hours of exposure a total of 48 hours was required for the visual luminescence response) and was quicker in thinner films than thick polymer monoliths. Both NH_3 and HCl exposure films dehydrated again to their original physical conditions when allowed to stand in ambient conditons (see Appendix A3). This indicated that the stability may of the simple p(HEMA-*co*-EGDMA) matrix in harsh environments (*i.e.* concentrated acid), was not a signficiant issue. These studies therefore demonstrated that the **[Eu.(122)$_3$]$^{3+}$@p(HEMA-*co*-EGDMA)** materials could be used both as the fully hydrated polymer gels or as thin films to respond to both solution and vapour stimuli.

3.8 Conclusions and future perspectives

In this Chapter, a structurally-related series of chiral naphthyl-**dpa** ligands, **121(*S,S*)** - **125(*S,S*)** and **121(*R,R*)** - **125(*R,R*)**, were synthesised possessing isosteric substituents at the pyridyl 4-position and complexes with Eu^{III} were formed under both thermodynamic and kinetic control. The ligands were either *O*- (**121** and **124**) or *N*-linked (**122**, **123** and **124**) and possessed either a pendent *N,N*-dimethyl ethylamine (**121** - **123**) or isopentyl (**124** and **125**) chain.

Ligands **121** – **125** were afforded through short synthetic routes in reasonable yields (*ca*. 60%) and were fully characterised for their structure and structural characteristics of the *O*- and *N*-substituted pyridyl ligands unambiguously assigned using ^{1}H- and ^{13}C- NMR spectroscopy, HRMS analysis and IR spectroscopy.

The photophysical characteristics of the ligands were studied using UV-visible absorption and fluorescence emission spectroscopy and revealed variable behaviour between the ligands dependent on the atom present at the 4-position of the central pyridyl units. *N*-linked ligands were more strongly absorbing at lower wavelengths (λ_{abs} = 270 – 320 nm) and the absorbance characteristics of the entire series were similar in CH_3CN and CH_3OH.

Chiral absorbance was detected for each ligand structure with each enantiomeric pair showing mirror image CD spectra consisting of a strong Cotton effect at λ_{abs} = 217 – 224 nm. The chiral absorbance was found to be solvent dependent and were not consistent with expected solvent screening effects, indicating a solvent-direction of the ligand conformations. Fluorescence emission from the ligands was found to be acid sensitive with **121**, **124** and **125** showing complete quenching of the emission upon protonation while the

N-linked ligands possessing terminal amines (**122** and **123**) gave substantial fluorescence enhancements of 400% and 500%, respectively. The fluorescence increases as a function of solvent, as well as of protonation, were accounted for through proposed PET pathways that were active under specific experimental conditions.

The Eu^{III} complexes of **121** - **125** were formed under thermodynamic conditions in CH_3OH in a microwave-assisted synthesis as the $CF_3SO_3^-$ salts and their photophysical properties were fully characterised in the solid-sate as well as in CH_3CN and CH_3OH. A coordination interaction with the Eu^{III} ion through the amide carbonyls was confirmed by the reduction of the stretching frequency of the C=O bond compared to the ligand spectra. The UV-visible absorption and CD absorption spectra showed the formation of complexes and intensity shifts in the spectra indicated the π-π interactions and coupling of ligand chromophores, following the directed-assembly of multiple ligands into close proximity around the central Eu^{III} ion.

Ligands **121** - **125** were all able to act as sensitising antenna for Eu^{III} when coordinated to the ion and the characteristic $^5D_0 \rightarrow {}^7F_J$ (J = 0 - 4) transitions from Eu^{III} were observed. The luminescence lifetimes of the ligands were determined in CH_3CN, CH_3OH, H_2O and D_2O demonstrating complexes of a single stoichiometry were formed (*via* thermodynamic synthesis) and were coordinatively saturated **Eu.L3** complexes. The structures of the Eu^{III} luminescence spectra were different between *O*-linked (**121** and **124**) and *N*-linked ligands (**122**, **123** and **125**) with respect to the ratio of the $^5D_0 \rightarrow {}^7F_1$ and $^5D_0 \rightarrow {}^7F_2$ transitions and in the splitting of the $^5D_0 \rightarrow {}^7F_2$ transition itself. These ratios served as 'spectral fingerprints' for the pyridyl 4-position distinguishing underivatised, *O*- and *N*-substituted ligand structures. CPL measurements demonstrated that the chiral environment generated by the *S,S* or *R,R* configuration of the ligands induced circular polarisation in the Eu^{III}-centred emission. Equal and opposite CPL spectra were recorded for each pair of enantiomers, which were consistent with other related systems. These empirically established 'CPL fingerprints' allowed the tentative assignment of Λ and Δ complexes to those of the *R,R* and *S,S* respectively.

The Eu^{III}-centred emission was parameterised and Φ_{tot} varied between 2% (**123** in neutral CH_3CN) to 12% (**125** in neutral CH_3CN) under various experimental conditions. The fundamental properties of the Eu^{III} emission (τ_r and Φ_{Ln}^{Ln}) were demonstrated to be dictated by the substitution at the 4-positon of the pyridine and correlated to the polarisability of the ligand field. The acid-dependence of the overall emission intensity and Φ_{tot} of Eu^{III}-centred

emission was found in the cases **122** and **123** (*N*-linked with pendent amine) in CH_3CN and **121** (*O*-linked with pendent amine) in CH_3OH. Three-fold increases in Φ_{tot} were recorded for **122** and **123** in CH_3CN when in acidic conditions and two-fold increases observed for **121** in CH_3OH treated with HCl. Again, active PET pathways competing with ligand-centred processes such as ISC and the ligand→Eu^{III} energy transfer accounted for these behaviours.

It was proposed that this effect would allow the development of Eu^{III}-luminescent acidity, or pH probes. Complex **[Eu.(122)$_3$]$^{3+}$** gave stable solutions in 5% CH_3OH in H_2O (0.1M NaCl) and was calibrated against pH between pH 2 - 12. Changes in the luminescence were recorded for both the Eu^{III}- and the ligand-centred emissions, providing complementary trends, where the emissions were sensitive within the region pH 5 - 9. The two responsive channels of emission gave strong visual colour changes to the eye from blue-purple through pink to red in basic, neutral and acidic conditions, respectively. The system was robust to "switching" and could be cycled, with little hysteresis observed.

To quantify the binding affinities, ligands **121** - **125** were studied for their self-assembly properties by titrating them with Eu^{III} in CH_3CN and CH_3OH. The spectral changes in UV-visible absorption, CD absorption, and the luminescence were monitored, and data fitted to binding models considering the stepwise formation of **L** → **Eu.L** → **Eu.L$_2$** → **Eu.L$_3$**. The results from the CD spectroscopy were particularly useful in elucidating the contribution and estimating the formation constant of **ML$_2$** stoichiometry species, when the UV-visible absorption changes were small and less reliable for analysis of the solution speciation. Similar binding constants were determined, however, for each ligand independent of the substitution of the pyridine moiety, suggesting that the substitution with *O*- or *N*- may affect the luminescence properties but not influence the overall stability of the complexes assembled in solution. Moreover, the binding constants in CH_3OH were similar in magnitude despite the more competitive solvent. Global stability constants were estimated in CH_3CN as $\log\beta_{MLn}$ *ca*. 7.0-7.4, 12.9-14.7 and 19.5-20.5 for the **ML**, **ML$_2$** and **ML$_3$** species, respectively (all in agreement to previously reported systems).[341,347,349]

Finally, complex **[Eu.(122)$_3$]$^{3+}$** was incorporated as a dopant into a polymer matrix of p(HEMA-*co*-EGDMA) *via* non-covalent encapsulation. The resulting **[Eu.(122)$_3$]$^{3+}$@p(HEMA-*co*-EGDMA)** materials were mechanically identical to un-doped p(HEMA-*co*-EGDMA) with T_g = 87.5 °C and a compressive modulus of 309 kPa; both consistent with independent literature reports[475] of p(HEMA) cross-linked with 1% EGDMA. The photophysical properties of **[Eu.(122)$_3$]$^{3+}$** were not substantially perturbed within the polymer matrix and the swelled polymer gels gave uniform emission that was

responsive to the external environment. Changes to the supernatant solutions of the polymer gels were equilibrated with the internal environment after 60 minutes and the gels responded to pH in the same manner as **[Eu.(122)$_3$]$^{3+}$** in solution. Hard polymer films were also shown to respond to NH_3 and HCl vapours. In addition to the emission intensity change recorded spectroscopically, strong colour changes were visible to the naked eye between blue-purple, pink and red in basic, neutral and acidic conditions, respectively.

Future work from this chapter can consider solubility challenges of naphthyl-**dpa** systems and further developments of the responsive doped polymers. Ligands **121** - **123** which possess pendent amine moieties are, in fact, the precursor compounds to the symmetrical sulfo-betaine materials described in Section 2.8. Related derivatives possessing an 'unmasked' amine may be used to derive additional functionalities such as bioconjugates[476] and (thio)ureas[477-479] which allow for responsive complexes or self-assembled materials.[480-483] Similarly, it is proposed that two complementary pendent chains could be exploited in the formation of organic soft matter through the crosslinking of complexes with inclusion complexes. For example, the use of CB[n] with ligands such as **121** - **123** possessing the terminal amine which can be quarternarised[484-486] or β-CD macrocycles[487-489] with alkyl ligand such as **124** - **125**. The future of the responsive polymer gels described above requires the limitations swelling and response times to be addressed. To form much thinner films (thus reducing the swelling time and diffusion distance) is not facile for free-standing films because of their lower mechanical robustness. It would, therefore, be proposed to prepare doped polymer gels as thin film coatings[490] which can be applied to a number of substrates through *in situ* polymerisation at an adhesive surface; etched PVC[491] and metal[492] substrates, for example, have been used to address needs in medical devices. Glass and quartz surfaces can be functionalised with methacrylate groups[493,494] allowing the direct polymerisation of dip-coated thin films, from a doped solution of monomers, onto the surface. This would generate supported thin films to allow rapid responses or the direct development of devices.

The use of luminescent ions as non-covalent dopants within p(HEMA)-based polymer gels will be extended further in the following chapter that will discuss dual-doping of hydrogel and organogels with responsive Eu^{III} and Tb^{III} complexes for the development of materials-based molecular logic gate mimics.

4. Luminescent Ln^{III} complexes and doped polymer gels as molecular logic gate mimics

4.1 Introduction

In the preceding chapters, the complex **[Eu.(122)$_3$]$^{3+}$** was described in both solution and polymer matrices. The pendant amine of **122** allowed the Eu^{III} complex to act as a Eu^{III} luminescent sensors for acidity and pH in organic and aqueous solutions, respectively. The strong luminescence response to H^+ was allowed through PET quenching of the ligand-centred excited-state competing with Eu^{III} sensitisation. To extend beyond this fundamental function into more versatile responsive probes, the complexes were analysed in the broader context of logic operations and will be discussed in this chapter. The field of logic has an ancient history and the eventual application of these concepts to the physical sciences gave rise to the digital age and computing technologies.[495] Within the chemical sciences, a similar interest arose from Aviram[496] and de Silva[497] in 1988 and 1993, respectively, to mimic familiar logic operations at the molecular level. In recent times, this has grown into a vast interest area with both simple molecular logic gates and complex circuits being demonstrated in single molecule[498], supramolecular assemblies[1,498] and 'materials devices'[499-506].

4.2 Molecular Logic and Molecular Logic Gate Mimics

The simplest of the logic functions are YES and NOT logic gates and are 'single input-single output' logic operations. A YES logic function has a binary output that mirrors that of the Input, *i.e.* if the Input is True then the Output is True, if the Input is False then the Output is False. This corresponds to the simplest form of chemical sensor (a single analyte "OFF/ON" sensor); when the analyte is present, above the limit of detection (LOD) of the responsive molecule, a positive readout is observed. With this in mind, over four hundred YES molecular logic gate mimics were published in 2015 alone (Scopus®). The NOT logic gate is just as common. This logic gate has a binary Output that is the inverse of the binary Input and chemical sensors that are "ON/OFF" probes can be described in this manner. The resting state of an "ON/OFF" sensor has a positive readout which is then 'switched off' following exposure to the appropriate analyte. These examples are relatively trivial. However, the true advantages of logical analysis are most available to supramolecular chemistry where there is a focus beyond single molecules towards larger constructs or systems.[507] For responsive

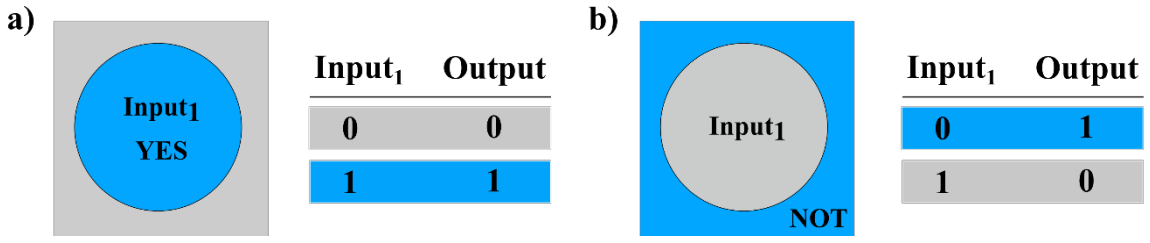

Figure 4.1 Venn diagram and truth table representations of single input-single output logic functions. **a)** YES gate; **b)** NOT gate. Areas of the Venn diagrams in blue indicate a positive output signal.

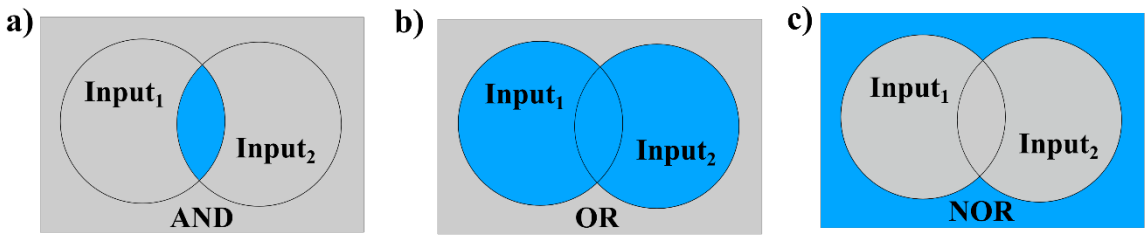

$Input_1$	$Input_2$	Output
0	0	0
1	0	0
0	1	0
1	1	1

$Input_1$	$Input_2$	Output
0	0	0
1	0	1
0	1	1
1	1	1

$Input_1$	$Input_2$	Output
0	0	1
1	0	0
0	1	0
1	1	0

Figure 4.2 Venn diagram and truth table representations of double input-single output logic functions. **a)** AND gate; **b)** OR gate; **c)** NOR gate. Areas of the Venn diagrams in blue indicate a positive output signal.

systems of the macro- and supra-molecular scales it is often the case that they go beyond simple "ON/OFF" or "OFF/ON" relationships and perform more advanced functions.[508]

When two Inputs are present, four different Input combinations are possible but sixteen potential Output combinations exist ranging from trivial unresponsive systems (PASS 1/0) to more complex logic operations;[509] three selected double input-single output gates are shown in Figure 4.2. Two key examples are AND logic and OR logic. For a positive readout from an AND gate it is prerequisite that two separate Input species be present above the defined threshold, under all other possible combinations the gate readout is nil ("0"), as described by the Venn diagram in Figure 4.2a. Where there is less selectivity between receptor sites and respective analytes, or multiple receptor sites that are similar in nature, there is a loss of exclusivity and an effective shift to OR logic.

In direct comparison to chemical sensors, the functions of XNOR and XOR/INHIBIT describe well-known types of probe. The truth table representations of these more advanced gates are given in Figure 4.3b. XNOR logic gates give an Output of ON/"1" in the cases where neither or both of the Inputs are present while the Output is OFF/"0" in the presence of either of the Inputs. On the other hand, XOR and INH give Outputs of OFF/ "0" in the absence and presence of both Inputs but "switch-on" in the presence of single Inputs. Sensors that behave through a bell-curve type relationship across a range of conditions (shown schematically in Figure 4.3b), therefore, can be considered in terms of these logic functions. These conditions can be combinations of physical conditions, chemical species, or repeated dosage of an equivalent Input such as light[510-512] or $[H^+]$[513]. Consequently, in the established chemical terminology, XNOR logic corresponds to "on-off-on" sensors[514,515] while various

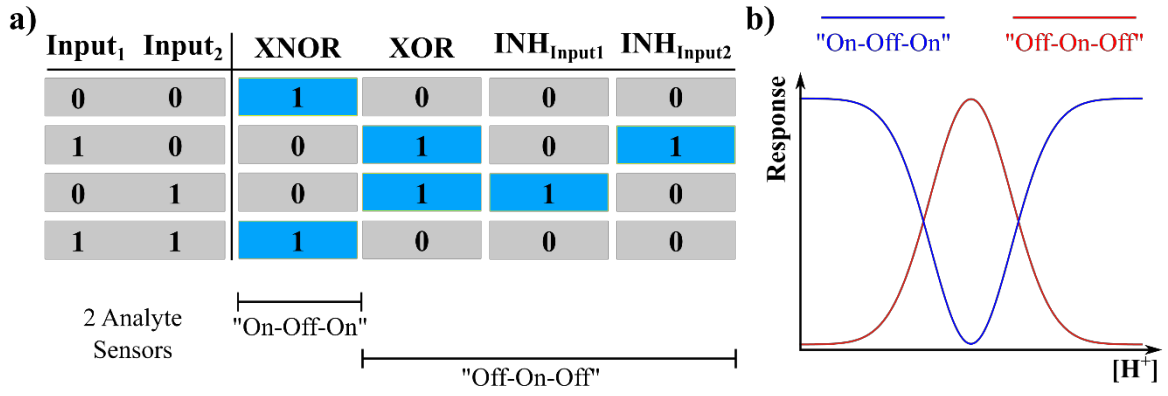

Figure 4.3 a) Truth table representations of more complex logic functions and their correspondence to chemical "On-Off-On" and "Off-On-Off" sensors. "1", or blue background, indicates an "ON" output; and **b)** representative pH sensor responses of "On-Off-On" and "Off-On-Off" compared for INHIBIT logic functions.

types of "off-on-off" sensors correspond to XOR[513,516] or INHIBIT[517] logic functions. For in depth analysis of this field the reader is directed to the monograph "Molecular Logic-based Computation" by de Silva.[509] However, only a limited number of examples have been reported using lanthanide luminescence and these are reviewed in the following section.

4.2.1 MLGMs based upon Ln^{III}-centred emission

The advantages of emissive *f-f* transitions in the manufacture of responsive probes was discussed in Section 1.3.3. While numerous examples exist of multiple-input responsive probes[518] and information-rich response curves,[513] few examples exist that have made explicit reference to a molecular logic despite the use of Ln^{III}-centred emission as Output channels in MLGMs representing a privileged approach (due to their wavelength-invariant emissive transitions). The earliest examples, **141**, were described by Parker,[519] and extended as **142** in collaboration with Gunnlaugsson,[520,521] based upon the DOTA scaffold and inputs of H^+ and pO_2. The complexes **141** and **142** are shown in Figure 4.4. In the case of **141**, it was suggested to operate as a NAND gate, a two-input NOT function, since the $^5D_4 \rightarrow {}^7F_{6\text{-}2}$ transitions of Tb^{III} were only observed in the conditions that both H^+ *and* O_2 were *not* present.

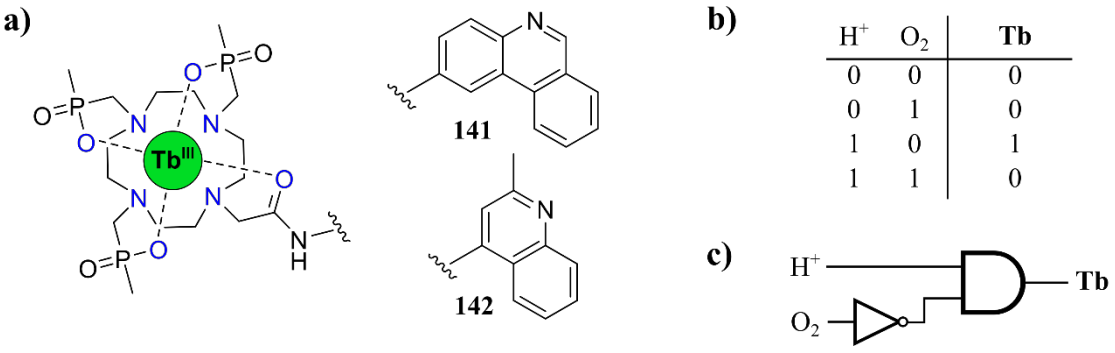

Figure 4.4 a) Structures of **141** and **142**, DOTA-based NAND and INH molecular logic gate mimics, respectively; **b)** truth table representation for behaviour of **141**, corresponding to INH_{pO_2}, and **c)** logic circuit diagram in standard schematic style representing the INH_{pO2}

Back-energy transfer was estimated to be greater in the case of the protonated phenanthridine accounting for the "OFF" output while pO_2 also promoting the switch to the OFF/"0" output through oxygen quenching of the phenanthridine triplet excited-state. A more complex logic circuit was achieved in **142**. The truth table and schematic logic circuit diagram are shown in Figure 4.4b and Figure 4.4c. The emission from the Tb^{III}-centre, the "ON" state, was observed in the presence of H^+. However, even under the acidic conditions the presence of pO_2 resulted in the switch to the OFF/"0" state. This corresponded to a two Input "Off-On-Off" relationship which translated into an $INHIBIT_{pO_2}$ logic gate mimic. In this case, the protonated form of the antenna was more efficient in the energy transfer to the Tb^{III} excited state levels while pO_2 again competed with energy transfer by quenching the chromophore triplet excited-state. These earlier examples use a single complex and single output in their logical analysis. Gunnlaugsson and co-workers[522] reported a further development and described a mixed Tb^{III}-Eu^{III} system as three unique logic gate mimics operating in parallel. The structure and truth table are shown in Figure 4.5. The multi-component line-like spectra of Tb^{III} and Eu^{III} were utilised to extract two Output channels from Eu^{III} ($^5D_0 \rightarrow {}^7F_2$ and $^5D_0 \rightarrow {}^7F_4$) and a single Output from Tb^{III} ($^5D_0 \rightarrow {}^7F_6$) as the two metal ions showed subtly different behaviours in response to the OH^- and pO_2 Inputs. The responses of **[Tb.(143)]$^{3+}$** and **[Eu.(143)]$^{3+}$** were continuous relationships; however, the definition of thresholds allowed for the digitisation of these analogue responses into specific ON/"1" and OFF/"0" states based upon emission intensity from Eu^{III} and Tb^{III} at specific wavelengths (λ_{em} = 545, 622 and 700 nm).

Self-assembly-based approaches have been used by Qu and-coworkers[523,524] to generate a set of "Plug and Play" molecular logic gates in the dynamic formation of Eu^{III}

a)

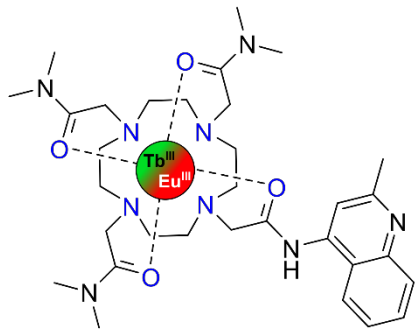

[Eu.(143)]$^{3+}$ - [Tb.(143)]$^{3+}$

b)

Inputs		**Outputs**		
OH^-	O_2	**545 nm**	**622 nm**	**700 nm**
0	0	1	1	1
0	1	1	0	1
1	0	1	0	0
1	1	0	0	0

545 nm = NAND
622 nm = NOR
700 nm =NOT

Figure 4.5 A two input-three output from Gunnlaugsson, responsive to OH^- and pO_2. **a)** Structure of **143** indicating a 1:1 solution mixture of Tb^{III} to Eu^{III}; **b)** truth table representation of the mixed **[Eu.(143)]$^{3+}$** or **[Tb.(143)]$^{3+}$** and the summary description of the logic function. Tb^{III}-centred output: 545 nm, Eu^{III}-centred output: 622 and 700 nm.

and Tb^{III} containing coordination polymer nanoparticles. Pischel *et al*. reported **144** as an INHIBIT (INH) logic gate with Inputs of Eu^{III} and pO_2.[525] Again, the quenching effect of O_2 on the triplet excited-state of the naphthalimide antenna was exploited to compete with energy transfer. The Output channel was Eu^{III} luminescence and, therefore, since Eu^{III} itself was an Input, the logic states (0,0) and (1,0) were "OFF/0" in a trivial fashion since Eu^{III} was not present. The presence of Eu^{III} with **144** in degassed solution, logic state (0,1), was emissive through the antenna sensitised mechanism; aeration of the solution to (1,1) resulted in O_2 quenching of the triplet excited-state of **144** reducing the energy transfer efficiency to Eu^{III} and inhibiting the emission to be "OFF/0".

Recently, the design of Ln^{III} containing logic gate mimics was shifted to materials by Tang and co-workers in the fabrication of paper-supported logic devices.[526] The devices employed simple complexes **145** and **146** which were absorbed onto filter paper and which were responsive to acidic and basic vapours. Materials of pure **145**, pure **146** and 1:1 mixed materials were successfully generated and operated with a clear "switch on" of Eu^{III} luminescence in basic conditions and of Tb^{III} luminescence in acidic conditions. The inverted behaviour was likely due to subtle mismatches of the protonated and unprotonated with energy levels of the respective lanthanide ions. These simple complexes combined to produce two different INHIBIT logic gate mimics based upon AND and OR logic in the case of **145** and **146**, respectively as shown in Figure 4.6c.

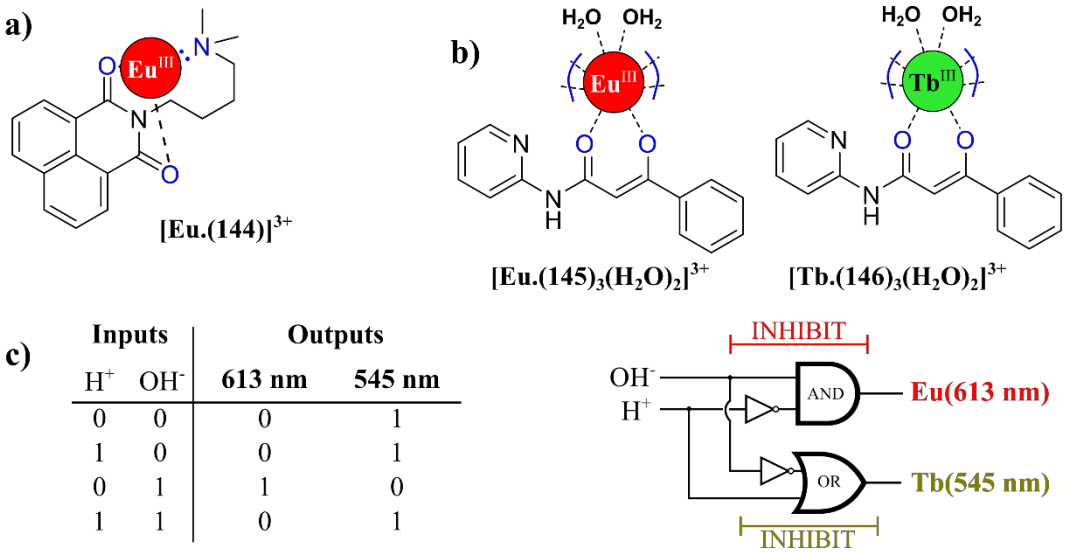

Figure 4.6 Structures of key MLGMs based on Ln^{III} emission and non-DOTA ligands. **a) 144**, a naphthalimide based INH logic gate responsive to Eu^{III} and O_2 as Input species; **b) [Eu.(145)$_3$(H$_2$O)$_2$]** and **[Tb.(146-H)$_3$(H$_2$O)$_2$]$^{3+}$**, parallel INH logic gates that are responsive to H^+ and OH^- as Inputs species and **c)** truth table and logic circuit diagram of the **[Eu.(145)$_3$(H$_2$O)$_2$]** and **[Tb.(146-H)$_3$(H$_2$O)$_2$]$^{3+}$** paper-based MLGM.

The future of molecular logic-based computation and MLGM therefore has been identified against two needs: i) the assimilation of logical analysis, and logical language, into research by a wider community as highlighted by many of the retrospective examples by de Silva[509]; and ii) the inclusion of such systems at surfaces or *into* materials translating the often less applicable solution chemistry within solids and into functional materials.[527] The research described in this chapter aimed to address the second of these criteria employing simple Ln^{III} luminescent complexes in a supramolecular approach to functional materials. Two ligands (**122** and **126**) were developed independently in the Gunnlaugsson group and were employed in the design of a mixed-Ln^{III} logic gate mimic. The design and photophysical characterisation of the responsive complexes are presented in the following sections, followed by the fabrication of MLGMs in solution and soft matter.

4.3 Design, synthesis and characterisation of the responsive probes

In the design of the dual-responsive system the complimentary characteristics of two scaffolds suitable for sensitised Ln^{III} emissions were considered simultaneously. These were naphthyl **dpa (6)** and bis(triazolyl)pyridine (**27**, **btp**). The **btp** scaffold has become increasingly popular as an alternative for Ln^{III} coordination. Systems based on bis-(naphthyl-**dpa)** are good sensitising ligands for Eu^{III} emission but are less effective for the sensitisation of Tb^{III} luminescence. In contrast to this, **btp** derivatives show improved sensitisation efficiency in complexes of both Eu^{III} and Tb^{III}. Furthermore, the **btp** excited-state is significantly more efficient in the sensitisation of Tb^{III} emission compared to Eu^{III} (quantum yields reported as 70±10 and 2.4±0.4 % for Tb^{III} and Eu^{III}, respectively).[353] Anion binding properties in **btp**-like motifs have been reported, with this arising from the acidic protons of the triazole moieties.[528,529] The sensitivity of **$[Tb.(126)_3]^{3+}$** to anionic species in solution was observed in previous work by the Gunnlaugsson group[530] and was investigated further herein

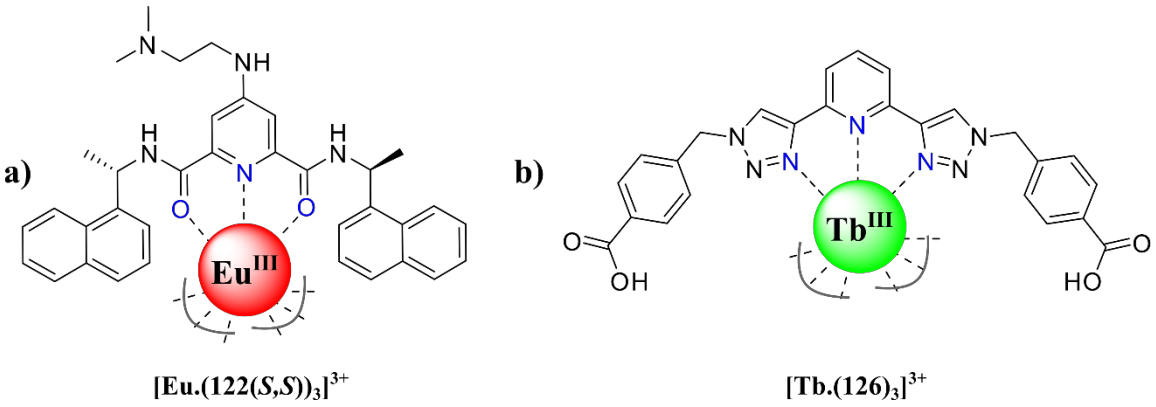

$[Eu.(122(S,S))_3]^{3+}$ **$[Tb.(126)_3]^{3+}$**

Figure 4.7 Structures of responsive complexes **a)** naphthyl **dpa** complex **$[Eu(122)_3]^{3+}$**; **b) btp** complex **$[Tb(126)_3]^{3+}$**.

through collaboration with Dr. Joseph Byrne; a selectivity in response to F^- and I^- over Br^- and Cl^- was found (Appendix A4). Both F^- and I^- resulted in the quenching of Tb^{III} centred emission with over 90% quenching having occurred after the addition of 12 and 3 equivalents of the anions, respectively; a concomitant fluorescence enhancement (*ca*. 6-fold) was observed with the additions of F^-. Interestingly, the mechanism of the response to the anions were different. The changes in UV-visible absorption demonstrated that F^- induced the dissociation of **[Tb.(126)$_3$]$^{3+}$** while I^- was likely involved in a supramolecular CH•••I^- interaction with the triazole proton. Similarly, dissociation of **[Tb.(126)$_3$]$^{3+}$** was observed upon exposure to H^+ (Appendix A4). A key responsive behaviour of **[Eu.(122)$_3$]$^{3+}$** with [H^+] was described in Chapter 3 as the result of PET quenching process. As expected, the opposite luminescence response to [F^-] was also observed for **[Eu.(122)$_3$]$^{3+}$**, this was the result of deprotonation of the pendent amine by the F^- and concomitantly increased PET efficiency. As a result of these complementary responses, it was proposed that the two scaffolds could be used in parallel to generate a dual input-dual output probe.

This chapter will discuss the implementation of **[Eu.(122)$_3$]$^{3+}$** and **[Tb.(126)$_3$]$^{3+}$** together in CH_3OH solution and their parallel spectroscopic responses to simple analytes analysed as MLGMs. The application as a materials-based MLGM will then be explored and the inclusion of the probes in polymer matrices with expectations of achieving versatile chemical devices.

4.3.1 Synthetic details

The synthesis and characterisation of **122** is reported in detail in Chapter 3 of this thesis and is restated only where necessary for coherent discussion. The synthesis of **btp** ligand **126** was completed by Dr. Joseph Byrne; the full synthetic scheme along with detailed procedures is provided in Appendix A4.

Ligand **126** was achieved from a one-pot deprotection/"click" synthesis that was established by Byrne and Gunnlaugsson.[352,353] 4-(Bromomethyl)benzoic acid was converted to the appropriate azide precursor *in situ* by nucleophilic substitution with NaN_3 and "*clicked*" to 2,6-bis(ethynyl)-pyridine (produced *in situ* by TMS deprotection by K_2CO_3) by the catalytic CuAAC reaction using Cu(I) generated from the reduction of $CuSO_4.5H_2O$ by sodium ascorbate. The reaction proceeded cleanly and following Cu(I) scavenging by aqueous EDTA/NH_4OH gave pure ligands in moderate yield, 63%. The complexes of **122** and **126** with Eu^{III} and Tb^{III}, respectively, were synthesised *via* a common microwave-assisted synthesis in CH_3OH with 0.33 equivalents of the appropriate trifluoromethane sulfonate salts and heated to reflux temperature for 30 minutes. The resultant solutions, once

concentrated, were added slowly to excess diethyl ether resulting in the precipitation of the emissive complexes in **ML$_3$** stoichiometry, as confirmed by emission lifetime (τ) and hydration state (q_{Tb} value) calculations, which are presented in Appendix Table A4.1.

The parallel application of both complexes, in practical terms, required that there be structural distinction but also photophysical coherence between them in both absorbance and luminescence properties; this necessitated coinciding absorbance features alongside the robustly distinguishable Ln^{III} luminescence. The basic photophysical assessment of **126** is presented in the following section and, while characterised fully in earlier discussion, key characteristics of **122** will be restated for comparison.

4.3.2 Photophysical summary in CH_3OH solution

The UV-visible absorption spectra of **126** and **122** were recorded at $c = 1 \times 10^{-5}$ M in CH_3OH and these spectra are shown in Figure 4.8, separated by ligand for clarity. Both the naphthyl **dpa** and **btp** derivatives shared a central pyridine core and showed similar absorbance features where $\lambda_{max} \approx 220$ nm, the feature arising collectively from high-energy electronic transitions ($\pi \rightarrow \pi^*$ and $n \rightarrow \pi^*$) of the pyridine unit. The lower energy transitions, however, differed between the two structures and the nature of their spectral changes between complexed and free-ligand forms also diverged.

In ligand **122**, these are assignable to naphthalene $\pi \rightarrow \pi^*$ transitions, showing the characteristic fine structure, while in **126** the assignment is made to $n \rightarrow \pi^*$ transitions of the extended **btp** core. The coordination of **122** to Eu^{III} did not result in appreciable wavelength shifts in any absorbance features, with only changes of ε in key regions of the spectrum observed. However, upon Tb^{III} being coordinated by **126** there was significant red-

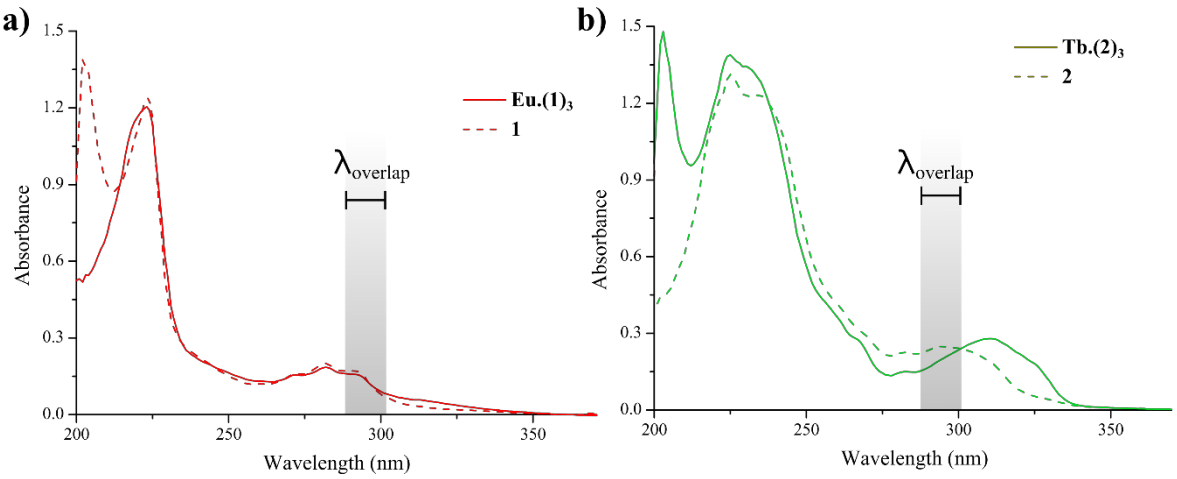

Figure 4.8 Overlaid UV-visible absorption spectra of ligand and complexes for: **a) 122** (dashed line) and **[Eu.(122)$_3$]$^{3+}$** (solid line) and; **b) 126** (dashed line) and **[Tb.(126)$_3$]$^{3+}$** (solid line). In both figures the same $\lambda_{overlap}$ is identified where absorbance coherence between all four species was achieved. All spectra were recorded at c = 1×10^{-5} M in CH_3OH at 24°C.

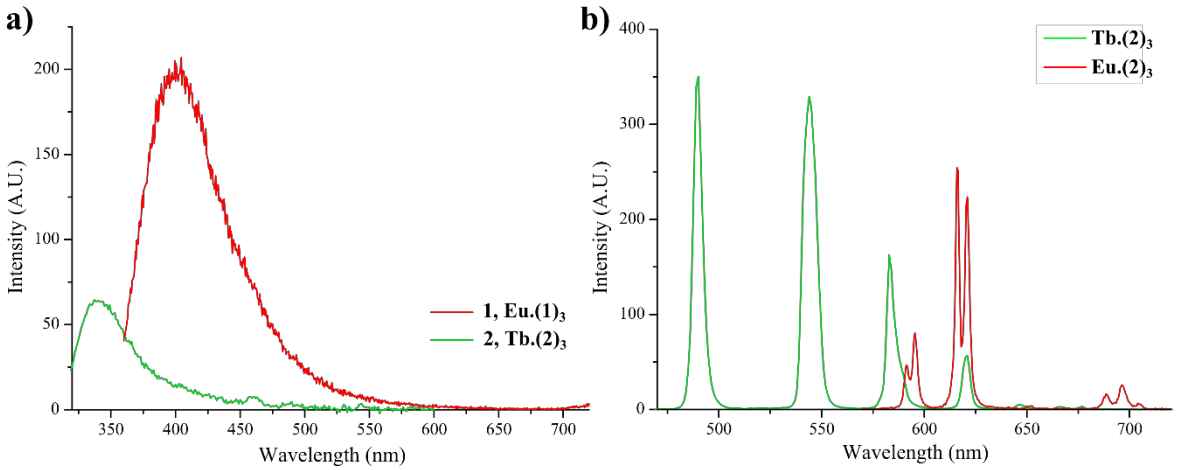

Figure 4.9 Overlaid luminescence spectra of **[Eu.(122)$_3$]$^{3+}$** (red) and **[Tb.(126)$_3$]$^{3+}$** (green): **a)** Fluorescence spectra showing ligand-centred emissions; **b)** time-gated emission spectra showing characteristic Eu^{III} and Tb^{III}-centred emissions. All spectra were recorded at c = 1 × 10^{-5} M in CH_3OH at 24 °C.

shift of both λ_{max} = 230 nm and λ_{max} = 300 nm absorbance features. In the case of λ_{max} = 300 nm, this red-shift had a magnitude of 15 nm which effectively generated an offset between the lowest energy absorbance features of **[Eu.(122)$_3$]$^{3+}$** and **[Tb.(126)$_3$]$^{3+}$**. This offset presented a window (λ_{abs} = 280 – 310 nm) in which simultaneous excitation could be achieved, with similar extinction coefficients (*ca.* 2 × 10^5 cm^{-1}M^{-1}) that corresponded appropriately to dose both complexes efficiently. Upon excitation both complexes exhibit luminescence properties in both the fluorescence and phosphorescence timescales, these emission spectra are presented in Figure 4.9a and Figure 4.9b, respectively.

The criteria of interest for analysis of luminescence signals was clarity of their differentiation, the fluorescence spectra clearly demonstrated that the Stokes shift in the emission from **122** was greater than for **126** resulting in offset emission maxima (λ_{em} = 330 nm and 380 nm for **122** and **126**, respectively). The shape of the emission bands were easily de-convoluted and differentiation made of the contributions from each complex; Eu^{III}- and Tb^{III}-centred transitions were not of appropriate intensity to monitor in fluorescence mode. Therefore, metal-centred luminescence was also recorded from both complexes as phosphorescence, as shown in Figure 4.9b. The features of Eu^{III} luminescence spectra have been referenced extensively and are discussed for **[Eu.(122)$_3$]$^{3+}$** in Section 3.3.6; the electronic transitions of Tb^{III} share a similar nature but show different λ_{em} and the spectral window of Tb^{III} is extended to higher energy. The sensitised emission of Tb^{III} by **126** resulted in measurable characteristic transitions resulting from $^5D_4 \rightarrow {}^7F_{6\text{-}2}$, the most intense transitions were also the highest in energy and corresponded to $^5D_4 \rightarrow {}^7F_6$ and $^5D_4 \rightarrow {}^7F_5$ while the lower energy transitions of reduced intensity; this was consistent with the selection rules for intra-conformational *f-f* transitions.[62]

The nature of the *f-f* electronic transitions have been discussed in detail and the narrow emission bands allowed for the required differentiation of the emission from Eu^{III} and Tb^{III}, since discrete "pure" transitions for each ion could be identified. These features are summarised in Table 4.1 (pure features are marked with *).

Table 4.1 Summary of transitions in Figure 4.9b indicating their emission purity and relative intensities from **[Eu.(122)$_3$]$^{3+}$** and **[Tb.(126)$_3$]$^{3+}$** at $c = 1 \times 10^{-5}$ M; *Transitions suitable for parallel monitoring; †Weak pure transitions

	Transition (Ln)	λ_{em} (nm)	Purity	Intensity	
1	$^5D_4 \rightarrow {}^7F_6$ (Tb)	490	Pure	Strong	*
2	$^5D_4 \rightarrow {}^7F_5$ (Tb)	545	Pure	Strong	*
3	$^5D_4 \rightarrow {}^7F_4$ (Tb)	582	Pure	Strong	*
4	$^5D_0 \rightarrow {}^7F_1$ (Eu)	590	Overlapped by 3	Weak	
5	$^5D_0 \rightarrow {}^7F_1$ (Eu)	595	Pure	Weak	†
6	$^5D_0 \rightarrow {}^7F_2$ (Eu)	615	Pure	Strong	*
7	$^5D_0 \rightarrow {}^7F_2$ (Eu)	622	Overlap 8	Strong	
8	$^5D_4 \rightarrow {}^7F_3$ (Tb)	622	Overlap 7	Weak	
9	$^5D_4 \rightarrow {}^7F_2$ (Tb)	650	Overlap 10	V. Weak	
10	$^5D_0 \rightarrow {}^7F_3$ (Eu)	650	Overlap 9	V. Weak	
11	$^5D_0 \rightarrow {}^7F_4$ (Eu)	695	Pure	Weak	†

Comparing the emission spectra of **[Eu.(122)$_3$]$^{3+}$** and **[Tb.(126)$_3$]$^{3+}$**, there was substantial overlap of one component of the $^5D_0 \rightarrow {}^7F_2$ transition of Eu^{III} and $^5D_4 \rightarrow {}^7F_3$ transition from Tb^{III}, as well as one component of the $^5D_0 \rightarrow {}^7F_1$ transition in Eu^{III} with the edge of the $^5D_4 \rightarrow {}^7F_4$ transition of Tb^{III}. The emissions at 622 nm and 590 nm were therefore not pure to a unique emissive species. However, the Tb^{III}-centred bands from $^5D_4 \rightarrow {}^7F_6$ (λ_{em} = 490 nm) and $^5D_4 \rightarrow {}^7F_5$ (λ_{em} = 550 nm) from **[Tb.(126)$_3$]$^{3+}$** were outside the emission window of Eu^{III} and strongly emissive and could be considered pure. This allowed the simultaneous and orthogonal monitoring of the emission output from both Eu^{III} and Tb^{III} ions. The distinguishable emissions were exploited to monitor the responsive behaviours of **[Eu.(122)$_3$]$^{3+}$** and **[Tb.(126)$_3$]$^{3+}$** in mixed solution.

4.4 Responsive behaviours of [Eu.(122)$_3$]$^{3+}$ and [Tb.(126)$_3$]$^{3+}$ in mixed CH_3OH solution

At equal concentration in CH_3OH, the complexes **[Eu.(122)$_3$]$^{3+}$** and **[Tb.(126)$_3$]$^{3+}$** displayed substantially different emission intensities. The mismatch in quantum yield was corrected for trivially by reducing the concentration of **[Tb.(126)$_3$]$^{3+}$**. The spectrum of the mixed

solution of complexes is shown in Figure 4.10a and Figure 4.10b for the phosphorescence and fluorescence emissions, respectively. In the spectra of **[Eu.(122)$_3$]$^{3+}$** and **[Tb.(126)$_3$]$^{3+}$** mixed in a 3:1 ratio, an equal intensity in the $^5D_0 \rightarrow {}^7F_2$ transition of Eu^{III} (λ_{em} = 615 nm) and the $^5D_4 \rightarrow {}^7F_2$ transition of Tb^{III} (λ_{em} = 490 nm) was observed. The absolute concentrations were determined such that a clear distinction in the intensities of the Eu^{III} and Tb^{III} transitions could be made after maximum enhancement and quenching of the emissions, respectively. The appropriate concentrations were determined at 2.5×10^{-5} M and 5×10^{-6} M for **[Eu.(122)$_3$]$^{3+}$** and **[Tb.(126)$_3$]$^{3+}$**, respectively.

The observations of **[Eu.(122)$_3$]$^{3+}$**, in Chapter 2, and of **[Tb.(126)$_3$]$^{3+}$**, in previous work,[530] suggested that the **ML$_3$** complexes were stable (likely due to cooperative interaction of π-π stacking in the coordination) at 1 – 10 μM. Therefore, under the experimental conditions of the mixed solution it was unlikely that dynamic sorting ('scrambling') of the ligand and Ln^{III} ions would occur. The potential abstraction of Eu^{III} and Tb^{III} by the F^- input, as result of the large lattice energies of lanthanide fluorides[63] was addressed by determining the reversibility of the responses observed in Section 4.4.1 below.

The same spectra, Figure 4.10, were obtained over time indicating mixed solution was kinetically stable under the operating conditions of 24 °C. This confirmed that: i) **[Eu.(122)$_3$]$^{3+}$** and **[Tb.(126)$_3$]$^{3+}$** were stable; ii) the ligands did not dynamically sort into mixed-ligand complexes; and iii) a constant, reproducible chemical and physical state could be achieved. The structure of the Ln^{III} luminescence spectrum from the mixed solution was also additive for overlapped Ln^{III}-centred transitions (*e.g.* the $^5D_0 \rightarrow {}^7F_2$ transition from **[Eu.(122)$_3$]$^{3+}$** with the $^5D_4 \rightarrow {}^7F_4$ transition from **[Tb.(126)$_3$]$^{3+}$** at λ_{em} = 621 nm),

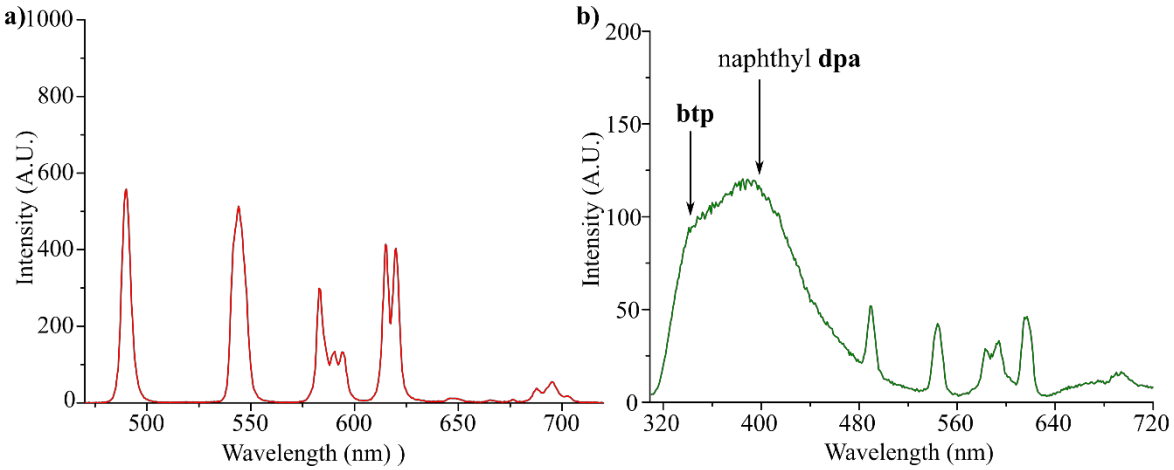

Figure 4.10 Emission spectra of mixed **Eu.(122)$_3$** and **Tb.(126)$_3$** in CH_3OH, **a)** phosphorescence emission showing Tb^{III}-centred emissions ($^5D_4 \rightarrow {}^7F_{6,5,4,3}$) and Eu^{III}-centred emissions ($^5D_0 \rightarrow {}^7F_{1,2,3,4}$); **b)** fluorescence emission showing **122**, **126**-centred emissions as well as Eu^{III}- and Tb^{III}-centred transitions. [**Eu.(122)$_3$**] = 2.5×10^{-5} M and [**Tb.(126)$_3$**] = 5×10^{-6} M in CH_3OH at 24 °C.

demonstrating that **[Eu.(122)$_3$]$^{3+}$** and **[Tb.(126)$_3$]$^{3+}$** remained photophysically independent in solution. No evidence for FRET-like quenching of ligand excited-states[531] or quenching of Tb^{III}-centred excited-states *via* $Ln^{III} \rightarrow Ln^{III}$ energy transfer to Eu^{III} centres was observed.[532] This was also supported by the excitation spectra of the $^5D_4 \rightarrow {}^7F_6$ transition of Tb^{III} (λ_{em} = 490 nm) and $^5D_0 \rightarrow {}^7F_6$ transition of Eu^{III} (λ_{em} = 695 nm) which indicated sensitisation of Tb^{III} and Eu^{III} emissons by **126** and **122**, respectively. Having established that the mixed solution was stable, the system was studied under the proposed stimuli conditions and the functions of the MLGM derived.

4.4.1 Solution model of a molecular logic circuit

Complexes **[Eu.(122)$_3$]$^{3+}$** and **[Tb.(126)$_3$]$^{3+}$** have been established to be responsive to H^+ and F^-, both showing significant changes in the metal- and ligand-centred emissions. The responsive behaviour of **[Eu.(122)$_3$]$^{3+}$** was discussed in Section 3.3.6 and those of **[Tb.(126)$_3$]$^{3+}$** are shown in Appendix A4. The Tb^{III}-centred emission in **[Tb.(126)$_3$]$^{3+}$** was quenched by the addition of H^+ and F^-, while the ligand-centred fluorescence was enhanced. In the case of F^- treatment, the quenching of Eu^{III} emission in **[Eu.(122)$_3$]$^{3+}$** was reversible with H^+ and therefore indicated that there was no abstraction of Eu^{III} by F^-. For **[Tb.(126)$_3$]$^{3+}$** the quenching was not reversible due to the dissociative mechanism and the abstraction of Tb^{III} was not determined, however no precipitation (i.e. TbF_3) was observed.

The Input concentrations to the MLGM for [H^+] and [F^-] were defined such that the maximum quenching or enhancement was reached instantaneously and are summarised in Table 4.2. The luminescence spectra of the mixed solution were then recorded under the varous combined conditions of [H^+] and [F^-]. For two input stimuli there are four possible combined Input states corresponding to: i) a "neutral" state where neither H^+ nor F^- are present, termed the (0,0) state; ii) two complementary states where a single component is present, the (1,0) and (0,1) states; and iii) a final (1,1) state, in which both stimuli are presented simultaneously.

Table 4.2 Summary of the solution concentrations of $Input_1$ and $Input_2$ in each possible logic state

Input State	**Concentration (M)**	
($Input_1$, $Input_2$)	H^+	F^-
(0,0)	-	-
(0,1)	-	1×10^{-3}
(1,0)	2×10^{-3}	-
(1,1)	2×10^{-3}	1×10^{-3}

The time-gated emission spectra of the mixed solution of **[Eu.(122)$_3$]$^{3+}$** (c = 2.5 × 10^{-5} M) and **[Tb.(126)$_3$]$^{3+}$** (c = 5 × 10^{-6} M) in CH_3OH are shown in Figure 4.11 from the four Input states. The corresponding fluorescence spectra are shown in Figure 4.12. Both Eu^{III}- and Tb^{III}-centred transitions were observed. The addition of H^+ to the (0,0) state switched the system into the (1,0) input state. The luminescence responses from **[Eu.(122)$_3$]$^{3+}$** and **[Tb.(126)$_3$]$^{3+}$** were in agreement with the expected behaviours.

A two-fold enhancement in Eu^{III} emission was observed (as expected from the restriction of PET quenching by protonation of the pendent amine of **122**). The emission from Tb^{III} was instantaneously lost as can be clearly seen in the 'pure' $^5D_4 \rightarrow {}^7F_{6,5}$ transitions at 490 and 585 nm, respectively. In the Eu^{III} emission spectrum, the $^5D_0 \rightarrow {}^7F_0$ transition was observed. This suggested that **[Eu.(122)$_3$]$^{3+}$** was slightly de-symmetrised under the acidic conditions which allowed the $^5D_0 \rightarrow {}^7F_0$ transition to gain intensity.[67] The fluorescence was quenched upon acidification for both the naphthyl-**dpa** (λ_{em} = 280 nm) and **btp** (λ_{em} = 240 nm) emission bands. This was contrary to the initial solution studies of **[Tb.(126)$_3$]$^{3+}$**, however, was a reproducible change and likely a result of energy transfer processes between **[Eu.(122)$_3$]$^{3+}$** and **[Tb.(126)$_3$]$^{3+}$**.

Treating the (0,0) state with TBAF (1 mM) achieved the (0,1) Input state and the expected quenching of both the Eu^{III}- and Tb^{III}-centred emission was observed (by 100% and 65%, respectively). In contrast, the ligand-centred fluorescence for both the **btp** and the

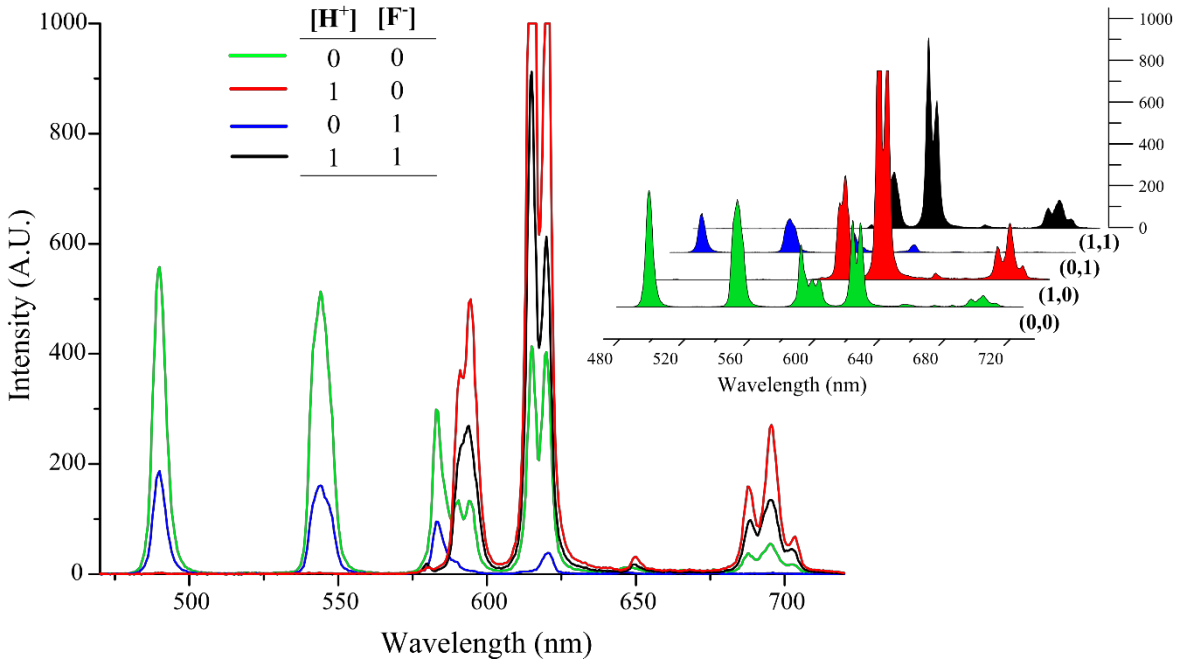

Figure 4.11 Phosphorescence emission spectra overlaid from each logical input state combining H^+ and F^-, showing (0,0) in green, (1,0) in red, (0,1) in blue and (1,1) in black, ***inset***: 3D representation of the emission spectra for clarity. Spectra were recorded at 298K in CH_3OH using the parameters described in Table 4.1.

naphthyl-**dpa** features were enhanced significantly (*ca*. five-fold increase). This was consistent with the dissociation of **[Tb.(126)$_3$]$^{3+}$** and the basic interaction of F^- with the 4-aminopyridyl moiety[468] resulting in increased fluorescence. Applying both H^+ and TBAF simultaneously resulted in the formation of the (1,1) input state. The Tb^{III}-centred emission was completely quenched, while the Eu^{III}-centred luminescence was enhanced. The fluorescence changes were equivalent to those seen on treatment with TBAF and emission from both **122** and **126** were enhanced.

In addition to unique spectra being recorded for each Input state, the visible colours of the solutions (as perceived by the 'naked eye' when irradiated with UV-light, λ_{exc} = 254 nm) were different in each of the Output states and provided an additional visual readout to the system. As a result of the three main emissions arising from the Eu^{III} and Tb^{III} emission and the ligand-centred fluorescence which are red, green and blue, respectively, the final colours of the solution were an additive result from three primary colour channels. This allowed access to various colours dependent on the relative levels of quenching and enhancement in each case for **[Eu.(122)$_3$]$^{3+}$** and **[Tb.(126)$_3$]$^{3+}$** gave rise to the distinguishable 'naked-eye' readouts, as shown in Figure 4.12b. Here, the solution was green in the (0,0) state, red in the (1,0) state, blue in the (0,1) state and pink-purple in the (1,1) state. The changes in the ratios of the Eu^{III}, Tb^{III} and ligand-centred emission were subsequently

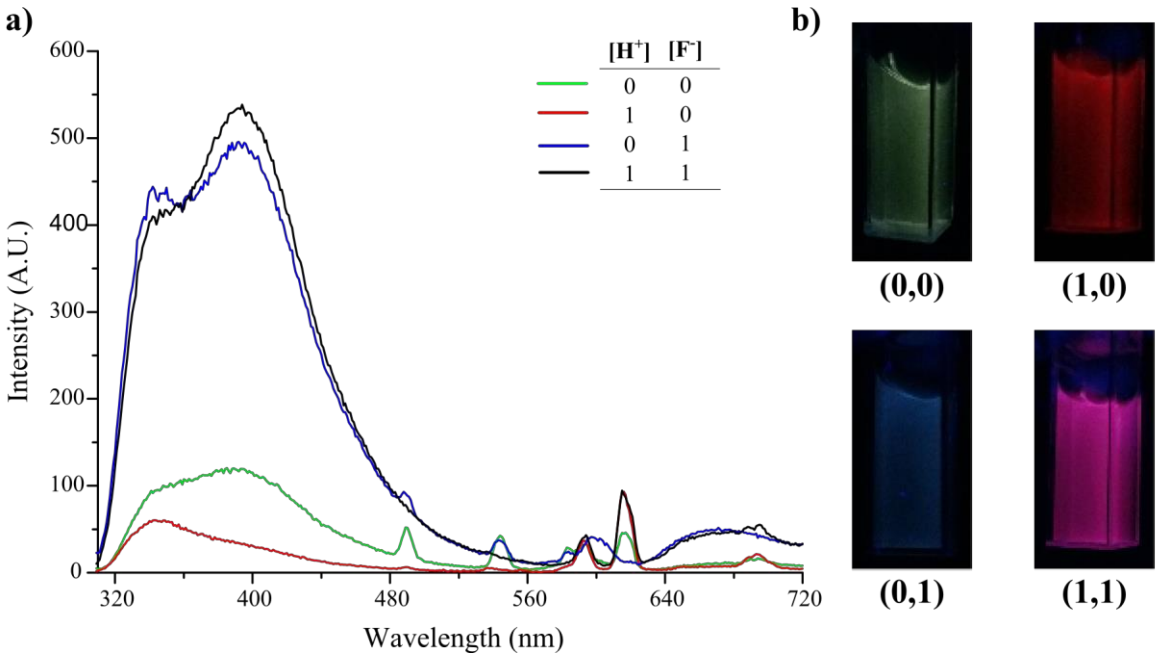

Figure 4.12 a) Fluorescence emission spectra overlaid from each logical input state combining H^+ and F^-, showing (0,0) in green, (1,0) in red, (0,1) in blue and (1,1) in black; **b)** photographs of experimental solutions from each logical input state under UV-light (λ_{em} = 254 nm) showing the clear naked-eye difference between conditions. Spectra were recorded at 298K in CH_3OH using the parameters described in Table 4.1.

described as logic functions with the analysis of the each emission Outputs as parameterised as a unique logic gate.[509]

4.4.2 Logical Analysis & Parameterisation

Additional conditions to the Inputs discussed above were imposed to generate a binary nature on each Output and define when the switch between OFF/"0" and ON/"1" occurred. The Output channels were simplified to single transitions that could be unambiguously assigned to **[Tb.(126)$_3$]$^{3+}$**, **[Eu.(122)$_3$]$^{3+}$** and **126**. These corresponded to the time-gated emission at λ_{em} = 490 nm, 615 nm and fluorescence at λ_{em} = 345 nm, respectively.

Normalised intensity thresholds (expressed as percentage changes in emission and independent of the arbitrary measurement parameters) were applied to the individual transitions in order to give the smallest probability of false switching and a maximum error of 10%. In absolute terms, these afforded the thresholds that are shown in Figure 4.13a-c. The thresholds applied represented one of a number of possible arbitrary assignments and were selected to provide the richest overall information from the system. For example, these thresholds avoided the simultaneous use of TRANSFER$_{[H+]}$ and NOT TRANSFER$_{[H+]}$ which in the same circuit would simply provide reciprocal information about the H^+ input, see Appendix A4 for further representations. A truth table, shown in Figure 4.14a, which described the relevant "1"/ON or "0"/OFF state for each emission channel, with respect to the four, Input states was constructed.

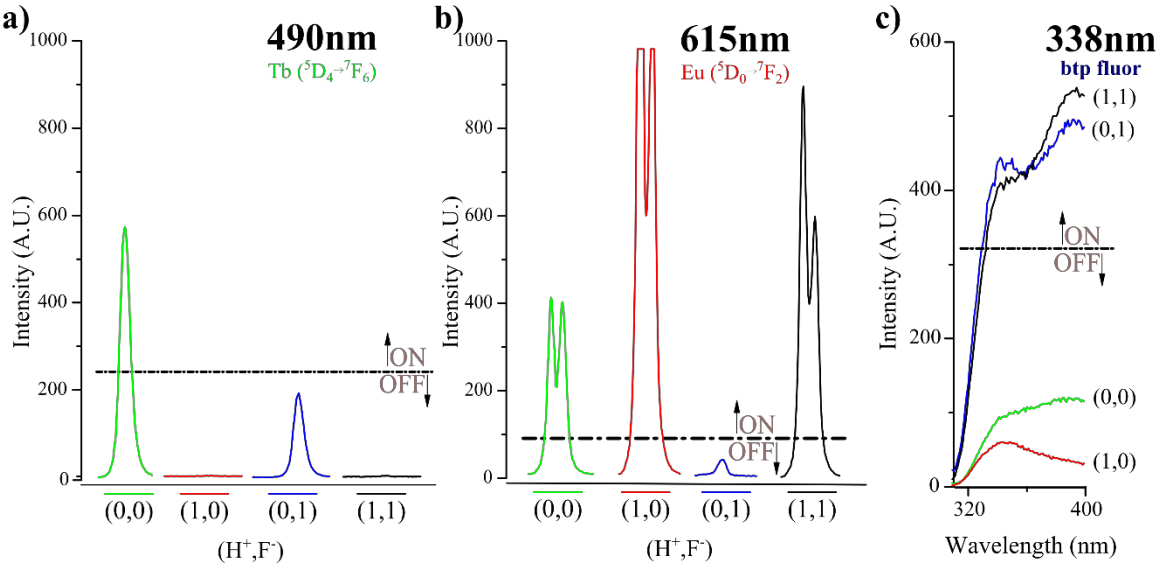

Figure 4.13 Spectroscopic Output thresholds applied to key emissions from the solution spectra in each logic input state: **a)** $^5D_4 \rightarrow {}^7F_6$ transition of **[Tb.(126)$_3$]$^{3+}$** (λ_{em} = 490 nm) representing NOR logic; **b)** $^5D_0 \rightarrow {}^7F_2$ transition of **[Eu.(122)$_3$]$^{3+}$** (λ_{em} = 615 nm) representing IMPLICATION logic: **c)** ligand fluorescence from **126** (λ_{em} = 345 nm) representing TRANSFER logic. Spectra were recorded at 298K in CH_3OH using parameters defined in Table 4.2. Ln^{III}-centred emissions were recorded as phosphorescence, **126**-centred emission was recorded as fluorescence.

The green channel from Tb^{III}-centred emission (λ_{em} = 490 nm) had a threshold applied of 62% quenching. Therefore, the output was determined to be "1"/ON in the (0,0) state only and "0"/OFF in all the stimulated states, Figure 4.13a. This corresponded to a NOR logic mimic, shown schematically in Figure 4.14c, which gave a positive output only when "neither H^+ *NOR* F^-" were present and gave the negative output under all other conditons. The red channel from Eu^{III}-centred emission (λ_{em} = 615 nm) was subject to the threshold of 90% quenching compared to the emission of the initial (0,0) state, shown in Figure 4.13b. This gave the Output as "1"/ON for all states except in the presence of F^- alone. This represented Reverse-IMPLICATION$_{[F^-]}$ logic, Figure 4.14b, which reports specifically on the presence of the F^- without H^+ by switching the Output state to "0"/OFF.

The fluorescence emission from **126**, the blue channel, was restricted by the threshold a 360% enhancement in emission from the initial (0,0) state to switch "0"/OFF to "1"/ON. This resulted in Outputs of "0"/OFF in the (0,0) and (1,0) states where neither Input was present and when was present H^+ alone, respectively. The system was then switched to "1"/ON in the states of (0,1) and (1,1) when F^- was present alone and when both F^- and H^+ Inputs were present together, respectively. This corresponded to the fundamentally simple logical idea of TRANSFER$_{[F^-]}$ and acted as a YES gate for F^- within the two-input system. Each of these logic functions is represented schematically using Venn diagrams, Figure

a)

Input$_1$ $[H^+]^a$	Input$_2$ $[F^-]^b$	Output$_1$ 615 nm^c	Output$_2$ 490 nm^c	Output$_3$ 345 nm^d
0	0	1	1	0
1	0	1	0	0
0	1	0	0	1
1	1	1	0	1
		Reverse IMPLICATION$_{[H^+]}$	NOR	TRANSFER$_{[F^-]}$

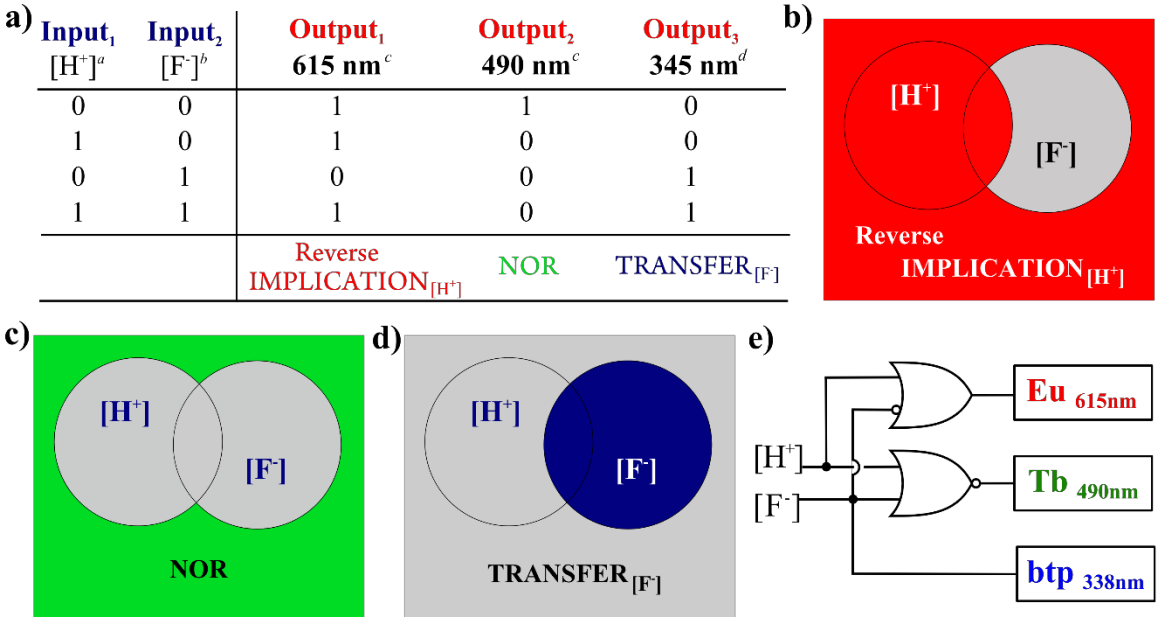

Figure 4.14 Logical analysis of solution MLGM. **a)** Truth table for each Input state indicating 1 or 0 as Output for each emission channel: λ_{em} = 615 nm (**[Eu.(122)$_3$]**$^{3+}$ metal-centred emission), λ_{em} = 490 nm (**[Tb.(126)$_3$]**$^{3+}$ metal-centred emission) and λ_{em} = 345 nm (**126** fluorescence) and the respective logic functions; **b)** Venn diagram for 615 nm (red) output as Reverse IMPLICATION logic; **c)** Venn diagram for 490 nm (green) output as NOR logic; **d)** Venn diagram for 345 nm (blue) output as TRANSFER logic; **e)** logic circuit diagram for parallel solution implementation of the MLGM outputs.

4.14b-d, which visually demonstrate the set of conditions in which the emission Output was defined as 1/"ON".

The three logic functions were combined to produce a logic circuit which implemented the different gates in parallel. This circuit is shown in Figure 4.14e using the established standards.[533] In addition to each Output channel mimicking a different logic function, each Input state corresponded to a unique combination of the binary Outputs (*e.g.* 110 and 101, for the (0,0) and (1,1) states, respectively) and therefore, the stimuli present could be identified unambiguously when the three Output states were considered simultaneously.

The solution-based logic circuit operated robustly and reproducibly to provide a rich information output. However, the solution system displayed limitations. The MLGM was not reversible since the dissociation products of **[Tb.(126)$_3$]$^{3+}$** (while being fundamental to the responsive behaviour) did not re-associate readily and the MLGM function could not be returned to the original (0,0) resting state. Moreover, as the containment of any free solution-phase system is low, and particularly since this system dissociated, there are no realistic prospects to the application within a bulk environment or those where contamination of the sample environment is inappropriate. Therefore, a similar approach to that described in Chapter 3 for the development of luminescent hydrogel pH probes was pursued to address the containment of the MGLM system and polymer gels were synthesised with the responsive complexes encapsulated with internal microenvironment.

4.5 Hydrogel and Organogel Inclusions

It is known that changes in the microenvironment can strongly influence the behaviour of encapsulated species and also their photophysical performance.[534,535] However, it was demonstrated for **[Eu.(122)$_3$]$^{3+}$** alone (Section 3.7) that the responsive behaviour was retained when encapsulated within p(HEMA-*co*-EGMDA). Furthermore, **[Eu.(122)$_3$]$^{3+}$**, which was not water soluble, could be used within an aqueous environment. Therefore, it was proposed that p(HEMA-*co*-EGDMA) could be used as a suitable matrix for both **[Eu.(122)$_3$]$^{3+}$** and **[Tb.(126)$_3$]$^{3+}$** to address the containment limitations. The development of hydrogels was not successful due to instability of **[Tb.(126)$_3$]$^{3+}$** to H_2O which resulted in the immediate quenching of Tb^{III} emission when swelled in an aqueous environment (Appendix A4). As a result, polymer organogels using p(HEMA-*co*-MMA-*co*-EGDMA) were developed as soft material hosts for the **[Eu.(122)$_3$]$^{3+}$** and **[Tb.(126)$_3$]$^{3+}$** complexes.

4.5.1 Synthesis and characterisation of organogels

The p(HEMA-*co*-MMA-*co*-EGDMA) materials were prepared in the same manner as in described for **[Eu.(122)$_3$]$^{3+}$** hydrogels in Section 3.7.1. However, small modifications were required for successful inclusion of **[Tb.(126)$_3$]$^{3+}$**. The **[Tb.(126)$_3$]$^{3+}$** complex was not directly soluble in HEMA and a co-solvent was required. It is well known in polymer gel synthesis that residual co-solvents can influence internal structure, emulsification and final porosity.[469,536] However, CH_3CN was found to be a suitable volatile solvent that would solubilise the complex initially but easily volatilise during the free radical polymerisation and heat curing. The resulting materials were consistent with p(HEMA-*co*-EGDMA) in terms complex distribution throughout the polymer solid phase and optical transparency.

Complex **[Eu.(122)$_3$]$^{3+}$** was dissolved into a mixture of 75% HEMA and 25% MMA (v/v) at 0.02 wt% with 1 wt% EGDMA, which was added as cross-linker. After the formation of a homogenous solution had occured, a concentrated solution of **[Tb.(126)$_3$]$^{3+}$** (1.0 mg in 200 µL CH_3CN) was added and the resulting mixture stirred until the solution was well homogenised within the HEMA-MMA-EGDMA mixture. The addition of AIBN at 1% w/w afforded the final precursor solution. This solution was transferred to a cast (thickness of 1.2 mm) and placed at 90 °C to initiate the thermal polymerisation. The bulk polymerisation of the hard acrylic monolith was complete after 90 minutes and the material was heat-cured at 90 °C for a further 4.5 hours. The materials were then cooled to ambient temperature, after which the hard materials could be released from the moulds.

The acrylic materials formed from a 25% MMA in HEMA monomer mixture can be swelled in neat CH_3OH and, unlike HEMA in CH_3OH, retain the structural integrity

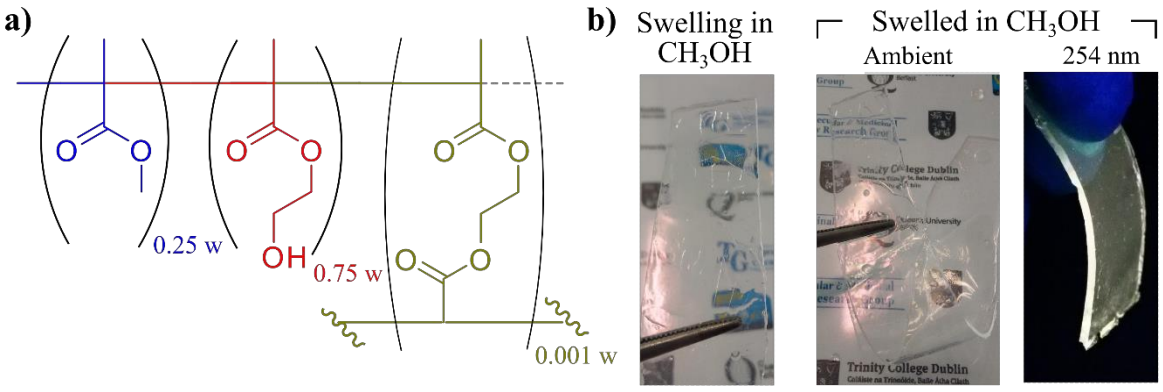

Figure 4.15 Co-polymer organogels containing **[Eu.(122)$_3$]$^{3+}$** and **[Tb.(126)$_3$]$^{3+}$**, **a)** structural representation of the polymer matrix as a random co-polymer of MMA (blue), HEMA (red) and EGDMA (green); **b)** photographs of visual inspection of **i)** polymer organogel during the swelling process in CH_3OH showing internal stress and 'cracking'; **ii)** polymer organogel equilibrated in CH_3OH showing the recovery of optical clarity and reducing in visible stresses and fractures; and **iii)** equilibrated organogel under UV light (λ_{exc} = 254 nm) showing stable emission from both **[Eu.(122)$_3$]$^{3+}$** and **[Tb.(126)$_3$]$^{3+}$** complexes.

necessary to handle and analyse the materials. The p(HEMA-*co*-MMA-*co*-EGDMA) swelled rapidly and softening was observed within 20 minutes of submersion in the CH_3OH solvent. The mechanism of organogel swelling was clearly different to the aqueous hydrogels and apparent "cracking" of the matrix during the swelling process was observed, as can be seen in Figure 4.15b. This effect was significant and uniform across the material during the first hours of swelling. Upon extended submersion in solvent, *i.e.* > 2 hours, the "cracks" disappeared and the materials were uniformly transparent. It is proposed that this was an effect of solvent swelling strain[537] and an optical effect caused by unequal swelling rates of partial phase separations[538] in the random copolymer. No evidence of detrimental effects on the internal porous structure from the swelling was observed. The emission and absorbance spectra of the supernatant solutions from CH_3OH swelled materials were measured. This did not show any evidence of leeching of either of the complexes and indicated that expansion of the material did not significantly increase the pore sizes. The polymer organogels were flexible, but remained mechanically, and the gels could be bent without immediate tearing of the samples. This robustness was a direct effect of the MMA additive as HEMA organogels swelled from CH_3OH split readily and were broken even on gentle handling.

Using CH_3OH as the swelling solvent gave a stable and reproducible initial (0,0) state that to 'naked-eye' observation, under UV irradiation at $\lambda_{exc} = 254$ nm, the gel materials appeared yellow to greenish-yellow in colour. The corresponding emission spectrum of the gels is shown in Figure 4.16a. The emission was uniform across the gels suggesting a

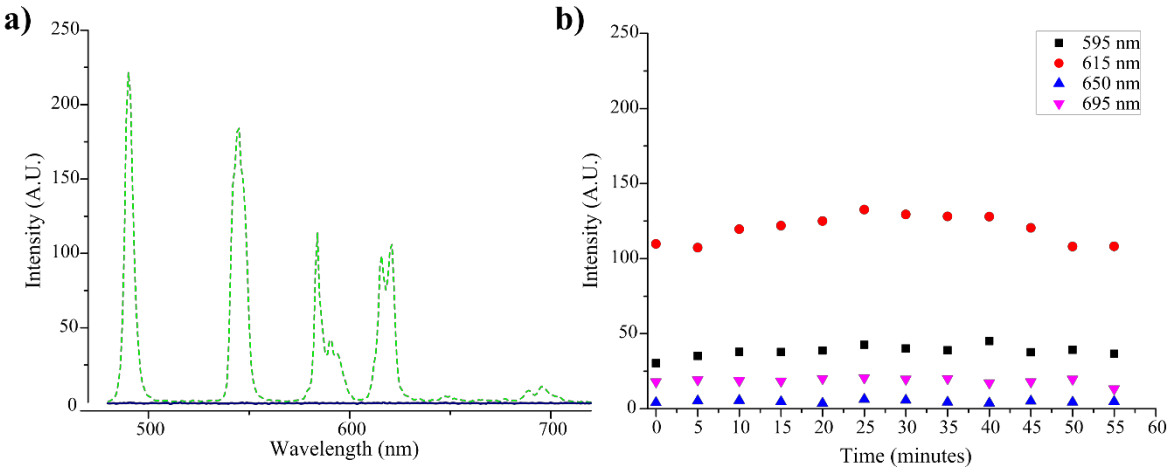

Figure 4.16 Luminescence measurements of poly(HEMA-*co*-MMA-*co*-EGDMA) organogels swelled in CH_3OH; **a)** Emission spectrum of the organogel + supernatant under neutral conditions (green, dashed) and the supernatant solution after treatment with 10-fold excess Tb^{III} for 60 minutes (blue, solid); **b)** intensities of emission from $^5D_0 \rightarrow {}^7F_{1,2,3,4}$ emissions of Eu^{III} over 60 minutes treatement with 10-fold excess Tb^{III} showing stable emission. All measurements were recorded at 298K, solutions were stirred between each recorded spectrum.

continuous and evenly distributed internal environment. The ratio of the lanthanide emissions were as expected from the loadings of the dry acrylic monoliths and demonstrated that **[Tb.(126)$_3$]$^{3+}$** remained stable. Satisfyingly, in the swelled materials enhancement in emission was retained and quenching by internal solvent[539] had a minimal effect.

The stability of the entire system was validated further by the emission behaviour of **[Eu.(122)$_3$]$^{3+}$** and **[Tb.(126)$_3$]$^{3+}$** when exposed to an excess of 'free' Tb^{III} ions. During the dissociation of **[Tb.(126)$_3$]$^{3+}$** 'free' Tb^{III} was generated, therefore the gel was exposed to an excess (> 10-fold) of Tb^{III}, as $Tb(CF_3SO_3)_3$, and the emission recorded over time, as shown in Figure 4.16b. The emission was stable which demonstrated there was no dynamic exchange of the ligands or changes in complex stoichiometry within the material. This was an encouraging result since the > 10-fold excess of these experiments was substantially greater than was ever generated under the material operating conditions where the ratio of Tb^{III}:Eu^{III} was ≈ 1:2. Having manufactured a stable emissive polymer gel, the responsive behaviour with $[H^+]$ and $[F^-]$ was studied in the same manner as the solution model and the output changes monitored using emission spectroscopy.

4.5.2 Spectroscopic Responses of organogel-based MLGMs

Samples (30 mm × 10 mm × 1.2 mm) were cut from the swelled gels and suspended in CH_3OH, within a quartz cuvette, and conditional changes were made to the supernatant solution in the same manner as for the free CH_3OH solution. The same definitions of $[H^+]$ and $[F^-]$ input conditions as for the solution were used (2 mM and 1 mM, respectively). The spectra were recorded at constant temperature (24 °C) to ensure the porosity of the equilibrated gels remained constant.[540] In the solution studies, described in Section 5.5.1, the equilibrium state of each conditional change was reached rapidly and the emission changes were instantaneous. However, the response times of the organogels were found to be much slower. The response time of the porous gels was diffusion controlled as was expected by the compartmentalisation of the internal solvent environment from the bulk supernatant. The diffusion effects of acrylate hydrogels are well studied and varies with gel thickness (diffusion length) and surface area (accessible pores).[537] Therefore, materials of constant thickness (1.2 mm) were used and the response was measured after 20 minutes equilibration. This corresponded to the timeframe in which major changes were complete. The time-gated and fluorescence emission spectra are shown in Figure 4.17 and Figure 4.18, respectively.

Upon acidification to afford the (1,0) state, the intensity of Eu^{III} emission was enhanced along with the concomitant quenching of the Tb^{III}-centred emission. A 50% enhancement in the fluorescence associated with **[Tb.(126)$_3$]$^{3+}$/126** at λ_{em} = 338 nm was

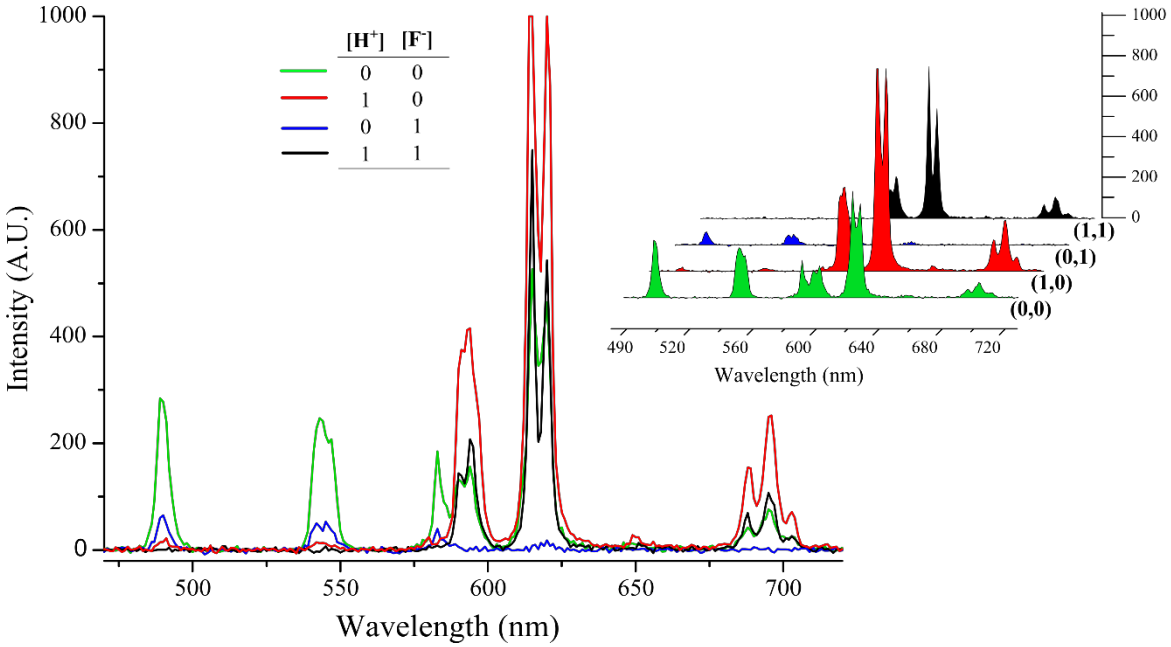

Figure 4.17 Phosphorescence emission spectra of the organogels, overlaid from each logical input state combining H^+ and F^-, showing (0,0) in green, (1,0) in red, (0,1) in blue and (1,1) in black, ***inset***: 3D representation of the emission spectra for clarity. Spectra were recorded at 298K while suspended in CH_3OH using the Inputs described in Table 4.1.

observed along with the loss of the shoulder of this band and enhanced Eu^{III} emission. The Ln^{III}-centred luminescence enhancement was consistent with the solution studies, while the fluorescence was inconsistent and indicated that the interactions in the microenvironment between solvent and the complexes were different. The changes observed were in agreement with the mechanisms of PET quenching and complex dissociation for **[Eu.(122)$_3$]$^{3+}$** and **[Tb.(126)$_3$]$^{3+}$**, respectively. Concomitant with the increase in intensity a red-shift of the emission maximum *ca.* 5 nm was observed. This emission wavelength was not equivalent to that recorded for **126** or **[Tb.(126)$_3$]$^{3+}$** in CH_3OH solution. Therefore, the emission was assigned to be characteristic of the protonated ligand **126-H$^+$** following dissociation of the Tb^{III} complex. The relative changes in the emissions were clearly reflected in the colour visible to the naked eye when the gels were irradiated with UV-light (λ_{em} = 254 nm). The Eu^{III} emission was dominant and resulted in gels that were strongly red luminescent, Figure 4.18b.

Alternatively, treating the gels with TBAF (c = 1 × 10^{-3} M) gave to (0,1) state and again resulted in a similar response to that seen in the solution studies. A quenching in the Tb^{III} emission to approximately the same extent was observed (*ca.* 80% reduction in intensity). The fluoridation also resulted in the complete quenching of the Eu^{III}-centred emission from **[Eu.(122)$_3$]$^{3+}$**. The change in Tb^{III}-centred luminescence was again assigned to the stimulated dissociation of **[Tb.(126)$_3$]$^{3+}$** by F^-, while the quenching of Eu^{III}-centred

emission was accounted for by the quantitative deprotonation of **[Eu.(122)$_3$]$^{3+}$** by F^-. The deprotonation of the pendent amine resulted increased PET efficiency that reduced the **122** → Eu^{III} sensitisation efficiency (as described in Chapter 3). As a result of the quenching of both red Eu^{III} and green Tb^{III} emission, the final colour of the materials was accounted for solely by the ligand fluorescence. On the fluorescence timescale, a significant enhancement in intensity across both ligand-centred bands (330 – 500 nm) was observed. The order of enhancements in the **126** and **122**-centred emission was not consistent with the solution-based MLGM and again demonstrated the influence of the matrix upon the chromophore excited-states and photophysical processes.

Furthermore, a larger red-shift (*ca*. 8 -10 nm) than that observed from treatment of the gels with H^+ was observed after fluoridation. This was thought to arise from a common dissociation process; however, in the presence of F^- there is also the possibility of the formation of a triazole-CH•••F interaction.[541,542] The dominant fluorescence gave the gels a strong blue colour to the naked eye, as shown in Figure 4.18b, which was consistent with the solution, Figure 4.12b.

The final conditional state, the (1,1) state, was achieved when both H^+ and F^- were simultaneously present in solution. This state was generated by the simultaneous addition of both F^- and H^+ to the system. However, it is important to note that, as an equilibrium position, the final state showed no difference in the response after 20 minutes equilibration if prepared

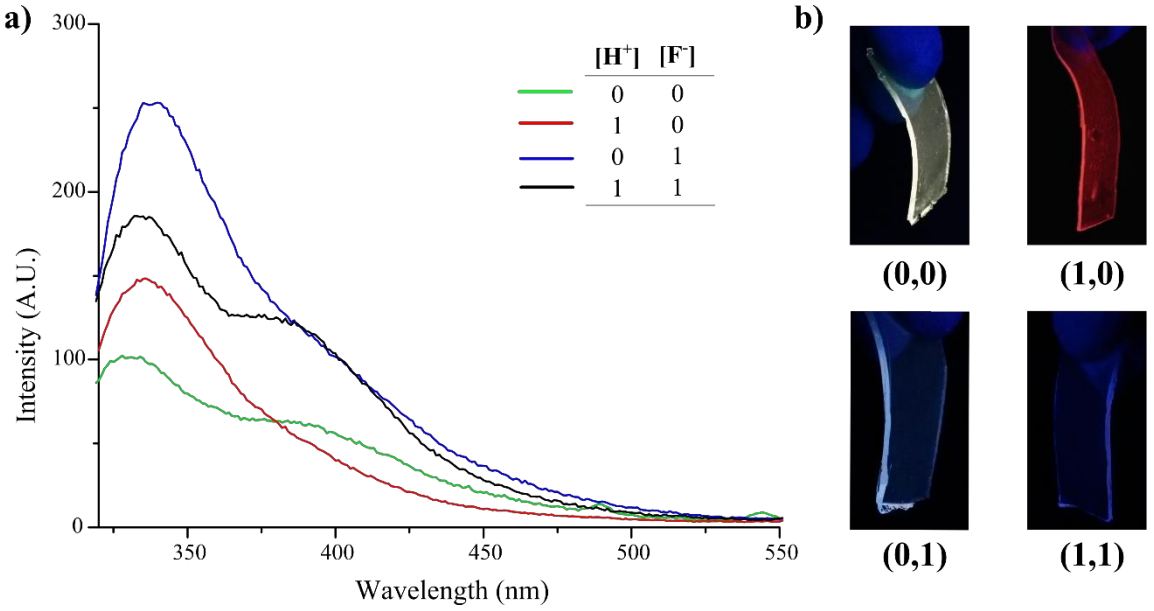

Figure 4.18 a) Fluorescence emission spectra from the organogels, overlaid from each logical input state combining H^+ and F^-, showing (0,0) in green, (1,0) in red, (0,1) in blue and (1,1) in black; **b)** photographs of experimental solutions from each logical input state under UV-light (λ_{exc} = 254 nm) showing the clear naked-eye difference between conditions. Spectra were recorded at 298K while suspended CH_3OH using the parameters described in Table 4.1

from sequential addition of acid and fluoride. In the (1,1) input state substantial quenching of the Tb^{III}-centred emission was observed with concomitant enhancement of Eu^{III}-centred transitions, as shown in Figure 4.17. The Tb^{III}-centred emission from **[Tb.(126)$_3$]$^{3+}$** was completely quenched (as was seen from treatment with H^+) and indicated complete dissociation. The Eu^{III}-centred emission enhanced to a smaller extent than that observed on treatment with H^+ alone which was consistent with the equilibrium achieved from protonation and deprotonation by H^+ and F^-, respectively. Simultaneously, the fluorescence emission of **126** and **[Eu.(122)$_3$]$^{3+}$** were enhanced, as shown in Figure 4.18, with both fluorescence bands increasing approximately two-fold. The emission maximum of **126**-centred fluorescence was again red-shifted *ca*. 5 nm and was consistent with the shift from treatment with H^+ alone suggesting the emission arose predominantly from dissociated **126-H$^+$** ligands. This was consistent with the conditions since H^+ was in excess with respect to F^-. The organogel appeared purple to the naked eye, consistent with combined Eu^{III}-centred emission and blue ligand fluorescence, as shown in Figure 4.18b.

The luminescence behaviours observed were consistent between the solution and gel systems and the responses of the organogels were also parameterised as logic functions.

4.5.3 Logical Analysis & Parameterisation

Thresholds were applied to the spectra recorded in the studies as described above for the solution model. The individual output emission spectra and the corresponding thresholds are shown in Figure 4.19. These thresholds represent the most versatile and robust logic functions. Despite the difference in fluorescence behaviour between the solution and gel, the two systems mimicked the same logic gates. Therefore, the truth table representations for each Output channel of the gel matched those shown in Figure 4.14a; although the fluorescence output maximum was shifted from λ_{max} = 345 nm to λ_{max} = 338 nm.

The fluorescence at 338 nm gave two states reporting ON/"1" and two states reporting OFF/"O". Both the ON/"1" Output values coincided only with the presence of F^- and the blue channel output mimicked a "proposition transfer" for [F^-] and operated as $TRANSFER_{[F-]}$ logic. Again, the emission from Tb^{III} at 490 nm behaved as $NOR_{[H+]/[F-]}$ and gave a positive readout only when neither stimulus was present in the system. The Eu^{III} emission was above the ON/"1" threshold in every condition except when [F^-] was presented to the system alone producing the $Reverse\text{-}IMPLICATION_{[H+]}$ function. However, the gel-based MLGM exhibited more freedom in threshold application and reconfiguration of the logical operations compared to the free solution model. This was a result of the change in fluorescence changes between the two systems. The conditions meant that only one threshold

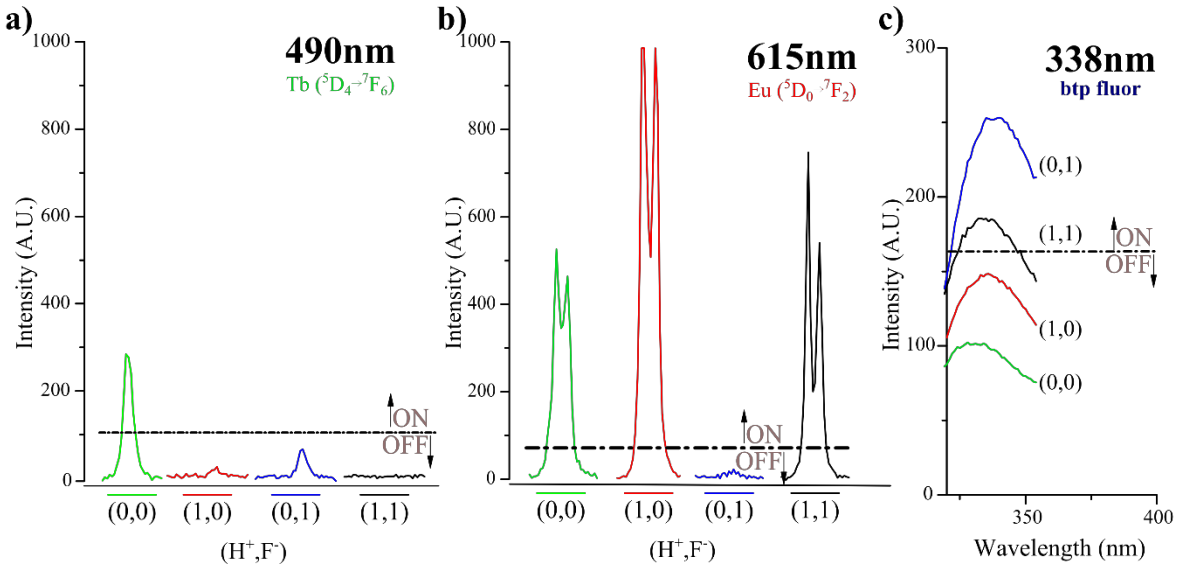

Figure 4.19 Spectroscopic Output thresholds as applied to key emissions from the organogel spectra in each logic input state: **a)** $^5D_4 \rightarrow {}^7F_6$ transition of **[Tb.(126)$_3$]$^{3+}$** (λ_{em} = 490 nm) representing NOR logic; **b)** $^5D_0 \rightarrow {}^7F_2$ transition of **[Eu.(122)$_3$]$^{3+}$** (λ_{em} = 615 nm) representing IMPLICATION logic: **c)** ligand fluorescence from **126** (λ_{em} = 338 nm) representing TRANSFER logic. Spectra were recorded at 298K in CH_3OH using parameters defined in Table 4.2. Ln^{III}-centred emissions were recorded as phosphorescence, **126**-centred emission was recorded as fluorescence.

for Tb^{III}-centred emission (λ_{em} = 490 nm) was valid. However, for the Eu^{III}-centred luminescence (λ_{em} = 615 nm) two possibilities were available, and in the case of **126**-centred fluorescence arbitrary reconfiguration was more significant.

The Eu^{III} and fluorescence outputs from the polymer MLGM with the possible logic gate mimics marked are shown in Figure 4.20a and Figure 4.20b, for emission at 338 nm

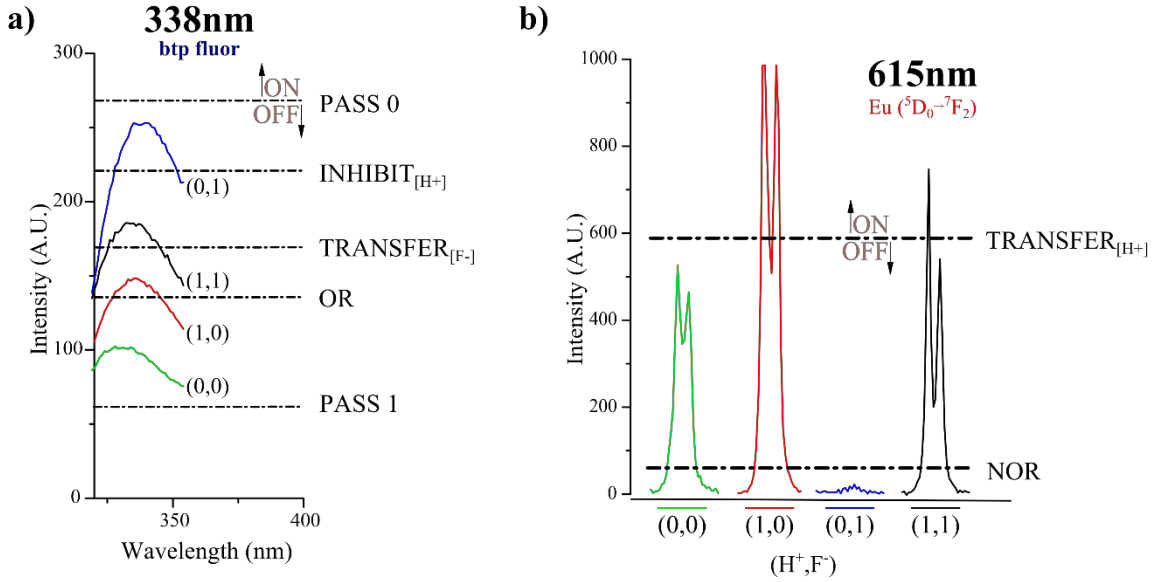

Figure 4.20 Possible threshold reconfigurations for organogel-based MGM in **a) [Tb.(126)$_3$]$^{3+}$/126**-centred fluorescence emission (λ_{em} = 338 nm) showing various logic functions of PASS, OR, TRANSFER and INHIBIT; **b) [Eu.(122)$_3$]$^{3+}$**-centred phosphorescence emission (λ_{em} = 615 nm) showing two functions NOR and TRANSFER. Thresholds are placed at intensities using the robustness criteria discussed above.

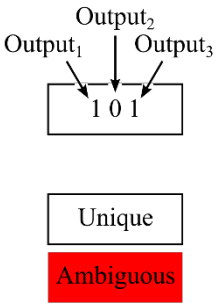

Logic Function Mimicked by Output$_3$ (λ= 338 nm fluorescence)

Input State	PASS 0	PASS 1	OR	TRANSFER [F⁻]	INHIBIT [H+]
(0,0)	1 1 0	1 1 1	1 1 0	1 1 0	1 1 0
(1,0)	1 0 0	1 0 1	1 0 1	1 0 0	1 0 0
(0,1)	0 0 0	0 0 1	0 0 1	0 0 1	1 0 1
(1,1)	1 0 0	1 0 1	1 0 1	1 0 1	1 0 0

Figure 4.21 The combined three-fold Output states for each of the four possible Input states to the organogel MLGM under the various reconfigurations of the thresholds of ON/OFF switching for **Output$_3$** (λ_{em} = 338 nm fluorescence from **126**) showing that only TRANSFER$_{[F-]}$ provides unique Output states for each Input state. Entries in red represent ambiguous Output states. **Output$_1$**: λ_{em} = 615 nm from Eu^{III}; **Output$_2$**: λ_{em} = 490 nm from Tb^{III}.

and 615 nm, respectively. The second valid threshold for Eu^{III}-centred emission at 615 nm converted the Reverse-IMPLICATION$_{[H+]}$ logic to a TRANSFER$_{[H+]}$ function and, in fact, reduced the available information provided by the circuit. There were numerous valid fluorescence thresholds for the Output at 338 nm because of the evenly stepped nature of each fluorescence maxima the spectra with respect to the initial (0,0) input state. As the threshold was placed at different levels, various functions could be considered varying between the trivial PASS 1/0 extremes and those which included more power, namely OR, NOR and INHIBIT. However, only when this Output was treated as TRANSFER$_{[F-]}$ could unique overall Output states be described for each Input combination (*i.e.* without Input states (1,0) and (1,1) being ambiguous) as shown in Figure 4.21.

Therefore, the parameterisation which takes the emissions of Eu^{III} as Reverse-IMPLICATION$_{[H+]}$, Tb^{III} as NOR$_{[H+]/[F-]}$ and **126**-centred fluorescence as TRANSFER$_{[F-]}$ was the most robust parameterisation in both systems and also the most rich information reduction. These three single-output MLGMs within the gel therefore mimicked the same double-input-three-output logic circuit observed in the solution model, Figure 4.14e. However, limitations to the operation and potential application were not successfully addressed.

4.5.4 Operational Robustness and Switching

While functioning as a MLGM, a number of issues were noted that limited the lifetime of operation and reversibility of the systems. Contrary to initial expectations from the hydrogel studies, the smaller **126** species (*i.e.* 'free', deprotonated or 'F^- bound') diffused out from the interior of the gel matrix and contaminated the supernatant solution; this leeching process was characterised further. As described above, the time-gated emission spectra recorded for the neutral system in the (0,0) state representing and strong characteristic emission from both

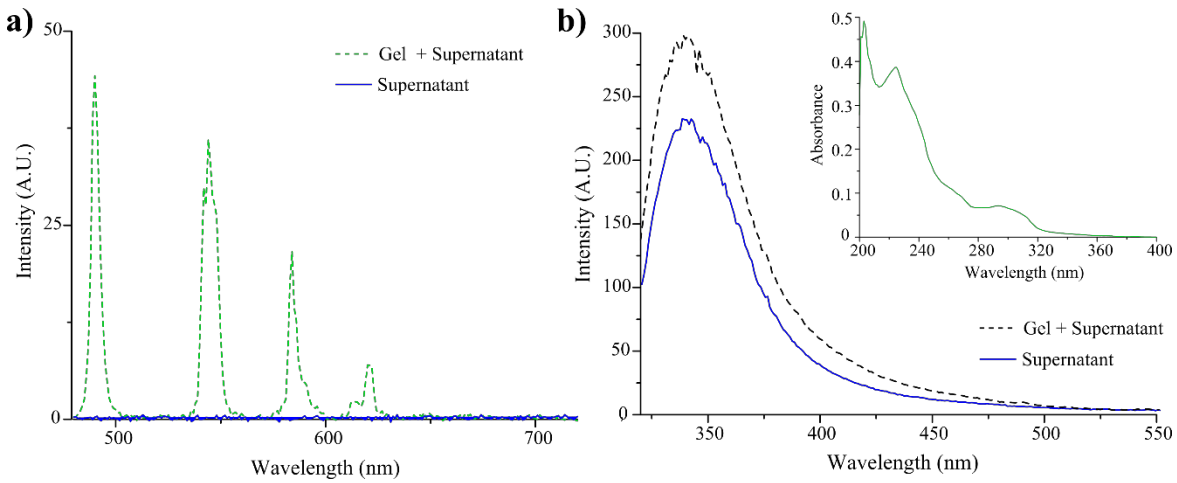

Figure 4.22 a) Phosphorescence emission spectra of the MLGM system (green dashed, organogel + supernatant solution) and the supernatant solution alone (blue) after treatment with TBAF, showing retention of **[Tb.(126)$_3$]$^{3+}$** within the polymer matrix; and **b)** fluorescence emission spectra of the MLGM system (black dashed, organogel + supernatant solution) and the supernatant solution alone (blue) after treatment with TBAF, showing diffusion of **126** (λ_{em} = 345 nm) into the bulk solution from inside the gel, ***inset*:** UV-visible absorption spectrum of supernatant solution showing key absorbance features of **126** external to the gel.

Eu^{III} and Tb^{III}, as shown in Figure 4.22a. The gels were suspended in stirred solutions for 18 hours and no decrease in emission was observed. The emission spectrum from the supernatant solution, also shown in Figure 4.22a, demonstrated that no emission from either **[Eu.(122)$_3$]$^{3+}$** and **[Tb.(126)$_3$]$^{3+}$** occurred outside the polymer matrix. This confirmed that there was no leeching of the complexes into the bulk solution and was in agreement with the measurements in excess Tb^{III} described in Section 4.6.3 above.

Treatment of the gels with F^- for 60 minutes resulted in the expected quenching in Eu^{III} and Tb^{III} emissions (by 100% and 75%, respectively). The luminescence spectrum of the supernatant, shown in Figure 4.23a, showed the remaining Tb^{III}-centred emission was still contained within the gel. The containment of **[Eu.(122)$_3$]$^{3+}$** after F^- treatment was also confirmed by the acidification of the gel and supernatant solutions. As shown in Figure 4.23b, Eu^{III}-centred emission was recovered within the gel matrix and not in the supernatant which implied **[Eu.(122)$_3$]$^{3+}$** was still contained by the polymer. A significant fluorescence signal was observed in the fluorescence spectra of the supernatant solution after exposure to F^- stimulus for the 60 minute period, shown in Figure 4.22, which was assigned exclusively to **126**. The UV-visible absorption spectra was also recorded of the supernatant, Figure 4.22b (inset), and confirmed the assignment **126** with the spectrum matching the structure known for the ligand.

The leeching that was observed for the organogels but not from hydrogels was most likely due to the mutual good solubility of **126** in both the internal microenvironment and

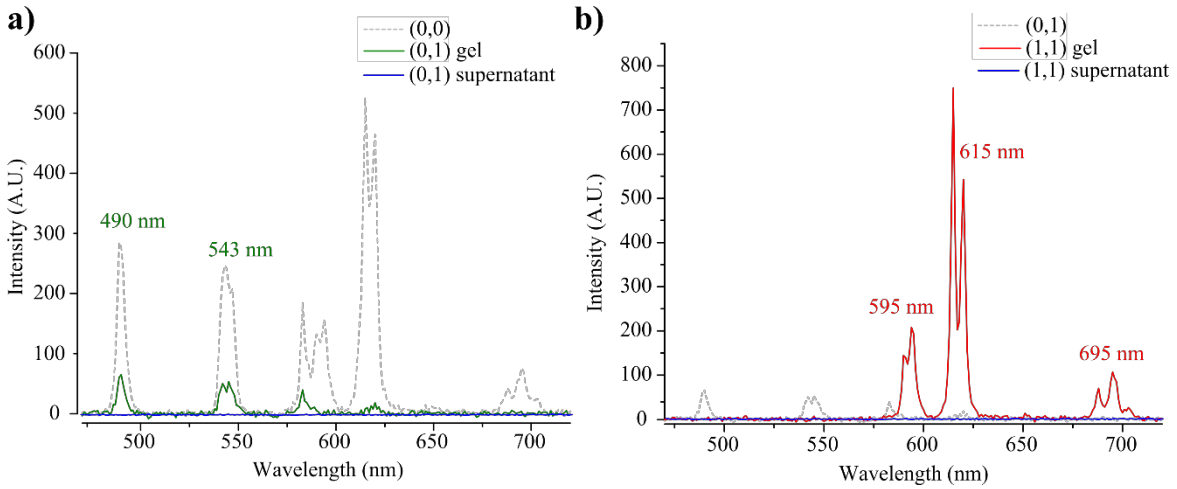

Figure 4.23 Phosphorescence spectra of a) the neutral organogel (grey dashed), the organogel treated with fluoride (green) and the supernatant solution (blue) and b) the organogel treated with fluoride (grey dashed), the organogel treated with fluoride then acid (red) and the supernatant solution (blue) showing the retention of both **Tb.(126)$_3$** and **Eu.(122)$_3$** within the gel matrix.

external bulk solvent. In hydrogel systems, the inclusion of species insoluble in aqueous media within the polymer microenvironment can be achieved by providing preferential solvation.[543,544] Since ligand **126** is both small and soluble in CH_3OH, organogel is not analogous since there are favourable solvation interactions both internally and externally to the gel material. Therefore upon dissociation of **[Tb.(126)$_3$]$^{3+}$** the small ligand **126** would not be expected to be size- or solvent- excluded from diffusion out of the gel. The release of **126** into the external environment weakened the MLGM by removing the reverse-switch since 'removal' of F^- by chemical means (*e.g.* silyl binding) would be ineffective as a fundamental probe would have been lost.

The consequence of the irreversibility was that the MLGM became a single use system. For the development of chemical sensors, one-time use (disposable) devices are common place across *in situ* diagnostic and point-of-care applications.[545-547] While not being suitable for long-time data processing, as a disposable sensor the use of Ln^{III} luminescent materials-based MLGM is an viable and attractive approach.

4.6 Conclusions and future perspectives

This chapter described the design and fabrication of a dual-probe responsive system from novel naphthyl-**dpa** and **btp** ligands (**122** and **126**, respectively) which operated as solution- and material-based MLGMs. The ligands and their respective complexes of **[Eu.(122)$_3$]$^{3+}$** and **[Tb.(126)$_3$]$^{3+}$** were characterised for their photophysical behaviour, **[Eu.(122)$_3$]$^{3+}$** having been discussed at length in Chapter 2, as independent species and isolated complexes. Complex **[Tb.(126)$_3$]$^{3+}$** showed unique behaviours with H^+ and F^- which were characterised by spectroscopic changes in Tb^{III}-centred phosphorescence, ligand-centred fluorescence, and

UV-visible absorption. Both H^+ and F^- were found to initiate dissociation of the complex resulting in Tb^{III} emission quenching with concomitant ligand fluorescence enhancement. A combined system of **[Eu.(122)$_3$]$^{3+}$** and **[Tb.(126)$_3$]$^{3+}$** in solution was studied as a solution-based MLGM. Photophysical independence of the two complexes was confirmed and the emissions from the ligands, Eu^{III} and Tb^{III} were found to be stable and reproducible. Analogous systems fabricated within polymer gels through the non-covalent inclusion of **[Eu.(122)$_3$]$^{3+}$** and **[Tb.(126)$_3$]$^{3+}$**. While hydrogels of p(HEMA-*co*-EGDMA) were unstable in their photophysical response, the formation of p(HEMA-*co*-MMA-*co*-EGDMA) organogels in CH_3OH was achieved. The fluorescence and time-gated emissions were monitored for the solution and organogel MLGMs under various combinations of $[H^+]$ and $[F^-]$ at 2 mM and 1 mM, respectively. The emissions at λ_{em} = 338, 490 and 615 nm were parameterised using intensity thresholds to converted emission to binary states of "1"/ON or "0"/OFF. From logical analysis, the responses of the materials were shown to mimic a parallel Reverse-IMPLICATION – TRANSFER – NOR logic circuit and colour mixing of the RGB Output signals gave 'naked eye' luminescent response. As a result of the Eu^{III}, Tb^{III} and **126** emissions corresponding to RGB colour channels, each states was found to have a distinct colour. The colour changes of both solutions and organogels were wide ranging (yellow green to red, blue or pink/purple under UV irradiation) when switching between all four logic states. Limitations of the MLGM were identified in both solution and polymer-gel systems. A leeching behaviour of **126** from the organogels under certain stimulus conditions was observed due to the dissociation of **[Tb.(126)$_3$]$^{3+}$** in CH_3OH systems. The free ligand **126** was too small to be retained within the polymer matrix and was subsequently released to the bulk.

In future development, the issue of leeching can be addressed or, in fact, exploited. While a limitation for sensing, the stimuli-initiated dissociation and subsequent diffusion of the free ligands from the gel could be exploited and applied in the controlled-release of functional **btp** ligands. Controlled release from polymer microgels has been well explored to date[469,548] and the privileged luminescence of the Ln^{III} ions could add an internal dosage-reporting mechanism for the level of a release. On the other hand, to directly address the leeching and prevent loss of the dissociated ligands approaches that covalently tethering the **btp** ligand to the polymer matrix should be considered. The structures shown in Figure 4.24, have been proposed for the development of Rehahn Type II metallopolymers (Section 1.7). A number of candidate ligand have been identified in **147 - 149**, derived from previous and currently research in the Gunnlaugsson group in collaboration with Dr. Joseph Byrne and

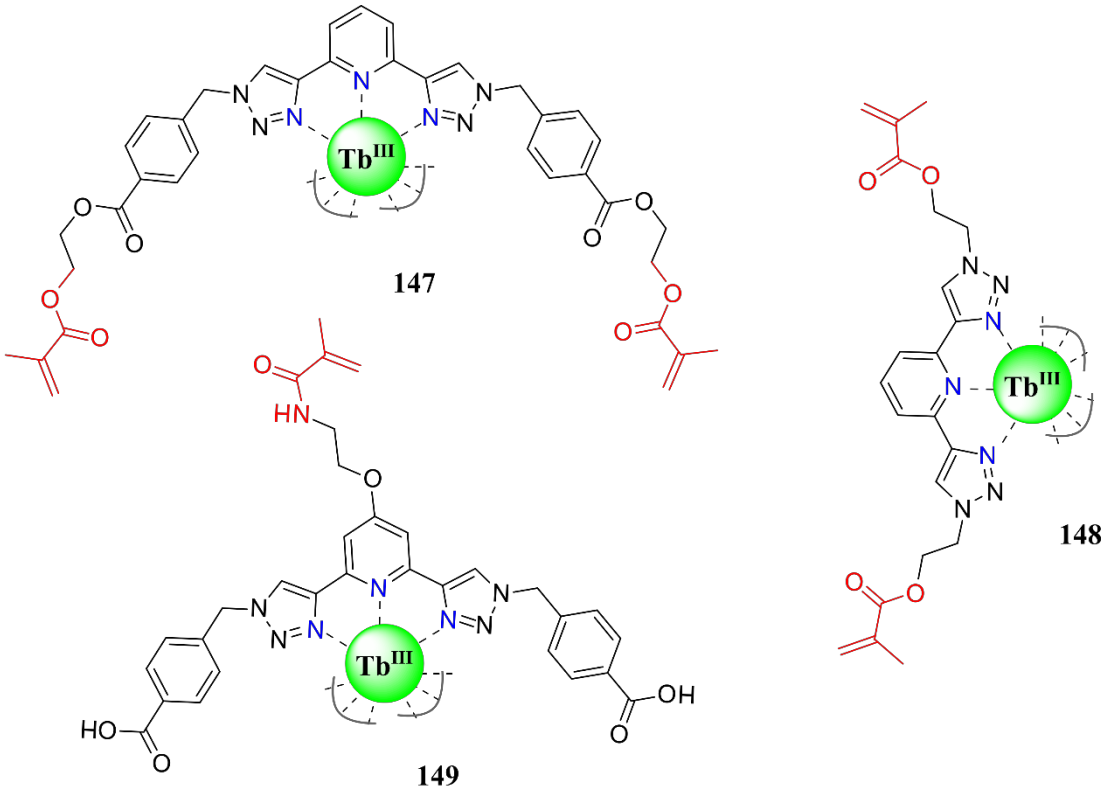

Figure 4.24 Structures of potential **btp**-derivatives (**147** - **149**) for covalent co-polymerisation of the Tb^{III}-complexes into the polymer matrix and prevent leeching upon complex dissociation.

Ms. Isabel Hegarty; further investigations within polymer systems will hopefully be forthcoming. The structures of **147** and **148** possess two methacrylate moieties and therefore may copolymerise to covalently link a **btp** unit into the hydrogel, or organogel, matrix. However, this would introduce additional structural modulations to the gels since they would certainly act as covalent crosslinkers in the same fashion as EGDMA. The consequences of this crosslinking could be to introduce additional response into the system or, rather, hinder the function further. In the case of **149**, the methacrylamide unit is introduced as a pendent chain and the bulk structure of the **btp** arms is equivalent to that seen in **126**; therefore, potentially retaining the same analyte interactions but unable to diffuse as a result of the covalent link. This ligand has a number of potentials applications (*c.f.* Chapter 5) and is currently under development in the Gunnlaugsson laboratory.

This type of covalent attachment of coordinating ligands within polymer hydrogels (Rehahn Type II polymer systems) and the luminescent materials formed in presence of Eu^{III} was investigated for naphthyl-**dpa** derivatives in collaboration with Prof. C. P. McCoy (Queen's University Belfast). The preliminary results of this work are presented in the following chapter.

5. Preliminary studies of naphthyl-dpa methacrylate monomers for the synthesis of Rehahn Type II supramolecular *co*-polymer gels

5.1 Introduction

Metallopolymers and their respective classes were reviewed in Section 1.6 and Section 1.7 in the context of luminescent Ln^{III}-containing materials. The ions were either: i) grafted onto organic-polymer chains (Rehahn Type I); ii) intrinsic to the construction of the bulk materials (Rehahn Type II); or iii) introduced as dopants (Rehahn Type III). The nature of the inclusion of the Ln^{III} ions led to various applications for each class of material. Rehahn Type III materials can be employed as sensors, as was demonstrated in Chapter 3 and Chapter 4 previously. The grafting of coordinating sites (Rehahn Type II) to polymers has led to the development of supramolecular cross-linked through metal complexes, most notably with transition ions such as Fe^{2+}, Zn^{2+} and Cu^{2+}.[209,549-551] Crosslinking density is fundamental to mechanical properties of polymer and other soft matter.[552-554] A driving force behind this has been the design of materials with tuneable structural properties by providing a highly controllable variation in the cross-linking density and strength.[209,319] Additionally, the reversible, or exchangeable, nature of coordination interactions (compared to covalent bonds) can allow for mechanical properties exhibiting chemical response[555] or self-healing properties since cross-linking density can be restored after 'damage' has occurred.[549] Examples of the forms that potential metal-centred crosslinks can take for *f*-metal and 6-coordinate *d*-metals are shown schematically in Figure 5.1, but these can be tuned through a number of approaches. The doped-metal concentration within a material will influence the cross-linking density and concomitant structural properties. Although these systems are under significant kinetic control, at lower concentrations it would be expected that saturated

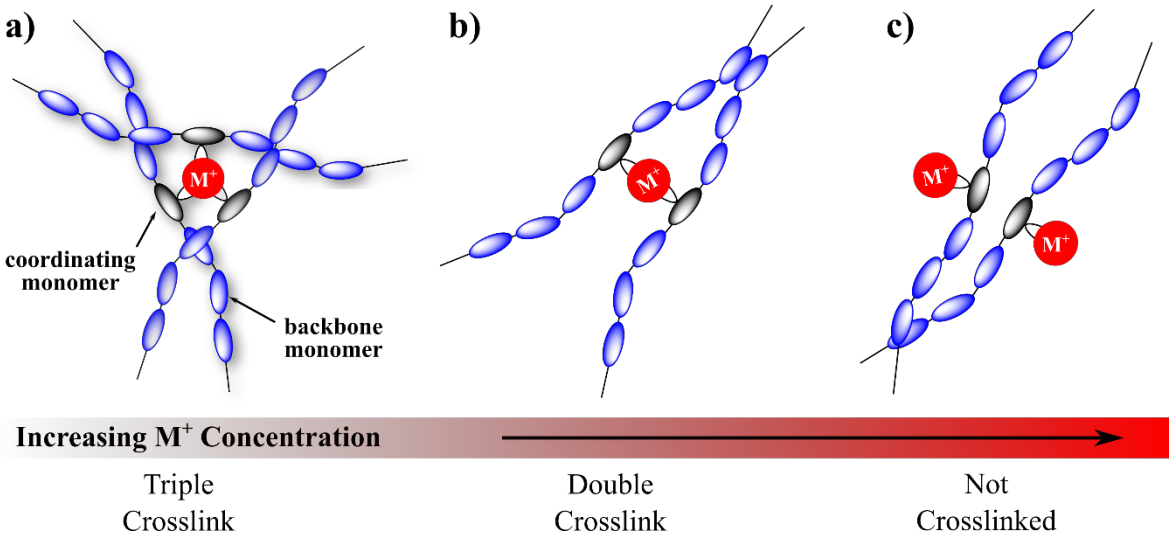

Figure 5.1 Schematic representation of the nature of crosslinks formed between organic copolymer chains by metal coordination complexes at different stoichiometries showing: **a)** triple crosslinks in ML_3 complexes; **b)** double crosslinks for ML_2 complexes; and **c)** no crosslinking for **ML** stoichiometry

complexes are formed that can give rise to 'triple crosslinks' where the metal ion connects three separate polymer chains. With increasing metal concentration (compared to coordinating sites in the polymer) the formation of unsaturated complexes could possibly become more prevalent. This could result in 'double crosslinks', which are less restricting than 'triple crosslinks'. Eventually, it is possible that an excess metal ion doping occurs, where no crosslinking takes place. The choice of metal centre influences the types and strengths of crosslinks that form, particularly so in the case of *d*-metal ions with octahedral, tetrahedral and square-planar geometries. The strongest supramolecular metallo-crosslinkers have tended to be transition metals due to their higher charge densities and strong coordination bonds compared to *f*-metal; for example, the Fe^{2+}-catechol interaction has been used very effectively.[549,556] The specific use of Ln^{III} ions has mostly involved the introduction of luminescent properties into such systems and a number of examples have structural changes as the result of Eu^{III}-based crosslinks.[239,332-334,354,355,357]

It was proposed that the naphthyl-**dpa** scaffold used in the previous chapters, could be functionalised with a pendent methacrylamide moiety that could then be copolymerised into methacryl-based materials, such as the p(HEMA-*co*-EGDMA) to yield responsive hydrogels. Two structures, **127(*S,S*)** and **128(*S*),** were designed with this in mind. These were functionalised with *N*-propylacrylamides in both a symmetrical and an asymmetrical arrangement, Figure 4.2. It has been established previously that both symmetrical and asymmetrical naphthyl-**dpa** systems are good sensitising antennae for Ln^{III}, and, hence the use of Eu^{III} (or Tb^{III} in the case of **128(*S*)**)[95,346,377] should introduce both crosslinking and concomitantly result in the generation of a luminescent material.

This chapter will present the preliminary studies carried out using polymer hydrogels made from p(HEMA-*co*-EGDMA) that were copolymerised with either **127(*S,S*)** or **128(*S*)**. The synthesis of the monomers and the assembly of their Eu^{III} complexes will be initially presented, followed by their copolymerisation into the hydrogels. The later sections will

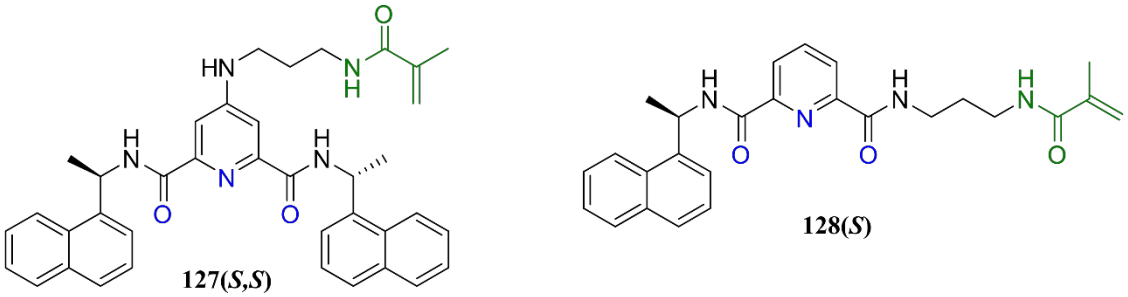

Figure 5.2 Structures of **127(*S,S*)** and **128(*S*)**, the proposed symmetrical and asymmetrical naphthyl-**dpa** methacrylate monomers, respectively. Coordinating atoms are shown in blue and the polymerisable unit in green.

describe the structural photophysical, and mechanical analysis of the resulting hard polymer materials and corresponding soft hydrogels. A potential application of such systems could be found in the monitoring of *in-situ* stability of soft materials by luminescence.

5.2 Design, synthesis and structural characterisation of monomers 127(*S,S*) and 128(*S*)

The synthesis of symmetrical ligand monomer **127(*S,S*)** is shown in Scheme 5.1. A 1,3-diaminopropyl- chain was introduced to the 4-position of the pyridine starting from chloro-substituted naphthyl-**dpa** intermediate **126** and was achieved through a similar methodology to that applied in Chapter 3 (Section 3.7.1). Intermediate **126** was heated in neat excess of 1,3-diaminopropane until the solid residues were fully dissolved and stirred at temperature for 18 hours. The resulting solution was allowed to cool to RT then poured into iced-water which afforded an off-white crude precipitate which was recovered by filtration. After drying under vacuum for 1 hour, the material was dissolved in CH_2Cl_2 and washed with 0.1M HCl, $NaHCO_3$ (sat. aq.) and NaCl (sat. aq.) to remove excess amine. The organic phases were then dried over $MgSO_4$, concentrated *in vacuo* to afford an off-white solid, which was purified on silica (RediSep®, 0 → 10% CH_3OH in CH_2Cl_2), from which product containing fractions were dried over $MgSO_4$ and concentrated *in vacuo* giving **141(*S,S*)** in 70% yield. Purified compound **141(*S,S*)** was dissolved in CH_2Cl_2 and treated with methacrylic anhydride and NEt_3 at RT. The reaction was monitored until starting materials had been consumed, after which the solvent was removed *in vacuo*, followed by flash chromatography

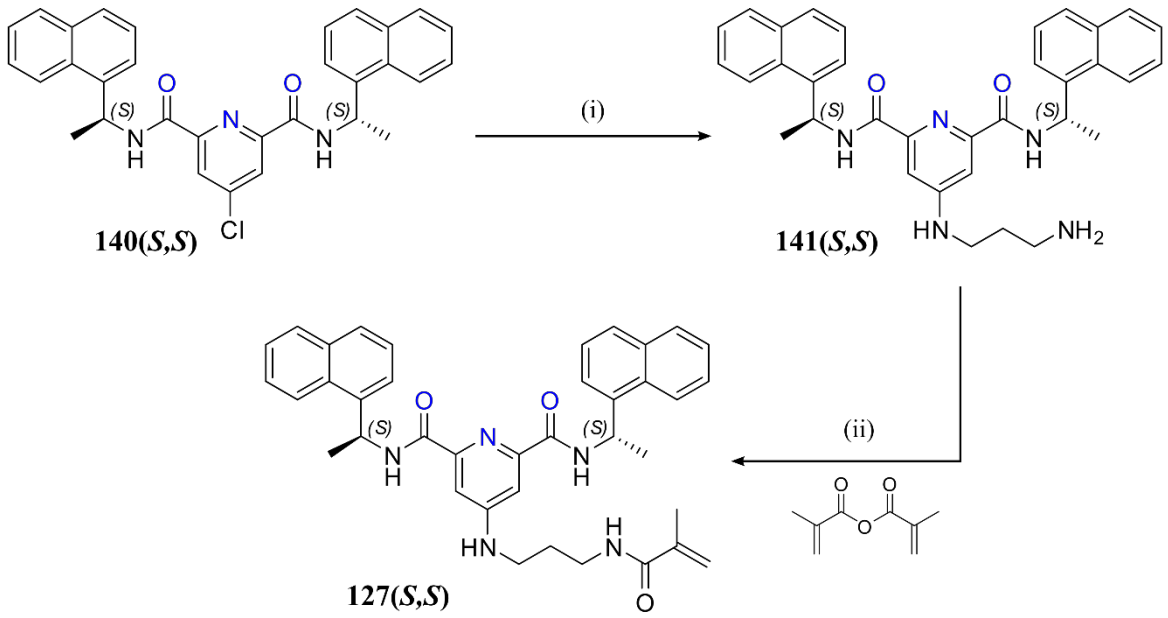

Scheme 5.1 Synthesis of symmetrical naphthyl-**dpa** ligand monomer **127(*S,S*)** possessing a pendent methacrylate moiety **(i)** 1,3-diaminopropane, Δ 135 °C, 18 hours; **(ii)** NEt_3 (1.1 equiv.), CH_2Cl_2.

(RediSep®, 0 → 5% CH_3OH in CH_2Cl_2), affording **127(*S*,*S*)** as a white solid in 65 % yield after workup.

The corresponding asymmetrical ligand monomer **128(*S*)** was synthesised in a seven-step synthesis from dipicolinic acid (**6**) and was carried out in collaboration with Dr. Oxana Kotova and Mr. Garrett Dee (a final year project student working in the Gunnlaugsson laboratory). Dipicolinic acid **6** was suspended in DMF and treated with benzyl bromide in the presence of suspended $NaHCO_3$ at RT for 24 hours. A yellow solution resulted, which was diluted with H_2O, adjusted to pH 8 with sat. aq. $NaHCO_3$ and extracted with EtOAc (removing the doubly-protected side product). The aqueous phase was acidified and extracted with EtOAc, dried over $MgSO_4$ and concentrated *in vacuo*. The crude solid obtained which was dissolved in CH_2Cl_2 and washed with H_2O and sat. aq. NaCl before drying over $MgSO_4$ and concentrating *in vacuo*. This afforded **142** as a white solid in 33% yield. Compound **142** was dissolved in THF and treated with (*S*)-1-(1-naphthyl)ethylamine in the presence of EDCI, HOBt and NEt_3 for 24 hours in order to couple the naphthyl antenna. The resulting material was dissolved in CH_2Cl_2 and with 1M HCl, sat. aq. $NaHCO_3$, H_2O and sat. aq. NaCl. After drying over $MgSO_4$ **143(*S*)** was afforded as a yellow oil in 85% yield which was subsequently deprotected by catalytic hydrogenation using Pd/C at 3 atm. of H_2 in CH_3OH, affording **144(*S*)** as an off-white solid in 90% yield after workup. 1,3-Diaminopropane was mono-protected with di-*tert*-butyldicarbonate in $CHCl_3$ (**145**) and

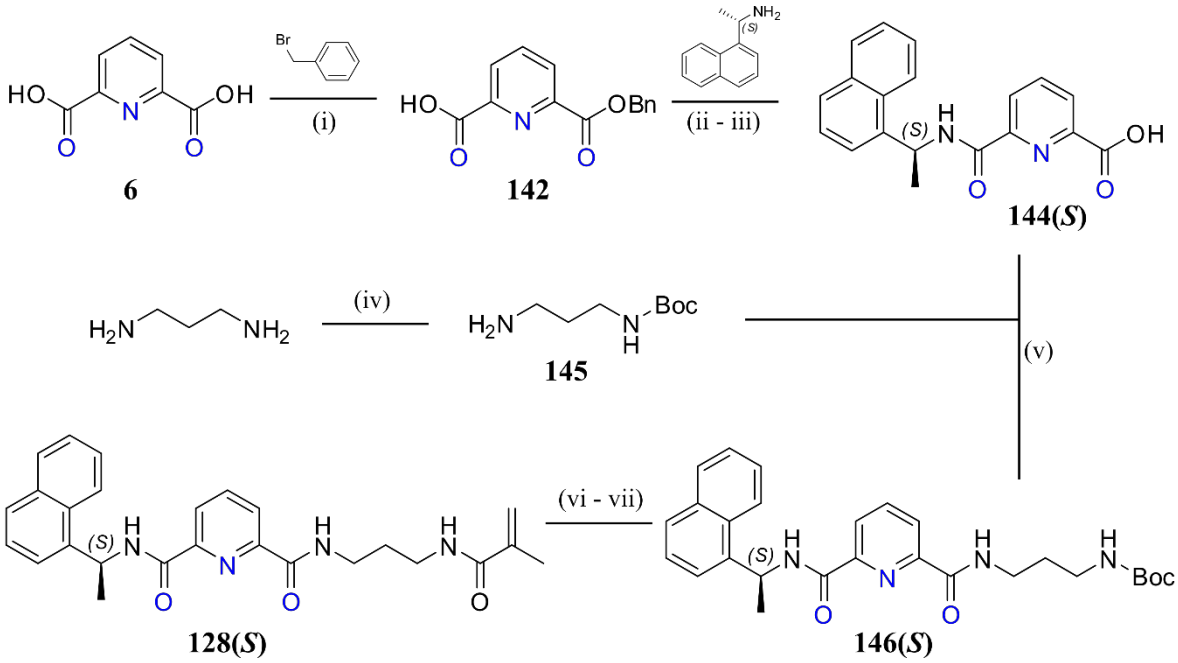

Scheme 5.2 Synthesis of asymmetrical naphthyl-**dpa** ligand **128(*S*)** possessing a methacrylate moiety. **(i)** $NaHCO_3$, DMF, RT; **(ii)** EDCI, HOBt, NEt_3, THF, 0 °C → RT; **(iii)** H_2 (3 atm), 10 wt% Pd/C (0.15 equiv.), CH_3OH, RT; **(iv)** Boc_2O, $CHCl_3$, RT; **(v)** EDCI, HOBt, NEt_3, THF, 0°C → RT; **(vi)** TFA:CH_2Cl_2 (1:3 v/v); **(vii)** methacrylic anhydride, NEt_3, CH_2Cl_2.

coupled to **144(*S*)** under the same amide coupling conditions as described above giving **146(*S*)** as a yellow solid in 79% yield after aqueous acid-base workup. Compound **146(*S*)** was subsequently de-protected using TFA in CH_2Cl_2 (1:3 v/v) followed by workup affording **147(*S*)** in 80% yield. Finally, **147(*S*)** was treated with methacrylic anhydride in CH_2Cl_2, the presence of NEt_3 at RT, for 24 hours after which the solvent was removed *in vacuo*. The recovered material was purified by flash chromatography on silica using 0 → 5% CH_3OH in CH_2Cl_2 as eluent then eluted further on silica using 100% EtOAc as eluent to afford clear glassy solid in 48% yield.

Both target monomers were structurally characterised by ^1H and ^{13}C NMR spectroscopy, IR and HRMS analysis. The ^1H NMR spectra of **127(*S,S*)** and **128(*S*)** are shown in **Figure 5.3**. The two ligands shared a number of features due to their related structures in the central core and antenna moieties. In addition to the distinctive signal for the chiral proton (H_8) adjacent to the antenna moiety at ≈ 6 ppm, the aromatic region showed a set of characteristic resonances (H_1 – H_7) which corresponded to naphthyl groups as well as those of the pyridine central core (H_{10} in **127(*S,S*)** and H_{10} – H_{12} in **128(*S*)**). These signals were more clearly resolved in **128(*S*)** (consistent with the lower anisotropy associated with the single naphthyl moiety) and the asymmetry of the ligand confirmed by three resonances associated with the pyridine moiety being observed. On the other hand, a single resonance *ca*. 7.5 ppm in **127(*S,S*)** confirmed the symmetrical pyridine unit and was in agreement with

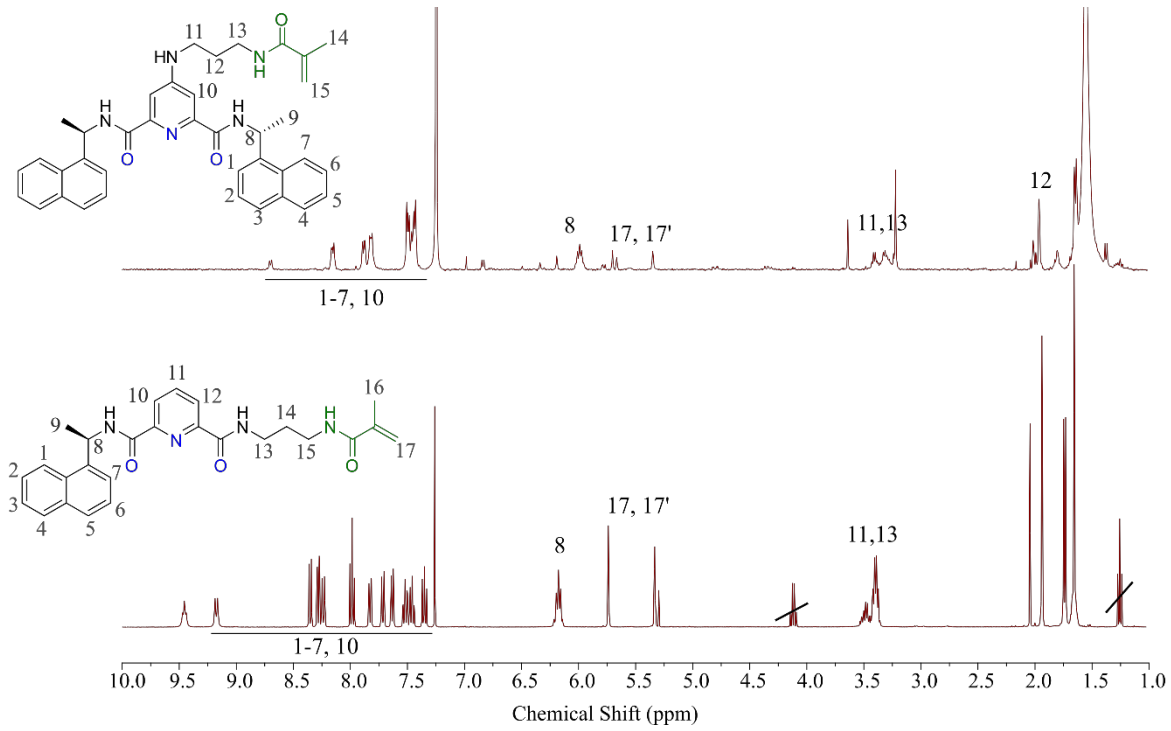

Figure 5.3 ^1H NMR spectra (400 MHz, $CDCl_3$) for ligands **a) 127(*S,S*)**; and **b) 128(*S*).**

N-linked naphthyl-**dpa** derivative **122**. The functionalisation with the propane methacrylamide moiety was confirmed by the resonances for the methylene protons of the propyl chain at 1.7, 3.3 and 3.5 ppm, along with the sharp signals corresponding to the non-chemically equivalent methacrylamide alkene (H_{17}) protons at 5.7 and 5.3 ppm.

The formation of complexes with Eu^{III} was subsequently achieved using microwave-assisted synthesis in CH_3OH by treating the ligands with 0.33 equivalents of $Eu(CF_3SO_3)_3$ at 70 °C for 20 minutes. The complexes formed were isolated by precipitating from CH_3OH into Et_2O, which afforded off-white solids. The formation of complexes was demonstrated by HRMS and ^1H NMR analysis (see Appendix A5). The ^1H NMR in CD_3OD showed lanthanide induced shifts (LIS) in both the naphthyl and the pyridyl resonances due to the paramagnetic effects of Eu^{III}. In both cases, the NMR experiments showed the presence of multiple Eu^{III} species in CD_3OD, rather than a single saturated **ML_3** species, as multiple sets of resonances were observed. This was later found to be consistent with the photophysical analysis discussed in the following sections.

5.3 Photophysical characterisation of 127(*S,S*) and 128(*S*) and their Eu^{III} complexes formed under thermodynamic conditions

The ligands and their complexes with Eu^{III} were studied in CH_3CN solution in order to probe their photophysical properties prior to their use within the polymer matrix. The UV-visible absorption spectra of **127(*S,S*)** with **[Eu.(127(*S,S*))$_3$]$^{3+}$** and **128(*S*)** with **[Eu.(128(*S*))$_3$]$^{3+}$** are shown in Figure 5.4a and Figure 5.4b, respectively. Symmetrical ligand **127(*S,S*)** showed a characteristic absorbance profile and extinction coefficients ($\varepsilon = 15 \times 10^4$ $M^{-1}cm^{-1}$ and 80×10^3 $M^{-1}cm^{-1}$ at $\lambda_{abs} = 224$ and 281 nm, respectively) associated the 4-position of the pyridine.

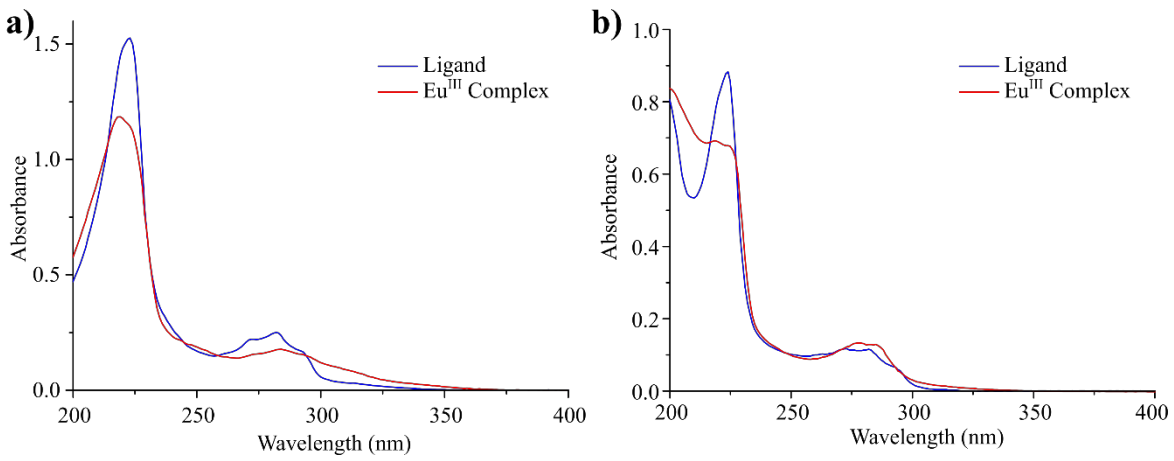

Figure 5.4 Overlaid UV-visible absorption spectra in CH_3CN for: **a) 127(*S,S*)** (blue) and **[Eu.(127(*S,S*))$_3$]$^{3+}$** (red); and **b) 128(*S*)** (blue) and **[Eu.(128(*S*))$_3$]$^{3+}$** (red). Spectra were recorded at effective ligand concentrations of $c = 1 \times 10^{-5}$ M at 24 °C.

The fine structure in lower wavelength absorbance (assigned to pyridyl n→π* and naphthyl π→π* transitions) was present in both ligands from the common chromophores.

Ligand **128(*S*)** was more weakly absorbing across the entire spectrum, also consistent with other 'half-helicate' naphthyl-**dpa** systems.[346] On the formation of the Eu^{III} complexes, hyperchromic shifts were observed for both **[Eu.(127(*S,S*))$_3$]$^{3+}$** and **[Eu.(128(*S*))$_3$]$^{3+}$** in the regions 300 – 350 nm and 200-220 nm. In the region of 279 – 300 nm, the two ligands behaved differently with **[Eu.(127(*S,S*))$_3$]$^{3+}$** undergoing significant hypochromism compared to **127(*S,S*)**, while **[Eu.(128(*S*))$_3$]$^{3+}$** showed a much smaller change. These changes were consistent with the formation of π-π interactions and chromophore, which was in agreement with previous work using related systems.

Excitation of both the **[Eu.(127(*S,S*))$_3$]$^{3+}$** and the **[Eu.(128(*S*))$_3$]$^{3+}$** complexes gave rise to Eu^{III}-centred luminescence, as shown in Figure 5.5a and Figure 5.5b, respectively. In the case of **[Eu.(127(*S,S*))$_3$]$^{3+}$** the ligand-centred fluorescence (λ_{em} = 390 nm) was quenched upon coordination of the Eu^{III} ion and participation in the sensitisation mechanism. The sensitisation of the Eu^{III} by the ligands was confirmed in the excitation spectra of the emission at λ_{em} = 615 nm (see Appendix A5) which closely matched the corresponding absorbance spectra. The $^5D_0 \rightarrow {}^7F_J$ (J = 1-4) transitions were observed in both fluorescence and time-gated emission spectra. As discussed in Chapter 3, each spectra was structured characteristically to the substitution type at the 4-position of the pyridine core and **[Eu.(128(*S*))$_3$]$^{3+}$** presented a single $^5D_0 \rightarrow {}^7F_2$ band, while **[Eu.(127(*S,S*))$_3$]$^{3+}$** showed a two component $^5D_0 \rightarrow {}^7F_2$ with each component in approximately 1:1 ratio. As further characterisation of the ligands, the kinetic assembly of these complexes were also probed in CH_3CN.

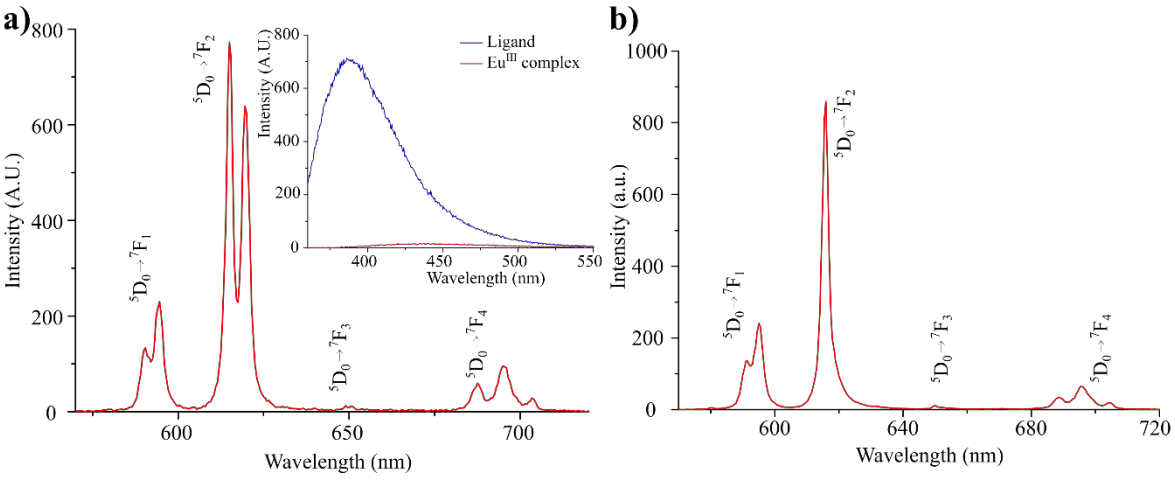

Figure 5.5 Time-gated emission spectra in CH_3CN for complexes: **a) [Eu.(127(*S,S*))$_3$]$^{3+}$** ***inset***: **127(*S,S*)**-centred fluorescence emission from **127(*S,S*)** and **[Eu.(127(*S,S*))$_3$]$^{3+}$** showing quenching upon coordination; and **b) [Eu.(128(*S*))$_3$]$^{3+}$**. Spectra recorded at effective ligand concentration $c = 1 \times 10^{-5}$ M at 24 °C.

5.4 Observing kinetic assemblies of 127(*S,S*) and 128(*S*) through self-assembly titration in CH_3CN

Spectrophotometric titrations monitoring the UV-visible absorption, fluorescence and Eu^{III}-centred emission changes were carried out on **127(*S,S*)** and **128(*S*)** in CH_3CN. The self-assembly behaviours of the ligands were mostly in agreement with related naphthyl-**dpa** based systems. The UV-visible absorption spectra and the respective key wavelength isotherms are shown for **127(*S,S*)** and **128(*S*)** upon titrating with Eu^{III} in Figure 5.6a and Figure 5.6b, respectively. Upon the first additions of Eu^{III}, hypochromic shifts in the higher energy absorbance at λ_{abs} = 224 nm were observed, reaching minima at 0.25 and 0.40 equivalents of Eu^{III} for **127(*S,S*)** and **128(*S*)**, respectively. This was in agreement with a dominant formation of $\mathbf{ML_3}$ complexes in the initial stages of the titration before these dissociate into $\mathbf{ML_2}$ and **ML** species.

Both ligands showed hyperchromism in the region 300 – 325 nm and reached a plateau in coincidence of the minimum absorbance at λ_{abs} = 224 nm. This was consistent with the conformational changes (and concomitant chromophore coupling) upon coordination. With further additions of Eu^{III} from ≈ 0.30 → 1.00 equivalents, the absorbance at λ_{abs} = 224 nm recovered; reaching a plateau at one equivalent in the cases of both **127(*S,S*)** and **128(*S*)**. This was consistent with dissociation of $\mathbf{ML_3}$ complexes into lower stoichiometry species as eluded to above. For **128(*S*),** the absorbance at λ_{abs} = 224 nm was fully recovered while for **127(*S,S*)** there was a smaller recovery (*ca.* 25%). This was consistent with related systems and the different chromophore interactions in the two scaffolds.

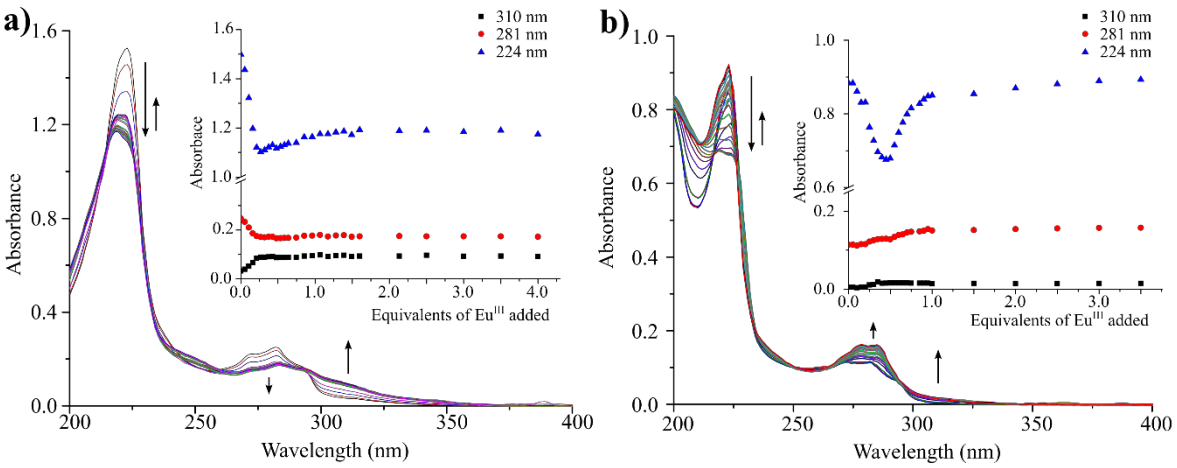

Figure 5.6 Overlaid UV-visible absorption spectra from titrations with 0.00 → 4.00 equivalents of $Eu(CF_3SO_3)_3$ in CH_3CN for: **a)** ligand **127(*S,S*)** ***inset:*** single wavelength binding isotherms at λ_{abs} = 310, 281 and 224 nm as a function of added equivalents of Eu^{III}; and **b)** ligand **128(*S*)** ***inset***: single wavelength binding isotherms at λ_{abs} = 310, 281 nm as a function of added equivalents of Eu^{III}. Spectra recorded from initial ligand concentrations of $c = 1 \times 10^{-5}$ M at 24 °C.

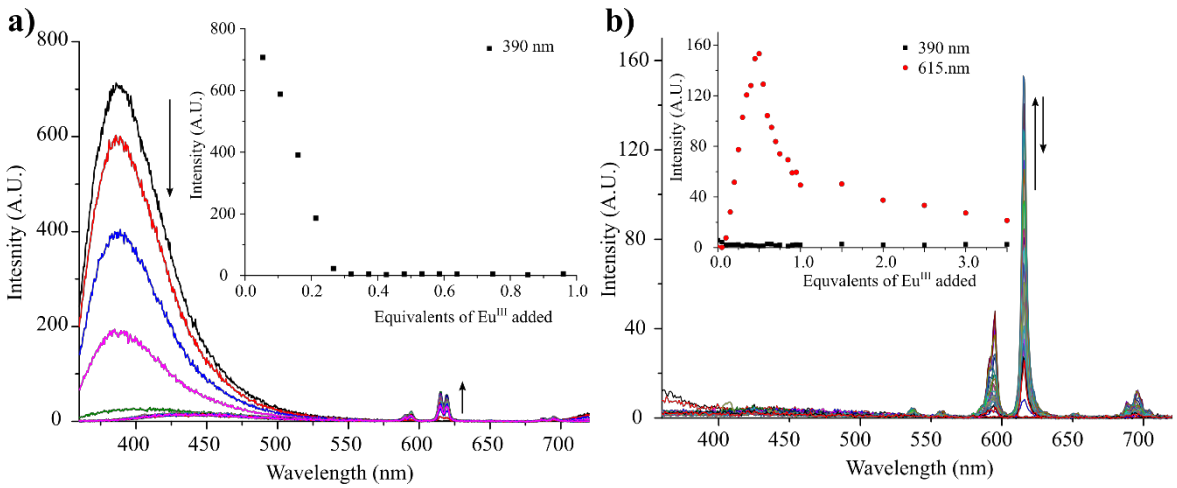

Figure 5.7 Overlaid fluorescence emission spectra from titrations with 0.00 → 4.00 equivalents of $Eu(CF_3SO_3)_3$ in CH_3CN for: **a)** ligand **127(*S,S*)** ***inset:*** single wavelength binding isotherms for ligand emission at λ_{em} = 390 nm as a function of added equivalents of Eu^{III}; and **b)** ligand **128(*S*)** ***inset***: single wavelength binding isotherms for ligand emission at λ_{em} = 390 nm and Eu^{III}-emission at λ_{abs} = 615nm as a function of added equivalents of Eu^{III}. Spectra recorded from initial ligand concentrations of $c = 1 \times 10^{-5}$ M at 24 °C.

The formation of the methacrylamide moiety quenched any PET activity similar to those observed in Chapter 3 for **127(*S,S*)** as well as for **128(*S*)**. Here, the emission behaviour was relatively simple and characteristic of that seen for non-PET active systems. The fluorescence spectra and the related single wavelength isotherms are shown in Figure 5.7a and Figure 5.7b for **127(*S,S*)** and **128(*S*)**, respectively. Ligand **127(*S,S*)** was fluorescent, with λ_{max} at 390 nm. Upon initial additions of Eu^{III}, an immediate fluorescence quenching was observed. This quenching continued until the additions of 0.30 equivalents of Eu^{III}. The emission was quenched in full in coincidence with the minima and maxima observed in the UV-visible absorption spectra and expected formation of **ML_3** species. In contrast to this, ligand **128(*S*)** was not fluorescent and remained non-emissive throughout the titration, Eu^{III}-centred emission was observed.

The time-gated emission spectra from the same titrations and their respective binding isotherms for the transitions at λ_{em} = 595, 615 and 695 nm ($^5D_0 \rightarrow {}^7F_{1,2,4}$) are shown in Figure 5.8a and Figure 5.8b for the titrations of **127(*S,S*)** and **128(*S*)**, respectively. Upon addition of Eu^{III} to the solution, an immediate evolution of the Eu^{III}-centred emission was observed, clearly showing the formation of complexes through the 'switch-on' of the sensitisation mechanism. This emission continued to enhance between 0.00 → 0.35 equivalents of Eu^{III} (in both cases) before reaching a maximum, and becoming rapidly quenched between 0.40 → 1.00 equivalents and into excess of Eu^{III}. The quenching by 1.00 equivalents was *ca*. 75% for **128(*S*)** and 25% for **127(*S,S*)** which showed different sensitisation efficiencies in the

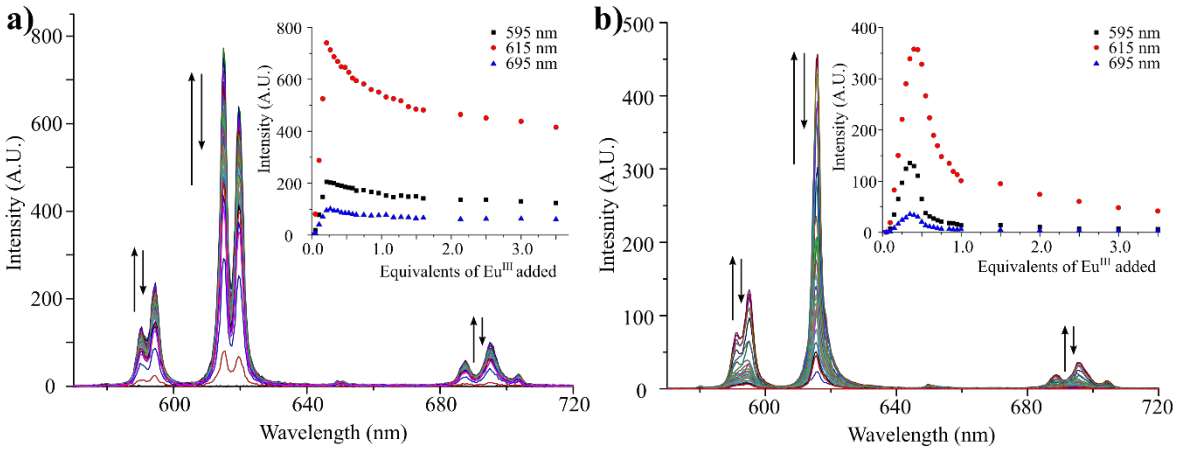

Figure 5.8 Overlaid time-gated emission spectra from titrations with 0.00 → 4.00 equivalents of $Eu(CF_3SO_3)_3$ in CH_3CN for: **a)** ligand **127(*S,S*)** ***inset:*** single wavelength binding isotherms for Eu^{III} emission at λ_{em} = 595, 615 and 695 nm as a function of added equivalents of Eu^{III}; and **b)** ligand **128(*S*)** ***inset***: single wavelength binding isotherms for Eu^{III} emission at λ_{em} = 595, 615 and 695 nm as a function of added equivalents of Eu^{III}. Spectra recorded from initial ligand concentrations of $c = 1 \times 10^{-5}$ M at 24 °C.

ML_2 and **ML** species; this was also consistent with behaviour observed in Chapter 3 and other previous work.[377]

These titrations could be fitted using the established methods of global using ReactLab EQUILIBRIA® and the behaviour of **127(*S,S*)** and **128(*S*)** were characteristic of their respective ligand families. The data was modelled and cumulative stability constants ($\log\beta_{MLn}$, n = 1, 2, 3) were determined for **127(*S,S*)** as 6.9 ± 0.1, 13.5 ± 0.2 and 20.5 ± 0.1 for $\log\beta_{ML1}$, $\log\beta_{ML2}$ and $\log\beta_{ML3}$, respectively. These were consistent with related **dpa** systems and similar to those calculated for **121** - **125**. The trends strongly indicated the formation of **ML_2** stoichiometry complexes in solution. In the case of **128(*S*)**, these stability constants were estimated as 7.6 ± 0.3, 14.5 ± 0.2 and 20.1 ± 0.4; being also in agreement with those determined for other asymmetrical naphthyl-**dpa** systems such as **105** - **108**. The self-assembly studies herein demonstrated the expected dynamic nature of the complexes formed which was probed further using the luminescence lifetimes of the Eu^{III} emission.

5.5 Luminescence lifetimes measurements of Eu^{III} complexes of ligands 127(*S,S*) and 128(*S*) in solution

Luminescence lifetime measurements were recorded in a range of solvents (H_2O, D_2O, CH_3OH, CD_3OD and CH_3CN) in order to characterise the stoichiometry and the speciation distribution of under thermodynamic control. The values determined from these experiments are summarised in Table 5.1. Complexes **$[Eu.(127(S,S))_3]^{3+}$** and **$[Eu.(128(S))_3]^{3+}$** showed various behaviours in the each solvent systems; this was likely due to the solvation variation in the two systems, arising from the balance of additional polarity provided by the methacrylate and lipophilicity of the naphthyl chromophores in the two ligands. It was

suggested that the effect of solvation was stronger for these systems compared to related ligands described in Chapter 3. The number of bound water molecules (*q*-values) could be determined in both aqueous and methanolic solutions for these systems using the models of Horrocks' and Parker (Equation 2.1). The calculated *q*-values are summarised in Table 5.2.

Table 5.1 Eu^{III}-centred luminescence lifetime measurements for **[Eu.(127(*S,S*))$_3$]$^{3+}$** and **[Eu.(128(*S*))$_3$]$^{3+}$** in H_2O, D_2O, CH_3CN and CH_3OH at λ_{em} = 615 nm. Uncertainty was determined as the standard deviation from independent replicates. (%) reflects ratio of *A* pre-exponents. [a]Only one emissive species was found in solution.

Complex	Solvent	τ_1 / ms	τ_2 / ms
[Eu.(127(*S,S*))$_n$]$^{3+}$	CH_3CN	1.43 ± 0.02 (91%)	0.44 ± 0.01 (9%)
	H_2O	1.33 ± 0.01 (100%)	-[a]
	D_2O	2.96 ± 0.02 (100%)	-[a]
	CH_3OH	1.29 ± 0.01 (95%)	0.48 ± 0.01 (5%)
	CD_3OD	2.54 ± 0.02 (95%)	0.84 ± 0.01 (5%)
[Eu.(128(*S*))$_n$]$^{3+}$	CH_3CN	1.43 ± 0.01 (100%)	-[a]
	H_2O	1.43 ± 0.01 (94%)	0.30 ± 0.01 (6%)
	D_2O	3.20 ± 0.05 (93%)	1.77 ± 0.30 (7%)
	CH_3OH	0.52 ± 0.01 (100%)	-[a]
	CD_3OD	2.49 ± 0.02 (100%)	-[a]

Table 5.2 Number of water molecules bound to Eu^{III} in **[Eu.(127(*S,S*))$_3$]$^{3+}$** and **[Eu.(128(*S*))$_3$]$^{3+}$** as estimated from *q*-value models of lifetime values in H_2O and D_2O and CH_3OH and CD_3OD (Table 4.1) from Horrocks and Parker. The associated error with each *q*-value is ± 0.5. [a]Only one lifetime was identified in solution.

Complex	Solvents	*q*-value (Horrock's)		*q*-value (Parker)	
		τ_1	τ_2	τ_1	τ_2
[Eu.(127(*S,S*))$_n$]$^{3+}$	H_2O/D_2O	0.2	-[a]	~ 0	-[a]
[Eu.(128(*S*))$_n$]$^{3+}$	H_2O/D_2O	0.2	3.1	~ 0	2.7
[Eu.(127(*S,S*))$_n$]$^{3+}$	CD_3OD/CH_3OH	0.2	3	~ 0	2.8
[Eu.(128(*S*))$_n$]$^{3+}$	CD_3OD/CH_3OH	3.1	-[a]	2.9	-[a]

Consistent distributions of lifetimes were determined from independent measurements. In CH_3CN complex **[Eu.(127(*S,S*))$_3$]$^{3+}$** gave a bi-exponential lifetime indicating that two species were present in solution with lifetimes of 1.43 and 0.44 ms, respectively, likely corresponded to **[Eu.(127(*S,S*))$_3$]$^{3+}$** and dissociated **[Eu.(127(*S,S*))$_2$]$^{3+}$** species. The pre-

exponential factors of the fitted lifetimes suggested dominant formation of the longer lifetime species and that the dissociated complexes were the minor species in solution; accurate distributions weighted by quantum yield were not determined. Similarly, in CH_3OH, two lifetimes were recorded of τ_{em} = 1.29 and 0.48 ms from solution. Again, this suggested the existence of two species in solution; these were most likely to be the **ML$_3$** and **ML$_2$** stoichiometries as suggested by the *q*-values of ≈ 0 and ≈ 3, respectively (Table 5.2). The lifetimes of **ML$_2$** stoichiometry complexes of symmetrical naphthyl-**dpa** systems have not been reported, however the lifetimes observed here were of a similar order to those reported for the asymmetrical systems.[347] Interestingly, the two species distribution of **[Eu.(127(*S,S*))$_n$]$^{3+}$** complexes was found to be specific to the CH_3CN and CH_3OH solutions as in H_2O, **[Eu.(127(*S,S*))$_3$]$^{3+}$** existed as a single species with τ_{em} =1.33 ms and a *q*-value of 0. The degree of protection of the Eu^{III} centre from coordinating solvent (the interactions of which can drive dissociation) appeared to affect the stability of complexes of different stoichiometry.

While **127(*S,S*)** formed **ML$_3$** species exclusively in aqueous solution, a bi-exponential lifetime was recorded from **[Eu.(128(*S*))$_n$]$^{3+}$** in aqueous systems with lifetimes of 1.43 ms and 0.30 ms, respectively in H_2O. These likely corresponded to a major **ML$_3$** species being formed and **ML$_2$** species existing as a minor product. This was supported by the *q*-values which were calculated as of ≈ 0 and ≈ 3, respectively. Furthermore, the speciation distribution of **[Eu.(128(*S*))$_n$]$^{3+}$** complexes in organic solution was also contrary to those observed for **[Eu.(127(*S,S*))$_n$]$^{3+}$**. In CH_3CN the formation of a a single species in solution was suggested by the mono-exponential lifetime (τ_{em} = 1.43 ms) which was likely to be **[Eu.(128(*S*))$_3$]$^{3+}$** with a lifetime consistent to those reported for related systems.[95,346,348,377] Similarly, in CH_3OH the **[Eu.(128(*S*))$_n$]$^{3+}$** formed as a single species. However, this species had a lifetime of 0.52 ± 0.01 ms which was suggested to be **[Eu.(128(*S*))$_2$]$^{3+}$** (**ML$_2$**) from the methanolic q-values (≈ 3 - 4) in solution. The lifetime for **[Eu.(128(*S*))$_2$]$^{3+}$** was in very close agreement with lifetimes reported for **[Eu.(105)$_2$]$^{3+}$** and **[Eu.(106)$_2$]$^{3+}$** of 0.57 and 0.58 ms, respectively although these were formed as the minor products in solution. This implied that for **[Eu.(128(*S*))$_n$]$^{3+}$** the solvation was inhibiting the formation of the fully saturated species and highlighted the subtle effect on speciation behaviour that could occur with small changes in external factors.

It was noted in the previous chapters that inclusion of naphthyl-**dpa** complexes within p(HEMA-*co*-EGDMA) materials did not give rise to significant changes in the luminescence lifetimes. Therefore, it was suggested that the recorded distribution of

lifetimes from a polymer gel containing Eu^{III}-based supramolecular crosslinking could reflect the effects of mechanical and physical stimuli to the materials. Hence, ligands **127(*S*,*S*)** and **128(*S*)** were copolymerised with HEMA and EGDMA to form polymer gels. The preliminary structural, photophysical and mechanical characterisations are described in the following sections.

5.6 Synthesis and physical characterisation of p(HEMA-*co*-EGDMA-*co*-127(*S*,*S*)) and p(HEMA-*co*-EGDMA-*co*-128(*S*))

Schematic structures of the copolymers with **127(*S*,*S*)** and **128(*S*)** are shown in Figure 5.9a and Figure 5.9b, respectively. The copolymers of p(HEMA-*co*-EGDMA-*co*-**127(*S*,*S*)**) and p(HEMA-*co*-EGDMA-*co*-**128(*S*)**) were synthesised from a modified procedure previously reported by the Gunnlaugsson group[358] and described in Section 3.7.

Both **127(*S*,*S*)** and **128(*S*)** were found to be soluble in neat HEMA at RT and, therefore, were polymerised directly with the HEMA and EGDMA monomers without the need of a co-solvent, or solution-phase synthesis. Solutions of **127(*S*,*S*)** and **128(*S*)** in HEMA (*ca*. 0.1 wt%) were stirred at RT until the ligand monomers were fully dissolved then treated with EGDMA (1 wt%) and AIBN (1 wt%). The mixture of monomers was transferred to a cast (formed between two glass plates with a siliconised PE liner) and placed into an oven for 6 hours at 90 °C. Within 30 minutes, the solution was viscous and within one hour a solid polymer material had formed which was cured at 90 °C for a further five hours. Following 6 hours total curing time, the casts were removed from the oven and allowed to cool to RT. The hard materials were removed from the cast and washed with deionised H_2O

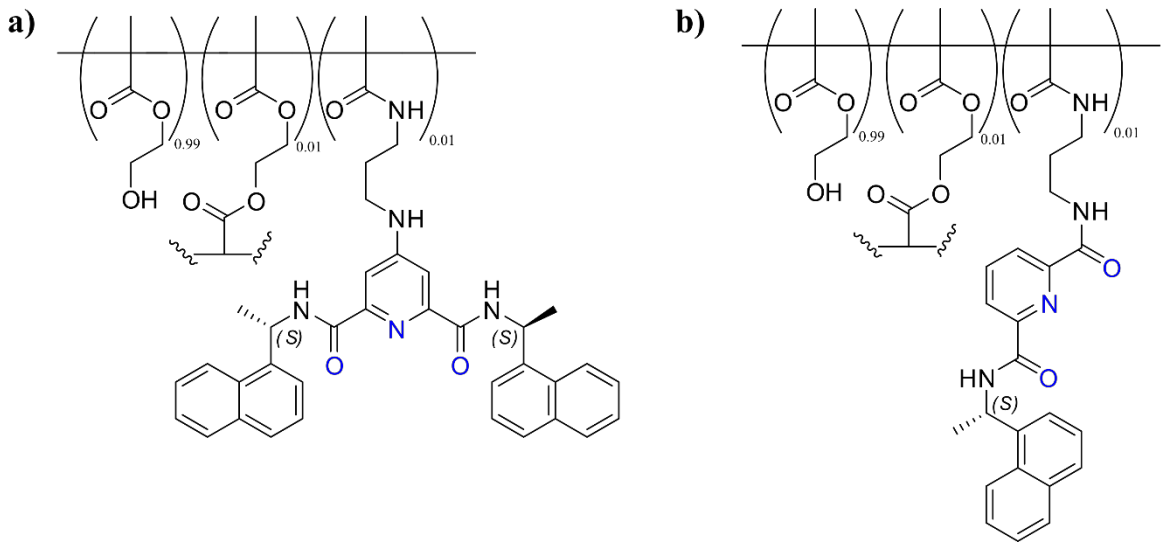

Figure 5.9 Schematic representation, showing wt% ratios, of the structures of the polymers: **a)** p(HEMA-*co*-EGDMA-*co*-**127(*S*,*S*)**); and **b)** p(HEMA-*co*-EGDMA-*co*-**128(*S*)**). Coordinating atoms from crosslinking monomers are shown in blue.

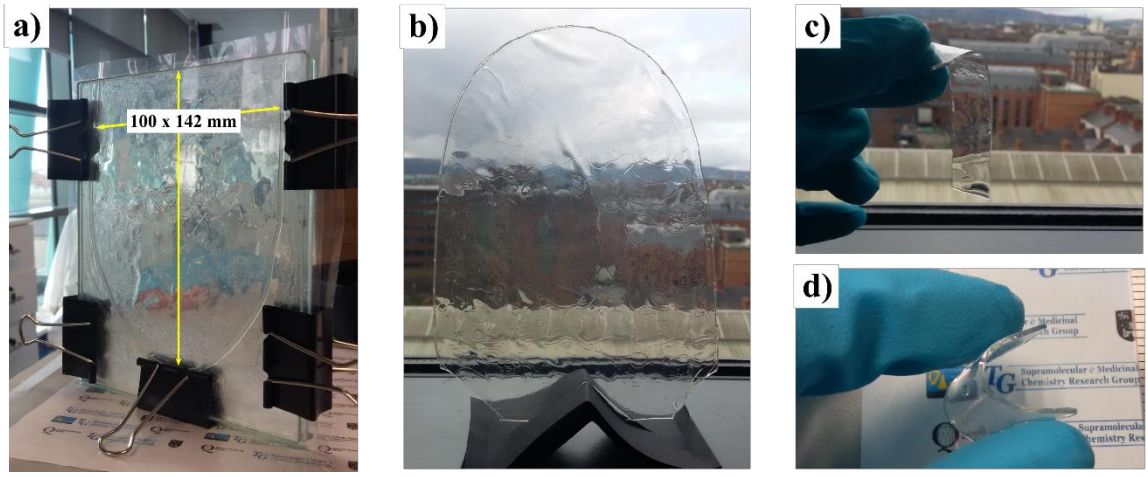

Figure 5.10 Photographs of: **a)** cast used to fabricate polymer monoliths made from glass and lined with a non-stick coating; **b)** polymer monolith of **127(*S,S*)** after 5 hours curing, transparent and hard; and **c)** and **d**) cut strips of hard polymer swelled in H_2O for 2 hours showing soft, flexible materials that remain transparent.

to remove initiator and inhibitor impurities. The solution ^{1}H NMR (see Appendix A5) the polymers swelled in CD_3OD showed residual signals of unreacted HEMA and EGDMA, however suggested that both **127(*S,S*)** or **128(*S*)** had been consumed during the polymerisation. The bulk materials yielded were hard, brittle and optically transparent with a solid thickness of *ca*. 1 mm. When submerged into H_2O the materials swelled to become soft and flexible while retaining their optical clarity, Figure 5.10. The average equilibration water content (EWC) was found to be 67±3 and 75±4 % for the copolymers of **127(*S,S*)** and **128(*S*)**, respectively, from mass measurements in the dehydrated and swelled states, which were in agreement with similar p(HEMA-*co*-EGDMA) hydrogels.[358]

The solid materials were characterised for their glass transition temperature (T_g) from DSC measurement. Heat flow traces for the second heating cycles for samples of the copolymers with **127(*S,S*)** and **128(*S*)** are shown in Figure 5.11a and Figure 5.11b, respectively. It was suggested that homogenous copolymers had formed with a single T_g observed in each sample at *ca*. 95 °C and 104 °C for p(HEMA-*co*-EGDMA-*co*-**127(*S,S*)**) and p(HEMA-*co*-EGDMA-*co*-**128(*S*)**), respectively. Both of these T_g values were higher than that of p(HEMA-*co*-EGDMA) blanks measured experimentally and from literature sources of *ca*. 86 °C.[475] Importantly, it was noted that the T_g recorded by DSC of samples doped with complexes that were non-covalently incorporated into the polymer matrix did not show a shift in T_g and therefore the change was supportive of successful copolymerisation. The increase in T_g was consistent with the bulky co-monomers **127(*S,S*)** ad **128(*S*)** reducing the mobility of the HEMA-*co*-EGDMA chains requiring more energy for them to flow in the copolymer samples.[557-559] Following this basic structural analysis, the

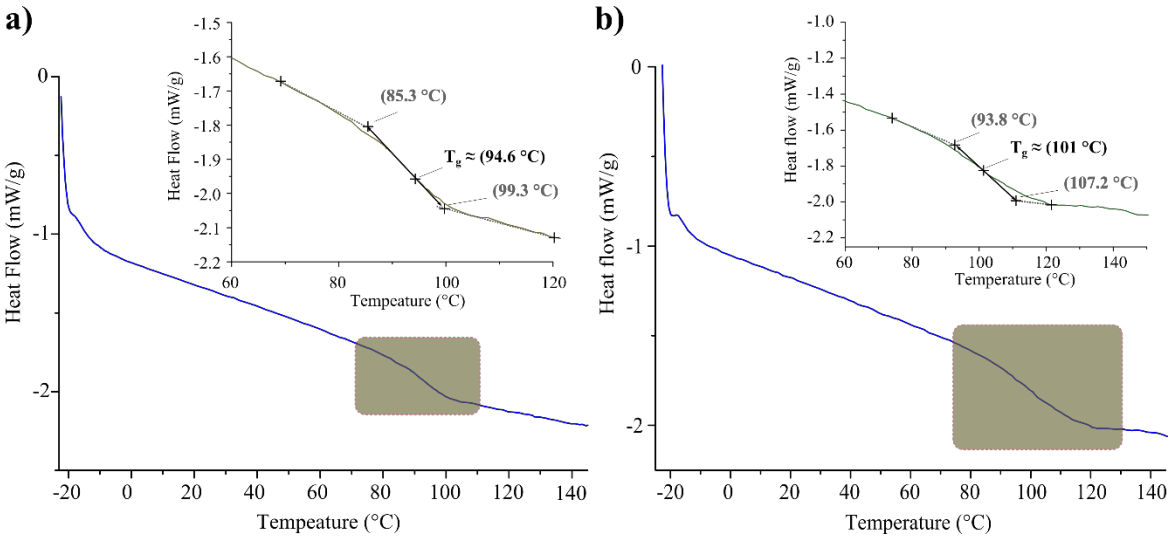

Figure 5.11 Dynamic scanning calorimetry (DSC) curves recorded from solids samples of: **a)** p(HEMA-*co*-EGDMA-*co*-**127(*S,S*)**) ***inset***: zoomed region and determination of T_g from extrapolation methods; and **b)** p(HEMA-*co*-EGDMA-*co*-**128(*S*)**) ***inset***: zoomed region and determination of T_g from extrapolation methods. Curves showns are second heating cycles and T_g was determined using therelevant instrument software.

photophysical properties of the bulk materials were investigated in both the swelled and dehydrated polymers gel forms.

5.6.1 Photophysical characterisation of swelled and dried polymer gels p(HEMA-*co*-EGDMA-*co*-127(*S,S*)) and p(HEMA-*co*-EGDMA-*co*-128(*S*))

The photophysical properties of **127(*S,S*)** and **128(*S*)** were transferred to the polymer materials as a result of their copolymerisation and the average behaviour of the bulk polymers were characterised using UV-visible absorption and luminescence spectroscopy.

5.6.2 p(HEMA-*co*-EGDMA-*co*-127(*S,S*)) and p(HEMA-*co*-EGDMA-*co*-128(*S*)): dry and in H_2O

Both the UV-visible absorption and the fluorescence emission spectra were recorded for the materials p(HEMA-*co*-EGDMA-*co*-**127(*S,S*)**) and p(HEMA-*co*-EGDMA-*co*-**128(*S*)**) and are shown in Figure 5.12a and Figure 5.12b, respectively. Absorbance from the bulk methacrylate polymer was strong in the region of 250 – 200 nm and therefore the usable region of the absorption spectrum was limited to λ_{abs} between 250 and 400 nm. However, in the both materials the inclusion of the naphthyl-**dpa** structure was confirmed by the presence of the characteristic fine structured absorbance band between 270 – 300 nm (as was described above for the ligand absorption spectra in Section 5.3). As has been observed for non-covalent inclusion of complexes (Section 3.7.1), no significant shifts in the absorbance were observed as a result of the inclusion of the ligands within the polymer. The p(HEMA-

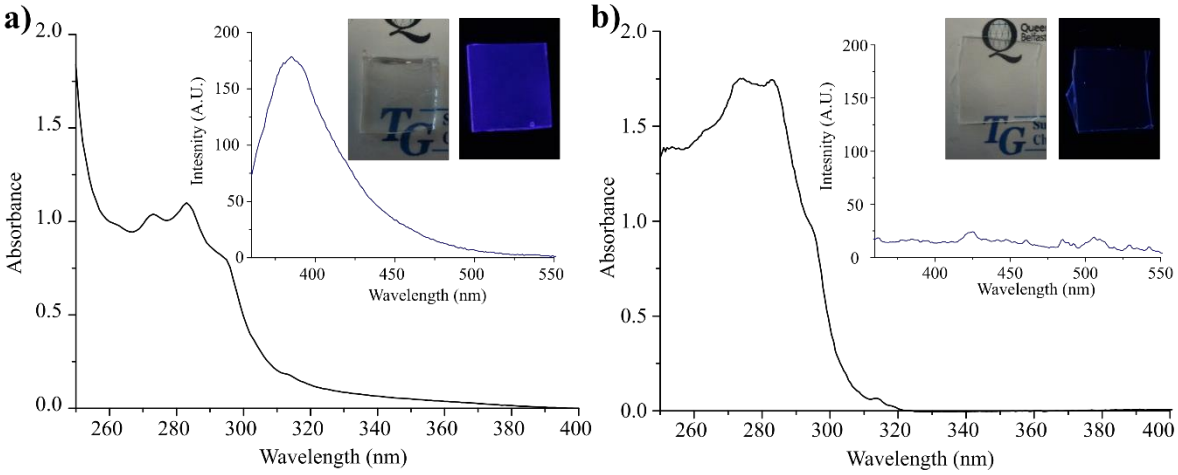

Figure 5.12 UV-visible absorption and fluorescence emission (***inset***) spectra of swelled samples of: **a)** p(HEMA-*co*-EGDMA-*co*-**127(*S,S*)**); and **b)** p(HEMA-*co*-EGDMA-*co*-**128(*S*)**). Materials were equilibrated in H_2O for 2 hours prior to measurement and fully swelled, the spectra were recorded of gels in supernatant H_2O at 24 °C.

co-EGDMA-*co*-**127(*S,S*)**) materials were shown to be fluorescent with a λ_{max} of 390 nm, which also gave rise to a strong blue fluorescence to the 'naked eye' (Figure 5.12), and the same fluorescence features were observed in both the dry polymer and the swelled hydrogels.

5.6.3 p(HEMA-*co*-EGDMA-*co*-127(*S,S*)) and p(HEMA-*co*-EGDMA-*co*-128(*S*)): swelled in aqueous Eu^{III}

Having generated gels in the manner described above, the next objective was to induce crosslinking in the gel through supramolecular interactions. The dry materials were swelled the material solutions of $Eu(CF_3SO_3)_3$ (at concentrations suitable to equilibrate *ca*. 0.33 equivalents of Eu^{III}) and the evolution of Eu^{III}-centred emission was observed. In the swelled polymer gels, p(HEMA-*co*-EGDMA-*co*-**127(*S,S*)**) was strongly emissive while p(HEMA-*co*-EGDMA-*co*-**128(*S*)**) only gave rise to a weak luminescence. The spectral details of the Eu^{III}-doped p(HEMA-*co*-EGDMA-*co*-**128(*S*)**) hydrogel was poorer than that seen for p(HEMA-*co*-EGDMA-*co*-**127(*S,S*)**), where the emission was well-resolved and the expected two-component $^5D_0 \rightarrow {}^7F_2$ transition was observed, see Figure 5.13. In fact, the ratios of the emission bands in the Eu^{III} spectrum of Eu^{III}@p(HEMA-*co*-EGDMA-*co*-**127(*S,S*)**) was in close agreement to those observed for **[Eu.(122(*S,S*))$_3$]**$^{3+}$ in 5% CH_3OH in H_2O and likely reflected the polarity of the solvent environment. This suggested that the tethering of the complex to the polymer matrix did not significantly distort the Eu^{III} coordination geometry. Luminescence lifetime measurements were recorded of the Eu^{III}-crosslinked samples described above and from the same materials once dehydrated. The lifetime values are summarised in Table 5.3 under various 'solvent' conditions.

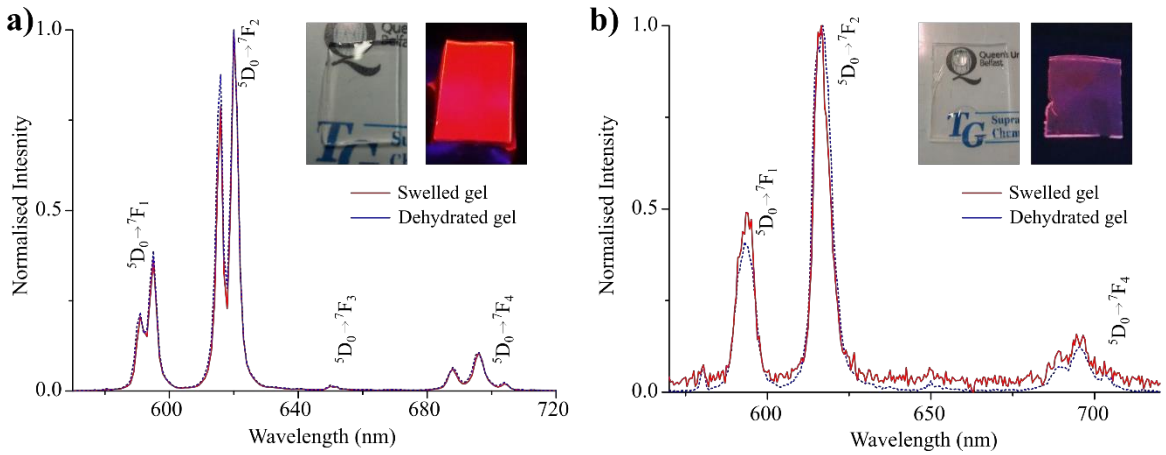

Figure 5.13 Normalised phosphorescence emission spectra from: **a)** p(HEMA-*co*-EGDMA-*co*-**127(*S,S*)**) swelled in 0.33 equivalents of Eu^{III} (red) and the corresponding dehydrated gel (blue), ***inset:*** photographs of materials swelled in 0.33 equivalents of Eu^{III} under ambient and UV light; and **b)** p(HEMA-*co*-EGDMA-*co*-**128(*S*)**) swelled in 0.33 equivalents of Eu^{III} (red) and the corresponding dehydrated gel (blue), ***inset:*** photographs of materials swelled in 0.33 equivalents of Eu^{III} under ambient and UV light. Spectra were recorded of the swelled gels in a supernatant of H_2O at 24 °C.

Table 5.3 Eu^{III}-centred luminescence lifetime measurements for p(HEMA-*co*-EGDMA-*co*-**127(*S,S*)**) and p(HEMA-*co*-EGDMA-*co*-**128(*S*)**) polymer gels after fully equilibrating with 0.33 equivalents $Eu(CF_3SO_3)_3$ at λ_{em} = 615 nm. Uncertainty was determined as the standard deviation from independent replicates. [a]Only one emissive species was found in solution. [b]Samples were dehydrated from swelled gels. [c]Absolute *q*-values could not be determined.

Complex	Solvent	τ_1 / ms	τ_2 / ms	*q*-value
$[Eu.(127(S,S))_n]^{3+}$	Dry[b]	1.31 ± 0.01 (86%)	0.56 ± 0.01 (14%)	-[c]
	H_2O	1.32 ± 0.01 (100%)	-[a]	0
	D_2O	2.79 ± 0.01 (100%)	-[a]	
$[Eu.(128(S))_n]^{3+}$	Dry[b]	0.40 ± 0.02 (51%)	0.91 ± 0.01 (49%)	-[c]
	H_2O	0.48 ± 0.03 (100%)	-[a]	3
	D_2O	2.65 ± 0.02 (100%)		

The bulk lifetime in H_2O for the Eu^{III}@p(HEMA-*co*-EGDMA-*co*-**127(*S,S*)**) hydrogel was determined to be mono-exponential giving τ_{em} = 1.32 ms and was consistent to the lifetime observed for **$[Eu.(127(S,S))_3]^{3+}$** in solution (see Table 5.1 above). Moreover, the materials were treated with Eu^{III} solutions from both H_2O and D_2O and allowed for the determination of *q*-values for these complexes, which confirmed the **ML_3** stoichiometry (*q*-values of 0). Similarly, luminescence lifetime recorded of Eu^{III}@p(HEMA-*co*-EGDMA-*co*-**128(*S*)**) was 0.48 ms from the hydrogel in H_2O and 2.65 ms in D_2O. These corresponded to a *q*-value of

3, and suggested that **[Eu.(128(*S*))$_2$]$^{3+}$** complexes were formed within the hydrogel matrix. This confirmed that the crosslinking was occurring within gel in the manner described in Figure 5.1 with Eu^{III}@p(HEMA-*co*-EGDMA-*co*-**127(*S,S*)**) and Eu^{III}@p(HEMA-*co*-EGDMA-*co*-**128(*S*)**) forming 'triple crosslinks' and 'double crosslinks', respectively. Changes in the lifetime distribution were observed during the dehydration of the hydrogels from H_2O, Table 5.3. The emission lifetimes recorded for both gels switched from mono-exponential to bi-exponential decay, suggesting that there was a redistribution of the complexes formed upon dehydration. Although the absolute *q*-values could not be determined, it was likely that this corresponded to **ML$_3$** and **ML$_2$** complexes. It might be expected that following dehydration the materials the reduced mobility of the chains and reorganisation of the polymer chains result in different stabilities of the **ML$_3$** and **ML$_2$** complexes as a result of geometric restrictions.[560,561] These changes in the lifetime distribution suggested that the physical and mechanical nature (*i.e.* freedom of movement) could be reflected in the emission lifetimes observed from the samples. A preliminary assessment was made whether a measurable difference in luminescent lifetimes or distribution of lifetimes occurred from mechanical strain of the swelled polymer gels. However, upon straining the material (by stretching and compression) no measureable differences in the lifetimes were found when the gels (Appendix A5).

The formation of crosslinks at low levels crosslinkers doping have been shown to influence bulk mechanical properties of polymer gels.[562] Therefore, mechanical analysis was undertaken on the p(HEMA-*co*-EGDMA-*co*-**127(*S,S*)**) as swelled polymer gels in the presence and absence of Eu^{III} ions.

5.7 Mechanical analysis of p(HEMA-*co*-EGDMA-*co*-127(*S,S*)) polymer gels in H_2O and aqueous Eu^{III} solution

Mechanical analysis was undertaken in the materials of p(HEMA-*co*-EGDMA-*co*-**127(*S,S*)**) polymer gels with 0.1 wt% additional crosslinking concentration as part of a collaboration with Prof. Colin P. McCoy, Dr. Nicola Irwin and Dr. John Hardy in the School of Pharmacy, Queen's University Belfast.

The hydrogels were evaluated for their compressive and tensile moduli as shown in Figure 5.14a and Figure 5.14b, respectively. Representative tensile measurements are shown in Appendix A5; in general, these showed larger elongation strains prior to yielding in the hydrogels doped with Eu^{III}. However, the tensile elastic moduli determined were not significantly different (*ca*. 500 kPa) in the presence and absence of Eu^{III}. The tensile analysis was less reproducible and the sample sizes correspondingly lower and, therefore, only the

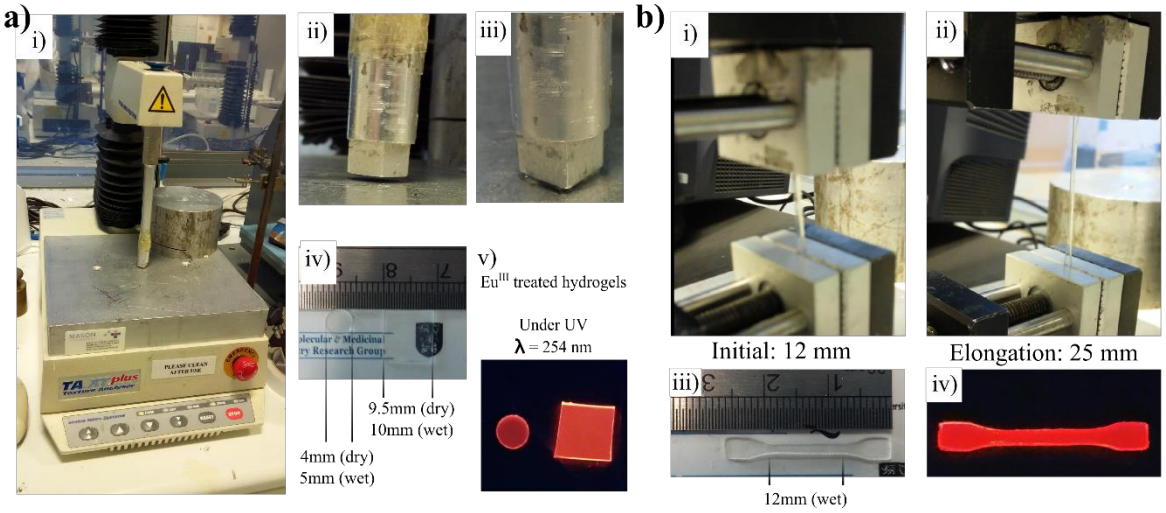

Figure 5.14 Photographs of: **a) i)** TextureAnalyser used to assess compressive and mechanical strength, **ii)** compression testing utility with surface area 100 mm^2, **iii)** square-cut hydrogel sample under compressive load showing expulsion of H_2O, **iv)** sample dimensions as die-cut circles (Ø 5mm) or square-cut (100 mm^2), **v)** Eu^{III}-treated samples under λ_{exc} = 254 nm showing formation the of Eu^{III} complexes; and **b) i)** initial state of tensile analysis with 12 mm sample, **ii)** strained sample at 100% elongation prior to yield, **iii)** die-cut sample for tensile analysis, iv) Eu^{III}-treated samples under λ_{exc} = 254 nm showing the formation of Eu^{III} complexes.

measurements and analysis from compression tests were deemed reliable. Samples were either die-cut as circles (ϕ = 5mm) or cut by scalpel as squares (10 mm x 10 mm) from various points across the swelled polymer gels. The swelled thickness of the gels was not uniform with variation between 0.97 – 1.20 mm, therefore, the thickness was measured for each sample and taken into account in each individual measurement. The material samples were then placed under compressive strain at a rate of 1 mm s^{-1} for 25% the original thickness of the materials (*i.e.* a sample of 1.2 mm was compressed by 0.3 mm). A single measurement was taken from each sample and at least 12 repetitions were performed for each condition of the polymer gels.

Representative stress *vs*. strain curves for p(HEMA-*co*-EGDMA-*co*-**127(*S,S*)**) are shown in Figure 5.15a in both H_2O and aqueous Eu^{III} (0.33 equivalents) solutions; the stress *vs*. strain curve showed a typical behaviour of porous polymer scaffolds.[563] The initial region of 5% compressive strain was non-linear in the stress response and can be consider as a 'toe region', likely being accounted for by the lateral straightening of some entangled polymer chains.[564] This was followed by a linear region (between *ca*. 5 – 15% strain magnitudes) which corresponded to the linear elastic response of the hydrogels after which a second non-linear stress response was observed. At 15 – 25% compressive strain the non-linear behaviour is likely accounted for by densification of the material caused by a significant collapse of the porous network of the gel and partial dehydration of the gel (by force). The materials did not reach compressive yield during these measurements. Both the Eu^{III}-doped

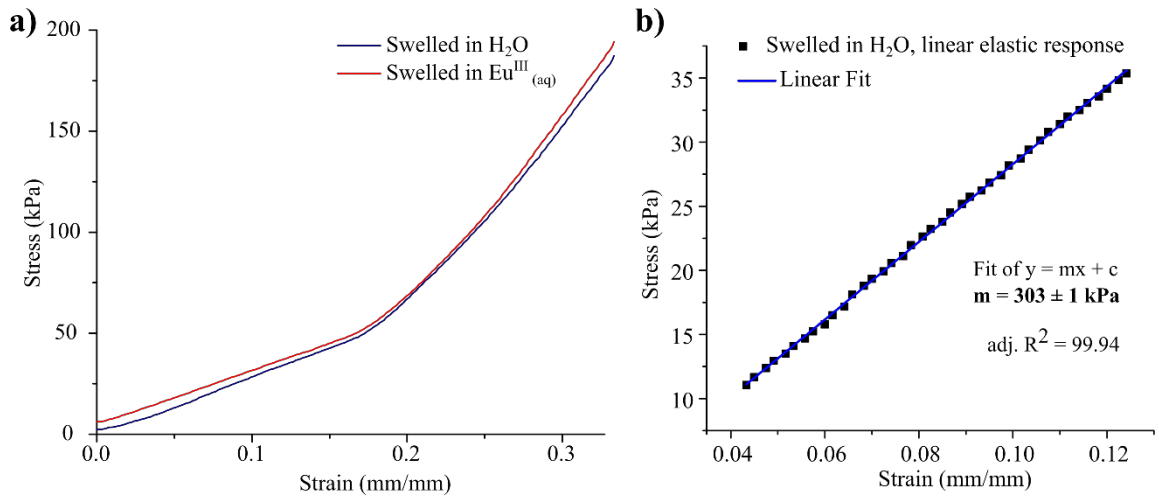

Figure 5.15 a) Representative stress *vs*. strain curves from compression tests recorded for p(HEMA-*co*-EGDMA-*co*-**127(*S,S*)**) swelled in H_2O (blue) and in 0.33 equivalents of Eu^{III} (red) between 0 → 25% compressive strain; and **b)** zoomed region of the linear elastic response between 0.04 → 0.12 mm/mm (5 → 10%) compressive strain (points) of for p(HEMA-*co*-EGDMA-*co*-**127(*S,S*)**) swelled in H_2O and the linear fit to calculate compressive modulus (m, line). These represent one repetition, final modulus values were determined as the average of 12 replicates.

and the control hydrogels gave similar stress *vs*. strain curves, this implying that there was little difference in the mechanical response introduced by the formation of the Eu^{III}-based crosslinks. The linear elastic region between 15 – 25% can be fitted to determine the compressive modulus from the gradient of elastic behaviour in the stress *vs*. strain responses. Values for the modulus were determined from each experiment (repetitions > 12) and the average modulus determined in each condition along with the standard deviation; the calculated values are summarised in Table 5.4.

Table 5.4 Compressive modulus values determined for p(HEMA-*co*-EGDMA-*co*-**127(*S,S*)**) polymer gels swelled in H_2O and 0.33 equivalents of aqueous $Eu(CF_3SO_3)_3$. [a]0% EGDMA crosslinking. Values were calculated as the mean average of multiple measurements and the error represents the standard deviation from the mean.

Crosslinker loading (wt%)	**Compressive modulus (kPa)**	
	H_2O	**0.33 equiv. Eu^{III} (aq.)**
0.01	300 ± 20	330 ± 20
0.1	310 ± 20	310±10
0.05[a]	220 ± 20	250 ± 30

Compressive modulus values were determined in H_2O and Eu^{III} as 300 ± 20 and 330 ± 20 kPa, respectively. However, the internal variation within, and between, the samples measured are not significantly different and cannot be distinguished within the error of the standard deviations. Moreover, these moduli values, and the onset of densification, were in

close agreement with those determined for blank p(HEMA-*co*-EGDMA) recorded experimentally and demonstrated the bulk properties still reflected the unmodified matrix.[475] At higher loadings of the crosslinker **127(*S,S*)** the same compressive elastic modulus was determined for neat and Eu^{III}-doped materials for both p(HEMA-*co*-EGDMA) and p(HEMA) materials at *ca*. 310 and 250 kPa, respectively. Interestingly, at 0.1 wt% loadings of **127(*S,S*)** the densification response (Appendix A5) was reproducibly perturbed by the presence of Eu^{III}, implying that the supramolecular crosslinking was influencing the behaviour. However, the elastic response remained unaffected. It would be expected that larger changes could be detected with significantly larger loadings of the cross-linking monomer. However, neither the materials nor the time was not available to prepare the required quantities of additional materials and study during this time. In fact, at substantially larger loadings of **127(*S,S*)** the crude synthetic procedures were not robust enough and uniform, optical transparent materials could not be obtained (Appendix A5). This was suggested to be because of poorer miscibility of **127(*S,S*)** in the neat mixtures of HEMA and EGDMA compared to the low loadings used in previous studies. These concerns and numerous other open-questions concerning will become the focus of further work and can be readily addressed.

5.8 Conclusions and future perspectives

This chapter described a set of preliminary studies from the initial stages of an ongoing larger project of smart, luminescent materials operating with emissive lanthanide complexes formed as supramolecular crosslinks intrinsic to the polymeric material. Two novel naphthyl-**dpa** structures, one symmetrical and the other asymmetrical, were synthesised with both possessing propyl methacrylamide pendent chains suitable for copolymerisation with other methacryl- species. The ligands were characterised for their structure and photophysical properties using various techniques including ^{1}H- and ^{13}C- NMR spectroscopy, IR analysis, HRMS and spectrophotometry of absorbance and emission properties. The formation of Eu^{III} complexes were demonstrated with $Eu(CF_3SO_3)_3$ from time-gated emission and UV-visible absorption spectroscopies showing characteristic Eu^{III} emission spectra and π-π stacking of ligand chromophores from the directed assembly, respectively. The directed self-assembly processes of Eu^{III} complexes under kinetic control were shown to be in agreement to the respective ligand families and pyridine substitution patterns from spectroscopic titrations in CH_3CN. Global stability constants were estimated as $\log\beta_{MLn}$ for **127(*S,S*)** as 6.9 ± 0.1, 13.5 ± 0.2 and 20.5 ± 0.1 for $\log\beta_{ML}$, $\log\beta_{ML2}$ and $\log\beta_{ML3}$, respectively. Similarly, for **128(*S*)** constants of 7.6 ± 0.3, 14.5 ± 0.2 and 20.1 ± 0.4

were determined. The various complexes were characterised in different solvent conditions and determined from the Eu^{III} luminescence lifetimes to have different speciation in these different solvents with *q*-values confirming the complex identities where possible as **ML_3** or **ML_2** stoichiometry. The complexes of **127(*S,S*)** showed partial (*ca*. 5%) dissociation in organic solvents while **128(*S*)** formed **ML_2** species uniquely in CH_3OH.

Polymer matrices of p(HEMA-*co*-EGDMA) were synthesised including the novel monomers **127(*S,S*)** and **128(*S*)** directly with the copolymers and formed as brittle, optically transparent monoliths. The resulting polymers were mechanically and photophysically characterised with the formation of a homogenous matrix suggested from DSC and ^1H NMR measurements. The photophysical properties of the individual ligands were transferred into the respective bulk solid materials and, on submerging in aqueous solutions, swelled into soft polymer gels which also retained these photophysical properties. p(HEMA-*co*-EGDMA-**127(*S,S*)**) containing a symmetrical *N*-linked naphthyl-**dpa** co-monomer were shown to be fluorescent under UV irradiation and both p(HEMA-*co*-EGDMA-**127(*S,S*)**) and p(HEMA-*co*-EGDMA-**128(*S*)**) gave rise to Eu^{III}-centred emission when treated in solutions containing Eu^{III}. The Eu^{III}-centred emission of the polymer materials was studied in detail for the spectral structure and these were comparable to those obtained in solution. The hydrogels were prepared in aqueous solutions of 0.33 equivalents Eu^{III} to promote the formation of triple-crosslinks during equilibration of the internal gel environment. The average distribution of the complexes formed within the polymer gels was characterised through the luminescence lifetime measurements (and confirmed where possible for stoichiometry by q-value estimated from the analogous deuterated system). The mobility and hydration of the polymer chains was shown to be reflected in the distribution luminescence lifetimes of the Eu^{III}-based complexes, from comparisons of hydrated and dehydrated gels. For the symmetrical naphthyl-**dpa** system, the formation of a bulk **ML_3** stoichiometry was suggested in the swelled material, while a disruption into intermediate species was shown in the dehydrated states. On the other hand, the asymmetrical naphthyl-**dpa system** showed the formation of **ML_2** stoichiometry complexes in the swelled material and again disruption into the other species in the dehydrated state. Mechanical stress on the swelled materials (in the forms of elongation, compression or cutting) was not measurably reflected in the emission or lifetime results. The bulk mechanical properties of p(HEMA-*co*-EGDMA-**127(*S,S*)**) were measured and compressive moduli determined for the swelled polymer gels in H_2O and in the presence of Eu^{III} as 300 ± 20 and 330 ± 20 kPa, respectively, for these samples. These demonstrated that no significant difference was observed.

The future direction of this research should address the number of open questions and the potential development routes. An improved understanding of the self-assembly behaviour would be desirable. This could be achieved by the design of titration protocols to study the self-assembly processes in the hydrogel matrix directly. Modified fabrication methods are required to allow increases in the loading of novel monomers (*i.e.* suitable solubility) and produce consistent homogenous materials across a wider range of cross-linker loadings. One approach to direct such improvement will be the use of solubility modelling, i.e. Hansen parameters,[565] to understand which ligands and which matrices will have the most compatible solubility in a predictive fashion. The challenge of *in-situ* spectroscopic measurement during the mechanical strains (*e.g.* shear, extension, compression *etc.*) rather than afterwards to eliminate the rapid dynamic rearrangement during the unloading and relaxation processes of the samples. This can only be addressed through the design of specialist instrumentation or customised sample holders and would require significant research efforts. However, in general, to address the potential of using luminescence changes (*e.g.* lifetime distribution) to monitor the hydrogels, spatial resolution in the spectroscopy is required. The distribution of ligands and complexes can be mapped spatially using techniques such as Raman[566] and confocal microscopy[86] while studies using fluorescence and phosphorescence lifetime microscopy (FLIM and PLIM, respectively) would also be of great potential.[567-572] These techniques are commonly applied to the biological sciences for studying dynamics within soft matrices, such as lipid bilayers, which can be viewed analogously to studying complexes dynamics in the polymer hydrogels.[568] A map of Eu^{III} lifetimes would allow the mapping of different crosslinking complexes throughout the materials, monitoring of specific strain points and potential identification of smaller changes. As a result of less background noise from dynamic rearrangements in the remaining bulk material, the Eu^{III}-based crosslinking may have potential in the development of both polymer materials and other soft matter.

6. Experimental Details

6.1 General methods and materials

All reagents and solvents were purchased from commercial suppliers and used without further purification. Dry solvents were prepared following standard procedures[573] or by solid-phase solvent purification. Synthesis was completed, unless stated, under inert atmospheres of N_2 or Ar. Flash chromatography was carried out using a TeledyneIsco CombifFlash Rf 200 automated purification system; pre-packed normal phase, amine or C-18 silica cartridges were used supplied by TeledyneIsco RediSep® or Grace Technologies. Thin-layer chromatography (TLC) was conducted using MerckMillipore Kiesegel 60 F_{254} silica or alumina plates and visualised under $\lambda = 254$ nm; amine containing compounds were visualised using Ninhydrin in EtOH. Melting points were determined using an Electrothermal IA900 digital apparatus. Infrared spectra were recorded (in cm^{-1}) using a PerkinElmer Spectrum One FT-IR Spectrometer fitted with a universal ATR sampling accessory from solid samples under 70 N compression. Elemental analysis for % carbon, hydrogen and nirogen was carried out at the Microanalytical Laboratory, School of Chemistry and Chemical Biology, University College Dublin. Microwave-assisted reactions were carried out in a Biotage Initiator Eight EXP microwave reactor using 2-5 mL or 10-20 mL sealed vials.

6.1.1 NMR Spectroscopy

NMR spectra were recorded using a Bruker DPX-400 Avance spectrometer or Agilent DD2/LH spectrometer at frequencies of 400.13 MHz and 100.6 MHz for ^{1}H-NMR and ^{13}C-NMR, respectively; or a Bruker AV-600 spectrometer at frequencies of 600.1 MHz and 150.2 MHz for ^{1}H-NMR and ^{13}C-NMR, respectively. All spectra were recorded in commercially sourced per-deuterated solvents and referenced to residual proton signals of those solvents. Recorded free-induction decay signals were Fourier-transformed and processed using MestreNova v.6 without apodization and chemical shifts expressed in parts per million (ppm / δ) and coupling constants (J) in Hz.

6.1.2 Mass Spectrometry

Mass spectrometry was completed in the departmental mass spectrometery service of the School of Chemistry, Trinity College Dublin. Electrospray mass spectra were measured on a Micromass LCT spectrometer calibrated against a leucine enkephaline standard. MALDI Q-ToF mass spectra were recorded on a MALDI Q-TOF Premier (Waters Corporation, Micromass MS Technologies, Manchester, UK) and high-resolution mass spectrometer was performed using Glu-Fib as an internal reference (m/z = 1570.677).

6.1.3 Photophysical measurements

All photophysical measurements were taken in spectroscopic grade solvents (Sigma-Aldrich®) were used in quartz cells purchased from HellmaAnalytics with path length 10mm. Spectroscopic solutions were prepared from stock solutions using Pipetman® Classic micropipettes (Gilson, Inc)

6.1.3.1 UV-visible absorption and luminescence spectroscopy

UV-visible absorption spectra were recorded using a Varian Cary 50 spectrophotometer, a spectroscopic window of 450 – 200 nm was used for all spectra with applied baseline correction from blank solvent. Luminescence spectra (fluorescence and time-gated emission) were recorded using a Varian Cary Eclipse spectrophotometer and reported in arbitrary units; spectral windows of 570 – 720 nm and 470 – 720 nm were applied for Eu^{III} emission and mixed Eu^{III}/Tb^{III} emission, respectively. Time-gated emission spectra were recorded over an average integration time for 0.1 seconds. The temperature was kept constant throughout the measurements at 298 K by using a thermostated unit block

6.1.3.2 Luminescence lifetime measurements

Luminescence lifetime measurements of Eu^{III}-centred emission was recorded using a Varian Cary Eclipse spectrophotometer as a time-resolved measurement at 298 K. Excitation was made at the maximum absorbance (*ca.* 281 – 310 nm) and, following a gate time, the decay in intensity of the $^5D_0 \rightarrow {}^7F_2$ transition of Eu^{III} was monitored. Final lifetimes were averaged from at least five measurements at different gate times between 0.02 – 0.04 ms. The recorded decay curves were fitted to mono- or bi-exponential decay functions using Origin® 8.5.

6.1.3.3 pH measurements

pH measuremetnts were made using either an Orion™ 9157BNMD Triode™ Ag/AgCl electrode (Thermo Scientific™) connected to a digital readout on a sympHony™ SB70P benchtop meter (VMR®), or using EcoTestr pH 2 handheld meter (Oakton Instruments). The probes were calibrated against pH standards provided by Fluka® and Hanna Instruments.

6.1.3.5 Circular dichrosm and circularly polarised luminescence spectroscopy

Circular dichroism (CD) spectra were recorded in solution on a Jasco J-810-150S spectropolarimeter under a constant flow of nitrogen. Each spectrum corresponded to a three-scan collection with applied baseline correction. Temperature-dependent CD measurements were carried out in the same spectrometer using a recirculating thermostatic bath. Circularly polarised luminescence (CPL) spectra were recorded by Dr. R. D. Peacock

at the University of Glasgow, UK. Circularly polarized luminescence (CPL) measurements were made on a home built instrument constructed round a Fluoromax 2. A Coherent 599 tunable dye laser (0.03 nm resolution) with argon ion laser as a pump source was used to excite the complexes and achieve Eu^{III}-centred luminescence. Calibration of the emission monochromator was accomplished by passing scattered light from a low power HeNe laser through the detection system. The optical detection system consisted of a photoelastic modulator (PEM, Hinds Int.) operating at 50 kHz and a linear polarizer, which together act as a circular analyzer, followed by a long pass filter, focusing lens and a 0.22 m double monochromator. The emitted light was analysed by passing it through a photoelastic modulator and plane polarizer. The signal from the photomultiplier, after a/d conversion, was processed by a lock-in amplifier which extracts the AC (CPL, $\Delta I = I_{left} - I_{right.}$) and DC ($I = I_{left} + I_{right,}$) signals

6.1.3.6 Dynamic light scattering

All DLS measurements were made from back scatter in using Malvern Instruments Zetasizer Nano Series at 25 ºC in acrylic cuvettes with a path length of 10 mm. Statistical distributions by intensity were determined using the instrument software with standard deviations determined from triple replicate measurements. Samples were prepared in H_2O filtered six times through a 0.45µm syringe filter (Acrodisc®, PTFE).

6.1.4 Microscopy

6.1.4.1 Scanning electron microscopy

Microscopy analysis of gel-aggregate samples by Scanning Electron Microscopy (SEM) was carried out under collaboration with Mr. Savyasachi A Jayanth and Ms. Amy D. Lynes from the Gunnlaugsson group and using the facilities of the Advanced Microscopy Laboratory (AML) in Trinity College Dublin. Samples were prepared by a drop-casting methodology onto clean silicon wafers (cleaned by sonication in HPLC-grade acetone followed by HPLC-grade propan-2-ol) from glass Pasteur pipettes.[355] The manually drop cast samples were dried overnight in ambient conditions and under high vacuum for 2 hours prior immediately to their imaging. Where stated, samples were coated with a conductive Au layer, by sputtering, in order to improve contrast where static charging interfered with the imaging. Low kV SEM was carried out using the Zeiss ULTRA Plus using an SE2 detector.

6.1.4.2 Fluorescence optical microscopy

Fluorescence optical microscopy of polymer hydrogel materials was completed during research visits with Prof. Colin P. McCoy at the School of Pharmacy, Queen's University

Belfast using a GXML3201LED from GX Microscopes with UV-excitation and objective lenses at 10X, 40X and 100X magnification.

6.1.5 Compressive and tensile modulus testing

Mechanical analaysis of polymer hydrogel samples were carried out in collaboration with Prof. Colin P. McCoy at the School of Pharmacy, Queen's University Belfast using a TA.XT Plus Texture Analyser (Stable Micro Systems). Samples for compression test were die-cut as cylinders (ϕ = 5mm) or cut square (10 mm x 10 mm) and were compressed to 75% of the original thickness at a rate of 12 mm/min. For tensile analysis, samples were die-cut to a standard "dog-bone" shape, clamped between two opposing plates and stretched at a rate of 12 mm/min (only runs which did not slip from the clamps and yielded in the centre of the sample were considered for analysis).

6.1.6 Thermal calorimetry

6.1.6.1 Isothermal titration calorimetry

Isothermal titration calorimetry (ITC) was carried out by Prof. Amir Khan at the School of Biochemistry, Trinity College Dublin using a MicroCal iTC200 instrument (Malvern Instruments). Ligand samples were prepared in filtered buffer solutions and dialysed against excess buffer to equilibrate salt concentrations using SpectraPor® dialysis tubing with a 100 – 500 D molecular weight cutoff. EuCl3 and TbCl3 solutions were supplied by SigmaAldrich® at high purity (>99.999% metal basis) and prepared from the dialysed buffer immediately prior to measurements.

6.1.6.2 Dynamic scanning calorimetry

Dynamic scanning calorimetry (DSC) was carried out either in at the School of Pharmacy, Queen's University Belfast using a DSC 2920 Modulated DSC (TA Instruments) or in the School of Chemistry, Trinity College Dublin using a DSC 8000 (Perkin Elmer). Samples were prepared in DSC pans provided by TA Instruments and PerkinElmer, respectively, and heat flows measured against a reference pan. Both instruments were fitted with recirculating coolers and programs run with heating and cooling rates of 5 °C min^{-1} and 10°C min^{-1}, respectively. The temperature extremes were held isothermally between each heating and cooling run. T_g values were estimated at the centre point by tangent extrapolation methods using TA Universal Analysis or Pyris® software associated with the respective instruments.

6.2 Synthesis

Protocol 1: Aryl amination by nucleophilic aromatic substitution for **121 - 125** and **141(*S,S*).**

Compound **126(S,S) or 126(R,R)** (1 equiv.) was refluxed in distilled *N,N*-dimethylethanolamine, *N,N*-dimethylethylenediamine, *N',N,N*-trimethylethylenediamine, isopentanol, isopentylamine or 1,3-diaminopropane (1.5 mL) for **121, 122, 123, 124, 125** and **141(*S,S*)** respectively. Upon completion by TLC reaction mixtures were poured into iced-water (3 mL) precipitating beige solids which were isolated by filtration and washed with excess H_2O and dried *in vacuo*. Crude mixtures were eluted on silica (RediSep® 40g, 10 CV DCM followed by gradient elution 0 → 15 % CH_3OH in DCM), product containing fractions were concentrated to give pure products as white solids.

Protocol 2: Preparation of complexes under microwave irradiation

Ligand was dissolved in CH_3OH (5 mL) and treated with 0.33 equivalents of the appropriate Ln^{III} salt for 30 minutes at 70 ºC. The resulting solutions were concentrated *in vacuo* then re-dissolved into minimal CH_3OH. The concentrated solution was subsequently precipitated in rapidly stirred diethyl ether (100 ml) to give white solids. Precipitates were collected by centrifuging and filtering the recovered solids; products were washed with Et_2O and dried under high vacuum.

6.2.1 Ligand synthesis & characterisation

4-Hydroxy-*N,N'*-bis((*S*)-1-(naphthalen-1-yl)ethyl)pyridine-2,6-dicarboxamide - 133(*S,S*)

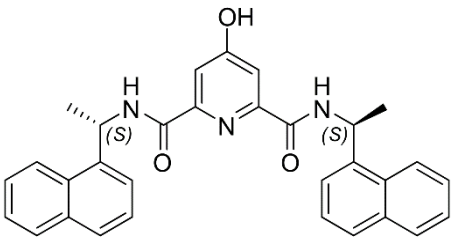

A solution of chelidamic acid monohydrate (0.50 g, 2.49 mmol), HOBt hydrate (0.98 g, 7.25 mmol), EDCI (0.9 mL , 5.10 mmol) and TEA (0.7 mL, 5.02 mmol) in anhydrous THF (50 mL) was stirred at 0 ºC for 30 minutes then treated with *(S)*-1-(1-naphthyl)ethylamine (0.85 mL, 5.30 mmol) dropwise. After 30 minutes the reaction was allowed to warm to RT and stirred for 48 hours. All insoluble residues were removed by filtration, the filtrate concentrated to dryness then re-dissolved into CH_2Cl_2 (150 mL). This solution was washed with 1M HCl (2 x 50 mL), sat. aq. $NaHCO_3$ (2 x 50 mL) and brine (50 mL) and the organic phase dried over $MgSO_4$, filtered and concentrated *in vacuo*. Elution on silica (RediSep® 12g, 0 → 5 % CH_3OH in DCM) afforded **133(*S,S*)** pure as an off-white solid (0.682 g, 1.39 mmol, 56%); m.p. 154.6 – 155.3 ºC ; HRMS (*m/z*) (ES^+) Calculated for

$C_{31}H_{28}N_3O_3$ *m/z* = 490.2151 $[M + H]^+$. Found *m/z* = 490.2125; ^{1}H NMR (400 MHz, $CDCl_3$) δ : 8.15 – 8.08 (2H, m, naph-CH), 8.02 (2H, s, pyr-CH) 7.90 (3H, dd, *J* = 6.6, 3.0 Hz, naph-CH), 7.84 (2H, dd, *J* = 5.9, 3.6 Hz, naph-CH), 7.55 – 7.48 (4H, m, naph-CH), 7.46 – 7.39 (3H, m, naph-CH), 6.00 (2H, app. dd, *J* = 14.6, 7.1 Hz, aliphatic CH), 1.67 (6H, d, *J* = 6.8 Hz, CH_3) ^{13}C NMR (100 MHz, $CDCl_3$) δ : 158.4, 137.8, 133.8, 130.7, 130.7, 128.9, 128.4, 126.6, 125.9, 125.3, 123.0, 122.8, 113.2, 45.7, 21.0, 15.2; IR ν_{max} (cm^{-1}): 3281, 2970, 2927, 2865, 1654, 1599, 1509, 1448, 1353, 1236, 1135, 996, 799, 774.

4-Hydroxy-*N,N'*-bis((*R*)-1-(naphthalen-1-yl)ethyl)pyridine-2,6-dicarboxamide - 133(*R,R*)

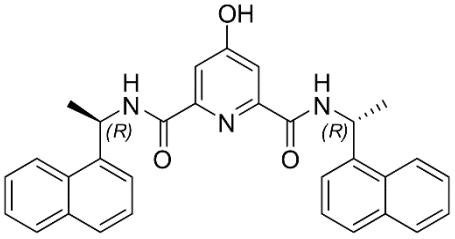

A solution of chelidamic acid monohydrate (0.50 g, 2.49 mmol), HOBt hydrate (0.98 g, 7.25 mmol), EDCI (0.9 mL , 5.10 mmol) and TEA (0.7 mL, 5.02 mmol) in anhydrous THF (50 mL) was stirred at 0 °C for 30 minutes then treated with *(R)*-1-(1-naphthyl)ethylamine (0.85 mL, 5.30 mmol) dropwise. After 30 minutes the reaction was allowed to warm to RT and stirred for 48 hours. All insoluble residues were removed by filtration, the filtrate concentrated to dryness then re-dissolved into CH_2Cl_2 (150 mL). This solution was washed with 1M HCl (2 x 50 mL), sat. aq. $NaHCO_3$ (2 x 50 mL) and brine (50 mL) and the organic phase dried over $MgSO_4$, filtered and concentrated *in vacuo*. Elution on silica (RediSep® 12g, 0 → 5 % CH_3OH in DCM) afforded **133(*S,S*)** pure as an off-white solid (0.682 g, 1.39 mmol, 56%); m.p. 154.0 – 155.1 °C ; HRMS (*m/z*) (ES^+) Calculated for $C_{31}H_{28}N_3O_3$ *m/z* = 490.2151 $[M + H]^+$. Found *m/z* = 490.2141. ^{1}H NMR (400 MHz, cdcl$_3$) δ 8.16 – 8.06 (m, 2H), 8.02 (s, 2H), 7.95 – 7.78 (m, 5H), 7.57 – 7.48 (m, 3H), 7.46 – 7.38 (m, 3H), 6.14 – 5.85 (m, 2H), 1.67 (d, *J* = 6.8 Hz, 6H). ^{13}C NMR (100 MHz, $CDCl_3$) δ : 158.4, 137.8, 133.9, 130.7, 130.7, 128.9, 128.5, 126.6, 125.9, 125.2, 123.1, 122.8, 113.2, 45.7, 21.0, 15.2; IR ν_{max} (cm^{-1}): 3280, 2971, 2928, 2864, 1654, 1597, 1509, 1447, 1353, 1236, 1135, 998, 797, 772.

3-(2,6-Bis((*S*)-1-(naphthalen-1-yl)ethylcarbamoyl)pyridin-4-yloxy)propane-1-sulfonate caesium salt - 120(*S,S*)

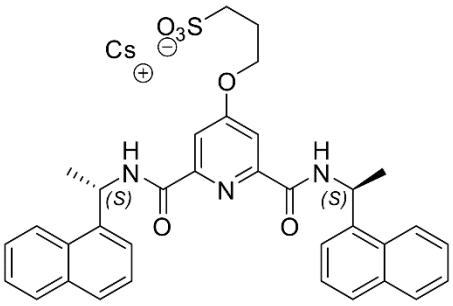

A solution of **133(*S,S*)** (1 equiv.) in anhydrous THF (25 mL) was treated with Cs_2CO_3 (2.5 equiv.) 1,3-propanesultone (0.98 equiv., as a volumetric solution in anhydrous THF) then heated at reflux for 2 hours. The reaction mixture was cooled and concentrated *in vacuo*, then the residue treated with acetone (50 mL) and sonicated for 30 minutes. Residues were isolated by filtration under suction; washed with acetone (250 mL) and Et_2O (100 mL) then dried under high vacuum to give a white solid, **122(*S,S*)** as the caesium salt. Yield: 71 %; m.p. 220.9 – 222.3 (decomposed at 224 ^oC); HRMS (*m/z*) (ES^-) Calculated for $C_{34}H_{32}N_3O_6S$ *m/z* = 61.2017[M – Cs]$^-$. Found *m/*z = 610.2015; ^1H NMR (400 MHz, CD_3OD) δ: 8.20 (2H, d, *J* = 8.3 Hz, naph-CH), 7.91 (2H, d, *J* = 7.8 Hz, naph-CH), 7.85 – 7.80 (4H, m, aryl-CH), 7.66 (2H, d, *J* = 7.0 Hz, naph-CH), 7.58 – 7.37 (6H, m, naph-CH), 6.09 (2H, q, *J* = 6.5 Hz, aliphatic CH), 4.36 (2H, t, *J* = 5.64 Hz, CH_2), 3.01 (2H, t, *J* = 7.1 Hz, CH_2), 2.32 (2H, m, CH_2), 1.74 (6H, d, *J* = 6.7 Hz, CH_3); ^{13}C NMR (100 MHz, CD_3OD) δ : 165.9, 162.19, 149.5, 137.1, 132.4, 129.3, 126.9, 126.0, 124.3, 123.7, 123.4, 121.2, 120.9, 109.4, 50.3, 49.9, 43.9, 43.7, 18.3; IR ν_{max} (cm^{-1}): 3300, 2932, 2570, 1638, 1599, 1521, 1393, 1351, 1180, 1137, 1034, 993, 884, 831, 800, 776, 733, 694, 661.

3-(2,6-Bis((*R*)-1-(naphthalen-1-yl)ethylcarbamoyl)pyridin-4-yloxy)propane-1-sulfonate caesium salt - 120(*R,R*)

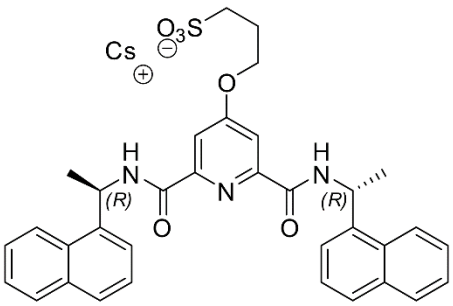

A solution of **133(*S,S*)** (1 equiv.) in anhydrous THF (25 mL) was treated with Cs_2CO_3 (2.5 equiv.) 1,3-propanesultone (0.98 equiv., as a volumetric solution in anhydrous THF) then heated at reflux for 2 hours. The reaction mixture was cooled and concentrated *in vacuo*, then the residue treated with acetone (50 mL) and sonicated for 30 minutes. Residues were isolated by filtration under suction; washed with acetone (250 mL) and Et_2O (100 mL) then dried under high vacuum to give a white solid, **122(*S,S*)** as the caesium salt. Yield: 70 %. m.p. 221 – 222 °C; HRMS (*m/z*) (ES^-) Calculated for $C_{34}H_{32}N_3O_6S$ *m/z* = 610.2017[M – Cs]$^-$. Found *m/*z = 610.2020. ^1H NMR (400 MHz, CD_3OD) δ 8.18 (d, *J* = 8.3 Hz, 2H), 7.88 (d, *J* = 7.1 Hz, 2H), 7.80 (d, *J* = 6 Hz,

2H), 7.63 (d, *J* = 7 Hz, 2H), 7.57 – 7.40 (m, 4H), 6.07 (q, *J* = 7.0 Hz, 2H), 4.33 (t, *J* = 6.2 Hz, 2H), 3.07 – 2.93 (m, 2H), 2.43 – 2.24 (m, 2H), 2.13 (s, 2H), 1.71 (d, *J* = 7.0 Hz, 6H). ^{13}C NMR (100 MHz, CD_3OD) δ : 165.9, 162.2, 149.5, 137.1, 132.4, 129.3, 126.9, 126.0, 124.3, 123.7, 123.4, 121.2, 120.9, 109.4, 50.3, 49.9, 43.9, 43.7, 18.3; IR ν_{max} (cm^{-1}): 3445, 3293, 3051, 1653, 1598, 1442, 1350, 1036, 997, 885, 776.

4-Chloro-*N,N'*-bis((*S*)-1-(naphthalen-1-yl)ethyl)pyridine-2,6-dicarboxamide - 126(*S,S*)

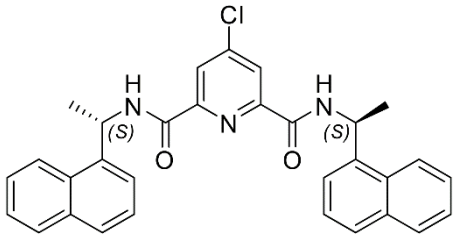

Chelidamic acid monohydrate was heated (0.40 g, 1.99 mmol) in $SOCl_2$ (5 mL) with cat. DMF (3 drops) at 50 °C for 18 hours until complete dissolution. Excess $SOCl_2$ was distilled under reduced pressure. The residue dried under high vacuum then dissolved into THF (50 mL) and treated with *(S)*-1-(1-naphthyl)ethylamine (0.64 mL, 3.99 mmol) and TEA (0.56 mL, 3.99 mmol) at 0 °C. After 30 minutes the reaction was allowed to warm to RT and stirred for 48 hours. Solvent was removed *in vacuo* then residues redissolved into CH_2Cl_2 (150 mL). This solution was washed with sat. aq. $NaHCO_3$ (2 x 50 mL), brine (50 mL) and the organic phase dried over $MgSO_4$, filtered and concentrated *in vacuo*. Trituration under CH_3OH and filtration of resultant solids yielded **126(*S,S*)** as a white solid (0.615 g, 1.21 mmol, 61%); m.p. 129.9 – 131.2 °C ; HRMS (*m/z*) (ES^+) Calculated for $C_{31}H_{27}ClN_3O_2$ *m/z* = 508.1766 $[M + H]^+$. Found *m/z* =507.1714; ^{1}H NMR (400 MHz, $CDCl_3$) δ : 8.34 (2H, s, pyridyl-CH), 8.13 (2H, br. d, *J* = 5.9 Hz, naph-CH), 7.85 (2H, br. d, *J* = 7.5 Hz, naph-CH), 7.63 (2H, d, *J* = 7.7 Hz, naph-CH), 7.55 – 7.49 (4H, m, naph-CH), 7.49 – 7.39 (4H, m, naph-CH), 6.12 – 5.89 (2H, m, pyr-CH), 1.67 (6H, d, *J* = 6.6 Hz, CH_3). ^{13}C NMR (100 MHz, $CDCl_3$) δ : 161.3, 150.0, 147.7, 137.8, 133.9, 130.9, 128.9, 128.6, 126.7, 126.0, 125.5, 125.2, 123.1, 122.7, 45.4, 20.8 ; IR ν_{max} (cm^{-1}): 3281, 2976, 1644, 1599, 1510, 1373, 1334, 1232, 1173, 1118, 1081, 998, 900, 860, 800, 777, 765, 681.

4-Chloro-*N,N'*-bis((*R*)-1-(naphthalen-1-yl)ethyl)pyridine-2,6-dicarboxamide - 126(*R,R*)

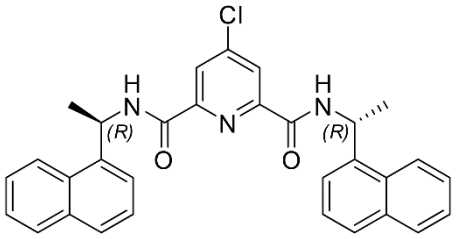

Compound **126**(R,R) was synthesised following the same procedures as **126**(S,S) coupling chelidamic acid with *(R)*-1-(1-naphthyl)ethylamine Compound **126**(R,R) was recovered as a white solid: Yield: 55%. m.p. 129.0 – 129.8 °C ; HRMS (*m/z*) (ES^+) Calculated for $C_{31}H_{26}ClN_3O_2Na$ *m/z* = 530.1611 $[M + Na]^+$. Found *m/z* = 530.1585. ^{1}H NMR (400

MHz, $CDCl_3$) δ 8.34 (s, 2H, pyridyl-CH), 8.22 – 8.07 (m, 2H, naphthyl-CH), 7.95 – 7.78 (m, 4H, naphthyl-CH), 7.62 (d, *J* = 8.1 Hz, 2H, naphthyl-CH), 7.52 (m, 4H, naphthyl-CH), 7.48 – 7.35 (m, 4H, naphthyl-CH), 6.12 – 5.92 (m, 2H, aliphatic-CH), 1.67 (d, *J* = 6.8 Hz, 6H, CH_3). ^{13}C NMR (101 MHz, $CDCl_3$) δ 161.3, 150.1, 147.8, 137.8, 134.0, 130.9, 128.9, 128.6, 126.7, 126.0, 125.5, 125.2, 123.2, 122.7, 45.4, 20.8. IR ν_{max} (cm^{-1}): 3276, 2985, 1650, 1523, 1396, 1328, 1237, 1169, 1133, 1081, 998, 893, 800, 778, 762, 684.

4-(2-(Dimethylamino)ethoxy)-*N,N*'-bis((*S*)-1-(naphthalen-1-yl)ethyl)pyridine-2,6-dicarboxamide - 121(*S,S*)

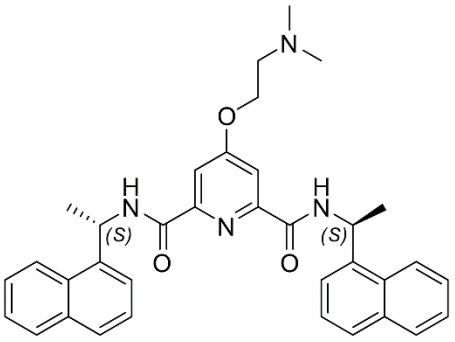

Compound **121(*S,S*)** was synthesised according to Protocol 1 – refluxing **126(*S,S*)** in *N,N*-dimethylethanolamine as solvent with reflux for 18 hours. Yield: 64 %; m.p. 197.6 – 198.2 ºC; HRMS (*m/z*) (ES^+) Calculated for $C_{35}H_{37}N_4O_3$ *m/z* = 561.2866 $[M + H]^+$. Found *m/*z = 561.2870; ^1H NMR (400 MHz, $CDCl_3$) δ : 8.23 – 8.08 (2H, m, naph-CH), 7.92 – 7.86 (2H, m, naph-CH), 7.86 – 7.76 (5H, m, aryl-CH), 7.51 (4H, dd, *J* = 5.5, 3.9 Hz, naph-CH), 7.45 – 7.40 (3H, m, naph-CH), 6.05 – 5.92 (2H, m, aliphatic CH), 4.28 (2H, app. s, CH_2), 2.90 (2H, app. d, *J* = 14.9 Hz, CH_2), 2.43 (6H, s, CH_3), 1.64 (6H, d, *J* = 6.8 Hz, CH_3). ^{13}C NMR (100 MHz, $CDCl_3$) δ : 162.2, 150.8, 138.1, 134.0, 130.9, 128.9, 128.5, 126.6, 125.9, 125.3, 123.3, 122.7, 111.3, 104.2, 57.2, 56.6, 45.3, 30.9, 21.0. ; IR ν_{max} (cm^{-1}): 3263, 3057, 2977, 2940, 2823, 2773, 1662, 1640, 1598, 1510, 1455, 1332, 1237, 1124, 1995, 1034, 890, 803, 779.

4-(2-(Dimethylamino)ethoxy)-*N,N*'-bis((R)-1-(naphthalen-1-yl)ethyl)pyridine-2,6-dicarboxamide - 121(*R,R*)

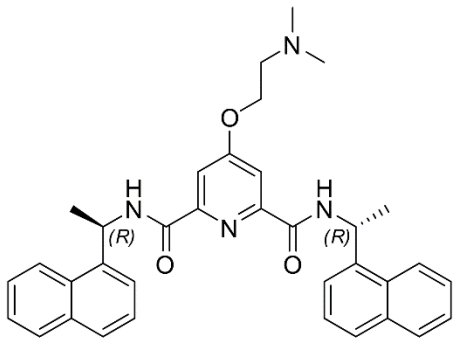

Compound **121(*R,R*)** was synthesised according to Protocol 1 – refluxing **126(*R,R*)** in *N,N*-dimethylethanolamine as solvent with reflux for 18 hours. Yield: 65 %; m.p. 197.0 – 197.5 °C; HRMS (*m/z*) (ES^+) Calculated for $C_{35}H_{37}N_4O_3$ *m/z* = 561.2866 $[M + H]^+$. Found *m/*z = 561.2872. ^1H NMR (600 MHz, $CDCl_3$) δ 8.18 – 8.11 (m, 2H, naphthyl-CH), 7.92 – 7.88 (m, 2H, naphthyl-CH), 7.86 (s, 2H, pyridyl-CH), 7.84 (d, *J* = 7.7 Hz, 2H, naphthyl-CH), 7.77 (d, *J* = 8 Hz, 2H, naphthyl-CH), 7.51 (dd, *J* = 6, 3 Hz, 4H, naphthyl-CH), 7.45 (q,

J = 7.5 Hz, 4H, naphthyl-CH), 6.18 – 5.67 (m, 2H, aliphatic-CH), 4.22 (t, *J* = 5.5 Hz, 2H, CH_2), 2.77 (t, *J* = 5.5 Hz, 2H, CH_2), 2.33 (s, 6H, CH_3), 1.66 (d, *J* = 7 Hz, 6H, CH_3), 1.58 (br. s, 2H). ^{13}C NMR (151 MHz, $CDCl_3$) δ 167.6, 162.0, 150.7, 138.2, 134.0, 131.0, 128.9, 128.5, 126.6, 125.9, 125.3, 123.3, 122.7, 111.4, 77.2, 77.0, 76.8, 67.0, 57.7, 45.9, 45.3, 21.0; IR ν_{max} (cm^{-1}): 3301, 3255, 3061, 2978, 2940, 2822, 2773, 1662, 1641, 1597, 1510, 1457, 1331, 1293, 1237, 1183, 1122, 1033, 995, 892, 802, 778.

4-(2-(Dimethylamino)ethylamino)-*N,N'*-bis((*S*)-1-(naphthalen-1-yl)ethyl)pyridine-2,6-dicarboxamide - 122(*S,S*)

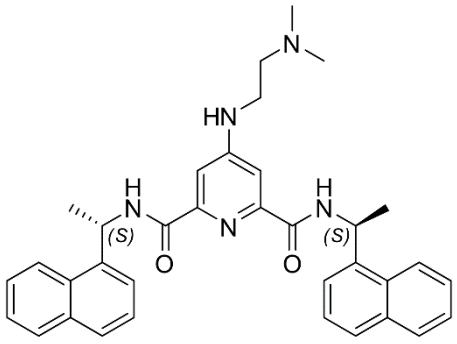

Compund **122(*S,S*)** was synthesised according to Protocol 1 – refluxing **126(*S,S*)** in *N,N*-dimethylethylenediamine as solvent with reflux for 18 hours. Yield: 75 %; m.p 129.6 – 130.5 °C; HRMS (*m/z*) (ES^+) Calculated for $C_{35}H_{38}N_5O_2$ *m/z* = 560.3026 $[M + H]^+$. Found *m/*z = 560.3033; ^1H NMR (400 MHz, $CDCl_3$+0.1%NaOD) δ : 8.28 – 8.12 (2H, m, naph-CH), 7.85 (5H, m, naph-CH), 7.58 – 7.36 (9H, m, aryl-CH), 6.07 – 5.87 (2H, m, CH), 3.42 (2H, br. s, CH_2), 2.84 (2H, br. s., aliphatic CH), 2.48 (6H, br. s, CH_3), 1.78 – 1.56 (6H, d, CH_3).: ^{13}C NMR (100 MHz, $CDCl_3$) δ : 163.5, 149.2, 138.5, 134.0, 130.9, 128.9, 128.3, 126.5, 125.8, 125.3, 123.3, 122.6, 117.0, 107.0, 48.1, 45.3, 38.5, 30.9, 21.2 ; IR ν_{max} (cm^{-1}): 3645, 3292, 3049, 2979, 2865, 2822, 2771, 1650, 1607, 1511, 1456, 1241, 1175, 1143, 991, 775.

4-(2-(Dimethylamino)ethylamino)-*N,N'*-bis((*R*)-1-(naphthalen-1-yl)ethyl)pyridine-2,6-dicarboxamide - 122(*R,R*)

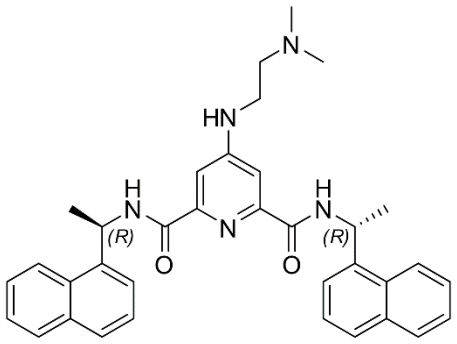

Compund **122(*R,R*)** was synthesised according to Protocol 1 – refluxing **126(*R,R*)** in *N,N*-dimethylethylenediamine as solvent with reflux for 18 hours. Yield: 62 %; m.p 130.1 – 130.9 °C ; HRMS (*m/z*) (ES^+) Calculated for $C_{35}H_{38}N_5O_2$ *m/z* = 560.3026 $[M + H]^+$. Found *m/*z = 560.3029*:* ^1H NMR (600 MHz, $CDCl_3$) δ 8.28 – 8.10 (m, 2H, naphthyl-CH), 7.95 – 7.86 (m, 2H, naphthyl-CH), 7.83 (d, *J* = 7.0 Hz, 4H, naphthyl-CH), 7.51 (dd, *J* = 9.2, 5.3 Hz, 4H, naphthyl-CH), 7.48 – 7.39 (m, 6H, aryl-CH), 6.12 – 5.91 (m, 2H, aliphatic-CH), 5.39 (br. s, 1H, aryl-NH), 3.27 (m, 2H, CH_2), 2.58 (m, 2H, CH_2), 2.26 (s, 6H, 2 × CH_3),

1.65 (d, J = 6.8 Hz, 6H, 2 × CH_3), 1.58 (br. s). ^{13}C NMR (151 MHz, $CDCl_3$) δ 163.3, 138.5, 134.0, 131.0, 128.9, 128.3, 126.5, 125.9, 125.3, 123.4, 122.6, 77.2, 77.0, 76.8, 57.0, 45.2, 44.9, 39.7, 21.1; IR ν_{max} (cm^{-1}): 3662, 3333, 3290, 2981, 2884, 2824, 2771, 1645, 1609, 1517, 1239, 1141, 991, 799, 779.

4-((2-(*N*-dimethyl-*N'*-methyl)ethylamino)-*N'',N'''*-bis((*S*)-1-(naphthalen-1-yl)ethyl)pyridine-2,6-dicarboxamide - 123(*S,S*)

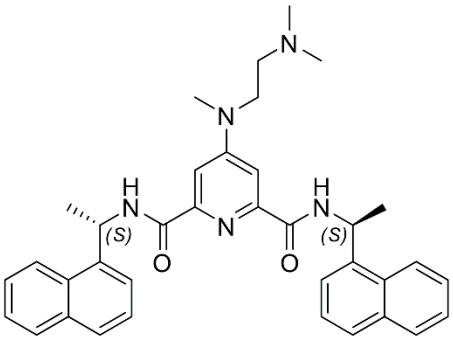

Compound **123(*S,S*)** was synthesised according to Protocol 1 – refluxing **126(*S,S*)** in *N,N,N'*-trimethylethylenediamine as solvent with reflux for 18 hours. Yield: 63 %; m.p. 169.2 – 169.9 ºC; HRMS (*m/z*) (ES^+) Calculated for $C_{36}H_{40}N_5O_2$ *m/z* = 574.3182 $[M + H]^+$. Found *m/z* = 574.3177; ^1H NMR (400 MHz, $CDCl_3$+0.1% NaOD) δ : 8.19 – 8.10 (2H, m, naph-CH), 7.95 – 7.86 (4H, m, aryl-CH), 7.86 – 7.79 (2H, m, naph-CH), 7.51 (5H, m, naph-CH), 7.47 – 7.37 (3H, m, naph-CH), 6.08 – 5.82 (2H, m, aliphiatic CH), 3.71 (2H, app. br. s, CH_2), 3.14 (3H, s, CH_3), 2.68 (2H, app. br. s, CH_3), 2.44 (6H, s, CH_3) 1.65 (6H, d, J = 6.8 Hz, **9**). ^{13}C NMR (100 MHz, $CDCl_3$) δ : 163.4, 155.4, 146.7, 138.4, 134.0, 130.9, 128.9, 128.3, 126.5, 125.8, 125.3, 123.3, 122.6, 113.5, 109.9, 106.8, 45.2, 38.4, 30.9, 21.1. IR ν_{max} (cm^{-1}): 3300, 2977, 2824, 2769, 1654, 1604, 1517, 1453, 1396, 1775, 1145, 1020, 866, 802, 776.

4-((2-(*N*-dimethyl-*N'*-methyl)ethylamino)-*N'',N'''*-bis((*R*)-1-(naphthalen-1-yl)ethyl)pyridine-2,6-dicarboxamide - 123(*R,R*)

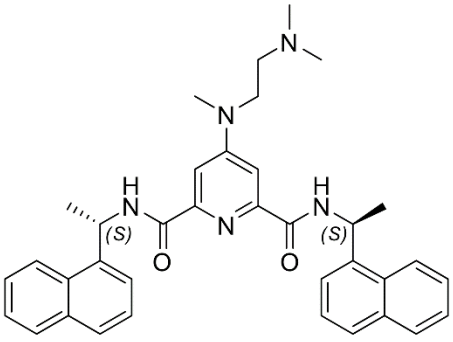

Compound **123(*R,R*)** was synthesised according to Protocol 1 – refluxing **126(*R,R*)** in *N,N,N'*-trimethylethylenediamine as solvent with reflux for 18 hours. Yield: 61 %; m.p. 168.8 – 169.8 ºC; HRMS (*m/z*) (ES^+) Calculated for $C_{36}H_{40}N_5O_2$ *m/z* = 574.3182 $[M + H]^+$. Found *m/z* = 574.3178. ^1H NMR (400 MHz, $CDCl_3$) δ 8.26 – 8.08 (m, 2H), 7.97 – 7.85 (m, 4H), 7.83 (dd, J = 5.7, 3.6 Hz, 2H), 7.58 – 7.47 (m, 6H, aryl-CH), 7.47 – 7.39 (m, 4H), 6.00 (app. p, J = 7 Hz, 1H, aliphatic-CH), 3.68 (m, 2H, CH_2), 3.13 (s, 3H, CH_3), 2.64 (m, 2H, CH_2), 2.53 – 2.30 (m, 6H, 2 × CH_3), 1.64 (d, J = 6.8 Hz, 3H, 2 × CH_3). ^{13}C NMR (101 MHz, $CDCl_3$) δ 163.4, 155.4, 149.3, 138.4, 134.0, 130.9, 128.9, 128.3, 126.5, 125.8, 125.3, 123.3,

122.6, 106.8, 77.3, 77.0, 76.7, 45.2, 38.4, 30.9, 21.12; IR ν_{max} (cm^{-1}): 3532, 3277, 2970, 2938, 2823, 2769, 1642, 1600, 1515, 1455, 1398, 1178, 1117, 1019, 864, 801, 778.

4-(Isopentyloxy)-*N,N'*-bis((*S*)-1-(naphthalen-1-yl)ethyl)pyridine-2,6-dicarboxamide - 124(*S,S*)

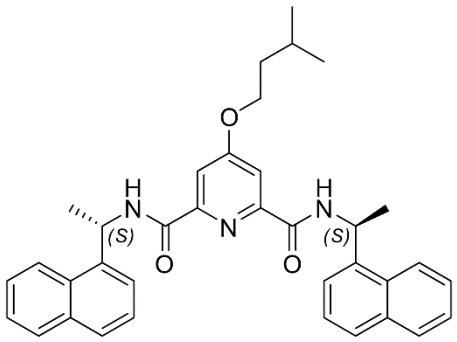

Compound **124(*S,S*)** was synthesised according to a modified procedure based on Protocol 1 – refluxing **126(*S,S*)** in isopentanol with Cs_2CO_3 (1.5 equiv.) as solvent with reflux for 18 hours. Yield: 30 %; m.p. decomposed over 220 ^oC; HRMS (*m/z*) (ES^+) Calculated for $C_{36}H_{38}N_3O_3$ *m/z* = 560.2913 $[M + H]^+$. Found *m/*z = 560.2901. ^1H NMR (400 MHz, cdcl$_3$) δ 8.21 – 8.09 (m, 2H), 7.93 – 7.87 (m, 2H), 7.86 – 7.81 (m, 4H), 7.77 (d, *J* = 8.2 Hz, 2H), 7.56 – 7.47 (m, 4H), 7.44 (t, *J* = 6.5 Hz, 4H), 6.10 – 5.94 (m, 2H), 4.16 (t, *J* = 6.6 Hz, 2H), 1.81 (dt, *J* = 19.5, 6.6 Hz, 1H), 1.72 (dd, *J* = 13.4, 6.7 Hz, 2H), 1.66 (d, *J* = 6.8 Hz, 6H), 0.96 (d, *J* = 6.6 Hz, 6H). ^{13}C NMR (100 MHz, $CDCl_3$) δ 162.2, 150.4, 138.2, 133.9, 130.9, 128.9, 128.4, 126.6, 125.9, 125.3, 123.2, 122.7, 111.5, 45.3, 37.3, 25.0, 22.4, 21.0. IR ν_{max} (cm^{-1}): 3306, 3259, 3040, 2957, 2873, 1661, 1639, 1598, 1512, 1455, 1354, 1239, 1183, 1121, 1029, 996, 890, 855, 804, 778, 732.

4-(Isopentyloxy)-*N,N'*-bis((*R*)-1-(naphthalen-1-yl)ethyl)pyridine-2,6-dicarboxamide - 124(*R,R*)

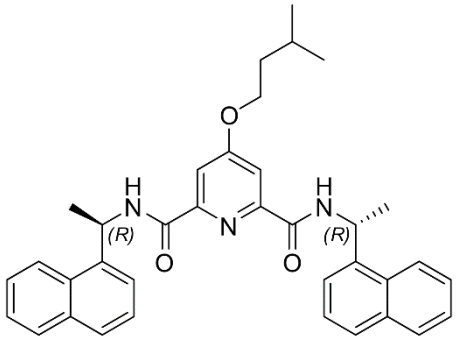

Compound **124(*R,R*)** was synthesised according to Protocol 1 – refluxing **126(*R,R*)** in isopentanol as solvent with reflux for 18 hours. Yield: 35 %; m.p. decomposed over 210 ^oC; HRMS (*m/z*) (ES^+) Calculated for $C_{36}H_{38}N_3O_3$ *m/z* = 560.2913 $[M + H]^+$. Found *m/*z =560.2897. ^1H NMR (400 MHz, $CDCl_3$) δ 8.16 – 8.05 (m, 2H), 7.89 – 7.83 (m, 2H), 7.82 – 7.76 (m, 4H), 7.72 (d, *J* = 8.2 Hz, 2H), 7.51 – 7.43 (m, 4H), 7.40 (t, *J* = 6.5 Hz, 4H), 6.05 – 5.89 (m, 2H), 4.11 (t, *J* = 6.6 Hz, 2H), 1.77 (dt, *J* = 19.5, 6.6 Hz, 1H), 1.67 (dd, *J* = 13.4, 6.7 Hz, 2H), 1.62 (d, *J* = 6.8 Hz, 6H), 0.92 (d, *J* = 6.6 Hz, 6H). 162.2, 150.4, 138.2, 134.0, 130.9, 128.9, 128.4, 126.6, 125.9, 125.3, 123.2, 122.7, 111.5, 45.3, 37.3, 24.9, 22.4, 20.9. IR ν_{max} (cm^{-1}): 3307, 3260, 3041, 2957, 2870, 1661, 1638, 1601, 1511, 1452, 1354, 1239, 1182, 1122, 1028, 997, 891, 855, 803, 778, 731.

4-(Isopentylamino)-*N,N'*-bis((*S*)-1-(naphthalen-1-yl)ethyl)pyridine-2,6-dicarboxamide - 125(*S,S*)

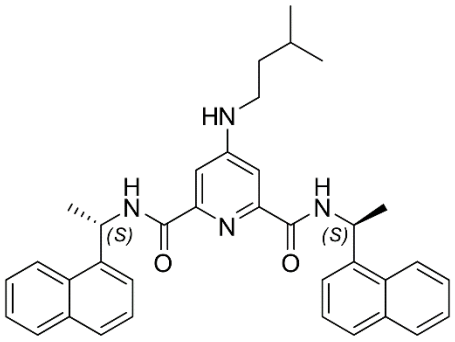

Compound **125(*S,S*)** was synthesised according to Protocol 1 – refluxing **126(*S,S*)** in isopentylamine as solvent with reflux for 18 hours. Yield: 65 %; m.p. 189.0 – 191.5 °C; HRMS (*m/z*) (ES^+) Calculated for $C_{36}H_{39}N_4O_2$ *m/z* = 559.3037 $[M + H]^+$. Found *m/z* = 559.3024. ^1H NMR (400 MHz, $CDCl_3$) δ 8.15 (dd, *J* = 7.1, 2.6 Hz, 2H), 7.99 – 7.86 (m, 2H), 7.86 – 7.74 (m, 6H), 7.56 – 7.48 (m, 4H), 7.48 – 7.36 (m, 4H), 6.16 – 5.93 (m, 2H), 4.15 (t, *J* = 6.6 Hz, 2H), 1.86 – 1.75 (m, 1H), 1.71 (q, *J* = 6.7 Hz, 2H), 1.66 (d, *J* = 6.8 Hz, 6H), 1.57 (br. s, 1H), 0.96 (d, *J* = 6.6 Hz, 6H). ^{13}C NMR (101 MHz, $CDCl_3$) δ 163.5, 162.7, 151.6, 147.0, 145.9, 138.4, 133.9, 130.9, 128.9, 128.0, 126.5, 125.8, 125.4, 123.2, 51.4, 45.7, 41.4, 29.7, 25.9, 22.4, 21.1. IR ν_{max} (cm^{-1}): 3406, 3281, 3256, 3041, 2925, 2964, 2869, 1657, 1605, 1517, 1475, 1365, 1293, 1240, 1184, 1116, 1143, 1081, 988, 879, 857, 803, 736

4-(Isopentylamino)-*N,N'*-bis((*R*)-1-(naphthalen-1-yl)ethyl)pyridine-2,6-dicarboxamide - 125(*R,R*)

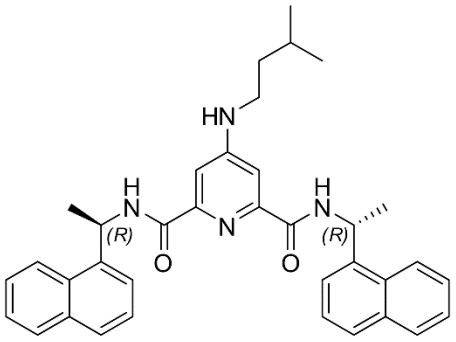

Compound **125(*R,R*)** was synthesised according to Protocol 1 – refluxing **126(*R,R*)** in isopentylamine as solvent with reflux for 18 hours. Yield: 70 %; m.p. 190.1 – 192.0 °C; HRMS (*m/z*) (ES^+) Calculated for Calculated for $C_{36}H_{39}N_4O_2$ *m/z* = 559.3037 $[M + H]^+$. Found *m/z* = 559.3029. ^1H NMR (400 MHz, $CDCl_3$) δ 8.15 (dd, *J* = 7, 3 Hz, 2H), 7.99 – 7.86 (m, 2H, pyridyl-CH), 7.85 – 7.73 (m, 6H, naph-CH), 7.56 – 7.48 (m, 4H, naph-CH), 6.14 – 5.91 (m, 2H, aliphatic-CH), 4.15 (t, *J* = 7 Hz, 2H, CH_2) , 1.86 – 1.75 (m, 1H, aliphatic-CH), 1.71 (app. q, *J* = 7 Hz, 2H, CH_2), 1.66 (d, *J* = 7Hz, 6H, CH_3), 1.57 (br. s., 1H, aryl-NH), 0.96 (d, *J* = 7 Hz, 6H). ^{13}C NMR (151 MHz, $CDCl_3$) δ 163.5, 162.7, 151.6, 147.1, 145.9, 138.4, 133.9, 130.8, 128.9, 128.3, 126.5, 125.8, 125.4, 123.1, 51.3, 45.6, 41.3, 25.87, 22.4, 21.1 IR ν_{max} (cm^{-1}): 3406, 3280, 3257, 3041, 2925, 2964, 2870, 1657, 1605, 1517, 1475, 1365, 1293, 1241, 1184, 1116, 1143, 1081, 990, 881, 857, 801, 732.

4-(3-Aminopropylamino)-*N,N'*-bis((*S*)-1-(naphthalen-1-yl)ethyl)pyridine-2,6-dicarboxamide - 141(*S,S*)

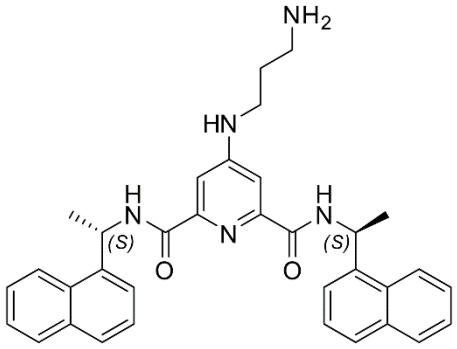

Compound **141(*S,S*)(*S,S*)** was synthesised according to Protocol 1 – refluxing **126(*S,S*)** in 1,3-diaminopropane as solvent with reflux for 18 hours. Yield: 45 %; m.p. 172 – 174 ºC; HRMS (*m/z*) (ES^-) Calculated for $C_{34}H_{34}N_5O_2$ *m/z* = 544.2713. Found *m/z* = 544.3138. $[M + H]^+$. ^1H NMR (600 MHz, $CDCl_3$, broad signals possible aggregation) δ 8.10 (m, 3H, aryl-CH), 7.79 (m, 4H, aryl-CH), 7.42 (m, 8H, aryl-CH), 5.96 (app. s, 1H, aliphatic-CH), 3.15 (m, 4H, CH_2), 2.07 (m, 2H, CH_2), 1.55 (app. s, 6H, CH_3). ^{13}C NMR (151 MHz, $CDCl_3$) δ 163.70, 155.70, 149.10, 138.72, 133.89, 130.81, 128.88, 128.11, 127.28, 126.45, 125.98, 125.78, 125.63, 125.44, 125.24, 123.23, 122.89, 122.61, 121.40, 46.51, 45.30, 30.92, 29.70, 24.74, 21.24. IR ν_{max} (cm^{-1}): 3285, 3048, 2934, 1654, 1605, 517, 1309, 1467, 1241 1144, 1116, 873, 9899, 777

4-(3-Methacrylamido-propylamino)-*N,N'*-bis((*S*)-1-(naphthalen-1-yl)ethyl)pyridine-2,6-dicarboxamide - 127(*S,S*)(*S,S*)

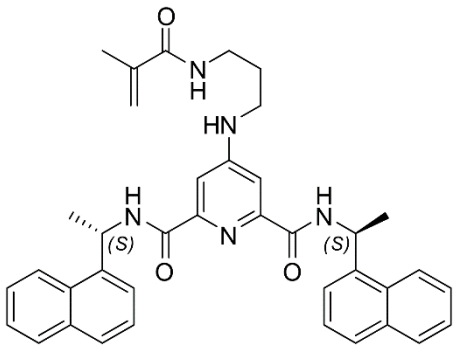

To a solution of **141(*S,S*)(*S,S*)** (0.250 g, mmol, 1 equiv.) in CH_2CL_2 (20 mL) at 0 °C methacrylic anhydride (0.2 mL, 1.26 mmol, 3.4 equiv.) was added and the reaction stirred at RT for 24 hours. The reaction mixture was subsequently diluted with CH_2Cl_2 (50 mL) and washed with H_2O (100 mL) and NaCl (sat. aq., 100 mL). The organic phase was dried over $MgSO_4$, filtered and concentrated *in vacuo* to afford a crude oily liquid which was eluted in silica (RediSep®, 5% CH_3OH in CH_2Cl_2). Product containing fractions were combined and concentrated *in vacuo* to give **127(*S,S*)** as a white solid. Yield: 65%; HRMS (*m/z*) (ES^+) Calculated for $C_{38}H_{38}N_5O_3$ *m/z* = 612.2975 $[M - H]^-$. Found *m/z* = 612.2964. ^1H NMR (400 MHz, $CDCl_3$) δ 8.11 (d, *J* = 4.5 Hz, 2H, aryl-CH), 7.85 (dd, *J* = 22.1, 17.2 Hz, 6H, aryl-CH), 7.58 – 7.33 (m, 8H, aryl-CH), 6.04 – 5.78 (m, 2H, aliphatic-CH), 5.66 (s, 1H, alkene-CH), 5.30 (s, 1H, alkene-CH), 3.25 (m, 4H, CH_2), 1.72 (m, 2H, CH_2) 1.61 (m, 6H, CH_3), 1.24 (s, 3H, CH_3). ^{13}C NMR (151 MHz, $CDCl_3$) δ 167.03, 156.55, 144.09, 135.33, 133.98, 133.38, 130.95, 128.91, 128.34, 127.28, 126.55, 125.84, 125.38, 123.30, 77.22,

77.01, 76.80, 45.52, 29.70, 21.05, 18.69, 18.58, 14.77. IR ν_{max} (cm^{-1}): 3290, 3051, 2961, 2935, 2870, 1763, 1651, 1607, 1519, 1451, 1376, 1172, 990, 868, 800, 776

6-((benzyloxy)carbonyl)pyridine-2-carboxylic acid[349] – 142[a]

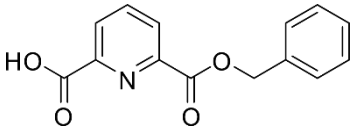

2,6-pyridinedicarboxylic acid (**6**, 2.043 g, 12.23 mmol, 1 equiv.) and $NaHCO_3$ (1.233 g, 14.66 mmol, 1.2 equiv.) were stirred in anhydrous N,N-dimethylformamide (DMF) (100 mL) at 60 °C under argon for 30 minutes. Benzyl bromide (1.7 mL, 15 mmol, 1.2 equiv.) was added dropwise and the reaction stirred under argon at 60 °C for 24 hours**.** The resulting yellow solution was diluted with water (100 ml), basified to pH 8 with $NaHCO_3$ (sat. aq.) and extracted with EtOAc (2 x 100 ml). The aqueous layer was then acidified to pH 3 with conc. HCl and extracted with EtOAc (2 x 100 ml). The organic layer was dried over $MgSO_4$, filtered and the solvent removed *in vacuo*. The resulting solid was dissolved in CH_2Cl_2 (100 ml). This solution was washed with water (100 ml) and NaCl (sat. aq., 3 x 100 mL) after which the organic layer was dried over $MgSO_4$, filtered and dried *in vacuo* to afford **142** as a white solid. Yield: 1.0205 g, 33 %; m.p. 133 - 134 °C; HRMS (*m/z*) (ES^-) Calculated for $[C_{14}H_{10}NO_4]^-$ *m/z* = 256.0610 $[M - H]^-$. Found *m/z* = 256.0615*;* ^1H NMR (400 MHz, $CDCl_3$) δ 8.46 – 8.34 (m, 2H, pyridine-CH), 8.12 (t, *J* = 7.8 Hz, 1H, pyridine-CH), 7.53 – 7.34 (m, 5H, phenyl-CH), 5.46 (s, 2H, CH_2); ^{13}C NMR (101 MHz, $CDCl_3$) δ 163.5, 146.7, 146.4, 139.7, 135.0, 128.9, 128.8, 128.6, 126.8, 68.1. IR ν_{max} (cm^{-1}): 2575, 1736, 1692, 1576, 1499, 1466, 1418, 1376, 1289, 1243, 1151, 1083, 994, 956, 941, 856, 797, 754, 729, 710, 691.

(*R*)-6-((1-(naphthalen-1-yl)ethyl)carbamoyl)-2-((benzyloxy)carbonyl)-pyridine[349] – 143(*S*)[a]

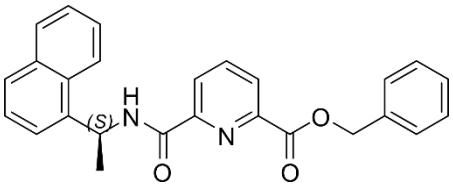

Compound **142** (1.021 g, 3.97 mmol, 1 equiv.), (*R*)-1-(1-naphthyl)-ethylamine (0.64 mL, 3.97 mmol, 1 equiv.), HOBt (0.536 g,3.97 mmol, 1 equiv.) and triethylamine (0.55 mL, 3.97 mmol, 1 equiv.) were stirred in anhydrous THF at 0 °C (50 ml) under argon 0.5 hours. To this solution, EDCI·HCl (0.760 g, 3.97 mmol, 1. equivalent) was then added and the reaction mixture left stirring at 0 °C for a further 0.5 hours. The mixture was allowed to warm to RT and stirred for an additional 24 hours. All insoluble residues were filtered and the filtrate concentrated *in vacuo* and dissolved in CH_2Cl_2 (100 ml) which was washed with 1 M HCl (2 x 100 ml), $NaHCO_3$ (sat. aq., 100 ml), water (100 ml) and NaCl (sat. aq., 100 ml). The organic layer was dried over $MgSO_4$, filtered and concentrated *in vacuo* to afford **143(*S*)** as a pale yellow oil. Yield: 1.3792 g, 85 %; HRMS (*m/z*) (ES^+)

Calculated for $[C_{26}H_{22}N_2O_3Na]^+$ *m/z* = 433.1528 $[M - Na]^+$. Found *m/*z = 433.1354. ^{1}H NMR (400 MHz, $CDCl_3$) δ 8.50 (d, *J* = 8.6 Hz, 1H, aryl-CH), 8.42 (d, *J* = 7.8 Hz, 1H, aryl-CH), 8.26 – 8.14 (m, 2H, aryl-CH), 7.98 (t, *J* = 7.8 Hz, 1H, aryl-CH), 7.87 (d, *J* = 7.9 Hz, 1H, aryl-CH), 7.81 (d, *J* = 8.6 Hz, 1H aryl-CH), 7.62 (d, *J* = 7.1 Hz, 1H, aryl-CH), 7.57 – 7.32 (m, 8H, aryl-CH), 6.29 – 6.02 (m, 1H, aliphatic CH), 5.40 (s, 2H, CH_2), 1.80 (d, *J* = 6.8 Hz, 3H, CH_3). ^{13}C NMR (101 MHz, $CDCl_3$) δ 164.1, 162.3, 150.1, 146.5, 138.5, 138.4, 135.4, 133.9, 131.0, 128.8, 128.6, 128.4, 128.2, 128.1, 127.3, 126.4, 125.7, 125.5, 125.3, 123.3, 122.6, 67.4, 44.9, 21.4. IR ν_{max} (cm^{-1}): 3385, 3301, 3049, 2979, 2875, 2319,, 1725, 1671, 1598, 1588, 1571, 1511, 1446, 1397, 1376, 1306, 1285, 1232, 1163, 1132, 1078, 998, 959, 908, 862, 843, 800, 778, 750, 733, 696

(*R*)-6-((1-(naphthalen-1-yl)ethyl)carbamoyl)pyridine-2-(carboxylic acid)[349] - 144(*S*) [a]

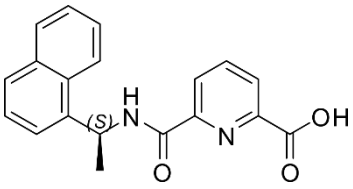

Compound **143(*S*)** (1.34g, 3.36 mmol, 1 equiv.) was dissolved in CH_3OH (60 mL) treated with 10 wt % Pd/C (0.054 g, 0.05 mmol, 0.15 equivalent). The reaction mixture was placed in a Parr hydrogen shaker under H_2 (3 atm.) and shaken for 24 hours. After the reaction had gone to completion, the mixture was filtered through Celite® and the filtrate concentrated *in vacuo* to afford **144(*S*)** as off white crystals. Yield: 0.95 g, 88 %; m.p. 102 – 104 °C; HRMS (*m/z*) (ES^-) Calculated for $[C_{19}H_{15}N_2O_3]^-$ *m/z* = 319.1088 $[M-H]^-$. Found *m/z* = 319.1085; ^{1}H NMR (400 MHz, $CDCl_3$) δ 8.44 (d, *J* = 7.8 Hz, 1H, aryl-CH), 8.27 (d, *J* = 7.7 Hz, 1H, aryl-CH), 8.15 (d, *J* = 8.2 Hz, 1H, aryl-CH), 8.09 (d, *J* = 8.4 Hz, 1H, aryl-CH), 8.03 (t, *J* = 7.8 Hz, 1H, aryl-CH), 7.82 (d, *J* = 8.2 Hz, 1H aryl-CH), 7.75 (d, *J* = 8.1 Hz, 1H, naphthyl-CH), 7.57 – 7.43 (m, 3H, aryl-CH), 7.43 – 7.37 (m, 1H, aryl-CH), 6.16 – 5.88 (m, 1H, aliphatic CH_2), 1.73 (d, *J* = 6.8 Hz, 3H, CH_3). ^{13}C NMR (101 MHz, $CDCl_3$) δ 163.8, 162.0, 149.2, 145.0, 139.5, 137.7, 133.8, 131.0, 128.8, 128.4, 126.7, 126.6, 125.8, 125.2, 123.1, 122.8, 50.8, 45.1, 20.8. IR ν_{max} (cm^{-1}): 3259, 2981, 1735, 1647, 1598, 1523, 1453, 1346, 1285, 1238, 1173, 1141, 1077, 1000, 920, 846, 800, 777, 745, 719

^{t}Butyl (3-aminopropyl)carbamate – 145

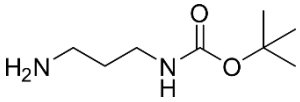

To a stirred solution of 1,3-diaminopropane (6 mL, 71.88 mmol, 1 equiv.) in $CHCl_3$ (50 mL) at 0 °C, a solution di-*tert*-butyldicarbonate (1.57 g, 7.19 mmol, 1 equiv.) in $CHCl_3$ (20 mL) was added dropwise and stirred at RT for 24 hours. The reaction mixture was subsequently washed with NaCl (sat. aq., 3 × 100 ml) and water (1 × 100 ml), dried over $MgSO_4$, filtered and concentrated *in vacuo* to afford **145** as a colourless oil. Yield: 1.05 g, 84 %; HRMS (*m/z*) (ES^-) Calculated

for $[C_8H_{17}N_2O_2]^-$ *m/z* = 173.1290 $[M-H]^-$. Found *m/z* = 173.1283; ^{1}H NMR (400 MHz, $CDCl_3$) δ 3.21 (m, 2H, CH_2), 2.76 (t, *J* = 7 Hz, 2H, CH_2), 1.61 (t, *J* = 7 Hz, 2H, CH_2), 1.44 (s, 9H, CH_3), 1.37 (br. S., 2H, NH_2). ^{13}C NMR (101 MHz, $CDCl_3$) δ 156.1, 78.9, 39.5, 38.2, 33.3, 28.3.

(*R*)-(3-(6-((1-(naphthalen-1-yl) ethyl)carbamoyl)pyridine-2-amido)propyl)carbamate[349] – 146(*S*)[a]

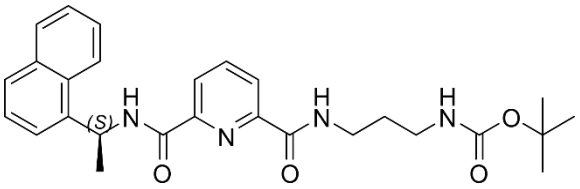

Compound **144(*S*)** (0.843 g, 2.63 mmol, 1 equiv.) was dissolved in anhydrous THF (50 mL) at 0 °C and HOBt (0.356 g, 2.63 mmol, 1 equiv.), NEt_3 (0.37 mL, 2.63 mmol, 1 equiv.) and **145** (0.4615 g, 2.63 mmol, 1 equiv.) were added to the solution. EDCI·HCl (0.50 g, 2.63 mmol, 1 equiv.) was then added and the mixture allowed to warm to RT after 0.5 hours. After 24 hours stirring at RT all insoluble materials were filtered, the filtrate concentrated *in vacuo* and the recovered residue dissolved in CH_2Cl_2. The organic phase was washed with 1M HCl (2 x 100 mL), $NaHCO_3$ (sat. aq., 100 mL), H_2O (100 mL) and NaCl (sat. aq., 100 mL). The organic phase was dried over $MgSO_4$, filtered and concentrated *in vacuo* to afford **146(*S*)** as a pale yellow solid. Yield: 0.99g, 79%; m.p. 80 – 83 °C; HRMS (*m/z*) (ES^+) Calculated for $[C_{27}H_{32}N_4O_4Na]^+$ *m/z* = 499.2321 $[M + Na]^+$. Found *m/z* = 499.2328. ^{1}H NMR (400 MHz, $CDCl_3$) δ 8.69 (s, 1H), 8.63 (s, 1H), 8.35 (d, *J* = 7.7 Hz, 1H), 8.27 (d, *J* = 7.8 Hz, 1H), 8.18 (d, *J* = 8.3 Hz, 1H), 7.97 (t, *J* = 7.8 Hz, 1H), 7.83 (d, *J* = 7.9 Hz, 1H), 7.73 (d, *J* = 8.2 Hz, 1H), 7.62 (d, *J* = 7.1 Hz, 1H), 7.56 – 7.42 (m, 2H), 7.38 (d, *J* = 8.0 Hz, 1H), 6.22 – 6.01 (m, 1H, aliphatic CH), 4.84 (s, 1H, amide-NH), 3.53 – 3.36 (m, 2H, CH_2), 3.19 – 3.08 (m, 2H, CH_2), 1.76 (d, *J* = 6.9 Hz, 3H, CH_3), 1.66 – 1.53 (m, 2H, CH_2), 1.40 (s, 9H, CH_3). ^{13}C NMR (101 MHz, $CDCl_3$) δ 163.7, 162.7, 148.9, 148.8, 138.7, 133.9, 130.9, 128.8, 128.0, 126.4, 125.6, 125.2, 124.9, 124.7, 123.3, 122.9, 79.5, 67.9, 45.3, 36.4, 34.8, 30.9, 30.5, 28.4, 28.4, 25.6, 21.2. IR ν_{max} (cm^{-1}): 3305, 2978, 2933, 2324, 1655, 1599, 1513, 1443, 1391, 1365, 1311, 1274, 1243, 1164, 1143, 1072, 999, 955, 935, 918, 845, 800, 777, 727, 675, 663.

(R)-6-((1-(naphthalen-1-yl)ethyl)carbamoyl)-2-((3-aminopropyl)carbamoyl)- pyridine – 147(*S*)[a]

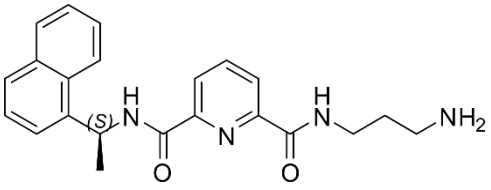

To a solution of **146(*S*)** in anhydrous CH_2Cl_2 (0.78, 2.08 mmol, 1 equiv.) TFA was added (5 mL, 65.3 mmol) and the reaction stirred under an argon

atmosphere. The reaction was monitored until completion then diluted with CH_2Cl_2 (50 mL) and basified to pH 10 with 1M NaOH. The organic phase was isolated and washed with H_2O (100 mL) and NaCl (sat. aq., 100 mL) before being dried over $MgSO_4$, filtered and concentrated *in vacuo* to afford **128(*S*)** as an off-white solid. Yield: 0.46g, 75%; m.p. 85 – 88 °C; HRMS (*m/z*) (ES^+) Calculated for $[C_{22}H_{25}N_4O_2Na]^+$ *m/z* = 377.1732 $[M + H]^+$. Found *m/z* = 377.1978; ^{1}H NMR (400 MHz, $CDCl_3$) δ 9.35 (br. s, 1H), 8.37 (d, *J* = 7.1 Hz, 1H), 8.28 (d, *J* = 7.7 Hz, 1H), 8.24 (d, *J* = 8.2 Hz, 1H), 8.13 (d, *J* = 7.9 Hz, 1H), 8.00 (t, *J* = 7.8 Hz, 1H), 7.88 (d, *J* = 7.2 Hz, 1H), 7.84 (d, *J* = 8.3 Hz, 1H), 7.63 (d, *J* = 7.1 Hz, 1H), 7.56 – 7.45 (m, 3H), 6.21 – 6.06 (m, 1H), 3.47 (t, *J* = 13.3 Hz, 2H), 2.77 – 2.62 (m, 2H), 1.81 (d, *J* = 6.7 Hz, 3H), 1.62 – 1.47 (m, 2H), 1.10 (s, 2H). ^{13}C NMR (101 MHz, $CDCl_3$) δ 163.3, 162.6, 149.0, 148.3, 138.8, 137.9, 133.9, 131.3, 128.7, 128.7, 126.9, 126.1, 125.0, 124.6, 124.5, 123.5, 122.7, 44.8, 41.6, 39.9, 30.0, 20.2. IR ν_{max} (cm^{-1}): 3283, 2981, 2932, 1648, 1598, 1522, 1442, 1376, 1340, 1311, 1239, 1173, 1119, 1074, 999, 966, 910, 845, 800, 777, 746, 719, 677

(R)-6-((1-(naphthalen-1-yl)ethyl)carbamoyl)-2-((3-methacrylamidopropyl)-carbamoyl)-pyridine – 128(*S*)[a]

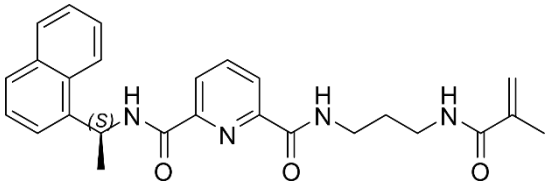

To a solution of **147(*S*)** (0.165g, 0.44 mmol, 1 equiv.) in CH_2CL_2 (20 mL) at 0 °C methacrylic anhydride (0.27 mL, 1.76 mmol, 4 equiv.) was added and the reaction stirred at RT for 24 hours. The reaction mixture was subsequently diluted with CH_2Cl_2 (50 mL) and washed with H_2O (100 mL) and NaCl (sat. aq., 100 mL). The organic phase was dried over $MgSO_4$, filtered and concentrated *in vacuo* to afford a crude oily liquid which was eluted in silica (RediSep®, 5% CH_3OH in CH_2Cl_2). Product containing fractions were combined and concentrated *in vacuo*, the recovered residue dissolved in EtOAc and eluted on silica (RediSep®, 100% EtOAc). Again, product containing fractions were combined and concentrated *in vacuo* to afford **128(*S*)** as a glassy oil. Yield: 0.095g, 48%; m.p. 90 – 92 °C; HRMS (*m/z*) (ES^-) Calculated for $[C_{26}H_{27}N_4O_3]^-$ *m/z* = 443.2089 $[M - H]^-$. Found *m/z* = 443.2093; ^{1}H NMR (400 MHz, $CDCl_3$) δ 9.42 (s, 1H), 9.18 – 9.12 (m, 1H), 8.35 (d, *J* = 7.8 Hz, 1H), 8.28 (d, *J*= 7.7 Hz, 1H), 8.24 (d, *J* = 8.5 Hz, 1H), 7.98 (t, *J* = 7.8 Hz, 1H), 7.83 (d, *J* = 8.0 Hz, 1H), 7.72 (d, *J*= 8.1 Hz, 1H), 7.64 (d, *J* = 7.1 Hz, 1H), 7.55 – 7.43 (m, 2H), 7.35 (t, *J* = 7.7 Hz, 1H), 6.22 – 6.11 (m, 2H), 5.73 (s, 1H), 5.33 (s, 1H), 3.55 – 3.34 (m, 4H), 1.94 (s, 3H), 1.75 (d, *J* = 6.9 Hz, 3H), 1.69 – 1.64 (m, 2H). ^{13}C NMR (101 MHz, $CDCl_3$) δ 169.7, 163.7, 162.8, 148.9, 139.5, 139.3, 138.7, 133.8, 131.0, 128.6, 127.7, 126.2, 125.5, 125.1, 124.8, 124.4, 123.5, 122.9, 120.5, 45.1, 35.4, 34.2, 29.9, 21.2, 18.9, 14.2. IR ν_{max} (cm^{-1}): 3295, 2980, 1654, 1613,

1517, 1443, 1397, 1374, 1311, 1226, 1174, 1119, 1088, 1073, 1000, 979, 924, 845, 800, 777, 744, 726, 676, 663

N.B. *a* denotes **s**ynthesis carried out by Mr Garrett Dee (Trinity College Dublin)

6.2.2 Complexes with Eu^{III}

[Eu.(121(*S,S*))$_3$](CF$_3$SO$_3$)$_3$: HRMS (*m/z*) (MALDI) Calculated for [**[Eu.(121(*S,S*)-H)$_2$](CF$_3$SO$_3$)**] *m/z* = 1571.3828. Found *m/z* = 1571.3844. IR ν_{max} (cm^{-1}): 3312, 3089, 2983, 1631, 1598, 1560, 1443, 1359, 1271, 1243, 1162, 1034, 959, 775.

[Eu.(121(*R,R*))$_3$](CF$_3$SO$_3$)$_3$: HRMS (*m/z*) (MALDI) Calculated for [**[Eu.(121(*R,R*)+H)$_2$](CF$_3$SO$_3$)$_2$**] *m/z* = 1573.3984. Found *m/z* = 1573.3943. IR ν_{max} (cm^{-1}): 3313, 3096, 2981, 1632, 1598, 1558, 1445, 1359, 1272, 1243, 1165, 1034, 957, 806, 776.

[Eu.(122(*S,S*))$_3$](CF$_3$SO$_3$)$_3$: HRMS (*m/z*) (MALDI) Calculated for **[Eu.(122(*S,S*))$_2$](CF$_3$SO$_3$)$_2$** *m/z* = 1569.4147. Found *m/z* = 1569.4039. IR ν_{max} (cm^{-1}): 3317, 3102, 2791, 1596, 1556, 1454, 1378, 1244, 1158, 1031, 859, 775.

[Eu.(122(*R,R*))$_3$](CF$_3$SO$_3$)$_3$: HRMS (*m/z*) (MALDI) Calculated for **[Eu.(122(*R,R*))$_2$](CF$_3$SO$_3$)$_2$ –H** *m/z* = 1420.4146. Found *m/z* = 1420.4865. IR ν_{max} (cm^{-1}): 3317, 3066, 2775, 1600, 1557, 1453, 1245, 1159, 1029, 863, 777.

[Eu.(123(*S,S*))$_3$](CF$_3$SO$_3$)$_3$: HRMS (*m/z*) (MALDI) Calculated for **[Eu.(123(*S,S*))$_2$](CF$_3$SO$_3$)$_2$** *m/z* = 1597.4460. Found *m/z* = 1597.4514. IR ν_{max} (cm^{-1}): 3325, 3101, 2982, 1619, 1595, 1560, 1531, 1455, 1402, 1279, 1241, 1160, 1025, 860, 775.

[Eu.(123(*R,R*))$_3$](CF$_3$SO$_3$)$_3$: HRMS (*m/z*) (MALDI) Calculated for **[Eu.(123(*R,R*))$_2$](CF$_3$SO$_3$)$_2$** *m/z* = 1597.4460. Found *m/z* = 1597.4525. IR ν_{max} (cm^{-1}): 3327, 3104, 2981, 1619, 1596, 1557, 1532, 1455, 1400, 1277, 1242, 1159, 1028, 860, 801, 778.

[Eu.(124(*S,S*))$_3$](CF$_3$SO$_3$)$_3$: HRMS (*m/z*) (MALDI) Calculated for **[Eu.(124(*S,S*))$_2$](CF$_3$SO$_3$)$_2$** *m/z* = 1569.3923. Found = 1569.3888. IR ν_{max} (cm^{-1}): 3267, 3114, 2961, 2871, 1620, 1595, 1555, 1445, 1361, 1291, 1236, 1145, 1030, 775.

[Eu.(124(*R,R*))$_3$](CF$_3$SO$_3$)$_3$: HRMS (*m/z*) (MALDI) Calculated for **[Eu.(124(*R,R*))$_2$](CF$_3$SO$_3$)$_2$** *m/z* = 1569.3923. Found = 1569.3911. IR ν_{max} (cm^{-1}): 3265, 3117, 2960, 2870, 1621, 1595, 1556, 1447, 1360, 1291, 1237, 1164, 1032, 775.

[Eu.(125(*S,S*))$_3$](CF$_3$SO$_3$)$_3$: HRMS (*m/z*) (MALDI) Calculated for **[Eu.(125(*S,S*) +H)$_2$](CF$_3$SO$_3$)$_2$** *m/z* = 1569.4399. Found = 1569.4039. IR ν_{max} (cm^{-1}): 3317, 3040, 2823, 1598, 1557, 1447, 1279, 1157, 1029, 960, 860, 775.

[Eu.(125(*R,R*))$_3$](CF$_3$SO$_3$)$_3$: HRMS (*m/z*) (MALDI) Calculated for **[Eu.(125(*R,R*)+H)$_2$](CF$_3$SO$_3$)** *m/z* = 1420.4879. Found = 1569.4865. IR ν_{max} (cm^{-1}): 3321, 3102, 2977, 2773, 1598, 1556, 1449, 1382, 1278, 1243, 1157, 1030, 962, 862, 775.

[Eu.(127(*S,S*)(*S,S*))$_3$](CF$_3$SO$_3$)$_3$: HRMS (*m/z*) (MALDI) Calculated for **[Eu.(127(*S,S*)(*S,S*))$_2$](CF$_3$SO$_3$)$_2$** m/z = 1677.4359. Found = 1667.4328. IR ν_{max} (cm^{-1}): 3328, 3067, 2981, 1598, 1558, 1524, 1380, 1245, 1158, 1245, 1028, 859, 776.

[Eu.(128(*S*)(*S*))$_3$](CF$_3$SO$_3$)$_3$: HRMS (*m/z*) (MALDI) Calculated for **[Eu.(128(*S*)(*S*))$_2$](CF$_3$SO$_3$)$_2$** *m/z* = 1339.2576. Found = *m/z* 1339.2639. IR ν_{max} (cm^{-1}): 3296, 3096, 2982, 1632, 1596, 1560, 1458, 1380, 1349, 1277, 1240,1224, 1161, 1028, 936, 862, 840, 802, 779, 753, 727, 660, 634, 572

6.2.3 Polymer gels

Polymer gels were fabricated from modified literature procedure previously reported by Gunnlaugsson and McCoy.[358]

[Eu.(122)$_3$]$^{3+}$@poly(HEMA-*co*-EGDMA)

[Eu.(**122**)$_3$](CF$_3$SO$_3$)$_3$ was dissolved in 2-hydroxyethyl methacrylate (HEMA, 10 mL) and ethylene glycol dimethacrylate (EGDMA, 0.1 mL) at RT. AIBN (100 mg) was added and the clear, homogenous solution injected into a non-stick mould and placed in a 90 °C oven for 6 hours. Then resulting acrylic materials were allowed to cool to RT, removed from the moulds and cut to the desired dimensions. IR ν_{max} (cm^{-1}): 2462, 2974, 2946, 2877, 1720, 1456, 1385, 1250, 1149, 1072, 1021, 948, 847, 749.

([Eu.(19)$_3$]$^{3+}$)$_3$([Tb.(20)$_3$]$^{3+}$)$_1$@poly(HEMA-*co*-EGDMA)

2-hydroxyethyl methacrylate (HEMA, 10 mL) and ethylene glycol dimethacrylate (EGDMA, 0.1 mL) were stirred at RT. Complexes **Eu.1$_3$** (3 mg) and **Tb.2$_3$** (1 mg) were added in CH$_3$CN (200 μL) to stirred until dissolution had occurred. AIBN (100 mg) was added and the clear, homogenous solution injected into a non-stick mould and placed in a 90 °C oven for 6 hours. Then resulting acrylic materials were allowed to cool to RT, removed from the moulds and washed in excess H$_2$O to remove initiator side-products and unreacted monomer. IR ν_{max} (cm^{-1}): 2462, 2978, 2943, 2880, 1718, 1451, 1382, 1250, 1150, 1070, 1019, 948, 850, 750.

(Eu.1$_3$)$_3$(Tb.2)$_1$@poly(HEMA-*co*-EGDMA-*co*-MMA)

2-hydroxyethyl methacrylate (HEMA, 7.5 mL), methyl methacrylate (MMA, 2.5 mL) and ethylene glycol dimethacrylate (EGDMA, 0.1 mL) were stirred at RT. Complexes **Eu.1$_3$** (3 mg) and **Tb.2$_3$** (1 mg) were added in CH$_3$CN (200 μL) to stirred until dissolution had

occurred. AIBN (100 mg) was added and the clear, homogenous solution injected into a non-stick mould and placed in a 90 °C oven for 6 hours. Then resulting acrylic materials were allowed to cool to RT, removed from the moulds and washed in excess CH_3OH to remove initiator side-products and unreacted monomer.. IR ν_{max} (cm^{-1}): 3439, 2980, 2943, 2896, 1721, 1485, 1449, 1385, 1247, 1147, 1071, 1025, 956, 899, 843, 748.

poly(HEMA-*co*-EGDMA-*co*-127(*S,S*))

2-hydroxyethyl methacrylate (HEMA, 10 mL), ethylene glycol dimethacrylate (EGDMA, 0.1 mL) and **127(*S,S*)** (1, 5 or 10 mg, 0 were stirred at RT till complete dissolution had occurred. AIBN (100 mg) was added and the clear, homogenous solution injected into a non-stick mould and placed in a 90 °C oven for 6 hours. Then resulting acrylic materials were allowed to cool to RT, removed from the moulds and washed in excess H_2O to remove initiator side-products and unreacted monomer. IR ν_{max} (cm^{-1}): 3412, 2946, 2884, 1702, 1453, 1384, 1244, 1151, 1071, 1021, 940, 896, 842, 748.

poly(HEMA-*co*-EGDMA-*co*-128(*S*))

2-hydroxyethyl methacrylate (HEMA, 10 mL), ethylene glycol dimethacrylate (EGDMA, 0.1 mL) and **128(*S*)** (13.1 mg) were stirred at RT till complete dissolution had occurred. AIBN (100 mg) was added and the clear, homogenous solution injected into a non-stick mould and placed in a 90 °C oven for 6 hours. Then resulting acrylic materials were allowed to cool to RT, removed from the moulds and washed in excess H_2O to remove initiator side-products and unreacted monomer. IR ν_{max} (cm^{-1}): 3412, 2933, 2873, 1719, 1453, 1388, 1239, 1151, 1067, 1023, 943, 897, 851, 748.

7. References

(1) Gust, D. *Faraday Discuss.* **2015**, *185*, 9.
(2) Ariga, K.; Kawakami, K.; Ebara, M.; Kotsuchibashi, Y.; Ji, Q.; Hill, J. P. *New J. Chem.* **2014**, *38*, 5149.
(3) Baji, A.; Abtahi, M.; Ramakrishna, S. *J. Nanosci. Nanotechnol.* **2014**, *14*, 4781.
(4) Xia, F.; Jiang, L. *Adv. Mater.* **2008**, *20*, 2842.
(5) Zimmerman, S. C. *Beilstein J. Org. Chem.* **2016**, *12*, 125.
(6) Lusby, P. J. *Annu. Rep. Prog. Chem. Sect. A: Inorg. Chem.* **2013**, *109*, 254.
(7) Lanigan, N.; Wang, X. *Chem. Commun.* **2013**, *49*, 8133.
(8) Zhang, K.; Zha, Y.; Peng, B.; Chen, Y.; Tew, G. N. *J. Am. Chem. Soc.* **2013**, *135*, 15994.
(9) Brassinne, J.; Bourgeois, J.-P.; Fustin, C.-A.; Gohy, J.-F. *Soft Matter* **2014**.
(10) Dastidar, P.; Ganguly, S.; Sarkar, K. *Chem. - Asian J.* **2016**, *11*, 2484.
(11) Li, B.; Wen, H.-M.; Cui, Y.; Zhou, W.; Qian, G.; Chen, B. *Adv. Mater.* **2016**, *28*, 8819.
(12) Blight, B. A.; Hunter, C. A.; Leigh, D. A.; McNab, H.; Thomson, P. I. T. *Nat. Chem.* **2011**, *3*, 244.
(13) Adachi, T.; Ward, M. D. *Acc. Chem. Res.* **2016**, *49*, 2669.
(14) Gale, P. A.; Steed, J. W.; Editors *Supramolecular Chemistry: From Molecules to Nanomaterials, Volumes 1-8*; John Wiley & Sons Ltd.: Chichester, UK, 2012.
(15) Martinez, C. R.; Iverson, B. L. *Chem. Sci.* **2012**, *3*, 2191.
(16) Salonen, L. M.; Ellermann, M.; Diederich, F. *Angew. Chem. Int. Ed.* **2011**, *50*, 4808.
(17) Grimme, S. *Angew. Chem. Int. Ed.* **2008**, *47*, 3430.
(18) Mahmudov, K. T.; Kopylovich, M. N.; Guedes da Silva, M. F. C.; Pombeiro, A. J. L. *Coord. Chem. Rev.*, In Press.
(19) Li, J.; Nowak, P.; Otto, S. *J. Am. Chem. Soc.* **2013**, *135*, 9222.
(20) Pedersen, C. J. *J. Am. Chem. Soc.* **1967**, *89*, 7017.
(21) Dietrich, B.; Lehn, J. M.; Sauvage, J. P. *Tetrahedron Lett.* **1969**, *10*, 2889.
(22) Weber, E.; Vögtle, F. *Inorg. Chim. Acta* **1980**, *45*, L65.
(23) Teyssandier, J.; Feyter, S. D.; Mali, K. S. *Chem. Commun. (Cambridge, U. K.)* **2016**, *52*, 11465.
(24) van Dongen, S. F. M.; Cantekin, S.; Elemans, J. A. A. W.; Rowan, A. E.; Nolte, R. J. M. *Chem. Soc. Rev.* **2014**, *43*, 99.
(25) Bruns, C. J.; Stoddart, J. F. *Top. Curr. Chem.* **2012**, *323*, 19.
(26) Stoddart, J. F. *Chem. Soc. Rev.* **2009**, *38*, 1802.
(27) Gale, Philip A.; Howe, Ethan N. W.; Wu, X. *Chem* **2016**, *1*, 351.
(28) Kim, S.-K.; Sessler, J. L. *Chem. Soc. Rev.* **2010**, *39*, 3784.
(29) Yeung, M. C.-L.; Yam, V. W.-W. *Chem. Soc. Rev.* **2015**, *44*, 4192.
(30) González-Álvarez, M. J.; Carmona, T.; Evren, D.; Mendicuti, F. *Supramol. Chem.* **2014**, *26*, 414.
(31) Bünzli, J.-C. G.; Eliseeva, S. V. *J. Rare. Earth.* **2010**, *28*, 824.
(32) Balzani, V.; Moggi, L.; Scandola, F. *NATO ASI Ser., Ser. C* **1987**, *214*, 1.
(33) Mendez-Ardoy, A.; Bassani, D. M. *Faraday Discuss.* **2015**, *185*, 549.
(34) Bassani, D. M. *Chimia* **2006**, *60*, 175.
(35) Bohne, C.; Pan, Q.; Ceroni, P.; Borjesson, K.; Rohacova, J.; Lewis, F.; Vlcek, A.; Bassani, D. M.; Wurthner, F.; Sartorel, A.; de Silva, A. P.; Nocera, D.; Scandola, F.; Lemon, C.; Allain, C.; Brudvig, G. W.; Marchesan, S.; Sundstrom, V.; Campagna, S.; Sheehan, S. W.; Plotz, P.-A.; Monti, F.; Kelly, J. M.; Gibson, E.; Maneiro, M.; Harriman, A.; Ruggi, A.; Galoppini, E.; Thummel, R.; Weinstein, J.; Vos, J.; Ishitani, O.; Gust, D.; Diaz-Moscoso, A. *Faraday Discuss.* **2015**, *185*, 187.

(36) Ceroni, P.; Pikramenou, Z.; Prodi, L.; Pan, Q.; Adams, D.; Weinstein, J.; Lewis, F.; Bohne, C.; Vlcek, A.; Bassani, D. M.; de Silva, A. P.; Moucheron, C.; Nocera, D.; Diaz-Moscoso, A.; Padilla, M.; Lemon, C.; Campagna, S.; Bradberry, S.; Galoppini, E.; Plotz, P.-A.; Kelly, J. M.; Rohacova, J.; Harriman, A.; Keane, P.; Gust, D.; Vos, J.; Mauro, M.; De Cola, L.; Nambalan Sivaraman, S. K.; Lemercier, G.; Osborne, S.; Monti, F. *Faraday Discuss.* **2015**, *185*, 311.
(37) van Dijken, D. J.; Chen, J.; Stuart, M. C. A.; Hou, L.; Feringa, B. L. *J. Am. Chem. Soc.* **2016**, *138*, 660.
(38) van Herpt, J. T.; Areephong, J.; Stuart, M. C. A.; Browne, W. R.; Feringa, B. L. *Chem. - Eur. J.* **2014**, *20*, 1737.
(39) Ramamurthy, V.; Mondal, B. *J. Photochem. Photobiol., C* **2015**, *23*, 68.
(40) Frampton, M. J.; Anderson, H. L. *Angew. Chem. Int. Ed.* **2007**, *46*, 1028.
(41) Gunnlaugsson, T.; Stomeo, F. *Org. Biomol. Chem.* **2007**, *5*, 1999.
(42) dos Santos, C. M. G.; Harte, A. J.; Quinn, S. J.; Gunnlaugsson, T. *Coord. Chem. Rev.* **2008**, *252*, 2512.
(43) Lincheneau, C.; Stomeo, F.; Comby, S.; Gunnlaugsson, T. *Aust. J. Chem.* **2011**, *64*, 1315.
(44) Kitchen, J. A.; Gunnlaugsson, T. In *The Rare Earth Elements: Fundamentals and Applications*; John Wiley & Sons Ltd.: Chichester, UK, 2012, p 481.
(45) Bünzli, J. C. G.; Piguet, C. *Chem. Soc. Rev.* **2005**, *34*, 1048.
(46) Bunzli, J.-C. G.; Eliseeva, S. V. *Chem. Sci.* **2013**.
(47) Bünzli, J.-C. G. *J. Coord. Chem.* **2014**, *67*, 3706.
(48) Parker, D.; Williams, J. A. G. *J. Chem. Soc., Dalton Trans.* **1996**, 3613.
(49) Bünzli, J.-C. G. *Acc. Chem. Res.* **2006**, *39*, 53.
(50) Katkova, M. A.; Bochkarev, M. N. *Dalton Trans.* **2010**, *39*, 6599.
(51) Butler, S. J.; Delbianco, M.; Lamarque, L.; McMahon, B. K.; Neil, E. R.; Pal, R.; Parker, D.; Walton, J. W.; Zwier, J. M. *Dalton Trans.* **2015**, *44*, 4791.
(52) Butler, S. J.; Lamarque, L.; Pal, R.; Parker, D. *Chem. Sci.* **2014**, *5*, 1750.
(53) Heffern, M. C.; Matosziuk, L. M.; Meade, T. J. *Chem. Rev.* **2014**, *114*, 4496.
(54) Comby, S.; Surender, E. M.; Kotova, O.; Truman, L. K.; Molloy, J. K.; Gunnlaugsson, T. *Inorg. Chem.* **2014**, *53*, 1867.
(55) Surender, E. M.; Comby, S.; Martyn, S.; Cavanagh, B.; Lee, T. C.; Brougham, D. F.; Gunnlaugsson, T. *Chem. Commun. (Cambridge, U. K.)* **2016**, *52*, 10858.
(56) Teo, R. D.; Termini, J.; Gray, H. B. *J. Med. Chem.* **2016**, *59*, 6012.
(57) Ungur, L.; Chibotaru, L. F. *Inorg. Chem.* **2016**, *55*, 10043.
(58) Zhang, P.; Zhang, L.; Tang, J. *Dalton Trans.* **2015**, *44*, 3923.
(59) MacDonald, M. R.; Bates, J. E.; Ziller, J. W.; Furche, F.; Evans, W. J. *J. Am. Chem. Soc.* **2013**, *135*, 9857.
(60) Evans, W. J. *Organomet.* **2016**, *35*, 3088.
(61) Moeller, T. In *Werner Centennial*; American Chemical Society: Washington, 1967; Vol. 62, p 306.
(62) Bünzli, J.-C. G.; Eliseeva, S. V. In *Lanthanide Luminescence*; Springer Berlin Heidelberg: Berlin, Germany, 2011; Vol. 7, p 1.
(63) Cotton, S. In *Lanthanide and Actinide Chemistry*; John Wiley & Sons, Ltd: Chichester, UK, 2006, p 1.
(64) Sorace, L.; Gatteschi, D. In *Lanthanides and Actinides in Molecular Magnetism*; Layfield, R. A., Murugesu, M., Eds.; John Wiley & Sons: Weinheim, Germany, 2015.
(65) Caravan, P.; Ellison, J. J.; McMurry, T. J.; Lauffer, R. B. *Chem. Rev.* **1999**, *99*, 2293.
(66) Bunzli, J. C. G.; Piguet, C. *Chem. Rev.* **2002**, *102*, 1897.

(67) Binnemans, K. *Coord. Chem. Rev.* **2015**, *295*, 1.
(68) Carnall, W. T.; Goodman, G. L.; Rajnak, K.; Rana, R. S. *J. Chem. Phys.* **1989**, *90*, 3443.
(69) Binnemans, K.; Gorller-Waldrand, C. *J. Rare. Earth.* **1996**, *14*, 173.
(70) Makhov, V. N.; Kirm, M.; Stryganyuk, G.; Vielhauer, S.; Zimmerer, G.; Malkin, B. Z.; Solovyev, O. V.; Korableva, S. L. *J. Lumin.* **2012**, *132*, 418.
(71) Laporte, O.; Meggers, W. F. *J. Opt. Soc. Am.* **1925**, *11*, 459.
(72) Eliseeva, S. V.; Bunzli, J.-C. G. *Chem. Soc. Rev.* **2010**, *39*, 189.
(73) *Spectral intensities of f-f transitions*; Gorller-Walrand, C.; Binnemans, K., Eds.; Elsevier: Amsterdam, 1998; Vol. 25.
(74) Rodger, A.; Norden, B. *Circular Dichroism and Linear Dichroism*; Oxford University Press: Oxford, UK, 1997.
(75) Tanner, P. A. *Chem. Soc. Rev.* **2013**, *42*, 5090.
(76) Mason, S. F.; Peacock, R. D.; Stewart, B. *Mol. Phys.* **1975**, *30*, 1829.
(77) Peacock, R. D. In *Rare Earths*; Springer Berlin Heidelberg: Berlin, Germany, 1975, p 83.
(78) Jørgensen, C. K.; Judd, B. R. *Mol. Phys.* **1964**, *8*, 281.
(79) Puntus, L. N.; Chauvin, A.-S.; Varbanov, S.; Bünzli, J.-C. G. *Eur. J. Inorg. Chem.* **2007**, *2007*, 2315.
(80) Pazos, E.; Vázquez, M. E. *Biotechnol. J.* **2014**, *9*, 241.
(81) Moore, E. G.; Samuel, A. P. S.; Raymond, K. N. *Acc. Chem. Res.* **2009**, *42*, 542.
(82) Chauvin, A.-S.; Thomas, F.; Song, B.; Vandevyver, C. D. B.; Bünzli, J.-C. G. *Philos. Trans. R. Soc., A* **2013**, *371*.
(83) Shavaleev, N. M.; Eliseeva, S. V.; Scopelliti, R.; Bünzli, J.-C. G. *Inorg. Chem.* **2015**, *54*, 9166.
(84) Smentek, L. *Mol. Phys.* **2003**, *101*, 893.
(85) Smentek, L.; Wybourne, B. G.; Hess, J. B. A. *J. Alloys Compd.* **2001**, *323–324*, 645.
(86) Surender, Esther M.; Comby, S.; Cavanagh, B. L.; Brennan, O.; Lee, T. C.; Gunnlaugsson, T. *Chem* **2016**, *1*, 438.
(87) Placide, V.; Pitrat, D.; Grichine, A.; Duperray, A.; Andraud, C.; Maury, O. *Tetrahedron Lett.* **2014**, *55*, 1357.
(88) D'Aléo, A.; Pointillart, F.; Ouahab, L.; Andraud, C.; Maury, O. *Coord. Chem. Rev.* **2012**, *256*, 1604.
(89) Weissman, S. I. *J. Chem. Phys.* **1942**, *10*, 214.
(90) Bünzli, J. C. G.; Choppin, G. R. *Lanthanide Probes in Life, Chemical and Earth Sciences: Theory and Practice*; Elsevier: Amsterdam, 1989.
(91) Crosby, G. A.; Whan, R. E.; Freeman, J. J. *J. Phys. Chem.* **1962**, *66*, 2493.
(92) Koziar, J. C.; Cowan, D. O. *Acc. Chem. Res.* **1978**, *11*, 334.
(93) Shimizu, Y.; Azumi, T. *J. Phys. Chem.* **1982**, *86*, 22.
(94) Montalti, M.; Credi, A.; Prodi, L.; Gandolfi, M. T. *Handbook of Photochemistry - Third Edition*; CRC Press LLC: Boca Raton, USA, 2006.
(95) Barry, D. E.; Caffrey, D. F.; Gunnlaugsson, T. *Chem. Soc. Rev.* **2016**, *45*, 3244.
(96) Ward, M. D. *Coord. Chem. Rev.* **2007**, *251*, 1663.
(97) Aboshyan-Sorgho, L.; Cantuel, M.; Petoud, S.; Hauser, A.; Piguet, C. *Coord. Chem. Rev.* **2012**, *256*, 1644.
(98) Chen, F.-F.; Chen, Z.-Q.; Bian, Z.-Q.; Huang, C.-H. *Coord. Chem. Rev.* **2010**, *254*, 991.
(99) Faulkner, S.; Tropiano, M. In *Luminescence of Lanthanide Ions in Coordination Compounds and Nanomaterials*; John Wiley & Sons Ltd: Chichester, UK, 2014, p 331.

(100) Forster, L. S. *Coord. Chem. Rev.* **2006**, *250*, 2023.
(101) Ward, M. D. *Coord. Chem. Rev.* **2010**, *254*, 2634.
(102) Nonat, A. M.; Allain, C.; Faulkner, S.; Gunnlaugsson, T. *Inorg. Chem.* **2010**, *49*, 8449.
(103) Aboshyan-Sorgho, L.; Nozary, H.; Aebischer, A.; Bünzli, J.-C. G.; Morgantini, P.-Y.; Kittilstved, K. R.; Hauser, A.; Eliseeva, S. V.; Petoud, S.; Piguet, C. *J. Am. Chem. Soc.* **2012**, *134*, 12675.
(104) Lazarides, T.; Sykes, D.; Faulkner, S.; Barbieri, A.; Ward, M. D. *Chem. Eur. J.* **2008**, *14*, 9389.
(105) Moriggi, L.; Aebischer, A.; Cannizzo, C.; Sour, A.; Borel, A.; Bunzli, J.-C. G.; Helm, L. *Dalton Trans.* **2009**, 2088.
(106) Imbert, D.; Cantuel, M.; Bünzli, J.-C. G.; Bernardinelli, G.; Piguet, C. *J. Am. Chem. Soc.* **2003**, *125*, 15698.
(107) Kleinerman, M. *J. Chem. Phys.* **1969**, *51*, 2370.
(108) D'Aléo, A.; Picot, A.; Beeby, A.; Gareth Williams, J. A.; Le Guennic, B.; Andraud, C.; Maury, O. *Inorg. Chem.* **2008**, *47*, 10258.
(109) Forster, T. *Discuss. Faraday Soc.* **1959**, *27*, 7.
(110) Horrocks, W. D.; Bolender, J. P.; Smith, W. D.; Supkowski, R. M. *J. Am. Chem. Soc.* **1997**, *119*, 5972.
(111) Faulkner, S.; Burton-Pye, B. P.; Khan, T.; Martin, L. R.; Wray, S. D.; Skabara, P. J. *Chem. Commun.* **2002**, 1668.
(112) Lazarides, T.; Davies, G. M.; Adams, H.; Sabatini, C.; Barigelletti, F.; Barbieri, A.; Pope, S. J. A.; Faulkner, S.; Ward, M. D. *Photochem. Photobiol. Sci.* **2007**, *6*, 1152.
(113) Dickins, R. S.; Parker, D.; de Sousa, A. S.; Williams, J. A. G. *Chem. Commun.* **1996**, 697.
(114) Beeby, A.; Clarkson, I. M.; Dickins, R. S.; Faulkner, S.; Parker, D.; Royle, L.; de Sousa, A. S.; Williams, J. A. G.; Woods, M. *J. Chem. Soc., Perkin Trans. 2* **1999**, 493.
(115) Wahsner, J.; Seitz, M. *Inorg. Chem.* **2013**, *52*, 13301.
(116) Escabi-Perez, J. R.; Nome, F.; Fendler, J. H. *J. Am. Chem. Soc.* **1977**, *99*, 7749.
(117) Almgren, M.; Grieser, F.; Thomas, J. K. *J. Am. Chem. Soc.* **1979**, *101*, 2021.
(118) Bonnet, C. S.; Pellegatti, L.; Buron, F.; Shade, C. M.; Villette, S.; Kubicek, V.; Guillaumet, G.; Suzenet, F.; Petoud, S.; Toth, E. *Chem. Commun.* **2010**, *46*, 124.
(119) Stasiuk, G. J.; Long, N. J. *Chem. Commun. (Cambridge, U. K.)* **2013**, *49*, 2732.
(120) Daumann, L. J.; Werther, P.; Ziegler, M. J.; Raymond, K. N. *J. Inorg. Biochem.* **2016**, *162*, 263.
(121) Cross, J. P.; Lauz, M.; Badger, P. D.; Petoud, S. *J. Am. Chem. Soc.* **2004**, *126*, 16278.
(122) Oxley, D. S.; Walters, R. W.; Copenhafer, J. E.; Meyer, T. Y.; Petoud, S.; Edenborn, H. M. *Inorg. Chem.* **2009**, *48*, 6332.
(123) Foucault-Collet, A.; Shade, C. M.; Nazarenko, I.; Petoud, S.; Eliseeva, S. V. *Angew. Chem., Int. Ed.* **2014**, *53*, 2927.
(124) Piguet, C.; Bünzli, J.-C. G. In *Handbook on the Physics and Chemistry of Rare Earths*; Elsevier: Amsterdam, 2010; Vol. Volume 40, p 301.
(125) Wang, K.-Z. In *Rare Earth Coordination Chemistry: Fundamentals and Applications*; John Wiley & Sons Ltd.: Hoboken, 2012, p 249.
(126) Werts, M. H. V.; Jukes, R. T. F.; Verhoeven, J. W. *Phys. Chem. Chem. Phys.* **2002**, *4*, 1542.
(127) Chauvin, A. S.; Gumy, F.; Imbert, D.; Bünzli, J. C. G. *Spectrosc. Lett.* **2004**, *37*, 517.
(128) Andres, J.; Hersch, R. D.; Moser, J.-E.; Chauvin, A.-S. *Adv. Funct. Mater.* **2014**, *24*, 5029.

(129) Muller, G. *Dalton Trans.* **2009**, 9692.
(130) Muller, G.; Riehl, J. P. *J. Fluoresc.* **2005**, *15*, 553.
(131) Gassner, A.-L.; Duhot, C.; G. Bünzli, J.-C.; Chauvin, A.-S. *Inorg. Chem.* **2008**, *47*, 7802.
(132) George, M. R.; Golden, C. A.; Grossel, M. C.; Curry, R. J. *Inorg. Chem.* **2006**, *45*, 1739.
(133) Andres, J.; Borbas, K. E. *Inorg. Chem.* **2015**, *54*, 8174.
(134) Vithanarachchi, S. M.; Kovacs, D.; Borbas, K. E. *Inorg. Chim. Acta* **2016**, Ahead of Print.
(135) Renaud, F.; Piguet, C.; Bernardinelli, G.; Bunzli, J.-C. G.; Hopfgartner, G. *Chem. - Eur. J.* **1997**, *3*, 1646.
(136) Leonard, J. P.; Jensen, P.; McCabe, T.; O'Brien, J. E.; Peacock, R. D.; Kruger, P. E.; Gunnlaugsson, T. *J. Am. Chem. Soc.* **2007**, *129*, 10986.
(137) Hua, K. T.; Xu, J.; Quiroz, E. E.; Lopez, S.; Ingram, A. J.; Johnson, V. A.; Tisch, A. R.; de Bettencourt-Dias, A.; Straus, D. A.; Muller, G. *Inorg. Chem.* **2011**, *51*, 647.
(138) Bonsall, S. D.; Houcheime, M.; Straus, D. A.; Muller, G. *Chem. Commun.* **2007**, 3676.
(139) Lemonnier, J.-F.; Babel, L.; Guénée, L.; Mukherjee, P.; Waldeck, D. H.; Eliseeva, S. V.; Petoud, S.; Piguet, C. *Angew. Chem. Int. Ed.* **2012**, *51*, 11302.
(140) Piguet, C.; Bernardinelli, G.; Hopfgartner, G. *Chem. Rev.* **1997**, *97*, 2005.
(141) Vandevyver, C. D. B.; Chauvin, A.-S.; Comby, S.; Bunzli, J.-C. G. *Chem. Commun. (Cambridge, U. K.)* **2007**, 1716.
(142) Chauvin, A.-S.; Comby, S.; Song, B.; Vandevyver, C. D. B.; Bunzli, J.-C. G. *Chem. - Eur. J.* **2008**, *14*, 1726.
(143) Deiters, E.; Song, B.; Chauvin, A.-S.; Vandevyver, C. D. B.; Buenzli, J.-C. G. *New J. Chem.* **2008**, *32*, 1140.
(144) Song, B.; Vandevyver, C. D. B.; Chauvin, A.-S.; Buenzli, J.-C. G. *Org. Biomol. Chem.* **2008**, *6*, 4125.
(145) de Bettencourt-Dias, A.; Barber, P. S. *C. R. Chim.* **2010**, *13*, 691.
(146) de Bettencourt-Dias, A.; Barber, P. S.; Viswanathan, S.; de Lill, D. T.; Rollett, A.; Ling, G.; Altun, S. *Inorg. Chem.* **2010**, *49*, 8848.
(147) de Bettencourt-Dias, A.; Viswanathan, S.; Rollett, A. *J. Am. Chem. Soc.* **2007**, *129*, 15436.
(148) de Bettencourt-Dias, A.; Barber, P. S.; Bauer, S. *J. Am. Chem. Soc.* **2012**, *134*, 6987.
(149) Yuasa, J.; Ohno, T.; Miyata, K.; Tsumatori, H.; Hasegawa, Y.; Kawai, T. *J. Am. Chem. Soc.* **2011**, *133*, 9892.
(150) Dai, Z.; Tian, L.; Song, B.; Liu, X.; Yuan, J. *Chem. Sci.* **2017**.
(151) Golkowski, R. T.; Settineri, N. S.; Zhao, X.; McMillin, D. R. *J. Phys. Chem. A* **2015**, *119*, 11650.
(152) Chen, P.; Holten-Andersen, N. *Adv. Opt. Mater.* **2015**, *3*, 1041.
(153) Muller, J. M.; Galley, S. S.; Albrecht-Schmitt, T. E.; Nash, K. L. *Inorg. Chem.* **2016**, *55*, 11454.
(154) Giraud, M.; Andreiadis, E. S.; Fisyuk, A. S.; Demadrille, R.; Pécaut, J.; Imbert, D.; Mazzanti, M. *Inorg. Chem.* **2008**, *47*, 3952.
(155) Andreiadis, E. S.; Imbert, D.; Pecaut, J.; Demadrille, R.; Mazzanti, M. *Dalton Trans.* **2012**, *41*, 1268.
(156) Di Pietro, S.; Gautier, N.; Imbert, D.; Pecaut, J.; Mazzanti, M. *Dalton Trans.* **2016**, *45*, 3429.
(157) Andres, J.; Chauvin, A.-S. *Inorg. Chem.* **2011**, *50*, 10082.

(158) Shavaleev, N. M.; Eliseeva, S. V.; Scopelliti, R.; Bunzli, J.-C. G. *Inorg. Chem.* **2014**, *53*, 5171.
(159) Shavaleev, N. M.; Eliseeva, S. V. *Inorg. Chim. Acta* **2015**, *427*, 81.
(160) Bozoklu, G.; Marchal, C.; Gateau, C.; Pecaut, J.; Imbert, D.; Mazzanti, M. *Chem. - Eur. J.* **2010**, *16*, 6159.
(161) Hussein, B. H. M.; Khairy, G. M.; Kamel, R. M. *Spectrochim Acta A Mol Biomol Spectrosc* **2016**, *158*, 34.
(162) Fernandez-Moreira, V.; Song, B.; Sivagnanam, V.; Chauvin, A.-S.; Vandevyver, C. D. B.; Gijs, M.; Hemmilae, I.; Lehr, H.-A.; Buenzli, J.-C. G. *Analyst (Cambridge, U. K.)* **2010**, *135*, 42.
(163) Zhao, C.; Sun, Y.; Ren, J.; Qu, X. *Inorg. Chim. Acta* **2016**, *452*, 50.
(164) Moore, E. G.; Xu, J.; Jocher, C. J.; Corneillie, T. M.; Raymond, K. N. *Inorg. Chem.* **2010**, *49*, 9928.
(165) McMahon, B. K.; Gunnlaugsson, T. *J. Am. Chem. Soc.* **2012**, *134*, 10725.
(166) Burke, H. M.; Gunnlaugsson, T.; Scanlan, E. M. *Org. Biomol. Chem.* **2016**, *14*, 9133.
(167) Burke, H. M.; Gunnlaugsson, T.; Scanlan, E. M. *Chem. Commun. (Cambridge, U. K.)* **2015**, *51*, 10576.
(168) Terai, T.; Ito, H.; Ueno, T.; Hanaoka, K.; Komatsu, T.; Nagano, T.; Urano, Y. *Bioorg. Med. Chem. Lett.* **2016**, *26*, 2314.
(169) Yao, Y.; Kong, C.; Yin, L.; Jain, A. D.; Ratia, K.; Thatcher, G. R. J.; Moore, T. W.; Driver, T. G.; Miller, L. W. *Chem. - Eur. J.* **2016**, Ahead of Print.
(170) Ai, K.; Zhang, B.; Lu, L. *Angew. Chem., Int. Ed.* **2009**, *48*, 304.
(171) Shipman, M. A.; Ramhit, K. J.; Blight, B. A. *J. Mater. Chem. B* **2016**, *4*, 3043.
(172) Sahoo, J.; Waghmode, S. B.; Subramanian, P. S.; Albrecht, M. *ChemistrySelect* **2016**, *1*, 1943.
(173) Sahoo, J.; Arunachalam, R.; Subramanian, P. S.; Suresh, E.; Valkonen, A.; Rissanen, K.; Albrecht, M. *Angew. Chem., Int. Ed.* **2016**, *55*, 9625.
(174) Nadella, S.; Selvakumar, P. M.; Suresh, E.; Subramanian, P. S.; Albrecht, M.; Giese, M.; Froehlich, R. *Chem. - Eur. J.* **2012**, *18*, 16784.
(175) Nadella, S.; Sahoo, J.; Subramanian, P. S.; Sahu, A.; Mishra, S.; Albrecht, M. *Chem. - Eur. J.* **2014**, *20*, 6047.
(176) Strassert, C. A.; Mauro, M.; De Cola, L. *Adv. Inorg. Chem.* **2011**, *63*, 47.
(177) Zinna, F.; Pasini, M.; Galeotti, F.; Botta, C.; Di Bari, L.; Giovanella, U. *Adv. Funct. Mater.* **2017**, *27*, 1603719.
(178) Eliseeva, S. V.; Kotova, O. V.; Gumy, F.; Semenov, S. N.; Kessler, V. G.; Lepnev, L. S.; Buenzli, J.-C. G.; Kuzmina, N. P. *J. Phys. Chem. A* **2008**, *112*, 3614.
(179) Biju, S.; Xu, L.-J.; Sun, C.-Z.; Chen, Z.-N. *J. Mater. Chem. C* **2015**, *3*, 5775.
(180) Li, Y.; Xu, Y.; Wang, Y. *Chem. - Eur. J.* **2016**, *22*, 10976.
(181) Yan, Y.; Wang, A.; Huang, J. *Soft Matter* **2014**.
(182) Yan, Y.; Huang, J. *Coord. Chem. Rev.* **2010**, *254*, 1072.
(183) Lim, H. L.; Hwang, Y.; Kar, M.; Varghese, S. *Biomater. Sci.* **2014**, *2*, 603.
(184) Svenson, S. *J. Dispersion Sci. Technol.* **2004**, *25*, 101.
(185) Lombardo, D.; Kiselev, M. A.; Magazu, S.; Calandra, P. *Adv. Condens. Matter Phys.* **2015**, *2015*, 22.
(186) Xu, J.; Wang, Z.; Wen, L.; Zhou, X.; Xu, J.; Yang, S. *Soft Matter* **2016**, *12*, 867.
(187) Kogej, K.; Fonseca, S. M.; Rovisco, J.; Azenha, M. E.; Ramos, M. L.; Seixas de Melo, J. S.; Burrows, H. D. *Langmuir* **2013**, *29*, 14429.
(188) Wang, S.; Ding, L.; Fan, J.; Wang, Z.; Fang, Y. *ACS Appl. Mater. Interfaces* **2014**, *6*, 16156.

(189) Debroye, E.; Eliseeva, S. V.; Laurent, S.; Vander Elst, L.; Muller, R. N.; Parac-Vogt, T. N. *Dalton Trans.* **2014**, *43*, 3589.
(190) Poznik, M.; Maitra, U.; Konig, B. *Org. Biomol. Chem.* **2015**, *13*, 9789.
(191) Isabettini, S.; Liebi, M.; Kohlbrecher, J.; Ishikawa, T.; Windhab, E. J.; Fischer, P.; Walde, P.; Kuster, S. *Langmuir* **2016**, *32*, 9005.
(192) Thevenaz, D. C.; Monnier, C. A.; Balog, S.; Fiore, G. L. *Biomacromolecules* **2014**, *15*, 3994.
(193) Arenz, S.; Babai, A.; Binnemans, K.; Driesen, K.; Giernoth, R.; Mudring, A.-V.; Nockemann, P. *Chem. Phys. Lett.* **2005**, *402*, 75.
(194) Driesen, K.; Nockemann, P.; Binnemans, K. *Chem. Phys. Lett.* **2004**, *395*, 306.
(195) Binnemans, K. *Chem. Rev. (Washington, DC, U. S.)* **2007**, *107*, 2592.
(196) Nockemann, P.; Beurer, E.; Driesen, K.; Van Deun, R.; Van Hecke, K.; Van Meervelt, L.; Binnemans, K. *Chem. Commun. (Cambridge, U. K.)* **2005**, 4354.
(197) Li, Z.; Wang, J.; Chen, M.; Wang, Y. *Chem. - Asian J.* **2016**, *11*, 745.
(198) Fan, B.; Wei, J.; Ma, X.; Bu, X.; Xing, N.; Pan, Y.; Zheng, L.; Guan, W. *Ind. Eng. Chem. Res.* **2016**, *55*, 2267.
(199) Selivanova, N. M.; Galeeva, A. I.; Gubaydullin, A. T.; Lobkov, V. S.; Galyametdinov, Y. G. *J. Phys. Chem. B* **2012**, *116*, 735.
(200) Binnemans, K.; Görller-Walrand, C. *Chem. Rev.* **2002**, *102*, 2303.
(201) Lunstroot, K.; Driesen, K.; Nockemann, P.; Van Hecke, K.; Van Meervelt, L.; Gorller-Walrand, C.; Binnemans, K.; Bellayer, S.; Viau, L.; Le Bideau, J.; Vioux, A. *Dalton Trans.* **2009**, 298.
(202) Guerra, S.; Dutronc, T.; Terazzi, E.; Buchwalder, K.-L.; Guénée, L.; Deschenaux, R.; Eliseeva, S. V.; Petoud, S.; Piguet, C. *Coord. Chem. Rev.*
(203) Goossens, K.; Nockemann, P.; Driesen, K.; Goderis, B.; Goerller-Walrand, C.; Van Hecke, K.; Van Meervelt, L.; Pouzet, E.; Binnemans, K.; Cardinaels, T. *Chem. Mater.* **2008**, *20*, 157.
(204) Yang, Y.; Driesen, K.; Nockemann, P.; Van Hecke, K.; Van Meervelt, L.; Binnemans, K. *Chem. Mater.* **2006**, *18*, 3698.
(205) Cardinaels, T.; Ramaekers, J.; Nockemann, P.; Driesen, K.; Van Hecke, K.; Van Meervelt, L.; Lei, S.; De Feyter, S.; Guillon, D.; Donnio, B.; Binnemans, K. *Chem. Mater.* **2008**, *20*, 1278.
(206) Cardinaels, T.; Driesen, K.; Parac-Vogt, T. N.; Heinrich, B.; Bourgogne, C.; Guillon, D.; Donnio, B.; Binnemans, K. *Chem. Mater.* **2005**, *17*, 6589.
(207) Galyametdinov, Y. G.; Knyazev, A. A.; Dzhabarov, V. I.; Cardinaels, T.; Driesen, K.; Gorller-Walrand, C.; Binnemans, K. *Adv. Mater.* **2008**, *20*, 252.
(208) Goossens, K.; Bruce, D. W.; Van Deun, R.; Binnemans, K.; Cardinaels, T. *Dalton Trans.* **2012**, *41*, 13271.
(209) Winter, A.; Schubert, U. S. *Chem. Soc. Rev.* **2016**, *45*, 5311.
(210) Rehahn, M. *Acta Polym.* **1998**, *49*, 201.
(211) Wolf, M. O. *Adv. Mater.* **2001**, *13*, 545.
(212) Wolf, M. O. *J. Inorg. Organomet. Polym. Mater.* **2006**, *16*, 189.
(213) Yamamoto, M.; Nakanishi, T.; Kitagawa, Y.; Fushimi, K.; Hasegawa, Y. *Mater. Lett.* **2016**, *167*, 183.
(214) Mohapatra, S.; Adhikari, S.; Riju, H.; Maji, T. K. *Inorg. Chem.* **2012**, *51*, 4891.
(215) Marchal, C.; Filinchuk, Y.; Imbert, D.; Buenzli, J.-C. G.; Mazzanti, M. *Inorg. Chem.* **2007**, *46*, 6242.
(216) Marchal, C.; Filinchuk, Y.; Chen, X.-Y.; Imbert, D.; Mazzanti, M. *Chem. - Eur. J.* **2009**, *15*, 5273.

(217) Liu, X.; Akerboom, S.; Jong, M. d.; Mutikainen, I.; Tanase, S.; Meijerink, A.; Bouwman, E. *Inorg. Chem.* **2015**, *54*, 11323.
(218) Huo, R.; Li, X.; Ma, D. *Eur. J. Inorg. Chem.* **2015**, *2015*, 852.
(219) Hirai, Y.; Nakanishi, T.; Miyata, K.; Fushimi, K.; Hasegawa, Y. *Mater. Lett.* **2014**, *130*, 91.
(220) Hatanaka, M.; Hirai, Y.; Kitagawa, Y.; Nakanishi, T.; Hasegawa, Y.; Morokuma, K. *Chem. Sci.* **2017**, *8*, 423.
(221) Chen, X.-Y.; Marchal, C.; Filinchuk, Y.; Imbert, D.; Mazzanti, M. *Chem. Commun. (Cambridge, U. K.)* **2008**, 3378.
(222) Duerrbeck, A.; Gorelik, S.; Hobley, J.; Yong, A. M.; Subramanian, G. S.; Hor, A.; Long, N. *J. Mater. Chem. C* **2015**, *3*, 8992.
(223) Campagnol, N.; Souza, E. R.; De Vos, D. E.; Binnemans, K.; Fransaer, J. *Chem. Commun. (Cambridge, U. K.)* **2014**, *50*, 12545.
(224) Stanley, J. M.; Holliday, B. J. *Coord. Chem. Rev.* **2012**, *256*, 1520.
(225) Douvali, A.; Tsipis, A. C.; Eliseeva, S. V.; Petoud, S.; Papaefstathiou, G. S.; Malliakas, C. D.; Papadas, I.; Armatas, G. S.; Margiolaki, I.; Kanatzidis, M. G.; Lazarides, T.; Manos, M. J. *Angew. Chem., Int. Ed.* **2015**, *54*, 1651.
(226) Wang, D.; Sun, L.; Hao, C.; Yan, Y.; Liang, Z. *RSC Adv.* **2016**, *6*, 57828.
(227) Li, Q.; Wang, C.; Tan, H.; Tang, G.; Gao, J.; Chen, C.-H. *RSC Adv.* **2016**, *6*, 17811.
(228) Zeng, H.-H.; Qiu, W.-B.; Zhang, L.; Liang, R.-P.; Qiu, J.-D. *Anal. Chem. (Washington, DC, U. S.)* **2016**, *88*, 6342.
(229) Liu, B.; Huang, Y.; Shen, Q.; Zhu, X.; Hao, Y.; Qu, P.; Xu, M. *RSC Adv.* **2016**, *6*, 100743.
(230) Huang, P.; Wu, F.; Mao, L. *Anal. Chem. (Washington, DC, U. S.)* **2015**, *87*, 6834.
(231) Xu, L.; Xie, M.; Huang, J.; Yan, Y. *Langmuir* **2016**, *32*, 5830.
(232) Wang, J.; Groeneveld, A.; Oikonomou, M.; Prusova, A.; Van As, H.; van Lent, J. W. M.; Velders, A. H. *Soft Matter* **2016**, *12*, 99.
(233) Xu, L.; Jing, Y.; Feng, L.; Xian, Z.; Yan, Y.; Liu, Z.; Huang, J. *Phys. Chem. Chem. Phys.* **2013**, *15*, 16641.
(234) Burnworth, M.; Rowan, S. J.; Weder, C. *Macromolecules (Washington, DC, U. S.)* **2012**, *45*, 126.
(235) Knapton, D.; Iyer, P. K.; Rowan, S. J.; Weder, C. *Macromolecules* **2006**, *39*, 4069.
(236) Balkenende, D. W. R.; Coulibaly, S.; Balog, S.; Simon, Y. C.; Fiore, G. L.; Weder, C. *J. Am. Chem. Soc.* **2014**, *136*, 10493.
(237) Escuder, B.; Miravet, J. F. *Functional Molecular Gels*; RSC: Cambridge, UK, 2014.
(238) Beck, J. B.; Rowan, S. J. *J. Am. Chem. Soc.* **2003**, *125*, 13922.
(239) Weng, W.; Beck, J. B.; Jamieson, A. M.; Rowan, S. J. *J. Am. Chem. Soc.* **2006**, *128*, 11663.
(240) Bhowmik, S.; Banerjee, S.; Maitra, U. *Chem. Commun. (Cambridge, U. K.)* **2010**, *46*, 8642.
(241) Banerjee, S.; Kandanelli, R.; Bhowmik, S.; Maitra, U. *Soft Matter* **2011**, *7*, 8207.
(242) Nonappa; Maitra, U. *Org. Biomol. Chem.* **2008**, *6*, 657.
(243) Gorai, T.; Maitra, U. *ACS Sens.* **2016**, *1*, 934.
(244) Bhowmik, S.; Maitra, U. *Chem. Commun. (Cambridge, U. K.)* **2012**, *48*, 4624.
(245) Kandanelli, R.; Sarkar, A.; Maitra, U. *Dalton Trans.* **2013**, *42*, 15381.
(246) Liu, Y.; Wang, T.; Liu, M. *Chem. - Eur. J.* **2012**, *18*, 14650.
(247) da Silva, F. F.; Lira de Menezes, F.; Lourenco da Luz, L.; Alves, S. *New J. Chem.* **2014**, *38*, 893.
(248) Kumar, P.; Soumya, S.; Prasad, E. *ACS Appl. Mater. Interfaces* **2016**, *8*, 8068.
(249) Wang, H.; Yi, C.; Li, X.; Fang, F.; Yang, Y. *J. Lumin.* **2011**, *131*, 603.

(250) Di Lorenzo, M. L.; Cocca, M.; Gentile, G.; Avella, M.; Gutierrez, D.; Della Pirriera, M.; Kennedy, M.; Ahmed, H.; Doran, J. *J. Colloid Interface Sci.* **2013**, *398*, 95.
(251) Yabuuchi, K.; Kato, T. In *Handbook of Liquid Crystals (2nd Edition)*; Wiley-VCH Verlag GmbH: Weinheim, Germany, 2014; Vol. 6, p 3.
(252) Cardinaels, T.; Hirai, Y.; Hanabusa, K.; Binnemans, K.; Kato, T. *J. Mater. Chem.* **2010**, *20*, 8571.
(253) Lunstroot, K.; Driesen, K.; Nockemann, P.; Goerller-Walrand, C.; Binnemans, K.; Bellayer, S.; Le Bideau, J.; Vioux, A. *Chem. Mater.* **2006**, *18*, 5711.
(254) Sutar, P.; Suresh, V. M.; Maji, T. K. *Chem. Commun.* **2015**, *51*, 9876.
(255) Zhu, Y.-M.; Xie, M.-Y.; Zhang, R.; Yang, Y.-Y.; Zeng, C.-H.; Zhao, F.-L.; Tong, Y.-X.; Su, C.-Y.; Wong, W.-T. *Photochem. Photobiol. Sci.* **2011**, *10*, 1760.
(256) Kim, H.; Chang, J. Y. *RSC Adv.* **2013**, *3*, 1774.
(257) Yakimanskii, A. V.; Goikhman, M. Y.; Podeshvo, I. V.; Anan'eva, T. D.; Nekrasova, T. N.; Smyslov, R. Y. *Polym. Sci., Ser. A* **2012**, *54*, 921.
(258) Hasegawa, Y.; Sogabe, K.; Wada, Y.; Kitamura, T.; Nakashima, N.; Yanagida, S. *Chem. Lett.* **1999**, 35.
(259) Sivakumar, S.; Reddy, M. L. P. *J. Mater. Chem.* **2012**, *22*, 10852.
(260) Yan, B.; Chen, X. *J. Optoelectron. Adv. Mater.* **2007**, *9*, 2091.
(261) Jiu, H.; Ding, J.; Sun, Y.; Bao, J.; Gao, C.; Zhang, Q. *J. Non-Cryst. Solids* **2006**, *352*, 197.
(262) Kai, J.; Felinto, M. C. F. C.; Nunes, L. A. O.; Malta, O. L.; Brito, H. F. *J. Mater. Chem.* **2011**, *21*, 3796.
(263) Raj, D. B. A.; Francis, B.; Reddy, M. L. P.; Butorac, R. R.; Lynch, V. M.; Cowley, A. H. *Inorg. Chem.* **2010**, *49*, 9055.
(264) Lunstroot, K.; Driesen, K.; Nockemann, P.; Viau, L.; Mutin, P. H.; Vioux, A.; Binnemans, K. *Phys. Chem. Chem. Phys.* **2010**, *12*, 1879.
(265) Moudam, O.; Rowan, B. C.; Alamiry, M.; Richardson, P.; Richards, B. S.; Jones, A. C.; Robertson, N. *Chem. Commun.* **2009**, 6649.
(266) Zhang, H.; Fan, R.; Wang, P.; Wang, X.; Gao, S.; Dong, Y.; Wang, Y.; Yang, Y. *RSC Adv.* **2015**, *5*, 38254.
(267) Biju, S.; Freire, R. O.; Eom, Y. K.; Scopelliti, R.; Bünzli, J.-C. G.; Kim, H. K. *Inorg. Chem.* **2014**, *53*, 8407.
(268) Bortoluzzi, M.; Paolucci, G.; Gatto, M.; Roppa, S.; Enrichi, F.; Ciorba, S.; Richards, B. S. *J. Lumin.* **2012**, *132*, 2378.
(269) Zhang, X.; Liu, L.; Yu, C.; Li, H.; Fu, G.; Lu, X.; Wong, W.-K.; Jones, R. A. *Inorg. Chem. Commun.* **2016**, *70*, 153.
(270) Yu, C.; Zhang, Z.; Liu, L.; Feng, W.; Lu, X.; Wong, W.-K.; Jones, R. A. *Inorg. Chem. Commun.* **2014**, *49*, 30.
(271) Hou, Z.; Liu, C.; Feng, G.; Li, Z.; Wang, Y. *Colloid. Polym. Sci.* **2016**, *294*, 1495.
(272) Biju, S.; Eom, Y. K.; Bunzli, J.-C. G.; Kim, H. K. *J. Mater. Chem. C* **2013**, *1*, 6935.
(273) Yu, C.; Zhang, Z.; Liu, L.; Li, H.; He, Y.; Lu, X.; Wong, W.-K.; Jones, R. A. *New J. Chem.* **2015**, *39*, 3698.
(274) Zhang, Z.; Liu, L.; Yu, C.; Li, H.; He, Y.; Lu, X.; Wong, W.-K.; Jones, R. A. *Inorg. Chem. Commun.* **2015**, *52*, 53.
(275) Liu, L.; Zhang, Z.; Feng, W.; Yu, C.; Lu, X.; Wong, W.-K.; Jones, R. A. *Inorg. Chem. Commun.* **2014**, *49*, 124.
(276) Bünzli, J.-C. G. *Coord. Chem. Rev.* **2015**, *293–294*, 19.
(277) Wang, H.; Wang, Y.; Zhang, L.; Li, H. *RSC Adv.* **2013**, *3*, 8535.
(278) Andreiadis, E. S.; Gauthier, N.; Imbert, D.; Demadrille, R.; Pecaut, J.; Mazzanti, M. *Inorg. Chem.* **2013**, *52*, 14382.

(279) Bai, G.; Tsang, M.-K.; Hao, J. *Adv. Funct. Mater.* **2016**, *26*, 6330.
(280) Lee, J. W.; Kim, D. K. *Colloids Surf., A* **2016**, *511*, 162.
(281) Buczko, K.; Karbowiak, M. *J. Lumin.* **2013**, *143*, 241.
(282) Garcia-Torres, J.; Bosch-Jimenez, P.; Torralba-Calleja, E.; Kennedy, M.; Ahmed, H.; Doran, J.; Gutierrez-Tauste, D.; Bautista, L.; Della Pirriera, M. *J. Photochem. Photobiol., A* **2014**, *283*, 8.
(283) Garcia-Torres, J.; Bosch-Jimenez, P.; Torralba-Calleja, E.; Kennedy, M.; Ahmed, H.; Doran, J.; Gutierrez-Tauste, D.; Bautista, L.; Della Pirriera, M. *J. Photochem. Photobiol., A* **2014**, *275*, 103.
(284) Kennedy, M.; Ahmed, H.; Doran, J.; Norton, B.; Bosch-Jimenez, P.; Pirriera, M. D.; Torralba-Calleja, E.; Tauste, D. G.; Aubouy, L.; Daren, S.; Solomon-Tsvetkov, F.; Galindo, S.; Voz, C.; Puigdollers, J. *Phys. Status. Solidi A* **2015**, *212*, 203.
(285) Parra, D. F.; Mucciolo, A.; Brito, H. F.; Thompson, L. C. *J. Solid State Chem.* **2003**, *171*, 412.
(286) Zhang, T.; Xu, Z.; Qian, L.; Tao, D. L.; Teng, F.; Gao, X.; Xu, X. R. *Chem. Phys. Lett.* **2005**, *415*, 30.
(287) Harrison, B. S.; Foley, T. J.; Knefely, A. S.; Mwaura, J. K.; Cunningham, G. B.; Kang, T.-S.; Bouguettaya, M.; Boncella, J. M.; Reynolds, J. R.; Schanze, K. S. *Chem. Mater.* **2004**, *16*, 2938.
(288) Tamaki, K.; Yabu, H.; Isoshima, T.; Hara, M.; Shimomura, M. *Colloids Surf., A* **2006**, *284+285*, 355.
(289) Hsu, S.-h.; Hung, K.-C.; Chen, C.-W. *J. Mater. Chem. B* **2016**, *4*, 7493.
(290) Mondragon, M.; Trujillo, G.; Moggio, I.; Arias, E. *Eur. Polym. J.* **2016**, *80*, 126.
(291) Alves, R.; Ravaro, L. P.; Pawlicka, A.; Silva, M. M.; de Camargo, A. S. S. *J. Braz. Chem. Soc.* **2015**, *26*, 2590.
(292) Chen, B.; Feng, J. *J. Phys. Chem. C* **2015**, *119*, 7865.
(293) Shahi, P. K.; Singh, A. K.; Rai, S. B.; Ullrich, B. *Sens. Actuators, A* **2015**, *222*, 255.
(294) Lin, J.-T.; Wang, Q.-M.; Tan, C.-L.; Chen, H.-Y. *Synth. Met.* **2010**, *160*, 1780.
(295) Zheng, Y.; Tan, C.; Drummen, G. P. C.; Wang, Q. *Spectrochim. Acta, Part A* **2012**, *96*, 387.
(296) Yang, D.; Wang, Y.; He, L.; Li, H. *ACS Appl. Mater. Interfaces* **2016**, *8*, 19709.
(297) Lenaerts, P.; Driesen, K.; Van Deun, R.; Binnemans, K. *Chem. Mater.* **2005**, *17*, 2148.
(298) Babel, L.; Hoang, T. N. Y.; Nozary, H.; Salamanca, J.; Guenee, L.; Piguet, C. *Inorg. Chem.* **2014**, *53*, 3568.
(299) Hoang, T. N. Y.; Wang, Z.; Babel, L.; Nozary, H.; Borkovec, M.; Szilagyi, I.; Piguet, C. *Dalton Trans.* **2015**, *44*, 13250.
(300) Munuera, L.; O'Reilly, R. K. *Dalton Trans.* **2010**, *39*, 388.
(301) Turchetti, D. A.; Nolasco, M. M.; Szczerbowski, D.; Carlos, L. D.; Akcelrud, L. C. *Phys. Chem. Chem. Phys.* **2015**, *17*, 26238.
(302) Bochkarev, L. N.; Rozhkov, A. V.; Bochkarev, M. N. *Polym. Sci., Ser. C* **2014**, *56*, 59.
(303) Chen, X.-Y.; Yang, X.; Holliday, B. J. *J. Am. Chem. Soc.* **2008**, *130*, 1546.
(304) Ghosh, K.; Balog, E. R. M.; Kahn, J. L.; Shepherd, D. P.; Martinez, J. S.; Rocha, R. C. *Macromol. Chem. Phys.* **2015**, *216*, 1856.
(305) Chen, B.; Wen, G.; Wu, J.; Feng, J. *Macromol. Rapid Commun.* **2015**, *36*, 1836.
(306) Jin, X.; Shi, L.; Li, X.; Liu, M.; Lu, J.; Sun, Z. *Mater. Lett.* **2015**, *145*, 59.
(307) Jin, Y.; Zuo, W.; Gao, H.; Fu, L.; Liu, Y.; Wu, W.; Xu, S.; Cao, S. *J. Appl. Polym. Sci.* **2015**, *132*, n/a.
(308) de Bettencourt-Dias, A.; Rossini, J. S. K. *Inorg. Chem.* **2016**, *55*, 9954.

(309) He, Y.; Liu, L.; Fu, G.; Lu, X.; Wong, W.-K.; Jones, R. A. *Inorg. Chem. Commun.* **2016**, *72*, 62.
(310) He, Y.; Fu, G.; Liu, L.; Li, H.; Li, B.; Guan, J.; Lu, X.; Wong, W.-K.; Jones, R. A. *Inorg. Chem. Commun.* **2016**, *69*, 62.
(311) Chauvin, A.-S.; Bunzli, J.-C. G.; Bochud, F.; Scopelliti, R.; Froidevaux, P. *Chem. - Eur. J.* **2006**, *12*, 6852.
(312) Balamurugan, A.; Reddy, M. L. P.; Jayakannan, M. *J. Mater. Chem. A* **2013**, *1*, 2256.
(313) McKenzie, B. M.; Wojtecki, R. J.; Burke, K. A.; Zhang, C.; Jákli, A.; Mather, P. T.; Rowan, S. J. *Chem. Mater.* **2011**, *23*, 3525.
(314) Yao, B.; Cong, Y.; Zhang, B. *RSC Adv.* **2015**, *5*, 87069.
(315) Yao, B.; Cong, Y.; Zhang, B.; Wang, Z.; Chen, F.; Sun, C. *RSC Adv.* **2016**, *6*, 42745.
(316) Yao, B.; Cong, Y.; Zhang, B. *Liq. Cryst.* **2016**, *43*, 1190.
(317) Yao, B.; Cong, Y.; Zhang, B. *New J. Chem.* **2016**, *40*, 3664.
(318) Zhang, L.; Tan, C.; Wang, Q.; Zhang, C. C. *Photochem. Photobiol.* **2011**, *87*, 1036.
(319) Whittell, G. R.; Hager, M. D.; Schubert, U. S.; Manners, I. *Nat. Mater.* **2011**, *10*, 176.
(320) Liu, S.; Ling, J.; Li, K.; Yao, F.; Oderinde, O.; Zhang, Z.; Fu, G. *RSC Adv.* **2016**, *6*, 63171.
(321) Liu, F.; Carlos, L. D.; Ferreira, R. A. S.; Rocha, J.; Gaudino, M. C.; Robitzer, M.; Quignard, F. *Biomacromolecules* **2008**, *9*, 1945.
(322) Wang, M. X.; Yang, C. H.; Liu, Z. Q.; Zhou, J.; Xu, F.; Suo, Z.; Yang, J. H.; Chen, Y. M. *Macromol. Rapid Commun.* **2015**, *36*, 465.
(323) Ma, Q.; Wang, Q. *Carbohydr. Polym.* **2015**, *133*, 19.
(324) Kawa, M.; Takahagi, T. *Chem. Mater.* **2004**, *16*, 2282.
(325) Yang, C.; Xu, J.; Zhang, R.; Zhang, Y.; Li, Z.; Li, Y.; Liang, L.; Lu, M. *Sens. Actuators, B* **2013**, *177*, 437.
(326) Zhou, Z.; Wang, Q.; Tan, C. *Soft Mater.* **2014**, *12*, 98.
(327) Jiang, Y.; Yang, X.; Ma, C.; Wang, C.; Li, H.; Dong, F.; Zhai, X.; Yu, K.; Lin, Q.; Yang, B. *Small* **2010**, *6*, 2673.
(328) Li, Q.-F.; Du, X.; Jin, L.; Hou, M.; Wang, Z.; Hao, J. *J. Mater. Chem. C* **2016**, *4*, 3195.
(329) Yao, Y.; Wang, Y.; Li, Z.; Li, H. *Langmuir* **2015**, *31*, 12736.
(330) Haring, M.; Diaz, D. D. *Chem. Commun.* **2016**, *52*, 13068.
(331) Meudtner, R. M.; Hecht, S. *Macromol. Rapid Commun.* **2008**, *29*, 347.
(332) Yuan, J.; Fang, X.; Zhang, L.; Hong, G.; Lin, Y.; Zheng, Q.; Xu, Y.; Ruan, Y.; Weng, W.; Xia, H.; Chen, G. *J. Mater. Chem.* **2012**, *22*, 11515.
(333) Yang, B.; Zhang, H.; Peng, H.; Xu, Y.; Wu, B.; Weng, W.; Li, L. *Polym. Chem.* **2014**, *5*, 1945.
(334) Yuan, J.; Zhang, H.; Hong, G.; Chen, Y.; Chen, G.; Xu, Y.; Weng, W. *J. Mater. Chem. B* **2013**, *1*, 4809.
(335) Bradberry, S. J.; Savyasachi, A. J.; Martinez-Calvo, M.; Gunnlaugsson, T. *Coord. Chem. Rev.* **2014**, *273–274*, 226.
(336) Lincheneau, C.; Leonard, J. P.; McCabe, T.; Gunnlaugsson, T. *Chem. Commun. (Cambridge, U. K.)* **2011**, *47*, 7119.
(337) Bonnet, C. S.; Devocelle, M.; Gunnlaugsson, T. *Org. Biomol. Chem.* **2012**, *10*, 126.
(338) Lincheneau, C.; Duke, R. M.; Gunnlaugsson, T. *Org. Biomol. Chem.* **2012**, *10*, 6069.
(339) Caffrey, D. F.; Gunnlaugsson, T. *Dalton Trans.* **2014**, *43*, 17964.
(340) Caffrey, D., Trinity College, The University of Dubin, 2013.
(341) Kotova, O.; Kitchen, J. A.; Lincheneau, C.; Peacock, R. D.; Gunnlaugsson, T. *Chem. Eur. J.* **2013**, *19*, 16181.

(342) Lincheneau, C.; Jean-Denis, B.; Gunnlaugsson, T. *Chem. Commun. (Cambridge, U. K.)* **2014**, *50*, 2857.
(343) Lincheneau, C.; Peacock, R. D.; Gunnlaugsson, T. *Chem. - Asian J.* **2010**, *5*, 500.
(344) Comby, S.; Stomeo, F.; McCoy, C. P.; Gunnlaugsson, T. *Helv. Chim. Acta* **2009**, *92*, 2461.
(345) Stomeo, F.; Lincheneau, C.; Leonard, J. P.; O'Brien, J. E.; Peacock, R. D.; McCoy, C. P.; Gunnlaugsson, T. *J. Am. Chem. Soc.* **2009**, *131*, 9636.
(346) Lincheneau, C.; Destribats, C.; Barry, D. E.; Kitchen, J. A.; Peacock, R. D.; Gunnlaugsson, T. *Dalton Trans.* **2011**, *40*, 12056.
(347) Kotova, O.; Blasco, S.; Twamley, B.; O'Brien, J.; Peacock, R. D.; Kitchen, J. A.; Martinez-Calvo, M.; Gunnlaugsson, T. *Chem. Sci.* **2015**, *6*, 457.
(348) Kitchen, J. A.; Barry, D. E.; Mercs, L.; Albrecht, M.; Peacock, R. D.; Gunnlaugsson, T. *Angew. Chem., Int. Ed.* **2012**, *51*, 704.
(349) Galanti, A.; Kotova, O.; Blasco, S.; Johnson, C. J.; Peacock, R. D.; Mills, S.; Boland, J. J.; Albrecht, M.; Gunnlaugsson, T. *Chem. - Eur. J.* **2016**, *22*, 9709.
(350) Barry, D. E.; Kitchen, J. A.; Albrecht, M.; Faulkner, S.; Gunnlaugsson, T. *Langmuir* **2013**, *29*, 11506.
(351) Cantuel, M.; Lincheneau, C.; Buffeteau, T.; Jonusauskaite, L.; Gunnlaugsson, T.; Jonusauskas, G.; McClenaghan, N. D. *Chem. Commun. (Cambridge, U. K.)* **2010**, *46*, 2486.
(352) Byrne, J. P.; Martínez-Calvo, M.; Peacock, R. D.; Gunnlaugsson, T. *Chem. Eur. J.* **2016**, *22*, 486.
(353) Byrne, J. P.; Kitchen, J. A.; O'Brien, J. E.; Peacock, R. D.; Gunnlaugsson, T. *Inorg. Chem.* **2015**, *54*, 1426.
(354) McCarney, E. P.; Byrne, J. P.; Twamley, B.; Martinez-Calvo, M.; Ryan, G.; Mobius, M. E.; Gunnlaugsson, T. *Chem. Commun. (Cambridge, U. K.)* **2015**, *51*, 14123.
(355) Martínez-Calvo, M.; Kotova, O.; Möbius, M. E.; Bell, A. P.; McCabe, T.; Boland, J. J.; Gunnlaugsson, T. *J. Am. Chem. Soc.* **2015**, *137*, 1983.
(356) Daly, R.; Kotova, O.; Boese, M.; Gunnlaugsson, T.; Boland, J. J. *ACS Nano* **2013**, *7*, 4838.
(357) Kotova, O.; Daly, R.; dos Santos, C. M. G.; Boese, M.; Kruger, P. E.; Boland, J. J.; Gunnlaugsson, T. *Angew. Chem. Int. Ed.* **2012**, *51*, 7208.
(358) McCoy, C. P.; Stomeo, F.; Plush, S. E.; Gunnlaugsson, T. *Chem. Mater.* **2006**, *18*, 4336.
(359) Gunnlaugsson, T.; McCoy, C. P.; Stomeo, F. *Tetrahedron Lett.* **2004**, *45*, 8403.
(360) Oshovsky, G. V.; Reinhoudt, D. N.; Verboom, W. *Angew. Chem. Int. Ed.* **2007**, *46*, 2366.
(361) Lindström, U. M. *Chem. Rev.* **2002**, *102*, 2751.
(362) Simon, M.-O.; Li, C.-J. *Chem. Soc. Rev.* **2012**, *41*, 1415.
(363) Jessop, P. G. *Green Chem.* **2011**, *13*, 1391.
(364) Laage, D.; Hynes, J. T. *Science* **2006**, *311*, 832.
(365) Ball, P. *Nature* **2003**, *423*, 25.
(366) Narayan, S.; Muldoon, J.; Finn, M. G.; Fokin, V. V.; Kolb, H. C.; Sharpless, K. B. *Angew. Chem. Int. Ed.* **2005**, *44*, 3275.
(367) Klijn, J. E.; Engberts, J. B. F. N. *Nature* **2005**, *435*, 746.
(368) Kubik, S.; Reyheller, C.; Stüwe, S. *J. Inclusion. Phenom. Macrocyclic. Chem.* **2005**, *52*, 137.
(369) Kataev, E. A.; Müller, C. *Tetrahedron* **2014**, *70*, 137.
(370) Davis, A. P.; Kubik, S.; Dalla Cort, A. *Org. Biomol. Chem.* **2015**, *13*, 2499.
(371) Jordan, J. H.; Gibb, B. C. *Chem. Soc. Rev.* **2015**, *44*, 547.

(372) chemicalize.org was used for prediction of logP, accessed 03/2017, ChemAxon (http://www.chemaxon.com).
(373) Kalepu, S.; Nekkanti, V. *Acta Pharm. Sin. B* **2015**, *5*, 442.
(374) Reddington, M. V. *Bioconjugate Chem.* **2007**, *18*, 2178.
(375) Peneva, K.; Mihov, G.; Nolde, F.; Rocha, S.; Hotta, J.-i.; Braeckmans, K.; Hofkens, J.; Uji-i, H.; Herrmann, A.; Müllen, K. *Angew. Chem. Int. Ed.* **2008**, *47*, 3372.
(376) Wang, H.; Lu, Z.; Lord, S. J.; Moerner, W. E.; Twieg, R. J. *Tetrahedron Lett.* **2007**, *48*, 3471.
(377) Barry, D. E., Trinity College, The University of Dublin, 2014.
(378) Nandi, I.; Bateson, M.; Bari, M.; Joshi, H. N. *AAPS PharmSciTech* **2003**, *4*, 1.
(379) Ghafourian, T.; Bozorgi, A. H. A. *Eur. J. Pharma. Sci.* **2010**, *40*, 430.
(380) Greenwald, R. B.; Choe, Y. H.; McGuire, J.; Conover, C. D. *Adv. Drug Delivery Rev.* **2003**, *55*, 217.
(381) Wuelfing, W. P.; Gross, S. M.; Miles, D. T.; Murray, R. W. *J. Am. Chem. Soc.* **1998**, *120*, 12696.
(382) Liu, Y.; Shipton, M. K.; Ryan, J.; Kaufman, E. D.; Franzen, S.; Feldheim, D. L. *Anal. Chem.* **2007**, *79*, 2221.
(383) Niu, S. L.; Ulrich, G.; Ziessel, R.; Kiss, A.; Renard, P.-Y.; Romieu, A. *Org. Lett.* **2009**, *11*, 2049.
(384) Wu, D.; O'Shea, D. F. *Org. Lett.* **2013**, *15*, 3392.
(385) Paape, N.; Wei, W.; Bosmann, A.; Kolbeck, C.; Maier, F.; Steinruck, H.-P.; Wasserscheid, P.; Schulz, P. S. *Chem. Commun.* **2008**, 3867.
(386) Murray, N. S., Trinity College, The University of Dublin, 2012.
(387) Smith, B. C. *Infrared Spectral Interpretation: A Systematic Approach*; Springer: Boca Ratan, USA, 1999.
(388) Berova, N.; Bari, L. D.; Pescitelli, G. *Chem. Soc. Rev.* **2007**, *36*, 914.
(389) Pescitelli, G.; Di Bari, L.; Berova, N. *Chem. Soc. Rev.* **2014**, *43*, 5211.
(390) Hembury, G. A.; Borovkov, V. V.; Inoue, Y. *Chem. Rev.* **2008**, *108*, 1.
(391) Berova, N.; Polavarapu, P. L.; Nakanishi, K.; Woody, R. W. *Comprehensive Chiroptical Spectroscopy, Volume 1: Instrumentation, Methodologies, and Theoretical Simulations*; John Wiley & Sons, Inc.: New York, USA, 2012.
(392) Berova, N.; Gargiulo, D.; Derguini, F.; Nakanishi, K.; Harada, N. *J. Am. Chem. Soc.* **1993**, *115*, 4769.
(393) Lightner, D. A.; Gurst, J. E. *Organic Conformational Analysis and Stereochemistry from Circular Dichroism Spectroscopy*; Wiley-VCH: New York, USA, 2000.
(394) Le Borgne, T.; Benech, J. M.; Floquet, S.; Bernardinelli, G.; Aliprandini, C.; Bettens, P.; Piguet, C. *Dalton Trans.* **2003**, 3856.
(395) Roosen, J.; Binnemans, K. *J. Mater. Chem. A* **2014**, *2*, 1530.
(396) Horrocks, W. D.; Sudnick, D. R. *J. Am. Chem. Soc.* **1979**, *101*, 334.
(397) Horrocks, W. D.; Sudnick, D. R. *Acc. Chem. Res.* **1981**, *14*, 384.
(398) Gregoliński, J.; Starynowicz, P.; Hua, K. T.; Lunkley, J. L.; Muller, G.; Lisowski, J. *J. Am. Chem. Soc.* **2008**, *130*, 17761.
(399) Chauvin, A. S.; Gumy, F.; Imbert, D.; Bünzli, J. C. G. *Spectrosc. Lett.* **2007**, *40*, 193.
(400) Aebischer, A.; Gumy, F.; Bunzli, J.-C. G. *Phys. Chem. Chem. Phys.* **2009**, *11*, 1346.
(401) Liu, G. K.; Chen, X. Y. *Handbook on the Physics and Chemistry of Rare Earths*; Elsevier Science B.V.: Amsterdam, 2007; Vol. 37.
(402) S. Dickins, R.; A. K. Howard, J.; M. Moloney, J.; Parker, D.; D. Peacock, R.; Siligardi, G. *Chem. Commun.* **1997**, 1747.
(403) S. Dickens, R.; A. K. Howard, J.; L. Maupin, C.; M. Moloney, J.; Parker, D.; D. Peacock, R.; P. Riehl, J.; Siligardi, G. *New J. Chem.* **1998**, *22*, 891.

(404) Bobba, G.; Bretonniere, Y.; Frias, J.-C.; Parker, D. *Org. Biomol. Chem.* **2003**, *1*, 1870.
(405) Zinna, F.; Di Bari, L. *Chirality* **2015**, *27*, 1.
(406) Richardson, F. S. *Inorg. Chem.* **1980**, *19*, 2806.
(407) Di Bari, L.; Salvadori, P. *Coord. Chem. Rev.* **2005**, *249*, 2854.
(408) Lunkley, J. L.; Shirotani, D.; Yamanari, K.; Kaizaki, S.; Muller, G. *Inorg. Chem.* **2011**, *50*, 12724.
(409) Dai, L.; Lo, W.-S.; Coates, I. D.; Pal, R.; Law, G.-L. *Inorg. Chem.* **2016**, *55*, 9065.
(410) Riehl, J. P.; Muller, G. In *Comprehensive Chiroptical Spectroscopy, Vol. 1: Instrumentation, Methodologies and Theoretical Simulations;*; John Wiley & Sons, Inc.: New York, USA, 2012; Vol. 1, p 65.
(411) Richardson, F. S.; Riehl, J. P. *Chem. Rev.* **1977**, *77*, 773.
(412) Pereira, C. C. L.; Dias, S.; Coutinho, I.; Leal, J. P.; Branco, L. C.; Laia, C. A. T. *Inorg. Chem.* **2013**, *52*, 3755.
(413) Maeder, M.; King, P. In *Chemometrics in Practical Applications*; InTech: Croatia, 2012, p 41.
(414) Kelly, S. M.; Jess, T. J.; Price, N. C. *Biochimica et Biophysica Acta (BBA) - Proteins and Proteomics* **2005**, *1751*, 119.
(415) Thordarson, P. *Chem. Soc. Rev.* **2011**, *40*, 1305.
(416) Jelesarov, I.; Bosshard, H. R. *J. Mol. Recognit.* **1999**, *12*, 3.
(417) Blandamer, M. J.; Cullis, P. M.; Engberts, J. B. F. N. *J. Chem. Soc., Faraday Trans.* **1998**, *94*, 2261.
(418) del Rosso, M. G.; Ciesielski, A.; Colella, S.; Harrowfield, J. M.; Samori, P. *ChemPhysChem* **2014**, *15*, 2743.
(419) Francisco, V.; Basilio, N.; Garcia-Rio, L. *J. Phys. Chem. B* **2014**, *118*, 4710.
(420) Ojida, A.; Mito-oka, Y.; Sada, K.; Hamachi, I. *J. Am. Chem. Soc.* **2004**, *126*, 2454.
(421) Ostermeier, M.; Berlin, M.-A.; Meudtner, R. M.; Demeshko, S.; Meyer, F.; Limberg, C.; Hecht, S. *Chem. - Eur. J.* **2010**, *16*, 10202.
(422) Mundoma, C.; Greenbaum, N. L. *Biopolymers* **2003**, *69*, 100.
(423) Barkleit, A.; Tsushima, S.; Savchuk, O.; Philipp, J.; Heim, K.; Acker, M.; Taut, S.; Fahmy, K. *Inorg. Chem.* **2011**, *50*, 5451.
(424) Brown, M. A.; Kropf, A. J.; Paulenova, A.; Gelis, A. V. *Dalton Trans.* **2014**, *43*, 6446.
(425) Michels, J. J.; Huskens, J.; Reinhoudt, D. N. *J. Am. Chem. Soc.* **2002**, *124*, 2056.
(426) Miguirditchian, M.; Guillaneux, D.; Guillaumont, D.; Moisy, P.; Madic, C.; Jensen, M. P.; Nash, K. L. *Inorg. Chem.* **2005**, *44*, 1404.
(427) Tian, G.; Martin, L. R.; Rao, L. *Inorg. Chem.* **2010**, *49*, 10598.
(428) Tian, G.; Zhang, Z.; Martin, L. R.; Rao, L. *Inorg. Chem.* **2015**, *54*, 1232.
(429) Good, N. E.; Winget, G. D.; Winter, W.; Connolly, T. N.; Izawa, S.; Singh, R. M. M. *Biochemistry* **1966**, *5*, 467.
(430) Schmidtchen, F. P. In *Analytical Methods in Supramolecular Chemistry (2nd Edition)*; Wiley-VCH Verlag GmbH & Co. KGaA: Weinheim, Germany, 2012; Vol. 1, p 67.
(431) Lamb, J. D.; Izatt, R. M.; Swain, C. S.; Bradshaw, J. S.; Christensen, J. J. *J. Am. Chem. Soc.* **1980**, *102*, 479.
(432) Lovatt, M.; Cooper, A.; Camilleri, P. *Eur. Biophys. J.* **1996**, *24*, 354.
(433) Patel, M. M.; Anchordoquy, T. J. *Biophys. J.* **2005**, *88*, 2089.
(434) Fairlie, W. D.; Perugini, M. A.; Kvansakul, M.; Chen, L.; Huang, D. C. S.; Colman, P. M. *Cell Death Differ.* **2005**, *13*, 426.

(435) Patterson, J. P.; Robin, M. P.; Chassenieux, C.; Colombani, O.; O'Reilly, R. K. *Chem. Soc. Rev.* **2014**, *43*, 2412.
(436) Gei; Gollwitzer, C.; Sikora, A.; Minelli, C.; Krumrey, M.; Resch-Genger, U. *Anal. Methods* **2015**, *7*, 9785.
(437) Schärtl, W. *Light Scattering from Polymer Solutions and Nanoparticle Dispersions*; Springer Berlin Heidelberg: Berlin, Germany, 2007.
(438) Balachandran, V. S.; Jadhav, S. R.; Pradhan, P.; De Carlo, S.; John, G. *Angew. Chem. Int. Ed.* **2010**, *49*, 9509.
(439) Seon Jeong, K.; Sang Jun, P.; Sun, I. K. *Smart Mater. Struct.* **2004**, *13*, 317.
(440) Kuang, Y.; Gao, Y.; Shi, J.; Li, J.; Xu, B. *Chem. Commun.* **2014**, *50*, 2772.
(441) Po, C.; Tam, A. Y.-Y.; Yam, V. W.-W. *Chem. Sci.* **2014**, *5*, 2688.
(442) Mezei, G.; Raptis, R. G. *New J. Chem.* **2003**, *27*, 1399.
(443) Gunderman, B. J.; Squattrito, P. J. *Inorg. Chem.* **1995**, *34*, 2399.
(444) Zweep, N.; van Esch, J. H. In *Functional Molecular Gels*; Escuder, B., Miravet, J. F., Eds.; The Royal Society of Chemistry: Cambridge, UK, 2014, p 1.
(445) Stubenrauch, C.; Giesselmann, F. *Angew. Chem., Int. Ed.* **2016**, *55*, 3268.
(446) Raghavan, S. R. *Langmuir* **2009**, *25*, 8382.
(447) Molloy, J. K.; Kotova, O.; Peacock, R. D.; Gunnlaugsson, T. *Org. Biomol. Chem.* **2012**, *10*, 314.
(448) Walton, J. W.; Carr, R.; Evans, N. H.; Funk, A. M.; Kenwright, A. M.; Parker, D.; Yufit, D. S.; Botta, M.; De Pinto, S.; Wong, K.-L. *Inorg. Chem.* **2012**, *51*, 8042.
(449) Neil, E. R.; Funk, A. M.; Yufit, D. S.; Parker, D. *Dalton Trans.* **2014**, *43*, 5490.
(450) Hu, Z.; Willard, A. P.; Ono, R. J.; Bielawski, C. W.; Rossky, P. J.; Vanden Bout, D. A. *Nat. Commun.* **2015**, *6*, 8246..
(451) Reichardt, C. *Chem. Rev.* **1994**, *94*, 2319.
(452) Reichaedt, C. *Solvents and Solvent Effects in Organic Chemistry, 3rd Edition*; John Wiley & Sons: Weinheim, Germany, 2003.
(453) Curutchet, C.; Scholes, G. D.; Mennucci, B.; Cammi, R. *J. Phys. Chem. B* **2007**, *111*, 13253.
(454) Harada, N.; Chen, S.-M. L.; Nakanishi, K. *J. Am. Chem. Soc.* **1975**, *97*, 5345.
(455) Heyn, M. P. *J. Phys. Chem.* **1975**, *79*, 2424.
(456) Turro, N. J. *Modern molecular photochemistry*; University Science Books: California, USA, 1991.
(457) Daly, B.; Ling, J.; de Silva, A. P. *Chem. Soc. Rev.* **2015**, *44*, 4203.
(458) Leach, S. J. *Physical Principles and Techniques of Protein Chemistry, Pt. A*; Academic Press: New York, USA, 1969.
(459) Yuasa, J.; Mukai, R.; Hasegawa, Y.; Kawai, T. *Chem. Commun.* **2014**, *50*, 7937.
(460) Imperio, D.; Giovenzana, G. B.; Law, G.-l.; Parker, D.; Walton, J. W. *Dalton Trans.* **2010**, *39*, 9897.
(461) Longhi, G.; Castiglioni, E.; Koshoubu, J.; Mazzeo, G.; Abbate, S. *Chirality* **2016**, *28*, 696.
(462) Sánchez-Carnerero, E. M.; Agarrabeitia, A. R.; Moreno, F.; Maroto, B. L.; Muller, G.; Ortiz, M. J.; de la Moya, S. *Chem. Eur. J.* **2015**, *21*, 13488.
(463) Luk, C. K.; Richardson, F. S. *J. Am. Chem. Soc.* **1975**, *97*, 6666.
(464) Parker, D. *Coord. Chem. Rev.* **2000**, *205*, 109.
(465) Prasanna de Silva, A.; Stewart, S. *Chem. Commun.* **1997**, 1891.
(466) Ye, Z.; Wang, G.; Chen, J.; Fu, X.; Zhang, W.; Yuan, J. *Biosens. Bioelectron.* **2010**, *26*, 1043.
(467) Gunnlaugsson, T.; Pope, S. J. A. In *Luminescence of Lanthanide Ions in Coordination Compounds and Nanomaterials*; John Wiley & Sons Ltd: 2014, p 231.

(468) Ingram, A. J.; Dunlap, A. G.; DiPietro, R.; Muller, G. *J. Phys. Chem. A* **2011**, *115*, 7912.
(469) McCoy, C. P.; Brady, C.; Cowley, J. F.; McGlinchey, S. M.; McGoldrick, N.; Kinnear, D. J.; Andrews, G. P.; Jones, D. S. *Expert Opin. Drug Delivery* **2010**, *7*, 605.
(470) Cao, Z.-Q.; Wang, G.-J. *Chem. Rec.* **2016**, *16*, 1398.
(471) Li, J.; Mooney, D. J. *Nature Reviews Materials* **2016**, *1*, 16071.
(472) Liu, D. E.; Dursch, T. J.; Taylor, N. O.; Chan, S. Y.; Bregante, D. T.; Radke, C. J. *J. Controlled Release* **2016**, *239*, 242.
(473) Surender, E. M.; Bradberry, S. J.; Bright, S. A.; McCoy, C. P.; Williams, D. C.; Gunnlaugsson, T. *J. Am. Chem. Soc.* **2017**, *139*, 381.
(474) Noda, A.; Watanabe, M. *Electrochim. Acta* **2000**, *45*, 1265.
(475) Guvendiren, M.; Yang, S.; Burdick, J. A. *Adv. Funct. Mater.* **2009**, *19*, 3038.
(476) Bünzli, J.-C. G. *Interface Focus* **2013**, *3*.
(477) dos Santos, C. M. G.; Fernandez, P. B.; Plush, S. E.; Leonard, J. P.; Gunnlaugsson, T. *Chem. Commun. (Cambridge, U. K.)* **2007**, 3389.
(478) dos Santos, C. M. G.; Gunnlaugsson, T. *Supramol. Chem.* **2009**, *21*, 173.
(479) Lincheneau, C.; Duke, R. M.; Gunnlaugsson, T. *Org. Biomol. Chem.* **2012**, *10*, 6069.
(480) Pandurangan, K.; Kitchen, J. A.; Blasco, S.; Paradisi, F.; Gunnlaugsson, T. *Chem. Commun.* **2014**, *50*, 10819.
(481) Fages, F.; Voegtle, F.; Zinic, M. *Top. Curr. Chem.* **2005**, *256*, 77.
(482) Smith, D. K.; John Wiley & Sons Ltd.: 2012; Vol. 7, p 3355.
(483) Steed, J. W. *Chem. Commun.* **2011**, *47*, 1379.
(484) Danylyuk, O.; Fedin, V. P.; Sashuk, V. *Chem. Commun.* **2013**, *49*, 1859.
(485) Barrow, S. J.; Kasera, S.; Rowland, M. J.; del Barrio, J.; Scherman, O. A. *Chem. Rev.* **2015**, *115*, 12320.
(486) Song, Q.; Gao, Y.; Xu, J.-F.; Qin, B.; Serpe, M. J.; Zhang, X. *ACS Macro Letters* **2016**, *5*, 1084.
(487) Harada, A.; Takashima, Y.; Nakahata, M. *Acc. Chem. Res.* **2014**, *47*, 2128.
(488) Kretschmann, O.; Choi, S. W.; Miyauchi, M.; Tomatsu, I.; Harada, A.; Ritter, H. *Angew. Chem. Int. Ed.* **2006**, *45*, 4361.
(489) Liu, D.; Wang, D.; Wang, M.; Zheng, Y.; Koynov, K.; Auernhammer, G. K.; Butt, H.-J.; Ikeda, T. *Macromolecules* **2013**, *46*, 4617.
(490) Jones, D. S.; Lorimer, C. P.; McCoy, C. P.; Gorman, S. P. *J. Biomed. Mater. Res., Part B* **2008**, *85B*, 417.
(491) Jones, D. S.; McCoy, C. P.; Andrews, G. P.; McCrory, R. M.; Gorman, S. P. *Mol. Pharmaceutics* **2015**, *12*, 2928.
(492) Indolfi, L.; Causa, F.; Netti, P. A. *J. Mater. Sci.: Mater. Med.* **2009**, *20*, 1541.
(493) Sola, L.; Cretich, M.; Damin, F.; Chiari, M. In *Nanomaterial Interfaces in Biology: Methods and Protocols*; Bergese, P., Hamad-Schifferli, K., Eds.; Humana Press: Totowa, NJ, 2013, p 95.
(494) Fixe, F.; Dufva, M.; Telleman, P.; Christensen, C. B. V. *Nucleic Acids Res.* **2004**, *32*, e9.
(495) Braun, E. L. *Digital Computer Design: Logic, Circuitry, and Synthesis*; Elsevier Science: New York, USA, 2014.
(496) Aviram, A. *J. Am. Chem. Soc.* **1988**, *110*, 5687.
(497) de Silva, A. P.; Gunaratne, N. H. Q.; McCoy, C. P. *Nature* **1993**, *364*, 42.
(498) Andreasson, J.; Pischel, U. *Chem. Soc. Rev.* **2015**, *44*, 1053.
(499) Asoh, T.-a.; Akashi, M. *Chem. Commun.* **2009**, 3548.

(500) Bychkova, V.; Shvarev, A.; Zhou, J.; Pita, M.; Katz, E. *Chem. Commun.* **2010**, *46*, 94.
(501) Kim, K.-W.; Kim, B. C.; Lee, H. J.; Kim, J.; Oh, M.-K. *Electroanalysis* **2011**, *23*, 980.
(502) Komatsu, H.; Matsumoto, S.; Tamaru, S.-i.; Kaneko, K.; Ikeda, M.; Hamachi, I. *J. Am. Chem. Soc.* **2009**, *131*, 5580.
(503) Matsui, J.; Mitsuishi, M.; Aoki, A.; Miyashita, T. *Angew. Chem. Int. Ed.* **2003**, *42*, 2272.
(504) Ogawa, A.; Maeda, M. *Chem. Commun.* **2009**, 4666.
(505) Privman, V.; Pedrosa, V.; Melnikov, D.; Pita, M.; Simonian, A.; Katz, E. *Biosens. Bioelectron.* **2009**, *25*, 695.
(506) Schneider, H. J.; Tianjun, L.; Lomadze, N.; Palm, B. *Adv. Mater.* **2004**, *16*, 613.
(507) de Silva, A. P.; Uchiyama, S.; Vance, T. P.; Wannalerse, B. *Coord. Chem. Rev.* **2007**, *251*, 1623.
(508) Fabbrizzi, L.; Poggi, A. *Chem. Soc. Rev.* **1995**, *24*, 197.
(509) Prasanna de Silva, A. *Molecular Logic-Based Computation*; Royal Society of Chemistry: Cambridge, UK, 2013.
(510) Andréasson, J.; Kodis, G.; Terazono, Y.; Liddell, P. A.; Bandyopadhyay, S.; Mitchell, R. H.; Moore, T. A.; Moore, A. L.; Gust, D. *J. Am. Chem. Soc.* **2004**, *126*, 15926.
(511) Andreasson, J.; Pischel, U.; Straight, S. D.; Moore, T. A.; Moore, A. L.; Gust, D. *J. Am. Chem. Soc.* **2011**, *133*, 11641.
(512) Andréasson, J.; Straight, S. D.; Kodis, G.; Park, C.-D.; Hambourger, M.; Gervaldo, M.; Albinsson, B.; Moore, T. A.; Moore, A. L.; Gust, D. *J. Am. Chem. Soc.* **2006**, *128*, 16259.
(513) Gunnlaugsson, T.; Leonard, J. P.; Sénéchal, K.; Harte, A. J. *J. Am. Chem. Soc.* **2003**, *125*, 12062.
(514) Vaishnavi, E.; Renganathan, R. *Analyst* **2014**, *139*, 225.
(515) Wan, S.; Zheng, Y.; Shen, J.; Yang, W.; Yin, M. *ACS Appl. Mater. Interfaces* **2014**, *6*, 19515.
(516) Amendola, V.; Bergamaschi, G.; Dacarro, G.; Denat, F.; Boschetti, F.; Nikolantonaki, M.; Gougeon, R.; D'Alessio, G.; Viaux, A. S.; Bertheau, L.; Guyot, S.; Sok, N.; Pallavicini, P. *Eur. J. Inorg. Chem.* **2016**, 5106.
(517) Gupta, V. K.; Mergu, N.; Kumawat, L. K.; Singh, A. K. *Talanta* **2015**, *144*, 80.
(518) Comby, S.; Gunnlaugsson, T. *ACS Nano* **2011**, *5*, 7184.
(519) Parker, D. *Chem. Commun.* **1998**, 245.
(520) Gunnlaugsson, T.; Mac Donail, D. A.; Parker, D. *Chem. Commun.* **2000**, 93.
(521) Gunnlaugsson, T.; Mac Dónaill, D. A.; Parker, D. *J. Am. Chem. Soc.* **2001**, *123*, 12866.
(522) Bonnet, C. S.; Gunnlaugsson, T. *New J. Chem.* **2009**, *33*, 1025.
(523) Pu, F.; Ren, J.; Qu, X. *ACS Appl. Mater. Interfaces* **2014**, *6*, 9557.
(524) Pu, F.; Ju, E.; Ren, J.; Qu, X. *Adv. Mater.* **2014**, *26*, 1111.
(525) de Sousa, M.; Kluciar, M.; Abad, S.; Miranda, M. A.; de Castro, B.; Pischel, U. *Photochem. Photobiol. Sci.* **2004**, *3*, 639.
(526) Li, X.; Chen, H.; Kirillov, A. M.; Xie, Y.; Shan, C.; Wang, B.; Shi, C.; Tang, Y. *Inorg. Chem. Front.* **2016**, *3*, 1014.
(527) Bassani, D. M.; Cucinotta, F.; Bohne, C.; Basilio, N.; Lemon, C.; Allain, C.; Sundstrom, V.; Campagna, S.; Rohacova, J.; Ketteler, Y.; Ryan, S. T. J.; Vos, J.; de Silva, A. P.; Slota, M. *Faraday Discuss.* **2015**, *185*, 399.
(528) Li, Y.; Flood, A. H. *Angew. Chem. Int. Ed.* **2008**, *47*, 2649.

(529) Schulze, B.; Friebe, C.; Hager, M. D.; Günther, W.; Köhn, U.; Jahn, B. O.; Görls, H.; Schubert, U. S. *Org. Lett.* **2010**, *12*, 2710.
(530) Byrne, J. P., Trinity College, The University of Dublin, 2015.
(531) Hemmilä, I.; Laitala, V. *J. Fluoresc.* **2005**, *15*, 529.
(532) Li, Q.; Li, T.; Wu, J. *J. Phys. Chem. B* **2001**, *105*, 12293.
(533) Wakerly, J. F. *Digital Design: Principles and Practices*; Pearson/Prentice Hall: Upper Saddle River, N.J., USA, 2006.
(534) Karg, M.; Hellweg, T. In *Hydrogel Micro and Nanoparticles*; Wiley-VCH Verlag GmbH & Co. KGaA: Weinheim, Germany, 2012, p 257.
(535) Monti, F.; Baschieri, A.; Matteucci, E.; Mazzanti, A.; Sambri, L.; Barbieri, A.; Armaroli, N. *Faraday Discuss.* **2015**, *185*, 233.
(536) Elbert, D. L. *Acta Biomater.* **2011**, *7*, 31.
(537) Wilson, A. N.; Salas, R.; Guiseppi-Elie, A. *J. Controlled Release* **2012**, *160*, 41.
(538) Sieglaff, C. L. *J. Polym. Sci.* **1959**, *41*, 319.
(539) Hanyková, L.; Spěváček, J.; Radecki, M.; Zhigunov, A.; Šťastná, J.; Valentová, H.; Sedláková, Z. *Colloid. Polym. Sci.* **2015**, *293*, 709.
(540) Yoon, S. C.; Jhon, M. S. *J. Appl. Polym. Sci.* **1982**, *27*, 4661.
(541) Lee, S.; Flood, A. H. In *Click Triazoles*; Košmrlj, J., Ed.; Springer Berlin Heidelberg: Berlin, Heidelberg, 2012, p 85.
(542) Watkinson, M. In *Click Triazoles*; Košmrlj, J., Ed.; Springer Berlin Heidelberg: Berlin, Heidelberg, 2012, p 109.
(543) Buenger, D.; Topuz, F.; Groll, J. *Prog. Polym. Sci.* **2012**, *37*, 1678.
(544) Tokarev, I.; Minko, S. *Soft Matter* **2009**, *5*, 511.
(545) Chan, H. N.; Shu, Y.; Xiong, B.; Chen, Y.; Chen, Y.; Tian, Q.; Michael, S. A.; Shen, B.; Wu, H. *ACS Sens.* **2016**, *1*, 227.
(546) Janegitz, B. C.; Cancino, J.; Zucolotto, V. *J. Nanosci. Nanotechnol.* **2014**, *14*, 378.
(547) Hierlemann, A.; Gutierrez-Osuna, R. *Chem. Rev.* **2008**, *108*, 563.
(548) Klinger, D.; Landfester, K. *Polymer* **2012**, *53*, 5209.
(549) Yang, Y.; Urban, M. W. *Chem. Soc. Rev.* **2013**, *42*, 7446.
(550) Jackson, A. C.; Beyer, F. L.; Price, S. C.; Rinderspacher, B. C.; Lambeth, R. H. *Macromolecules* **2013**, *46*, 5416.
(551) Jackson, A. C.; Walck, S. D.; Strawhecker, K. E.; Butler, B. G.; Lambeth, R. H.; Beyer, F. L. *Macromolecules* **2014**, *47*, 4144.
(552) Safranski, D. L.; Gall, K. *Polymer* **2008**, *49*, 4446.
(553) Varma, A. J.; Deshpande, S. V.; Kennedy, J. F. *Carbohydr. Polym.* **2004**, *55*, 77.
(554) Wei, P.; Yan, X.; Huang, F. *Chem. Soc. Rev.* **2015**, *44*, 815.
(555) Gohy, J.-F.; Lohmeijer, B. G. G.; Schubert, U. S. *Macromol. Rapid Commun.* **2002**, *23*, 555.
(556) Chiper, M.; Fournier, D.; Hoogenboom, R.; Schubert, U. S. *Macromol. Rapid Commun.* **2008**, *29*, n/a.
(557) Cypcar, C. C.; Camelio, P.; Lazzeri, V.; Mathias, L. J.; Waegell, B. *Macromolecules* **1996**, *29*, 8954.
(558) Matsumoto, A.; Tanaka, S.; Otsu, T. *Macromolecules* **1991**, *24*, 4017.
(559) Rogers, S.; Mandelkern, L. *J. Phys. Chem.* **1957**, *61*, 985.
(560) Hollinger, J. O. *An Introduction to Biomaterials, Second Edition*; CRC Press: Boca Ratan, USA, 2012.
(561) Sirkecioglu, A.; Mutlu, H. B.; Citak, C.; Koc, A.; Güner, F. S. *Polym. Eng. Sci.* **2014**, *54*, 1182.

(562) Hongke, T.; Fengfeng, X. In *Proceedings of the 2013 International Conference on Material Science and Environmental Engineering-2013*; DEStech Publications, Inc: Lancaster, USA, 2013.
(563) Hutmacher, D. W.; Schantz, T.; Zein, I.; Ng, K. W.; Teoh, S. H.; Tan, K. C. *Journal of Biomedical Materials Research* **2001**, *55*, 203.
(564) Fang, F.; Lake, S. P. *Interface Focus* **2016**, *6*.
(565) Hansen, C. M. *Hansen Solubility Parameters: A User's Handbook*; 2nd ed.; Taylor and Francis: Hoboken, USA, 2012.
(566) Smith, R.; Wright, K. L.; Ashton, L. *Analyst* **2016**, *141*, 3590.
(567) Biskup, C.; Hoffmann, B.; Benndorf, K.; Rück, A. In *Flim Microscopy in Biology and Medicine*; CRC Press: 2009, p 211.
(568) Bastos, A. E. P.; Scolari, S.; Stöckl, M.; de Almeida, R. F. M. In *Methods Enzymol.*; conn, P. M., Ed.; Academic Press: 2012; Vol. Volume 504, p 57.
(569) Li, D. D.-U.; Ameer-Beg, S.; Arlt, J.; Tyndall, D.; Walker, R.; Matthews, D. R.; Visitkul, V.; Richardson, J.; Henderson, R. K. *Sensors* **2012**, *12*, 5650.
(570) Sarder, P.; Maji, D.; Achilefu, S. *Bioconjugate Chem.* **2015**, *26*, 963.
(571) Esposito, A.; Gerritsen, H. C.; Wouters, F. S. In *Standardization and Quality Assurance in Fluorescence Measurements II: Bioanalytical and Biomedical Applications*; Resch-Genger, U., Ed.; Springer Berlin Heidelberg: Berlin, Heidelberg, 2008, p 117.
(572) Grichine, A.; Haefele, A.; Pascal, S.; Duperray, A.; Michel, R.; Andraud, C.; Maury, O. *Chem. Sci.* **2014**, *5*, 3475.
(573) Armarego, W. L. F.; Chai, C. L. L. In *Purification of Laboratory Chemicals (Sixth Edition)*; Butterworth-Heinemann: Oxford, 2009, p 88.

A2. Chapter 2 Appendix

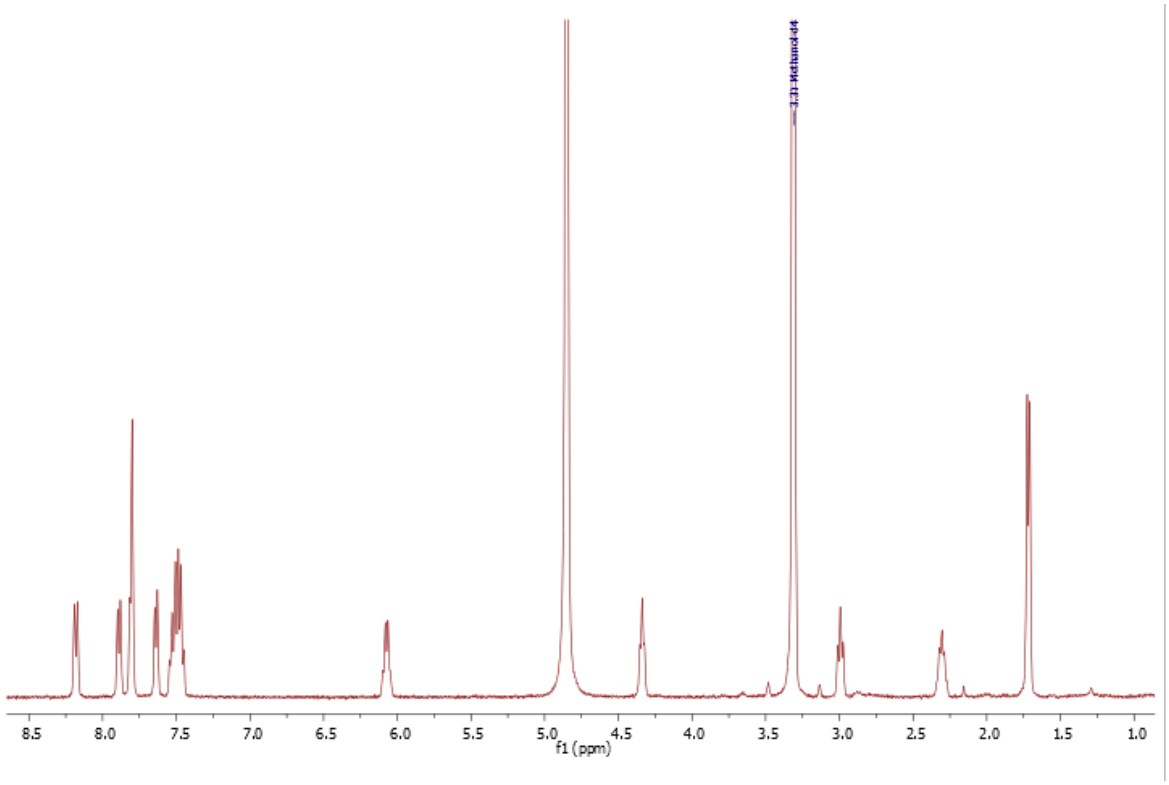

Figure A2.1 ^{1}H NMR (600 MHz, CD_3OD) spectrum of **120(*S,S*)**

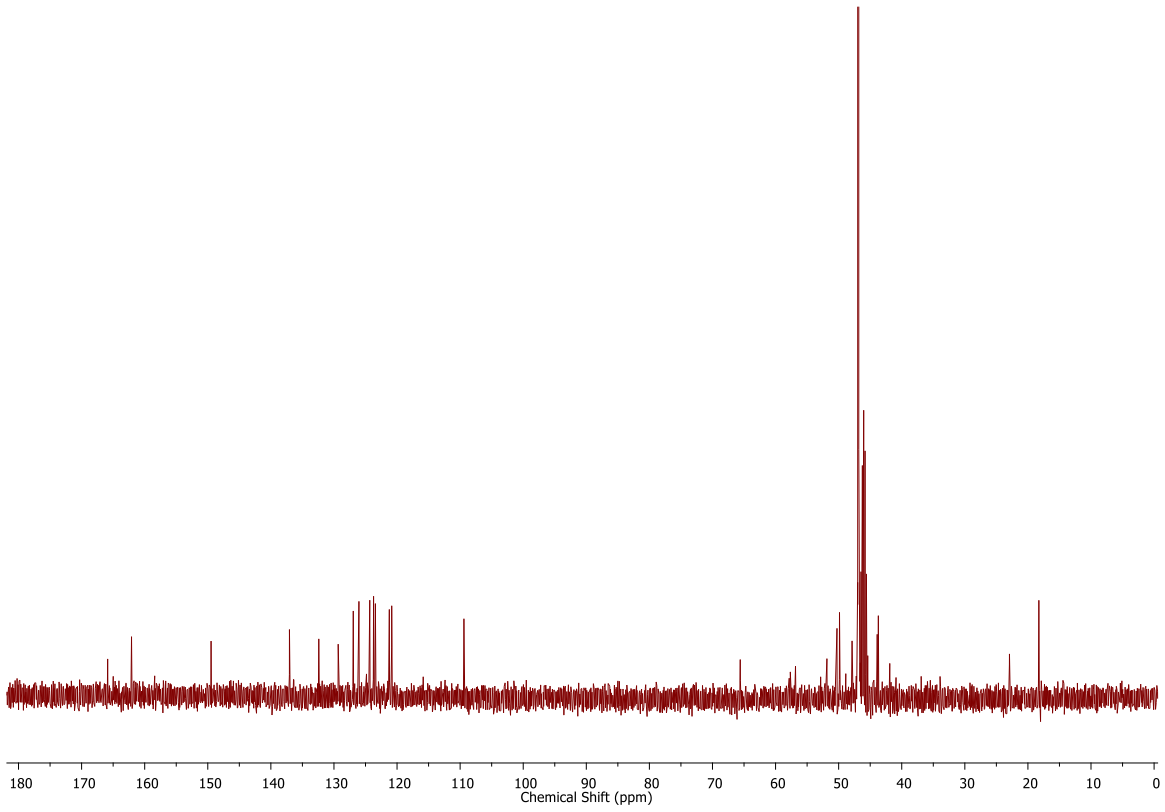

Figure A2.2 ^{13}C NMR (150 MHz, CD_3OD) spectrum of **120(*S,S*)**

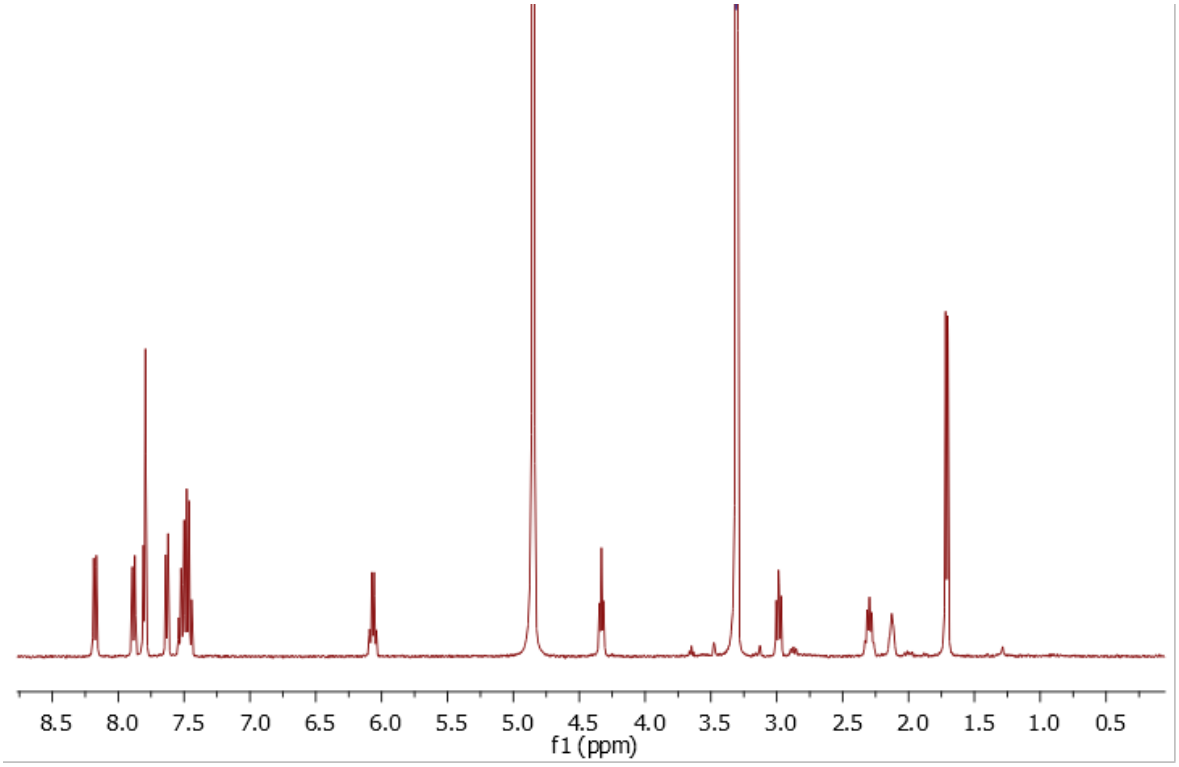

Figure A2.3 ^{1}H NMR (600 MHz, CD_3OD) spectrum of **120(*R*,*R*)**

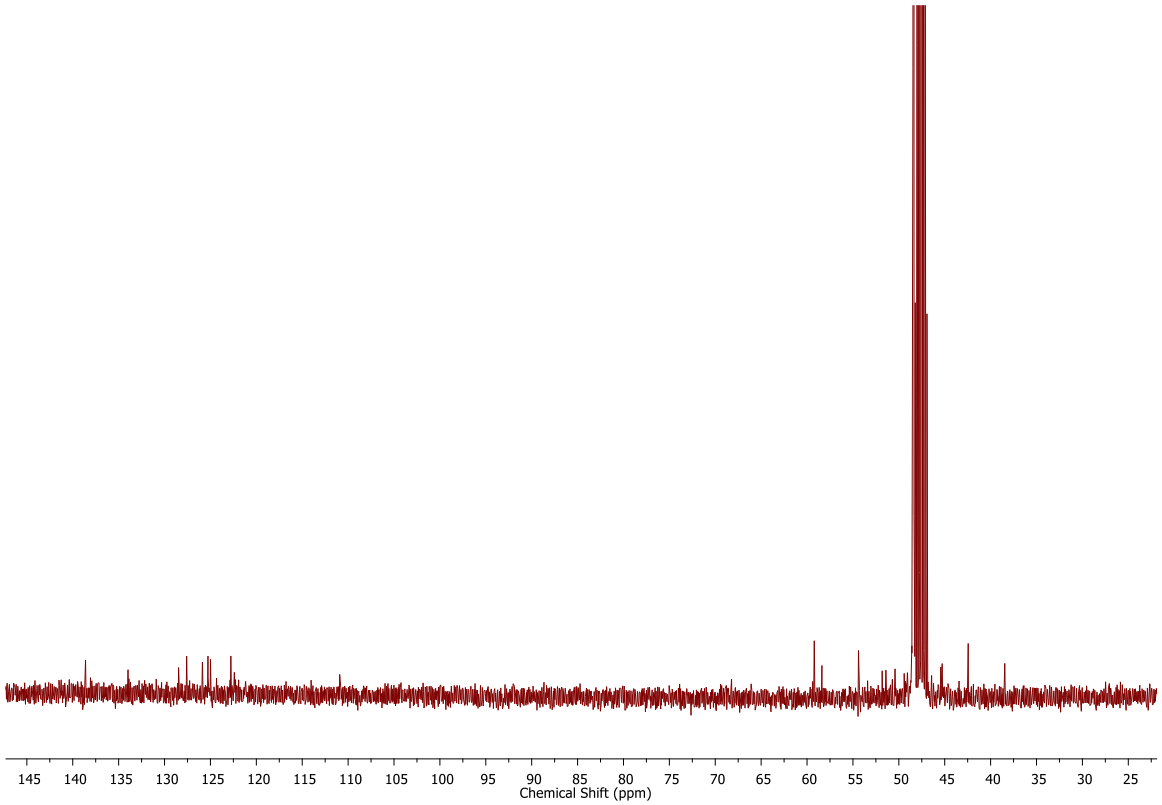

Figure A2.4 ^{13}C NMR (150 MHz, CD_3OD) spectrum of **120(*S*,*S*)**

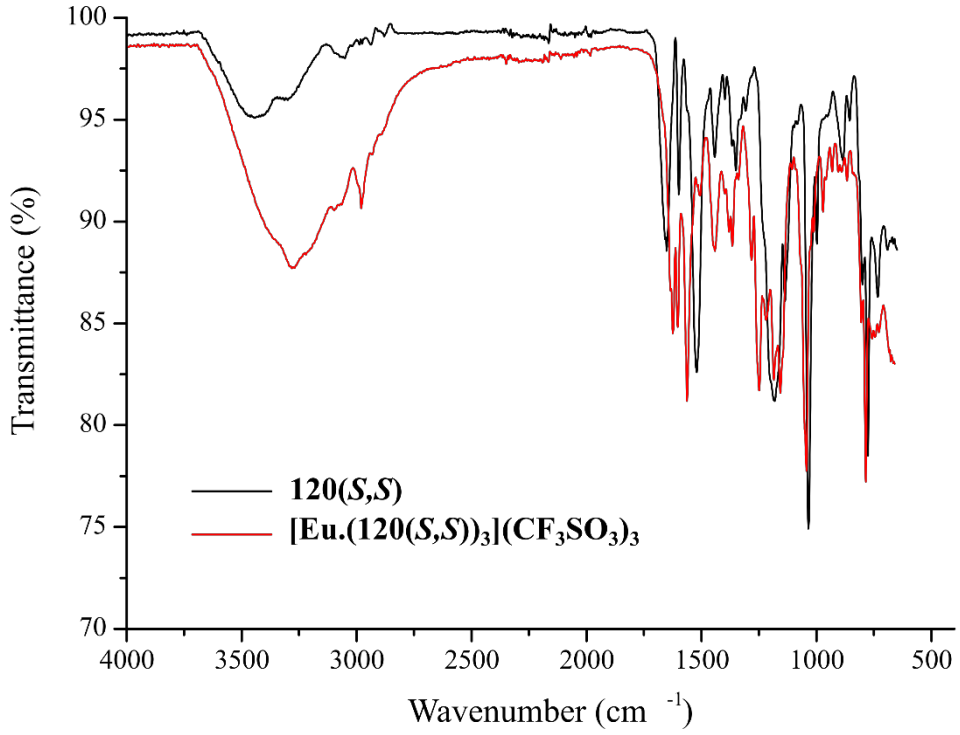

Figure A2.5 Overlaid IR spectra of **120(*S*,*S*)** and **[Eu.(120(*S*,*S*))$_3$]**$(CF_3SO_3)_3$

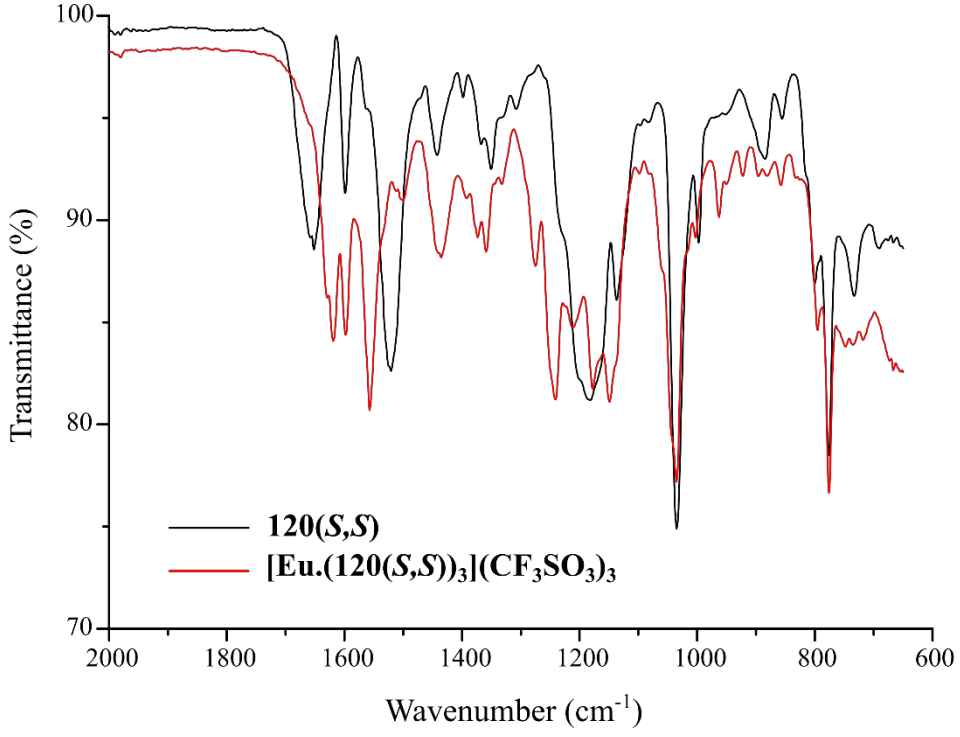

Figure A2.6 Zoomed region of overlaid IR spectra of **120(*S*,*S*)** and **[Eu.(120(*S*,*S*))$_3$]**$(CF_3SO_3)_3$ showing key carbonyl stretches and shifts between ligand and complex.

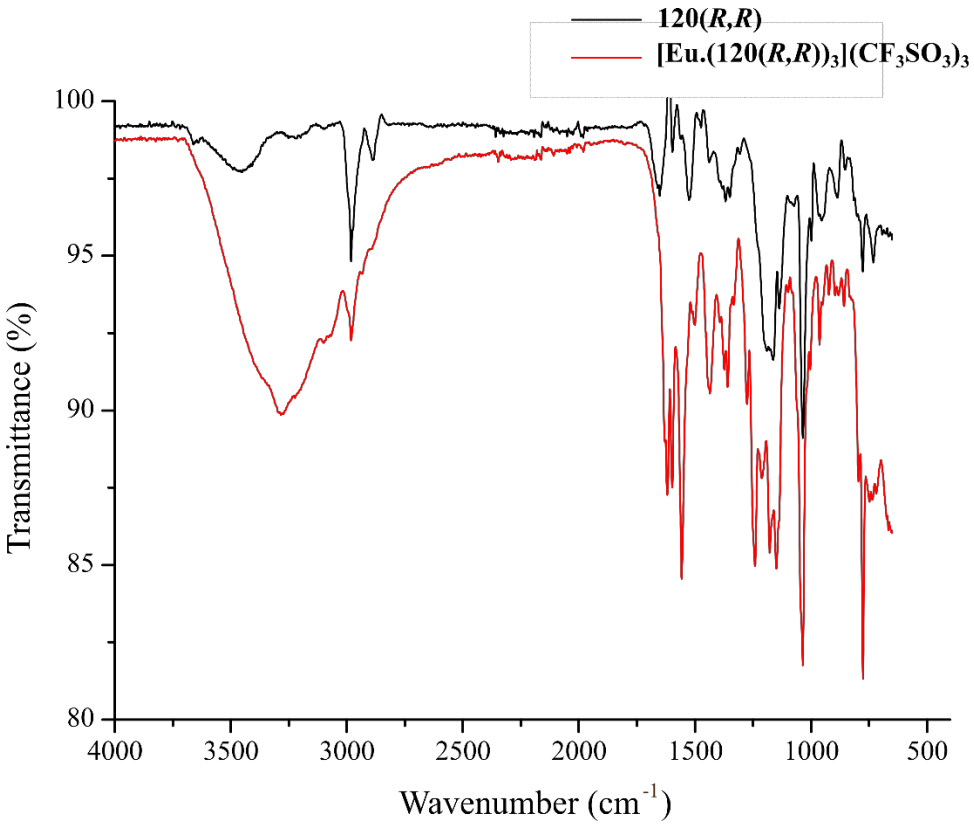

Figure A2.7 Overlaid IR spectra of **120(*R*,*R*)** and **[Eu.(120(*R*,*R*))$_3$]**$(CF_3SO_3)_3$

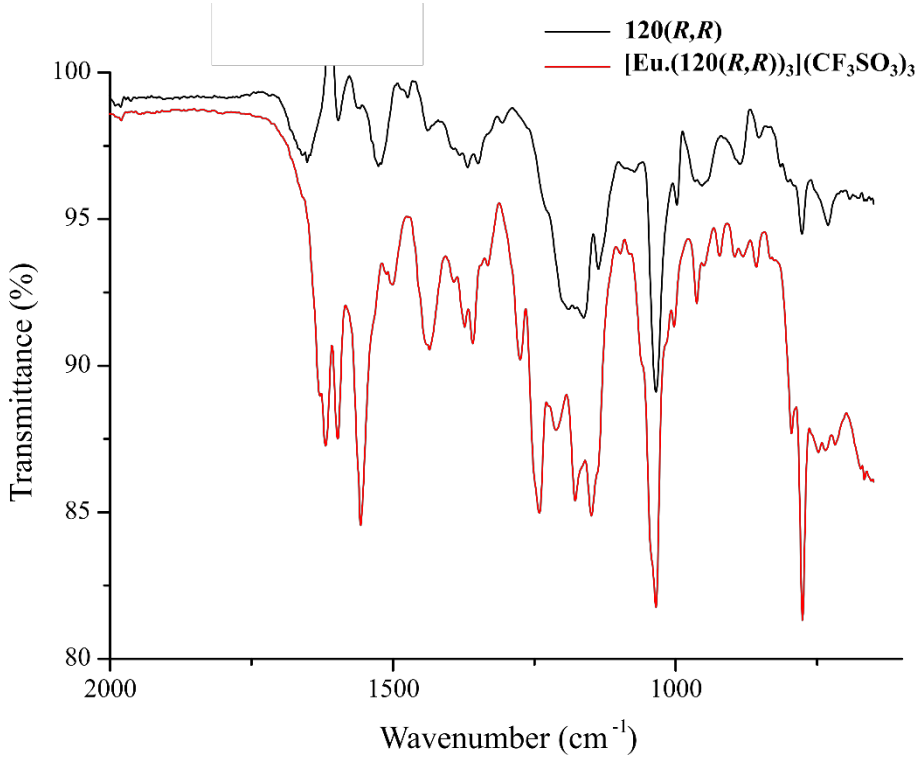

Figure A2.8 Zoomed region of overlaid IR spectra of **120(*R*,*R*)** and **[Eu.(120(*R*,*R*))$_3$]**$(CF_3SO_3)_3$ showing key carbonyl stretches and shifts between ligand and complex

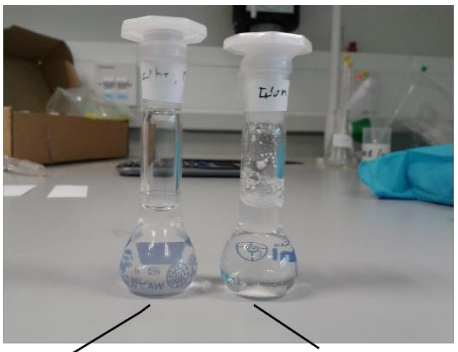

Figure A2.9 Photograph of solutions of 5 mg of **120(*S*,*S*)** and **133(*S*,*S*)** sonicated in H_2O showing full dissolution and flocculation, respectively;

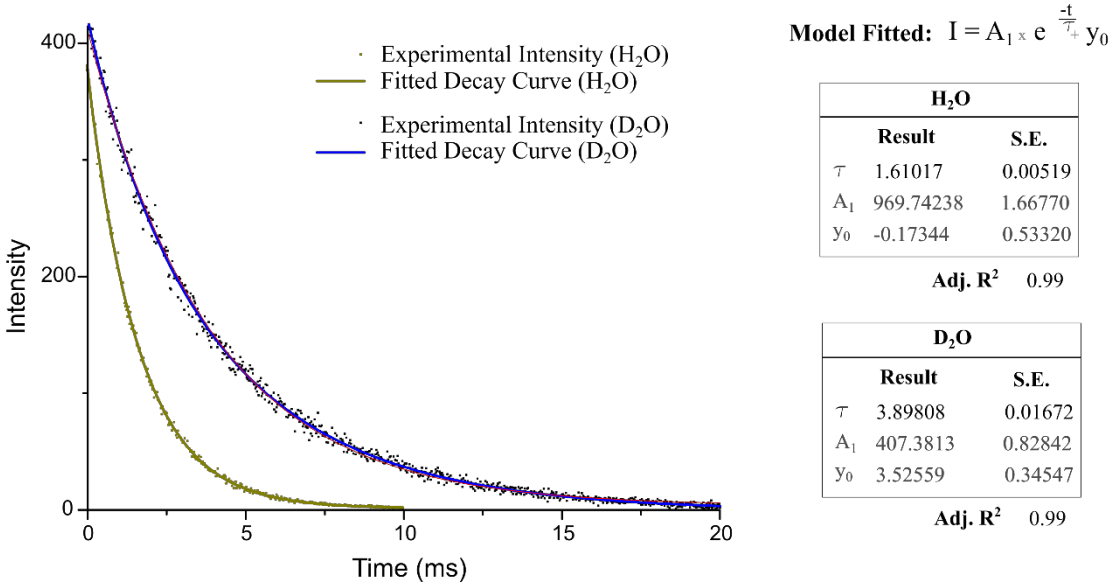

Model Fitted: $I = A_1 \times e^{\frac{-t}{\tau}} + y_0$

H_2O		
	Result	**S.E.**
τ	1.61017	0.00519
A_1	969.74238	1.66770
y_0	-0.17344	0.53320
Adj. R^2	0.99	

D_2O		
	Result	**S.E.**
τ	3.89808	0.01672
A_1	407.3813	0.82842
y_0	3.52559	0.34547
Adj. R^2	0.99	

Figure A2.10 Luminescence lifetime decay curves in H_2O and D_2O fitted to mono-exponential decay models Lifetimes recorded with 0.025 ms gate times and is representative of at least 5 independent measurements used to determined average lifetime values and *q*-values.

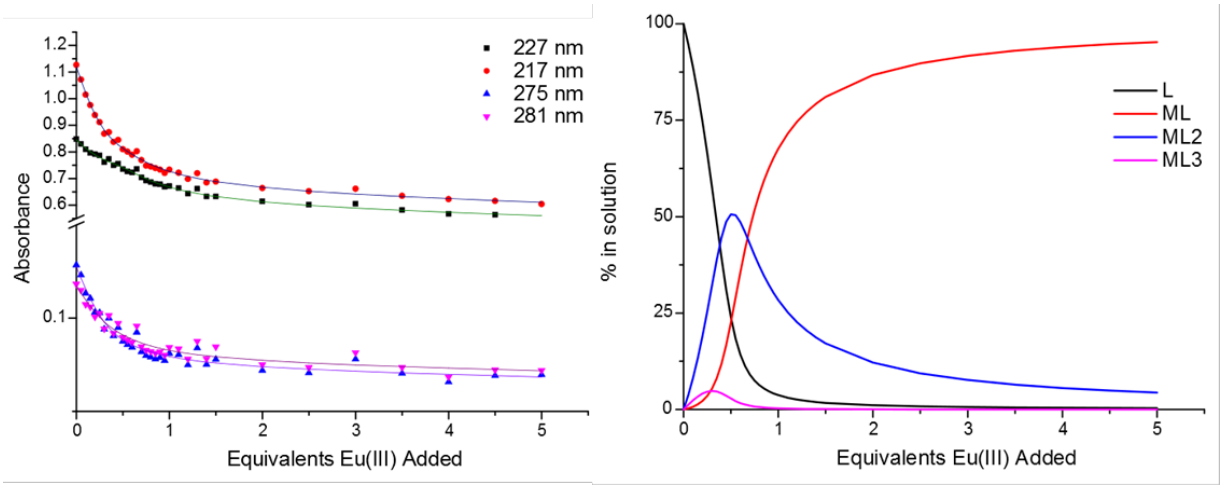

Figure A2.11 Fitting results of UV-visible titration of **120(*R,R*)** with $Eu(CF_3SO_3)_3$ in H_2O: **a)** Spectral changes at various wavelengths (points, S15b) and their calculated fits from non-linear regression analysis in ReactLab EQUILIBRIA®; and **b)** speciation distribution diagram from regression analysis of UV-changes.

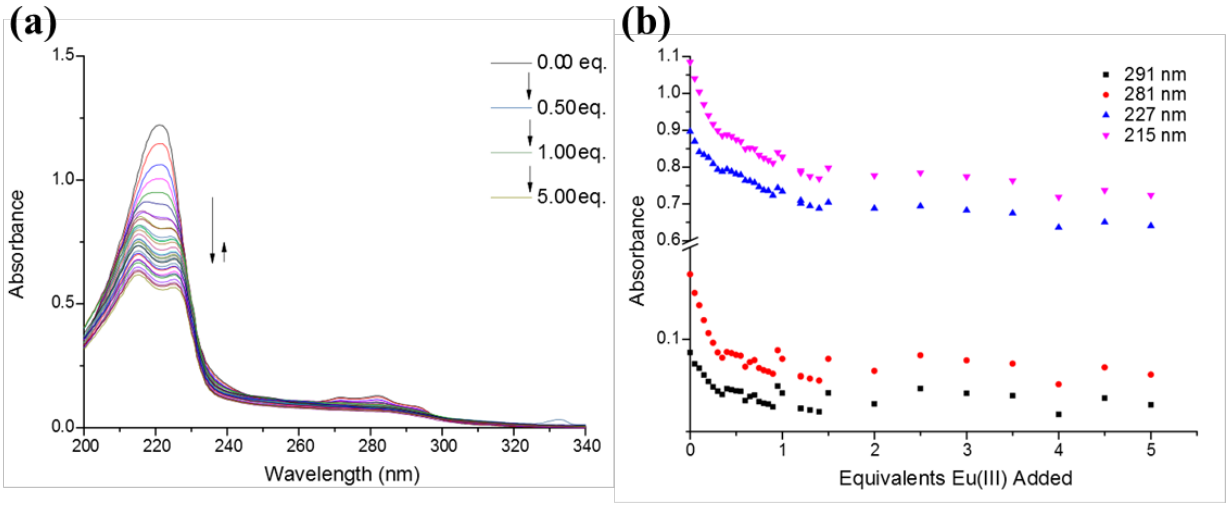

Figure A2.12 Representative UV-visible absorption titration of **120(*R,R*)** in H_2O: **a)** overlaid spectra of additions of Eu^{III} as $Eu(CF_3SO_3)_3$ to **120(*R,R*)** at c = 1 × 10^{-5} M; and **b)** Spectral changes at various wavelengths (291, 281, 227 and 215 nm) upon sequential additions of $Eu(OTf)_3$. Recorded at 24°C. This titration is representative of reproducible trends.

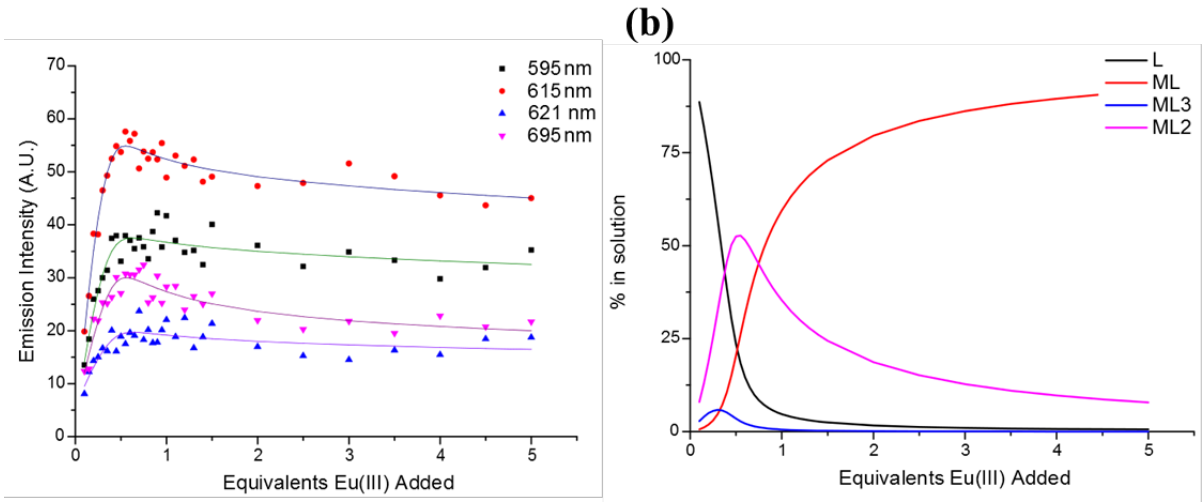

Figure A2.13 Fitting results of fluorescence emission titration of **120(*R,R*)** with $Eu(CF_3SO_3)_3$ in H_2O: **a)** Spectral changes at various wavelengths (points, S15b) and their calculated fits from non-linear regression analysis in ReactLab EQUILIBRIA®; and **b)** speciation distribution diagram from regression analysis of emission changes.

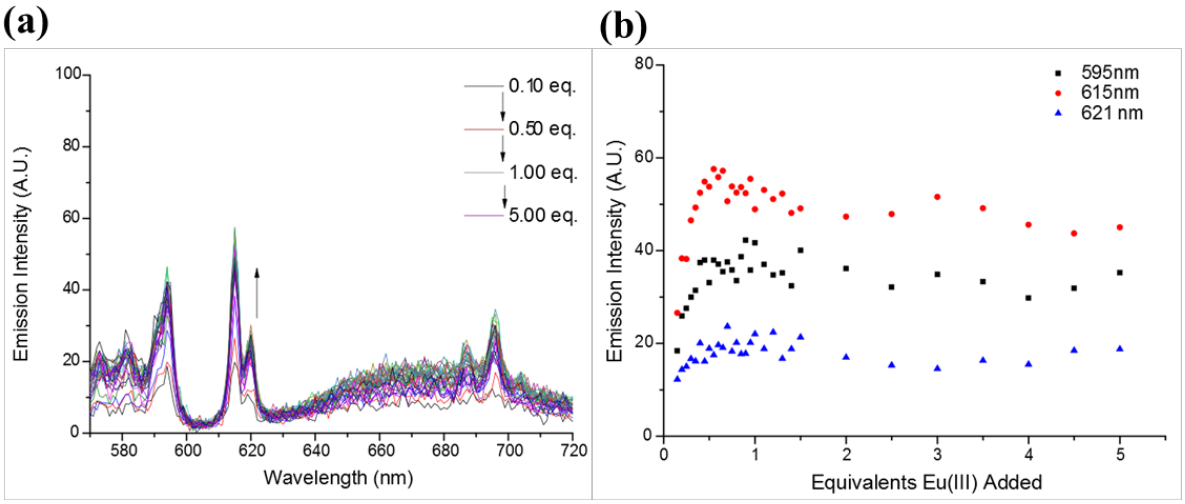

Figure A2.14 Fluorescence emission titration with low signal:noise ratio for **120(*R,R*)** with $Eu(CF_3SO_3)_3$ at c = 1 x 10^{-5} M in water: **a)** overlaid spectra of additions of Eu^{III}; and **b)** Spectral changes at various wavelengths of interest (595 (*J*=1), 615 and 621 (*J=2*) nm) upon sequential additions of $Eu(CF_3SO_3)_3$. Recorded at 24°C. This titration is representative of reproducible trends.

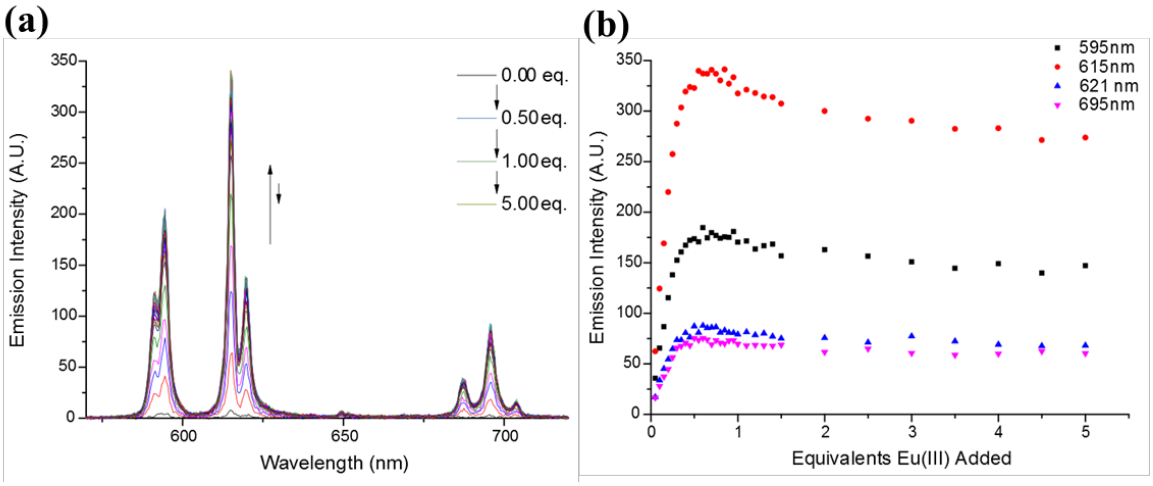

Figure A2.15 Time-gated luminescence (phosphoresence mode) titration for **120(*R,R*)** with $Eu(CF_3SO_3)_3$ in H_2O at c = 1 x 10^{-5} M in water: **a)** overlaid spectra of additions of Eu^{III}; **b)** Spectral changes at various wavelengths of interest (595 (*J*=1), 615, 621 (*J=2*) nm and 695 (*J=3*)) upon sequential additions $Eu(CF_3SO_3)_3$. Recorded at 24°C. This titration is representative of reproducible trends.

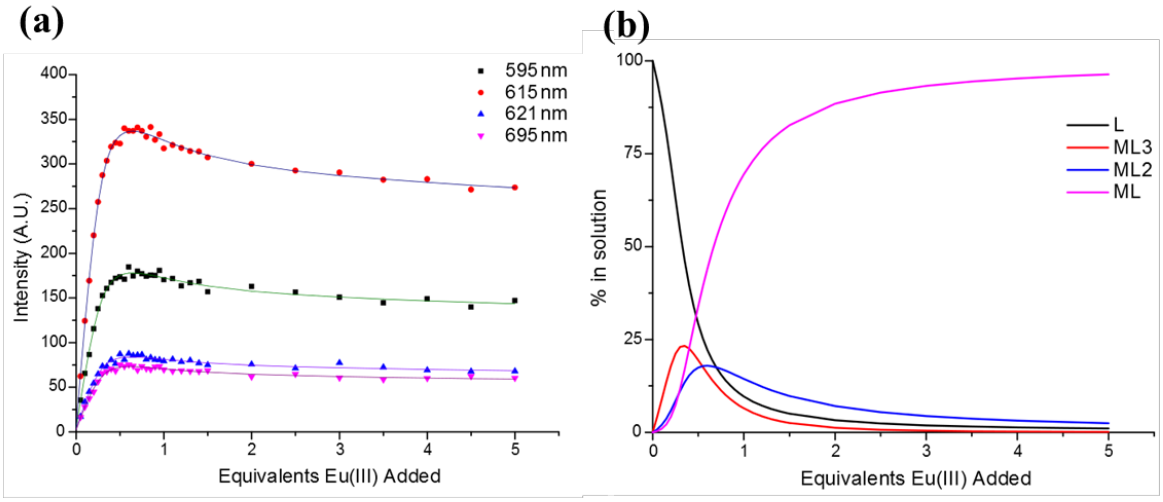

Figure A2.16 Fitting results of time-gated emission titration of **120(*R,R*)** with $Eu(CF_3SO_3)_3$ in H_2O: **a)** Spectral changes at various wavelengths (points, S15b) and their calculated fits from non-linear regression analysis in ReactLab EQUILIBRIA®; and **b)** speciation distribution diagram from regression analysis of emission changes

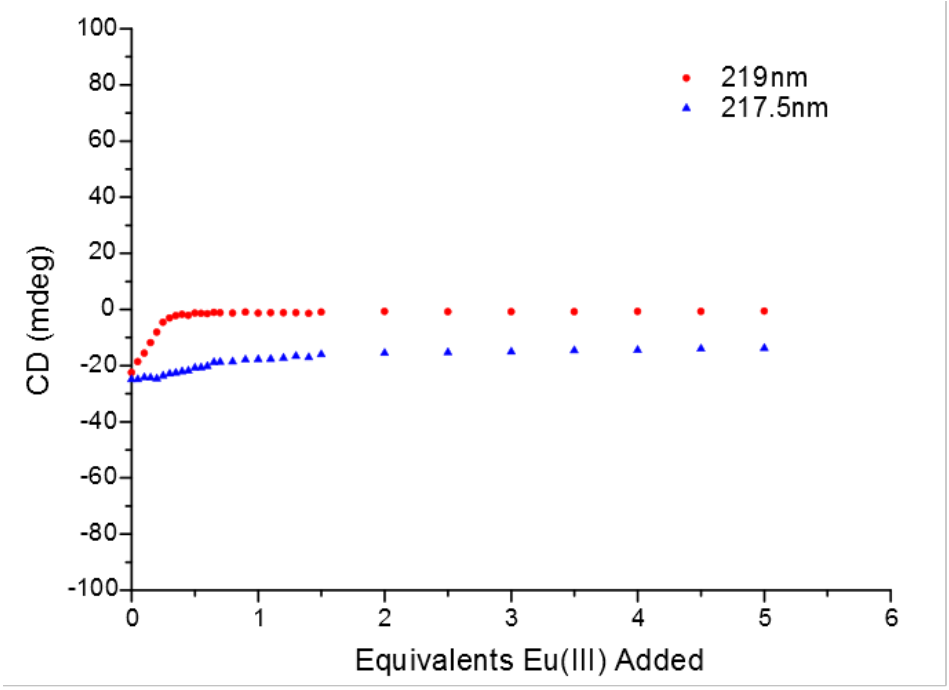

Figure A2.17 Spectral changes for two isoelipitc points observed at different stages of the titration of **120(*R*,*R*)** with $Eu(CF_3SO_3)_3$ 219 nm (0.3→excess) and 217.5 nm (0→0.3 equivalents).

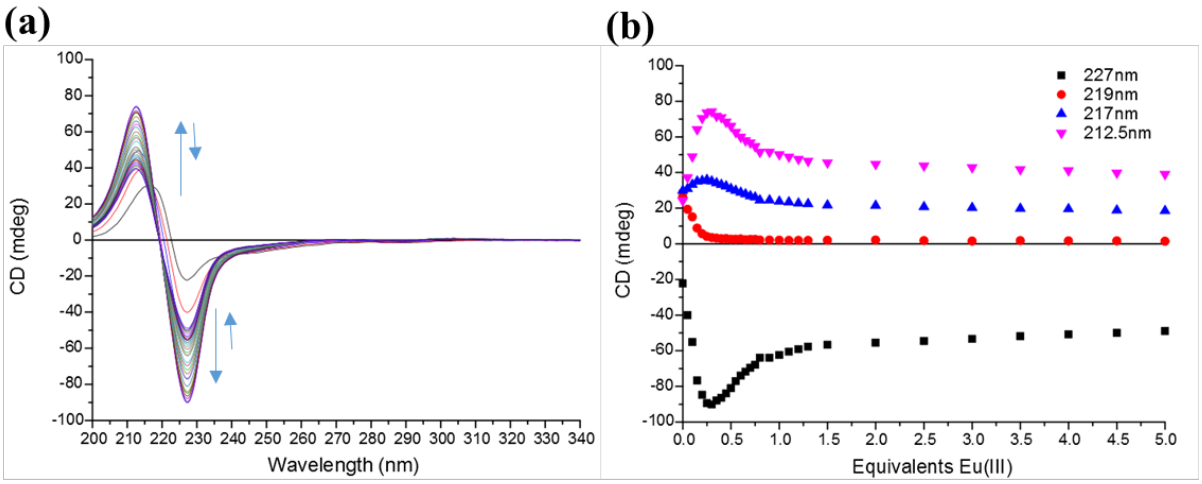

Figure A2.18 CD titration of **120(*R*,*R*)** with $Eu(CF_3SO_3)_3$ in water at c = 1 × 10^{-5} M: **a)** Full spectra from CD titration overlaid **b)** Spectral changes in key absorbance wavelengths (227, 219, 217 and 212.5 nm) upon addition of Eu^{III}. Recorded at 24°C. This titration is representative of reproducible trends.

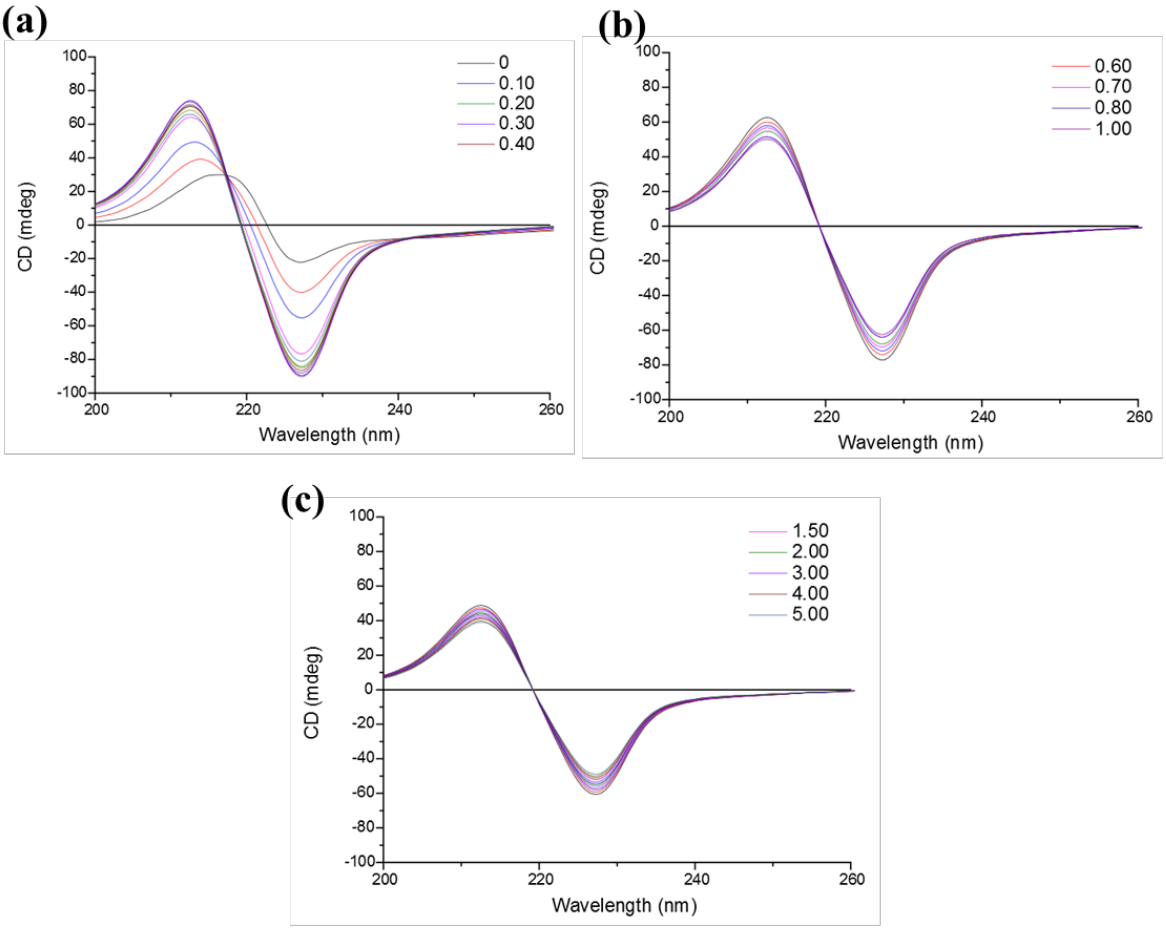

Figure A2.20 CD spectra represented between key equivalents of Eu^{III} for **120(*R,R*)** upon additions of $Eu(OTf)_3$ to **120(*R,R*)** at c = 1 × 10^{-5} M in water showing sequential isoeliptic features within the profiles: **a)** CD spectra recorded between 0→0.4 equivalents Eu^{III}; **b)** CD spectra recorded between 0.5→1.0 equivalents Eu^{III}; and **c)** CD spectra recorded between 1.5→5.0 (excess) equivalents Eu^{III}. Recorded at 24°C. This titration is representative of reproducible trends.

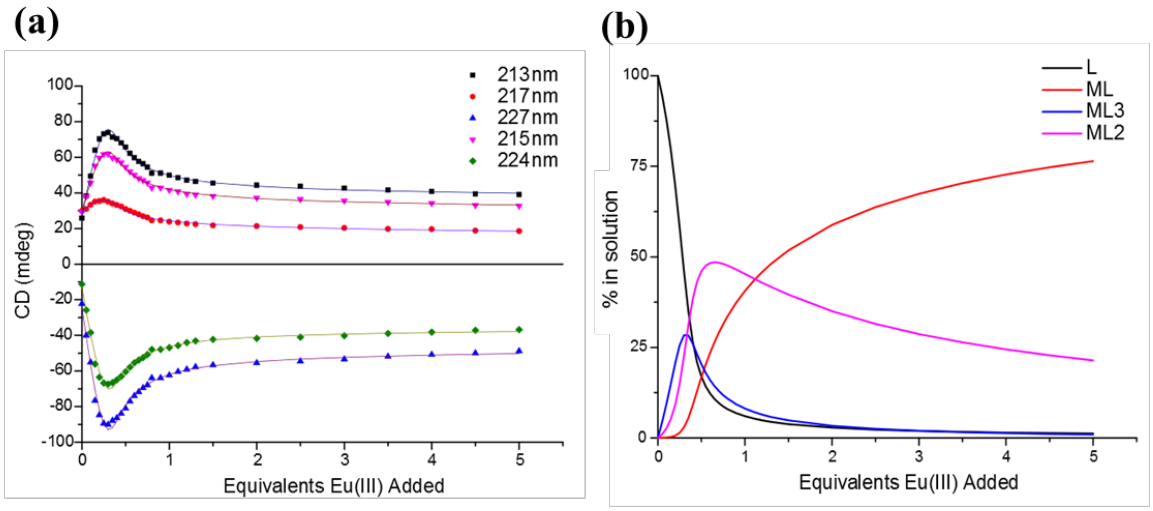

Figure A2.19 Fitting results of CD titration of **120(*R,R*)** with $Eu(CF_3SO_3)_3$ in H_2O: **a)** Spectral changes at various wavelengths and their calculated fits from non-linear regression analysis in ReactLab EQUILIBRIA®; and **b)** speciation distribution diagram from regression analysis of changes in the CD spectra.

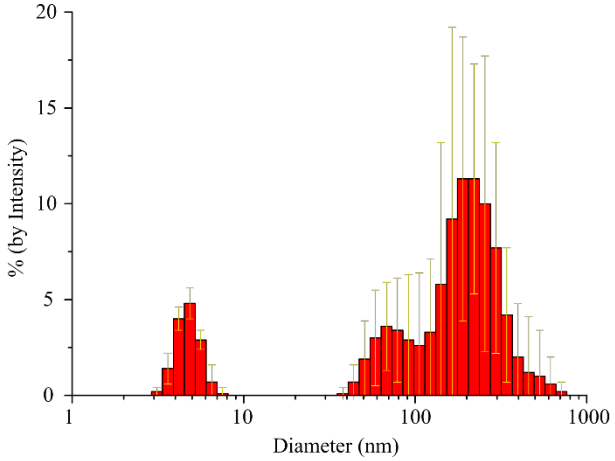

Figure A2.21 DLS results from solutions of **120(*S,S*)** in H_2O at $c = 1 \times 10^{-3}$ M showing results consistent with multiple scattering effects from excessive concentration for the analytical technique. Sample also was strongly absorbing and therefore the size distribution model is treated with caution. Error bars are standard deviations determined from 6 independent measurements.

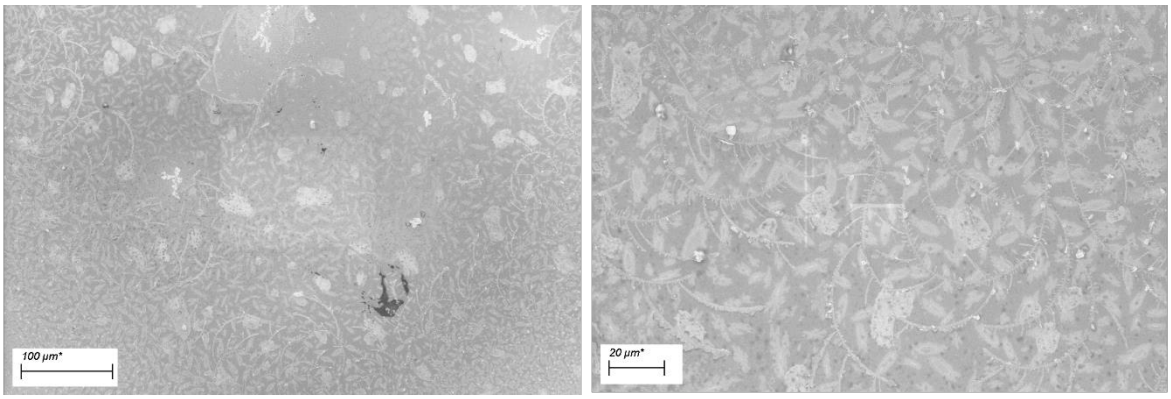

Figure A2.22 SEM images of **120(*S,S*)** in H_2O treated with 0.33 equivalents of $Eu(CF_3SO_3)_3$ showing no significant aggregates or morphological features upon drying of the solution samples.

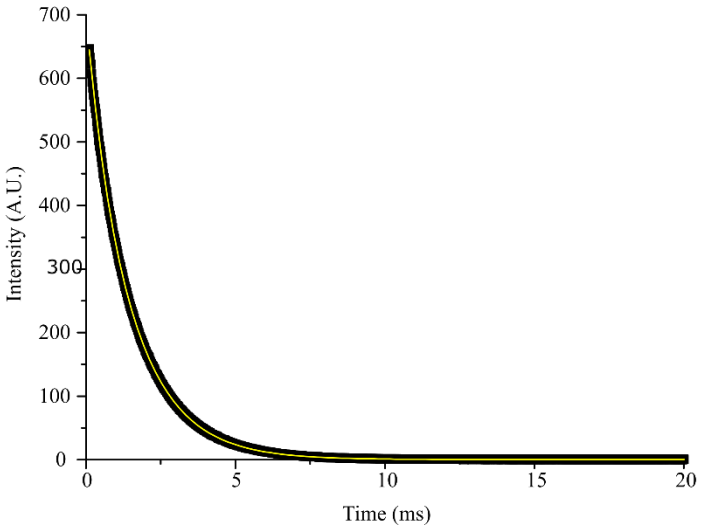

Model Fitted: $I = A_1 \times e^{\frac{-t}{\tau_1}} + y_0$

H_2O		
	Result	**S.E.**
τ_1	1.51082	0.00126
A_1	638.99614	0.99961
y_0	0.25591	0.01587
τ_2	0.4602	0.00734
A_2	65.40042	0.86325
Adj. R^2	0.99	

Figure A2.23 Luminescence emission decay curve recorded from the precipitate formed upon the treatment of gels of **120(*S,S*)** with $EuCl_{3\,(aq.)}$ and the results of the fit to a mono-exponential decay.

A3. Chapter 3 Appendix

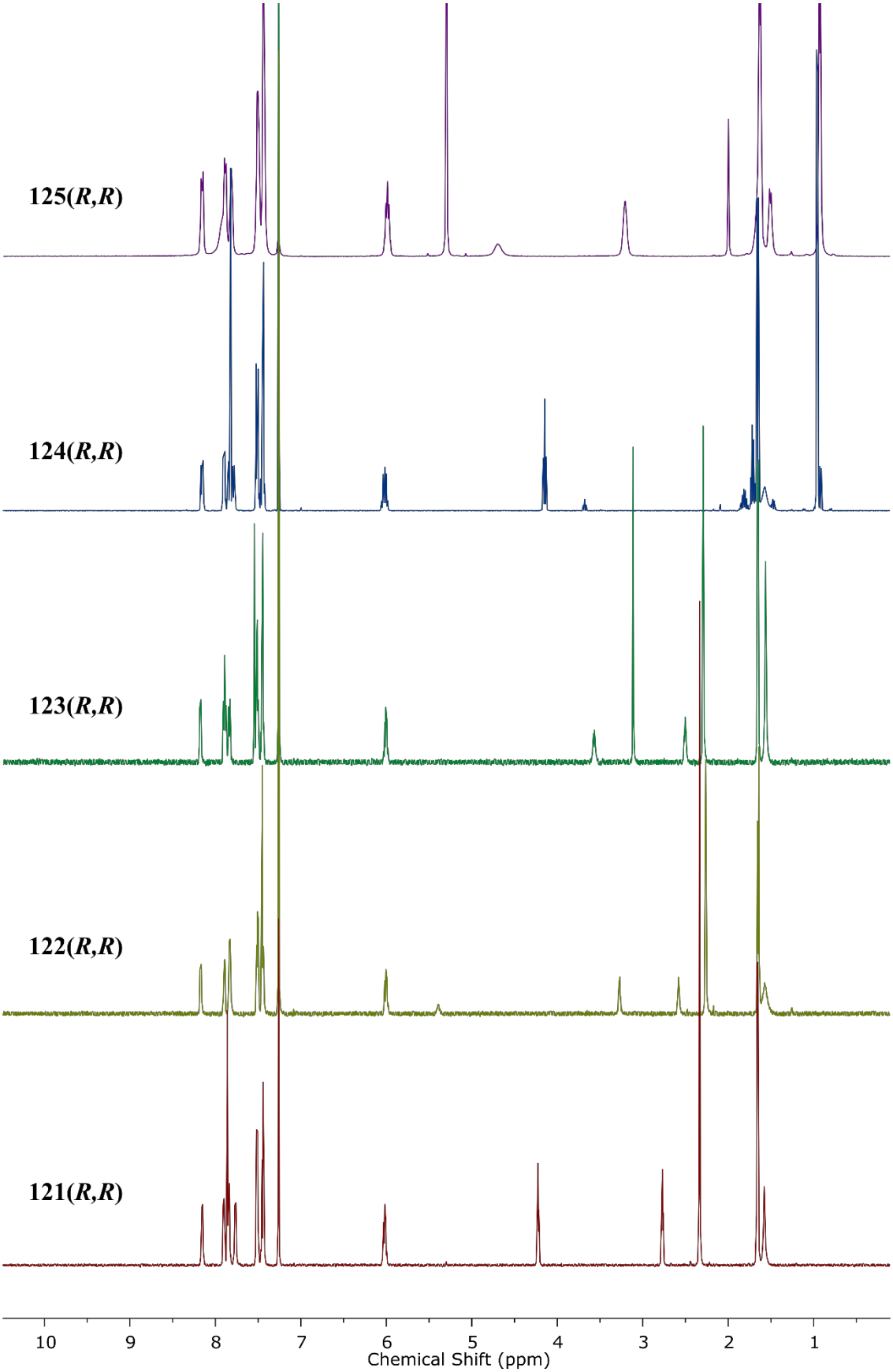

Figure A3.1 ^{1}H NMR spectra (600 MHz, $CDCl_3$) of **121(*R*,*R*)** - **125(*R*,*R*)**

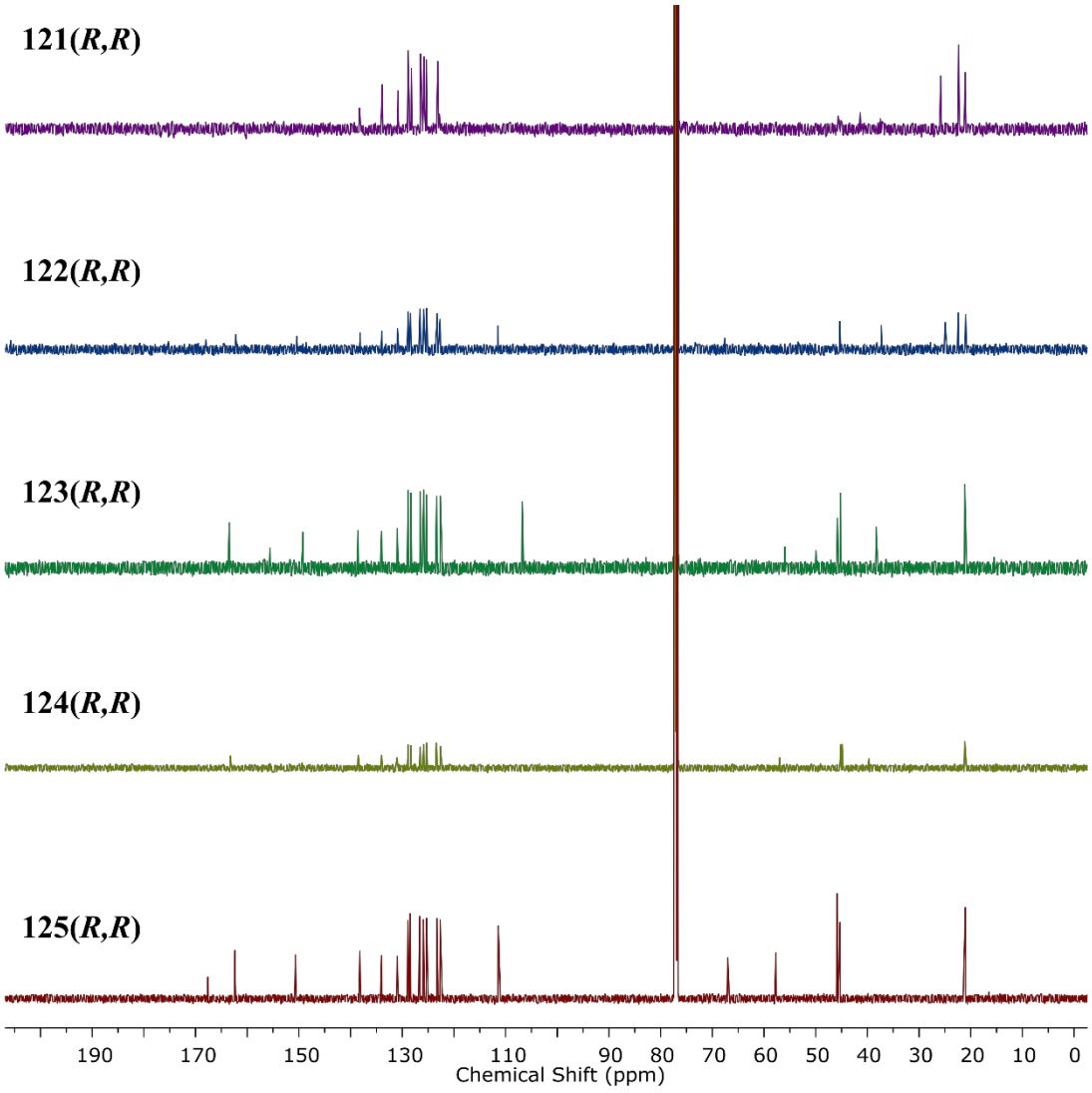

Figure A3.2 ^{13}C NMR (150 MHz, $CDCl_3$) of **121(*R*,*R*)** - **125(*R*,*R*)**

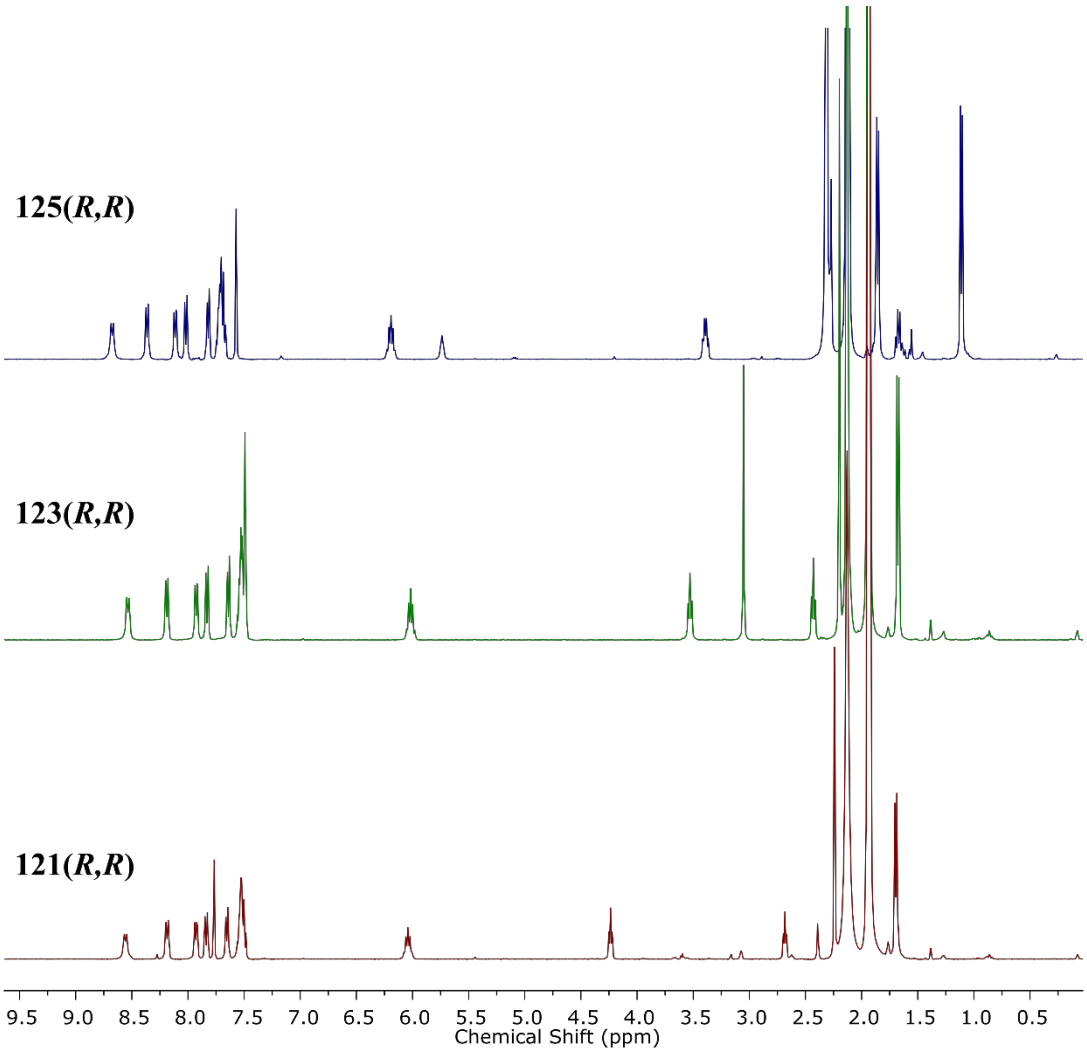

Figure A3.3 Selected ^{1}H NMR spectra (400 MHz, MeCN-d_3) for **121(*S*,*S*)**, **123(*S*,*S*)** and **125(*S*,*S*)** showing improved resolution of the vicinal coupling in the case of **121(*S*,*S*)** and **123(*S*,*S*)** compared to $CDCl_3$

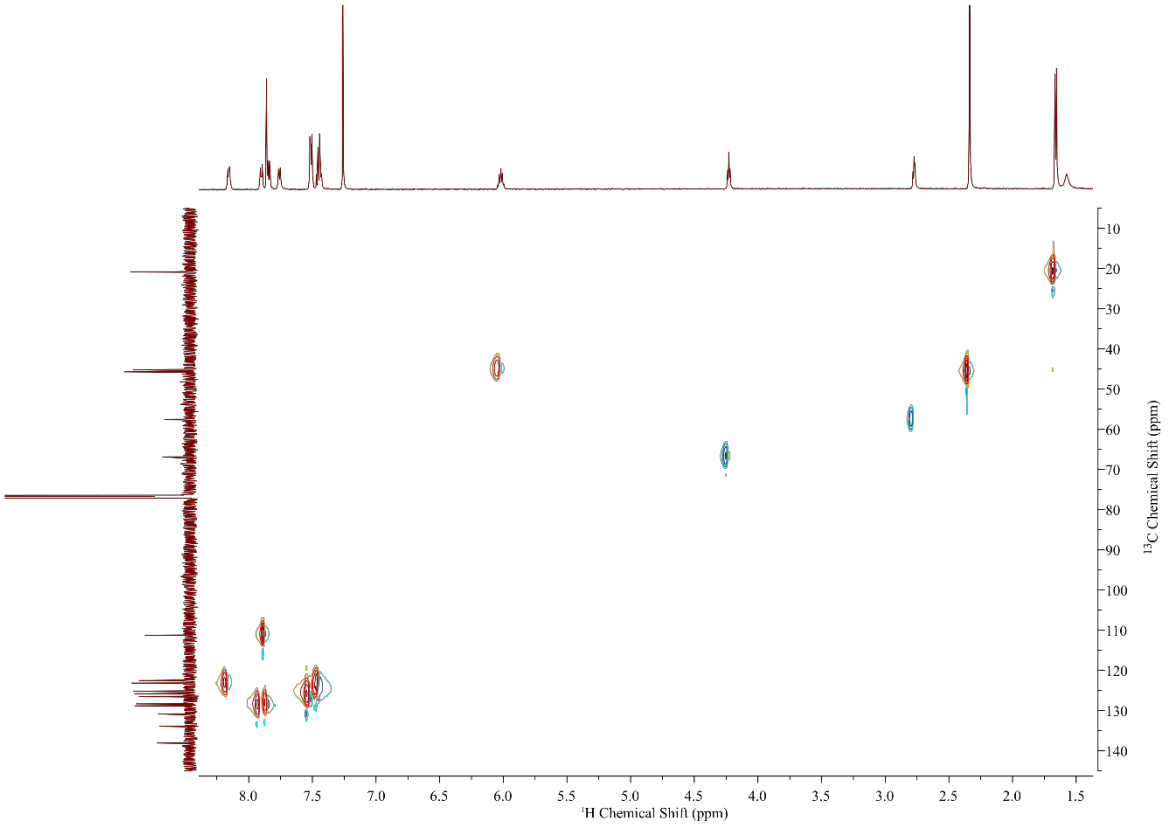

Figure A3.4 HSQC (phase-sensitive) spectrum (600, 150 MHz, $CDCl_3$) of **121(*R*,*R*)**

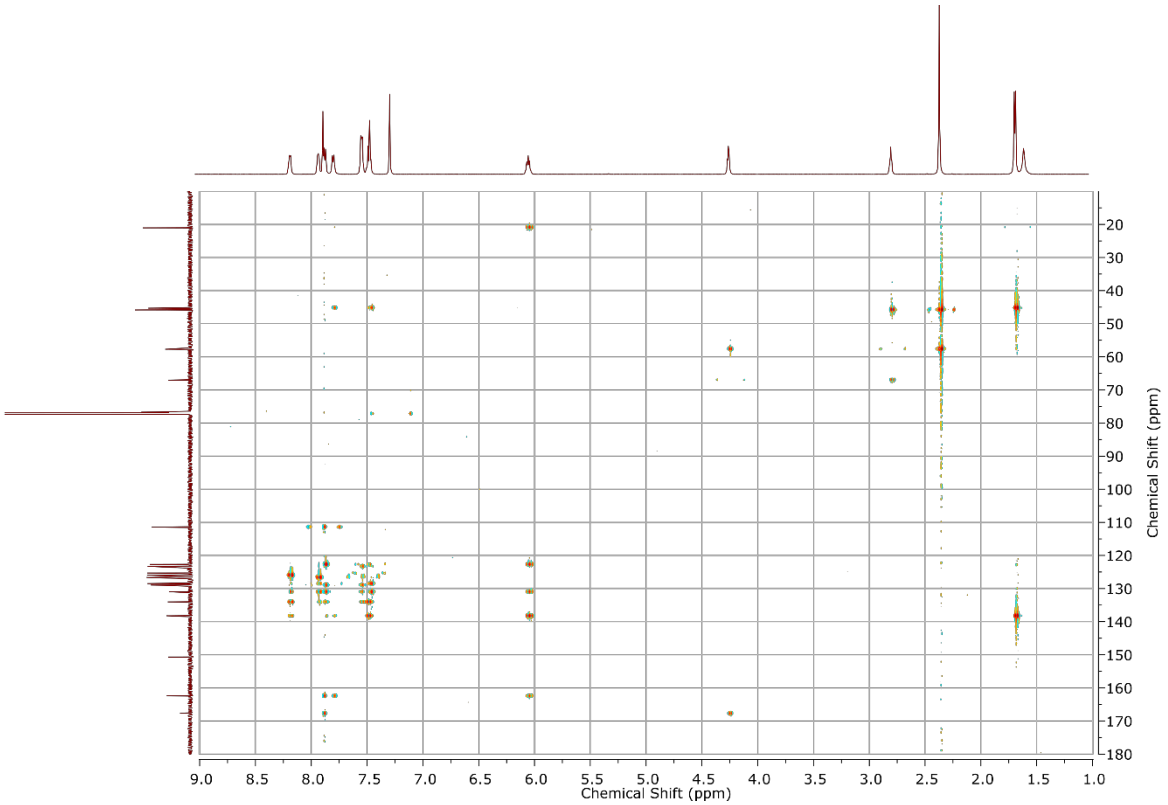

Figure A3.5 HMBC spectrum (600, 150 MHz, $CDCl_3$) of **121(*R*,*R*)**

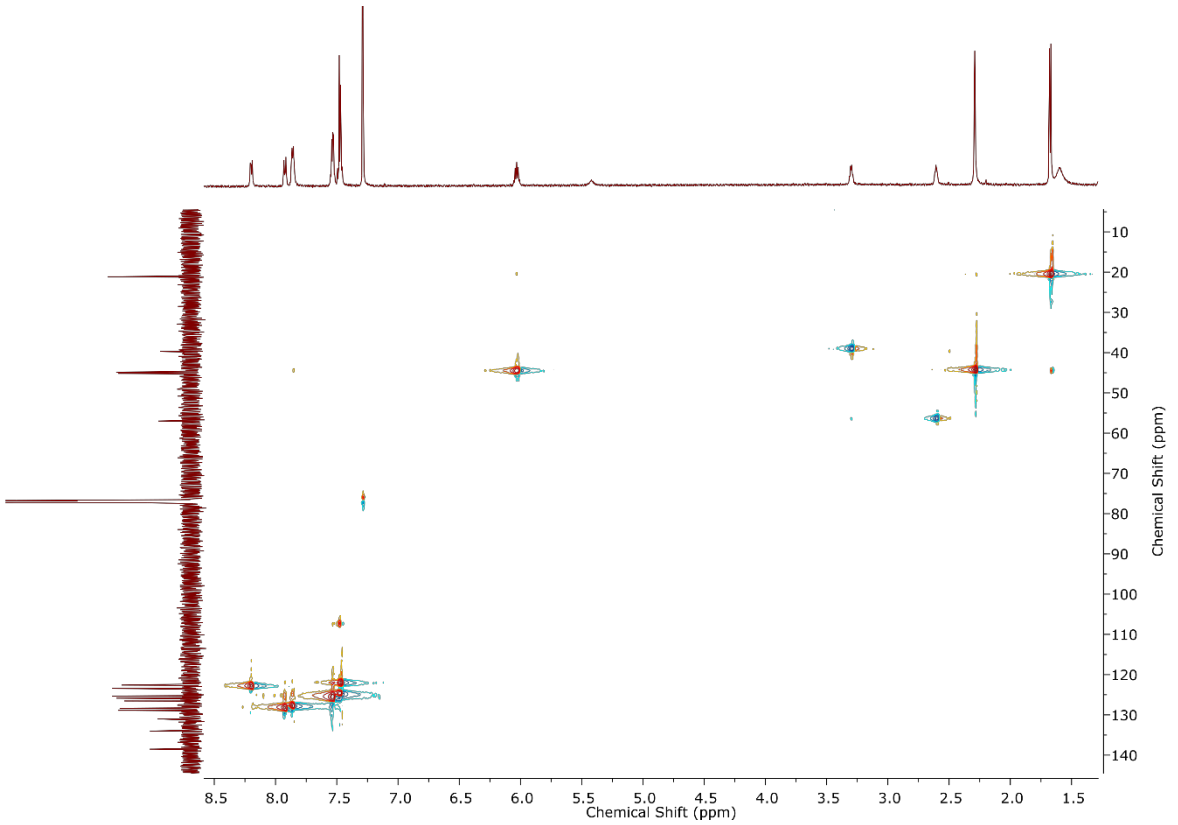

Figure A3.6 HSQC (phase-sensitive) spectrum (600, 150 MHz, $CDCl_3$) of **122(*R*,*R*)**

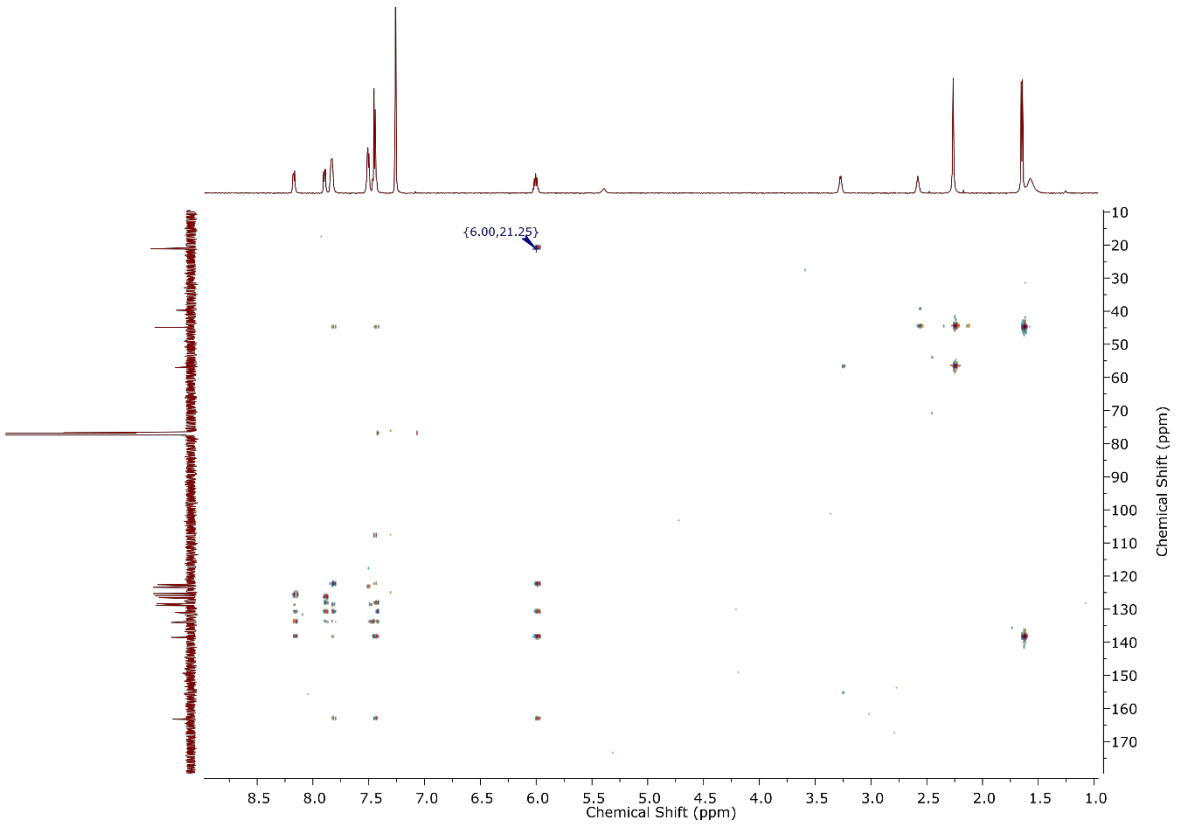

Figure A3.7 HMBC spectrum (600, 150 MHz, $CDCl_3$) of **122(*R*,*R*)**

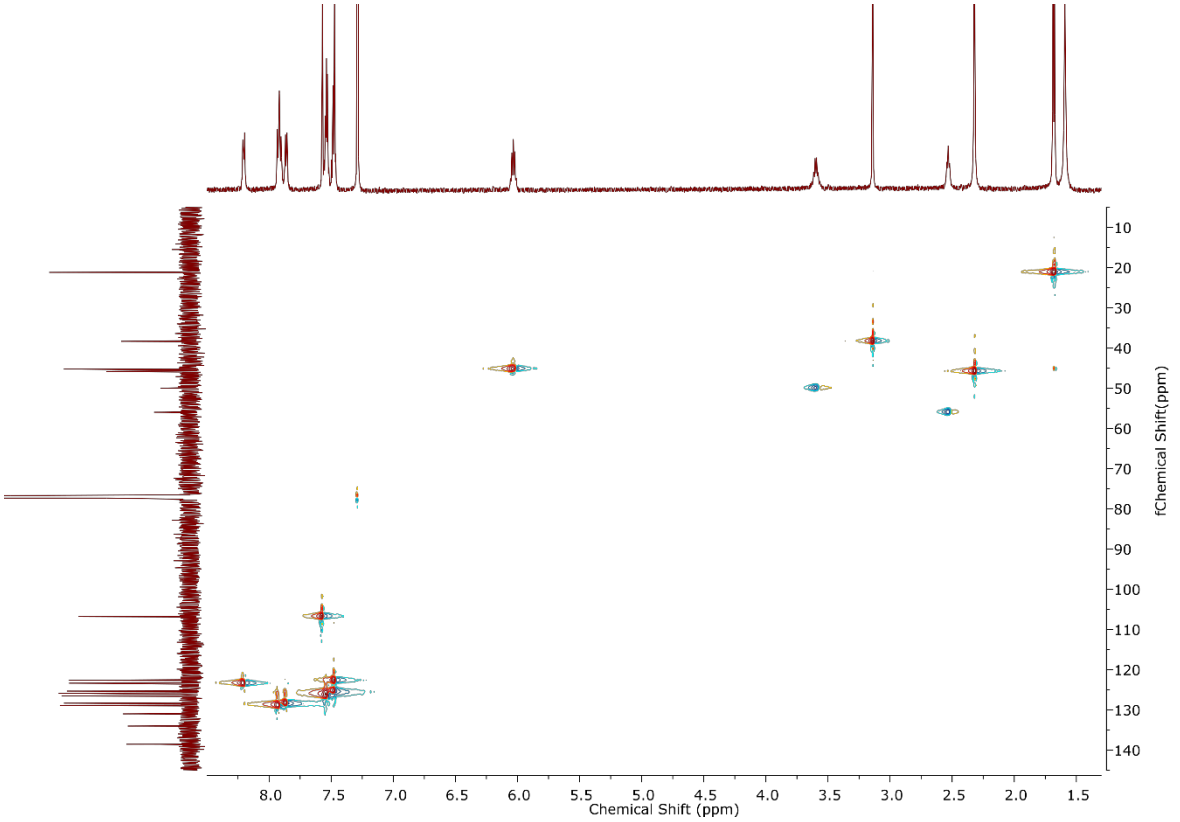

Figure A3.8 HSQC (phase-sensitive) spectrum (600, 150 MHz, $CDCl_3$) of **123(*R*,*R*)**

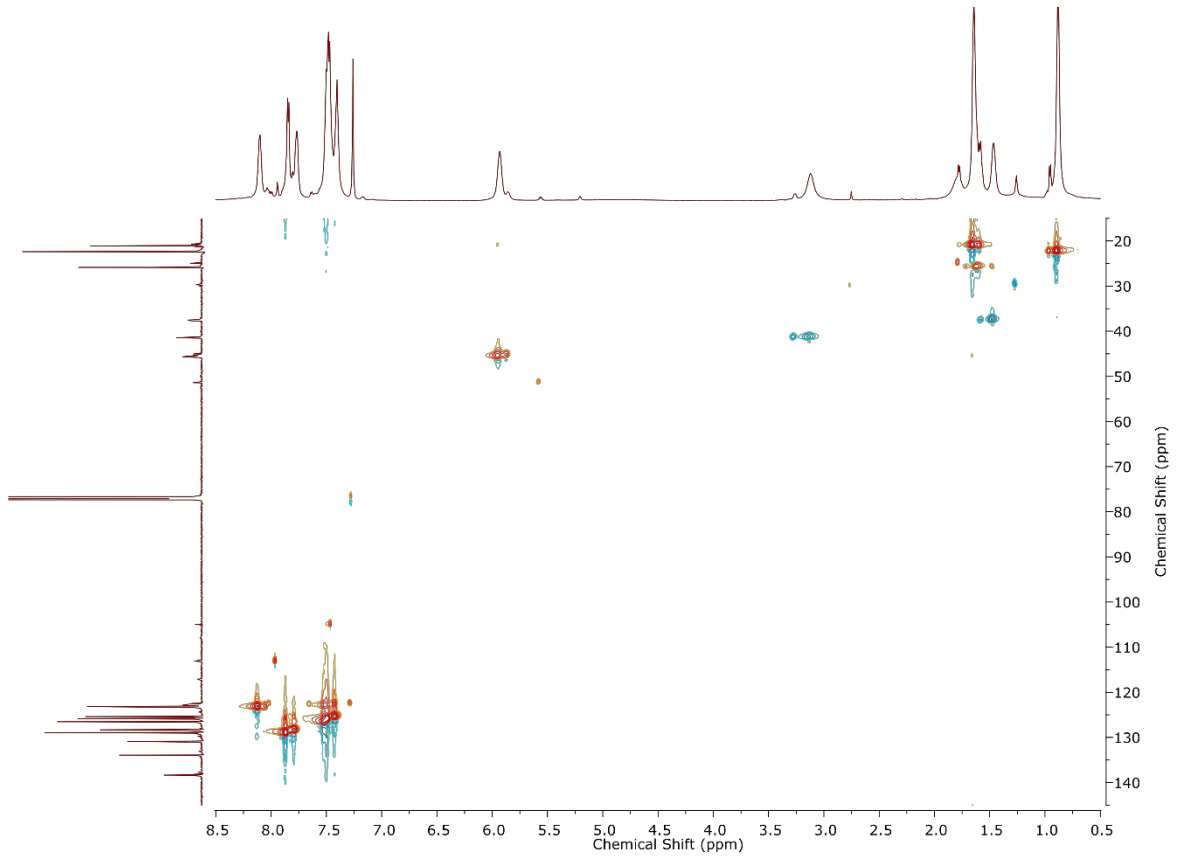

Figure A3.9 HSQC (phase-sensitive) spectrum (600, 150 MHz, $CDCl_3$) of **125(*R*,*R*)**

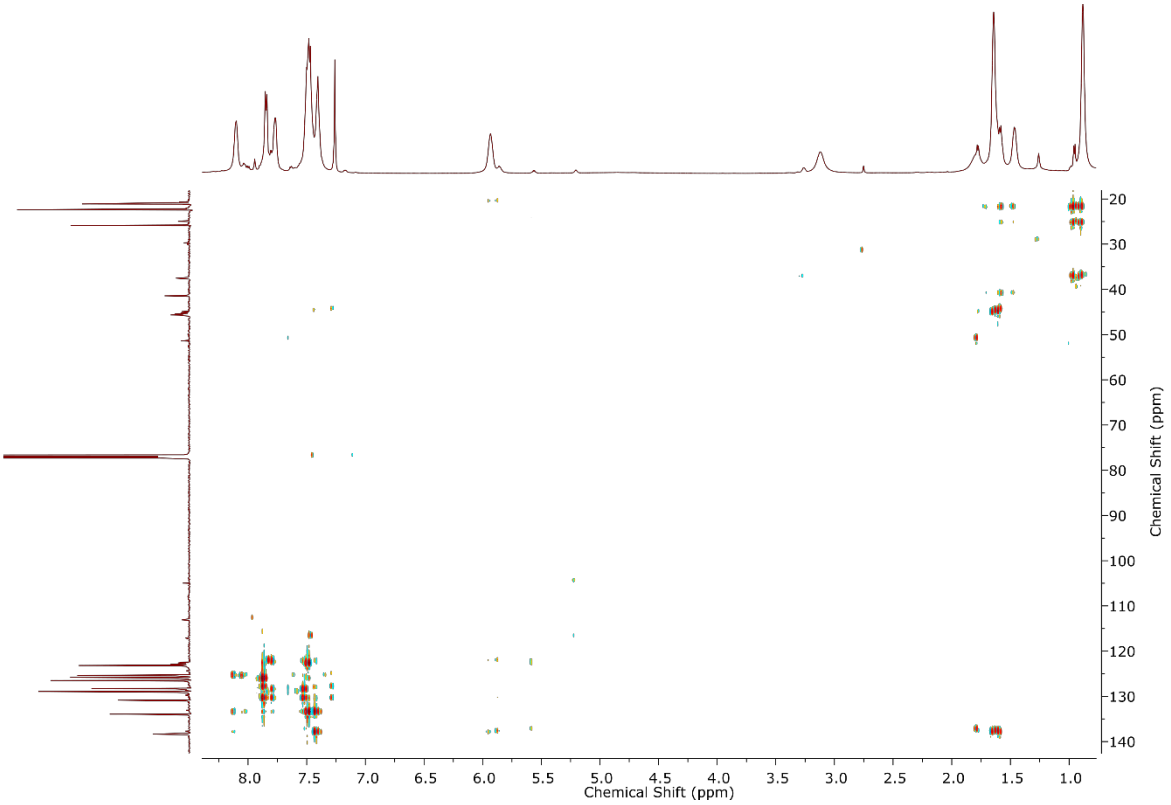

Figure A3.10 HMBC spectrum (600, 150 MHz, $CDCl_3$) of **125(*R*,*R*)**

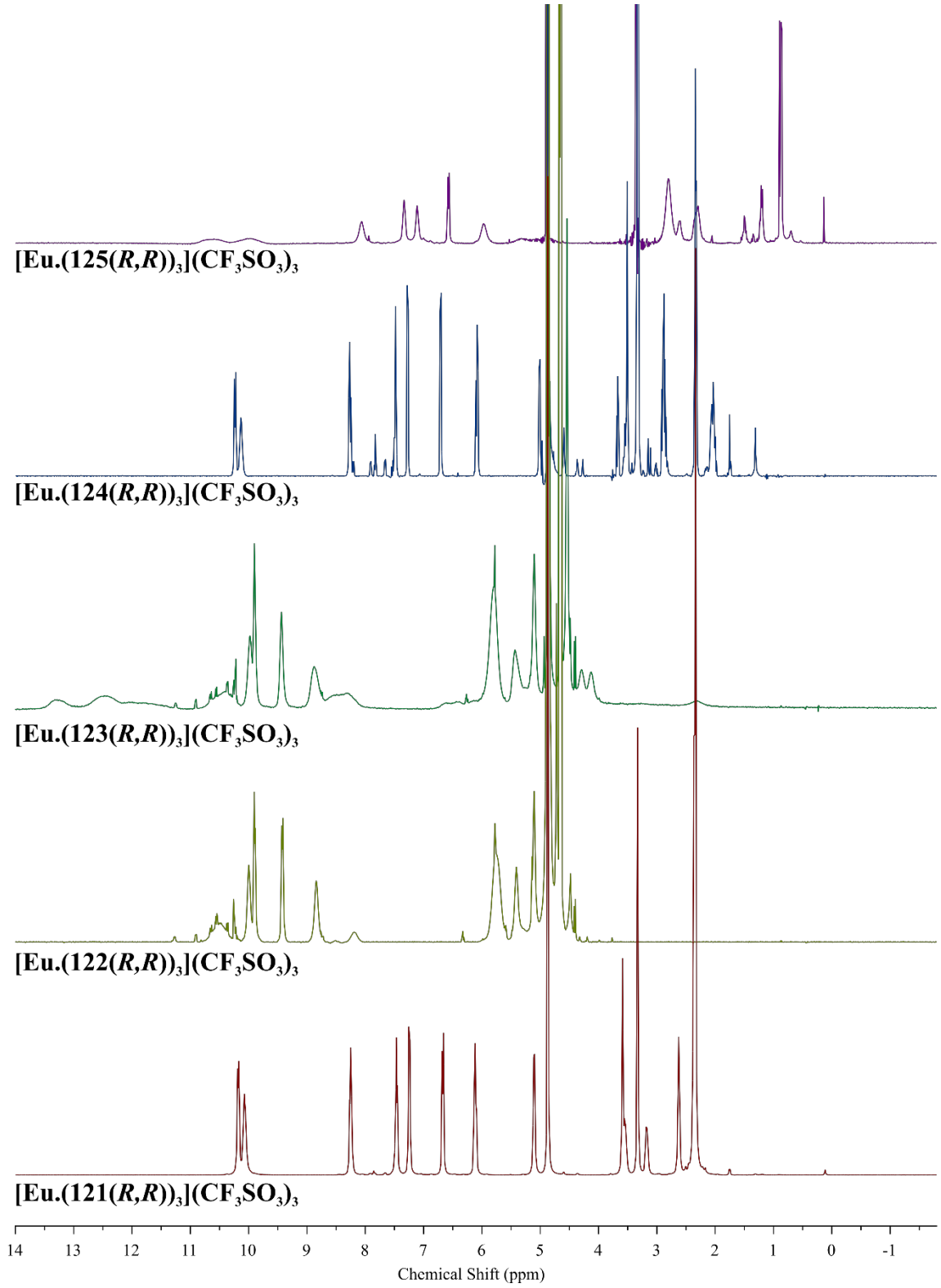

Figure A3.11 ^{1}H NMR (400 MHz, CD_3OD) of **[Eu.(121(*R*,*R*)$_3$]**$(CF_3SO_3)_3$ - **[Eu.(125(*R*,*R*)$_3$]**$(CF_3SO_3)_3$ showing various LIS in the resonance chemical shifts.

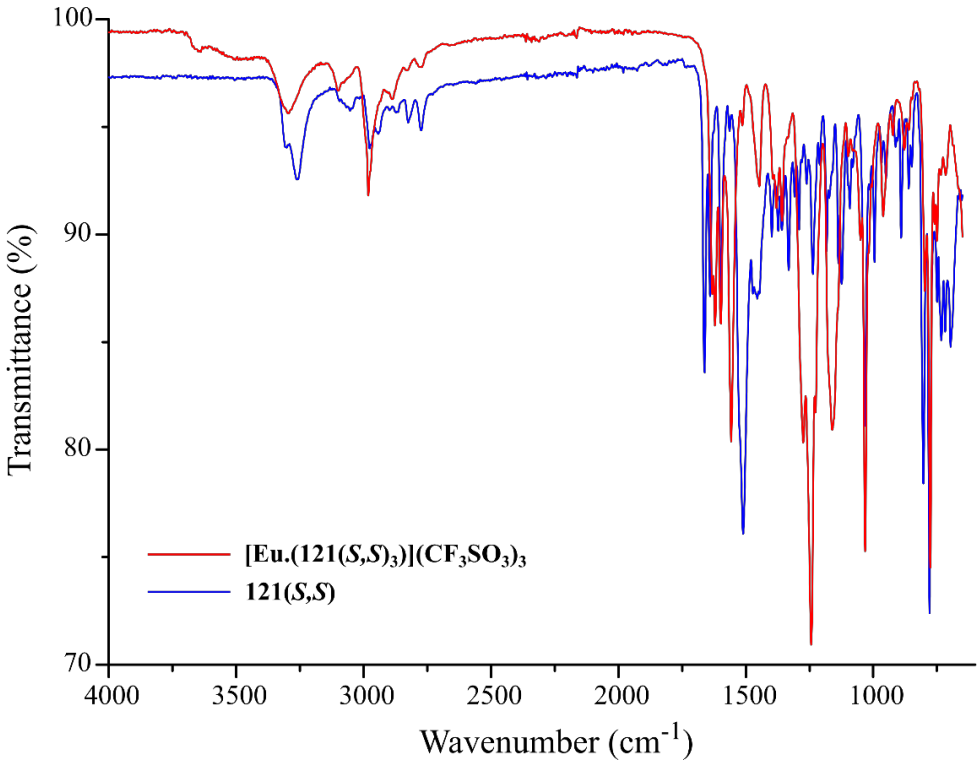

Figure A3.12 IR spectra (ATR) of **121(*S*,*S*)** (blue) and **[Eu.(121(*S*,*S*)$_3$]**$(CF_3SO_3)_3$ (red), showing key shifts in carbonyl stretches (1750 – 1500 cm^{-1}) upon complexation. The spectra for **121(*R*,*R*)** and **[Eu.(121(*R*,*R*)$_3$]**$(CF_3SO_3)_3$ were identical.

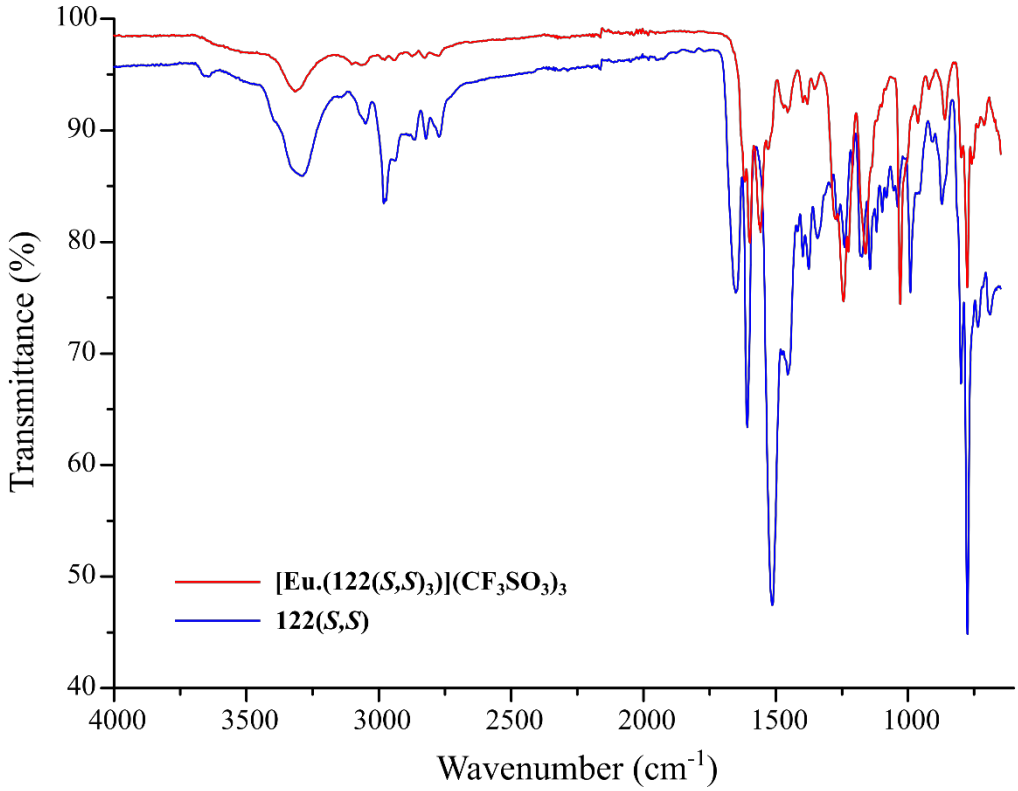

Figure A3.13 IR spectra (ATR) of **122(*S*,*S*)** (blue) and **[Eu.(122(*S*,*S*)$_3$]**$(CF_3SO_3)_3$ (red), showing key shifts in carbonyl stretches (1750 – 1500 cm^{-1}) upon complexation. The spectra for **122(*R*,*R*)** and **[Eu.(122(*R*,*R*)$_3$]**$(CF_3SO_3)_3$ were identical.

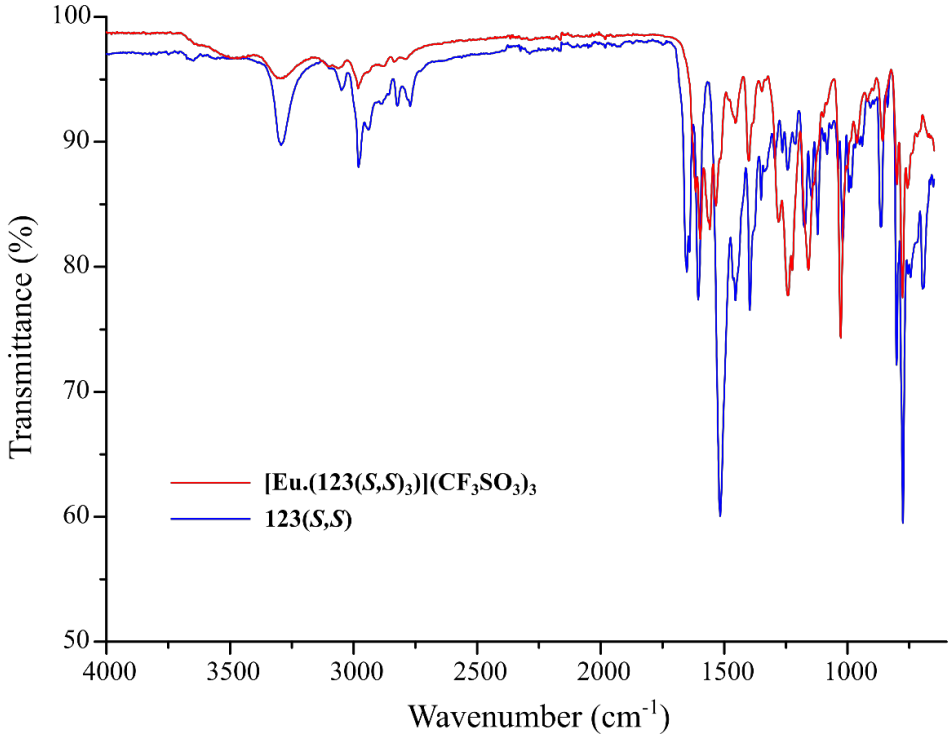

Figure A3.14 IR spectra (ATR) of **123(*S*,*S*)** (blue) and **[Eu.(123(*S*,*S*)$_3$]**$(CF_3SO_3)_3$ (red), showing key shifts in carbonyl stretches (1750 – 1500 cm^{-1}) upon complexation. The spectra for **123(*R*,*R*)** and **[Eu.(123(*R*,*R*)$_3$]**$(CF_3SO_3)_3$ were identical.

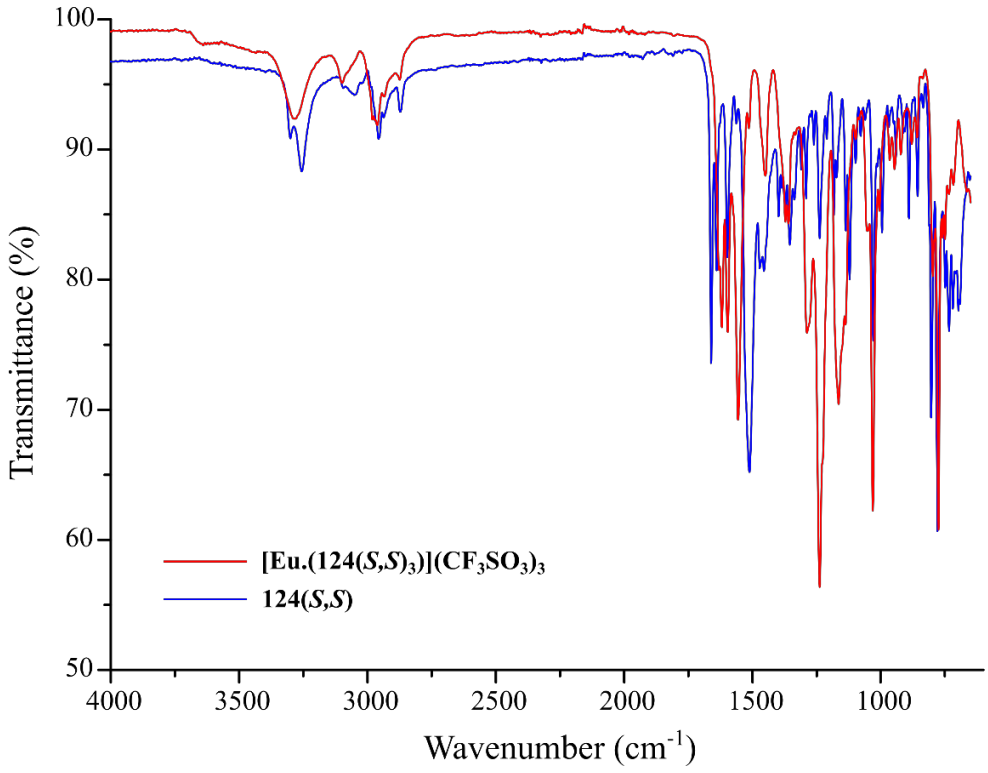

Figure A3.15 IR spectra (ATR) of **124(*S*,*S*)** (blue) and **[Eu.(124(*S*,*S*)$_3$]**$(CF_3SO_3)_3$ (red), showing key shifts in carbonyl stretches (1750 – 1500 cm^{-1}) upon complexation. The spectra for **124(*R*,*R*)** and **[Eu.(124(*R*,*R*)$_3$]**$(CF_3SO_3)_3$ were identical.

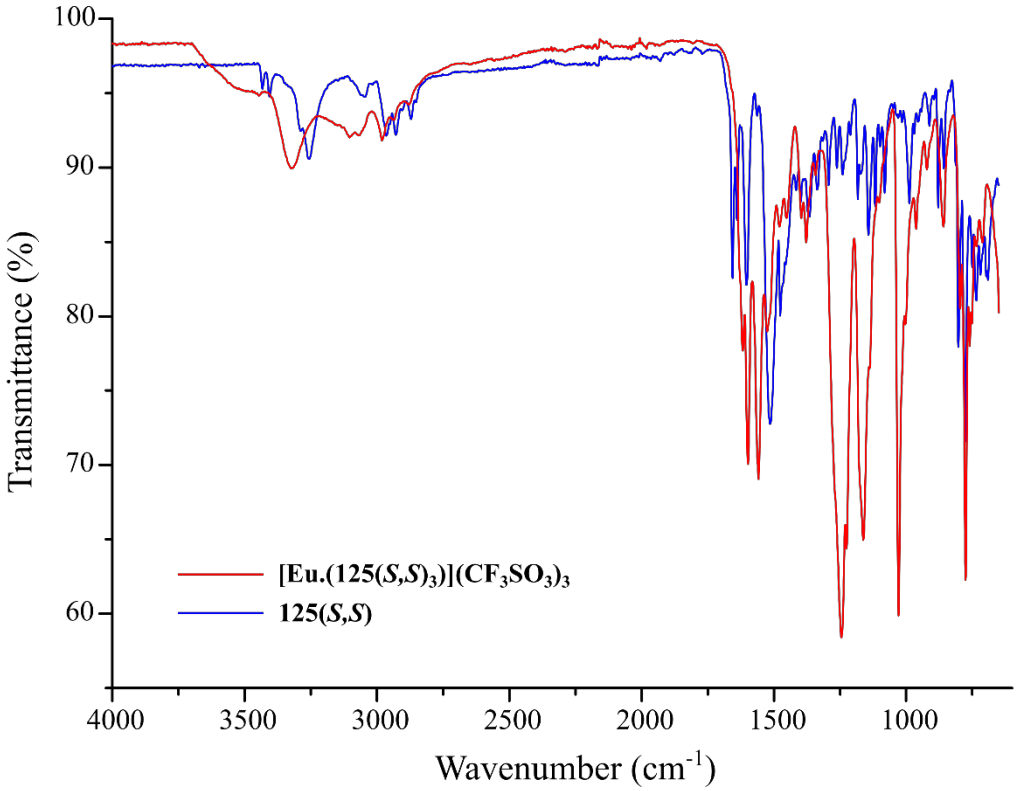

Figure A3.16 IR spectra (ATR) of **125(*S*,*S*)** (blue) and **[Eu.(125(*S*,*S*)$_3$]**$(CF_3SO_3)_3$ (red), showing key shifts in carbonyl stretches (1750 – 1500 cm^{-1}) upon complexation. The spectra for **125(*R*,*R*)** and **[Eu.(125(*R*,*R*)$_3$]**$(CF_3SO_3)_3$ were identical.

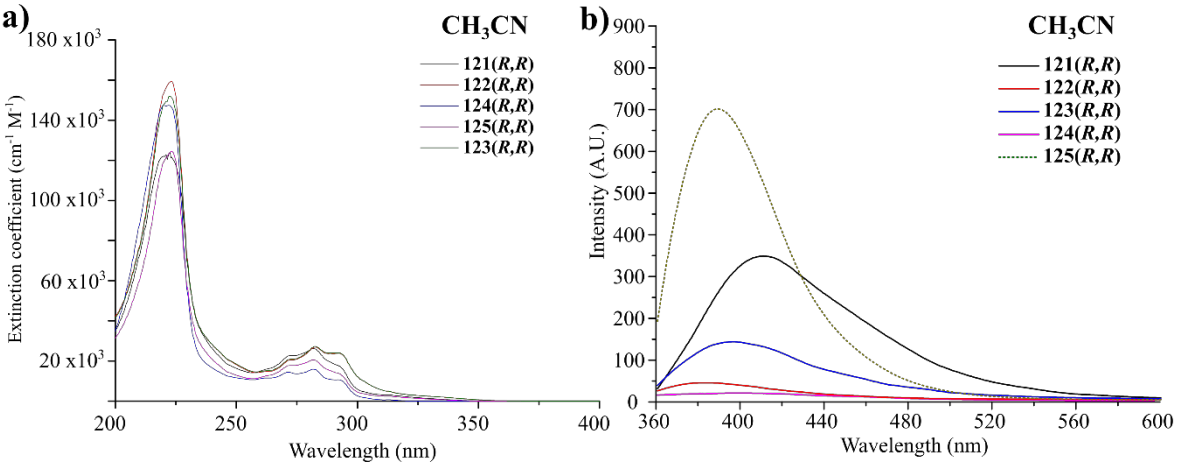

Figure A3. 17 a) Overlaid UV-visible absorpton spectra comparing the molar excition coefficients (ϵ) of ligands **121(*R*,*R*)** - **125(*R*,*R*)** in CH_3CN, showing common features and variation in ϵ with changes in *O*- or *N*-susbsitution of the 4-postion of the pyridine. **b)** Fluorescence emission spectra recorded from ligands **121(*R*,*R*)** - **125(*R*,*R*)** in CH_3CN, showing varying intensity and emission maxima in each ligand. Ligand **125** (green, dashed) was substantially more emissive and was recorded at a lower PMT voltage to demonstrate the maxima however intensity is not comparable to the other spectra. Spectra recorded at 24 °C and ϵ determined as the average of measurements from at least 5 different solutions.

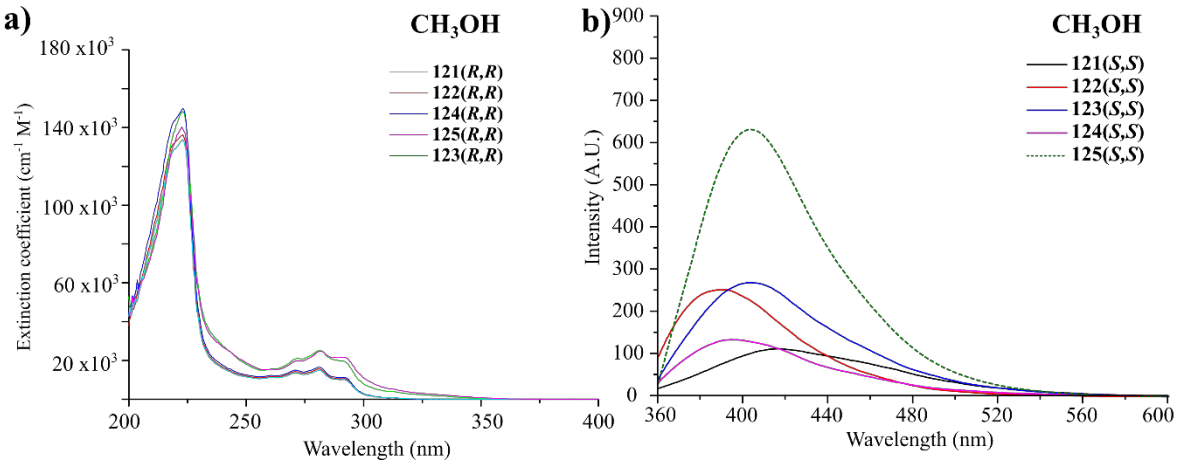

Figure A3.18 a) Overlaid UV-visible absorpton spectra comparing the molar excition coefficients (ϵ) of ligands **121(*R,R*) - 125(*R,R*)** in CH_3OH, showing common features and variation in ϵ with changes in *O*- or *N*-susbsitution of the 4-postion of the pyridine. **b)** Fluorescence emission spectra recorded from ligands **121(*R,R*) - 125(*R,R*)** in CH_3OH, showing varying intensity and emission maxima in each ligand. Ligand **125** (green, dashed) was substantially more emissive and was recorded at a lower PMT voltage to demonstrate the maxima however intensity is not comparable to the other spectra. Spectra recorded at 24 °C and ϵ determined as the average of measurements from at least 5 different solutions.

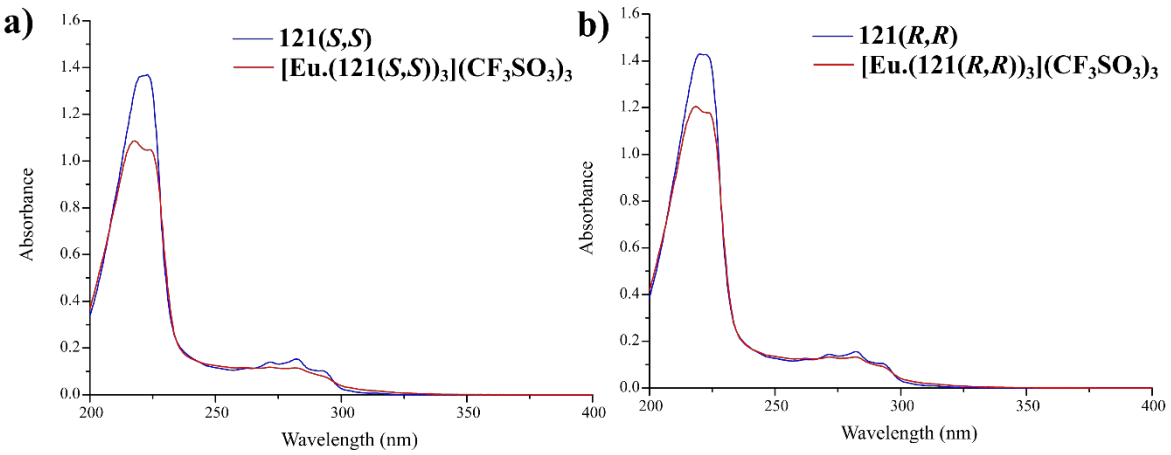

Figure A3.19 Overlaid UV-visible absorption spectra in CH_3CN for: **a) 121(*S*,*S*)** and **[Eu.(121(*S*,*S*))$_3$]**$(CF_3SO_3)_3$; and **b) 121(*R*,*R*)** and **[Eu.(121(*R*,*R*))$_3$]**$(CF_3SO_3)_3$showing hypo- and hyper-chromic shifts. All spectra recorded at ligand $c = 1 \times 10^{-5}$ M at 24 °C and represent consistent observations from repeated measurements.

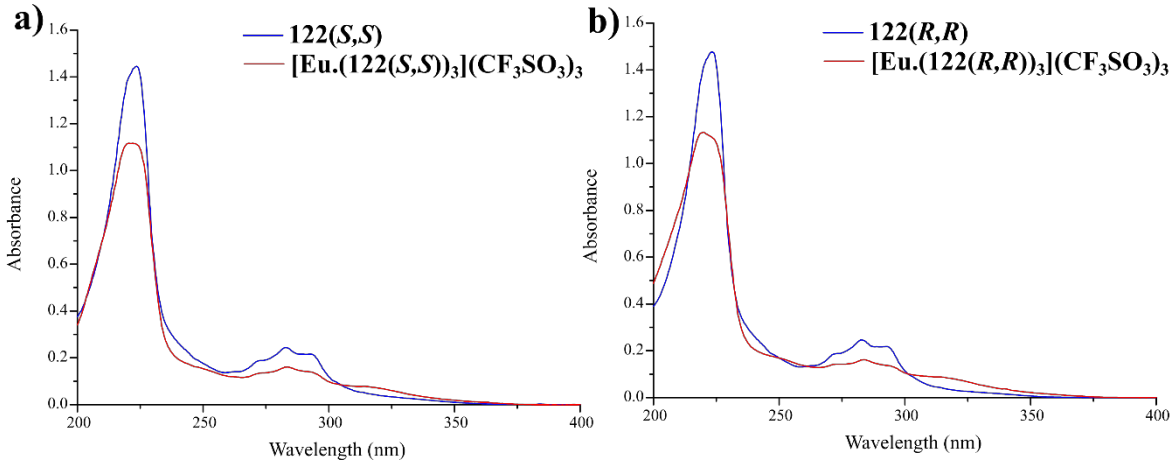

Figure A3.20 Overlaid UV-visible absorption spectra in CH_3CN for: **a) 122(*S*,*S*)** and **[Eu.(122(*S*,*S*))$_3$]**$(CF_3SO_3)_3$; and **b) 122(*R*,*R*)** and **[Eu.(122(*R*,*R*))$_3$]**$(CF_3SO_3)_3$showing hypo- and hyper-chromic shifts. All spectra recorded at ligand $c = 1 \times 10^{-5}$ M at 24 °C and represent consistent observations from repeated measurements.

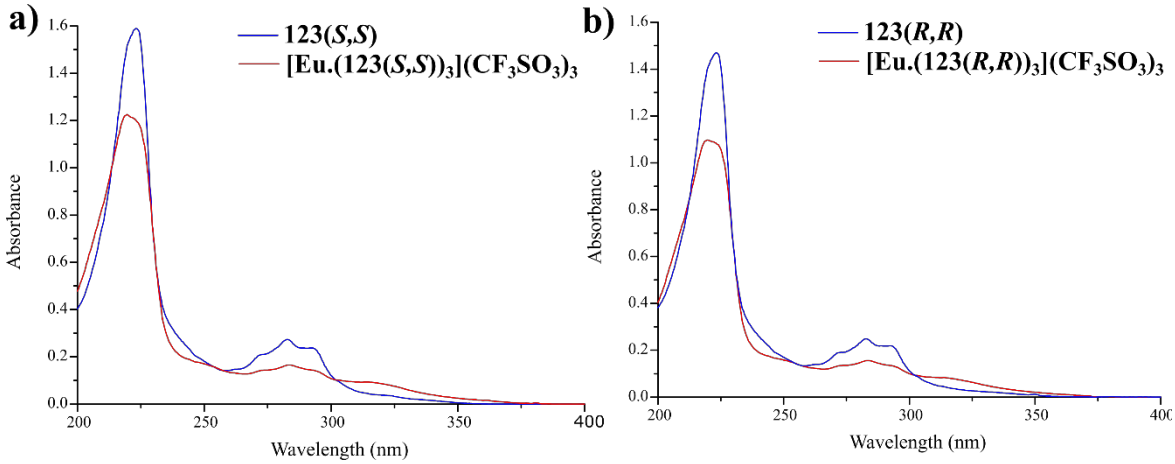

Figure A3.21 Overlaid UV-visible absorption spectra in CH_3CN for: **a) 123(*S,S*)** and **[Eu.(123(*S,S*))$_3$]**$(CF_3SO_3)_3$; and **b) 123(*R,R*)** and **[Eu.(123(*R,R*))$_3$]**$(CF_3SO_3)_3$showing hypo- and hyper-chromic shifts. All spectra recorded at ligand $c = 1 \times 10^{-5}$ M at 24 °C and represent consistent observations from repeated measurements.

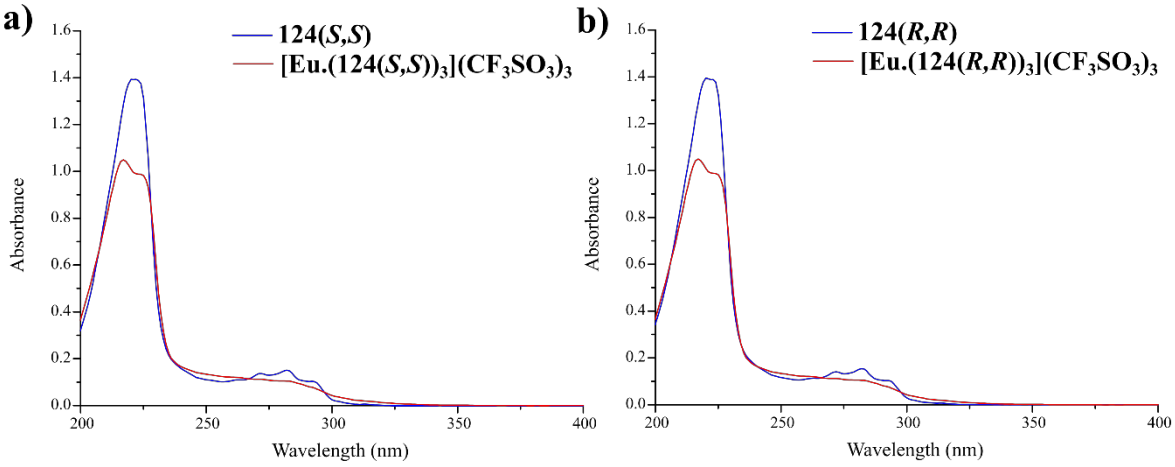

Figure A3.22 Overlaid UV-visible absorption spectra in CH_3CN for: **a) 124(*S,S*)** and **[Eu.(124(*S,S*))$_3$]**$(CF_3SO_3)_3$; and **b) 124(*R,R*)** and **[Eu.(124(*R,R*))$_3$]**$(CF_3SO_3)_3$showing hypo- and hyper-chromic shifts. All spectra recorded at ligand $c = 1 \times 10^{-5}$ M at 24 °C and represent consistent observations from repeated measurements.

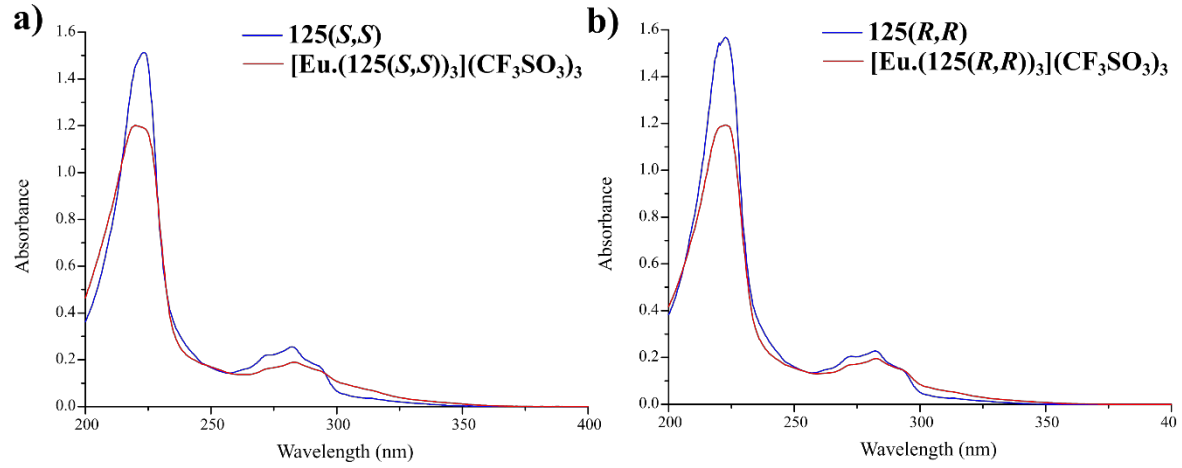

Figure A3.24 Overlaid UV-visible absorption spectra in CH_3CN for: **a) 125(*S*,*S*)** and **[Eu.(125(*S*,*S*))$_3$]**$(CF_3SO_3)_3$; and **b) 125(*R*,*R*)** and **[Eu.(125(*R*,*R*))$_3$]**$(CF_3SO_3)_3$showing hypo- and hyper-chromic shifts. All spectra recorded at ligand $c = 1 \times 10^{-5}$ M at 24 °C and represent consistent observations from repeated measurements.

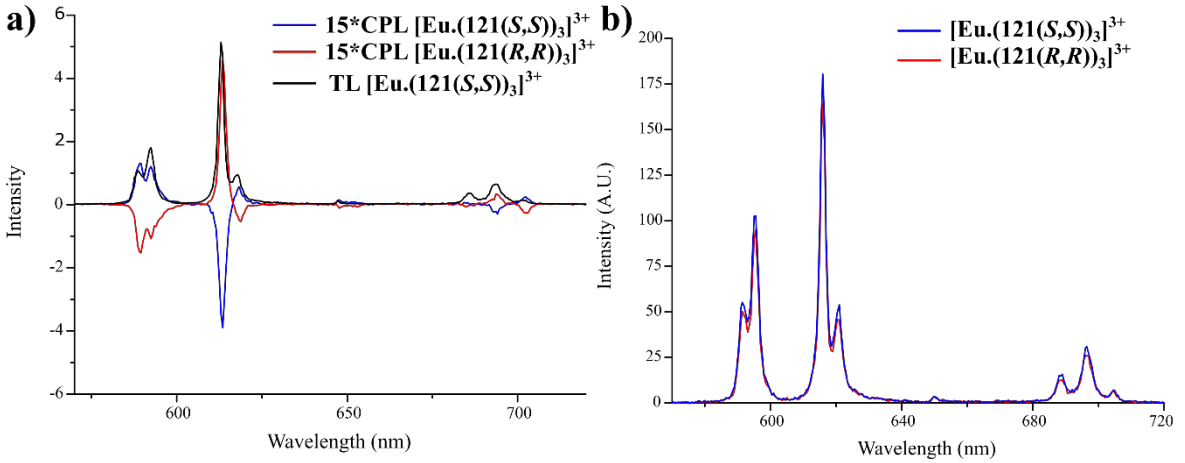

Figure A3.25 a) TL emission (black) CPL spectra for **[Eu.(121(*S*,*S*))$_3$]**$(CF_3SO_3)_3$ (blue) and **[Eu.(121(*R*,*R*))$_3$]**$(CF_3SO_3)_3$ (red) in CH_3CN; and **b)** time-gated emission spectra of for **[Eu.(121(*S*,*S*))$_3$]**$(CF_3SO_3)_3$ (blue) and **[Eu.(121(*R*,*R*))$_3$]**$(CF_3SO_3)_3$ (red) in CH_3OH.

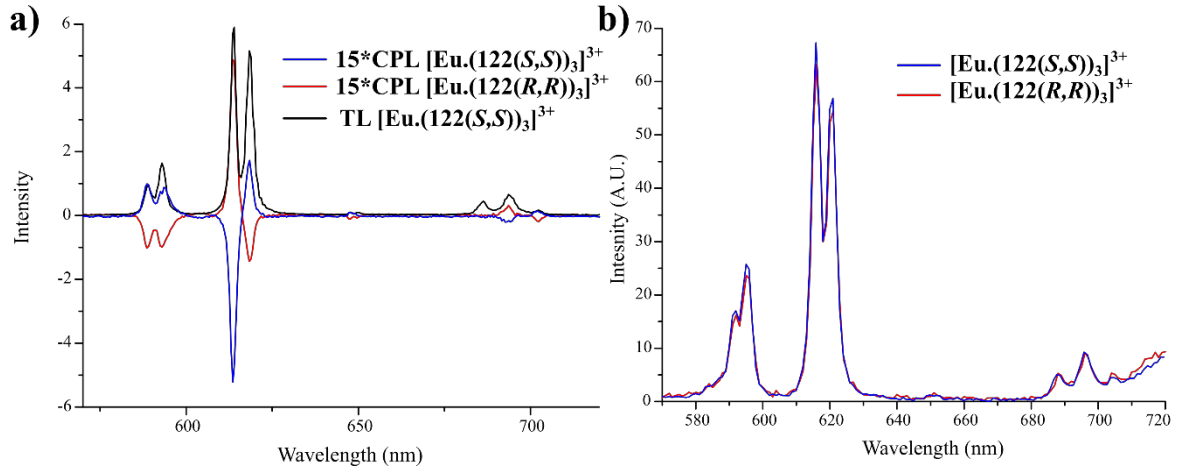

Figure A3.26 a) TL emission (black) CPL spectra for **[Eu.(122(*S*,*S*))$_3$]**$(CF_3SO_3)_3$ (blue) and **[Eu.(122(*R*,*R*))$_3$]**$(CF_3SO_3)_3$ (red) in CH_3CN; and **b)** time-gated emission spectra of for **[Eu.(122(*S*,*S*))$_3$]**$(CF_3SO_3)_3$ (blue) and **[Eu.(122(*R*,*R*))$_3$]**$(CF_3SO_3)_3$ (red) in CH_3OH.

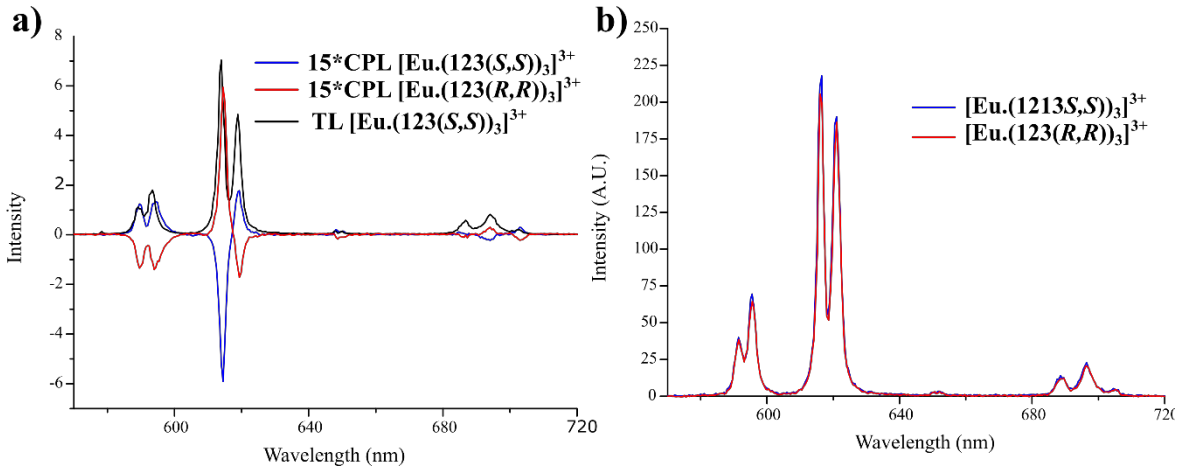

Figure A3.27 a) TL emission (black) CPL spectra for **[Eu.(123(*S*,*S*))$_3$]**$(CF_3SO_3)_3$ (blue) and **[Eu.(123(*R*,*R*))$_3$]**$(CF_3SO_3)_3$ (red) in CH_3CN; and **b)** time-gated emission spectra of for **[Eu.(123(*S*,*S*))$_3$]**$(CF_3SO_3)_3$ (blue) and **[Eu.(123(*R*,*R*))$_3$]**$(CF_3SO_3)_3$ (red) in CH_3OH.

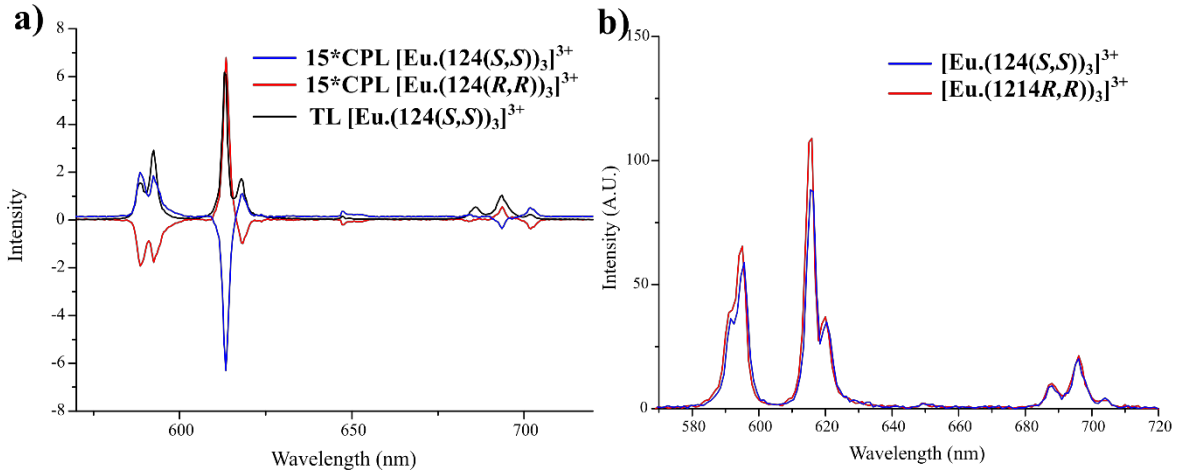

Figure A3.28 a) TL emission (black) CPL spectra for **[Eu.(124(*S*,*S*))$_3$]**$(CF_3SO_3)_3$ (blue) and **[Eu.(124(*R*,*R*))$_3$]**$(CF_3SO_3)_3$ (red) in CH_3CN; and **b)** time-gated emission spectra of for **[Eu.(124(*S*,*S*))$_3$]**$(CF_3SO_3)_3$ (blue) and **[Eu.(124(*R*,*R*))$_3$]**$(CF_3SO_3)_3$ (red) in CH_3OH.

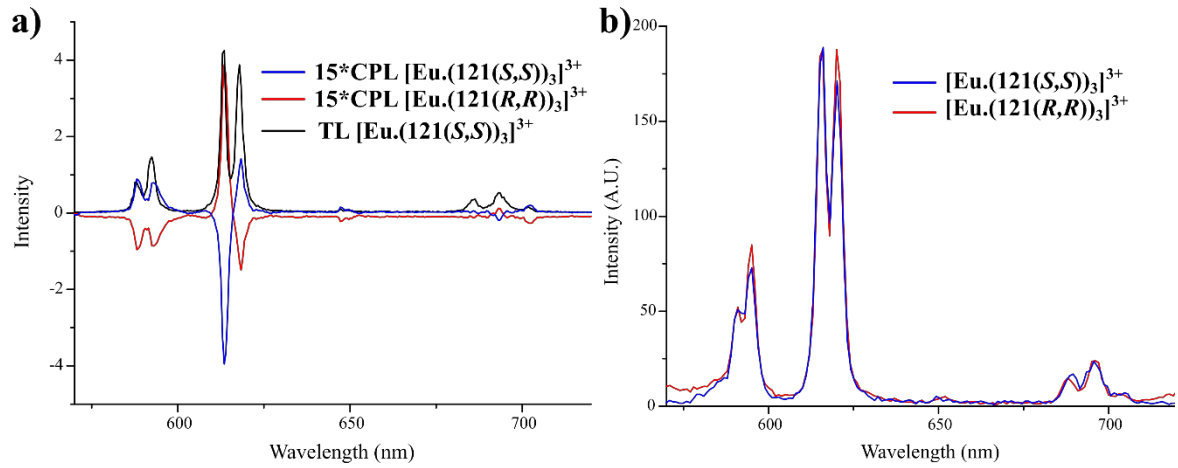

Figure A3.29 a) TL emission (black) CPL spectra for **[Eu.(125(*S*,*S*))$_3$]**$(CF_3SO_3)_3$ (blue) and **[Eu.(125(*R*,*R*))$_3$]**$(CF_3SO_3)_3$ (red) in CH_3CN; and **b)** time-gated emission spectra of for **[Eu.(125(*S*,*S*))$_3$]**$(CF_3SO_3)_3$ (blue) and **[Eu.(125(*R*,*R*))$_3$]**$(CF_3SO_3)_3$ (red) in CH_3OH.

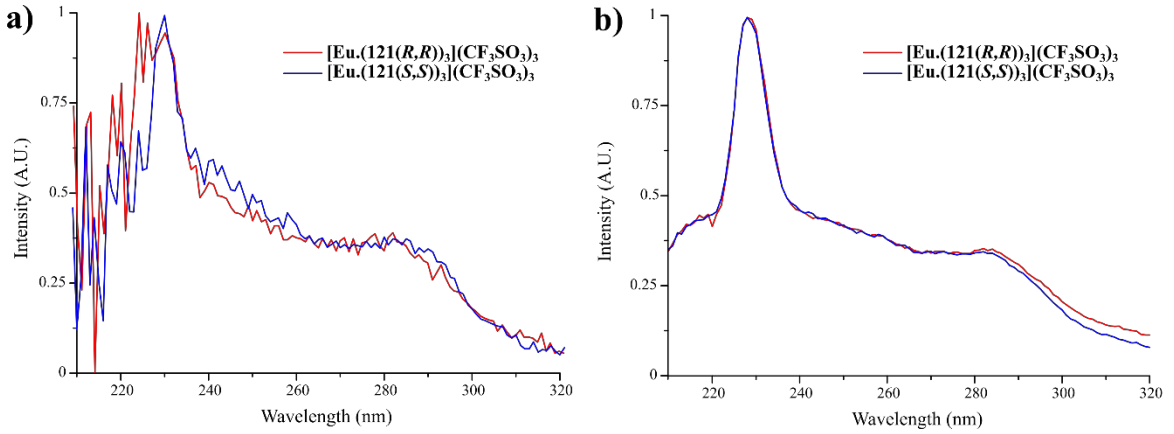

Figure A3.30 Normalised excitation spectra of emission at λ_{em} = 615 nm for **[Eu.(121(*R*,*R*))$_3$](CF$_3$SO$_3$)$_3$** (red) and **[Eu.(121(*S*,*S*))$_3$](CF$_3$SO$_3$)$_3$** (blue) recorded in: **a)** CH_3CN; and **b)** CH_3OH.

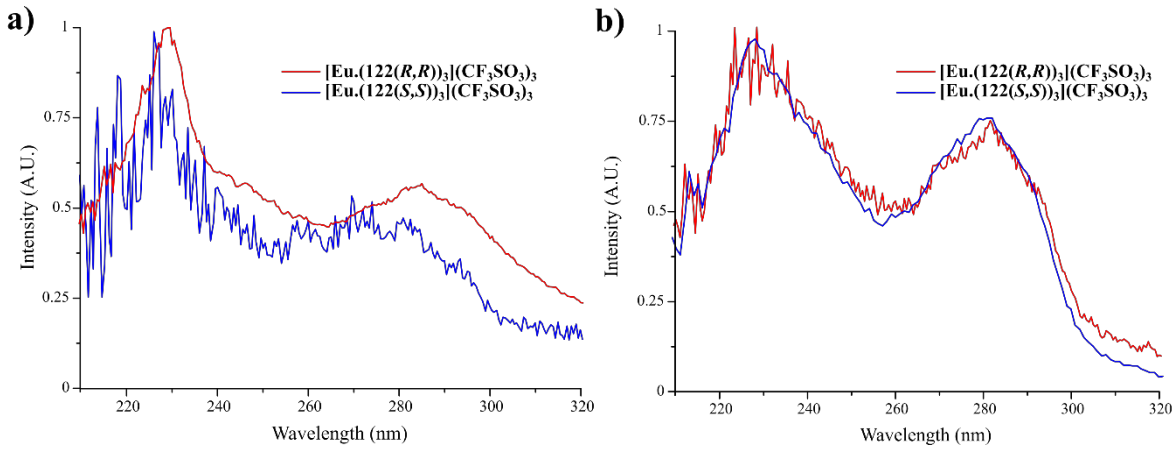

Figure A3.31 Normalised excitation spectra of emission at λ_{em} = 615 nm for **[Eu.(122(*R*,*R*))$_3$](CF$_3$SO$_3$)$_3$** (red) and **[Eu.(122(*S*,*S*))$_3$](CF$_3$SO$_3$)$_3$** (blue) recorded in: **a)** CH_3CN; and **b)** CH_3OH.

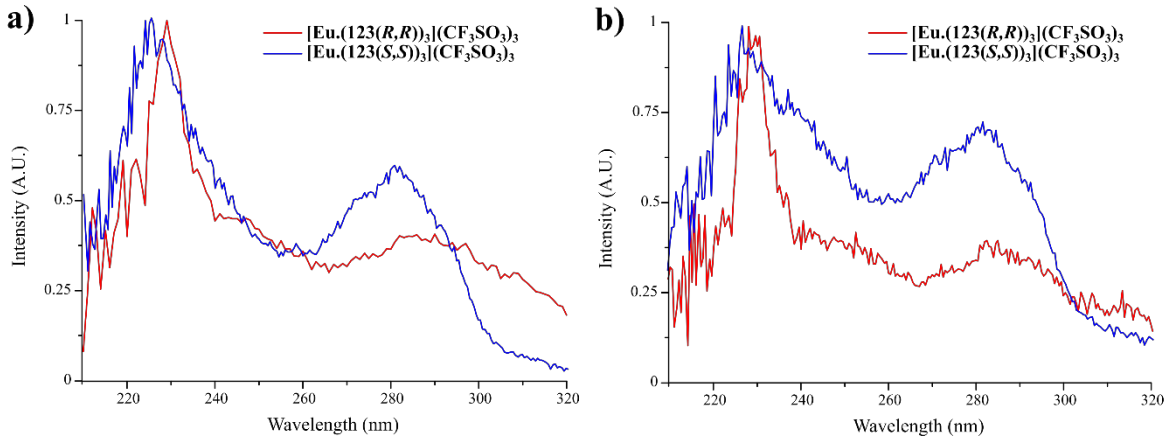

Figure A3.32 Normalised excitation spectra of emission at λ_{em} = 615 nm for **[Eu.(123(*R*,*R*))$_3$](CF$_3$SO$_3$)$_3$** (red) and **[Eu.(123(*S*,*S*))$_3$](CF$_3$SO$_3$)$_3$** (blue) recorded in: **a)** CH_3CN; and **b)** CH_3OH.

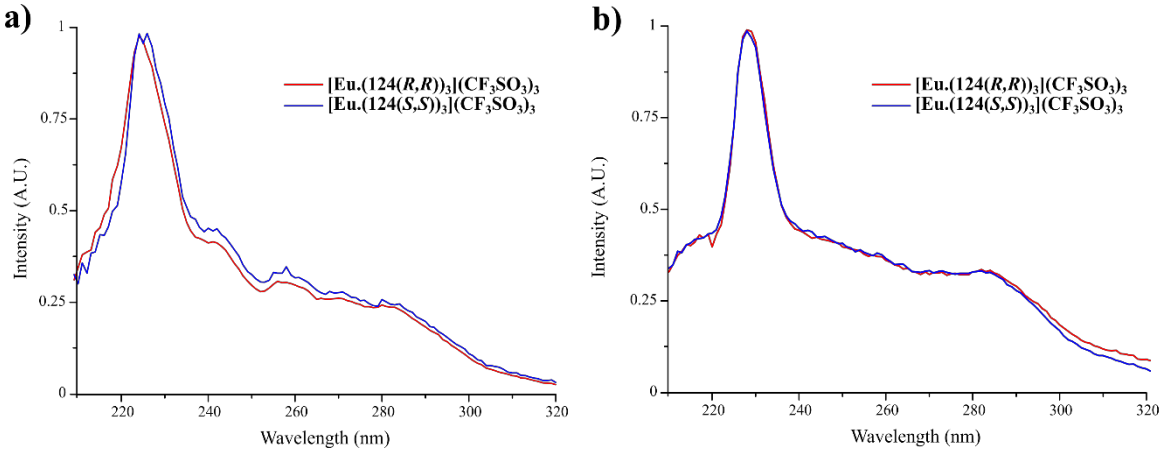

Figure A3.33 Normalised excitation spectra of emission at λ_{em} = 615 nm for **[Eu.(124(*R*,*R*))$_3$](CF$_3$SO$_3$)$_3$** (red) and **[Eu.(124(*S*,*S*))$_3$](CF$_3$SO$_3$)$_3$** (blue) recorded in: **a)** CH_3CN; and **b)** CH_3OH.

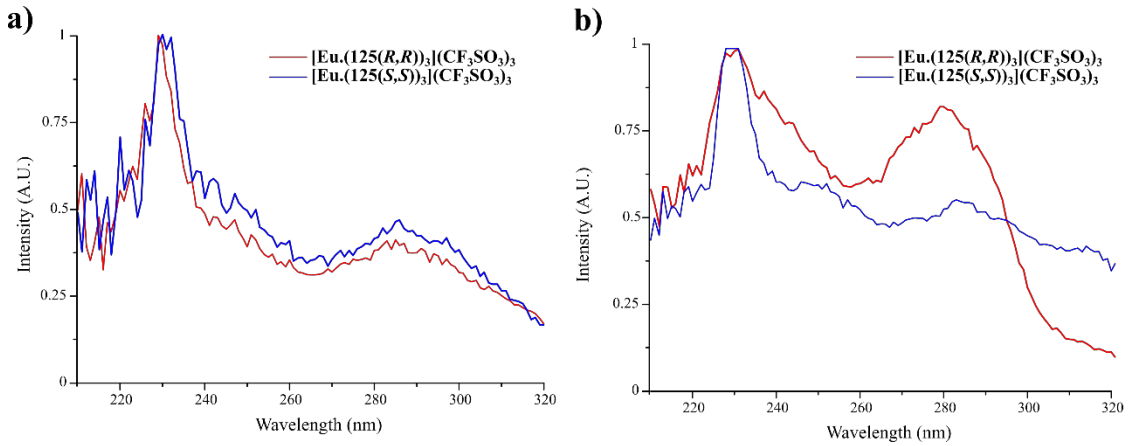

Figure A3.34 Normalised excitation spectra of emission at λ_{em} = 615 nm for **[Eu.(125(*R*,*R*))$_3$](CF$_3$SO$_3$)$_3$** (red) and **[Eu.(125(*S*,*S*))$_3$](CF$_3$SO$_3$)$_3$** (blue) recorded in: **a)** CH_3CN; and **b)** CH_3OH

Table A3.2 Summary of Eu^{III} luminescence emission lifetimes (τ, ms) recorded from complexes in H_2O and D_2O and the number of bound water molecules (*q*-value) determined from Horrocks' and Parker's equations. Average lifetimes were determined from five independent measurements.

Complex	τ_{H_2O} (ms)	τ_{D_2O} (ms)	*q*-value (Horrocks)	*q*-value (Parker)
[Eu.(121(*R*,*R*))$_3$]$^{3+}$	1.55±0.02	3.79±0.02	0.21	-0.24
[Eu.(122(*R*,*R*))$_3$]$^{3+}$	1.26±0.01	2.29±0.02	0.18	-0.27
[Eu.(123(*R*,*R*))$_3$]$^{3+}$	1.34±0.01	2.81±0.02	0.22	-0.23
[Eu.(124(*R*,*R*))$_3$]$^{3+}$	1.57±0.02	2.79±0.02	0.08	-0.37
[Eu.(125(*R*,*R*))$_3$]$^{3+}$	1.31±0.01	2.35±0.2	0.16	-0.29

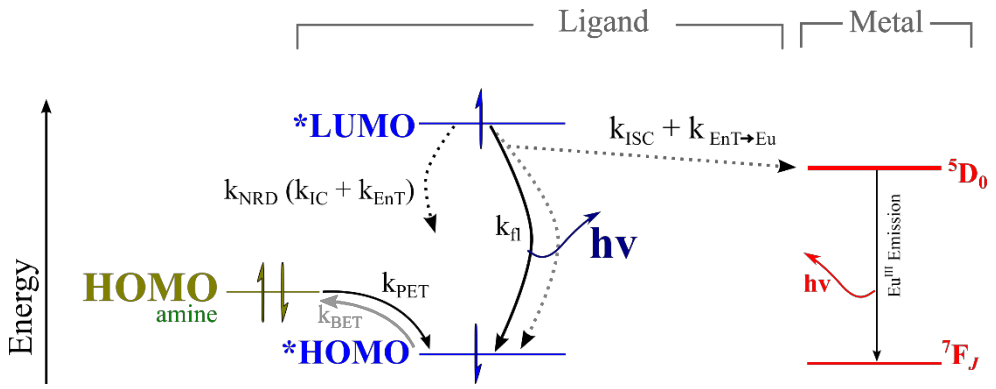

Figure A3.35 Extended schematic Jablonski diagram showing various competing processes in PET active ligands showing the singlet excited-state (blue, HOMO/LUMO), amine PET donor (green, HOMO) and lanthanide excited-state (red, $^5D_0$ state) and group-state (red, ^7F_J). Various key processes shown are: ligand-centred fluorescence (k_{fl}), non-radiative decay (k_{NRD}) combining deactivation by internal conversion (k_{IC}) and solvent coupling (k_{EnT}), the sensitisation process of intersystem crossing to a triplet state (k_{ISC}) followed by energy transfer to the Eu^{III} ion (kEnT→Eu).

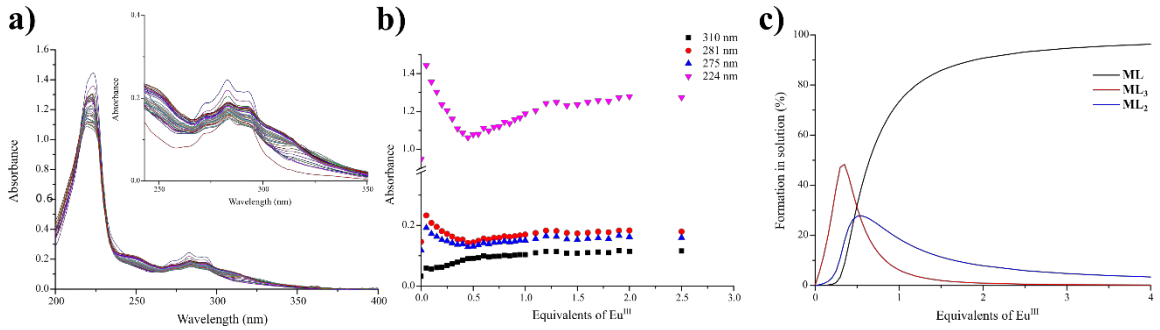

Figure A3.36 UV-visible absorption titration of **122(*S*,*S*)** with $Eu(CF_3SO_3)_3$ in CH_3CN. **a**) overlaid spectra recorded between 0.00 → 4.00 equivalents of Eu^{III}; **b)** single wavelength binding isotherms for key absorbance wavelengths; and **c)** the speciation distribution diagram generated from the non-linear regression analysis of the spectral changes. This titration represents one of multiple replicates which showed consistent behaviour.

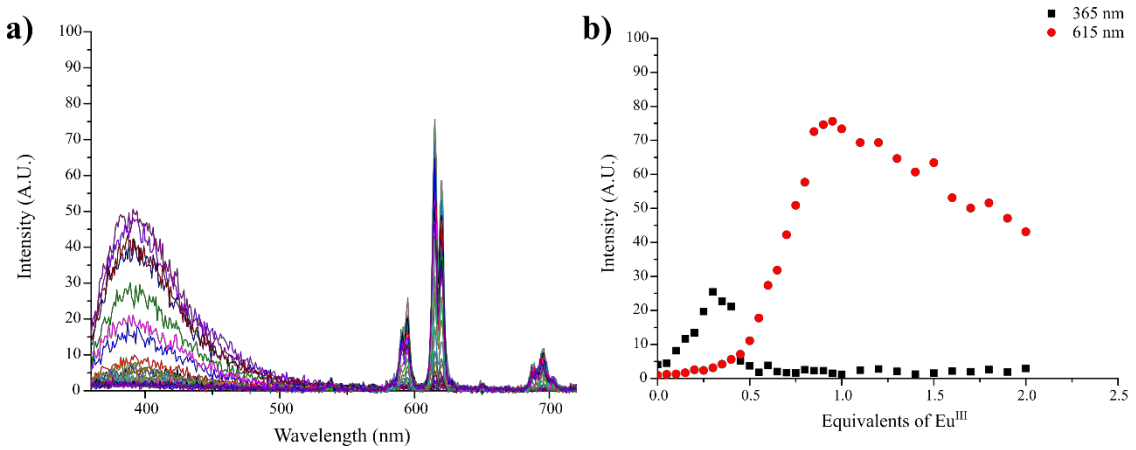

Figure A3.37 Fluorescence time-scale emission titration of **122(*S,S*)** with $Eu(CF_3SO_3)_3$ in CH_3CN. **a**) overlaid spectra recorded between 0.00 → 4.00 equivalents of Eu^{III}; and **b)** single wavelength binding isotherms between 0.00 → 2.00 equivalents for the ligand-and the metal-centred emissions at 390 and 615 nm, respectively. This titration represents one of multiple replicates which showed consistent behaviour.

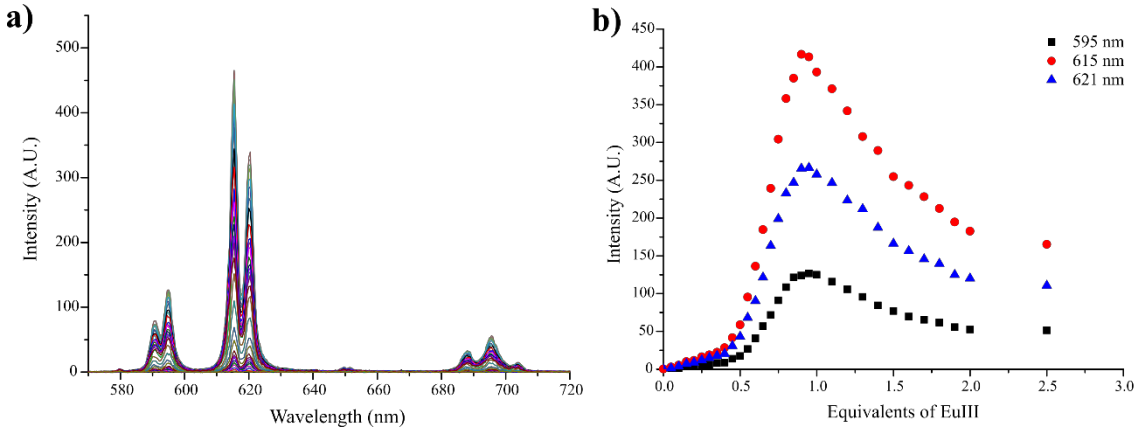

Figure A3.38 Time-gated emission titration of **122(*S,S*)** with $Eu(CF_3SO_3)_3$ in CH_3CN. a) overlaid emission spectra recorded between 0.00 → 4.00 equivalents of Eu^{III}; and **b)** single wavelength binding isotherms between 0.00 → 2.50 equivalents for $^5D_0 \rightarrow {}^7F_{1,2}$ transitions at 595, 615 and 621 nm. This titration represents one of multiple replicates which showed consistent behaviour.

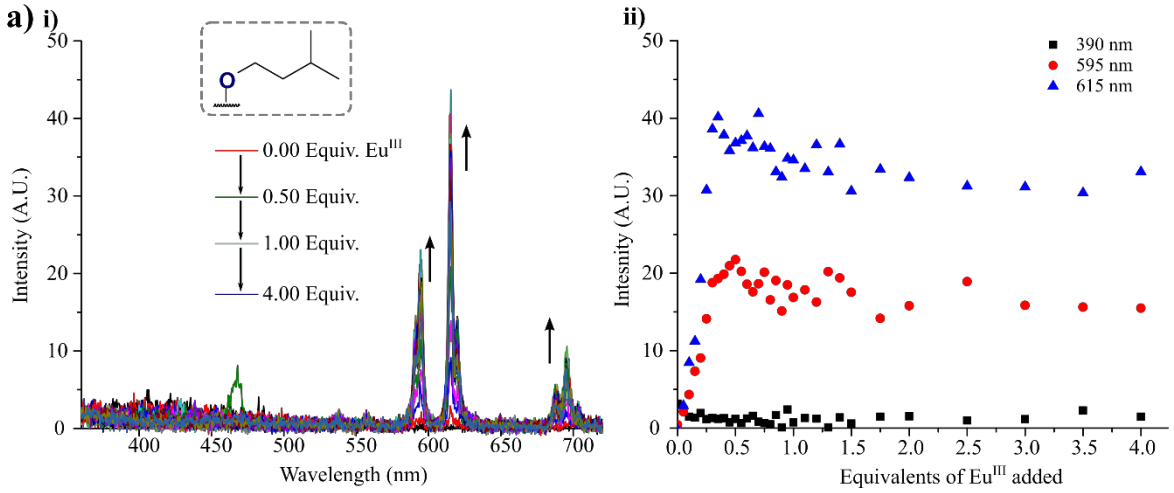

Figure A3.39 Fluorescence time-scale emission titration of **124(*S,S*)** with Eu(CF3SO3)3 in CH3CN (c.f. Figure 3.x). **a)** overlaid emission spectra between 0.00 → 4.00 equivalents of EuIII, showing only metal-centred transitions; and **b)** single wavelength isotherms of 'ligand fluorescence' at 390 nm (showing no change) and $^5D_0 \rightarrow {}^7F_{1,2}$ transitions at 595 and 615 nm. This titration represents one of multiple replicates which showed consistent behaviour.

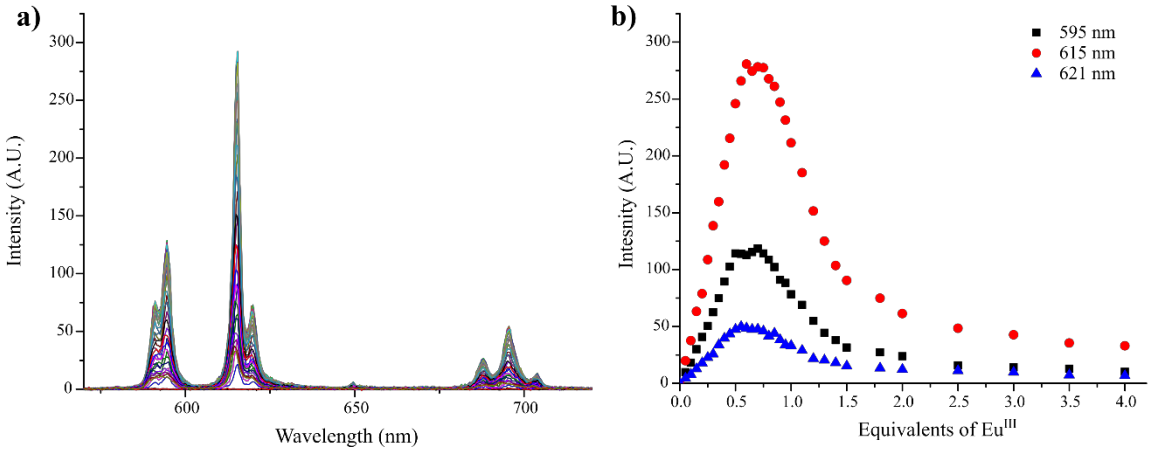

Figure A3.40 Time-gated emission titration of **121(*R,R*)** with $Eu(CF_3SO_3)_3$ in CH_3CN. **a)** overlaid spectra recorded between 0.00 → 4.00 equivalents of Eu^{III}; and **b)** single wavelength isotherms for the $^5D_0 \rightarrow {}^7F_{1,2}$ transitons at 595, 615 and 621 nm. This titration represents one of multiple replicates which showed consistent behaviour.

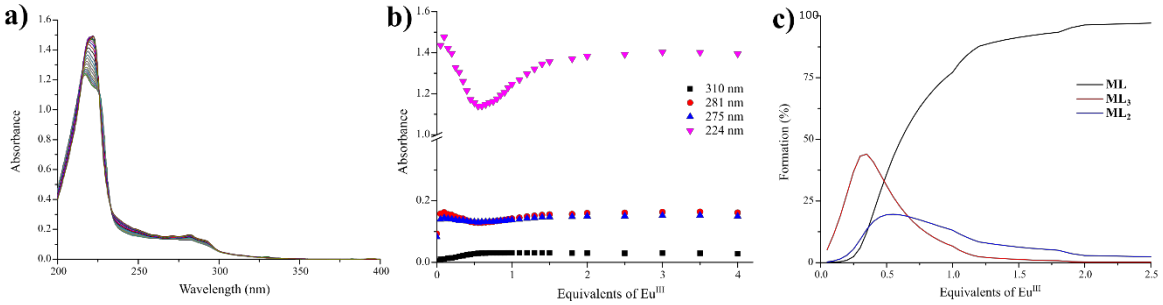

Figure A3.41 UV-visible absorption titration of **121(*R,R*)** with $Eu(CF_3SO_3)_3$ in CH_3CN. **a**) overlaid spectra recorded between 0.00 → 4.00 equivalents of Eu^{III}; **b)** single wavelength binding isotherms for key absorbance wavelengths; and **c)** the speciation distribution diagram generated from the non-linear regression analysis of the spectral changes. This titration represents one of multiple replicates which showed consistent behaviour.

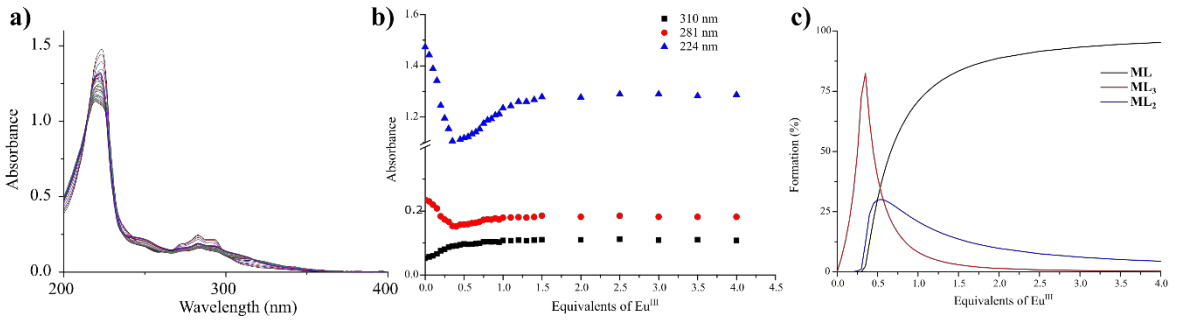

Figure A3.42 UV-visible absorption titration of **122(*R,R*)** with $Eu(CF_3SO_3)_3$ in CH_3CN. a) overlaid spectra recorded between 0.00 → 4.00 equivalents of Eu^{III}, b) single wavelength isotherms for key absorbance wavelengths; and c) the speciation distribution diagram generated from the non-linear regression analysis of the absorbance changes. This titration represents one of multiple replicates which showed consistent behaviour.

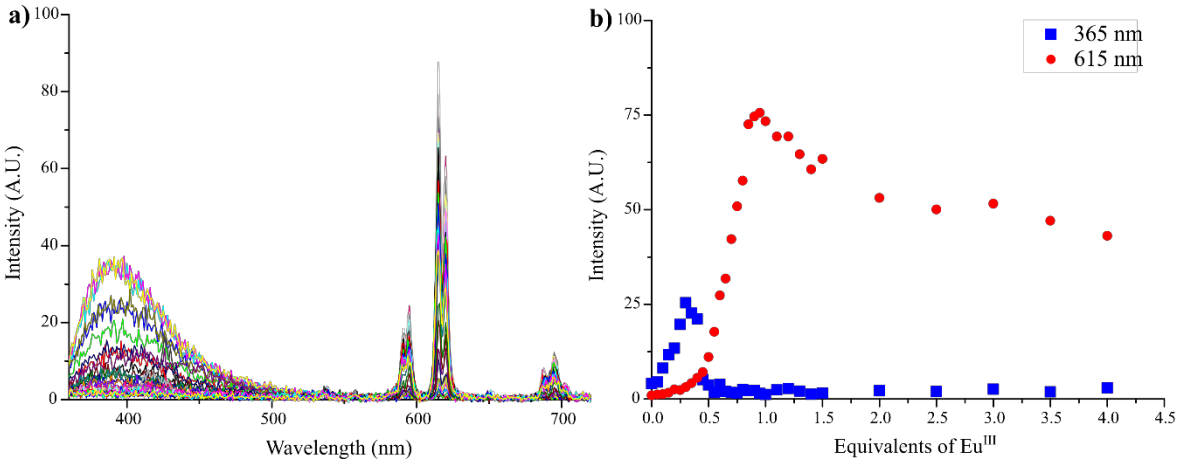

Figure A3.43 Fluorescence time-scale emission titration of **122(*R,R*)** with $Eu(CF_3SO_3)_3$ in CH_3CN. a) overlaid emission spectra recorded between 0.00 → 4.00 equivalents of Eu^{III}; and **b)** single wavelength isotherms for the ligand- and the metal-centred emissions at 395 and 615 nm, respectively. This titration represents one of multiple replicates which showed consistent behaviour.

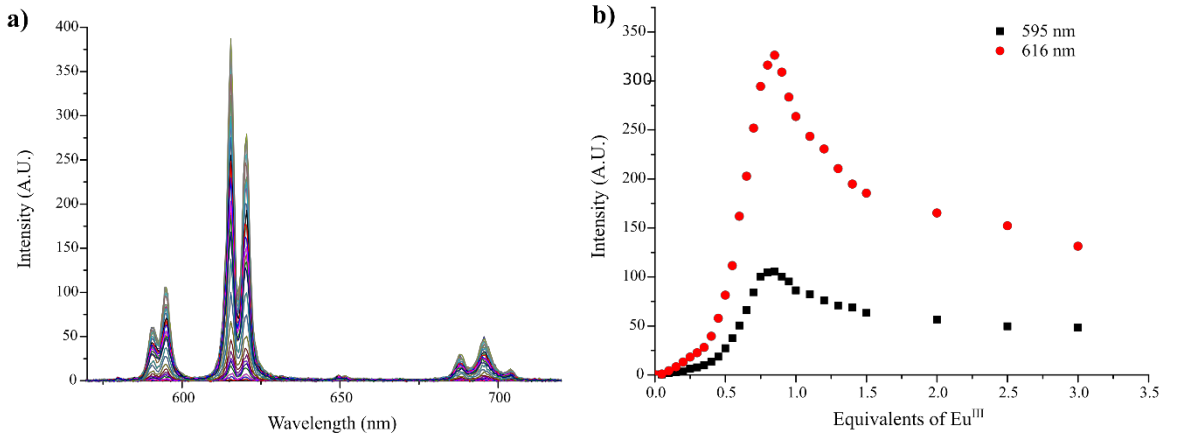

Figure A3.44 Time-gated emission titration of **122(*R,R*)** with $Eu(CF_3SO_3)_3$ in CH_3CN. a) overlaid emission spectra recorded between 0.00 → 4.00 equivalents of Eu^{III}; and **b)** single wavelength between 0.00 → 3.00 equivalents for the $^5D_0 \rightarrow {}^7F_{1,2}$ transitions at 595 and 616 nm, respectively. This titration represents one of multiple replicates which showed consistent behaviour.

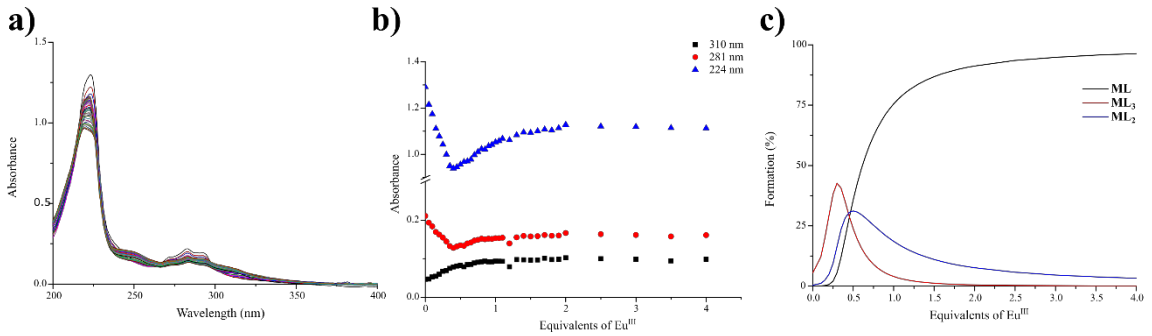

Figure A3.45 UV-visible absorption titration of **123(*R*,*R*)** with $Eu(CF_3SO_3)_3$ in CH_3CN. **a)** overlaid spectra recorded between 0.00 → 4.00 equivalents of Eu^{III}; **b)** single wavelength isotherms for key absorbance wavelengths during the titrations; and **c**) the speciation distribution diagram generated from the non-linear regression analysis of the absorbance changes. This titration represents one of multiple replicates which showed consistent behaviour.

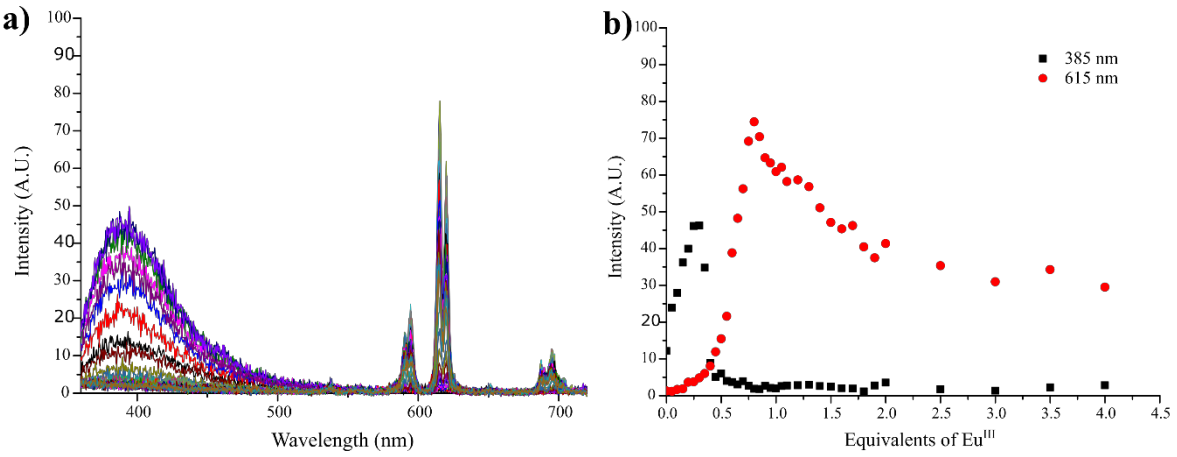

Figure A3.46 Fluorescence time-scale emission titration of **123(*R*,*R*)** with $Eu(CF_3SO_3)_3$ in CH_3CN. **a)** overlaid spectra recorded between 0.00 → 4.00 equivalents of Eu^{III}; and **b)** single wavelength isotherms for the ligand- and the metal-centred emissions at 395 and 615 nm, respectively. This titration represents one of multiple replicates which showed consistent behaviour.

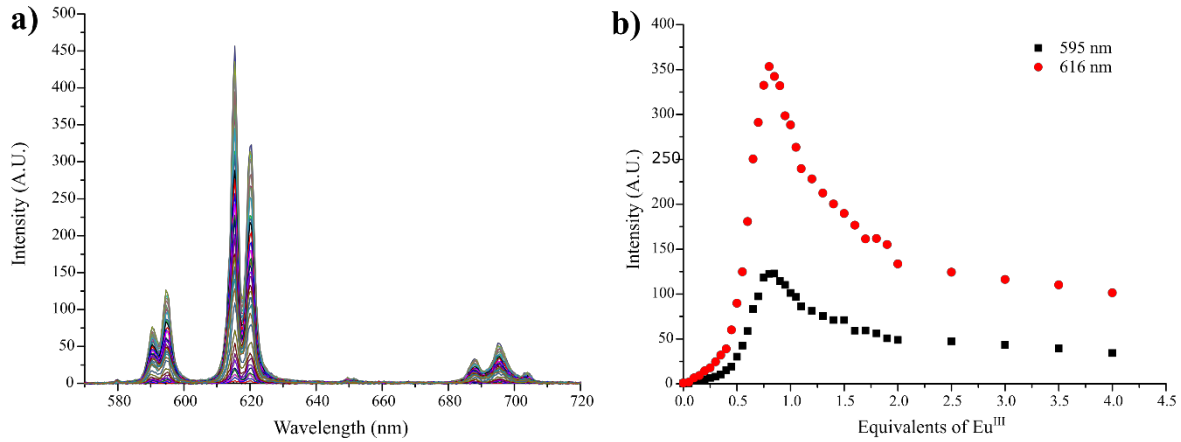

Figure A3.47 Time-gated emission titration of **123(*R,R*)** with $Eu(CF_3SO_3)_3$ in CH_3CN. a) overlaid emission spectra recorded between 0.00 → 4.00 equivalents of Eu^{III}; and **b)** single wavelength isotherms for the $^5D_0 \rightarrow {}^7F_{1,2}$ transitions at 595 and 615 nm, respectively. This titration represents one of multiple replicates which showed consistent results.

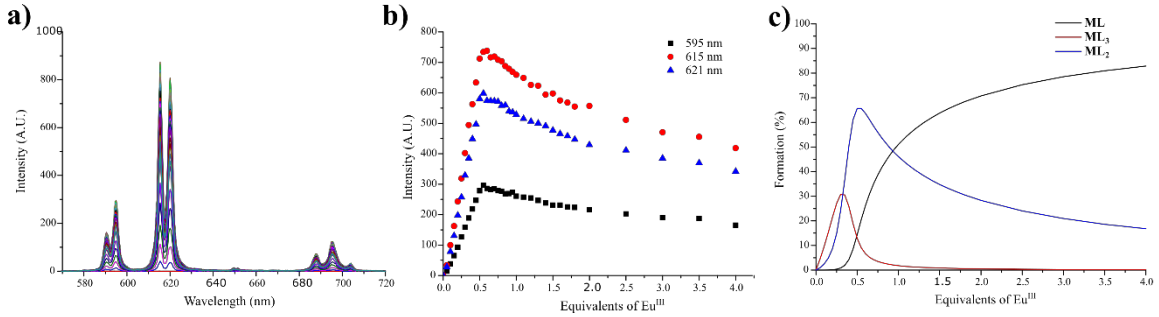

Figure A3.48 Time-gated emission titration of **125(*R,R*)** with $Eu(CF_3SO_3)_3$ in CH_3CN. **a)** overlaid emission spectra recorded between 0.00 → 4.00 equivalents of Eu^{III}; **b)** single wavelength isotherms for the $^5D_0 \rightarrow {}^7F_{1,2}$ transitions at 595, 615 and 621 nm; and **c)** the speciation distribution diagram generated from the non.-linear regression analysis of the luminescence changes. This titrations represents one of multiple replicates which showed consistent behaviour.

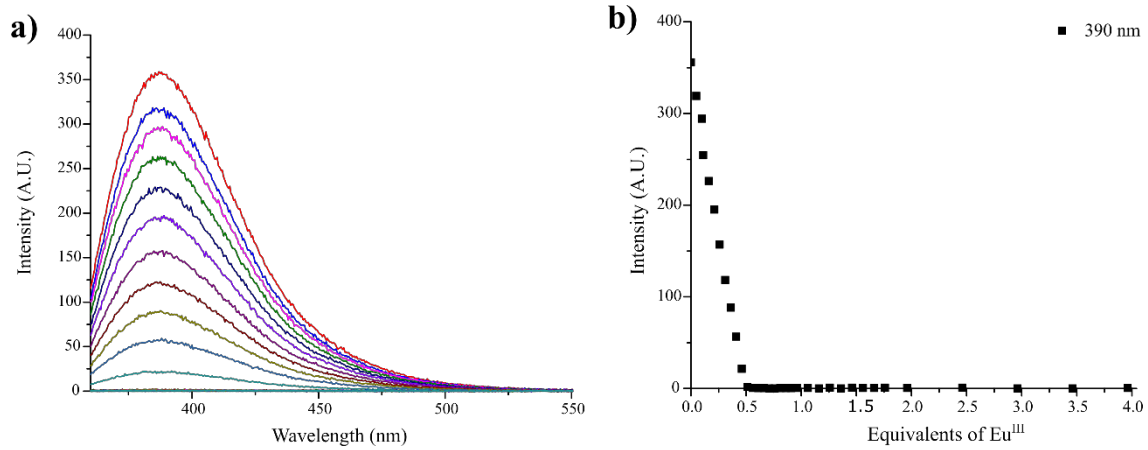

Figure A3.49 Fluorescence time-scale emission titration of **125(*R,R*)** with $Eu(CF_3SO_3)_3$ in CH_3CN. **a)** overlaid ligand fluorescence spectra recorded between 0.00 → 4.00 equivalents of Eu^{III}; and **b)** single wavelength isotherms for λ_{max} = 390 nm. This titration represents one of multiple replicates which showed consistent behaviour

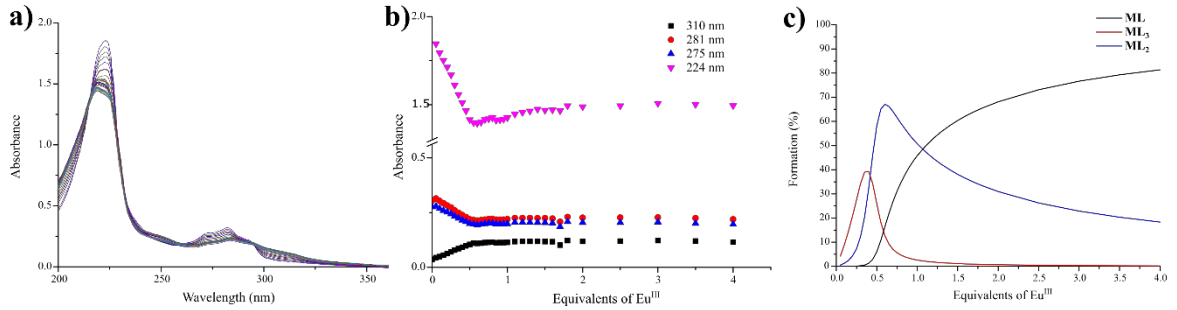

Figure A3.50 UV-visible absorption titration of **125(*R*,*R*)** with $Eu(CF_3SO_3)_3$ in CH_3CN. **a)** overlaid spectra recorded between 0.00 → 4.00 equivalents of Eu^{III}; **b)** single wavelength isotherms for key absorbance wavelengths during the titration; and **c)** the speciation distribution diagram generated from the non-linear regression analysis of the absorbance changes. This titration represents one of multiple replicates which showed consistent behaviour.

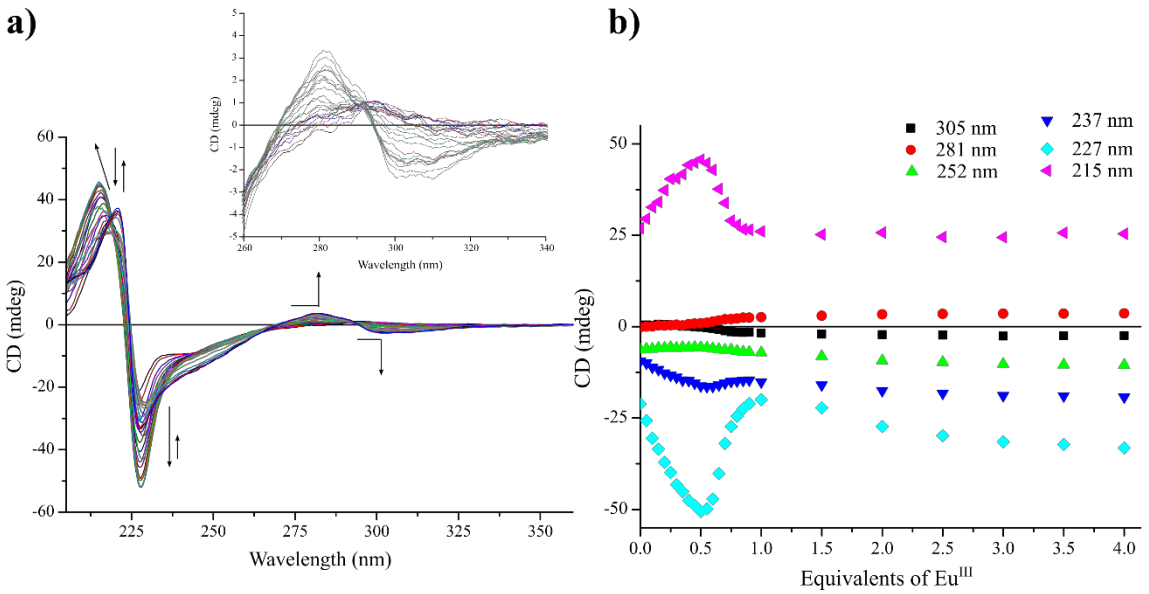

Figure A3.51 CD titration of **123(*R*,*R*)** with $Eu(CF_3SO_3)_3$ in CH_3CN. **a)** Overlaid spectra recorded between 0.00 → 4.00 equivalents of Eu^{III}, *inset*: expanded region between 260 – 340 nm; and **b)** single wavelength isotherms for key maxima in the CD spectra throughout the course of the titration. This titration represents one of multiple replicates which showed consistent behaviour.

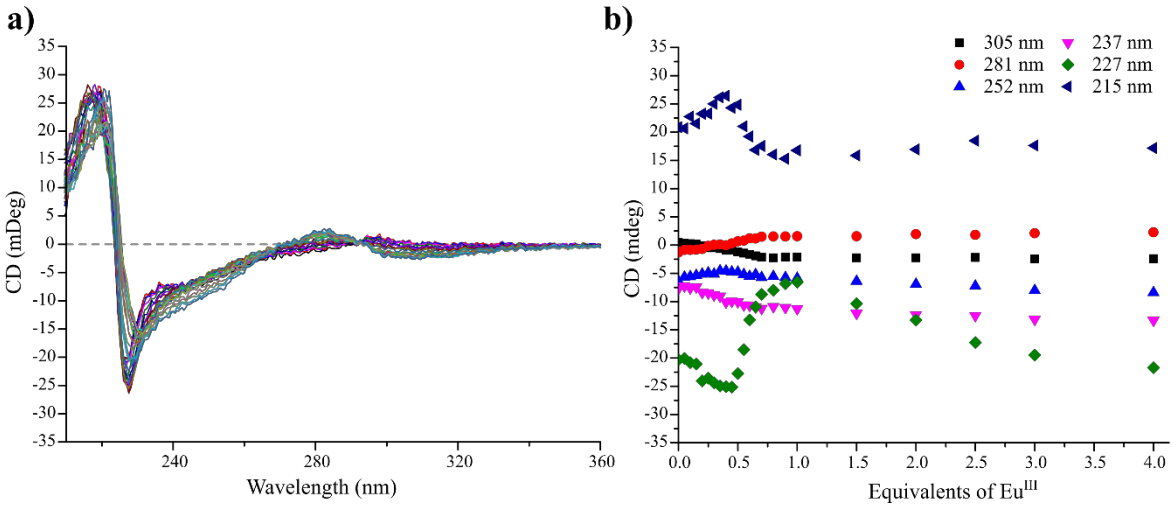

Figure A3.52 CD titration of **123(*R,R*)** with $Eu(CF_3SO_3)_3$ in CH_3OH. **a)** Overlaid spectra recorded between 0.00 → 4.00 equivalents of Eu^{III}, *inset*: expanded region between 260 – 340 nm; and **b)** single wavelength isotherms for key maxima in the CD spectra throughout the course of the titration. This titration represents one of multiple replicates which showed consistent behaviour.

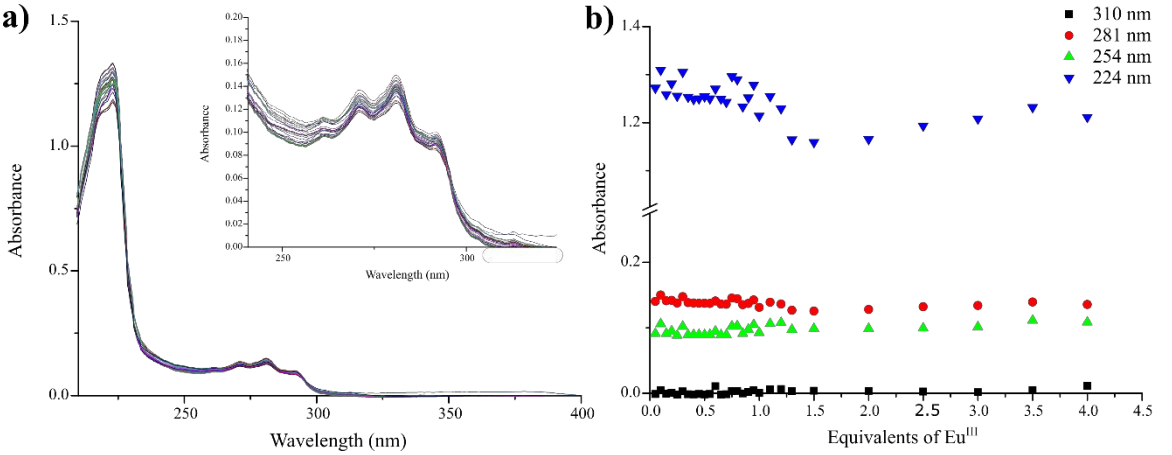

Figure A3.53 UV-visible absorption titration of **121(*R,R*)** with $Eu(CF_3SO_3)_3$ in CH_3OH. **a)** overlaid spectra recorded between 0.00 → 4.00 equivalents of Eu^{III}; and **b)** single wavelength isotherms for key absorbance wavelengths throughout the course of the titration. This behaviour was not very reproducible with the small changes (as were see in the S,S enantiomer) introducing large variation and noise, and therefore was not probed further.

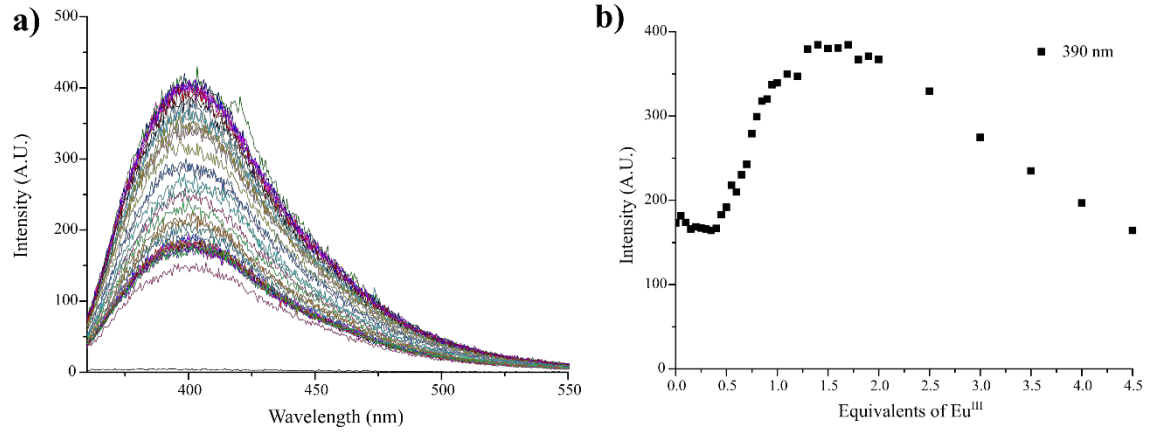

Figure A3.54 Fluorescence time-scale emission titration of **123(*R,R*)** with $Eu(CF_3SO_3)_3$ in CH_3OH. **a)** overlaid emission spectra between 0.00 → 5.00 equivalent of Eu^{III}; and **b)** single wavelength isotherm for λ_{max} = 390 nm throughout the course of the titration. This titration represents one of multiple replicates which showed consistent behaviour.

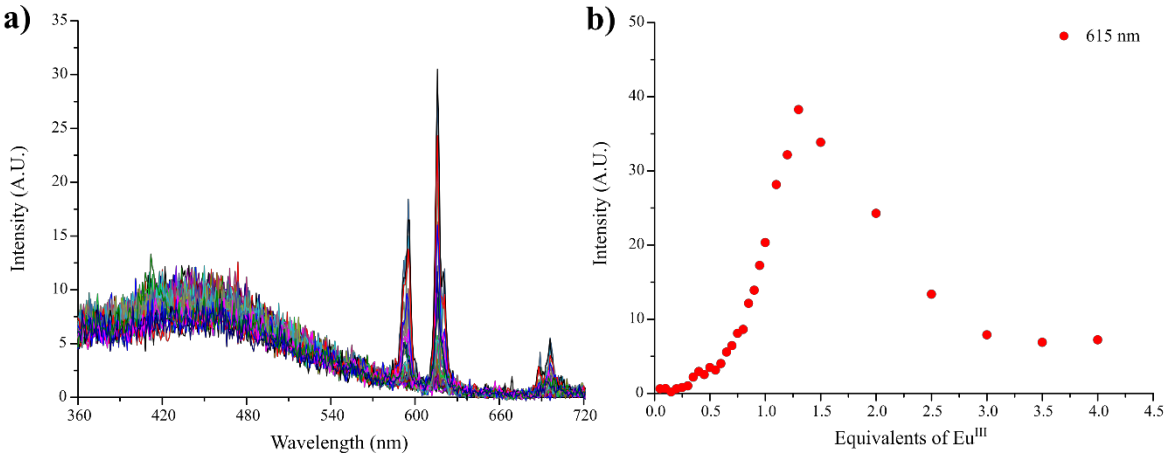

Figure A3.55 Fluorescence time-scale emission titration of **121(*R,R*)** with $Eu(CF_3SO_3)_3$ in CH_3OH. **a)** overlaid spectra recorded between 0.00 → 4.00 equivalents of Eu^{III}, showing weak and unchanging ligand-centred fluorescence; and **b)** single wavelength isotherm for the $^5D_0 \rightarrow {}^7F_2$ transition throughout the course of the titration. The luminescence behaviour was reproducible in multiple experiments and between enantiomers (more so that the absorbance changes); however, the behaviours could not be modelled.

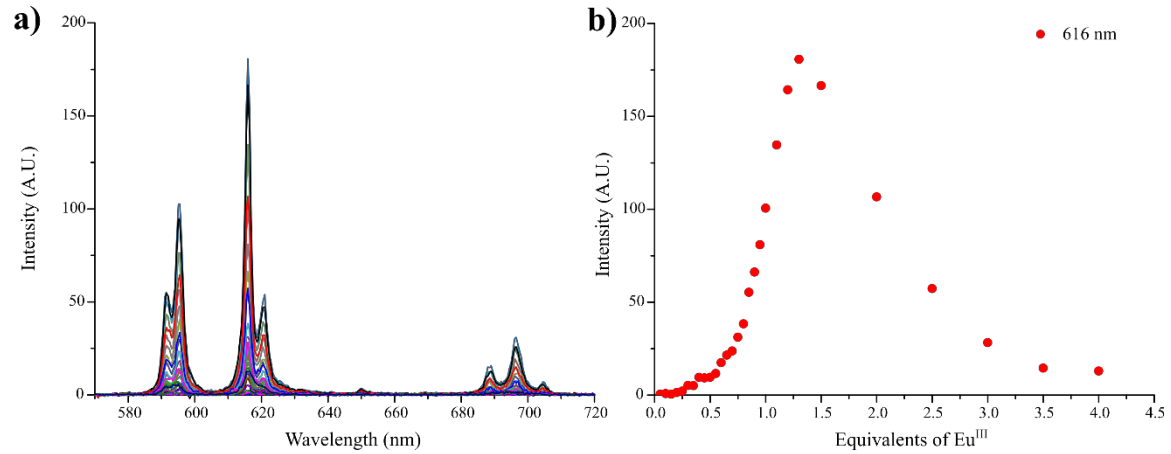

Figure A3.56 Time-gated emission titration of **121(*R,R*)** with $Eu(CF_3SO_3)_3$ in CH_3OH. **a)** overlaid spectra between 0.00 → 4.00 equivalents of Eu^{III}; and **b)** single wavelength isotherm showing the changes in the $^5D_0$ → $^7F_2$ transition during the course of the titration. The luminescence changes were again more reproducible than the UV-changes and they suggested significant quenching in the **ML_3** species.

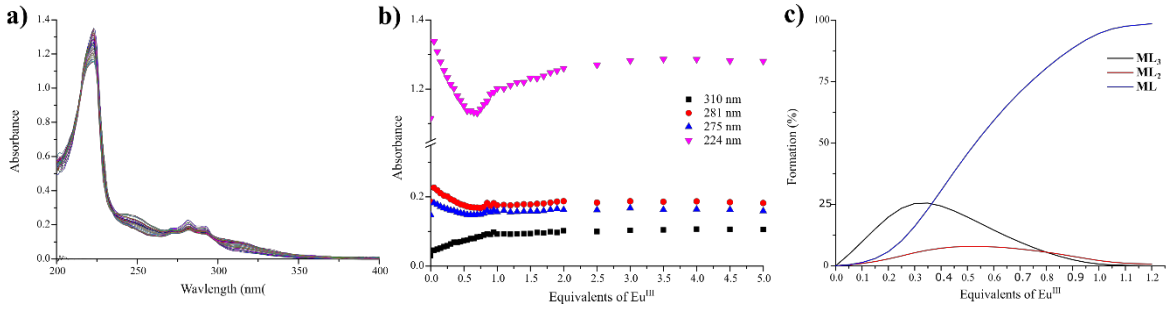

Figure A3.57 UV-visible absorption titration of **123(*R,R*)** with $Eu(CF_3SO_3)_3$ in CH_3OH. **a)** overlaid spectra recorded between 0.00 → 5.00 equivalents of Eu^{III}; **b)** single wavelength isotherms between 0.00 → 5.00 equivalents of Eu^{III} for key absorbance wavelengths; and **c)** speciation distribution diagram between 0.00 → 1.20 equivalents generated from the non-linear regression analysis of the absorbance changes, showing the main changes in solution species. This titration represents one of multiple replicates which showed consistent behaviour.

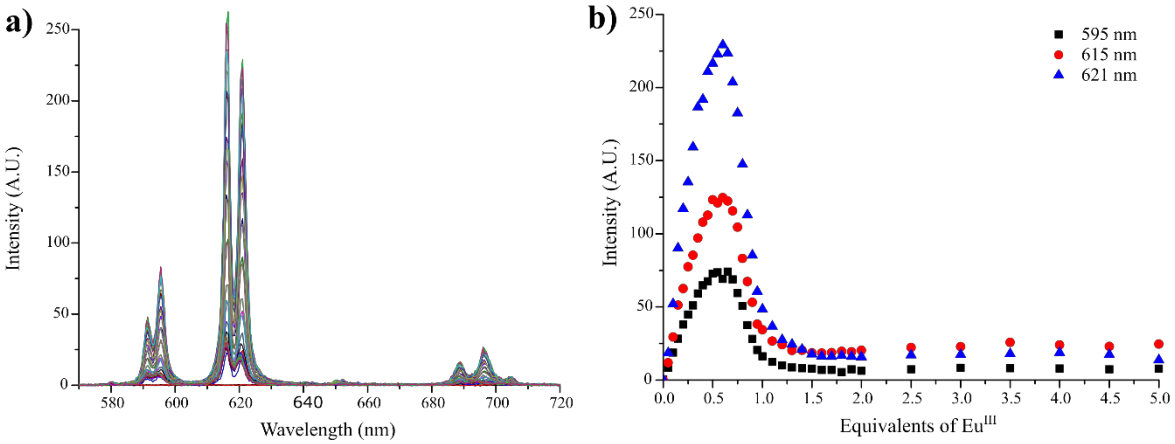

Figure A3.58 Time-gated emission titration of **123(*R*,*R*)** with $Eu(CF_3SO_3)_3$ in CH_3OH. **a)** overlaid emission spectra recorded between 0.00 → 5.00 equivalents of Eu^{III}; and **b)** single wavelength isotherms of the $^5D_0 \rightarrow {}^7F_{1,2}$ transitions at 595, 615 and 621 nm throughout the course of the titration. This titration represents one of multiple replicates which showed consistent behaviour.

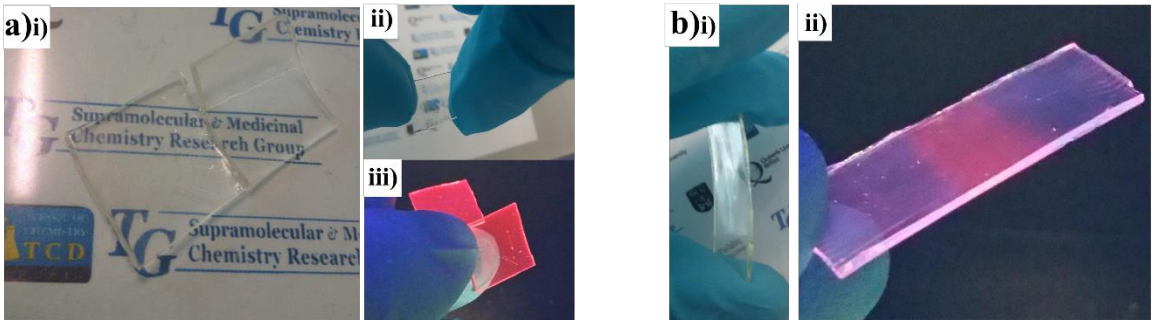

Figure A3.59 Photographs of vapour-treated gels after dehydration showing return to key properties, such as loss of flexibility (return to hard brittle materials) while retaining optical transparency and **[Eu.(122(*S*,*S*))$_3$]$^{3+}$** luminescence response: **a)** i) HCl-treated samples under ambient light showing hard, clear materials, ii**)** sample of HCl-treated polymer under mechanical stress, showing loss of flexibility, iii) polymer under λ_{exc} = 254 nm, showing strong red response ; and **b)** i) sample of NH_3-treated polymer under mechanical stress, showing loss of flexibility but retention optical clarity, ii) polymer under λ_{exc} = 254 nm, showing purple emission (loss of Eu^{III} emission), equivalent to that seen in the soft material.

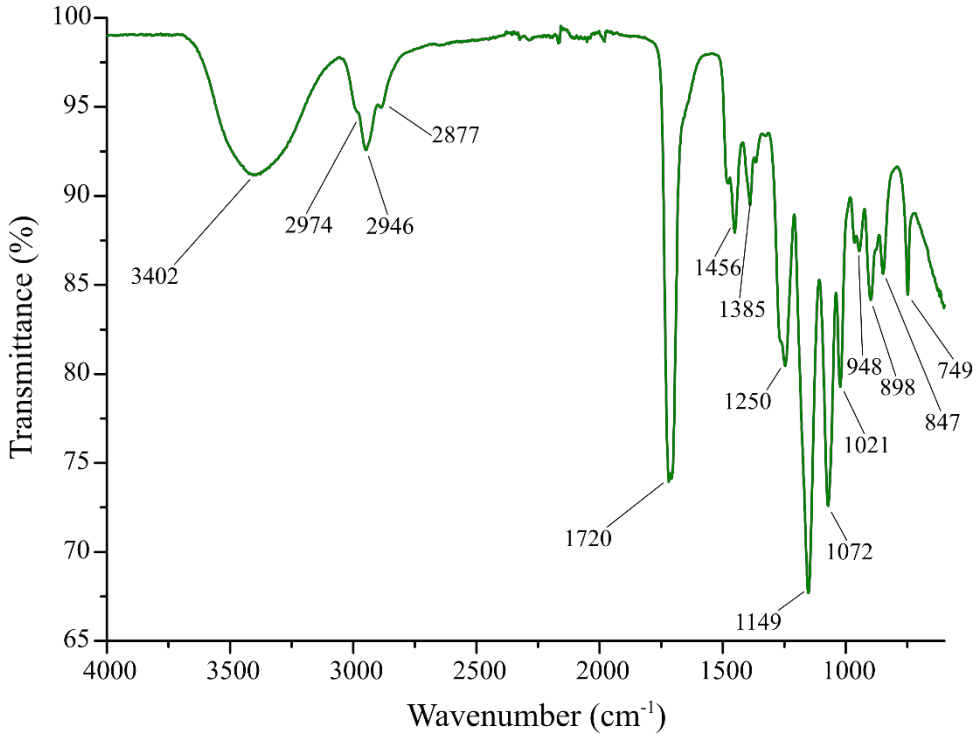

Figure A3.60 IR spectrum (ATR) of **[Eu.(123(*S*,*S*))$_3$]@p(HEMA-*co*-EGDMA)** showing the characteristic peaks of p(HEMA) backbone at 1721 cm^{-1}.

A4. Chapter 4 Appendix

Synthetic Procedure for 126

2,6-Bis(1-(4-(carboxy)benzyl)-1,2,3-triazol-4-yl)pyridine (126)

To a solution of 4-(bromomethyl) benzoic acid (4.65 mmol) in 15 mL DMF/water (4:1) was added sodium azide (0.332 g, 4.65 mmol) and the reaction mixture stirred for 1 hour, yielding the azide derivative, which was not isolated, and therefore used without further purification.

To this solution was added 2,6-bis(trimethylsilylethynyl)pyridine (0.631 g, 2.33 mmol). $CuSO_4 \cdot 5H_2O$ (0.232 g, 0.93 mmol) and sodium ascorbate (0.368 g, 1.86 mmol) were added to the reaction mixture, followed by anhydrous K_2CO_3 (0.650 g, 4.70 mmol) and stirred at room temperature for 18 hours in a further 15 mL 4:1 DMF/water. EDTA/NH_4OH solution was added to the reaction mixture and stirred for 1 hour before isolating the product.

The product was isolated upon acidification of the EDTA/NH_4OH solution by dropwise addition of concentrated HCl solution until pH 7 was reached. 2 was collected as a beige solid upon suction filtration (0.705 g, 1.46 mmol, 63%). Product decomposed over 284 °C. HRMS (m/z) (ESI^-): Calculated for $C_{25}H_{18}N_7O_4^-$ m/z = 480.1426 $[M-H]^-$. Found m/z = 480.1423; Calculated for $C_{25}H_{19}N_7O_4 \cdot 0.5H_2O$, C = 57.46, H = 3.86, N = 18.76. Found C = 57.39, H = 3.75, N = 18.92. ^1H NMR (600 MHz, DMSO-d_6): δ (ppm) = 5.80 (s, 4H, CH_2), 7.45 (d, 4H, J = 8.7 Hz, Ph CH), 7.91–8.03 (m, 7H, Ph CH and pyr CH), 8.74 (s, 2H, triazolyl CH); ^{13}C NMR (150 MHz, DMSO-d_6): δ (ppm) = 52.8 (CH_2), 118.7 (3- and 5-pyr CH), 124.1 (triazolyl CH), 128.2 (phenyl CH), 129.9 (Ph CH), 130.6 (Ph qt), 138.1 (4-pyr CH), 140.8 (Ph qt), 147.5 (triazolyl qt), 149.8 (2- and 4-pyr qt), 167.03 (C=O); IR ν_{max} (cm^{-1}): 3083 (ar C–H st), 2938 (C–H st), 1719, 1692 (C=O st), 1642, 1614, 1531, 1467, 1420, 1400, 1285, 1242, 1198, 1176, 1106, 1047, 942, 822, 800, 725.

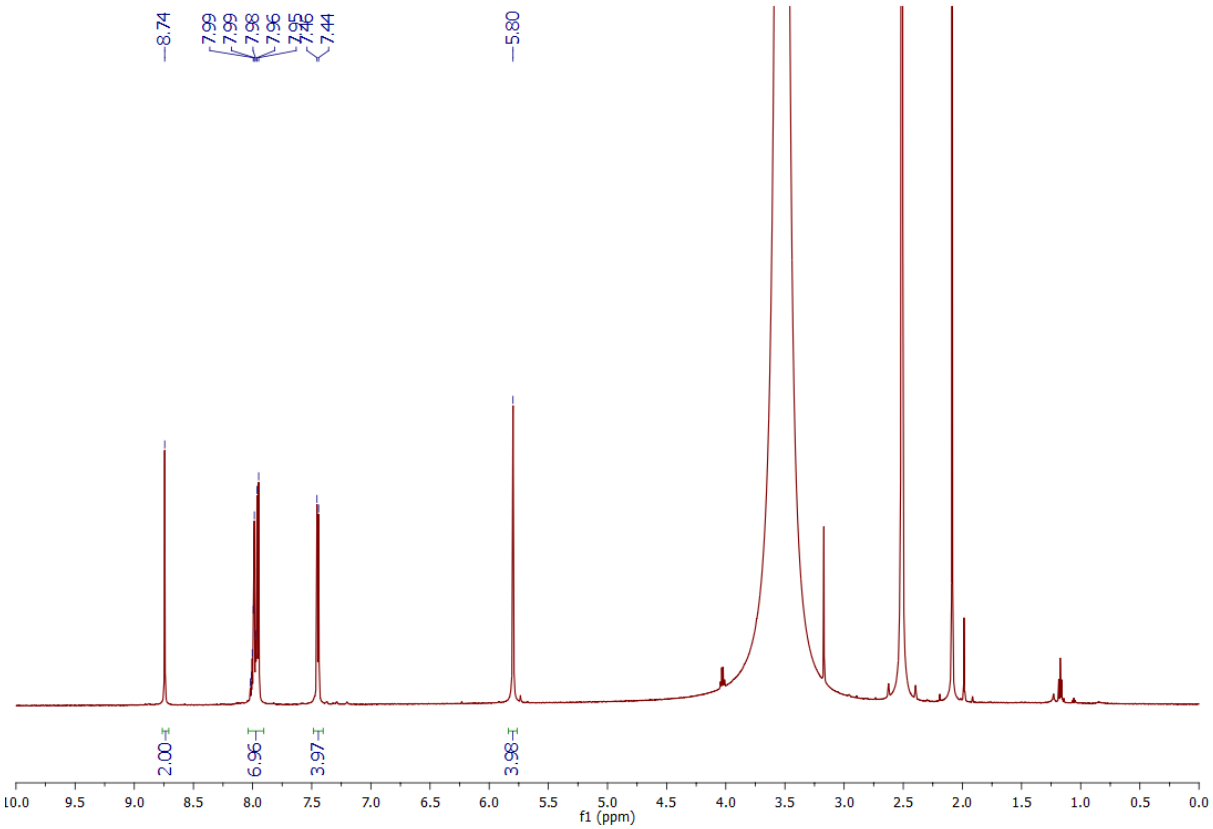

Figure A4.1 ^{1}H NMR (600 MHz, DMSO-d6) spectrum of **126**

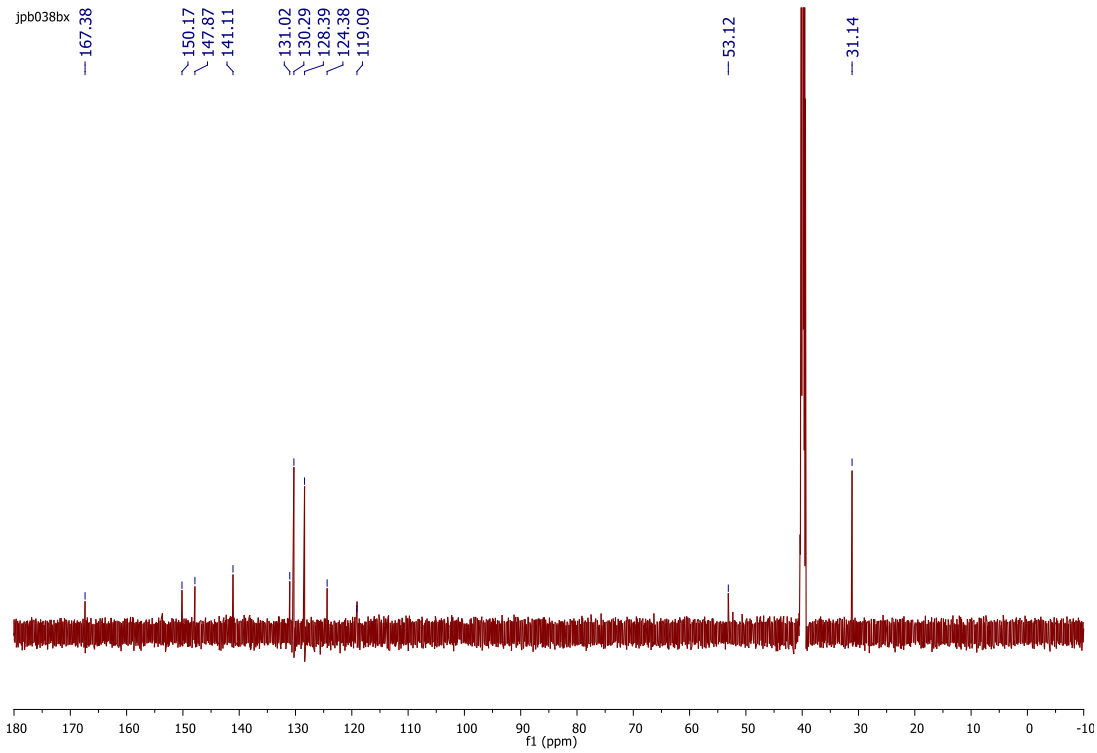

Figure A4.2 ^{13}C NMR (150 MHz, DMSO-d_6) spectrum of **126**

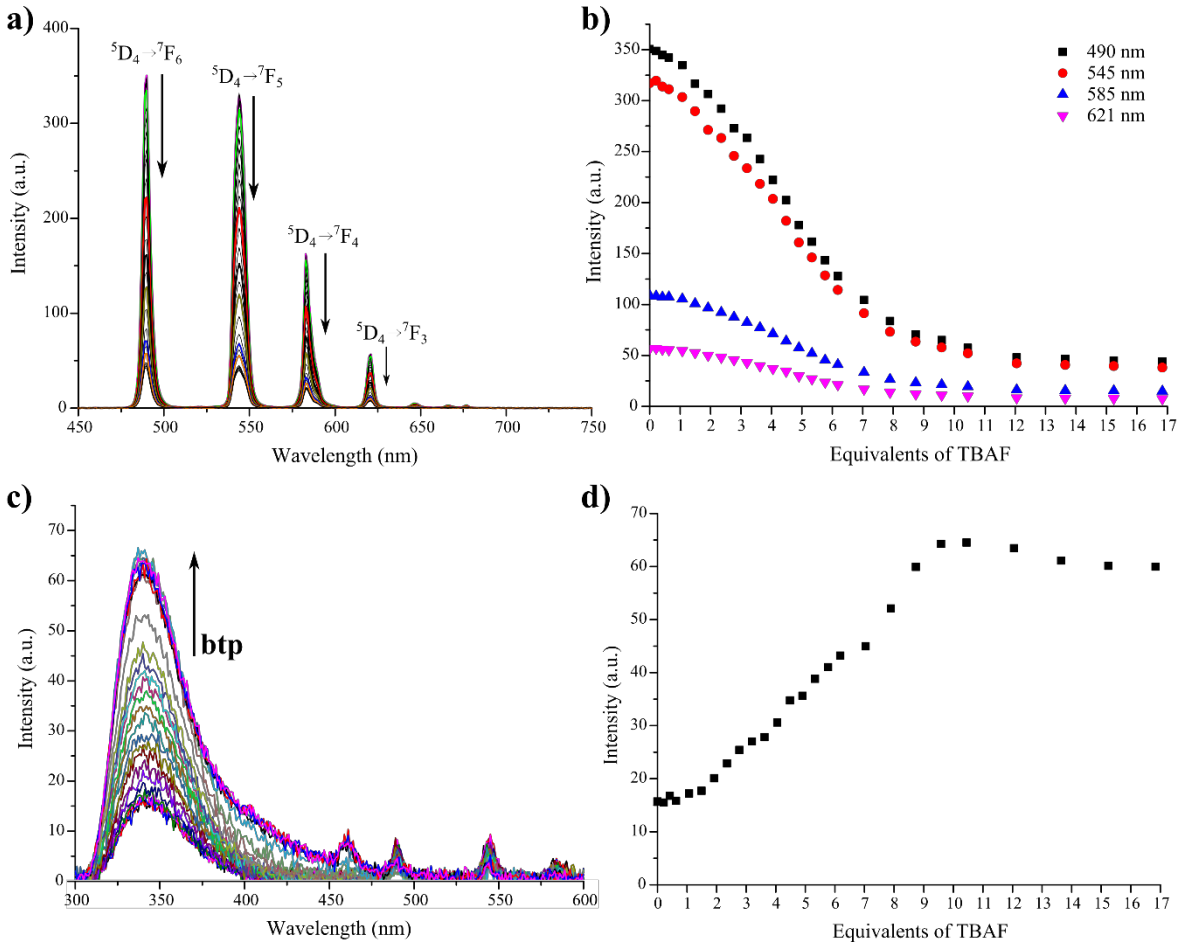

Figure A4.3 Titration of **[Tb.(126)$_3$](CF$_3$SO$_3$)$_3$** with TBAF in CH_3OH. **a)** Overlaid time-gated emission spectra upon addition of TBAF from 0 → 17 equivalents of TBAF, the arrows indicate the general trends of quenching in the $^5D_4 \rightarrow {}^7F_J$ transitions; **b)** isotherm trends of the $^5D_4 \rightarrow {}^7F_{6,5,4,3}$ transitions of **[Tb.(126)$_3$]$^{3+}$**; **c)** fluorescence spectra upon addition of TBAF from 0 → 17 equivalents of TBAF showing enhancement of the **126**-centred fluorescence; **d)** isotherm trends of λ_{em} = 345 nm showing enhancement and plateau in fluorescence signal. All measurements were made at 25 °C with **[Tb.(126)$_3$]$^{3+}$** at $c = 1 \times 10^{-5}$ M.

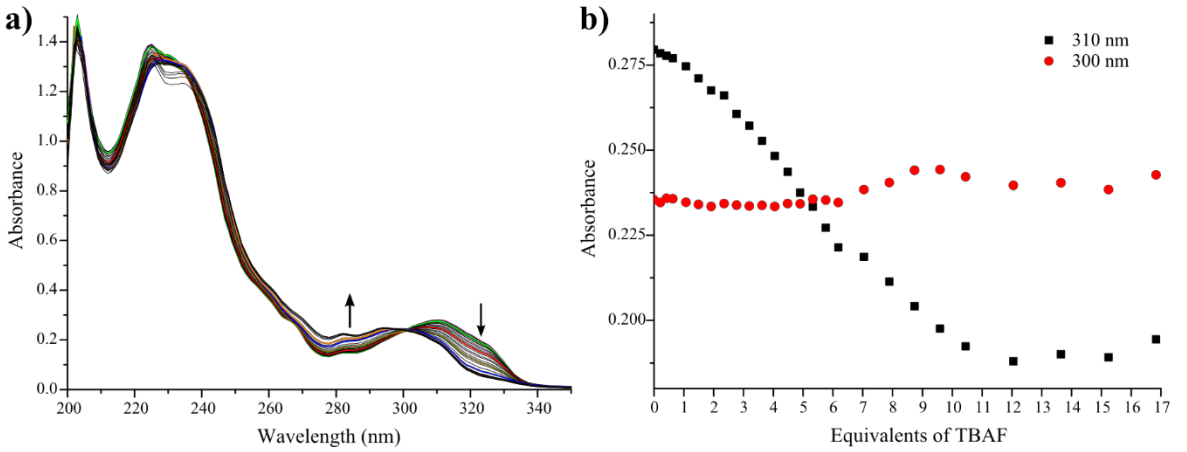

Figure A4.4 UV-visible absorption titration of **[Tb.(126)$_3$](CF$_3$SO$_3$)$_3$** with TBAF in CH_3OH: **a)** overlaid absorption spectra from 0 → 17 equivalents of TBAF showing dissociation of **[Tb.(126)$_3$]$^{3+}$** into **126** with intensity changes around an isosbestic point at λ_{abs} = 300 nm; **b)** overall absorbance change isotherms for λ_{abs} = 300 and 310 nm showing decrease in λ_{abs} = 310 associated with **[Tb.(126)$_3$]$^{3+}$** and opposite trends to self-assembly titrations.

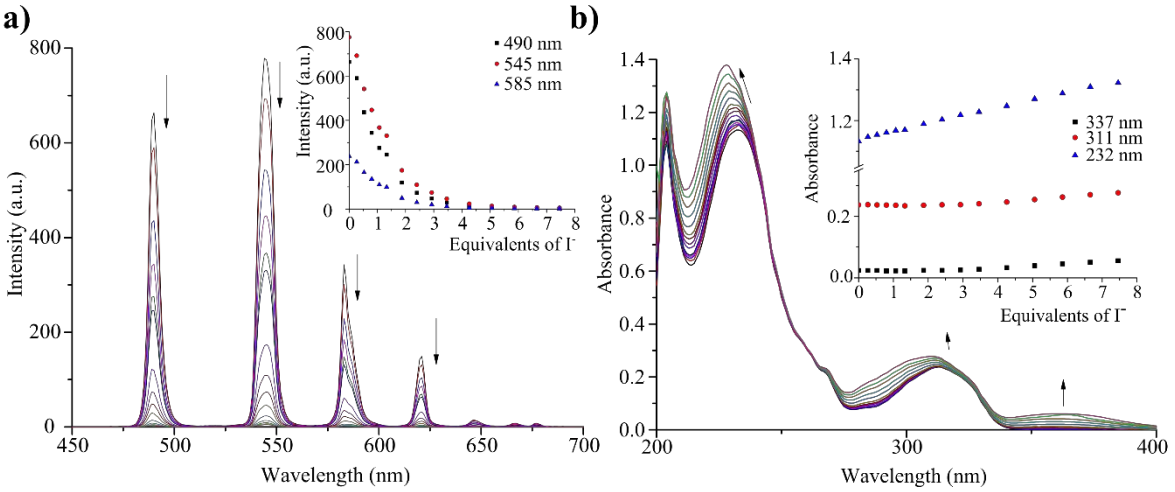

Figure A4.5 Titration of **[Tb.(126)$_3$](CF$_3$SO$_3$)$_3$** with TBAI in CH_3OH. **a)** Overlaid time-gated emission spectra upon addition of TBAI from 0 → 8 equivalents of TBAI, the arrows indicate the general trends of quenching in the $^5D_4 \rightarrow {}^7F_J$ transitions, *inset*: isotherm trends of the $^5D_4 \rightarrow {}^7F_{6,5,4,3}$ transitions of **[Tb.(126)$_3$]$^{3+}$**; and **b)** overlaid absorption spectra from 0 → 8 equivalents of TBAI showing intensity increases across the entire spectrum, most signficiantly in the band of λ_{max} = 232 nm, *inset*: overall absorbance change isotherms associated with **[Tb.(126)$_3$]$^{3+}$**.

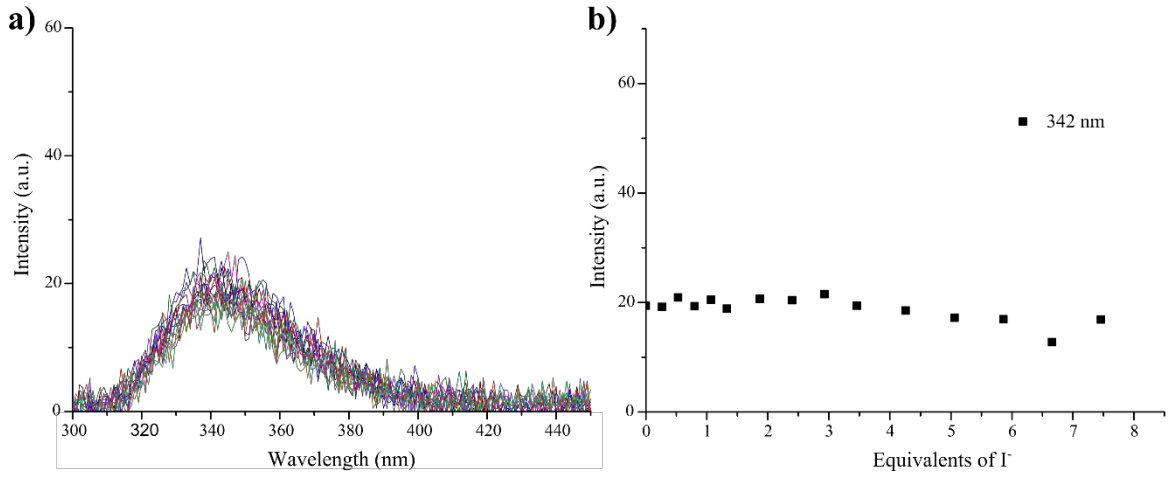

Figure A4.6 Titration of **[Tb.(126)$_3$](CF$_3$SO$_3$)$_3$** with TBAI in CH_3OH. **a)** fluorescence spectra upon addition of TBAI from 0 → 8 equivalents of TBAI showing enhancement of the **126**-centred fluorescence; **b)** isotherm trends of λ_{em} = 342 nm showing no change in fluorescence signal. All measurements were made at 25 °C with **[Tb.(126)$_3$]$^{3+}$** at $c = 1 \times 10^{-5}$ M.

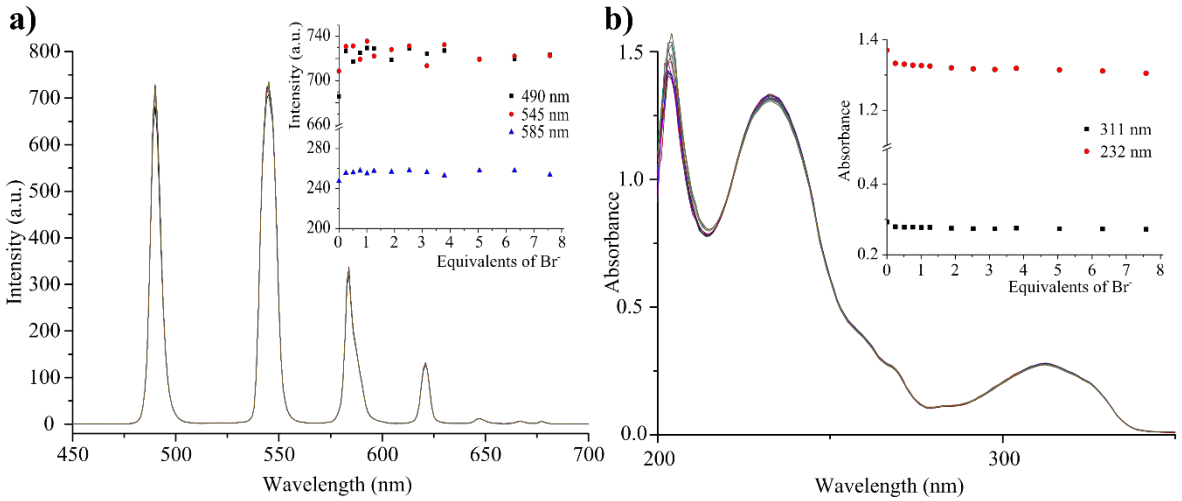

Figure A4.7 Titration of **[Tb.(126)$_3$](CF$_3$SO$_3$)$_3$** with TBACl in CH$_3$OH. **a)** Overlaid time-gated emission spectra upon addition of TBAI from 0 → 8 equivalents of TBACl, showing no changes, *inset*: isotherm trends of the $^5D_4 \rightarrow {}^7F_{6,5,4,3}$ transitions of **[Tb.(126)$_3$]$^{3+}$**; and **b)** overlaid absorption spectra from 0 → 8 equivalents of TBACl, showing no interaction with Cl^-, *inset*: overall absorbance change isotherms associated with **[Tb.(126)$_3$]$^{3+}$**.

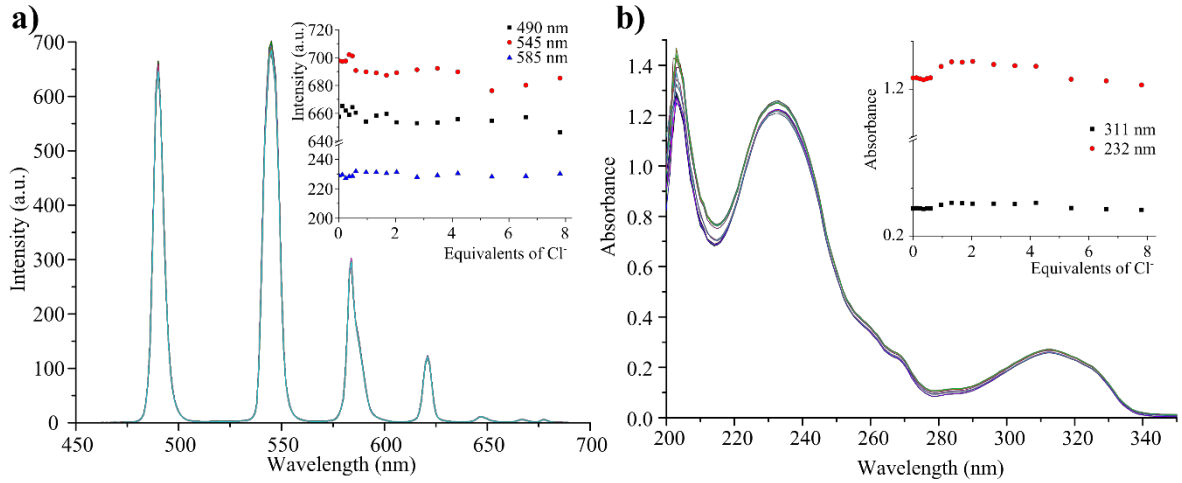

Figure A4.8 Titration of **[Tb.(126)$_3$](CF$_3$SO$_3$)$_3$** with TBABr in CH$_3$OH. **a)** Overlaid time-gated emission spectra upon addition of TBABr from 0 → 8 equivalents of TBABr, showing no changes, *inset*: isotherm trends of the $^5D_4 \rightarrow {}^7F_{6,5,4,3}$ transitions of **[Tb.(126)$_3$]$^{3+}$**; and **b)** overlaid absorption spectra from 0 → 8 equivalents of TBABr, showing no interaction with Br^-, *inset*: overall absorbance change isotherms associated with **[Tb.(126)$_3$]$^{3+}$**.

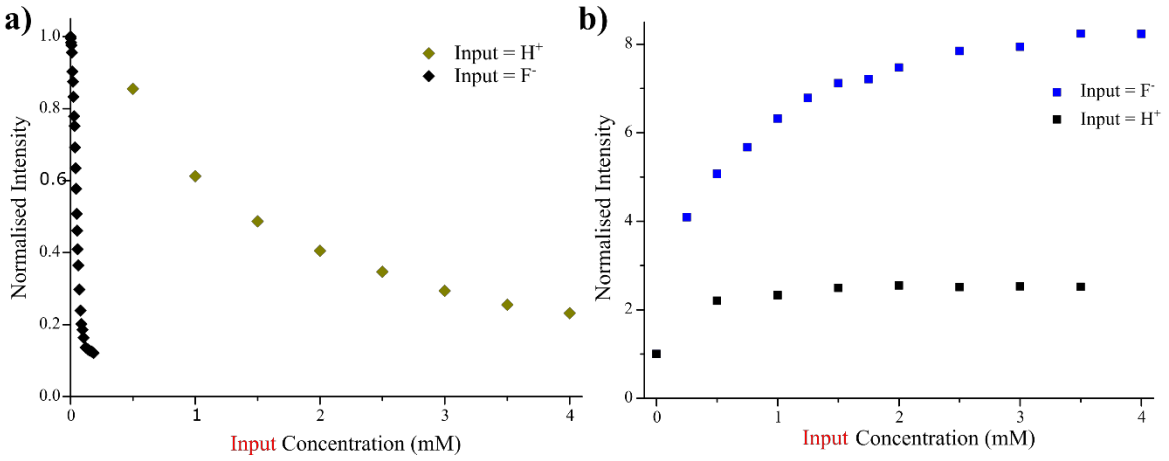

Figure A4.9 Continuous relationships between normalised luminescence intensity and [H^+] and [F^-] between 0 – 4 mM for **a)** $^5D_4 \rightarrow {}^7F_6$ transition (λ_{em} = 490 nm) of **[Tb.(126)$_3$]$^{3+}$** measured as time-gated emission upon treatment with H^+ (green) and F^- (black); **b) 57**-centred fluorescence emission (λ_{em} = 340 nm) upon treatment with H+ (black) and F- (blue).

Table A4.1 Lifetimes in H_2O and D_2O for **[Eu.(123(*S,S*))$_3$]$^{3+}$** and **[Tb.(126)$_3$]$^{3+}$** along with the calculated *q*-values from Horrocks' and Parker's models. [a]also reported in Chapter 3. [b]measured by Dr Joseph Byrne.

Complex	τOH , ms	τOD, ms	Horrocks *q* (± 0.5)	Parker *q* (± 0.5)
[a]**[Eu.(123(*S,S*))$_3$]$^{3+}$**	1.33±0.01	2.44±0.01	0.11 (~ 0)	-0.34 (~ 0)
[b]**[Tb.(126)$_3$]$^{3+}$**	1.06±0.05	1.98±0.01	0.01 (~ 0)	-0.2 (~ 0)

Comment A4.1 Comment upon the attempted formation of p(HEMA-*co*-EGDMA) hydrogels containing **[Eu.(123(*S,S*))$_3$]$^{3+}$** and **[Tb.(126)$_3$]$^{3+}$** and operation of an aqueous MLGM.

The precursor polymer monoliths for poly(HEMA-*co*-EGDMA) hydrogels were synthesised in the same manner as in described for **[Eu.(123(*S,S*))$_3$]$^{3+}$** hydrogels in Section 3.7.1; however, small modifications were required for successful inclusion of **[Tb.(126)$_3$]$^{3+}$**. The complex **[Eu.(123(*S,S*))$_3$](CF$_3$SO$_3$)$_3$** was dissolved into HEMA at 0.02 % w/w (*ca.* 2.5 mg in 10 mL) with 1 % w/w EGDMA added as cross-linker. After the formation of a homogenous solution, a concentrated solution of **[Tb.(126)$_3$](CF$_3$SO$_3$)$_3$** (1.0 mg in 200 μL) was added and the resulting mixture stirred until **[Tb.(126)$_3$](CF$_3$SO$_3$)$_3$** was also fully dissolved. AIBN (1% w/w) was added and the solution was transferred to a mould lined with

a non-stick coating with a thickness of 1.2 mm and placed at 90 °C to initiate thermal polymerisation. The bulk polymerisation of the hard acrylic monolith was complete after 90 minutes and the material was heat-cured at 90 °C for a further 4.5 hours before removing and allowing the material to cool to ambient temperature, after which the hard acrylic materials were released from the mould.

Visual inspection, shown in Figure A4.11, prior to conditioning showed the materials to be emissive and this emission visible to the naked eye, under irradiation at λ_{ex} = 254 nm. The colour was additive from Eu^{III} and Tb^{III} centred emission and samples were Yellow Green (YG-gY) to Yellow (Y) in colour. The encapsulation of the two complexes within the p(HEMA) matrix was found to enhance the luminescence performance of both complexes independently, with the dry materials not displaying the same intensity balance determined for a 3:1 concentration ratio in solution. The acrylic materials were conditioned by swelling in deionised water for several days periodically exchanging the external solution to wash the internal environment of the polymer hydrogels of unreacted monomers, initiator and contaminants such as monomer stabilisers. Swelling the hydrogels in deionised water there was an immediate quenching of Tb^{III}-centred emission; no similar quenching upon swelling was observed for Eu^{III} emission from **[Eu.(123(*S*,*S*))$_3$]$^{3+}$**. The selectivity of this quenching for the Tb^{III} complex was confirmed and, indeed, the fully aqueous p(HEMA) anion sensing has not been successfully reproduced following our preliminary investigation; the cause remains unknown. The water instability of **[Tb.(126)$_3$]$^{3+}$** was later confirmed by the titration of the complex in CH_3OH against added water. Mixed solvent systems were explored and aqueous mixtures with miscible spectroscopic-grade organic solvents were used to swell the p(HEMA) gels described above; the success of this approach was limited. In the case of CH_3OH, the swelling in low and high percentage mixed systems resulted in mechanical damage to the materials and made the gels inappropriate to handle; additionally these materials lacked the clarity necessary for spectroscopic measurements to be made reproducibly. A solvent system of CH_3CN/H_2O was found to sustain the Tb^{III} luminescence for an increased period of time, however this effect was limited and there was substantial sensitivity towards the CH_3CN content and small changes readily led to dehydration of the material. It is proposed that the resilience of the Tb^{III}-centred emission in CH_3CN/H_2O arose simply from the reduced wetting and slower wetting kinetics of the bulk material and was not appropriately reproducible in equilibration and optical properties. It has been established that ionic strengths can aid in the stabilisation of charged species in solution. A further approach was undertaken and the polymer gels were swelled in ionic strengths of NaCl that

did not dehydrate the material (0 → 1 M) however, this also failed to stabilise the cationic **[Tb.(126)$_3$]$^{3+}$** complex. No conditional change was found to be appropriate to address the quenching of Tb^{III}-centred emission by water, therefore the polymers gels were developed for anhydrous operation. As described above, p(HEMA) was structurally unstable in CH_3OH, therefore a change in the co-polymer matrix was made as a potential solution to the problem..

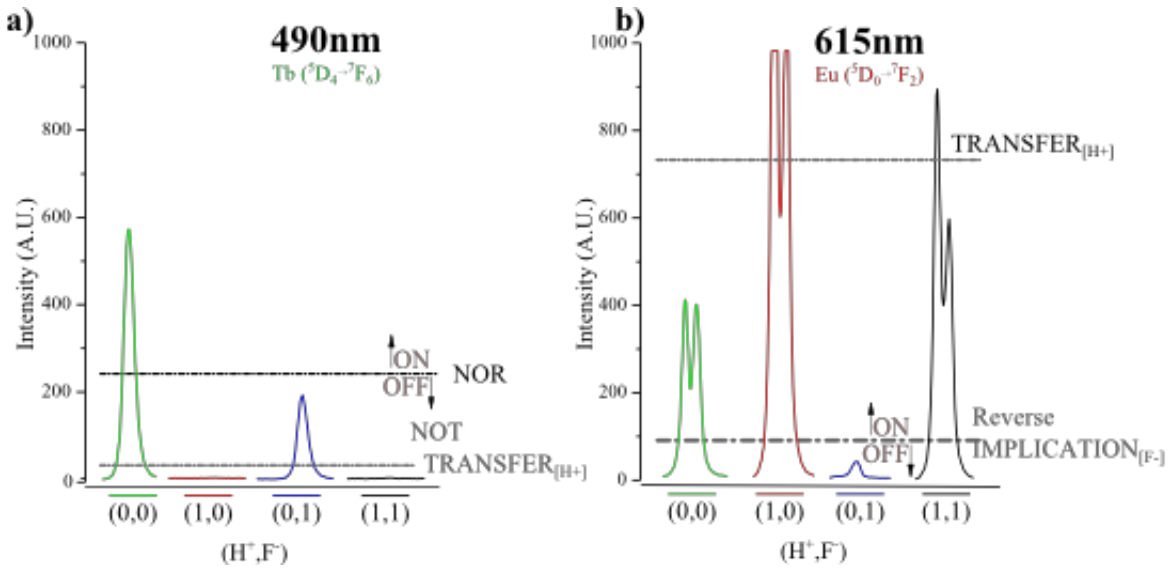

Figure A4.10 Additional thresholds possible for the parameterisation of the solution-based MLGM on: **a)** Tb^{III}-centred emission from **[Tb.(126)$_3$]$^{3+}$** resulting in NOR or NOT-TRANSFER$_{[H+]}$ logic functions; and **b)** Eu^{III}-centred emission from **[Eu.(123(*S,S*))$_3$]$^{3+}$** resulting in TRANSFER$_{[H+]}$ and Reverse-IMPLICATION$_{[F-]}$

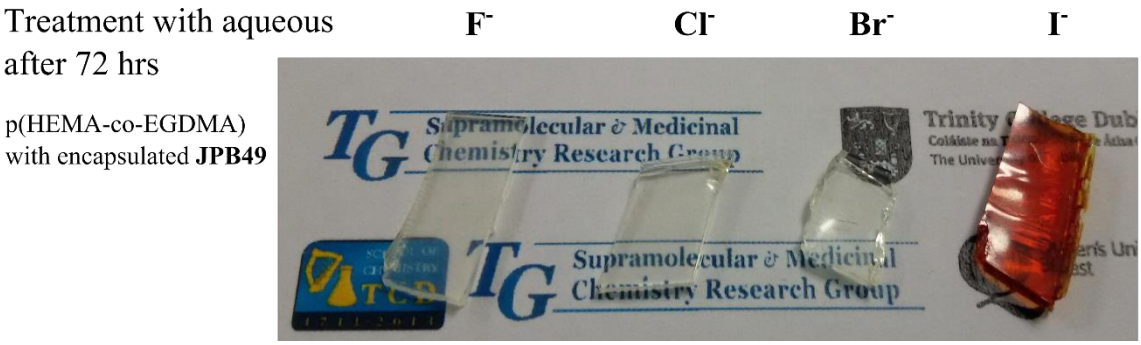

Figure A4.11 a) Photographs of **[Tb.(126)$_3$]$^{3+}$**@p(HEMA-*co*-EGDMA) treated with KF, KCl, KBr and KI over the period of 48 hours showing optical ageing in the presence of I^-.

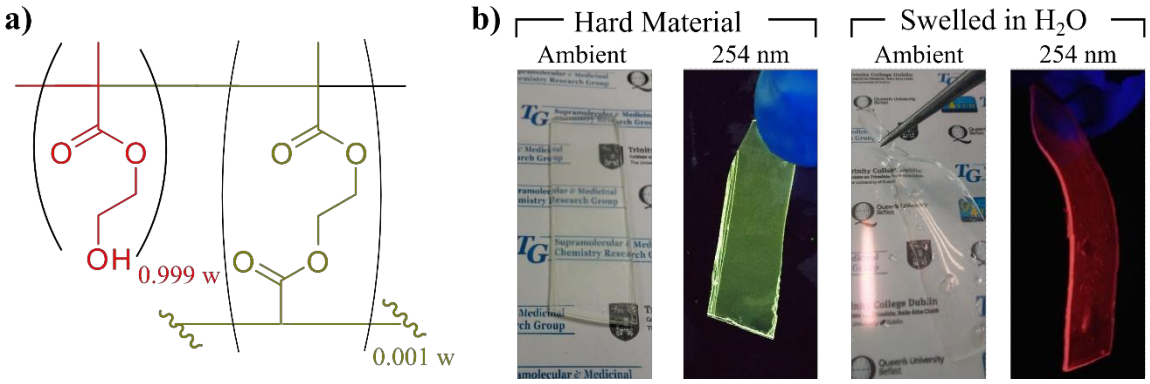

Figure A4.12 Polymer hydrogels containing **[Eu.(123(*S*,*S*))$_3$]$^{3+}$** and **[Tb.(126)$_3$]$^{3+}$**, **a)** structural representation of the polymer matrix as a random co-polymer of HEMA (red) and EGDMA (green); **b)** photographs of visual inspection of **i)** unconditioned hard acrylic monolith under ambient light; **ii)** swelled polymer hydrogel after conditioning under ambient light; **iii)** uncondtitioned hard acrylic monolith under UV-light (λ = 254 nm) showing "YG-gY-Y" emission; and iv) swelled polymer hydrogel after conditioning under UV-light (λ = 254 nm) showing quenched emission from **[Tb.(126)$_3$]$^{3+}$**.

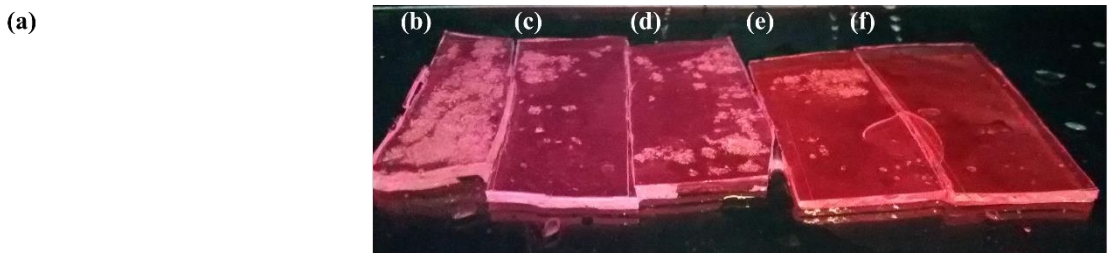

Figure A4.13 Photographs under UV-light (λ_{em} = 254 nm) of attempted ionic strength stabilisation of **[Tb.(126)$_3$]$^{3+}$** using NaCl (aq.) at various concentrations showing different degrees of hydration reflected in the emission colour. **a)** hard polymer showing Yg-mixed emission from **[Tb.(126)$_3$]$^{3+}$** and **[Eu.(123(*S*,*S*))$_3$]$^{3+}$**; and the material swelled in aq. NaCl at: **b)** 1M; **c)** 0.5 M; **d)** 0.25 M; **e)** 0.1 M; and **f)** 0 M, showing quenched terbium emission and more pink emission from **[Eu.(123(*S*,*S*))$_3$]$^{3+}$** with high salt concentrations swelling volumes (reduced swelling volumes).

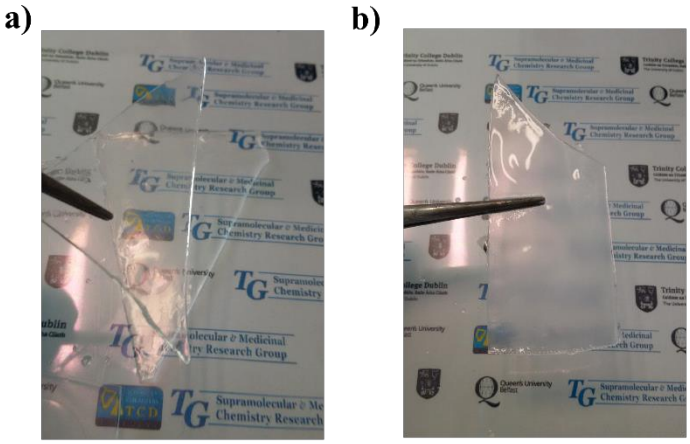

100% HEMA in CH_3OH | 100% HEMA in EtOH (2hrs)

Figure A4.14 Photographs of **a)** p(HEMA-*co*-EGDMA) swelled in CH_3OH showing poor mechanical stability and is broken by gentle flexing of the soft material: and **b)** p(HEMA-*co*-EGDMA) swelled in EtOH, showing loss of optical clarity after swelling.

Table A4.2 Tabulated threshold criteria applied to the solution-based MLGM.

Emission Wavelength (nm)	Centre	Type	Nature	Normalised Threshold (% enhancement)
490	Tb	Phosph.	$^5D_4 \rightarrow {}^7F_6$	-62
615	Eu	Phosph.	$^5D_0 \rightarrow {}^7F_2$	-90
338	**126**	Fluor.	S* → S	+360

Table A4.3 Tabulated threshold criteria applied to the organogel MLGM.

Emission Wavelength (nm)	Centre	Type	Nature	Normalised Threshold (% enhancement)
490	Tb	Phosph.	$^5D_4 \rightarrow {}^7F_6$	-50
615	Eu	Phosph.	$^5D_0 \rightarrow {}^7F_2$	-85
345	**126**	Fluor.	S* → S	+70

a)

Input$_1$ $[H^+]^a$	**Input$_2$** $[F^-]^b$	**Output$_1$** **615 nm**^{c}	**Output$_2$** **490 nm**^{c}	**Output$_3$** **338 nm**^{d}
0	0	1	1	0
1	0	1	0	0
0	1	0	0	1
1	1	1	0	1
		Reverse IMPLICATION$_{[H^+]}$	NOR	TRANSFER$_{[F^-]}$

b)

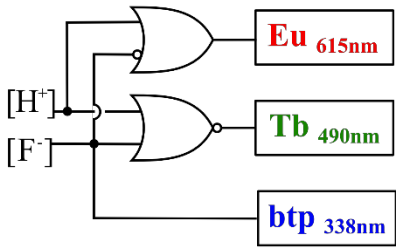

Figure A4.15 Logical analysis of organogel MLGM. **a)** Truth table for each Input state indicating 1 or 0 as Output for each emission channel: λ_{em} = 615 nm (**[Eu.(123(*S*,*S*))$_3$]**$^{3+}$ time-gated emission), λ_{em} = 490 nm (**[Tb.(57)$_3$]**$^{3+}$ time-gted emiission) and λ_{em} = 338 nm (**126**-centred fluorescence) and the respective logic functions which mirror the solution model, Figure 5.18; **b)** logic circuit diagram for parallel solution implementation of the MLGM outputs.

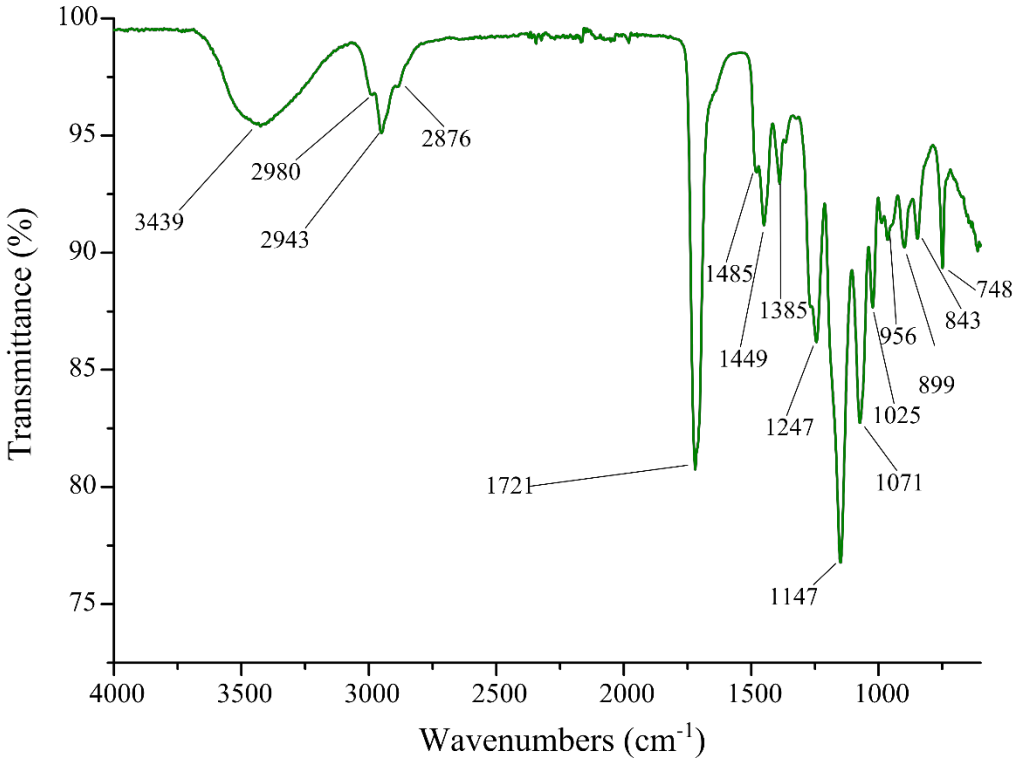

Figure A4.16 IR spectrum (ATR) of **[Eu.(123(*S*,*S*))$_3$]$_2$[Tb.(126)$_3$]$_1$@p(HEMA-*co*-EGDMA-*co*-MMA)** showing the characteristic peaks of p(HEMA) backbone at 1721 cm^{-1}.

A5. Chapter 5 Appendix

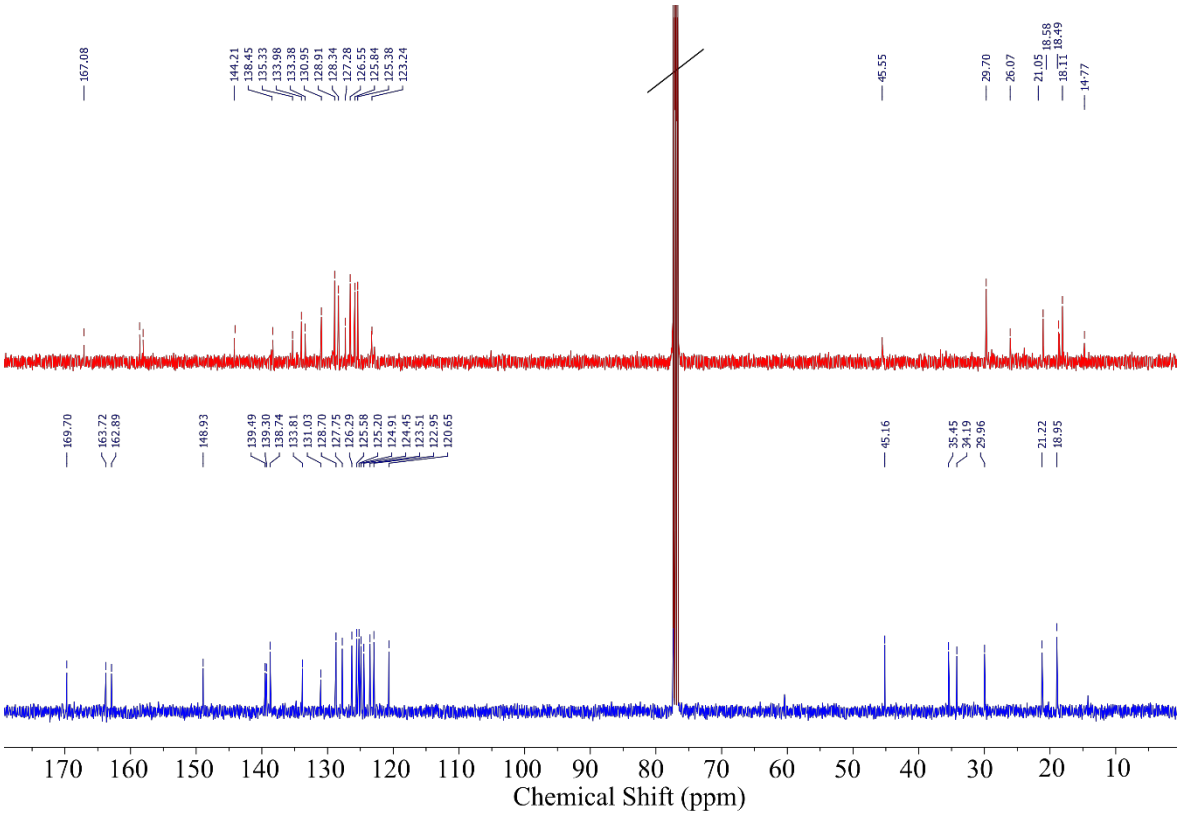

Figure A5.1 ^{13}C NMR (600 MHz, $CDCl_3$) for **127(*S*,*S*)** (red) and **128(*S*)** (blue).

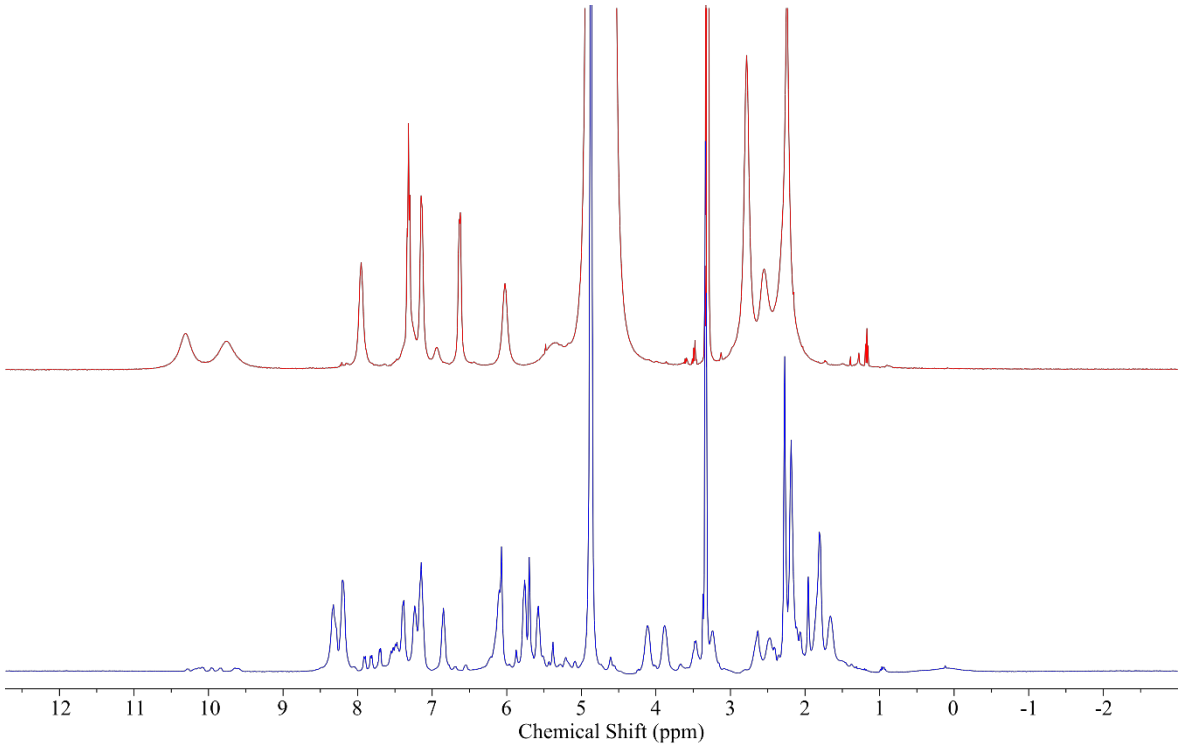

Figure A5.2 ^{1}H NMR (400 MHz, CD_3OD) for **[Eu.(127(*S*,*S*))$_3$](CF$_3$SO$_3$)$_3$** (red) and **[Eu.(128(*S*))$_2$](CF$_3$SO$_3$)$_3$** (blue), showing similar LIS consistent with similar geometry and crystal field splitting. Multiple species clearly visible for **[Eu.(128(*S*))$_2$](CF$_3$SO$_3$)$_3$** (blue) while **[Eu.(127(*S*,*S*))$_3$](CF$_3$SO$_3$)$_3$** (red) showed more broadening.

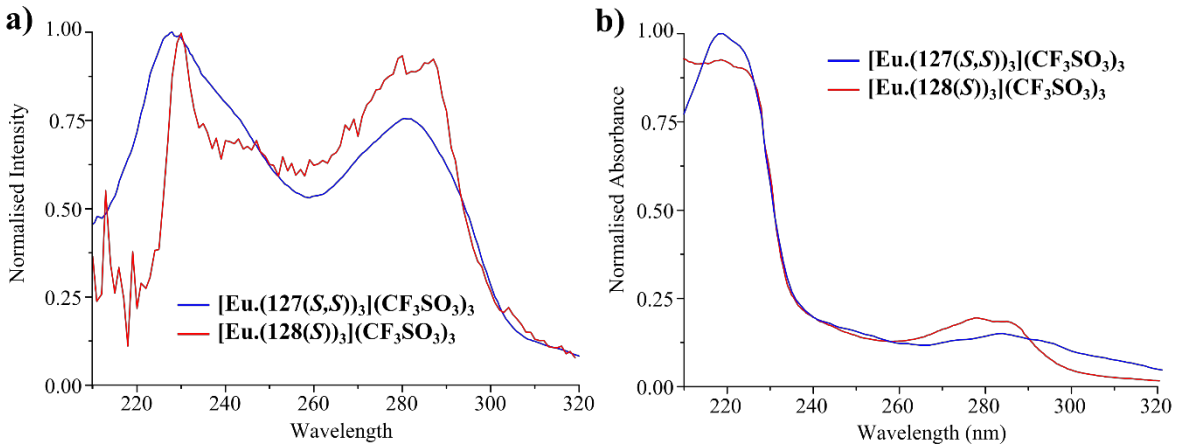

Figure A5.3 a) Normalised excitation spectra of **[Eu.(127(*S,S*))$_3$](CF$_3$SO$_3$)$_3$** (blue) and **[Eu.(128(*S*))$_2$](CF$_3$SO$_3$)$_3$** (red), showing key structural features of the ligand absorbance bands in CH_3CN; and **b)** normalised absorption spectra for **[Eu.(127(*S,S*))$_3$](CF$_3$SO$_3$)$_3$** and **[Eu.(128(*S*))$_3$](CF$_3$SO$_3$)$_3$** in CH_3CN.

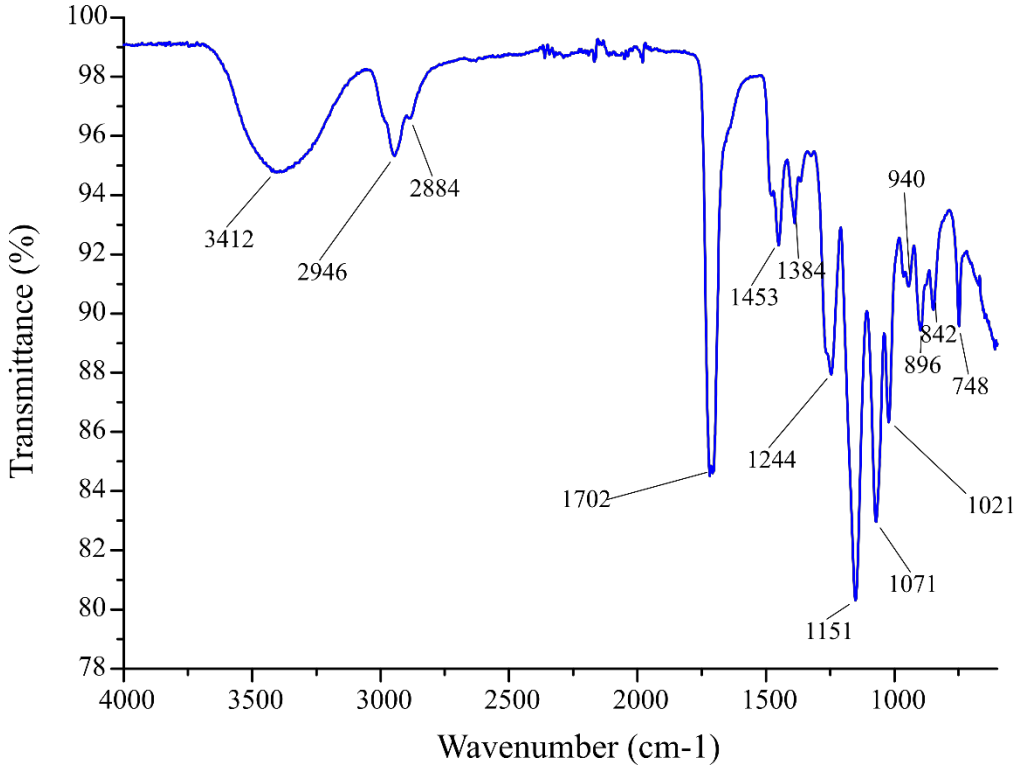

Figure A5.4 IR spectrum (ATR) of p(HEMA-co-EGDMA-co-**127(S,S)**)

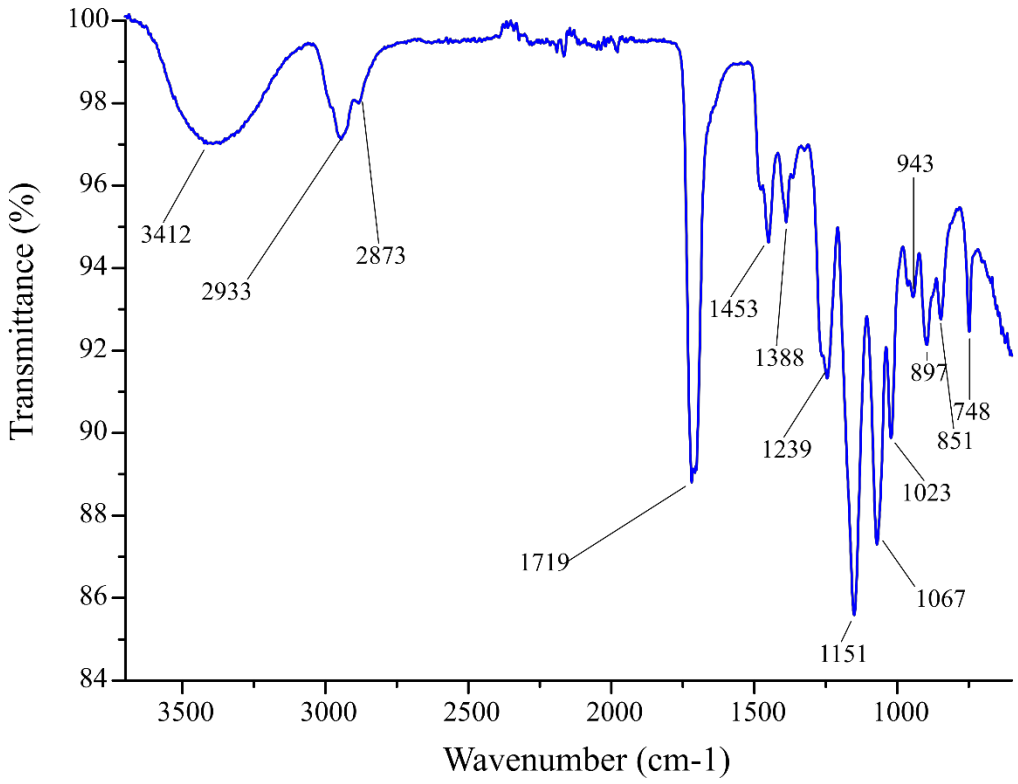

Figure A5.5 IR spectrum (ATR) of p(HEMA-co-EGDMA-co-**128(*S*)**)

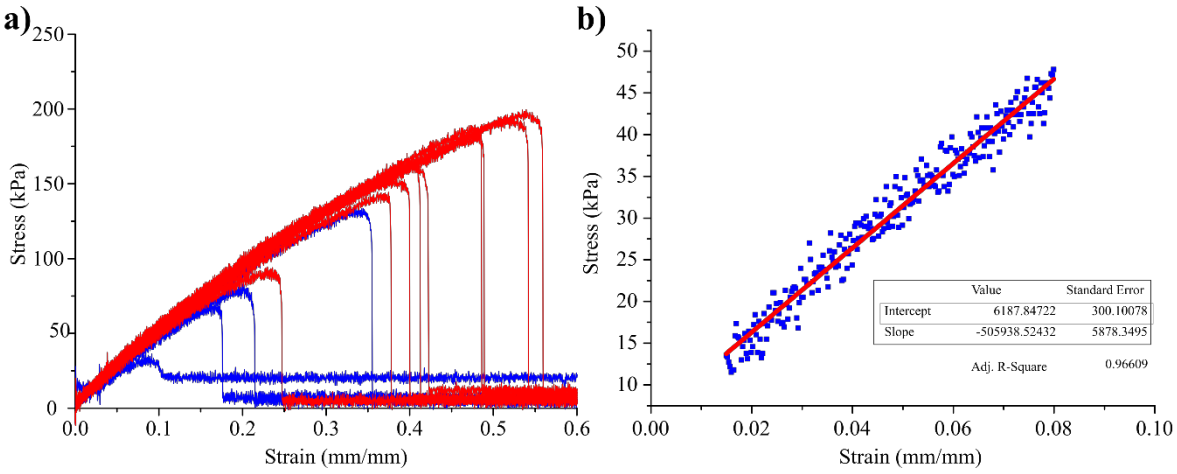

Figure A5.6 a) Representative stress vs. strain curves from tensile tests recorded for p(HEMA-co-**127(S,S)**) containing 0.05 wt% **127(S,S)** swelled in H_2O (blue) and in 0.33 equivalents of Eu^{III} (red); and **b)** zoomed region of the linear elastic response between 0.02 → 0.10 mm/mm tensile strain (points) of for p(HEMA-co-EGDMA-co-**127(S,S)**) swelled in H_2O and the linear fit to calculate elastic tensile modulus (m, line). These represent one repetition, final modulus values were determined as the average of 10 replicates. Similar moduli were calculated with H_2O and Eu^{III}(aq), minor increases in average elongation was observed in Eu^{III} but was not statistically signficant as a result of limited sample size.

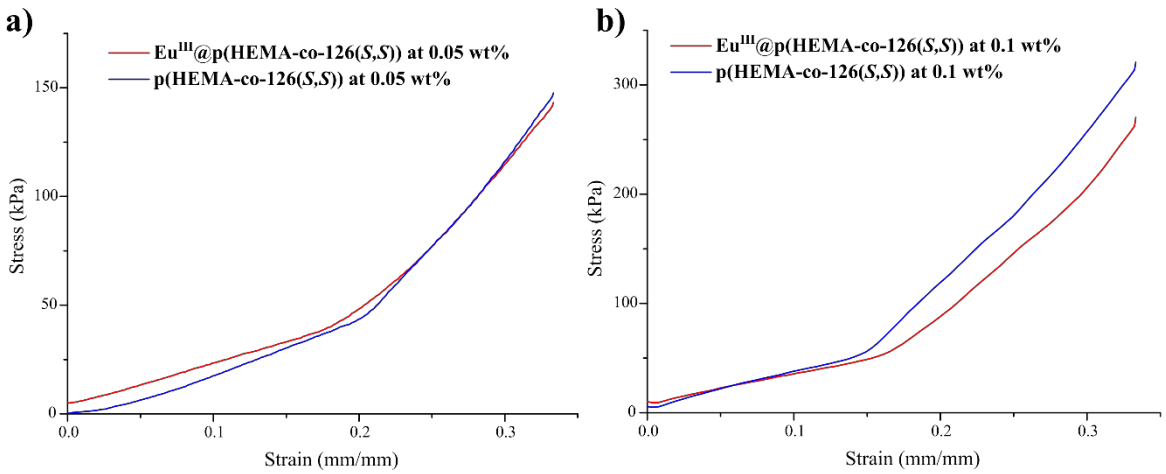

Figure A5.7 a) Representative stress vs. strain curves from compression tests recorded for p(HEMA-co-**127(S,S)**) containing 0.05 wt% **127(S,S)** swelled in H_2O (blue) and in 0.33 equivalents of Eu^{III} (red) between 0 → 25% compressive strain; and **b)** representative stress vs. strain curves from compression tests recorded for p(HEMA-co-EGDMA-co-**127(S,S)**) containing 0.1 wt% **127(S,S)** swelled in H_2O (blue) and in 0.33 equivalents of Eu^{III} (red) between 0 → 25% compressive strain. These represent one repetition, final modulus values were determined as the average of 12 replicates.

A6. Publications

Coordination Chemistry Reviews 273–274 (2014) 226–241

Contents lists available at ScienceDirect

Coordination Chemistry Reviews

journal homepage: www.elsevier.com/locate/ccr

Review

Development of responsive visibly and NIR luminescent and supramolecular coordination self-assemblies using lanthanide ion directed synthesis

Samuel J. Bradberry, Aramballi Jayant Savyasachi, Miguel Martinez-Calvo, Thorfinnur Gunnlaugsson*

School of Chemistry and Trinity Biomedical Sciences Institute, Trinity College Dublin, University of Dublin, Dublin 2, Ireland

Contents

ARTICLE INFO

Article history:
Received 9 January 2014
Received in revised form 19 March 2014
Accepted 20 March 2014
Available online 4 April 2014

This review is dedicated to Professor David Parker FRS for his inspiration, guidance, support and friendship for the last 18 years.

Keywords:
Supramolecular chemistry

ABSTRACT

This review details the progress made in our laboratory in Dublin within the area of supramolecular lanthanide chemistry; where the main objective has been to develop functional lanthanide luminescent systems that emit within the visible or the near-infrared regions of the electromagnetic spectrum. The application of the lanthanide-centred assembly is two-fold, firstly to use it for sensing application of biologically and environmentally relevant anions, and secondly to use the emission to report on the formation of lanthanide directed self-assembly processes. This review begins with the progress made from the use of lanthanide cyclen (1,4,7,10-tetraazacyclododecane) complexes: to develop: displacement assays for sensing or probing applications; for their incorporations onto gold nanoparticles where the lanthanide emission can be 'switched on-off' by external stimuli; and their application in the formation of mixed *f–d* metal ion based self-assemblies and sensors and imaging agents for DNA. The second part of this review focuses on the development of self-assemblies formed using 2,6-diamidopyridyl based ligands. A variety of ligands are presented that have been employed in the formation of chiral self-assembly bundles,

Abbreviations: BTA, benzene-1,3,5-tricarboxamide; Cyclen, 1,4,7,10-tetraazacyclo-dodecane; bipy, 2,2′-bipyridine; CD, circular dichroism; CPL, circularly polarised luminescence; DNA, deoxyribose nucleic acid; dpa, dipicolinic acid; EDCI, 1-ethyl-3-(3-dimethylaminopropyl)carbodiimide; EDX, energy-dispersive X-ray spectroscopy; ESMS, electro-spray mass spectrometry; HEMA, (2-hydroxyethyl)methacrylate; HRMS, high resolution mass spectrometry; IR, infrared; MLCT, metal-to-ligand charge transfer; MRI, magnetic resonance imaging; NMR, nuclear magnetic resonance; phen, 1-10-phenanthroline; MMA, methylmethacrylate; RCM, ring closing metathesis; SAMs, self-assembled monolayers; SEM, scanning electron microscopy; TEM, transmission electron microscopy; *terpy*, 2,2′:6′,2″-terpyridine.

* Corresponding author. Tel.: +353 1 896 3459; fax: +353 1 671 2826.
E-mail address: gunnlaut@tcd.ie (T. Gunnlaugsson).

http://dx.doi.org/10.1016/j.ccr.2014.03.023
0010-8545/

Faraday Discussions

Cite this: *Faraday Discuss.*, 2015, **185**, 413

PAPER

Quantifying the formation of chiral luminescent lanthanide assemblies in an aqueous medium through chiroptical spectroscopy and generation of luminescent hydrogels†

Samuel J. Bradberry,[a] Aramballi Jayant Savyasachi,[a] Robert D. Peacock[b] and Thorfinnur Gunnlaugsson*[a]

Received 10th June 2015, Accepted 26th June 2015
DOI: 10.1039/c5fd00105f

Herein we present the synthesis and the photophysical evaluation of water-soluble chiral ligands (**2**·(*R*,*R*) and **2**·(*S*,*S*)) and their application in the formation of lanthanide directed self-assembled structures. These pyridine-2,6-dicarboxylic amide based ligands, possessing two naphthalene moieties as sensitising antennae, that can be used to populate the excited state of lanthanide ions, were structurally modified using 3-propanesultone and caesium carbonate, allowing for the incorporation of a water-solubilising sulfonate motif. We show, using microwave synthesis, that Eu(III) forms chiral complexes in 1 : 3 (M : L) stoichiometries (Eu·[**2**·(*R*,*R*)]$_3$ and Eu·[**2**·(*S*,*S*)]$_3$) with these ligands, and that the red Eu(III)-centred emission arising from these complexes has quantum yields (Φ_{tot}) of 12% in water. Both circular dichroism (CD) and circular polarised luminescence (CPL) analysis show that the complexes are chiral; giving rise to characteristic CD and CPL signatures for both the Λ and the Δ complexes, which both possess characteristic luminescence dissymmetry factors (g_{lum}), describing the structure in solution. The self-assembly process was also monitored *in situ* by observing the changes in the ligand absorption and fluorescence emission, as well as in the Eu(III) luminescence. The change, fitted using non-linear regression analysis, demonstrated high binding affinity for Eu(III) which in part can be assigned to being driven by additional hydrophobic effects. Moreover, using CD spectroscopy, the changes in the chiroptical properties of both (**2**·(*R*,*R*) and **2**·(*S*,*S*)) were monitored in real time. Fitting the changes in the CD spectra allowed for the step-wise binding constants to be determined for these assemblies; these matched well with those determined from both the ground and the excited state changes. Both the ligands and the Eu(III)

[a]*School of Chemistry and Trinity Biomedical Sciences Institute (TBSI), Trinity College Dublin, University of Dublin, Dublin 2, Ireland. E-mail: gunnlaut@tcd.ie; Fax: +353 1 671 2826; Tel: +353 1 896 3459*
[b]*School of Chemistry, University of Glasgow, Glasgow, G12 8QQ, Scotland, UK*

† Electronic supplementary information (ESI) available. See DOI: 10.1039/c5fd00105f

JACS
JOURNAL OF THE AMERICAN CHEMICAL SOCIETY
Article
pubs.acs.org/JACS

Luminescent Lanthanide Cyclen-Based Enzymatic Assay Capable of Diagnosing the Onset of Catheter-Associated Urinary Tract Infections Both in Solution and within Polymeric Hydrogels

Esther M. Surender,[†] Samuel J. Bradberry,[†] Sandra A. Bright,[‡] Colin P. McCoy,[§] D. Clive Williams,[‡] and Thorfinnur Gunnlaugsson*[,†]

[†]School of Chemistry, Trinity Biomedical Sciences Institute (TBSI), Trinity College Dublin, The University of Dublin, Dublin 2, Ireland

[‡]School of Biochemistry and Immunology, Trinity Biomedical Sciences Institute (TBSI), Trinity College Dublin, The University of Dublin, Dublin 2, Ireland

[§]School of Pharmacy, Queen's University Belfast, 97 Lisburn Road, Belfast, BT9 7BL, Northern Ireland, U.K.

Supporting Information

ABSTRACT: Herein we present a supramolecular (delayed luminescent) Eu(III)-based pH-responsive probe/sensor with the ability to detect the urease-mediated hydrolysis of urea in aqueous solution. A series of photophysical titrations show this Eu(III) chelate behaves as an "*on*−*off*" luminescent switching probe, with its luminescence being quenched upon urea being enzymatically converted into ammonia and carbon dioxide. Calculation of the rate constant (k) and activation energy (E_a) for this hydrolysis reaction are detailed; the results demonstrate a direct observation of enzymatic activity in solution by the sensor. The potential application of this probe in detecting the onset of catheter-associated urinary tract infections (CAUTIs) is also demonstrated by incorporating **1.Eu** into water-permeable hydrogels that can be utilized as an alternative coating for catheters.

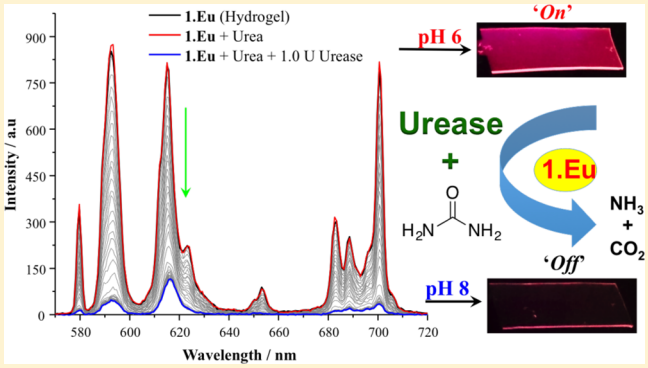

INTRODUCTION

Catheter-associated urinary tract infection (CAUTI) is one of the most common health-care associated infections worldwide, accounting for up to 40% of all nosocomial infections.[1,2] Approximately 20% of all hospitalized patients are catheterized.[2] Currently, the most commonly deployed prosthetic medical device is the Foley indwelling urethral catheter.[1d,2b] The development of CAUTIs has been directly linked to the duration of catheterization; nearly 100% of patients undergoing long-term catheterization (≥28 days) are found to develop catheter-associated bacteriuria (CAB).[1a−c] While most cases of CAB are asymptomatic and do not require treatment, some individuals can experience symptomatic episodes of CAUTI, which can result in pyelonephritis, septicaemic or endotoxic shock, and ultimately death.[1c,2b] These episodes are triggered by the occurrence of catheter encrustation, where the formation of crystalline polymicrobial-based biofilms on the inner and outer surfaces of the catheter tube causes the device to become blocked, and as such obstructs urinary flow.[3] The bacterial species most associated with catheter encrustation and CAUTI are urease-producing microorganisms, specifically *Proteus mirabilis*, *Proteus vulgaris*, and *Providencia rettgeri*.[1,2] Their ability to secrete urease, an enzyme that catalyzes the hydrolysis of urea (one of the primary constituents within urine) into ammonia and carbon dioxide, results in the pH of the urine being increased toward alkaline, which induces the precipitation of calcium and magnesium phosphate crystals from the urine.[4] These crystals accumulate within the bacterial layers of the biofilm, making it highly crystalline with increased resistance both to the hosts immune system and to antibiotic treatment.[3a,5] Several strategies have been employed to prevent the onset of CAUTI, the majority of which involve coating or impregnating the catheter material (hydrogels and other related soft materials) with antimicrobial agents that will counteract bacterial adhesion.[1c,2a] These agents include silver alloys,[6] antibacterials,[7] liposomes,[8] and urease inhibitors.[9] Nevertheless, no single prosthetic medical device currently exists that is able to completely inhibit CAB from developing during catheterization. Consequently, focus has turned to finding ways in which CAUTI can be quickly diagnosed in order to permit early treatment. The primary diagnostic tool currently utilized in the clinic to monitor CAB is the bromothymol blue colorimetric sensor developed by Stickler, which changes from a yellow (pH 6) to blue (pH 8) color in response to the pH of the urine being elevated by the presence of *Proteus* bacteria.[10]

Received: October 24, 2016
Published: December 7, 2016

DOI: 10.1021/jacs.6b11077
J. Am. Chem. Soc. 2017, 139, 381−388

ChemComm

COMMUNICATION

View Article Online
View Journal | View Issue

Cite this: *Chem. Commun.*, 2015, 51, 16565

Received 17th June 2015,
Accepted 22nd September 2015

DOI: 10.1039/c5cc05009j

www.rsc.org/chemcomm

Lanthanide luminescent logic gate mimics in soft matter: [H^+] and [F^-] dual-input device in a polymer gel with potential for selective component release†

Samuel J. Bradberry,*[a] Joseph P. Byrne,[a] Colin P. McCoy[b] and Thorfinnur Gunnlaugsson*[a]

The non-covalent incorporation of responsive luminescent lanthanide, Ln(III), complexes with orthogonal outputs from Eu(III) and Tb(III) in a gel matrix allows for *in situ* logic operation with colorimetric outputs. Herein, we report an exemplar system with two inputs ([H^+] and [F^-]) within a p(HEMA-*co*-MMA) polymer organogel acting as a dual-responsive device and identify future potential for such systems.

Molecular-based logic and computation has been developing since the first reports of the principles of storing logical states at the molecular level in 1988.[1] While representing a fundamentally young field of chemistry, a vast array of molecular systems have been reported to date either through single molecule[2] or supramolecular[3] paradigms. The parallel advances in receptor molecules for various ionic and molecular species, alongside probe species for chemical environment, have allowed for the construction of logic gates within solution- and solid-based chemical systems.[4] Logic systems of binary nature are most common, with "0" and "1" states only, while the calibrated properties of many chemical sensors have extended this to higher order, multi-level, logic.[5] Complexes, probes and sensors based on 4f-metal complexes have received much attention[6] and are appealing for their narrow-band emission spectra which are well resolved in spectroscopy and result in characteristic colours to the naked eye.[7] A range of luminescent and responsive lanthanide complexes have been developed to date by our group and by others exhibiting switching behaviour[7,8] with various solution analytes. Use of Ln(III) ions in logic functions has limited precedence in the literature from our research[9] and others[10] for a number of circuit types. The resistance of Ln(III)-centred emission to wavelength shifts with environmental change, such as the switching of states, is ideally suited to digitisation of intensity at well-defined wavelengths for outputs from a logic gate. The *in situ* applications of luminescent sensors have been demonstrated in systems immobilised upon metal and mineral surfaces *via* various self-assembly techniques; inclusion within hybrid-materials has been demonstrated effectively by Binnemans.[11] Polymeric and soft materials also have promise, with increasing versatility of sensitive ionogel materials.[12] We are interested in using polymer cross-linked hydrogel materials as intrinsic chemical devices.[13] Thus herein, we report the design and construction of a logic system with inputs of [H^+] and [F^-] through combination of two responsive emissive complexes of Eu(III) and Tb(III) with red and green emission, respectively.

Ligands that sensitise Eu(III) and Tb(III) emission were derived from scaffolds of dipicolinic acid (**dpa**), **1**, and **btp**,[14] **2**, respectively. The self-assembly of mono-nuclear complexes of ligands of these types have been studied previously in our laboratory.[15] Both ligands, shown in Fig. 1, were synthesised through optimised procedures in short, facile syntheses (Fig. S1–S4, ESI†). Ligands **1** and **2** were then coordinated with $Eu(OTf)_3$ and $Tb(OTf)_3$, respectively, to produce complexes **Eu.1$_3$** and **Tb.2$_3$** that were emissive under excitation at λ_{ex} = 291 nm. These complexes were obtained by reaction of respective ligands and Ln(III) triflates in 3 : 1 ratio in CH_3OH under microwave-assisted heating. The resultant complexes were directly precipitated from diethyl ether and characterised as having 1 : 3 stoichiometry from emission lifetimes.[16]

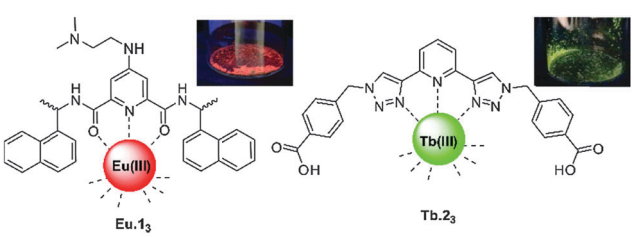

Eu.1$_3$ Tb.2$_3$

Fig. 1 Structures of ligand **1** and **2** and complexes with **Eu.1$_3$** and **Tb.2$_3$**. Inset: The emission arising from solid complexes irradiated under λ = 254 nm.

[a] *School of Chemistry and Trinity Biomedical Sciences Institute (TBSI), Trinity College Dublin, 152 – 160 Pearse Street, Dublin 2, Ireland. E-mail: gunnlaut@tcd.ie, bradbers@tcd.ie*

[b] *School of Pharmacy, Queen's University Belfast, Belfast, BT9 7BL, UK*

† Electronic supplementary information (ESI) available: Synthetic details, characterisation, additional spectroscopic data and animated figure. See DOI: 10.1039/c5cc05009j